Title
Multiphase Flow Vertical Aerated Column with Superhydrophobic Internals using X-ray Computed Tomography and Wire Mesh Sensors

Author
Rodriguez, Angel Francisco

Publication Date
2022

Peer reviewed|Thesis/dissertation

Multiphase Flow Vertical Aerated Column with Superhydrophobic Internals using X-ray Computed Tomography and Wire Mesh Sensors

By

Angel Francisco Rodriguez

A dissertation submitted in partial satisfaction of the

requirements for the degree of

Doctor of Philosophy

in

Engineering - Mechanical Engineering

in the

Graduate Division

of the

University of California, Berkeley

Committee in charge:

Professor Simo A. Mäkiharju, Chair
Professor Omer Savas
Professor Evan Variano

Spring 2022

Multiphase Flow Vertical Aerated Column with Superhydrophobic Internals using X-Ray Computed Tomography and Wire Mesh Sensors

Angel Francisco Rodriguez

Abstract

Multiphase Flow Vertical Aerated Column with Superhydrophobic Internals using X-Ray Computed Tomography and Wire Mesh Sensors

by

Angel Francisco Rodriguez

in Mechanical Engineering

University of California, Berkeley

Assistant Professor Simo A. Mäkiharju , Chair

This thesis addresses the influence of superhydrophobic material on bubble dynamics within a bubble column and simulated nuclear fuel cell channels through the use of X-ray Computed Tomography and iterative reconstruction algorithms. Pressurized water reactors operate in a single-phase flow. Localized nucleation sites arise to promote convectional heat transfer to the bulk liquid. During an event of flow loss or any condition that can result in bulk liquid temperatures exceeding saturation temperatures, bubbles will form more frequently, creating a boiling casualty called Departure from Nucleate Boiling. A Departure from Nucleate Boiling condition results from the bulk liquid temperature reaching and exceeding Critical Heat Flux. If a superhydrophobic-coated material is introduced into a fuel cell assembly, the vapor bubbles will show an affinity to the air layer in these coatings and therefore escape faster from the flow regime, resulting in a larger margin to reach Critical Heat Flux. This evaluation is made based on our findings using only an air and liquid mixture with similar characterization to vapor bubbles that would be found in a saturated system. Additionally, bubble column reactors rely on bubbly flow to promote mixing to meet chemical requirements for their applications. Superhydrophobic internals may modify the bubble regime to promote larger mixing with minimal changes in superficial gas velocity. The bubble dynamics that arise from dispersed bubble flow to slug flow can be measured by its void fraction. A superhydrophobic surface will enable bubbles to escape faster to the surface and therefore result in a void fraction value that remains lower as compared to void fraction conditions without superhydrophobic coated internals. With higher multiphase flow rates, these techniques become complex and difficult to measure. Advanced measurement techniques are required to measure void fraction in these partially opaque systems. Our findings suggests that lower void fractions are achievable with a modification of surface wall characteristics to promote superhydrophobicity. Additionally, superhydrophobic coatings do promote a transition to churn-turbulent flow without any modification to superficial gas velocity or bubble column dimensions. We show how geometric constraints, varied by adjusting the rod configuration,

also play a role in localized gas holdup but not as substantial as replacing a single fuel rod with a superhydrophobic-coated rod. Lastly, advanced measurement techniques, such as X-ray computed tomography, have proven effective at providing a non-intrusive and spatial and temporal resolution of void fraction measurements in dynamic multiphase flow systems.

To Jacqueline, my love and soulmate, and to Angel, Jaime and Gabriella, my biggest accomplishments

Thank you for putting up with my long hours of research and studying, always having a project and so many missed vacation opportunities. This year apart from you has been very challenging, but I know soon we will be together again. Military family members make huge sacrifices to move around with their servicemember. I know through these 22 years of service, it has been difficult on our family as I have uprooted you from your schools, friends and careers to a new location. I have the utmost love for you and words cannot express how grateful I am for your love, understanding, sacrifice and true friendship.

To Simo Mäkiharju,

Thank you for taking a chance on me. After so many years removed from academia and having spent these four years attending college with students that are the same age as my oldest son, I felt a substantial amount of stress but relieved that I had an advisor and now friend that was willing to not only advise but teach me. I am forever grateful for your support through the years. Your patience with me as a fellow family man, timeliness at offering assistance well into the late hours and technical expertise are unmatched and I wish you the utmost success in your life endeavors.

Contents

List of Figures

List of Tables

Acknowledgments

This accomplishment would not have been possible without the support of my wife, my three children, my research advisor, and my labmates in the FLOW lab. Their continued support, patience and technical expertise were pivotal in completion of this thesis.

Chapter 1

Review of Previous Experimental Measurements of Bubble Dynamics

We will briefly review previous studies in bubble dynamics. There are several areas of interests involved within bubble dynamics that make each experiment unique. Bubble size, bubble interaction in still versus flowing fluid medium, and proximity to the wall are a few of the factors which separate the point of interest in these previous experiments. An accurate measurement of flow rates of both phases of gas-liquid pipe flows is essential in several industries and applications [39] (Shaban, 2015). In petroleum industry applications, gas-liquid flow is encountered during different stages of extraction and transport. In nuclear reactor safety analysis, which is one of our focus areas, water-steam flows are encountered in fuel channels during accident scenarios. Accurate measurements are important to ensure our prediction of liquid flow rate under certain conditions are providing adequate cooling for fuel rods [39] (Shaban, 2015). One of the methods utilized in Multiphase Flow regime measurements is differential pressure measurement in bare tubes or fuel cell arrays. This method looks at differential pressures in bare tubes. One of the downfalls of this method is the time response for the differential pressure sensing assembly. This method has been used in correlation with conductivity wire mesh sensor (WMS).

1.1 Wire Mesh Sensor Void Fraction Measurements

The WMS was first introduced by Prasser et al [29] (Prasser, 1998). The WMS consists of two perpendicular arrays of electrodes that form a grid of conductivity-sensing nodes, which allows the measurement of gas-liquid phase distribution in a cross-section of the flow. This assumes the liquid has a much higher electrical conductivity than the gas. We will be using the WMS to measure void fraction and observe bubble size distribution. Shaban et al research's objective was to develop a multiphase flow model that can estimate the gas and liquid flow rates in a air-water mixture, based solely on WMS signals [39] (Shaban, 2015).

Shaban et al's experiment setup, displayed in Figure 1.1, consisted of a 32.5mm inner

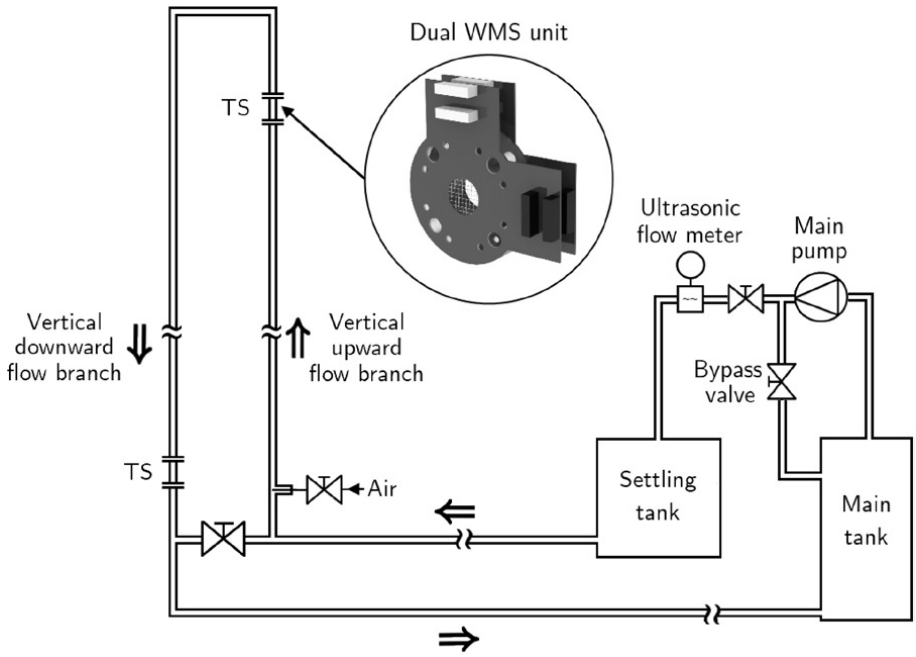

Figure 1.1: Schematic diagram of the air-water flow loop [39] (Shaban, 2015)

diameter clear polyvinyl chloride (PVC) tubing with filtered tap water that was pumped into the tubing. The air was injected through a porous stainless steel injector (100μm pore size). The WMS consisted of two mutually perpendicular arrays of eight parallel wires separated by 2mm. The device measured the instantaneous connectivity of the flowing mixture within the nodes. The flow regime of the air was adjusted to produce bubbly, slug, churn or annular flow regime. Measurements were taken using 1000 cross-sectional frames/second (fps), which were efficient to achieve convergence of the statistical properties of area-averaged void fraction in the ranges of flow rates. Figure 1.2 shows examples of relative frequency of area-averaged void fraction obtained using WMS in different flow regimes. The figure shows how the appearance of relative frequencies change with different flow regimes. In a single phase water flow, there is a sharp peak at $\alpha_k = 0$. In single phase air flow, there is a sharp peak at $\alpha_k = 1$. For bubbly flow, slug flow, churn flow, and annular flow, the void fraction varies as expected [39] (Shaban, 2015). The cross-correlation method used with two WMS proved more accurate than the machine learning algorithms proposed by Shaban.

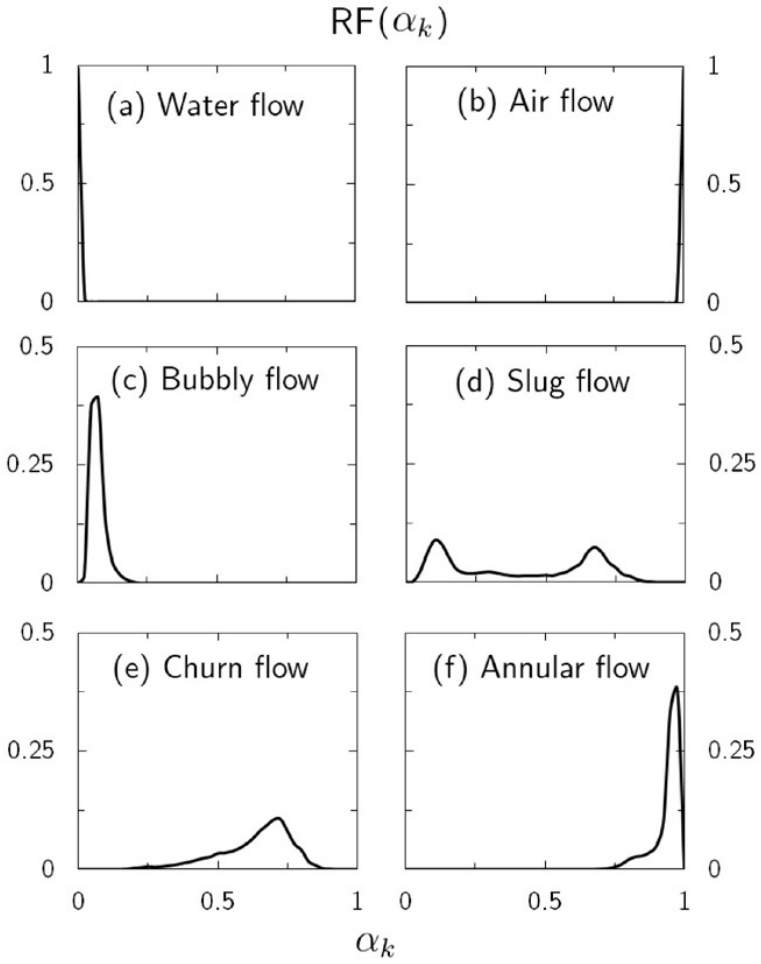

Figure 1.2: Relative frequencies of area-averaged void fraction in different flow regimes. [39] (Shaban, 2015)

1.2 Electrical Capacitance Tomograhy

Shafquet et al's experimental study of bubbly flow was conducted by producing two-phase bubble flow regime in a vertical online Electrical Capacitance Tomography (ECT) column. The study measured the values of raw capacitance and voltages of air and water flow. ECT provides quantitative measures of flow which is used for image and flow information. Void fraction is an important physical structure to determine other essential parameters, such as two-phase density, viscosity, and flow pattern transitions. ECT technology is based on measuring the changes in capacitance that are caused by the change in dielectric material distribution. ECT system consist of three main units: a sensor, data acquisition unit and an image reconstruction computer. A ring of 12 electrodes are mounted on the outer periphery of the sensor. The sensor includes measuring the capacitance between all possible combination pairs of electrodes and converting the measured capacitance value into the voltage signals. Figure 1.3. displays a schematic diagram of the vertical co-current two-phase flow experimental loop. The 12 electrodes are connected to a data acquisition unit which measures the inter-electrode capacitance and is dependent on the cross-sectional permitivity distribution inside the pipe.

Figure 1.4 shows the tomographic images corresponding to their flow patterns. The images were constructed using the back-projection reconstruction algorithm. This reconstruction provides qualitative results vice quantitative. The color scale of the reconstruction images displays the permitivity between 0 and 1, where 0 is low permitivity and 1 is the high permitivity.

Void fraction/gas holdup is calculated as a fraction that is occupied by the gas phase in the total volume of a two-phase mixture in the bubble column. Shafquet used the following equation to measure the void fraction via pressure difference measurements:

$$\epsilon = 1 - \frac{1}{\rho_l g}\frac{\delta p}{\delta z} \tag{1.1}$$

where ϵ is the local void fraction, ρ_l is liquid density, g is acceleration due to gravity, $\Delta p = p_1 – p_2$ are the pressures at location z_1 and z_2 with a Δz = 0.47m for Shafquet's experiment. Table 1.1 displays Shafquet's void fraction measurements using differential pressure. The superficial velocity was varied to evaluate the ECT measurements[41].

$U_l/U_g(m/sec)$		0.013	0.017	0.021	0.026	0.03
0.0085	ϵ	0.2	0.262	0.27	0.279	0.31
0.017	ϵ	0.214	0.23	0.262	0.273	0.292
0.026	ϵ	0.198	0.193	0.219	0.228	0.237
0.034	ϵ	0.179	0.176	0.187	0.2	0.208

Table 1.1: Void Fraction Measurement [41] (Shafquet, 2010)

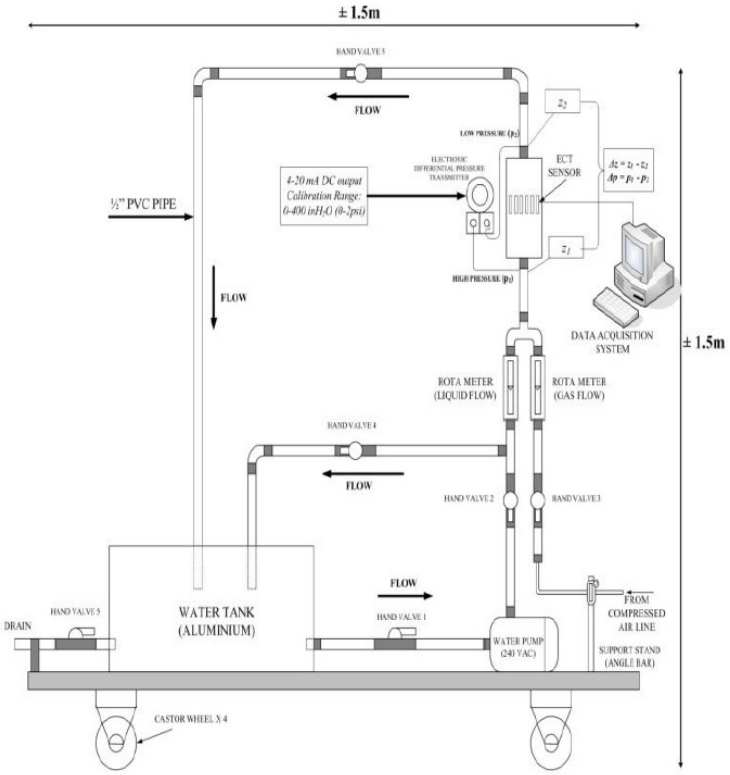

Figure 1.3: Schematic of test-rig for air-water flow [41] (Shafquet, 2010)

1.3 Ultra-Fast X-ray Compyted Tomography

Another method of calculating void fraction that provides an accurate assessment of bubble dynamics is ultra-fast X-ray Computed Tomography (CT). Along with WMS, X-ray CT can acquire instantaneous void fraction distributions over the entire measuring cross section with a time resolution in the order of milliseconds. X-ray tomography is not as intrusive as the WMS. Both methods are counterpart based on the accuracy and resolution of both techniques. Prasser, Misawa and Tiseanu compare measurements between X-ray CT and WMS using a 42mm inner diameter vertical pipe filled with an air-water mixture [30]. Traditionally, X-ray CT is based on the acquisition of several projections using the attenuation of the radiation. The X-ray source is rotated around the object. However, for ultra-fast CT used by Prasser, Misawa and Tiseanu [30], Schafer[35] and Yoon[48] nothing is physically moved, rather an electron beam is deflected changing source location as place where beam meets target material changes. The intensity from the source is measured by the detector on the other side, rotated with the detector. Understanding the projection distribution and material absorption properties, one can utilize tomographic reconstruction techniques

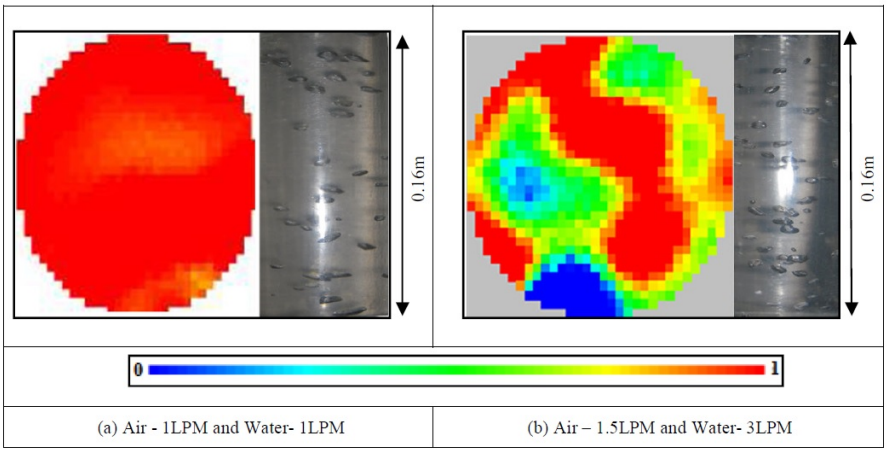

Figure 1.4: Tomographic ECT images and flow patterns [41] (Shafquet, 2010)

to reconstruct the flow regime. Cone beam tomography is a 3D visualization technique that allows collection of multi-slice data in a vertical direction within the same scanning time as 2D systems. One of the limitations with X-ray CT is the frame rate limitations due to mechanical rotation of the X-ray source around the object. In order to improve efficiency against this disadvantage, time-resolved X-ray CT scanners have been developed. With regards to frame rates, Prasser et al discusses two different devices in his research utilized to capture bubble dynamics. The first device captures a complete set of projection within 5ms. This is designed to determine the time needed to acquire a single frame. The second device has a framing time of 3.8ms and was utilized in Prasser et al's experiment with modifications for improved X-ray generators and detectors. Based off numerical calculations, the experiment required 18 X-ray sources placed along a circle of radius 120.5mm from the center of the measurement region. Figure 1.5 , displays the design of the ultra-fast X-ray computer tomography.

The X-ray source produced an electric field of 40-160kV which hit a Tungsten target. The X-ray generates a fan beam that spreads over an angle of 24 degrees. The radiation penetrating the object is detected by a ring of 256 CdTe detectors, arranged with an axial offset of 10-20mm for the X-ray plane. A sensitive detector was required in order to achieve a fast scanning capability. The radiation of each source reaches a sector of 60 pixels located opposite to the X-ray source. The image reconstruction is based on a filtered back-projection. The filtered back-projection method is used for a 2D reconstruction in a 101 x 101 pixel format over a 50mm area of interest. Prasser utilized a sensor with 16 receiver and 16 transmitter wires of 120 μm diameter, sampled with a frequency of 1053 Hz.

Figure 1.6 displays the test section location of the X-ray source and the wire mesh sensors. Since the fast X-ray CT system is non-invasive, it was 15mm upstream of the WMS. The

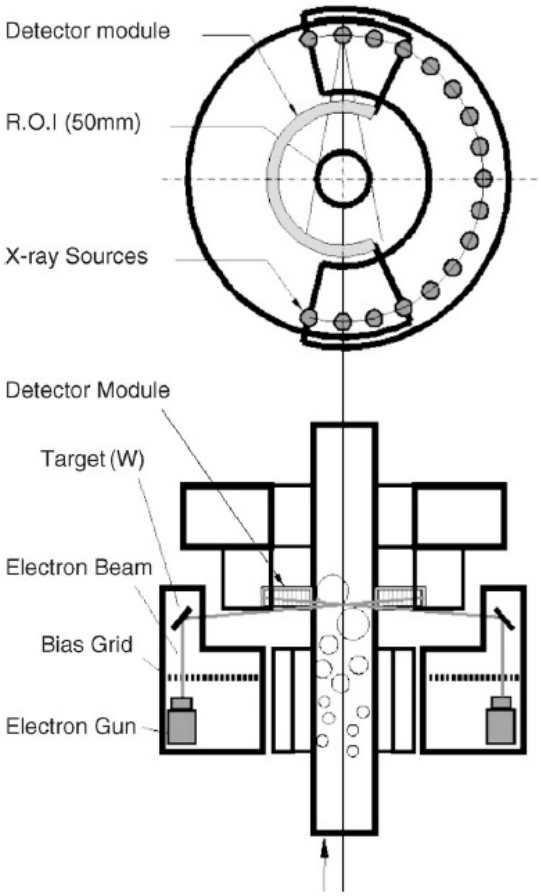

Figure 1.5: Design of the ultra-fast X-ray computer tomography [30] (Prasser, 2005)

starting trigger was shared by both systems and data was recorded for 4.0s.

Figure 1.7 shows an example of a comparison between instantaneous void fraction distributions measured by X-ray tomography with those obtained from the WMS. In the example, every seventh frame produced by the X-ray source is compared to every 28th frame of the WMS.

The instantaneous distribution are in good agreement besides a time delay caused by the time distance of 15mm between the two measuring sensors. The X-ray tomography displays show a slight shift towards the right lower corner of the region of interest. This was caused by difficulties in centering the sensor within the measuring plane of the scanner detector.

Figure 1.8 displays the instantaneous values of the void fraction averaged over the projection chord from the source and are plotted against time which are receiving radiation that

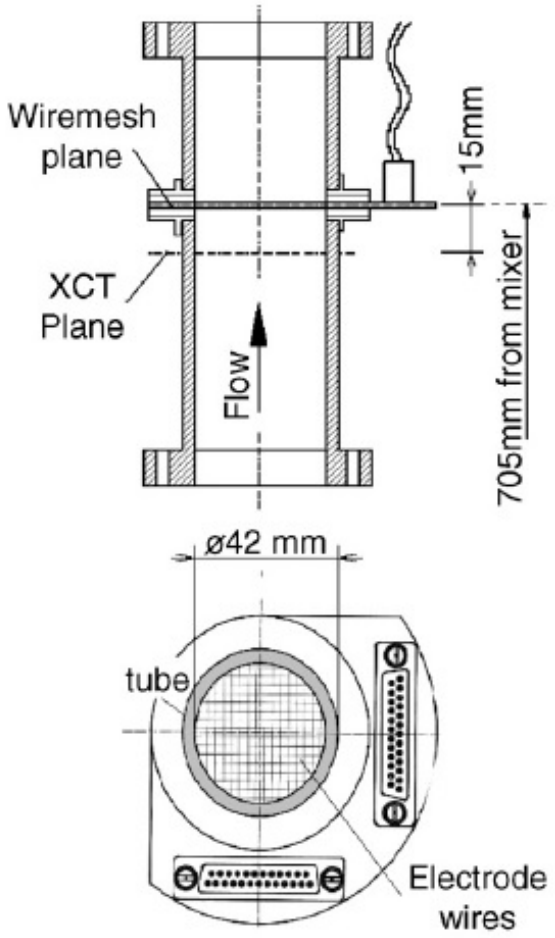

Figure 1.6: Part of Test Section with Wire-Mesh Sensor and the location of the X-ray CT [30] (Prasser, 2005)

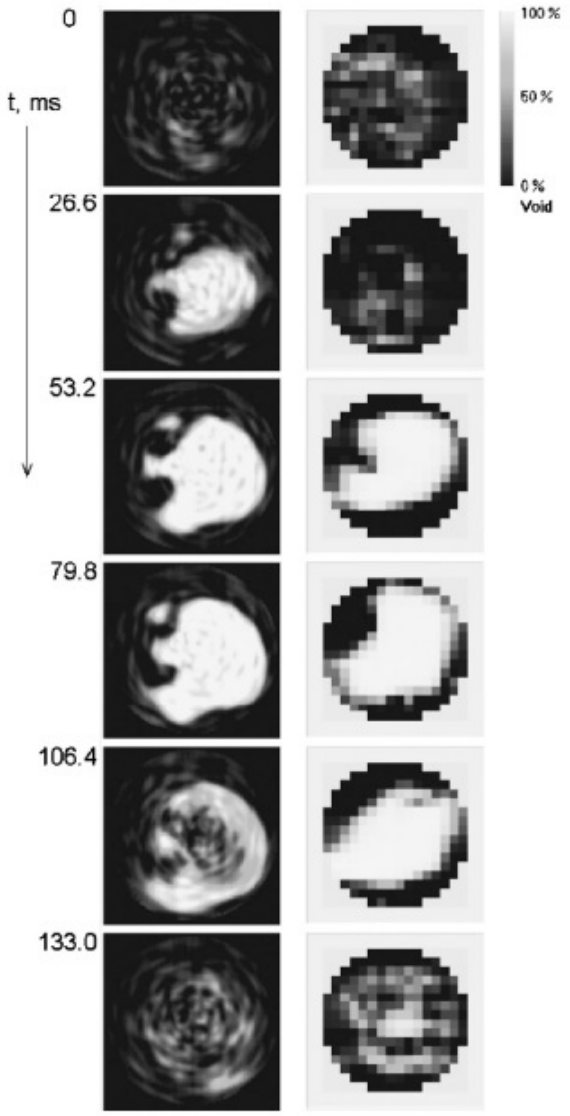

Figure 1.7: Time series of selected void fraction distributions during the passage of a gas plug in the test with $J_{water} = 0.24$m/s and $J_{air} = 0.30$m/s. Left: X-ray scanner, Right: wire mesh sensor [30] (Prasser, 2005)

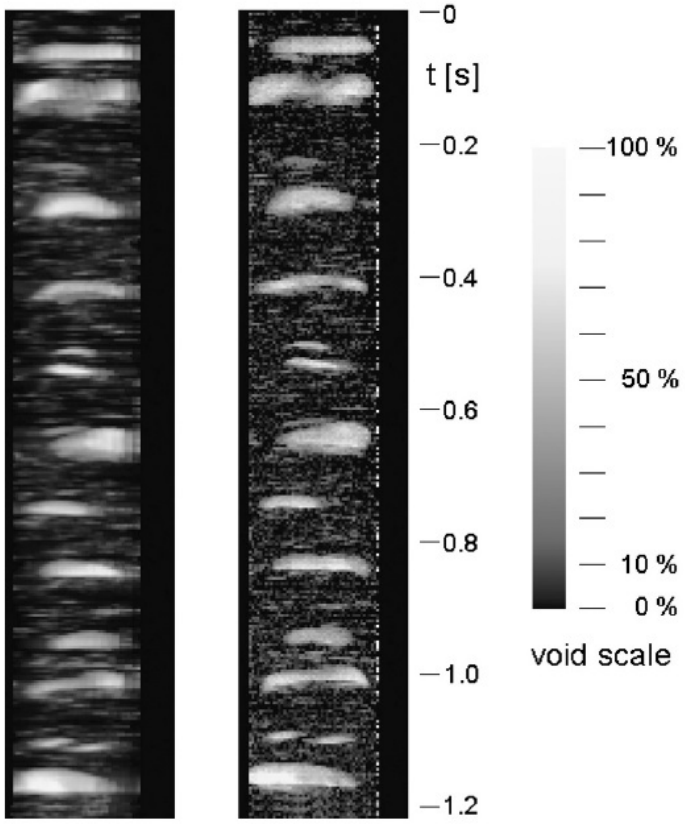

Figure 1.8: Void fraction averaged along the projection lines between source and detector as a function of time. Left: numerically projected wire mesh sensor data; Right: measured by X-ray scanner; parameters: $J_{air} = 0.15$ m/s, $J_{water} = 0.24$ m/s, gas injection A (4 orifices, D=5mm). [30]

are passed the measuring cross section (right column). The wire mesh sensor tends to underestimate the gas fraction due to the formation of liquid films in the wake of the electrode wires. The problems found with the X-ray results of small bubbles dealt with reconstruction difficulties. Void fraction measurements averaged without using a reconstruction algorithm yielded better results. Improvements in this area were accomplished by reducing the quantum noise rather than the electrical noise. The study found that in order to collect more photons for better resolution, the detector pixel should be enlarged or the number of photons increased [29] (Prasser, 2005).

Chapter 2

Pressurized Water Reactor Vapor Bubble Dynamics and Heat Transfer

2.1 Pressurized Water Reactors

Pressurized Water Reactors (PWR) operate in an indirect cycle where the primary coolant is heated and pressurized in the reactor core and cooled through the steam generator where a secondary system recirculates through the steam generator transferring heat from the primary coolant. The recirculated pressurized water is pumped back into the reactor core vessel using reactor coolant pumps. The steam generated in the secondary loop is fed towards a turbine which drives an electrical generator. The coolant acts as a neutron moderator and is usually pressurized to about 15.5 MPa in the pressurizer and forced to recirculate to cool the core with a single-phase flow with minimal occurrence of boiling. The density variation in the core is small as a result of the single-phase flow.

2.2 Reactor Safety Analysis

In the analysis of safe reactor operations, we investigate many conceivable failures in order to design a reactive protective and mitigation system to prevent accidents, with the ultimate goal of preventing release of fission products in the event of an accident. This leads to careful evaluation of neutron dynamics, fuel rod and vessel designs, and reactivity worth caused by changes in temperature, density, and pressure within a closed loop system.

The integrity of the fuel elements, pressure vessel and containment structure is intended to prevent the release of radionuclides. This leads to further design of reactor components that prevent pressure, thermal and transient stresses that can lead to a fracture of a component in such away that affects the integrity of the system, leading to radiological damage and health effects to the population caused by release of radionuclides. The majority of the casualty scenarios within the reactor core vessel, consistently rely on adequate flow of the moderator

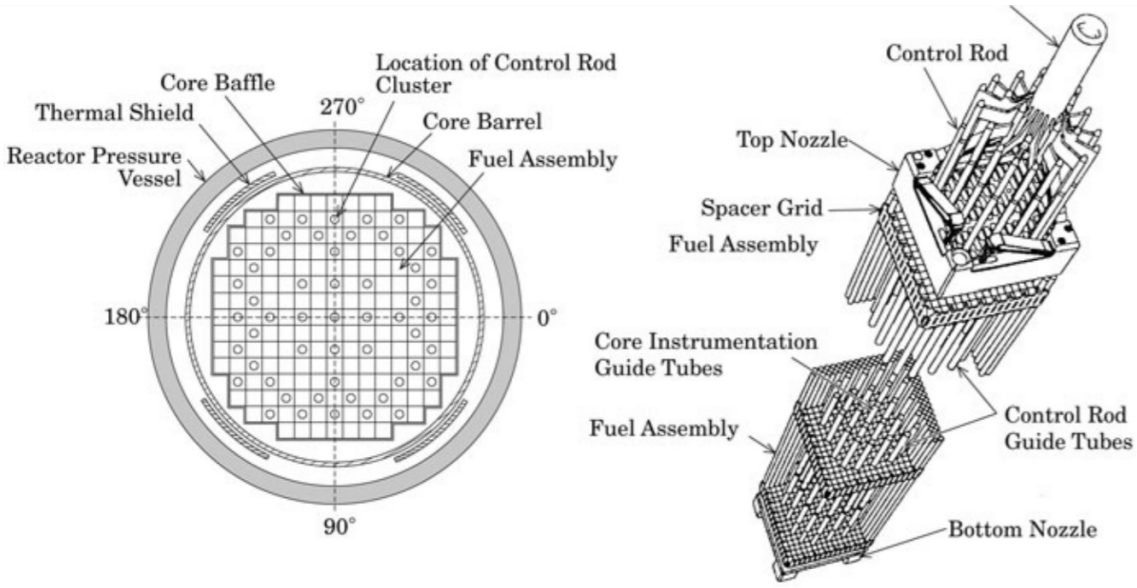

Figure 2.1: Cross-sectional view and fuel assembly of a PWR core [27] (Oka, 2014)

to slow down the neutrons and maintain forced or natural convection to remove heat from the fuel cells.

The accident scenarios we will evaluate are classified by initiating a boiling crisis event caused by the loss of flow or loss of coolant inside the fuel channels.

Loss of Flow or Loss of Coolant

Our study will deal primarily with a loss-of-flow accident (LOFAs), which results in increased temperature and reduced density of the coolant. A loss-of-coolant accident (LOCA) may be caused by a rupture of a primary coolant line, failure of primary coolant pump seal, inadvertent opening of a pressure relief or safety valve, which would result in increased temperature and decreased density of the coolant and possibly uncovering of the reactor core.

Loss of a Heat Sink

A Loss of Heat Sink accident (LOHA) occurs as a result of a significant decrease of steam flow in the secondary system due to a turbine trip or reduction or a loss of feed water in the secondary system. This accident will result in a reduction or elimination of heat removal

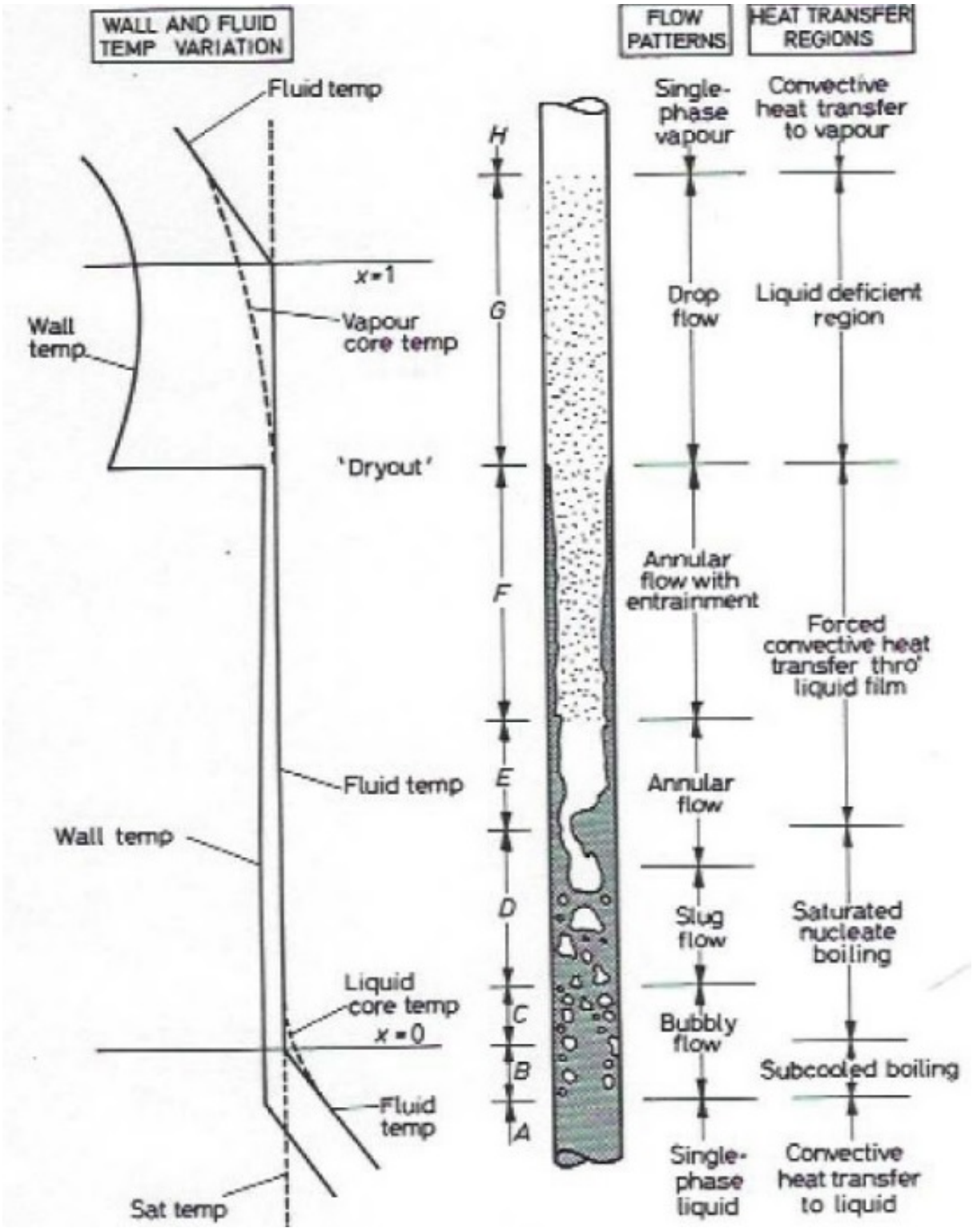

Figure 2.2: Flow Boiling Regime (Almenas and Lee, 2013)

from the primary coolant system, causing the primary coolant temperature to increase and the density to decrease.

In both cases, a negative temperature coefficient of Pressure Water Reactors and Boiling Water Reactors, provides an immediate power reduction, which is important for avoiding such accidents.

2.3 Pool Boiling Regimes

The impetus of the study involves an understanding of boiling in vertical channels and how that affects heat transfer properties and margin to reaching critical temperature constraints along the surface walls. Boiling heat transfer occurs when the temperature of the solid surface is sufficiently higher than the saturation temperature of the liquid that comes into contact with the surface walls. The solid-liquid interface heat transfer is accomplished by the transformation of heat generated from vapor bubbles, jets and films. The vapor bubbles are carried away by both buoyancy forces and the force flow of the liquid that is sweeping through the vertical channel.

To explain the process of boiling and different stages of boiling, we will start with a configuration description of heat transfer structures utilized. We will refer to a heat surface as T_w, which is immersed in a pool of initially stagnant liquid, referred to as T_l. The engineering complexity for heat transfer is comprised of understanding the relationship between surface heat flux, q'_w, and temperature differences (T_w - T_{sat}) where T_{sat} is the saturation temperature of the liquid. This function and the stages leading to a boiling crisis is depicted in Figure 2.2.

The vapor bubbles collapse (recondense) as they rise through a subcooled liquid. The generated vapor bubbles will migrate to the free surface of the channel when the temperature at the heater surface reaches saturation temperatures. It follows that the liquid in the pool is all saturated ($T_l = T_{sat}$).

Figure 2.3 shows a a particular curve that corresponds to the pool boiling of water at atmosphere pressure. The relationship between heat flux and excess temperatures is due to various forms of bubbles that start from the newly generated vapor that occurs in vicinity of the heater surface. The shape of the curve shows different pool boiling regimes. Region I is an area where there is very low excess temperatures (in water, at T_w - $T_{sat} < 5°$) and heat transfer occurs without appearance of bubbles on the heat surface. In this region, the surface becomes superheated and the vapor bubbles rise in the form of natural convection currents to the free surface of the pool. Region II is the area of nucleate boiling , which is characterized by the generation of vapor bubbles. At the low end of the nucleate boiling regions, the bubbles are isolated. At higher temperature, the frequency of the bubbles increase, the nucleation sites multiply and the bubbles start to interact with each other and form slugs and vapor columns.

The nucleate boiling area heat flux has a lowering slope caused by the formation of more and more vapors in vicinity of the surface. This starts to insulate the surface against the

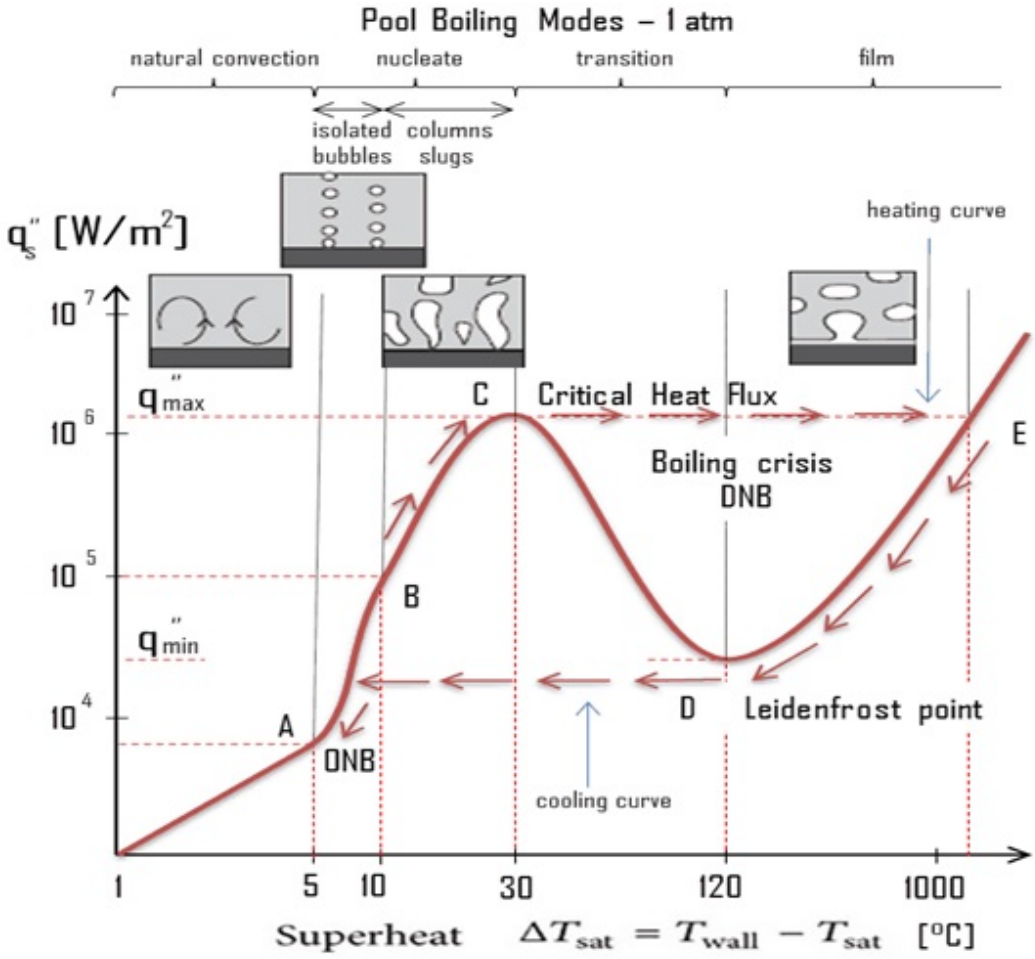

Figure 2.3: Regimes of pool boiling in water at atmospheric pressure (www.nuclear-power.net)

T_{sat}-cold liquid. At this point the nucleate boiling heat flux reaches a maximum heat flux, referred to as the Critical Heat Flux (CHF), which corresponds with an excess temperature value of 30°C [4].

The next regime defines a transition area where the heat flux decrease as the excess temperature (T_w - T_{sat}) increases. The explanation for the increased heat flux results from greater portions of the heater surface becoming more coated with a continuous film of vapor. As the vapor becomes unstable, it is intermittently replaced by nucleate boiling periods. This region is referred to as the transition boiling phase. This region expires when the heat flux reached its minimum value (q''_{min}). At this value of heat flux, the temperature is high enough to maintain a stable vapor film on the heater surface. This region occurs at an excess temperature in the range of 100-200°C.

The last region is comprised of a vapor film covering the entire surface and the heat flux resume its increase with (T_w - T_{sat}). At this point, radiation heat transfer dominates the heat transfer across the film and plays a larger role as excess temperatures increase. The high-temperature phase is referred to as the film boiling regime, which persist until T_w reaches a melting point of the surface material. Temperatures that reach this regime in nuclear reactor hot channels can cause possible breech of the fuel cladding, causing release of fission products into the coolant.

The nucleate boiling regime is the most important for our studies and where the most attention is placed to avoid reaching the level of film boiling. Within the nucleate boiling region, the heat transfer coefficient,

$$h = \frac{q''_w}{T_w - T_{sat}} \tag{2.1}$$

reached large values. One of the most popular equations of heat transfer was proposed by Roshenow:

$$T_w - T_{sat} = \frac{h_{fg}}{C_{P,l}} Pr_l^s C_{sf} \left[\frac{q''_w}{\mu_l h_{fg}} \left(\frac{\sigma}{g(\rho_l - \rho_v)} \right)^{\frac{1}{2}} \right]^{\frac{1}{3}} \tag{2.2}$$

This equation applies to clean surfaces and is insensitive to the shape and orientation of the surface. The subscripts l and v denote saturated liquid and saturated vapor. The dimensionless number C_{sf} accounts for the particular combination of liquid and surface material and the Prandtl number exponent s differentiates only between water and other liquids (Bejan, 2004)[4].

The surface tension is an important parameter in the life cycle of a vapor bubble. In equilibrium, the radius of a spherical vapor bubble is $\frac{2\sigma}{(P_v - P_l)}$ where P_l and P_v are the pressures inside and outside the bubble. We will discuss the comparison between vapor bubbles and gas bubbles to explain why our research can use gas bubbles to evaluate superhydrophobic surfaces on a simulated 2x2 array fuel channel.

2.4 Comparison of vapor bubbles and gas bubbles

The evolution of vapor bubbles is highly affected by liquid inertia and heat transfer between the bubble and the surrounding liquid. The momentum and energy equations in the liquid are related to each other through the thermodynamic equilibrium at the bubble surface. At the onset of vapor bubbles, inertial effects drive bubble motion. At later stages, inertial forces are not as dominant as the heat flux provided by the liquid at the bubble surface. The understanding of hydrodynamic forces on vapor bubbles is important to understand their trajectory and our confidence in using gas bubbles to evaluate the bubbles interaction with the air layer on superhydrophobic surfaces (Legendre, 1998)[19].

Andrea Properetti's study of vapor bubbles discussed the differences between vapor bubbles and gas bubbles and found that both types rely mainly on the diffusion phenomena in the liquid. The thermal diffusivity, in comparison to mass diffusivity, has an effect on bubble dynamics, making the vapor bubble more susceptible to physical change as compared to gas bubbles (Prosperetti, 2017)[32].

The vapor bubbles that we aspire to simulate with gas bubbles in our research into fuel cell array bubble dynamics in the presence of superhydrophobic-coated surfaces, are developed from bubbles that nucleate in a superheated liquid due to vaporization of liquid molecules in the vicinity of a dry cavity on a heating. Initially, the formation of the bubble is governed by mechanical forces. heat transfer rates and diffusion rates at the interface. The bubble grows at a rate influenced by inertia and surface tension forces. A boiling bubble grows in a liquid at superheated temperatures. In this category of vapor bubble, as opposed to cavitation bubbles, the heat transfer rate at the interface controls the growth rate. The energy equation is required to understand bubble growth pass inertial forces. The diffusion equation is also required if the vapor bubble contains some portion of gas. As a boiling bubble starts to grow, the surface tension force reduces and the growth rate is accelerated. Within a short period, studies show that the pressure and temperature drop become the dominant forces upon detachment from the surface. The bubble will either grow or start collapsing based on whether the surrounding fluid is super-heated or sub-cooled (Prosperetti, 2017)[32].

The motion of the bubble surface can be approximated by the combination of the momentum equation and Rayleigh equation into the following equation (Sha, 1977)[38]:

$$R\ddot{R} + \frac{3}{2}\dot{R}^2 = \frac{1}{\rho}\left(P_v - P_\infty - \frac{2\sigma}{R}\right) \tag{2.3}$$

Since the vapor pressure depends on vapor temperature,the energy equation must also be considered in bubble growth rate:

$$\rho\left(\frac{de}{dt} + u_r\frac{de}{dr}\right) = -P\left(\frac{du_r}{dr} + \frac{2u_r}{r}\right) + \frac{4\mu}{3}\left(\frac{du_r}{dr} - \frac{u_r}{r}\right)^2 + k\left(\frac{d^2T}{dr^2} + \frac{2}{r}\frac{dT}{dr}\right) + \rho\dot{q}''' \tag{2.4}$$

where q''' is the heat source and e is the specific internal energy.

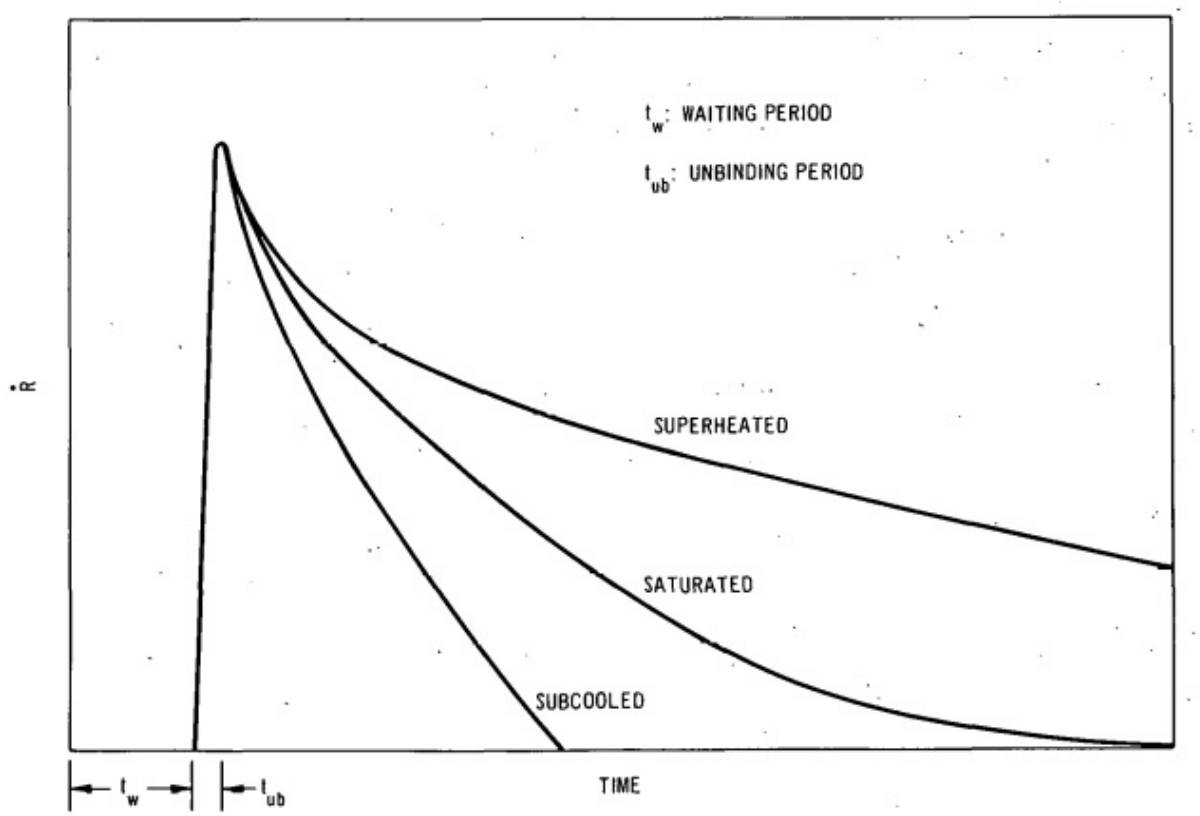

Figure 2.4: Variation of growth rate in Superheated, Saturated and Subcooled liquid regimes (Sha, 1977) [38]

The energy at the interface is governed by:

$$k\frac{dT}{dr} = \frac{L}{4\pi R^2}\frac{d}{dt}\left(\frac{4}{3}\pi R^3 \rho_v\right) \tag{2.5}$$

The description of this process is displayed on Figures 2.4 and 2.5. Similar to bubble growth in superheated liquid, our gas bubbles expand as they rise inside the bubble column under the forces of buoyancy.

Equation 2.3 is sufficient to predict bubble growth when inertial forces dominate. When the thermal effect becomes dominant, the energy equation, Equation 2.3, and the energy balance at the interface, Equation 2.4, dominate bubble growth and trajectory.

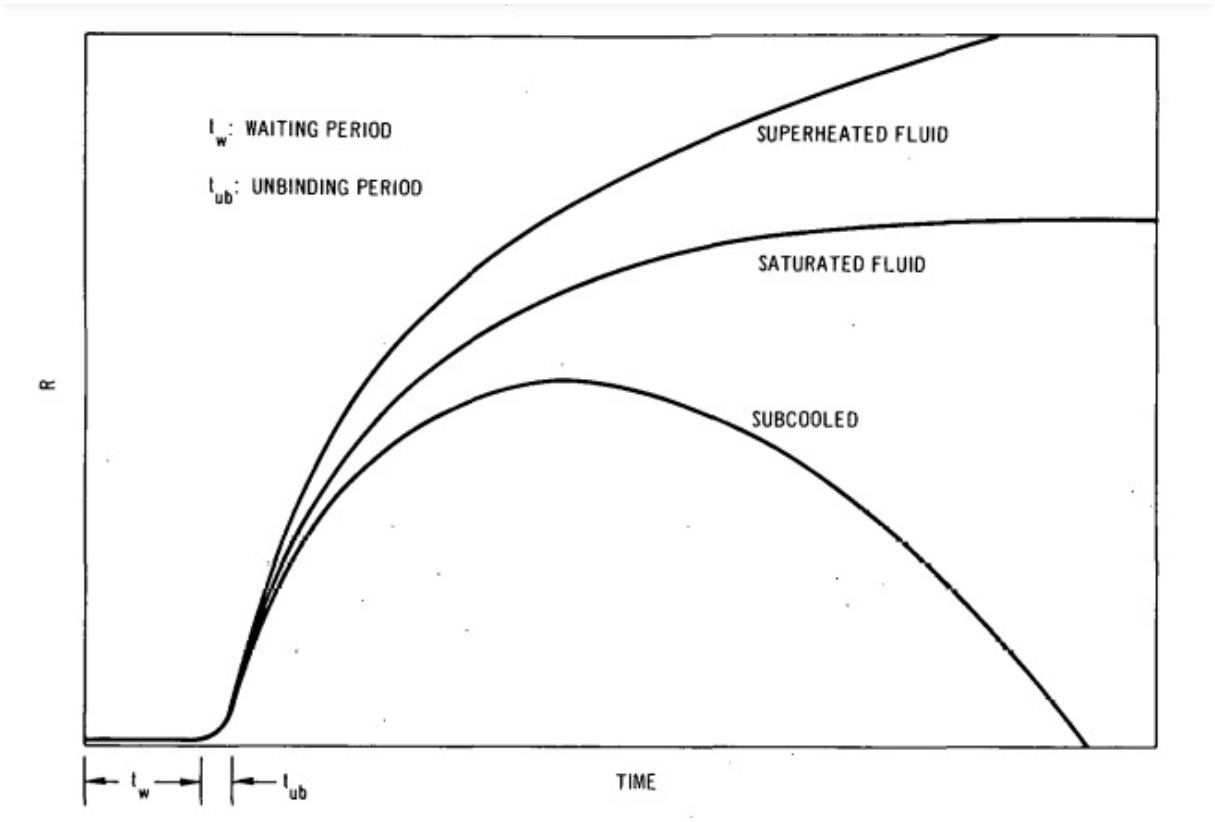

Figure 2.5: Variation of bubble radius in Superheated, Saturated and Subcooled liquid regimes (Sha, 1977)[38]

Chapter 3

Bubble Structural Dynamics

The phenomena of interest for our research is the presence of boundaries separating a given phase from an adjacent phase and evaluating how these adjacent phases interact with one another. Multiphase systems are systems that contain two or more phases. These systems are found in nature and engineering applications. Processes of distribution, rectification and cooperation are a few of the processes that govern multiphase flow systems.

Following the rubric of classic single phase hydrodynamics, a liquid or gas is considered a continuous medium. Therefore, any small volume element contains a large number of molecules. Furthermore, we deduce that any volume is much larger in comparison with inter-molecular distances. For homogeneous mixtures, where components are intermixed, methods of the mechanics of continuous medium provide the basis of theory for describing the laws of motion. Our discussion will deal with heterogeneous gas-liquid mixtures, which involve characteristics of macroscopic inhomogeneities.

In each macroscopic one phase region, the laws of continuum mechanics apply to explain inter-molecular interactions using fundamental laws of conservation of mass, momentum and energy. The boundaries between the individual regions are discontinuous. The interfacial surfaces experience jumps in density, internal energy, enthalpy and so on (Avdeev,2016)[3].

In a dispersed system, one phase forms a single connected area where the second one occupies numerous discrete regions. Bubble systems are an example of a dispersed system. The fundamental laws of conservation of mass, momentum and energy, are reflected within each macroscopic region.

3.1 Theory of Two-Phase System

We can look at a mathematical model of a two-phase systems, by utilizing the conventional equations of continuum mechanics for each single phase. Boundary conditions that reflect the laws of phase interaction must be satisfied on the interfacial surfaces.

Two phase mixture is represented as a set of unit cells. Although two phase mixtures can be stochastic, we will evaluate the processes in each cell to provide adequate level of

understanding. Since we work with bubble columns for our study, we will evaluate the ascending motion of bubbles. The bubbles are split into two groups: large bubbles rising with respect to liquid and small bubbles, transported by the liquid like a passive tracer.

When evaluating the different groups of bubbles, you have slug flow on one end and small single bubble flows on the other end of the spectrum. This approach is semi-empirical. The transition from a real two-phase system to a unit cell is subjective based on the investigator, so this is a drawback in bubble dynamics research.

Dynamics of Bubbles in Infinite Volume

Before discussing kinematics of column wall interactions, we will discuss bubbles in an infinite volume. In this particular situation, we are removing the forces introduced by heat and evaporation. The forces acting on a single bubble are governed by the relevant forces, pressure difference, inertia-forces, viscosity and surface tension forces.

We will look at the dynamic growth of a single bubble. Assume that at time $t = 0$, a spherical bubble of radius, R_o, filled with air originates in a still liquid. Pressure inside the spherical cavity is P_v, and P_l is the ambient liquid pressure. We assume a pressure difference of $\Delta P = P_v - P_l$ is constant in time. If the pressure inside the cavity is larger than the pressure in the liquid, the bubble protruding from the base will grow under the loading of the pressure difference. The rate of expansion will depend upon the pressure difference and the competing forces of the inertial forces in the liquid, surface tension forces, and viscosity effects. The surface tension forces are responsible for a pressure surge on the interfacial boundary. In small bubbles, the surface tension is enough to counteract the pressure difference, keeping the bubble growth impossible. The difference in growth is governed by the dynamic effects which prevail over thermal effects. For large growth times, the thermal effects/heat supply prevail over the interfacial boundary, resulting in a thermally controlled bubble growth model.

Bubble Growth and Collapse - The Rayleigh-Lamb Equation

If the $p_v < p_\infty$, the bubble radius decreases to the point that the bubble collapse. In the early stages of the process, while the current radius, R, of a collapsing bubble is still above $0.63R_o$, where R_o is the initial radius, the distribution of the pressure in the liquid is monotone in nature. Subsequently for $R < 0.63\ R_o$, the law of pressure variation in the liquid becomes monotone until the pressure achieves a maximum value. As the collapse process starts, the maximum value moves towards the bubble surface direction. Bubbles of these radius lose their spherical shape throughout the course of their trajectory. The farther a bubble is away from the wall, the more likely it is to retain its spherical shape. The maximum deformation for near-wall bubbles occurs right prior to their collapse due to liquid pressure differences at the wall (Avdeev,2016)[3].

Assume the pressure over the entire volume of the bubble is constant and equals p_v, and the pressure of the liquid is p_∞. If $p_v > p_\infty$, then the bubble will grow and will decrease if $p_v < p_\infty$. Figures 3.1 and 3.2 give a qualitative representation of bubble expansion and

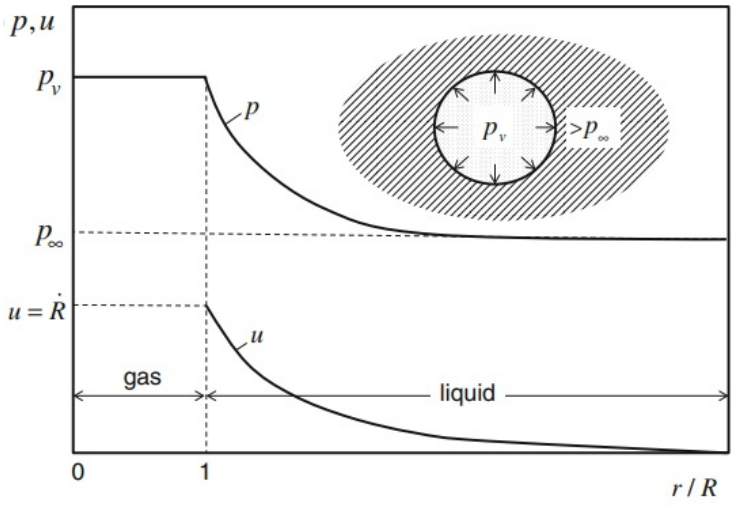

Figure 3.1: Bubble Growth Qualitative Representation (Avdeev,2016)[3]

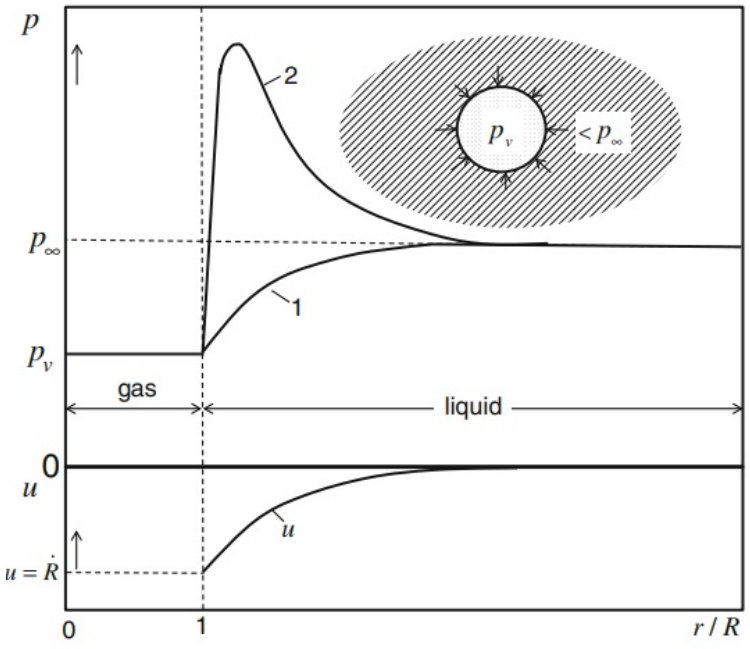

Figure 3.2: Bubble Collapse Qualitative Rendering (Avdeev,2016)[3]

collapse. The continuity equation for the liquid in the spherical polar system is as follows (Avdeev,2016)[3]:

$$\frac{1}{r^2}\frac{d}{dr}(r^2 u) = 0, \tag{3.1}$$

where u is the liquid velocity.

With respect to interfacial boundary, the velocity of the liquid on the bubble boundary, u_r, will equal the rate of change of its radius (Avdeev,2016)[3],

$$\dot{R} = \frac{dR}{dt} \tag{3.2}$$

The integral of Equaion 3.1 is the following:

$$r^2 u = R^2 u_r = R^2 \dot{R} = const = F(t) \tag{3.3}$$

where F(t) is a function of time.

We therefore have a field of radial velocity in the liquid (Avdeev,2016)[3]:

$$u = R^2 \frac{\dot{R}}{r^2} \tag{3.4}$$

The velocity of the liquid decays as $u \sim \frac{1}{r^2}$ as we move away from the bubble surface along a radial coordinate. The liquid at infinity from the bubble remains unperturbed (Avdeev,2016)[3].

The equation of conservation of momentum for a liquid is the Navier-Stokes equation in the spherical polar system:

$$\begin{aligned}\rho\left(\frac{du_r}{dt} + u_r\frac{du_r}{dr} + \frac{u_\phi}{rsin(\theta)}\frac{du_r}{d\phi} + \frac{u_\theta}{r}\frac{du_r}{d\theta} - \frac{u_\phi^2 + u_\theta^2}{r}\right) = \\ -\frac{dP}{dr} + \rho g_r + \mu\left[\frac{1}{r^2}\frac{d}{dr}\left(r^2\frac{du_r}{dr}\right) + \frac{1}{r^2 sin(\theta)^2}\frac{d^2 u_r}{d\phi^2}\right. \\ + \frac{1}{r^2 sin(\theta)}\frac{d}{d\theta}\left(sin(\theta)\frac{du_r}{d\theta}\right. \\ \left.\left. - 2\frac{u_r + \frac{du_\theta}{d\theta} + u_\theta cot(\theta)}{r} - \frac{2}{r^2 sin(\theta)}\frac{du_\phi}{d\phi}\right]\right.\end{aligned} \tag{3.5}$$

Based on the flow regime in a small confined liquid, only the radial velocity is considered and the terms from the Navier-Stokes equation that deal with axial and axisymmetric directions are eliminated (Avdeev,2016)[3].

$$\frac{-1}{\rho_l}\frac{dp}{dr} = \frac{du}{dt} + u\frac{du}{dr} - \upsilon_l\left[\frac{1}{r^2}\frac{d}{dr}(r^2\frac{du}{dr}) - \frac{2u}{r^2}\right] \tag{3.6}$$

where ρ_l and v_l are the density and kinematic viscosity coefficient of liquid.

When we substitute velocity, u, from Equation 3.4 into Equation 3.5, the following bubble dynamics equation is derived:

$$\frac{1}{r^2}(2R\dot{R}^2 + R^2\ddot{R}) - \frac{2}{r^2}R\dot{R}^2 = -\frac{1}{\rho_l}\frac{dp}{dr} \tag{3.7}$$

We will also look at a one-dimensional flow of viscous incompressible liquid (Avdeev,2016)[3]. The viscous term in the Navier-Stokes equation reads as:

$$W_0 = v_l\frac{d^2u}{dx^2} \tag{3.8}$$

for a plane flow.

For an axially symmetric flow in the cylindrical coordinate system, viscous term is represented as:

$$W_1 = v_l\left(\frac{d^2u}{dr^2} + \frac{1}{r}\frac{du}{dr} - \frac{u}{r^2}\right), \tag{3.9}$$

and for a spherically symmetric flow, the term is the following:

$$W_2 = v_l\left[\frac{1}{r^2}\frac{d}{dr}\left(r^2\frac{du}{dr}\right) - \frac{2u}{r^2}\right] \tag{3.10}$$

The effect of viscosity forces on the bubble dynamics is manifested in terms of the boundary conditions on the interfacial boundary (Avdeev,2016)[3].

Equation 3.6 is integrated from $r = R$ to $r = \infty$, we obtain the distribution of pressure in the liquid:

$$\frac{P(r) - P_\infty}{\rho_l} = \frac{2R\dot{R}^2 + R^2\ddot{R}}{r} - \frac{R^4\dot{R}^2}{2r^4} \tag{3.11}$$

where $\ddot{R} = \frac{d^2R}{dt^2}$

Equation 3.11 holds for volume of liquid upto the boundary of the bubble where r=R and $P = P_l$. The vapor pressure is constant and equals P_v.

On the interfacial boundary, the dynamic coupling condition is applied in conjunction with the relationship between P_v and P_l (Avdeev,2016)[3].

$$P_v - P_l = 4\frac{\mu_l\dot{R}}{R} + 2\frac{\sigma}{R} \tag{3.12}$$

where μ_l is the dynamic viscosity of the liquid and σ is the surface tension coefficient.

The right hand side of Equation 3.11 shows the viscous resistance of liquid on the spherical expansion (compression) of a bubble (Avdeev,2016)[3].

The value of 2σ is the Laplace jump of pressures due to the curvature of the interfacial boundary. Equation 3.11 is combined with Equation 3.12, to form the following relationship:

$$P_v - P_l = \frac{3}{2}\dot{R}^2 + R\ddot{R} + 4v_l\dot{R}R + 2\frac{\sigma}{\rho_l R} \tag{3.13}$$

Viscous effects are introduced in terms of the dynamic coupling condition on the interfacial boundary. The following boundary conditions are applied:

as $r \longrightarrow R(t) : P = P_v + \frac{2\sigma}{R(t)}$
as $r \longrightarrow \infty : P = P_\infty$
The initial condition applies as a pressure homogeneity condition across the entire space of the liquid:
for t = 0: $r = R_o$; $P = P_\infty$
In the absence of viscosity and surface tension ($v_l = \sigma = 0$), we can apply these to Equation 3.13:

$$\frac{P_v - P_\infty}{\rho_l} = \frac{3}{2}\dot{R}^2 + R\ddot{R} \tag{3.14}$$

Eq.(3.14) is referred to as the classical Rayleigh's equation. Eq.(3.13), with accountability for surface tension and viscosity, was obtained by Lamb in 1923 and will be referred to as the Rayleigh-Lamb equation (Avdeev,2016)[3].

The Rayleigh-Lamb equation assumes the interfacial boundary is impermeable, enabling the assumption that liquid velocity on the bubble surface is equal to the velocity of surface motion. The Rayleigh equation relates the variation of the bubble radius in time R(t) with the pressure drop, ΔP(t) (Avdeev,2016)[3].

3.2 Rayleigh - Plesset Equation Derivation

The derivation of the Rayleigh-Plesset equation starts with the implementation of a Navier-Stokes equation that is utilized to describe the dynamics of a single bubble under uniform conditions and in the absence of gravity (Brennen,2005) [5].

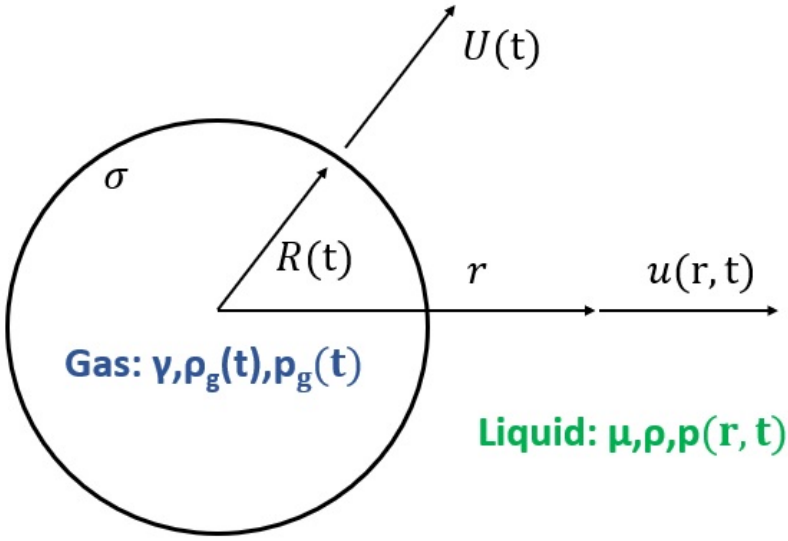

Figure 3.3: Dynamics of a gas bubble surrounded by a liquid with density and viscosity

The following assumptions are applied (Brennen,2005) [5]:

- absence of gravity
- conditions in the bubble are assumed uniform
- flow is incompressible
- flow is radial

Step 1: Apply the Spherical Continuity Equation

$$\frac{1}{r^2}\frac{d}{dr}(r^2 v_r) + \frac{1}{r sin\theta}\frac{d}{d\theta}(v_\theta sin\theta) + \frac{1}{r sin\theta}\frac{dv_\theta}{d\theta} = 0 \tag{3.15}$$

$$\frac{1}{r^2}\frac{d}{dr}(r^2 v_r) + \frac{1}{r sin\theta}\frac{d}{d\theta}(v_\theta sin\theta) + \frac{1}{r sin\theta}\frac{dv_\theta}{d\theta} = 0 \tag{3.16}$$

where v_θ is canceled due to the velocity being purely radial

$$\frac{1}{r^2}\frac{d}{dr}(r^2 v_r) = 0 \tag{3.17}$$

$$\frac{d}{dr}(r^2 v_r) = 0 \tag{3.18}$$

$$\frac{d}{dr}(r^2 u) = 0 \tag{3.19}$$

Step 2: Integrate the results of the spherical continuity equation to find that $u(r,t)$ is inversely proportional to square of distance (Brennen,2005) [5].

$$u(r,t) = \frac{F(t)}{r^2} \tag{3.20}$$

Step 3: Apply Radial Momentum Equation. Assuming the liquid is a Newtonian liquid, the Navier Stokes equation can be applied and appropriate cancellations are implemented to account for radial motion only and symmetry (Brennen,2005) [5].

$$\rho\frac{Du}{Dt} = \frac{-dP}{dr} + \rho g_r + \mu\left(\frac{d^2u}{dr^2} + \frac{1}{r}\frac{du}{dr} + \frac{1}{r^2}\frac{d^2u}{d\theta^2} + \frac{d^2u}{dz^2} - \frac{2u}{r^2}\right) \tag{3.21}$$

$$\rho\frac{Du}{Dt} = \frac{-dP}{dr} + \rho g_r + \mu\left(\frac{d^2u}{dr^2} + \frac{1}{r}\frac{du}{dr} + \frac{1}{r^2}\frac{d^2u}{d\theta^2} + \frac{d^2u}{dz^2} - \frac{2u}{r^2}\right) \tag{3.22}$$

$$\frac{d}{dt}\frac{F(t)}{r^2} = \frac{F'(t)}{r^2} \tag{3.23}$$

$$\frac{udu}{dr} = \frac{1}{2}\frac{du^2}{dr} \tag{3.24}$$

The following is Euler's equation:

$$\rho\left(\frac{udu}{dr} + \frac{du}{dt}\right) = -\frac{dP}{dr} \tag{3.25}$$

The bubble radius $R(t)$ oscillates about some equilibrium radius R_o with bubble wall velocity $\dot{R(t)}$ (Brennen,2005) [5].

$$\left(\frac{udu}{dr} + \frac{du}{dt}\right) = -\frac{1}{\rho}\frac{dP}{dr} \tag{3.26}$$

Step 4: Apply substitutions to equate velocity equation as a function of time to the pressure gradient (Brennen,2005) [5].

$$\frac{1}{2}\frac{du^2}{dr} + \frac{F'(t)}{r^2} = -\frac{1}{\rho}\frac{dP}{dr} \tag{3.27}$$

$$-\frac{1}{\rho}\frac{dP}{dr} = \frac{F'(t)}{r^2} + \frac{1}{2}\frac{du^2}{dr} \tag{3.28}$$

$$-\frac{1}{\rho}\int_{R(t)}^{\infty} dP = \int_{R(t)}^{\infty} \frac{F^{'}(t)}{r^2} + \int_{R(t)}^{\infty} \frac{1}{2}\frac{du^2}{dr}dr \tag{3.29}$$

Step 5: Evaluate the integral from the bubble surface (R(t)) to infinity (Brennen,2005) [5].

$$\frac{-1}{\rho}(P(R(t)) - P_{\infty}) = \frac{-F^{'}(t)}{R(t)} + \frac{1}{2}U^2(t) \tag{3.30}$$

$$U(t) = \frac{dR(t)}{dt} = \dot{R} \tag{3.31}$$

Step 6: Use the following relationships from the continuity equation:

$$F(t) = u(r,t)r^2 = R^2(t)U(t) = \frac{1}{3}\frac{dR^3}{dt} \tag{3.32}$$

$$F^{'}(t) = 2R\dot{R}^2 + R^2\ddot{R} = \frac{1}{3}\frac{d^2(R^3)}{dt^2} \tag{3.33}$$

Step 7: Apply Boundary Conditions. Find a relationship between the pressure gradient and surface tension at the bubble surface:

Surface tension has the following pressure differential:

$$\Delta P_{\sigma} = \frac{2\sigma}{R} \tag{3.34}$$

The viscous stress tensor has a normal component to the surface which equates to a pressure (Brennen,2005) [5]:

$$\Delta P_{\mu} = -2\mu\frac{du}{dr}\bigg|_R = 4\mu\frac{F(t)}{R^3} = 4\mu\frac{\dot{R}}{R} \tag{3.35}$$

Step 8: Combine Equations (20), (21) and the relationships identified in equations (16),(18) and (19) to arrive at the Rayleigh-Plesset equation (Brennen,2005) [5]:

$$R\ddot{R} + \frac{3}{2}\dot{R}^2 = \frac{1}{\rho}\left(P_g(t) - P_{\infty}(t) - 4\mu\frac{\dot{R}}{R} - \frac{2\sigma}{R}\right) \tag{3.36}$$

Expanding Bubble Dynamics

As the bubbles rise through the bubble column, they will expand under the differences of hydrostatic pressure. We will consider the expansion of the gas in an isentropic condition:

$$P(t)R(t)^{3\rho g} = constant \tag{3.37}$$

where $V(t) = \frac{4\pi R(t)^3}{3}$

There is an initial pressure, p1, and a radius R(0) = a. At the bubble surface, we neglect surface tension and liquid viscosity contributions to the pressure jump across the bubble. We also make the assumption that the liquid is incompressible.

These assumptions simplify the Rayleigh-Plesset equation to the following:

You start off with the Rayleigh-Plesset equation:

$$R\ddot{R} + \frac{3}{2}\dot{R}^2 = \frac{1}{\rho}\left(P_g(t) - P_\infty(t) - 4\mu\frac{\dot{R}}{R} - \frac{2\sigma}{R}\right) \tag{3.38}$$

Based on the neglect of surface tension and liquid viscosity and liquid pressure at infinity, the equation reduces to the following (Brennen,2005) [5]:

$$R\ddot{R} + \frac{3}{2}\dot{R}^2 = \left(\frac{P_1}{\rho}\right)^2\left(\frac{a}{R}\right)^{3\rho g} \tag{3.39}$$

Understanding the relationship of $U = \frac{dR}{dt}$, Equation 3.25 is integrated to the following equation:

$$\dot{R}^2 = \frac{2b^2}{3(\rho g - 1)}\left[\left(\frac{a}{R}\right)^3 - \left(\frac{a}{R}\right)^{3\rho g}\right] \tag{3.40}$$

where $b = \frac{P_1}{\rho_l}$

This yields a maximum surface velocity of:

$$U^2{}_{max} = \frac{2b^2}{3}\gamma^{\frac{-\gamma}{\gamma-1}} \tag{3.41}$$

where $\gamma = \rho g$

3.3 Richardson's Energy Cascade in Bubble Dynamics

Richardson posed in 1922 the following summary of turbulence/energy cascade:

Big whorls have little whorls,
Which feed on their velocity
And little whorls have lesser whorls
And so on to viscosity
(in the molecular sense)

Evaluation of free stress flows lend to the observation that turbulent motions range in size at variable scales getting progressively smaller as Reynolds number increases. We will look at energy cascade and Kolmogorov hypotheses to discuss variable turbulent scales (Pope, 2000)[28].

Energy cascade, introduced by Richardson, is that kinetic energy that enters the turbulence at the largest scales of motion, and transferred by inviscid processes to smaller and smaller scales until the energy is dissipated via viscous interaction. Richardson's view was comprised of the energy cascade theory centered on a turbulence comprised of eddies of variable sizes.

Richardson discussed having eddies with a size of l and a characteristic velocity, $u(l)$ and timescale, $\tau(l) = \frac{l}{u(l)}$. This eddy is a motion of localized turbulence within a region defined by size l. This region can also be comprised of smaller eddies (Pope, 2000)[28]. The eddies in the largest size range are at a comparable scale associated with U. These eddies have characteristics velocity $u_o = u(l_o)$, which is in the order of the r.m.s turbulence intensity,

$$u' \equiv \left(\frac{2k}{3}\right)^{\frac{1}{2}} \tag{3.42}$$

The eddies have a Reynolds number $\equiv \frac{u_o l_o}{\nu}$, which is large and the effect of the eddies directly associated with viscosity are negligibly small.

Richardson discussed that large eddies are unstable and breakup, and therefore conserve energy by transferring their energy to smaller eddies. This process continues to smaller eddies until the Reynolds number, $\frac{u(l)l}{\nu}$ is sufficiently small that resultant eddy motion is stable and molecular viscosity handles kinetic energy dissipation (Pope, 2000)[28]. Rate of dissipation is determined by the transfer of energy from the largest eddies. Near the hard fixed wall, the energy containing turbulent eddies is proportional to the distance from the wall. Due to turbulent flow, the circular regimes that from in a downward motion towards the wall away from the core may cause interface deformation due to impinging turbulent eddies. The impingement of turbulent eddies cause perturbations based on oscillatory motion in the interface surface. Another set of eddies that form but are less dominant than turbulent eddies, are the eddies that form behind rising bubbles[3]. Eddies have energy in the order of u_o^2 and time scale $\tau_o = \frac{l_o}{u_o}$ so the rate of heat transfer is $\frac{u_o^3}{l_o}$.

Studies conducted by Cui and Fan (2005)[9] distinguished the liquid velocity fluctuations, caused by shear-induced turbulence and bubble induced turbulence (BIT), where BIT has the larger effect on liquid turbulence fluctuations. Recent experimental results from Riboux et al (Riboux, 2010) [20] show a power-law relationship to the volume fraction of the bubble swarm. Their experiment revealed several items that are of particular interest to our experiment evaluations in terms of mean bubble velocity and complications introduced by an unstable bubble column. Here are the particular conclusions from their research which are relevant to our research:

- mean bubble velocity lowers with increasing void fraction
- mean bubble velocity scales with single bubble rise velocity and void fraction for void fractions less than 0.1, by the following equation:

$$< V > \propto V_o \alpha^{-0.1} \tag{3.43}$$

- mean bubble velocity scales with single bubble rise velocity and void fraction for large volume fractions, by the following equation:

$$< V > \propto V_o(1 - \alpha^{0.49} \tag{3.44}$$

- velocity fluctuations were found to be independent of void fraction even though there is a scaling relationship between average velocity and void fraction
- due to the large density differences between gas and liquid, the bubble velocity varies and this variation results in a complex agitation
- this complex agitation is predominantly governed by shear-induced turbulence at the walls and bubble-induced agitation by the bubble swarm

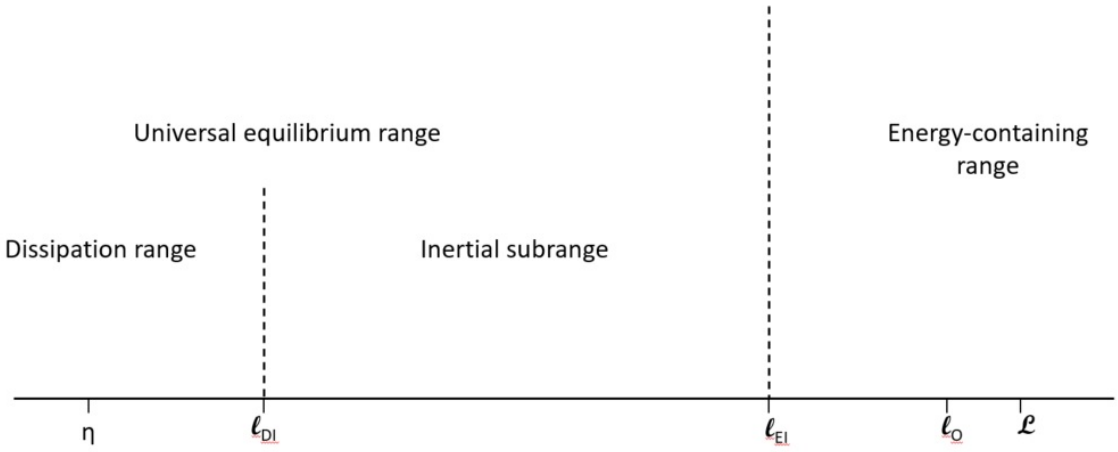

Figure 3.4: Eddy sizes at very high Reynolds number, showing the various length scales and ranges (Pope, 2000)[28]

Bubble Column Dynamics

We want to draw your attention to our own research experiment , which is comprised of a bubble column. The bubble column measures 1.1m in height and 77.9mm in diameter. Controlled air injection is used to evaluate bubble phase fraction. Figure 3.5 shows the bubble column computer-aid design to illustrate the bubble colander base section with a connection to two wire mesh sensor sections. Each wire mesh sensor area is connected with a 30mm flange spacer and two 6mm spacers that are connected by adhesive and silicon to the

tube sections above and below the wire mesh sensor. The spacers are connected using oil-resistant Buna-N-O-rings 1/8 fractional width with ID of 95.25mm. Figure 3.5 displays the bubble column with all measurement instrumentation utilized to measure air flow, absolute pressure and differential pressure across the bubble column.

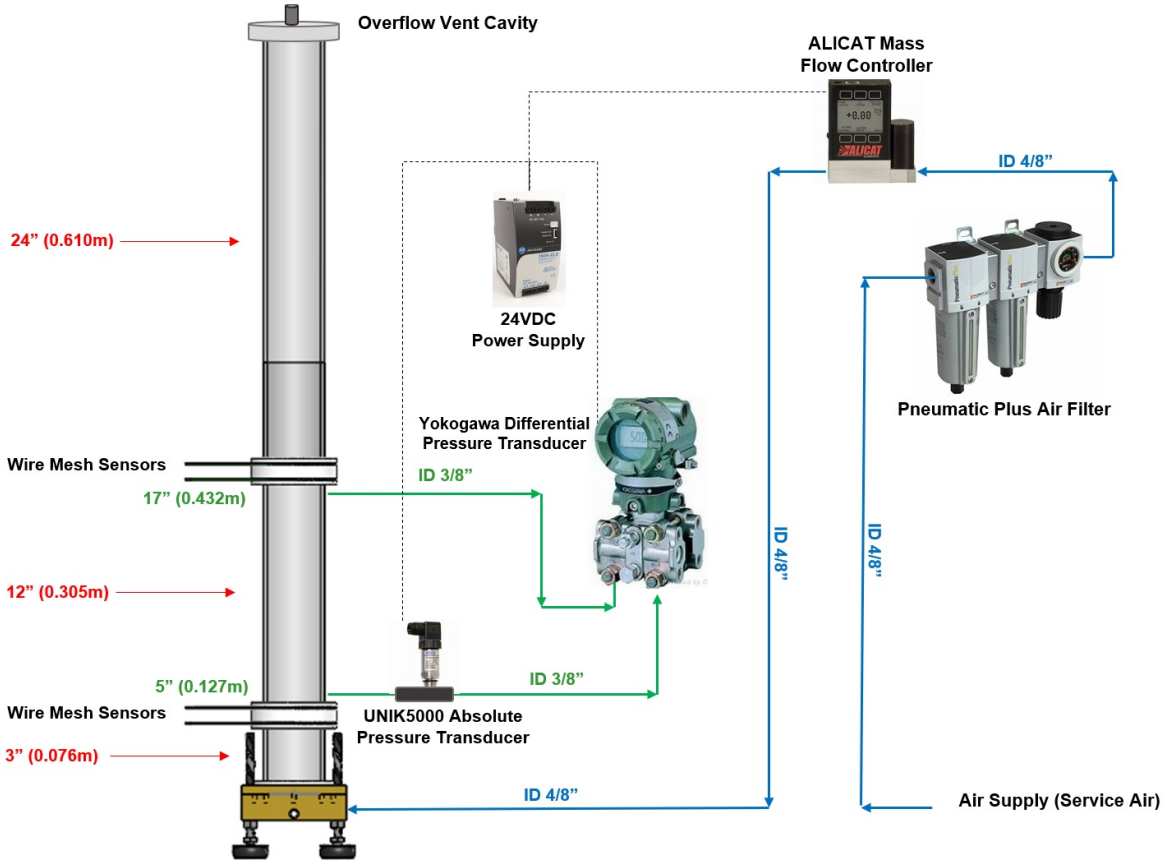

Figure 3.5: Bubble Column - SOLIDWORKS Computer-Aided Design with associated instrumentation

With our bubble column, we assume that the energy lost by the bubbles due to drag is converted to turbulent kinetic energy in the wake of the bubbles which is then dissipated by eddies until it reaches the Kolmogorov scale and is then dissipated to heat.

Bubble-induced agitation is caused by (Risso, 2018)[33]:

- flow disturbances generated in vicinity of each bubble
- turbulence that develops when the flow through the swarm of bubbles become unstable beyond a certain Reynolds number

The total fluctuations is defined as:

$$u(x,t) = \bar{u}(x) + u'(x,t) \tag{3.45}$$

where $\bar{(u)}(x)$ is the spatial distribution and $u'(x,t)$ is the temporal distribution of these fluctuations.

Figure 3.6 was produced by Riboux et al. who started to investigate the flow of water through a swarm of bubbles by using Large Eddy Simulations [33].

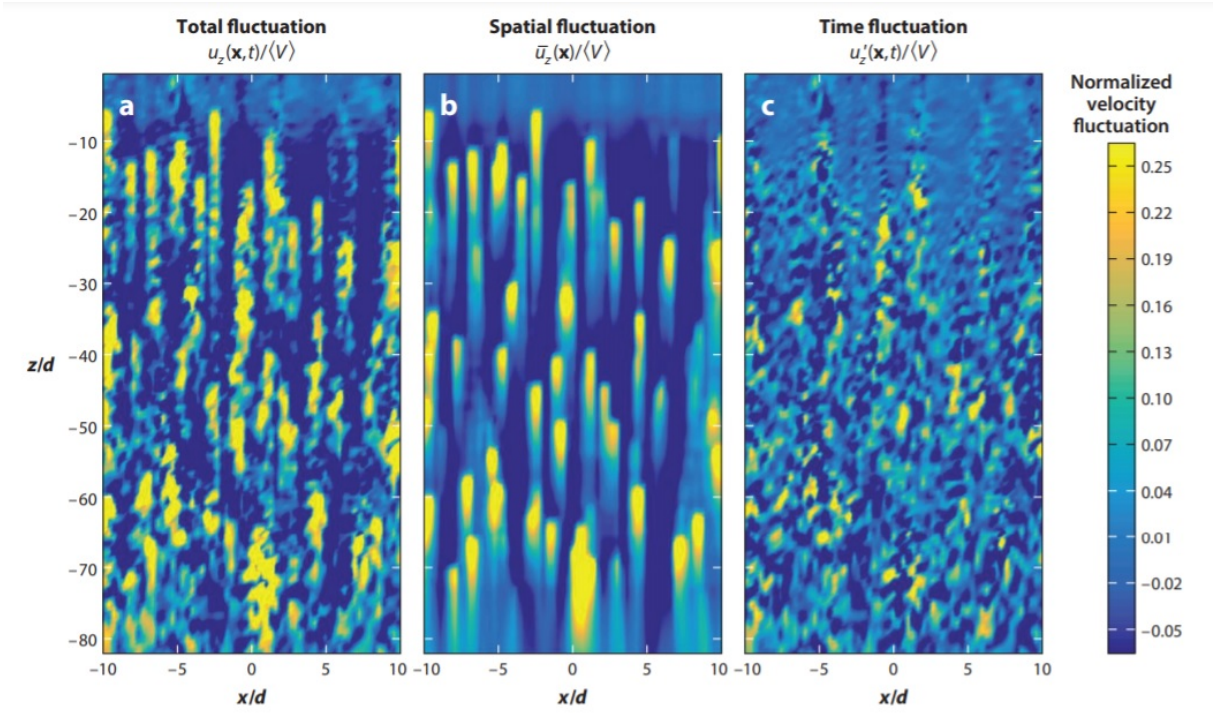

Figure 3.6: Fields of vertical velocity plane computed by large-eddy simulation (Riboux et al. 2013) (Risso, 2018)[33]

Energy of fluctuations in the bubble swarm depends on the nature of the dispersed phase and fluctuations caused by motion of bubbles' structure, which results mainly from large interactions between wakes.

Bubbles affect the flow by both spatial and temporal fluctuations. Spatial fluctuation are introduced by flow disturbances caused by each bubble. Temporal fluctuations account for the turbulence. Both fluctuations are generated at a k^{-3} subrange (Risso, 2018)[33].

Studies have found the following relationships in regards to bubble swarm dynamics (Risso, 2018)[33]:

- average velocity of the bubble swarm is lower than that of an isolated bubble of the same gas volume as an individual bubble in the bubble swarm
- bubble velocity fluctuations are dominated by wake-induced path oscillations, and their variance is weakly dependent on the gas volume fraction

Future studies are required to understand the transition between the length scale overlap between Shear-induced Turbulence and Bubble-inducted Turbulence. The bubble column also includes scales that are concerned with buoyancy-driven forces, which are much larger than the scale attributed to bubble-induced agitation. While the inlet gradient of a bubble column increases,the bubble column is no longer stable and homogeneous, leading to fluctuations of smaller and smaller scales cascading as proposed by Richardson. Our research does not specifically measure or address these fluctuations in our bubble column but these are areas that could possibly be measured with wire mesh sensors at high frequency rates.

Understanding the dynamic nature of our research, complexities are introduced with respect to capturing a time-resolved and spatial-resolved void fraction measurement that truly reflects the bubble regime characteristics of our experiment. Knowing that there are spatial and temporal fluctuations, we need to consider the adequate amount of collection that gives us a converged dataset representative of the lateral and temporal distribution of void fraction. We discuss further on how we selected a time period of 30-35 seconds to collect a substantial amount of bubble flow that represents a converged dataset, where spatial and temporal fluctuation will not predominantly skew the results.

Chapter 4

Single Bubble Dynamics Theory and Bubble Dynamics within Confined Spaces

4.1 Saffman's Theoretical Understanding and Experimentation of Bubble Dynamics

Spiraling Bubble Motion

Dynamics of bubbles are very complex and multilayered. The interaction between a gas bubble and heated inclined surface is essential to address the underlying fluid motion and the significant convective heat transfer enhancement. A study by Christopher Brücker, explores the flow in the wake of single and two interacting air bubbles freely rising in the water. A separate study performed by R. O'Reilly Meechan et al, explores the interaction between fluid dynamics and enhanced heat transfer capabilities (Brücker, 1999) [6].

In bubbly two phase flows, the bubbles have the shape of spheres, ellipsoid, or spherical caps which rise in rectilinear, spiraling, zig-zag or rocking motion. These aspects of bubble motion depend on system characteristics, such as bubble diameter and the properties of liquid (Brücker, 1999). Earlier studies by Saffman experimentally found bubbles with a radius less than 1mm have a zig-zag motion, while bubbles with a larger radius can either zig-zag or spiral.

Saffman's research, used in our understanding of bubble dynamics, is concerned with motion of air bubbles in water where the equivalent spherical radius range from 0.5 - 4.0mm. The governing equations obtained are relationships of geometrical parameters.

Bubble experiments show that bubbles with a radius of 0.7mm rise steadily in a straight line. When the radius exceeds 0.7mm, the motion shifts to either zig-zag from side-to-side and spirals in a uniform manner. Saffman's experiments found the frequency of the zigzag motion is about seven per second and independent of size of bubble. The study also found

that the angular velocity of spiraling motion appears to be independent of the size also and about 30 radians per second (5 revolutions per second about the spiral axis) (Saffman, 1956) [34].

It was shown that bubbles with a radius between 1.0mm and 2.3mm would either zig-zag or spiral. Bubbles with radius less than 1.0mm were always observed to zig-zag, even when interfering with other objects or release in a wake of a spiraling bubble. The tendency to spiral was more evident as the bubble radius increased. The summary of Saffman's small air bubble experiments concluded that bubbles rise steady in a straight line until the radius reaches a value where the flow becomes unstable. The zig-zag motion appears first. At a slightly large radius, the zig-zag motion is unstable due to large disturbances and gives way to spiraling motion.

Saffman discussed that a bubble is nearly spherical when the Re number is large, if $\frac{2gR}{W^2}$ (inverse of Froude number) and $\frac{2\rho RW^2}{T}$ (Weber number) are less than 1 , where T is the surface tension, R is the bubble radius, W is the velocity rise and ρ is the density if the fluid (Saffman, 1956) [34].

For spiraling and zig-zagging bubbles, $\frac{2gR}{W^2}$ is small but $\frac{2\rho RW^2}{T}$ is of order of unity. This concluded that the spiraling bubbles are not spherical but approximately oblate spheroids, displayed in Figure 4.1.

As we look to gain a theoretical understanding of bubble dynamics, we turn to Saffman's theoretical explanation of bubble rise motion. Saffman started with a calculation of pressure, P, in water. Motion of fluid in front of the bubble is assumed inviscid and irrotational. The boundary conditions for pressure (neglecting pressure in bubble) are satisfied over the entire surface in the following equation:

$$P + T\left(\frac{1}{R_1} + \frac{1}{R_2}\right) = const \tag{4.1}$$

where R_1 and R_2 are principle radii of surface curvature.

Calculation of pressure is denoted by vertical velocity of rise, W, and angular velocity for the spiral, denoted by Ω, and the radius of spiral by d.

Saffman used spherical coordinates (μ, ζ, ω) defined by:

$$x = k\mu\zeta \tag{4.2}$$

$$y = k(1-\mu^2)^{1/2}(1+\zeta^2)^{1/2}cos(\omega) \tag{4.3}$$

$$z = k(1-\mu^2)^{1/2}(1+\zeta^2)^{1/2}sin(\omega) \tag{4.4}$$

The surface of the bubble corresponds to ζ=ζ_o such that eccentricity of the median plane of the bubble is $\frac{1}{\sqrt{1+\zeta_o^2}}$ and the spherical radius is $k[\zeta_o(1+\zeta_o^2)]^{1/3}$

χ is defined as the angle between axis of symmetry of bubble and the upward vertical.

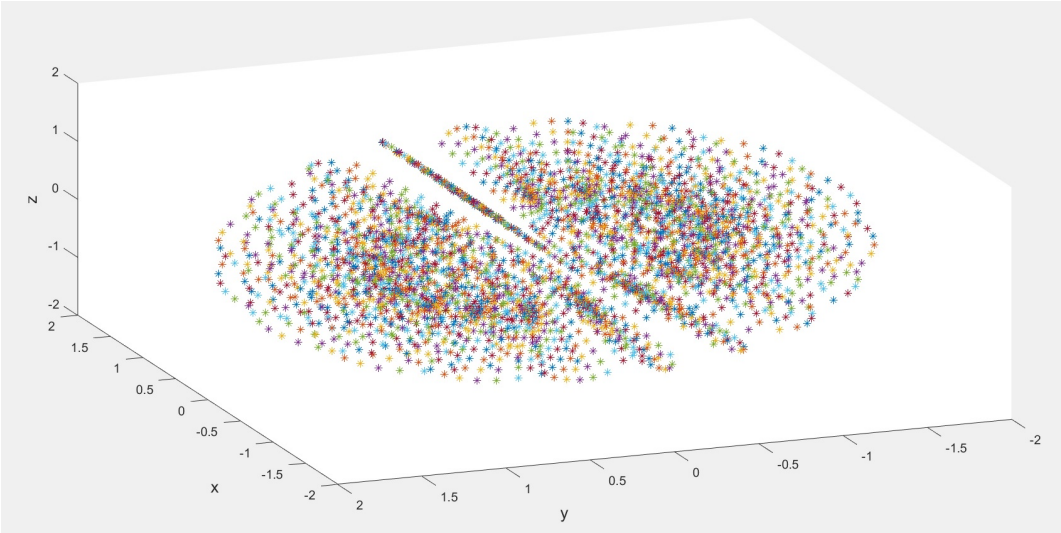

Figure 4.1: Oblate Spheroid (axes are non-dimensional and the points only define the surface if the spheroid)

A velocity $-W$ and angular velocity $-\Omega$ are imposed on the fluid, where W=(W cos(χ), W sin(χ), 0) and Ω=(Ω cos(χ), Ω sin(χ), 0). Saffman defined the velocity of undisturbed fluid as -W - Ω x (d+r) where d = (0,0,d) and r=(x,y,z).

The velocity potential of undisturbed fluid caused by bubble disturbance is

$$V = \Delta\phi - W - \Omega x(d + r) \tag{4.5}$$

relative to axis (x,y,z)

Surface of the bubble is a streamline where V $\cdot$ n = 0 on $\zeta = \zeta_o$ and n is defined outward from the surface.

The following boundary condition must be satisfied:

$$\begin{aligned}\left(\frac{\delta\phi}{\delta\zeta}\right)_{\zeta=\zeta_o} &= \mu k(Wcos(\chi) + \Omega dsin(\chi)) + k(1-\mu^2)^{1/2}(1+\zeta_o^2)^{-1/2}\zeta_o(Wsin(\chi) \\ &\quad -\Omega dcos(\chi))cos(\omega) + \Omega k^2\mu(1-\mu^2)^{1/2}(1+\zeta_o^2)^{-1/2}sin(\chi)sin(\omega)\end{aligned} \tag{4.6}$$

With the assumptions of the fluid being incompressible, $\nabla^2\phi = 0$ is satisfied.

The following suitable solution was found by Saffman to satisfy the boundary condition:

$$\begin{gathered}\mu(1 - cos(\zeta^{-}1)\zeta), \\ (1-\mu^2)^{1/2}(1+\zeta^2)^{-1/2}[\zeta - (1+\zeta^2)cot^{-1}(\zeta)]cos(\omega), \\ \mu(1-\mu^2)^{1/2}(1+\zeta^2)^{1/2}[3\zeta cot^{-1}(\zeta) - 3 + (1+\zeta^2)^{-1}]sin(\omega)\end{gathered}$$

By brevity, Saffman reduced velocity potential equation to the following solution sets where $\zeta = \zeta_o$:

$$X = \zeta + \frac{3\zeta cot^(-1)\zeta - 3 + (1+\zeta^(2))^{-1}}{(6\zeta^(2)+3)cot^(-1)\zeta - 6\zeta - \zeta(1+\zeta^2)^{-1}}$$
$$Y = 2 + \zeta^(2) - \zeta(1+\zeta^(2))cot^(-1)\zeta^{-1}$$
$$Z = (1+\zeta^2)(1+\zeta^2)cot^(-1)(\zeta) - \zeta$$

From the velocity potential, the following velocities are derived:

$$\begin{aligned}(\mu^2)+\zeta^2)^{\frac{1}{2}}V_\mu = -Z^{-1}(1+\zeta^2)(Wcos(\chi)+\Omega dsin(\chi))((1-\mu^2)^{\frac{1}{2}}) \\ +2Y(1+\zeta^2)^{\frac{1}{2}}(Wsin(\chi)-\Omega dcos(\chi))\mu cos(\omega) \\ +\Omega ksin(\chi)((1+\zeta^2)^{\frac{1}{2}}[-\zeta+(1-2\mu^2)(X-\zeta)]sin(\omega)\end{aligned} \tag{4.7}$$

$$\begin{aligned}V_w = 2Y(Wsin(\chi)-\Omega dcos(\chi))sin(\omega) - \Omega kcos(\chi)(1+\zeta^2)^{\frac{1}{2}}(1-\mu^2)^{\frac{1}{2}} \\ +\Omega ksin(\chi)X\mu cos(\omega)\end{aligned} \tag{4.8}$$

V_ω and V_μ are zero at the stagnation point.

The pressure is derived to the following equation:

$$\frac{P}{\rho} + \frac{1}{2}V^2 gH - \frac{1}{2}\Omega^2\omega^2 = const \tag{4.9}$$

where g is acceleration due to gravity

$\omega = [(d+z)^2 + (xsin(\chi) - ycos(\chi)^(2)]^{\frac{1}{2}}$ is the perpendicular distance from axis of spiral

$H = xcos(\chi) + ysin(\chi)$ is the vertical height above center of bubble

$\frac{1}{R_1} + \frac{1}{R_2} = \frac{\zeta((\zeta^2+1)^{\frac{1}{2}}}{k(\zeta^2+\mu^2)^{\frac{3}{2}}} + \frac{\zeta}{k(\zeta^2+1)^{\frac{1}{2}}(\zeta^2+\mu^2)^{\frac{1}{2}}}$ are results of solid geometry.

Saffman applied the pressure boundary condition as follow:

$$\left(\frac{\delta}{\delta\mu}, \frac{\delta}{\delta\omega}, \frac{\delta^2}{\delta\mu^2}, \frac{\delta^2}{\delta\mu\delta\omega}, \frac{\delta^2}{\delta\omega^2}\right)\left(\frac{-1}{2}V^(2) - gH + \frac{1}{2}\Omega^2\omega^2 + \frac{T}{\rho}\left(\frac{1}{R_1}+\frac{1}{R_2}\right)\right) = 0 \tag{4.10}$$

with derivatives evaluated at stagnation point (μ_s, ω_s)

By considering equations of the same order of magnitude, considering second order derivatives of Equation 4.10, and using assumptions that X and $(1-\mu^2)^{\frac{1}{2}}$ are small, Saffman obtained the velocity of rise as follow:

$$\frac{W^2}{gk} = \frac{Z^2}{1+\zeta^2}\left(\frac{4T\zeta}{\rho gk^2(1+\zeta^2)^2} + \zeta\right) \tag{4.11}$$

Saffman obtained the shape parameter as a function of the bubble radius as follow:

$$\frac{4T}{\rho gk^2(1+\zeta^2)^2} = \frac{1+\zeta^2}{2Y\zeta(Z-X)} - 1 \tag{4.12}$$

Saffman composed the theoretical results and compared them with experiment results from several authors. He concluded agreement between velocity of rise and bubble shape predicted from Equations 4.11 and 4.12 and experimental observations (Saffman, 1956) [34].

Saffman's findings include the following:

- no bubble can spiral unless it is flatter than the oblate spheroid corresponding to $\zeta = 1.52$
- for values of r less than 3.6mm, ζ decreases as r increases
- surface tension tends to keep the bubble spherical, where the magnitude of the surface tension effect is inversely proportional to the radius of the bubble
- spiraling motion is not possible for bubbles of radius larger than 3.6mm
- Equations 4.11 and 4.12 become more inaccurate as bubble radius become larger

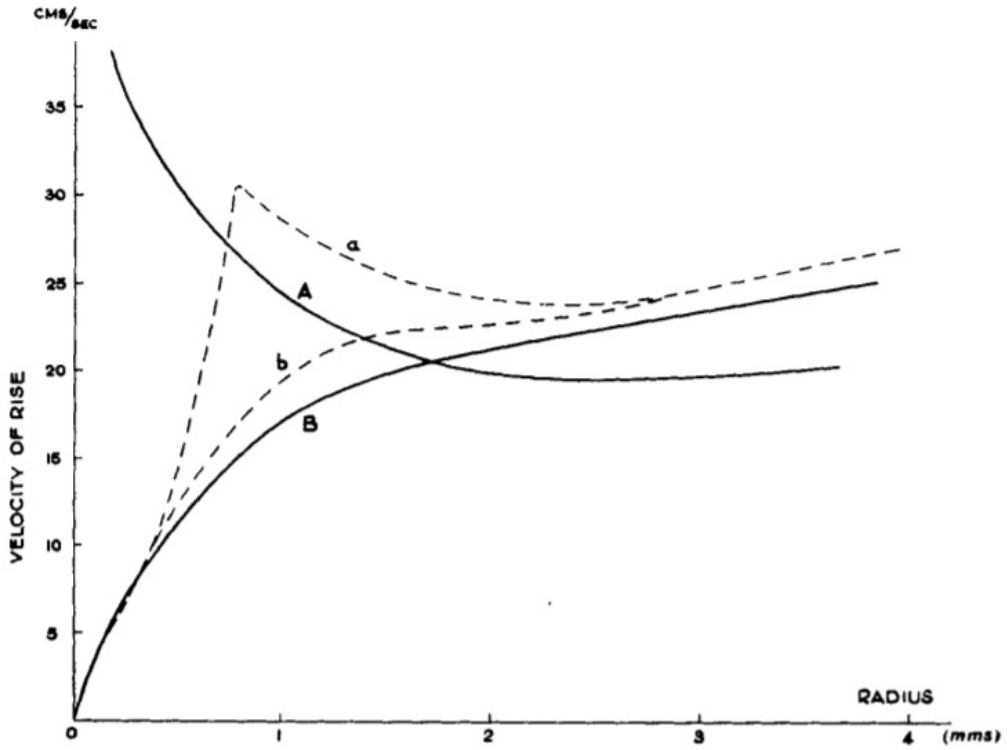

Figure 4.2: Broken lines (a) and (b) display approximate experimental results. Full lines (A) and (B) display results of Equations 4.11 and 4.12 and modified results due to separation of flow (Saffman, 1957)[34]

Discrepancies between theoretical and experimentation results stem from neglect of term $\frac{kgZX}{W\Omega d} = \Lambda$. Λ's physical meaning is unclear, but it must be small to account for condition that variations of hydrostatic pressure over the bubble surface are small as compared to hydrostatic pressure. Λ can be neglected with impact to velocity calculations for r less than 1.5mm. Λ increases rapidly with r greater than 3.0mm. This will drive equations (4.11) and (4.12) to be inaccurate (Saffman,1957) [34].

Stability of Rising Bubble

Analysis of bubble motion near the front of the bubble does not give information in regards to zig-zag motion. Saffman found that if the bubble is more oblate than a spheroid corresponding to ζ =1.52mm, there will be unstable motion in an irregular fashion. This condition suggests a departure of motion from rectilinear motion of a spheroidal bubble.

4.2 Void Distribution and Bubble Motion in Bubbly Flows in Reactor Rod Bundles

With a minimal repository of studies regarding two-phase flows in tube bundles, it is difficult to validate numerical methods for predicting gas-liquid mixture within the tube bundle. We will review void fraction calculations from Laser Doppler Velocimetry (LDV). The experiments performed by Hosokowa et al, from Kobe University in 2013, showed void fraction distribution in inner and side sub-channels depend not only on lift force acting on bubbles but also on geometrical constraints, in-depth look on effects of rod walls on bubble shape and rise velocity.

These additional studies evaluated average void fraction in rod bundles:

- Void fraction under high pressure, low flow (Anklam):
  Anklam et al, conducted experiments on high pressure, low heat and mass flux experiments. Experiment results show variations in void fraction and mixture swell parameter are dominated by changes in pressure and volumetric vapor generation rate. The vapor generation rate is a dominant factor and the swell parameter follows a linear relationship with vapor generation rate (Anklam, 1983)[26].

- Evolution of cross-sectional averaged void fraction (Morooka):
  Morooka et al, found that the distribution parameter from Drift Flux model is larger than unity, the void distribution across the rod bundle is not uniform and the void fraction across the outer channel wall is lower than the central void fraction. Additionally, at a constant mass flux, the void fraction decreases with increasing pressure (Morooka, 1988)[49].

Kamei et al conducted experiments evaluating gas-liquid two phase flow to obtain conclusions involving dependence of the void fraction on the gas volume flux due to the flow pattern

transition. In the case of a failure of flow through a reactor fuel cell, the vapor generated in reactor core forms two phase flow in a stagnant liquid and raises water level in the reactor core.

Kamei et al's experiment apparatus involved a test section, an upper and lower tank. The test section consisted of a channel box and sixteen rods positioned to upper and lower tie-plates. The rod diameter was 10mm, rod pitch was 12.3mm and the hydraulic diameter was 9mm. The gas was supplied through a diffuser plate of porous media (4mm thickness). The gas volume injector rate (J_G) was varied from 0.03 to 8.0$\frac{m}{s}$ to cover a wide range of void fractions, α. Pressure was measured using pressure transducers located at four sides of the channel box, with a sampling frequency of 200Hz. Figures 4.3 and 4.4 display the experiment apparatus and cross section of the tube bundle (Kamei, 2010) [16].

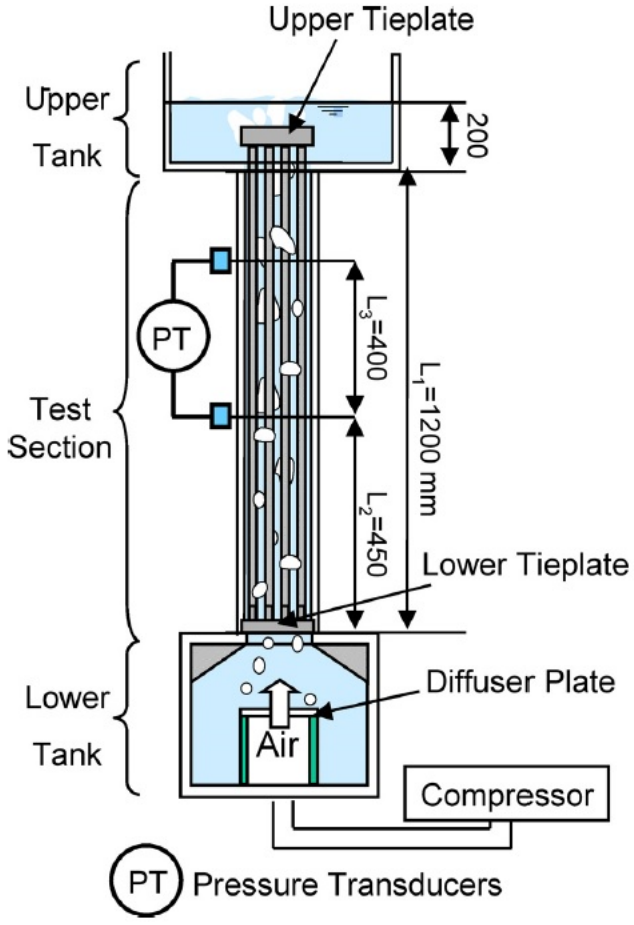

Figure 4.3: Experimental Apparatus (Kamei, 2010)[16]

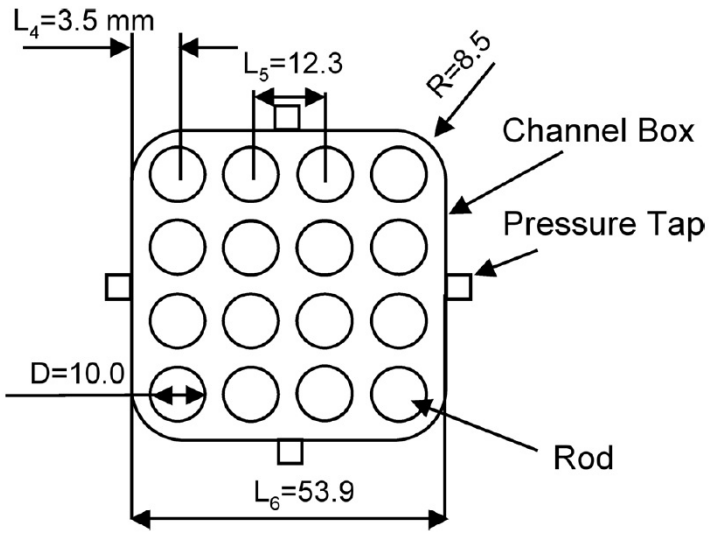

Figure 4.4: Cross Section of Rod Bundle (Kamei, 2010)[16]

ΔP was calculated using the following formula:

$$\Delta P = \frac{1}{T}\int_0^T \Delta P(t)\, dt \tag{4.13}$$

Void fraction was calculated from pressure drops by using the following equation:

$$\alpha = 1 - \frac{\Delta P}{(\rho_l - \rho_g)gL} \tag{4.14}$$

where ρ = density, g = acceleration of gravity, and L = length of the section L_3 Phase-averaged gas velocity, V_G, was evaluated from the pressure drops, ΔP, by using the following equation:

$$V_G = \frac{J_G}{\alpha} \tag{4.15}$$

where subscript G denotes the gas phase

Using a high-speed camera, flow patterns in the rod bundle were classified into six regimes. As J_G increases, the flow pattern transitions from bubbly to churn flow and eventually to annular flow.

- $0.1\frac{m}{s}$ - transition from bubbly to churn
- $1.5\frac{m}{s}$ - transition from churn A to churn B
- $6.0\frac{m}{s}$ - transition from churn to churn to annular

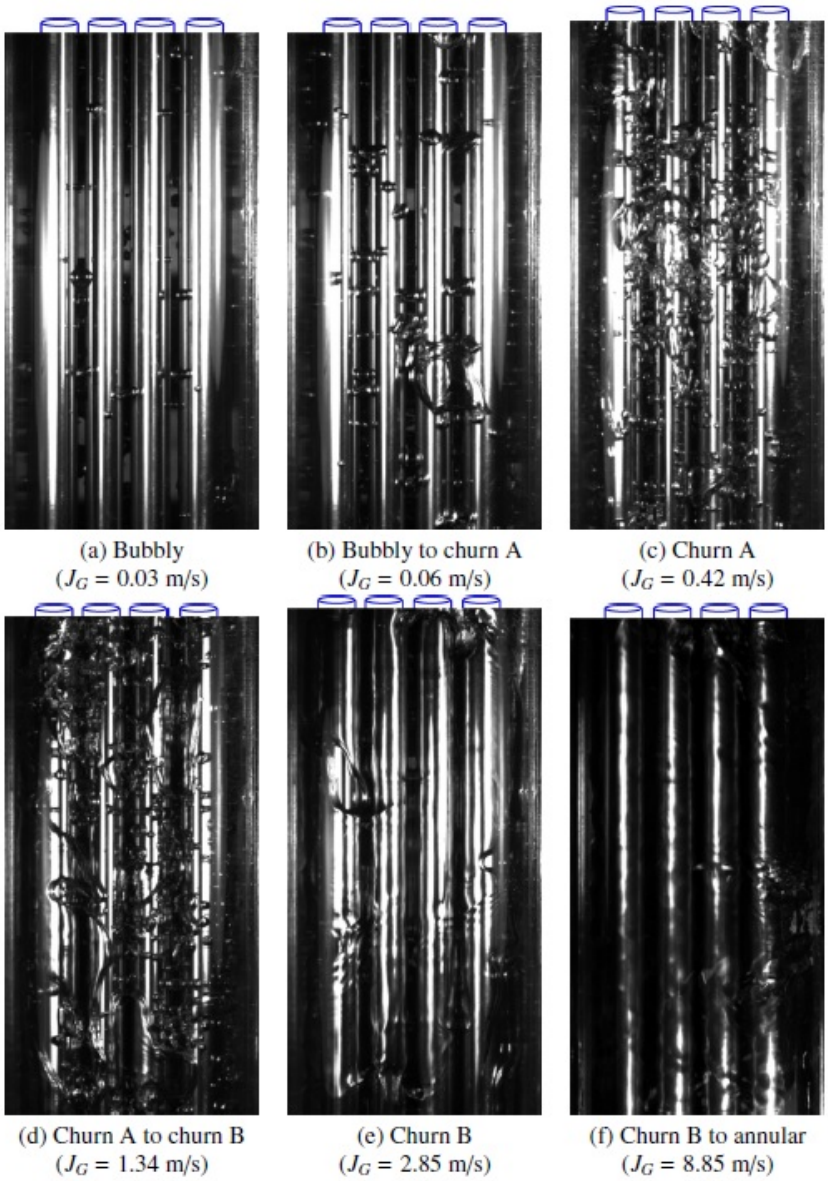

Figure 4.5: Flow Regime based on observation of transitions with an increase in superficial gas velocity (Kamei, 2010)

The phase averaged gas velocity, V_G, increases with J_G. The void fraction gradient decreases with increasing J_G at $J_G < 1.5\frac{m}{s}$ and it increases at $J_G = 1.5\frac{m}{s}$ and subsequently decreases again with increasing J_G. By separating calculations at $J_G = 1.5\frac{m}{s}$, α and V_G are correlated by use of the drift-flux model.

$$\alpha = \frac{J_G}{C_o J_G + V_{GJ}} \tag{4.16}$$

$$V_G = C_o J_G + V_{GJ} \tag{4.17}$$

where C_o is the distribution parameter and V_{GJ} is the drift velocity, which is the velocity measurement of the phase (in two phase flow) that is lagging in an entire flow phase.

The correlation coefficient, C_o, changes across $J_G = 1.5\frac{m}{s}$ due to flow pattern transition based on formation of large bubbles, which blocks the cross-section. Measured experimentation values agreed well with Murase et al's proposed void correlation of gas-liquid two-phase flows in rod bundles.

$$\alpha = 0.037Y^{1.68}\alpha <= 0.33 \tag{4.18}$$

$$1 - \alpha^{1.45} = e^{-0.0161Y}\alpha > 0.33 \tag{4.19}$$

where $Y = \frac{1}{1.7D^{0.125}}\frac{J_G^*}{\alpha}$ and J_G^* is the dimensionless gas volume flux defined by $J_G^* = J_G\left[\frac{\rho_l^2}{g\sigma(\rho_l - \rho_g}\right]^{\frac{1}{4}}$

Chapter 5

Bubble Column Construction

5.1 Bubble Column Experiment Setup and Instrumentation

Experiments conducted using a bubble column (BC) will analyze the behavior of bubbles rising in water under buoyancy and amidst superhydrophobic coated internal parts which is an active area of research. Furthermore, the BC provides an easy-to-use test bed to compare various phase fraction measurement techniques (electrical impedance, optical, X-ray, or differential pressure). In this experiment setup, we have a bubble column exposed to atmosphere, and supplied with air via a colander of 800 holes or variable needles protruding from a brass base plate. An open bubble column may introduce environmental impurities that may contaminate the water over time and affect the velocity of the bubbles so this is minimized by frequent exchange of water and a vented cap positioned at the top of the BC. Bubble rising in different types of water attain velocities corresponding to stresses at interfaces and no slip boundary conditions at surfaces. Evaluation of these bubbles encounter complexities due to particle motions, inter-facial interactions and deformations that occur at different length scales.

5.2 Bubble Column Setup

The bubble column measures 1.3m in height and 77.8mm in diameter. Controlled air injection is used to evaluate bubble phase fraction. Figure 5.1 shows the bubble column computer-aided design to illustrate the bubble colander base section with a connection to two wire mesh sensor sections. Each wire mesh sensor area is connected with a 30mm flange spacer and two 6.5mm spacers that are connected by adhesive and silicone sealant to the 77.9mm tube sections above and below the wire mesh sensor. The spacers are connected using oil-resistant Buna-N-O-rings 1/8 fractional width with ID of 95.25mm.

Figure 5.1 also displays the bubble column with all measurement instrumentation utilized

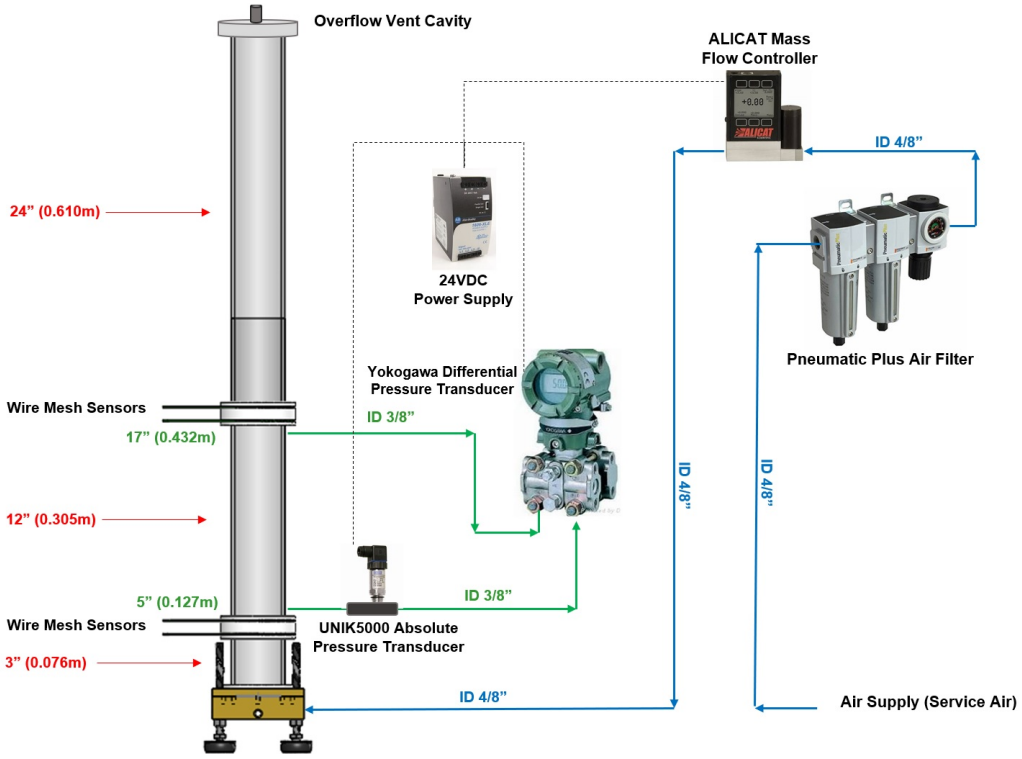

Figure 5.1: Bubble Column - SOLIDWORKS Computer-Aided Design with associated Instrumentation

to measure air flow, absolute pressure and differential pressure across the bubble column. The bubble column has two 0.8mm penetrations between both wire mesh sensor sections, measured at 12.7cm and 43.2cm from the brass base. The two penetrations connect to a YOKOGAWA EJX110A differential pressure transducer via a 1/4 inch ID plastic tubing. The high pressure connection of the differential pressure transducer passes through a UNIK 5000 absolute pressure transducer before entering the differential pressure transducer. The differential pressure transducer and cylindrical geometry can simplify calculation of void fractions. These measurements will be used later to validate wire mesh sensor and X-ray CT void fraction results.

Figure 5.1 includes the connections from the air source to the bubble column via an ALICAT mass flow controller and PneumaticPlus Air Filter with pressure regulator. The ALICAT mass flow controller is equipped with a read-out and control display, that indicates air flow and allows setpoint adjustment for the air flow. A PneumaticPlus PPC4C-N04DG-Q1 3 Stage Air Drying System, is connected upstream of the ALICAT mass flow controller to provide a filtered and steady pressure air supply to the bubble column.

The following table lists the instrumentation utilized with the bubble column. The model type, range and uncertainty are provided for each instrument as applicable.

Measurement	Equipment/Instrumentation	Range	Uncertainty
Differential Pressure	YOKOGAWA EJX110A-EMS4G-B22NM/FF1/D1	0-35 inH2O Linear	0.04 percent (MFG)
Absolute Pressure	UNIK 5000	0-60 PSI absolute	0.04 percent (MFG)
Mass Flow Rate (Air Flow)	Alicat Scientific MC Series Mass Flow Controllers	0-20 SLPM 0-20,000 SCCM	0.04 percent (MFG)
Pressure (Air Flow)	PneumaticPlus PPC4C-N04DG-Q1	Max Operating Pressure: 150 PSI, Particulate Filter: 5 Micron Sight Glass 0-150PSI,	N/A
Height	Measuring Tape	Measured in Inches	N/A
Temperature	Fluke 52II Thermometer	-250°to 400°C	+/-0.05% + 0.3°C

Table 5.1: Bubble Column Instrumentation Specifications

Figure 5.2 displays the bottom of the brass base where four air hoses are connected from an air source via a mass flow control valve. The bubble bottom plate is usually filled with water. The bottom base plate has four 1/2 inch connections to allow uniform air injection to the BC. All 4 inlets are attached to the air source.

Figure 5.3 displays the top portion of the brass base with 800 holes of 0.008in ID to diffuse bubbles into the vertical column. The holes are arranged in a convex position with larger diameter on the bottom of the top plate. The top brass plate and bottom brass plate are connected via four bolts providing base adjustable legs for the vertical column - which is to be leveled using these legs. The vertical column is connected to the top brass plate using 8 1/4 inch allen socket head cap screws and an O-ring between the spacer and the top brass plate.

A UNIK 5000 absolute pressure transducer with range from 0 to 60psi is utilized for absolute pressure measurements. A YOKOGAWA Differential Pressure Transducer with a range of 0-35inH2O is utilized to provide differential pressure measurements at three different wall pressure taps. Figure 5.4 is the UNIK 5000 pressure transducer. Figure 5.5 is an image of the YOKOGAWA D/P transducer.

Figure 5.6 displays the mass flow controller and pneumatic air filters utilized along the air line supply to the bubble column. The mass flow can be controlled and adjusted via setpoint

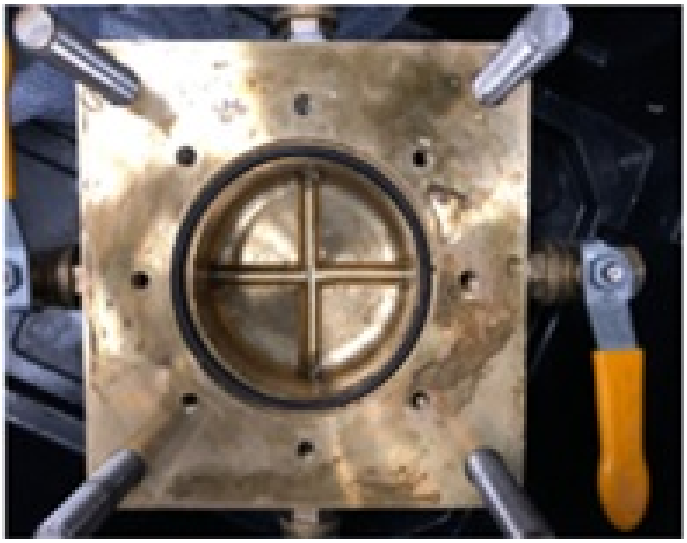

Figure 5.2: Bubble Column - Bottom Brass Plate

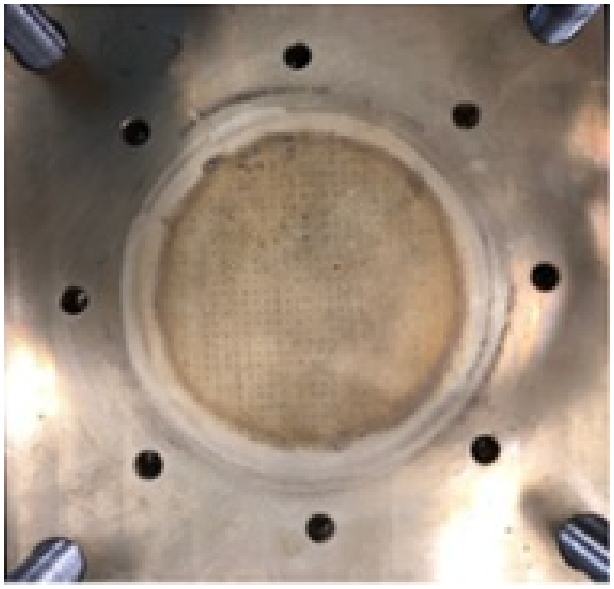

Figure 5.3: Bubble Column - Top Brass Plate

Figure 5.4: UNIK5000 - Absolute Pressure Transducer

Figure 5.5: YOKOGAWA - EJA110A - Differential Pressure Transducer

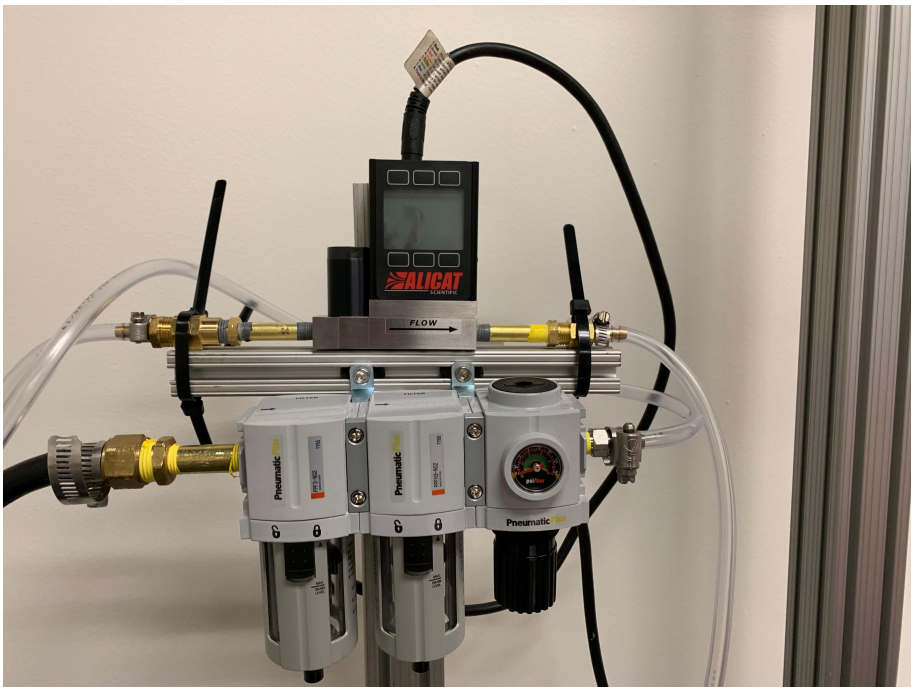

Figure 5.6: Mass Flow Controller and PneumaticPlus Air Filter

adjustments in the ALICAT readout screen. The pneumatic air filters have a pressure regulator that needs adjustment in the open position so it does not interfere with the desired mass flow rate.

A wire mesh sensor, purchased from Helmholtz Zentrum Dresden Rossendorf (HZDR), displayed in Figures 5.7 and 5.8, measures local conductivity of two-phase mixture at the intersection of the grid points for two electric fields. Time and spatial resolution are used to measure void fraction. In a wire mesh conductivity measurement, one plane of wires is used as a transmitter and another plane is used as a receiver. During measurements, switches are used to activate the transmitter to send a current through each row of wires. The receiver wires are transformed to voltages by amplifiers which are then sampled.

The wire mesh sensors are separated by a flange and connected to the flanges and spacers through 8 1/4" allen screw openings. The flanges and spacers were designed to provide minimal disruption of flow along the walls of the tubing.

5.3 Height Measurements by Differential Pressure

The differential pressure transducer was used against water column height measurements. Using the calculation of void fraction from column height difference, we were able to com-

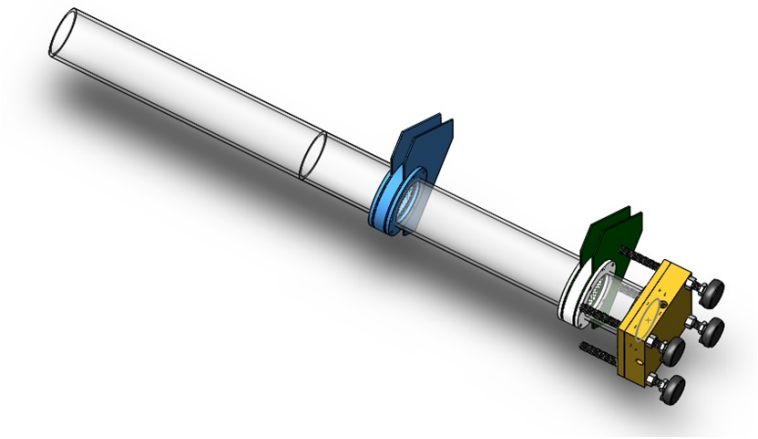

Figure 5.7: Wire Mesh Sensor Location

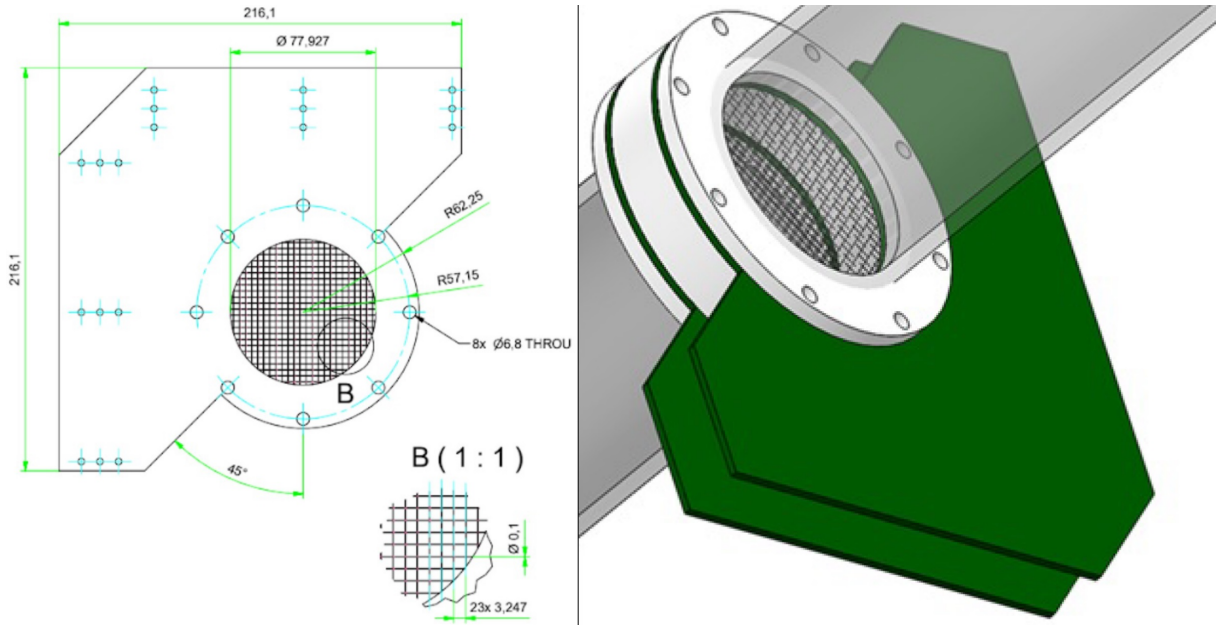

Figure 5.8: a) Wire mesh sensor computer-aided design with dimensions in millimeters b) Wire Mesh Sensor - Single Pair computer-aided design

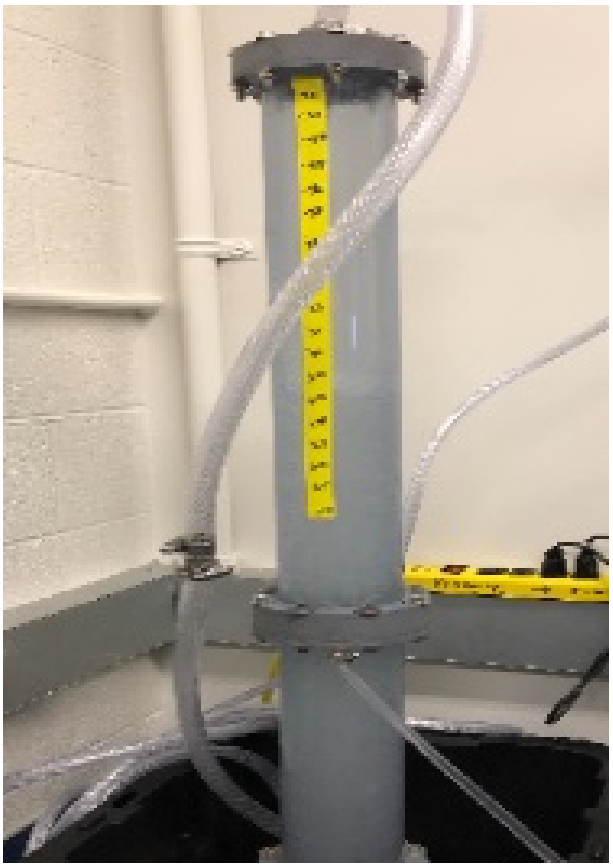

Figure 5.9: Calibration Bubble Column Markings

pare differential pressure recordings against calculated void fraction from column height. If phase fraction within column is homogeneous, the two should provide matching void fraction measurements.

A comparison was conducted by controlling inlet air flow at variable flow rates and slowly adjusting the flow rate to increase water level in the bubble column by 1 inch increment to a span total of ten inches. National Instruments LABVIEW 2018 VI was utilized to monitor and record differential pressure and absolute pressure readings.

To calibrate the differential pressure transducer, we incrementally changed height difference by one inch and applied the calibration sheet slope equation to the measure differential pressure transducer voltage to calculate the expected height difference. Figure 5.11 displays void fraction calculation from differential pressure transducer readings versus void fraction calculation from vertical column height variations performed a one inch increments versus the void fraction calculation based off the calibration sheet slope equation. Figure 5.11 is only valid for our particular experiment based on the height difference between the two

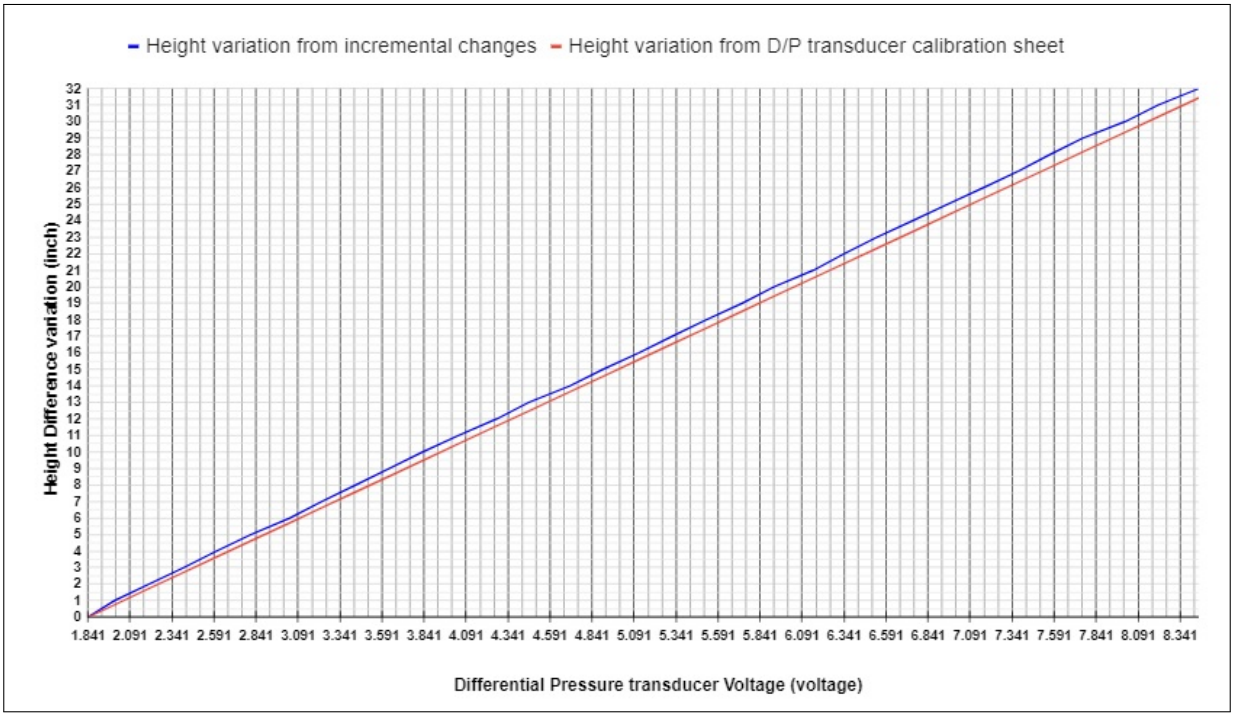

Figure 5.10: Differential pressure transducer calibration versus height increments

pressure taps.

$$\Delta P = \rho_{avg} g \Delta h$$

$$\rho_{mixture} = \rho_{air}\alpha + \rho_{water}(1-\alpha)$$

Hence the gas phase fraction α is

$$\alpha_{dp} = \frac{\rho_{mixture} - \rho_{water}}{\rho_{air} - \rho_{water}} = \frac{-\Delta P}{g\delta h(\rho_{air} + \rho_{water})} \tag{5.1}$$

Based on height change, hold up, the void fraction is

$$\alpha_{\delta h} = \frac{\delta h}{h_{water} + \delta h} \tag{5.2}$$

Figure 5.12 displays the assembled BC without the wire mesh sensors but with the differential pressure detector connections and air injected into the water-filled space.

Figure 5.13 displays three images of the bubble column test section with variable mass flow rates of 2 SLPM, 9 SLPM and 15 SLPM. The images display the bubble flow regime

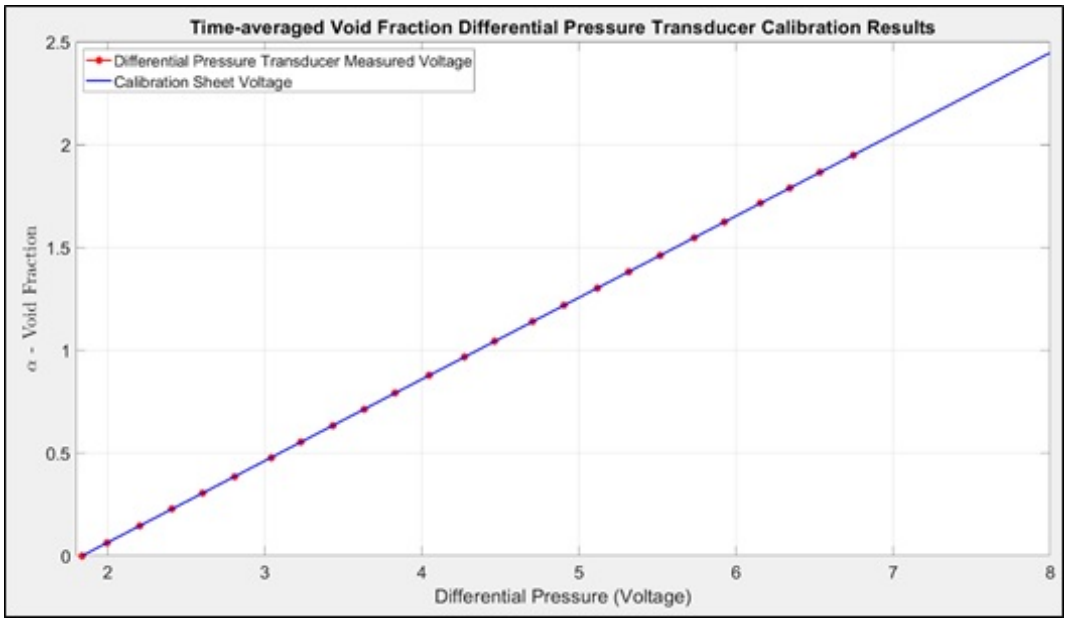

Figure 5.11: Differential Pressure Transducer Calibration - (red points) delineate sample points constructed by moving the differential pressure transducer, (blue line) delineates the calibration values for void fraction using the differential pressure transducer calibration sheet

observed throughout our expected measurements. We see that the bubble regime is homogeneous and remains dispersed throughout the designated variable air injection rates for our experiments. This presents a adequate model for our next steps at calibrating wire mesh sensor bubble properties and velocities.

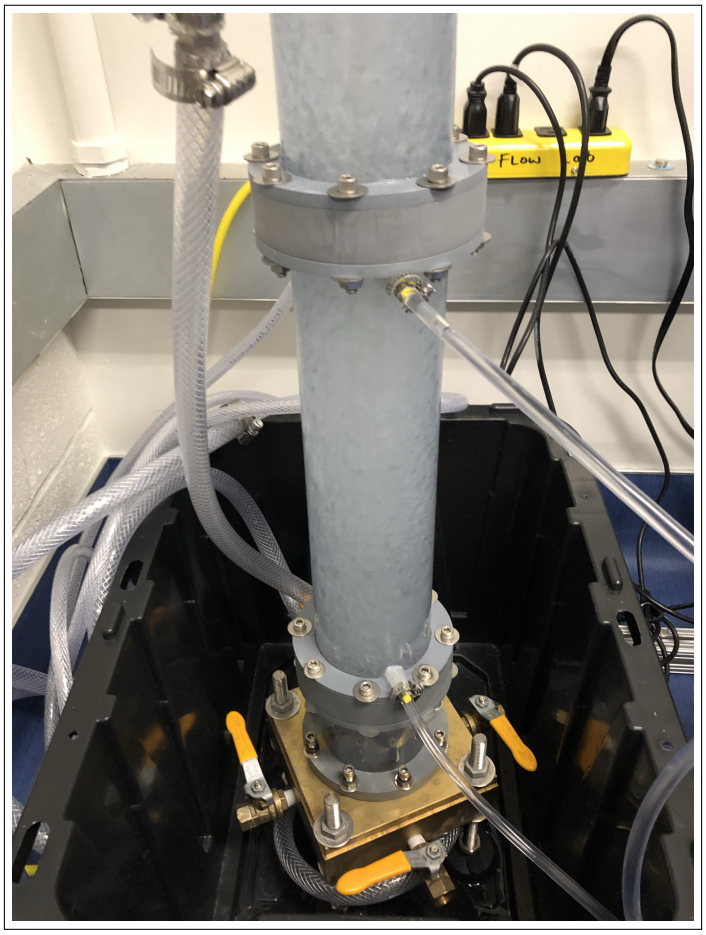

Figure 5.12: Bubble Column - Three Sections

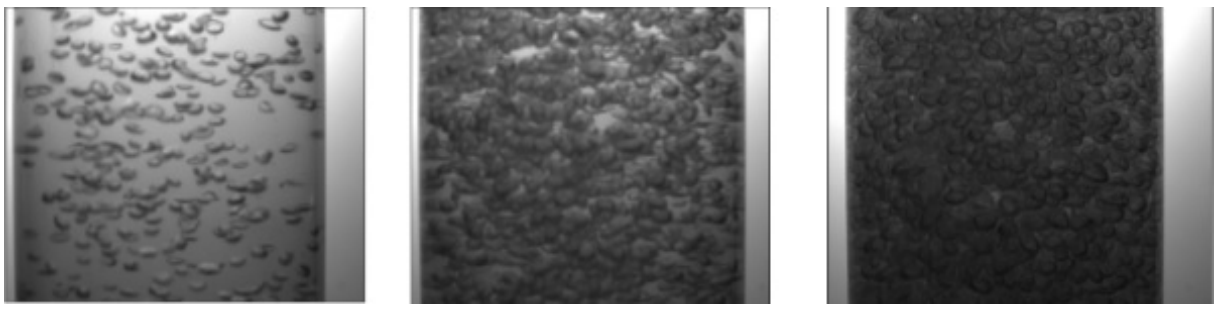

Figure 5.13: Bubble column dispersed bubble flow regime

Chapter 6

Experimental Setup and Measurement Complexities

Our research involves evaluation of flow conditions within an empty bubble column and a bubble column with suspended fuel cell assemblies scaled to mimic rod bundle spacing found in pressurized water reactors. The flow conditions are governed by the nature of the injection rate, the geometrical composition of the fuel cells, the pitch between fuel cells and the type of material.

The air injection rate is comprised of a steady air flow rate that injects bubbles into our simulated fuel cell assemblies from the base comprised of 800 holes of 0.008in inner diameter. The air is used from shop air maintained at 80psia and controlled by an Alicat Flow Controller. The air then passes through an air filter. The air pressure overcomes the hydrostatic pressure before it can reach a steady flow rate.

The typical reactor core vessel, displayed in Figure 6.1, measures 13m high and 6.2m in diameter (Knief, 2014)[17]. The vessels are constructed from low-alloy carbon steel with a wall thickness of 23cm and 3mm clad on inner surface. The coolant enters the vessel via inlet nozzles, flows downward between the vessel and the core barrel, and then distributed through the lower core plenum and onto the core fuel cell assemblies. The coolant leaves the core through outlet nozzles.

The typical fuel cell assembly is comprised of a diameter of 10mm with a pitch of 12mm, depicted in Figure 6.3. In this figure, you can see how the geometrical constraints of the fuel assembly defined by lines displaying the 10mm rod diameter and 12mm pitch. The fuel cells are constructed from Zircaloy cladding which have a high resistance to corrosion.

The fuel assemblies of Zircaloy-clad fuel rods are enriched with UO_2 pellets. A 17x17 array is used to enhance linear heat rate limits and flow mixing between adjacent units. Figure 6.2 shows a top view of the reactor core depicting typical layout of fuel assemblies. Figure 6.2 also displays a typical layout of a fuel rod bundle that supports the fuel rod assembly.

Figure 6.3 shows a typical fuel rod cell lattice with the geometrical makeup of a fuel cell found in a Pressurized Water Reactor. The diameter of a fuel rod is 10mm and the pitch

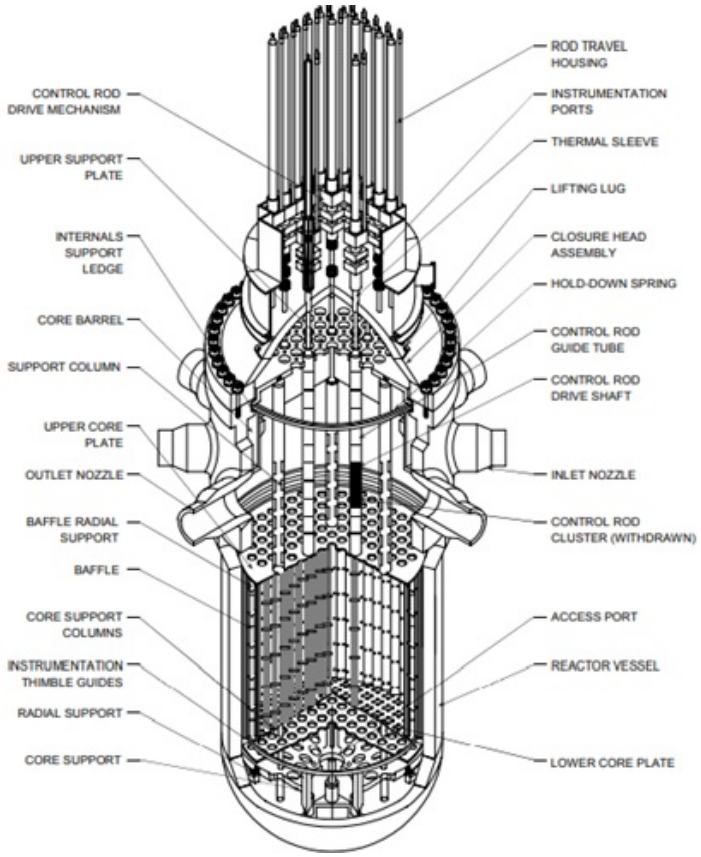

Figure 6.1: Nuclear Reactor Vessel Core (cutaway) (USNRC Technical Training Center)

between the fuel rods is 12.6mm. The heat transfer equations are governed by the hydraulic diameter based on the surface areas that interact with the fluid. Since the spacing between the fuel cells are not confined, the cross flow of the fluid also interact with the upward flow of the moderator along the fuel cell assembly.

Figure 6.4 is a zoomed in picture of the rod bundle displaying a possible velocity profile in one channel. You can notice the increased velocity towards the center of the channel, which is indicative of the viscous forces that are acting on the fluid as it travels upward through the fuel channel. It is evident to see how the no-slip condition at the walls of the fuel rods plays a significant role on the velocity profile. There are viscous effects throughout the entire flow but they are more dominant at the walls due to the no-slip condition.

Bubble coalescing in fuel cells is resultant of excessive vapor layer buildup along the fuel cell assembly. Figure 6.5 depicts a typical flow boiling regime, with the variable bubble regimes stemming from bubbly flow to annular flow. The flow conditions are important towards understanding the points where you can recover a system to normal operating con-

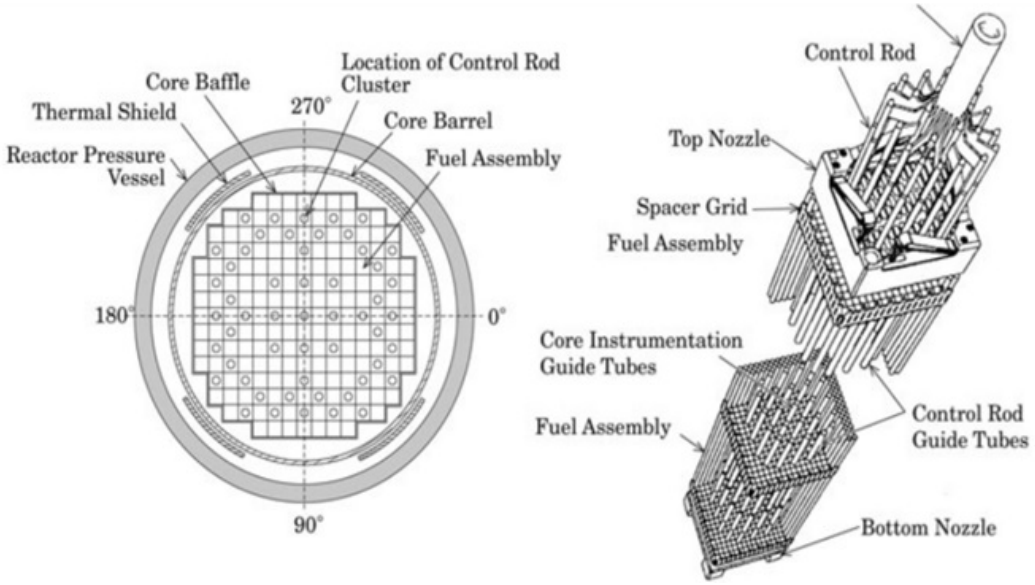

Figure 6.2: a) Cross-sectional View; b) Fuel assembly of a PWR (Oka, 2014)

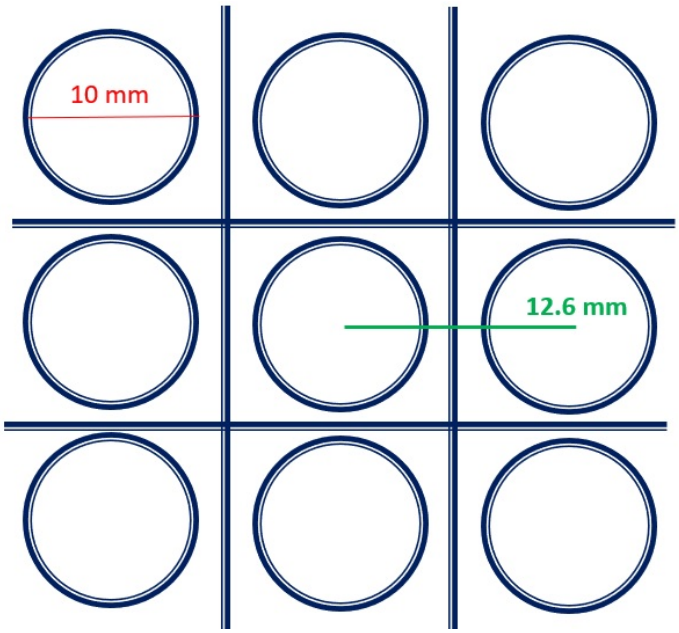

Figure 6.3: Typical fuel rod cell lattice(Tong and Weisman, 1996)[44]

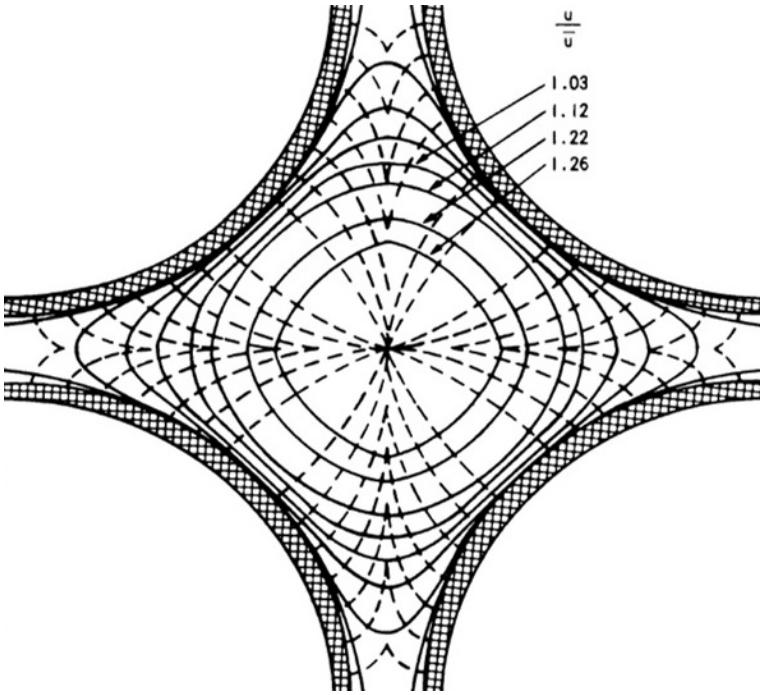

Figure 6.4: Typical Velocity Profile for a square array fuel rod arrangement (Reynolds Number: 40,000) (Tong and Weisman, 1996)[44]

ditions. As discussed previously, when the wall temperature exceeds saturation temperature at a particular pressure, bubbles will form on the walls. Based on the length of time the wall temperature remains above saturation temperature will determine the bubble flow regime in the fluid. Excessive wall temperatures above saturation temperatures can lead to a significant drop in flow causing single phase vapor and an increased proximity to Critical Heat Flux. Understanding that bubble coalescing is a key initial stage prior to bulk boiling and subsequent dryout, we want to pose the following hypothesis.

We hypothesize that the addition of a superhydrophobic-coated submerged rod into a fuel cell assembly can act as an air scavenger to lower air accumulation in fuel cell assemblies during bubbly flow, extending the proximity to Critical Heat Flux of fuel cells. Figure 6.6 shows the geometrical setup that we will use in our experiment to evaluate the effects on void fraction found by an addition of a superhydrophobic surface to the constrained flow found in a fuel cell channel.

Evaluating gas holdup, using a wire-mesh sensor, X-ray intensity field variations and X-ray Computed Tomography, are the methods we will use to evaluate gas holdup occurring in narrow fuel channels with a single non-fuel superhydrophobic-coated rod. Figure 6.6 displays a top view of our 2x2 simulated fuel cell array and shows how our experiment will

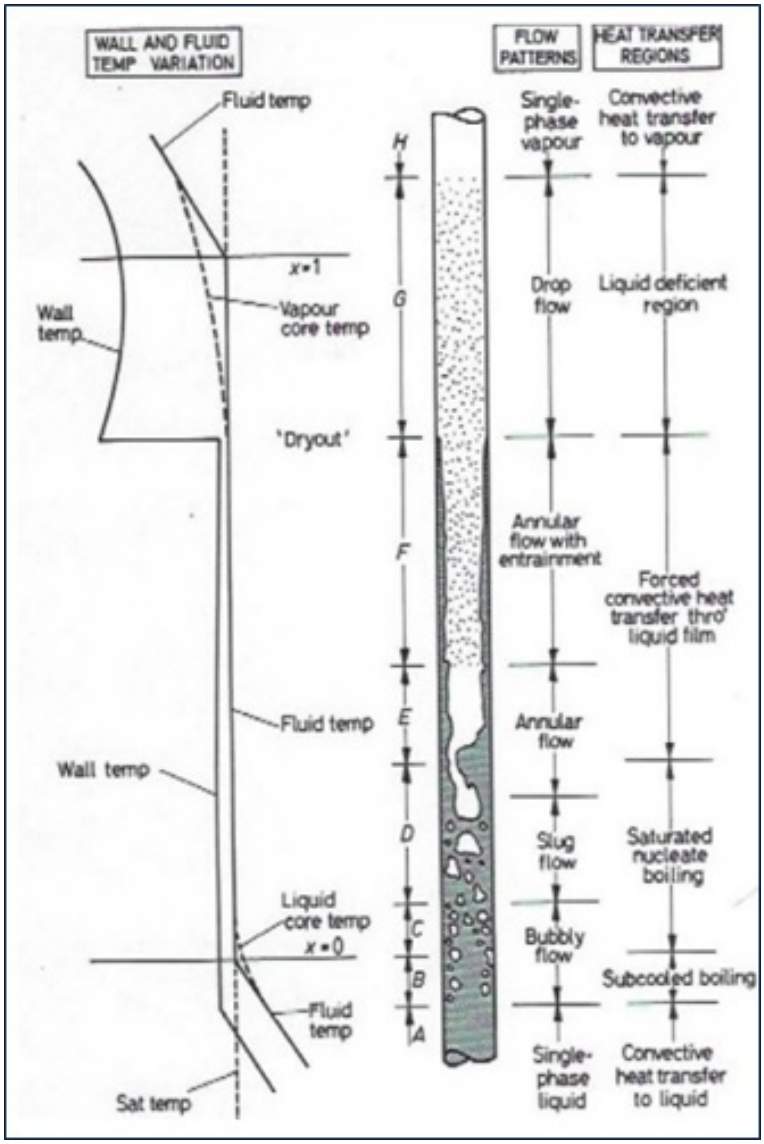

Figure 6.5: Flow Boiling Regime (Collier and Thorne, 1994)[8]

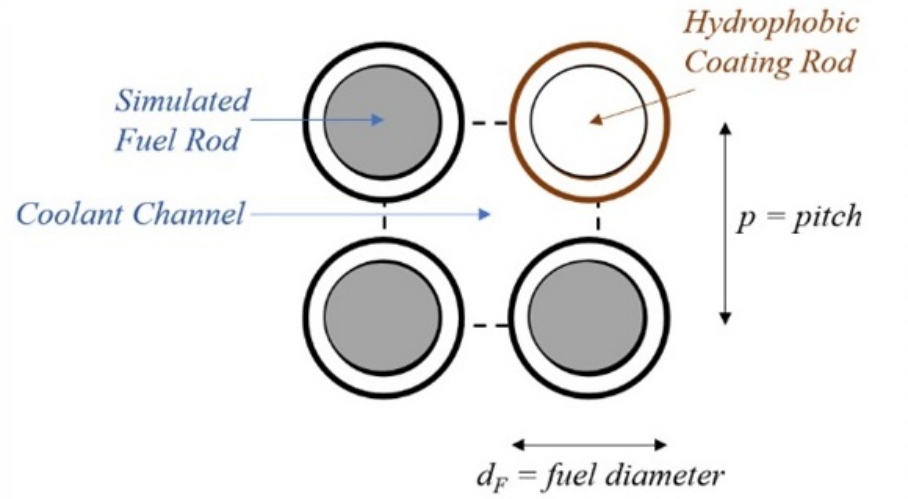

Figure 6.6: Fuel Cell Assembly with Hydrophobic-coated Rod (Top View)

use a superhydrophobic rod to substitute a fuel rod. We will evaluate the impact that one coated rod will have in bubble dynamics and localization of local void areas. We will also look at different rod configurations to evaluate the impact that both superhydrophobicity and geometric constraints have on gas holdup. We will later show how a single-coated rod comparison with a non-coated rod proves our hypothesis.

Because of the relative low density of steam compared to liquid water, the steam vapor phase is called a void. Void fraction, α, is defined as the ratio of local vapor volume to the local flow volume. Under normal Pressurized Water Reactor operating conditions, the mass flux is 2800 $\frac{kg}{m^2-s}$. At this flux, and with the water properties found at a particular Pressurized Water Reactor temperature, dispersed flow is expected in developing hot channels. At lower velocities, bubble and churn flow is expected. During a Loss of Coolant Accident (LOCA), you may encounter annular flow. Figure 6.7 displays 5 types of flow patterns of bubbly flow. Our research will focus on bubbly and dispersed flow primarily and will focus on the transition from bubbly flow to slug flow or churn flow based on the achieved bubbly flow conditions and introduction of hydrophobic internal modifications.

Figure 6.8 displays a qualitative view of void fraction in the boiling regime. In Region I, where the bulk of the liquid is still subcooled, the void is a thin layer attached to the wall. In Region II, where subcooling is low, void fraction increases and bubbles are detached from the wall and recondensed very slowly. In Region III, the bulk liquid has reached saturation and bulk boiling occurs. When nucleate boiling occurs, heat fluxes may increase up to a point where heat fluxes reached a maximum heat flux, referred to as the Critical Heat Flux (CHF). At CHF, the temperature gradient corresponds with an excess temperature value of

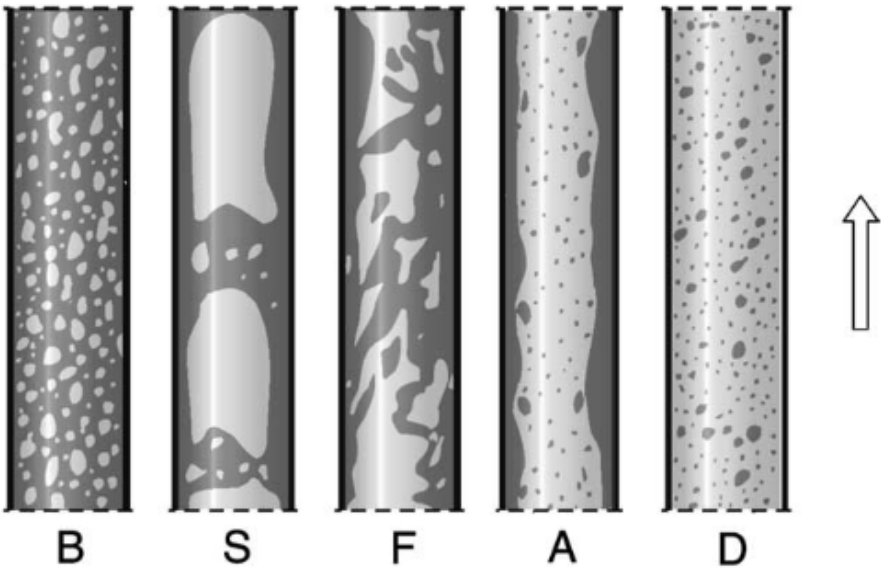

Figure 6.7: Basic flow structures in vertical upward flow: B-bubble flow, S-slug flow, F-froth flow, A-annular flow, D-dispersed flow (Dziubinski, 2003)[11]

30°(Bejan, 2004)[4].

6.1 Rod Configuration Studies

Hosokawa, from Kobe University, published an article in the Journal of Nuclear Science and Technology, titled: Void Distribution and Bubble Motion in Bubbly Flows in a 4x4 Rod Bundle. The distribution of local void fraction and bubble velocity in each subchannel in a 4x4 rod bundle were measured using a double-sensor conductivity probe. The superficial gas velocity and liquid velocity ranged from 0.06 to $0.15\frac{m}{s}$ and from 0.9 to $1.5\frac{m}{s}$ respectively[14].

Experimental results showed that the distributions of void fraction in inner and side channels depend not only on lift force acting on the bubbles but also on the geometrical constraints on bubble dynamics, i.e. the effects of rod walls on bubble shape and rise velocity. Figure 6.9 displays a cross section of the experimental apparatus utilized by Hosokawa et al. Air and tap water at atmospheric conditions were used for gas and liquid phases. Air was supplied to a channel box using a pressure regulating valve, a flow meter and a circular plate with pores that generated 1 to 5mm diameter spherical-equivalent bubbles. Water was supplied to a tank in the lower section from four different branch pipes. Sixteen rods of 10mm outside diameter and 800mm in length were installed in a channel box in a 4 x 4 square lattice arrangement with a 2.5mm gap between adjacent rods.

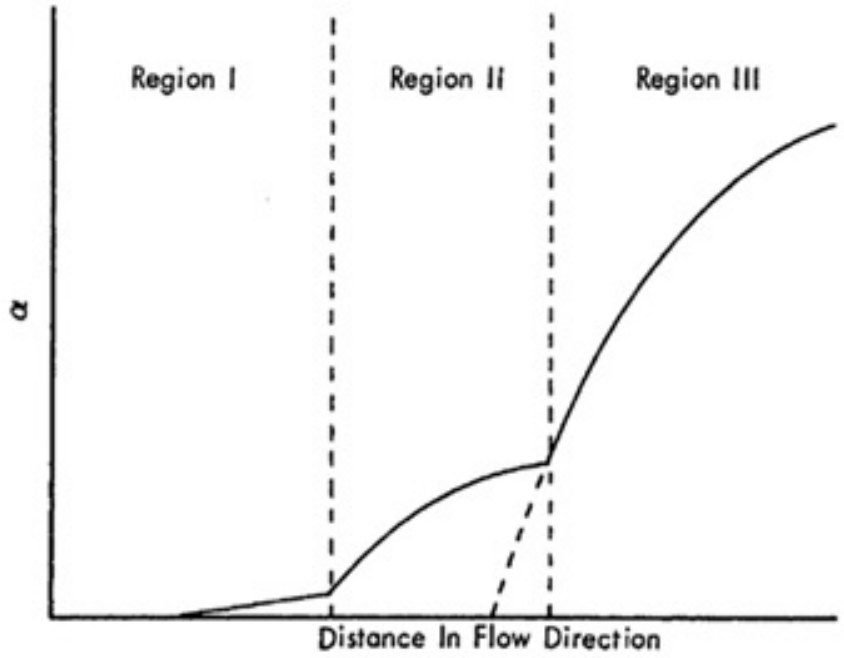

Figure 6.8: Void Fraction in Boiling Region (Tong and Weisman, 1996)[44]

Figure 6.10 shows that void fraction in the side and corner subchannels take lower values than those in inner subchannels. The distribution in the inner subchannels are wall-peaking in all cases. Bubbles tend to accumulate near the rod surface except for the gap region. Figure 6.11 shows the shape of bubbles in the side subchannel. The bubble, located near the rod wall, is elongated in the axial direction due to the presence of the wall and the lift force directed towards the wall[14].

6.2 Characterization of Bubble Size and Dynamics

Our research will focus on evaluating bubbly flow to more physically mimic coalescing vapor bubbles in a departure from nucleate boiling approach. This flow will also allow us to differentiate bubble regimes using measurement techniques provided through wire mesh sensors, high speed cameras and primarily X-ray CT.

Figure 6.12 displays bubbles of typical diameters that we will encounter in the evaluated flow regimes. These bubbles are not spheroid but ellipsoid or oblate spheroids. The majority of these bubbles either zig zag or spiral as predicted by several experiments and theories discussed by Saffman [34].

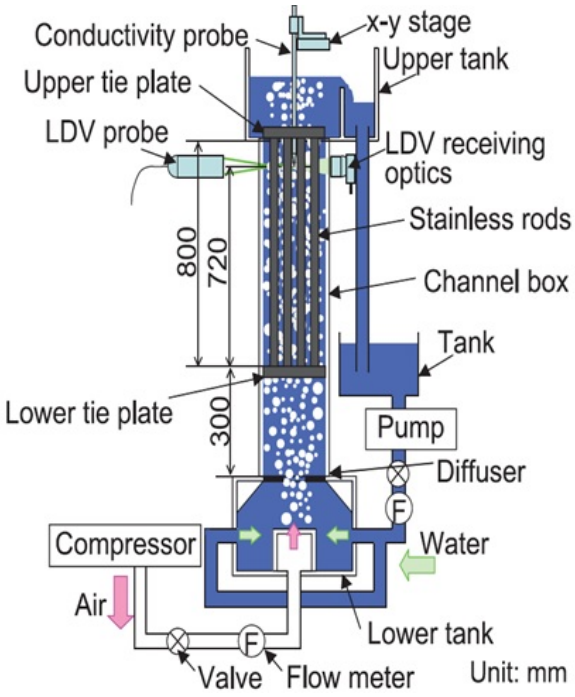

Figure 6.9: Experimental Apparatus (Hosokowa, 2013)[14]

We calculated the dimensionless equations to verify the bubble type which then allows us to figure out the forces that control the dynamics of their movements under hydrostatic pressure, interfacial stresses and surface tension. The highlighted box in Figure 6.13 displays the area where the bubble regime of interests resides for our research given the values for the dimensionless equations of Bond number, Morton and Reynolds number, summarized in Table 6.1. The following summarizes the definition of each dimensionless number with their corresponding equation.

- Eotvos number: relates the importance of gravitational force to surface tension force

$$E_o = \frac{g\Delta\rho d_e^2}{\sigma} \tag{6.1}$$

- Morton number: works with the Eotvos number to characterize the shape of bubbles in a continuous phase

$$M = \frac{g\mu^4\Delta\rho}{\rho^2\sigma^3} \tag{6.2}$$

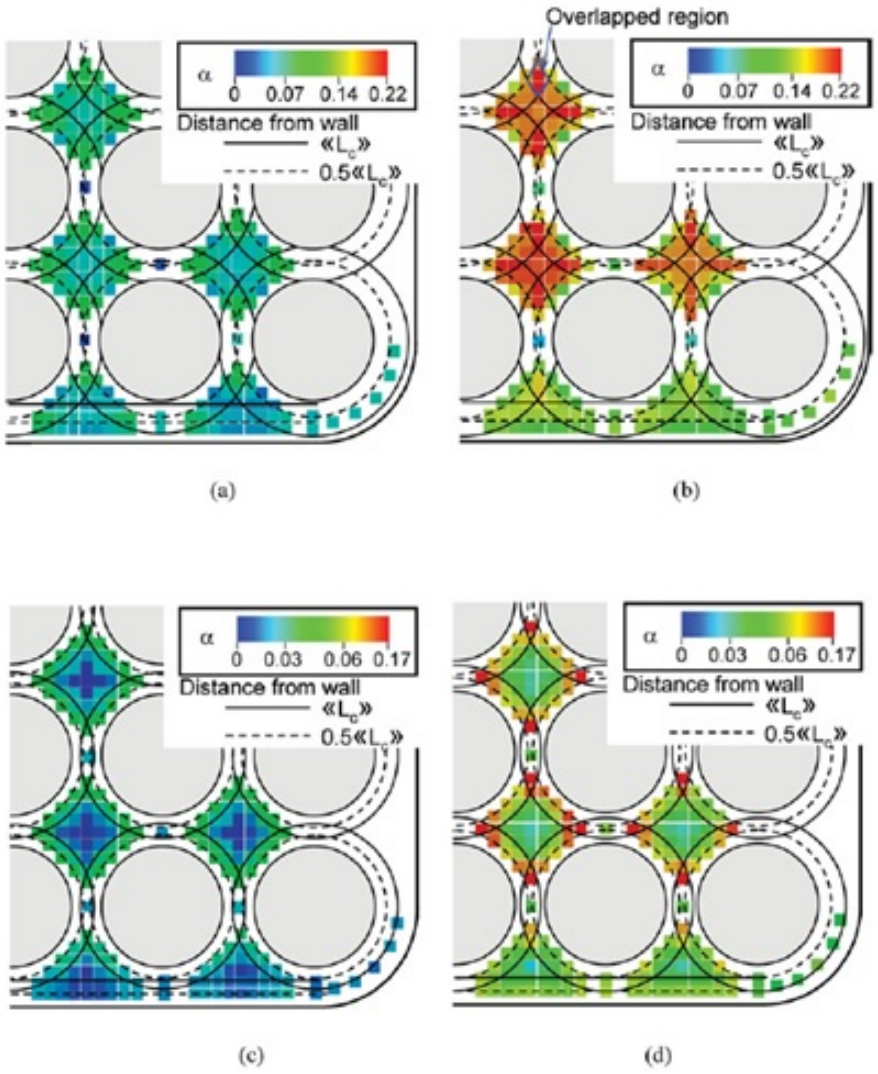

Figure 6.10: Void distributions. (a) Case 1: $J_L = 0.9$m/s, $J_G = 0.06$m/s;(b) Case 2: $J_L = 0.9$m/s, $J_G = 0.15$m/s; (c) Case 3: $J_L = 1.5$m/s, $J_G = 0.06$m/s;(d) Case 4: $J_L = 1.5$m/s, $J_G = 0.15$m/s (Hosokowa, 2013)[14]

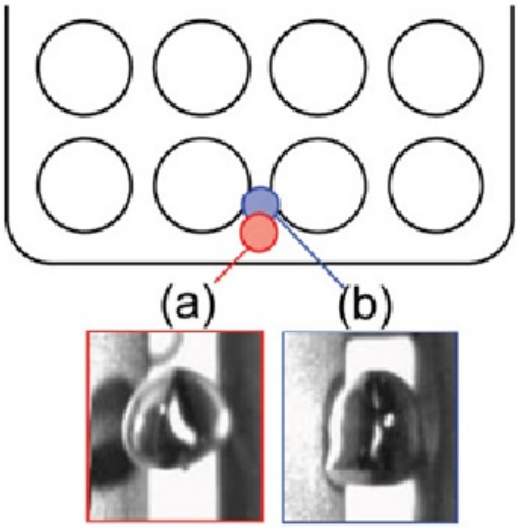

Figure 6.11: Bubble elongation in the presence of walls (Hosokowa, 2013)[14]

- Reynolds number: importance of inertial forces to viscous forces

$$Re = \frac{\rho d_e u}{\mu} \tag{6.3}$$

De(mm)	Eo	M	Re	U_{t-calc} (m/s)	$U_{t-image}(m/s)$
3.33	1.49	$5.23x10^{-11}$	499	0.118	0.15
7.33	7.20	$5.23x10^{-11}$	1390	0.175	0.19
5.35	3.83	$5.23x10^{-11}$	977	0.149	0.18
10.00	13.39	$5.23x10^{-11}$	2196	0.204	0.22

Table 6.1: Typical bubble properties encountered in the Bubble Column experiment

Figure 6.13 is used to estimate terminal velocity as well as the bubble regime. This figure is a useful tool to evaluate the specific characteristics that apply to different flow regimes. The following form of bubble terminal velocity has been suggested by Clift et al.[7]:

$$U_T = \left[\frac{2.14\sigma}{\rho d_e} + 0.505 g d_e\right]^{\frac{1}{2}} \tag{6.4}$$

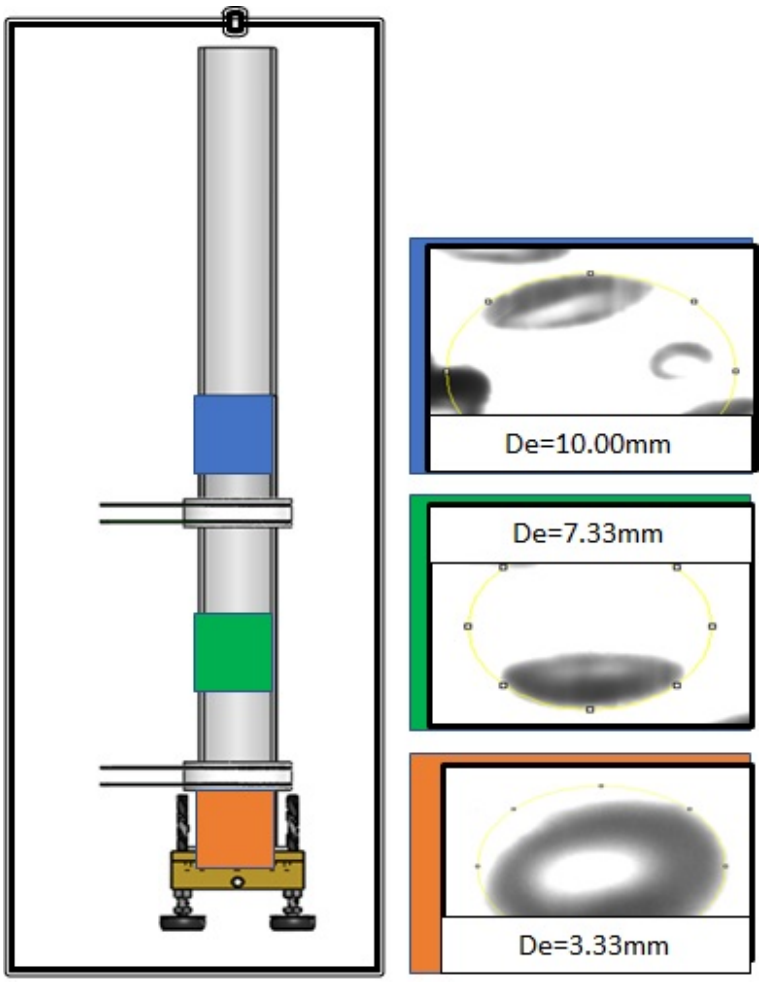

Figure 6.12: Expected Bubble Types with expected equivalent diameters

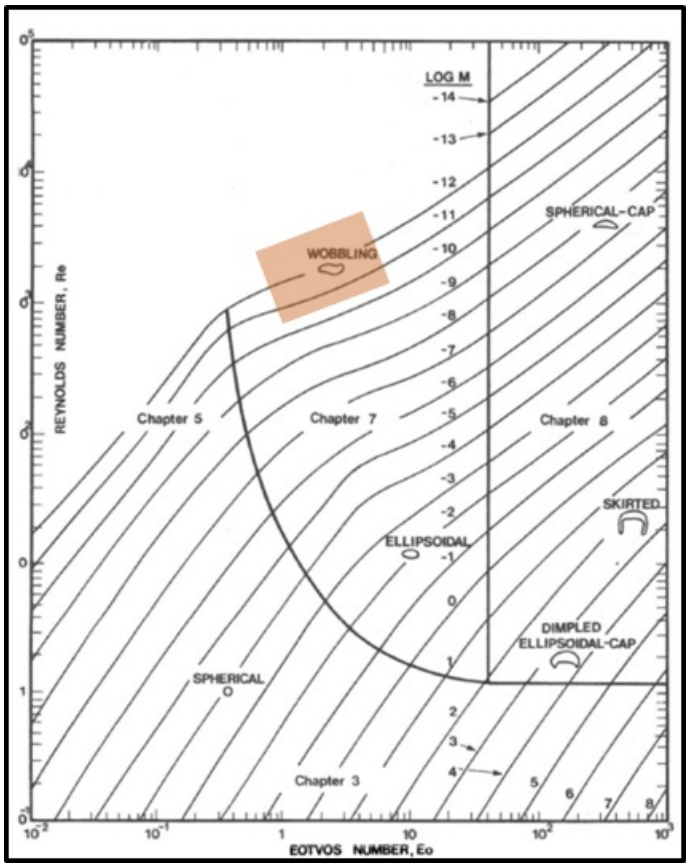

Figure 6.13: Expected Bubble types based on Eotvos, Morton and Reynolds numbers (Clift,2013) [7]

6.3 Submerged Superhydrophobicity Studies

Superhydrophobicity is a type of wetting circumstance where drops on a coated-surface assume a nearly spherical shape and are very mobile and bubbles spread due to the interaction between the air bubble and the air layer along the superhydrophobic surface plastrons. Surface contact angles with angles greater than 90° are hydrophobic. When the contact angles increase above 150°, the surface is called superhydrophobic. Anti-wetting is the most important attribute of a superhydrophobic surface. Superhydrophobicity requires a combination of a hydrophobic surface chemistry with a pronounced micro and nanoscale roughness. Some superhydrophobic surfaces are so water-repellent that the surface structure is not penetrated by liquid upon submersion; i.e. they retain air when submerged. This hold up at the air layer is overcome at a particular liquid pressure when the liquid can push deeper into the structure when the Laplace pressure prevails over capillary forces. The Laplace pressure is

the theoretical pressure difference between the inner and outer portions of a curved surface, which has formed a boundary between two fluid mediums. When some superhydrophobic surfaces are submerged into water, it is possible to observe a silvery mirror-like sheen on the submersed surface. This is due to the reflection of light from a sheathing layer of air retained at the surface.

Figure 6.14 shows the Cassie-Baxter state which defined the superhydrophobic state of a water droplet on a surface. When the surface is submerged in water, the figure displays a silver reflection that is caused by the presence of an air layer along the surface of the grooves on the surface.

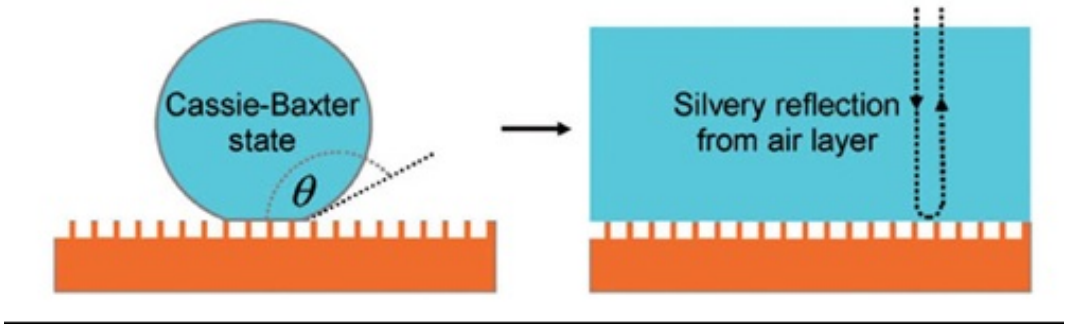

Figure 6.14: Schematics of (a) a droplet in a Cassie-Baxter state on a superhydrophobic surface in air (b) an immersed superhydrophobic surface with a silvery reflection from a plastron (McHale, 2010)[25]

Several studies have evaluated superhydrophobicity of objects immersed in water(McHale[25], Shi[42] and Valkereski[45]). Superhydrophobicity is either introduced by an applied polymer coating or manufactured to fabricate a surface that includes the necessary roughness features to promote superhydrophobicity. In a 2015 study conducted by Shi et al, a sequence of fast speed camera images were collected and played back to show spreading of an air bubble on a superhydrophobic-coated surface laying at the bottom of a water-filled tank. Figure 6.15 displays still images captured from 5,000 frames per second. These still images, starting from top left to bottom right, show a bubble being pushed from a needle onto a flat plate coated with superhydrophobic coating. The bubble makes its way out of the needle as expected, when it overcomes hydrostatic forces on the air to water interface. As the bubble is released onto the flat surface, the bubble spreads across the flat surface, which contains an air layer, separating the surface from the water[42].

Another study involves a high-speed camera snapshot of a 10mm radius steel sphere immersed in a liquid with various surface modifications held at 95° C water temperature of identical levels of air supersaturation. Figure 6.16(a) includes a plasma-cleaned hydrophilic

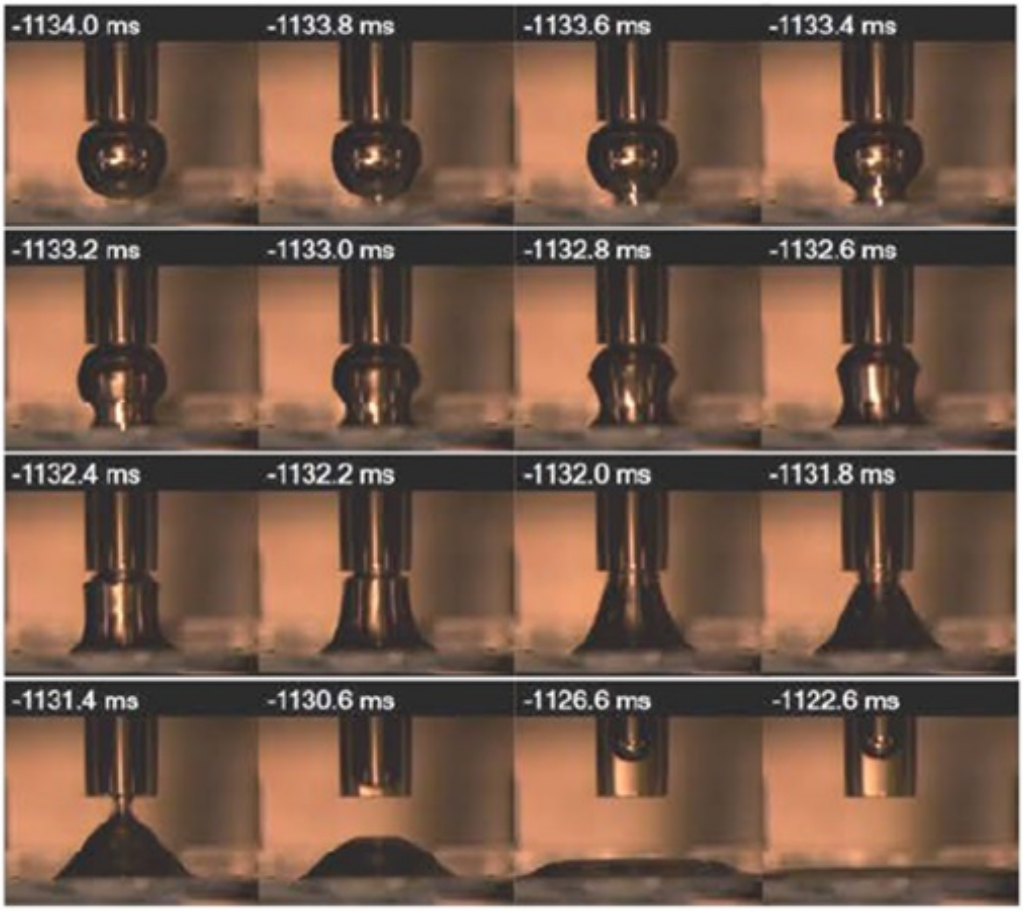

Figure 6.15: Sequence of fast speed camera images show spreading of an air bubble on a superhydrophobic-coated surface in water (5000 fps) (Shi, 2015)[42]

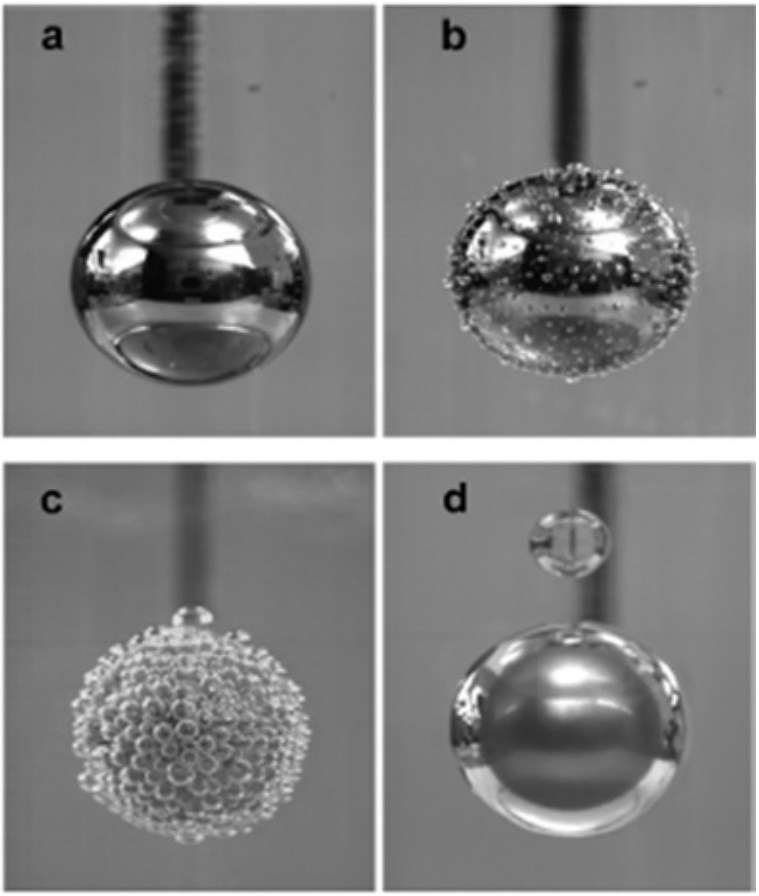

Figure 6.16: a) plasma-cleaned hydrophilic sphere, b) organic solvents only cleaned weakly hydrophilic sphere, c) hydrophobic sphere and d) superhydrophobic sphere (Vakarelski, 2013) [45]

sphere. The sphere has an affinity to water. Figure 6.16(b) involves an organic solvents-only cleaned weakly hydrophilic sphere. You notice the debris that builds on the sphere. Figure 6.16(c) includes a hydrophobic sphere where you can clearly see the affinity to air bubbles as they coalesce around the steel sphere. Figure 6.16(d) includes an image of the steel sphere coated with superhydrophobic coating with a strong affinity to air. The silvery layer is the air layer around the sphere, which is typical of objects covered with superhydrophobic coatings. The coated sphere is not touching the water. The same characteristics is observed for all superhydrophobic objects immersed in water. This is a characteristic that will become helpful as we continue our research and are always looking at methods to ensure the immersed surfaces remain superhydrophobic (Vakarelski, 2013) [45].

In order to conduct a quick evaluation of the phenomena of superhydrophobicity charac-

teristics immersed in water, we placed a superhydrophobic-coated plastic cylinder of 19mm in diameter into the water-filled bubble column and performed a series of void fraction calculations using height differences to evaluate the effectiveness of superhydrophobic surfaces on the bubble column's void fraction calculations at variable air injection rates. Figure 6.17 shows a non-coated plastic cylinder immersed in the bubble column. Figure 6.18 shows a superhydrophobic-coated cylinder immersed in the bubble column with a visible air layer, substantially different than the non-coated cylinder.

Figure 6.17: Non-SHS Plastic Cylinder Immersed in Water

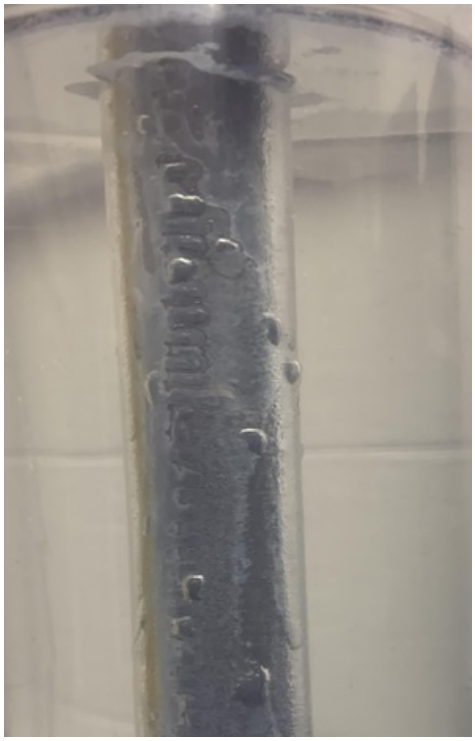

Figure 6.18: SHS-coated Plastic Cylinder Immersed in Water

Figure 6.19 shows eight measurement runs conducted to evaluate how effective a single superhydrophobic-coated cylinder is against the void fraction values obtained at variable air injection rates. The first four runs were conducted on non-coated cylinders immersed in a bubble column where air injection rates were varied from 1 SLPM to 16 SLPM. The second set of four runs were conducted on a superhydrophobic-coated cylinder immersed in the bubble column where air injection rates were varied from 1 SLPM to 16 SLPM. Figure 6.19 displays the calculated void fractions using height differences with an accuracy of 0.25 inches. All four measured void fractions from a non-coated cylinder were higher than all the four measured void fractions from our SHS-coated cylinder runs. The void fraction measurements for superhydrophobic runs were 30% lower. These results were favorable towards our hypothesis and allows us to continue to pursue this phenomena to gain an

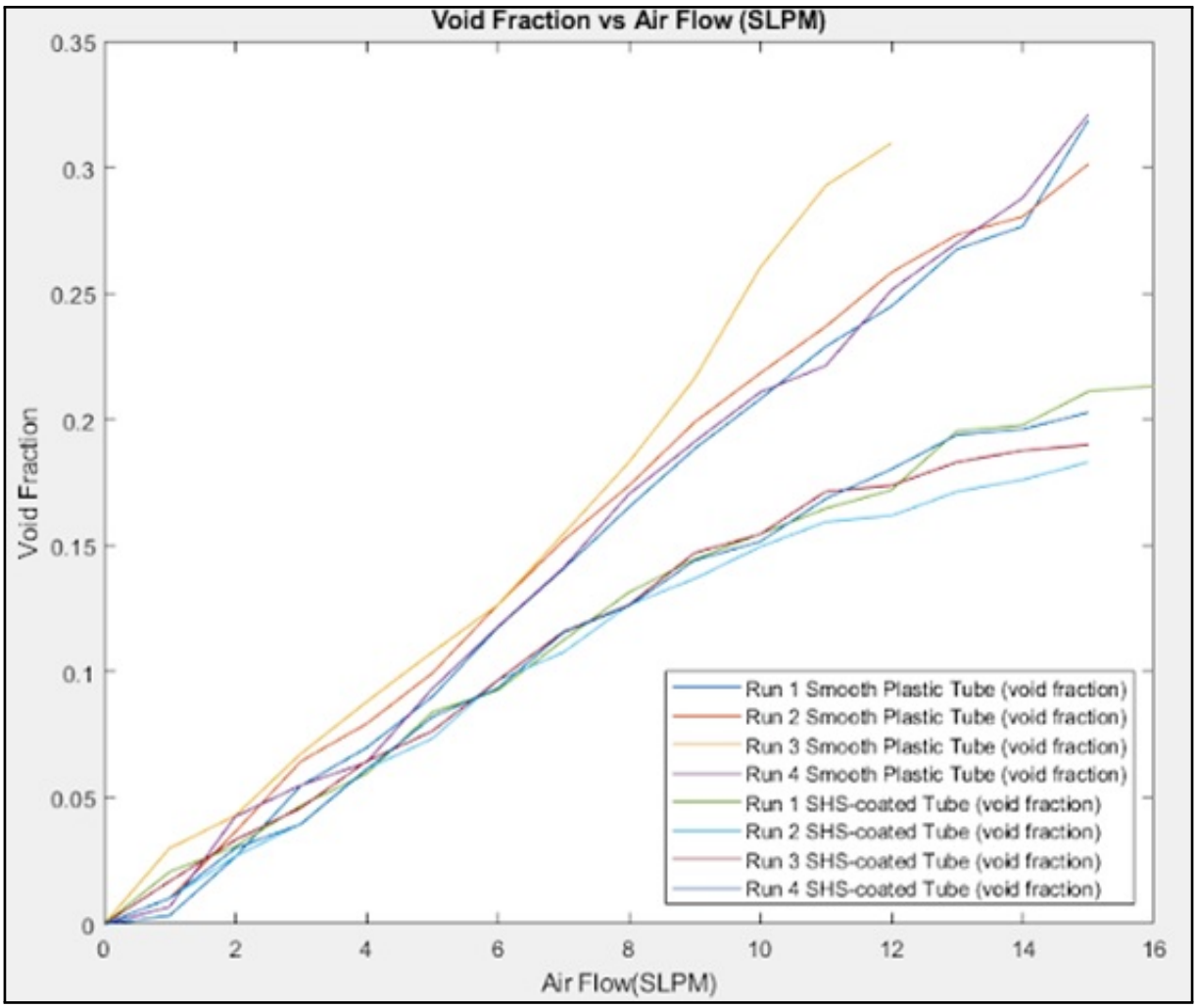

Figure 6.19: Void Fraction vs Air Flow(SLPM) for Superhydrophobic Coating and Smooth Surface Plastic Tube (void fraction calculated by height variation method)

understanding of the bubble dynamics that are occurring in this flow regime.

Figures 6.20 and 6.21 display a still image captured at 50 frames per second of the bubble column with a 16 SLPM air injection rate and superficial gas velocity of $0.055\frac{m}{s}$ with a non-coated and SHS-coated cylinder immersed in the center of the bubble column, respectively. Figure 6.20 shows the expected dispersed flow of the air bubbles as they accumulate and interact with one another within the geometric constraints of the bubble column wall and the immersed non-coated plastic cylinder. The calculated void fraction was estimated at 0.3. Figure 6.21 displays a different flow due to the reduced void fraction that exists because of

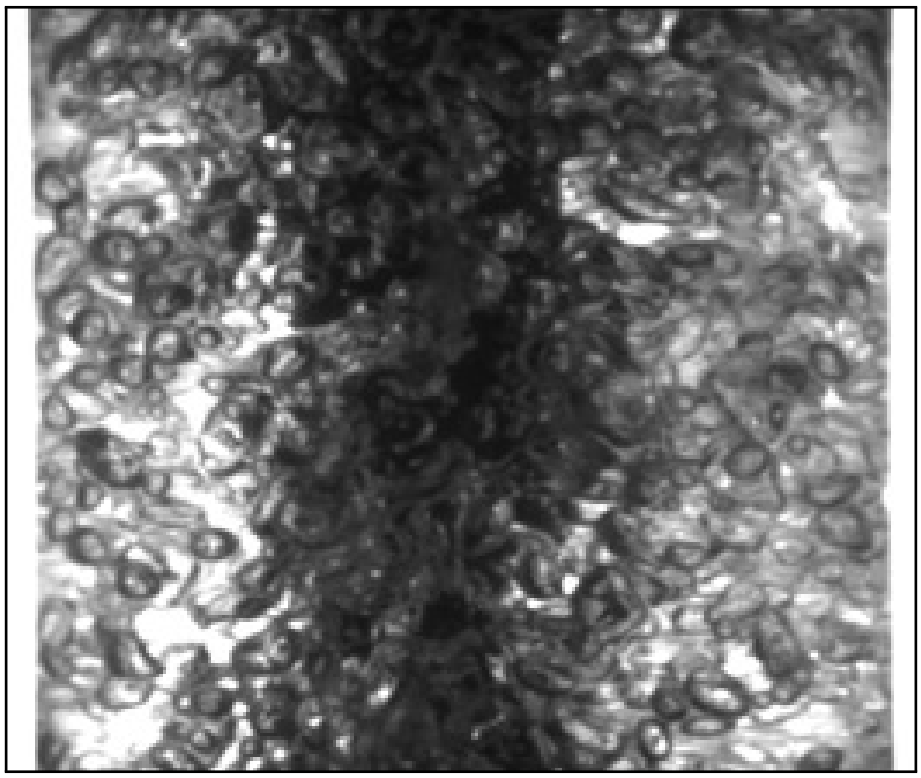

Figure 6.20: Non-SHS Coating Plastic Tube (Superficial Gas Velocity = 0.0545m/s)

what we suspect are characteristics introduced by the superhydrophobic coating applied to the plastic cylinder. The bubbles appear larger than the non-coated case due to coalescing along the plastic cylinder until buoyancy forces detachment of the bubble from the cylinder wall or the bubbles escape to the free surface and no longer migrate towards the liquid medium. We also noticed that the bubbles migrate towards the coated cylinder which we assess provides a larger escape route to bubbles and therefore lowering the void fraction. The void fraction calculations for the SHS-coated cylinder averaged at 0.2, considerably lower than 0.3 from the non-coated situation.

6.4 Bubble Column Fuel Rod Configuration Explanation

We built the bubble column, displayed in Figure 6.22, to evaluate fuel cell assemblies in a multiphase flow system with the ability to monitor bubble dynamics visually to validate our measurements performed using wire mesh sensors and X-ray computed tomography. The

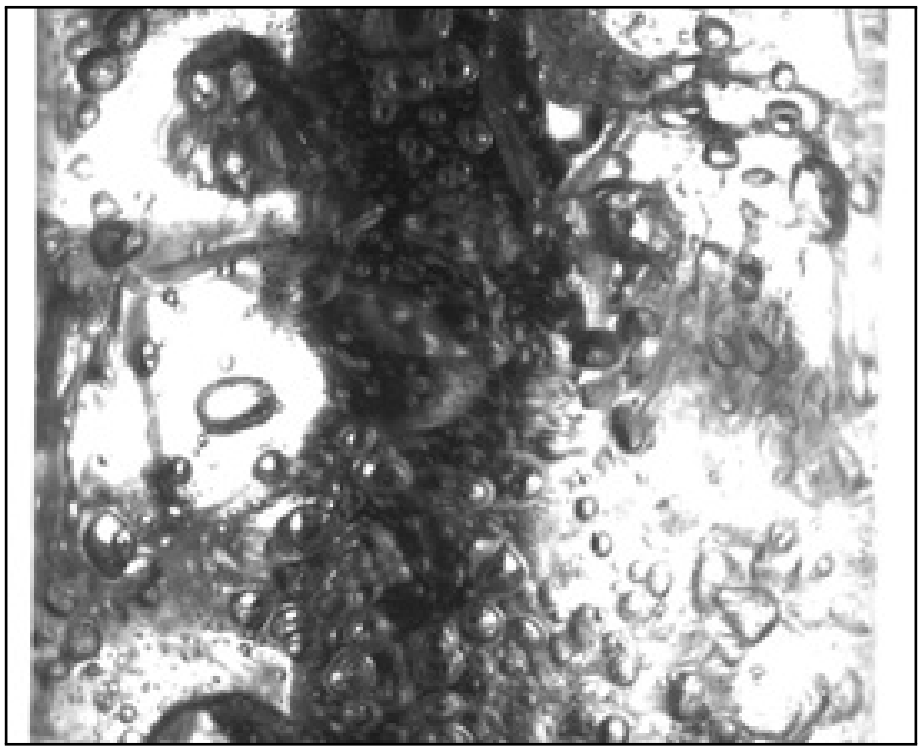

Figure 6.21: SHS-Coated Plastic Tube ((Superficial Gas Velocity = 0.0545m/s)

bubble column contains a differential pressure transducer, wire mesh sensors (2 pairs) and two brass plates (one with 800 holes 0.008in ID and one for variable needle adjustments). We will not generate vapor bubbles but will generate bubbles using constant air injection provided through an air filter and controlled by an adjustable ALICAT flow meter. Void fraction estimates from X-ray computed tomography measurements are validated against void fractions calculated by height differential, differential pressure transducer and wire mesh sensors.

Our overall research goal is to evaluate the void fraction within variable rod bundle configurations. This research should yield void fraction estimates in a 2x2 bundle array where one tube will be coated with SHS-coating polymer and show through five measurement techniques of void fractions how the void fraction value and lateral distribution is modified due to the presence of a coated SHS-tube. We will then take those results to evaluate the parameters that influence the superhydrophobic effects on gas holdup.

We will start characterizing bubbly flow in the configuration displayed in Figure 6.23 by using height difference, differential pressure detectors, wire mesh sensors and finish with X-ray intensity variation and computed tomography. Our main focus is to evaluate spatial resolution and limitations of the measurement techniques with variable rod configurations

along with incremental changes in air injection rates. Rod fuel cells will be simulated for the sake of evaluating geometrical constraints on gas holdup and continue to evaluate X-ray CT reconstruction techniques and algorithms.

Figure 6.22 shows how congested the system can get with high air injections, making the column opaque. Visual observations are unable to evaluate lateral void fraction distribution at high injection rates. Differential pressure transducers can also provide a method for void fraction calculations but are limited to localized measurements averaged between two pressure taps and do not capture lateral void fraction distribution. Our research hopes to show wire mesh sensors and X-ray computed tomography techniques that capture a lateral time-averaged void fraction distribution.

Figure 6.24 shows our plan of rod configuration that will be adjusted accordingly to evaluate geometrical contribution to wall effects on gas holdup. The experimental setup will include four cylinders that will mimic the geometrical constraints of a 2 x 2 fuel cell assembly. As in the actual fuel cell assembly, our experimental setup will allow for cross-flow between the rods. Our final 2 x 2 cell array configuration will be utilized for wire mesh sensor and X-ray CT measurements. Three of the four tubes will be maintained in its original state and a single rod will be coated with superhydrophobic coatings to achieve superhydrophobic characteristics. The typical fuel rod diameter is 10mm and the pitch between the rods is 12.5mm with approximate vapor bubble sizes of 1mm. Our simulated fuel rod is 21mm and the pitch is 28mm, which is commensurate to scaling the actual dimensions by 2.1 and fits our produced gas bubbles of 2.3mm diameter upon injection into the bubble column. These dimensions will allow comparison of the superhydrophobic-cylinder effects with the non-hydrophobic cylinder by scaling appropriately to evaluate spatial patterns.

Figure 6.24 displays the evolution of the rod configuration that we will utilize to build rod configuration complexities from 2 rods to 4 rods in one pattern. We will utilize wire mesh sensors to evaluate void fractions across a lateral field to investigate and differentiate effects driven by geometrical constraints and those caused by the change to an aerophilic surface.

Material Properties with Superhydrophobic Characteristics

As a point of discussion only and academic understanding of what type of material will be survivable in the harsh environments of nuclear reactors, we want to make a distinction between the nuclear reactions expected on a surface that is superhydrophobically-coated and a surface that is manufactured for superhydrophobicity. While our research doesn't address these items, we will specifically discuss here in detail the nuclear interactions expected with a material that will withstand the pressure and thermal gradients experienced in pressurized water reactors. Both materials are superhydrophobic, so we will specifically address neutron bombardment on both surfaces to explain the expected nuclear reactions. The material used during our research testing is a coated polymer. Although the polymer, NeverWet, used to achieve and maintain superhydrphobic properties can maintain stable temperatures up to $400^{\circ}F$, we will theoretically look at an actual hydrophobic material com-

Figure 6.22: Bubble Column Nominal Flow at Dispersed Flow

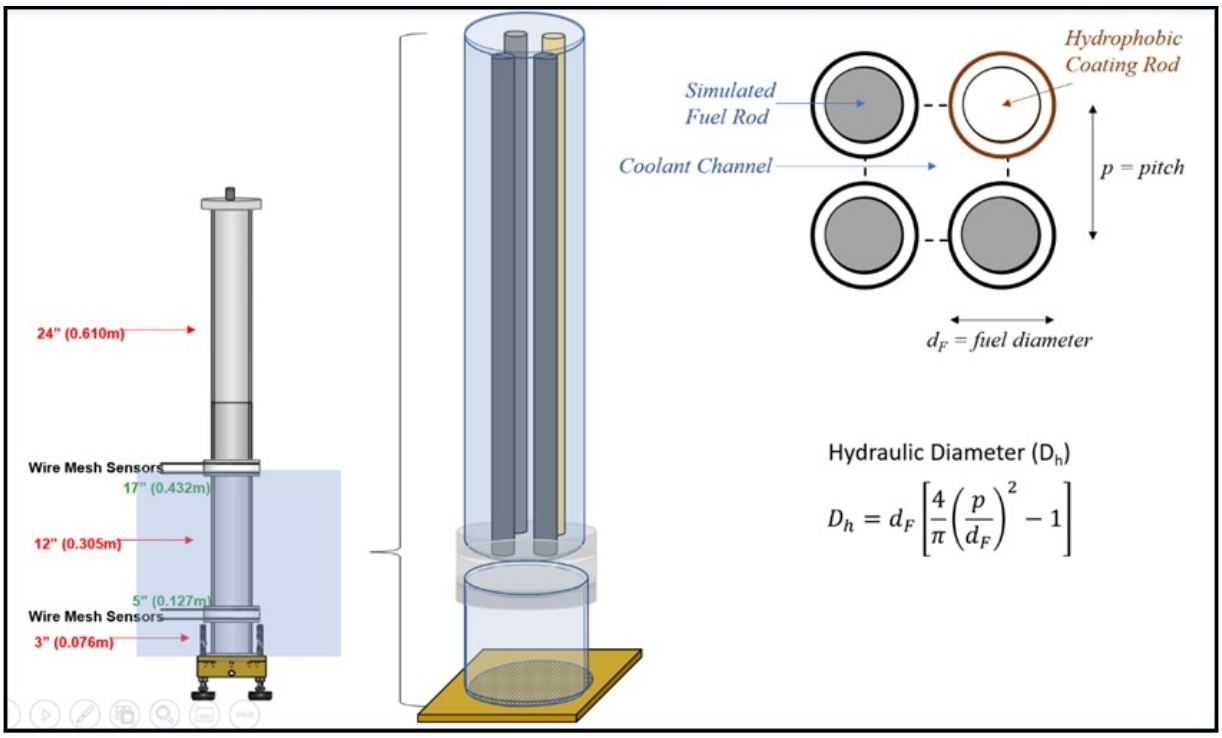

Figure 6.23: Bubble Column with installed tube bundle (3 simulated fuel cells and 1 super-hydrophobic coated rod

ponent found in a reactor vessel, designed to withstand the high pressure and temperatures found in a pressurized water reactor. These materials can act as a heavy reflector to protect itself efficiently from neutron embrittlement as well as providing superhydrophobic characteristics. Figure 6.25 displays the various metal components found in a typical nuclear reactor plant. Several internal components of a reactor vessel are made up from stainless steel. These reactor vessel components can be manufactured to gain superhydrophobic surface characteristics while maintaining the intrinsic characteristics of strength, durability and corrosion-resistance. Some of the methods to fabricate superhydrophobic surfaces on stainless steel include chemical etching, chemical deposition, electrochemical disposition and anodic oxidation process, sol-gel technique and laser processing [46].

The intended coating for research purposes is NeverWet. NeverWet is a polymer coating that can provide a contact angle of 160-175°. The chemical compound used in NeverWet is most likely comprised of heptadecafluorodecyltrimethoxysilame, with a molecular formula of $C_{13}H_{13}F_{17}O_3Si$. Aliphatic, fluorinated aliphatic or substituted aromatic hydrocarbon substituent are the hydrophobic entities which enable silanes to induce surface hydrophobicity. Silane is a common type of water repellent, derived from the silicone, Si, molecule. When

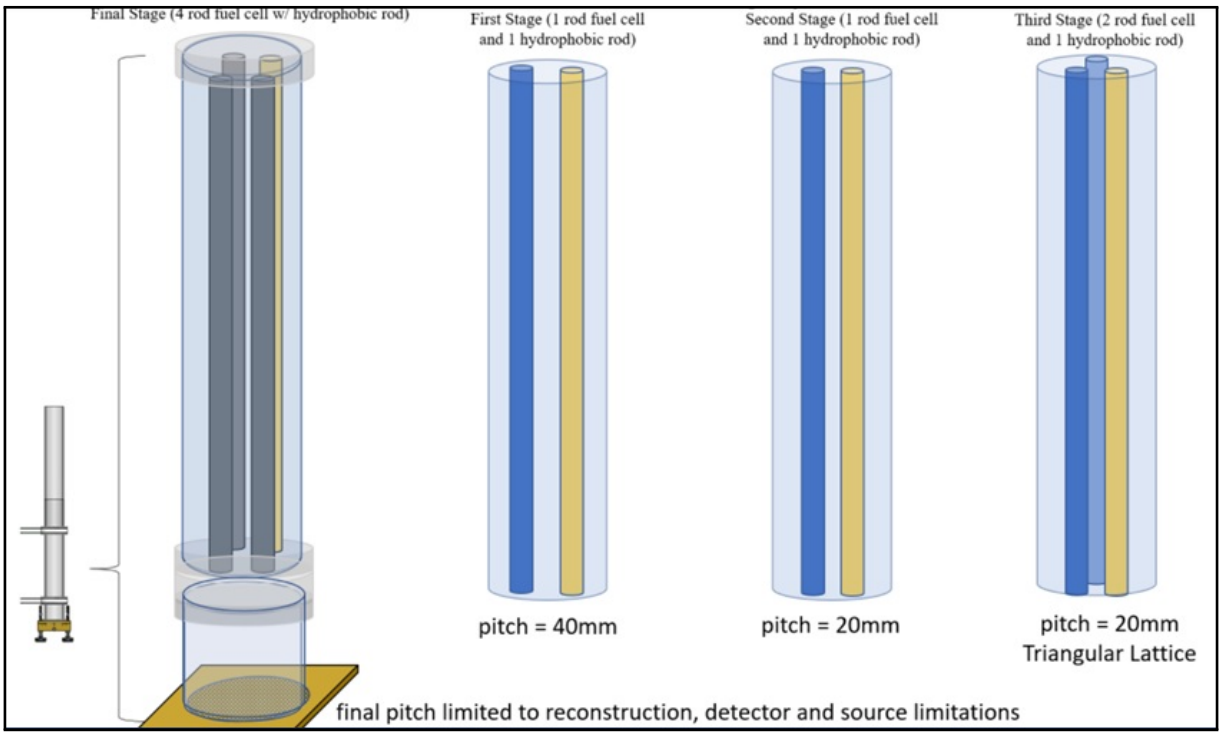

Figure 6.24: Bubble Column with installed tube bundle (3 simulated fuel cells and 1 superhydrophobic coated rod)

silane is applied, it reacts chemically with calcium hydroxide to form a hydrophobic, water repellent resin within the pores on the surface. The following nuclear reactions can be expected when the elements of Silicon and Fluorine are exposed to neutron bombardment (Fermi, 1934)[37]:

Silicon reactions:

$$Si_{14}^{28} + n_0^1 \longrightarrow Al_{13}^{28} + H_1^1 \tag{6.5}$$

Fluorine reactions:

$$F_9^{19} + n_0^1 \longrightarrow N_7^{16} + He_2^4 \tag{6.6}$$

$$N_7^{16} \longrightarrow O_6^{16} + e_1^0 \tag{6.7}$$

Superhydrophobic metals are important because of their applications in industrial settings, specifically for applications requiring self-cleaning, drag reduction and corrosion resistance. These types of features require a high static contact angle combined with low droplet

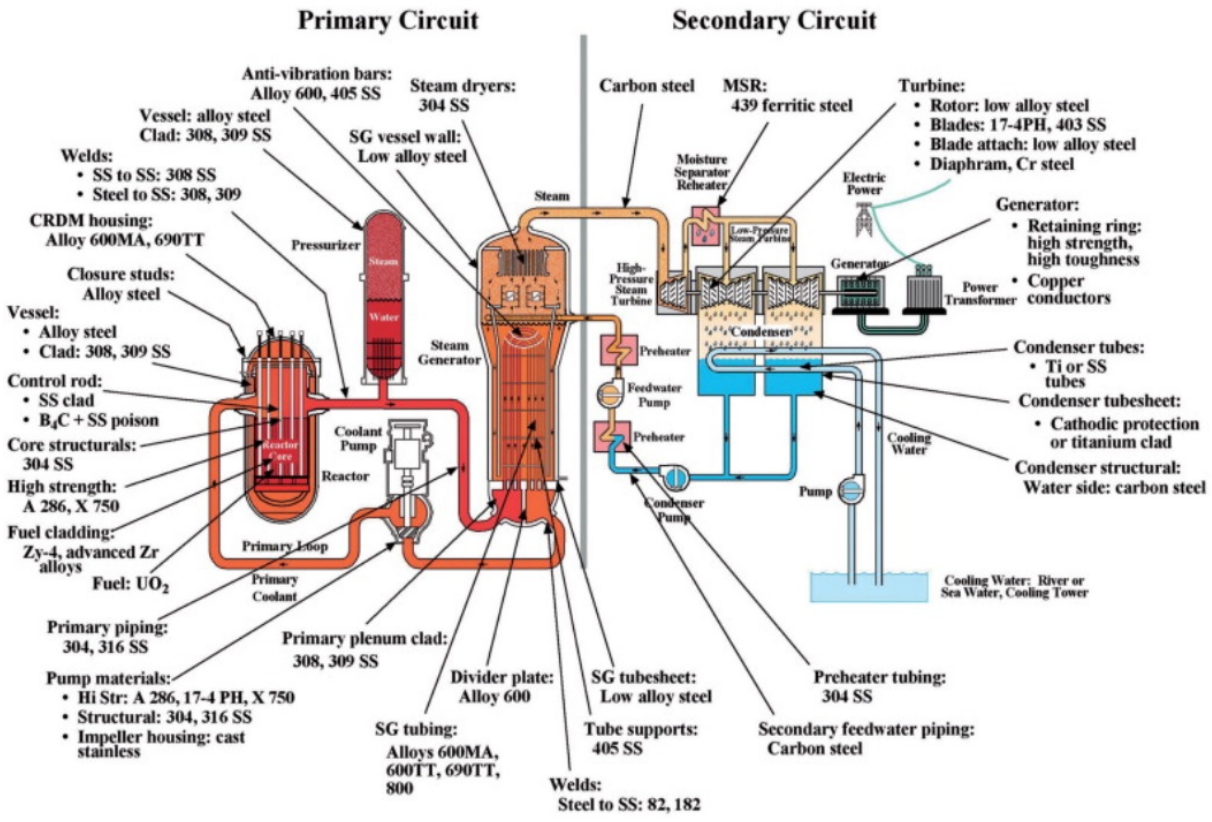

Figure 6.25: Reactor Vessel Metallic Components (Allen, 2010)[2]

adhesion. Copper, aluminum, titanium and numerous metallic alloys have been surface-modified to attain a superhydrophobic condition. To achieve these conditions, a surface roughness at a proper length scale must be used with a low surface energy. These techniques include electroless deposition, sol-gel methods, and anodization (Li, 2012)[22].

Stainless steel, which can be modified for superhydrophobicity, has been used substantially in nuclear reactor components due to its anti-corrosion properties. It is a useful combination of high corrosion resistance with excellent metallic strength. The main processes that involve fabrication of superhydrophibic stainless steel is ablation with a femtosecond laser used to create the necessary surface roughness. Other processes include coating of a stainless steel surface with another material to add roughness, but these coatings lack mechanical durability.

One study, conducted by Li et al, particularly looked at selective etching of amorphous phase of cellulose in an oxygen plasma while leaving the crystalline phase, creating a roughness at the required scale. The key advantage in this process lies in generating a roughness

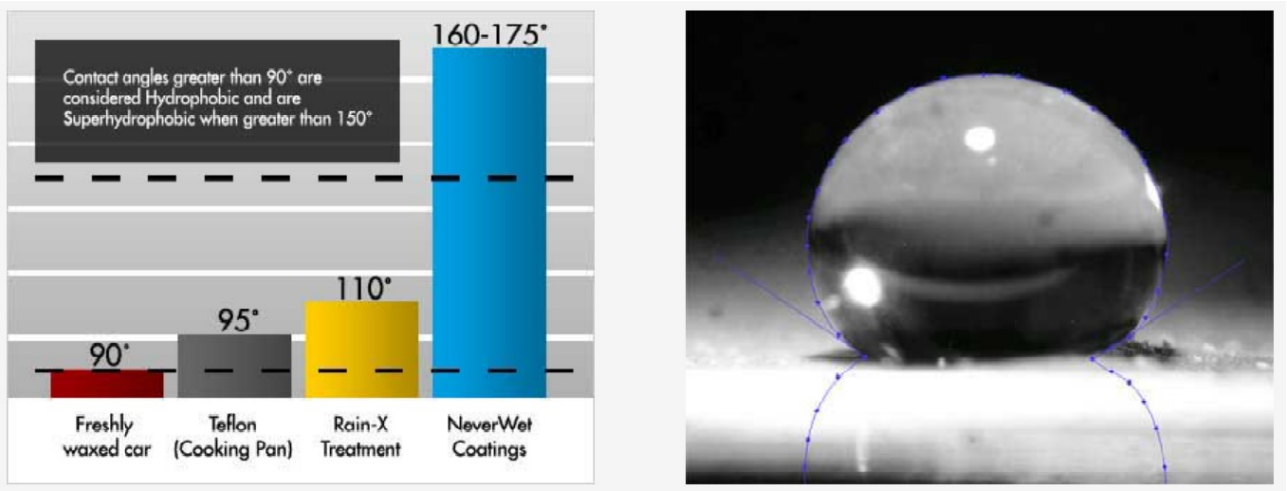

Figure 6.26: a) Degrees of Hydrophobicity. b) Contact Angle (NeverWet Whitepaper- https://www.neverwet.com/applications/productcharacteristics.php)

directly on the material vice adding it through deposition of particles or residue which tend to lack material durability (Li, 2012)[22].

Metal surfaces have a high surface energy, negatively charged and hydrophilic, which means it has a low contact angle. Polymers have low surface energy and are hydrphobic. Hydrophobicity is determined by contact angle. If the water spreads over the surface without forming a droplet, the surface is said to be hydrophilic. When the water beads on the surface, it is called hydrophobic. A contact angle is measured as the angle from the surface under the droplet to the edge of the droplet as displayed in Figure 6.24b by the purple lines.

Surface contact angles with angles greater than 90° are hydrophobic. When the contact angles increase above 150°, the surface is called superhydrophobic. Antiwetting is the most important attribute of a superhydrophobic surface. NeverWet coatings have been tested during long periods of exposure to temperatures up to 205°C ($400°F$) and temperature transients up to 288° C (550°F). The samples still remained superhydrophobic under these conditions. NeverWet coatings are applied by using sprays and the typical coating thickness is between 25-75 microns. NeverWet coatings can achieve contact angles between 160° and 175°.

Stainless steel is a term used to describe iron-based metals that contain $> 12\%$ chromium and have resistance to corrosive environments. Stainless steel alloy compositions vary greatly based on the desired application, with different mixtures for various corrosive resistance, hardening and mechanical strength (Li, 2012)[22].

Stainless steel is a heavy reflector that provides protection from irradiation embrittlement. The nuclear reactions associated with neutron bombardment of stainless steel are the

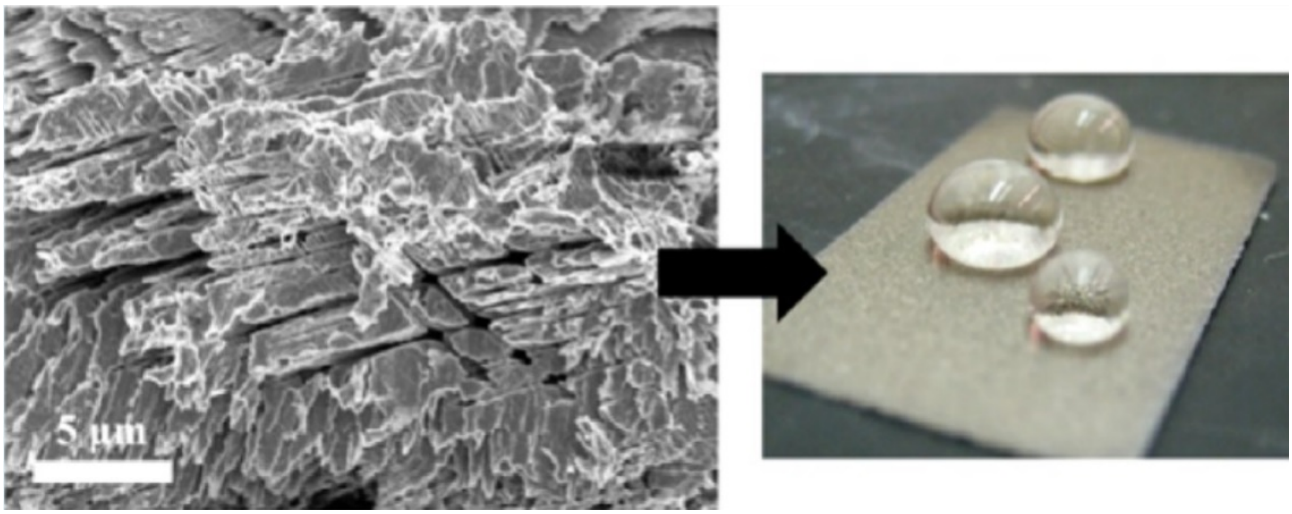

Figure 6.27: Superhydrophobicity on an Etched Stainless Steel surface (Li, 2012)[22]

following:

Iron reactions:

$$Fe_{26}^{56} + n_0^1 \longrightarrow Mn_{25}^{56} + H_1^1 \tag{6.8}$$

Chromium reactions:

$$Cr_{24}^{52} + n_0^1 \longrightarrow V_{23}^{52} + H_1^1 \tag{6.9}$$

The etching process involves selectively attacking grain boundaries through inter-granular corrosion, leading to the formation of micrometer and submicrometer scale roughness. By passivating the etched stainless steel, the advantageous corrosion resistance properties of the stainless steel material are re-established.

Figure 6.28 shows static contact angles, hysteresis, and mean roughness of 304 Stainless Steel etches with Hydrofluoric (HF) acid at $50°C$ as a function of etch time. This particular experiment shows that by etching stainless steel in HF acid, followed by passivation in nitric acid and fluoropolymer deposition, the technique demonstrates an ability to create superhydrophobic stainless steel surfaces that maintain corrosion-resistant properties of untreated stainless steel, while changing the wetting properties significantly.

X-ray Computed Tomography considerations

Understanding the geometry of our bubble column experiment and the desired resolution to differentiate bubbles, water and the material of the suspended tubes and bubble column

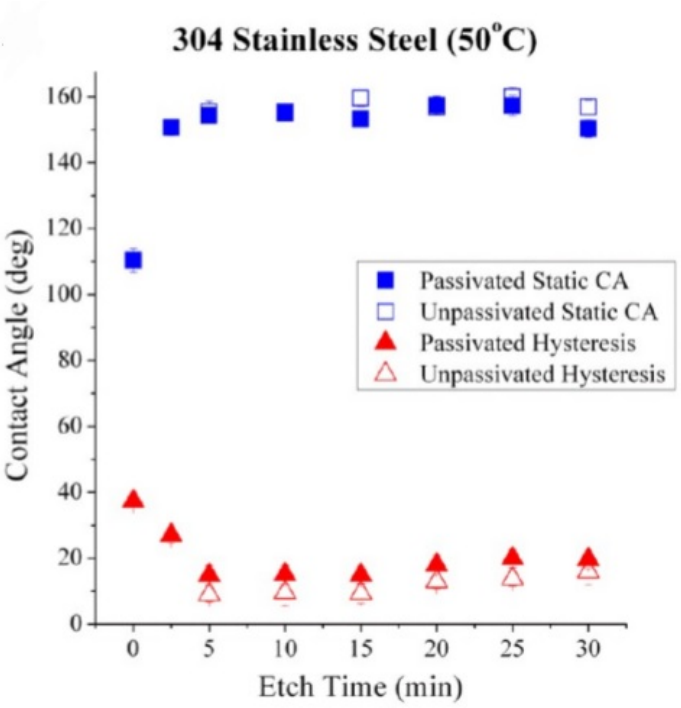

Figure 6.28: Static contact angles and hysteresis (Li, 2012)[22]

walls, we set up an experiment displayed in Figure 6.29. First, we assembled the flooring for the bubble column and detector linear stages. An optical table, measuring 1.83m x 0.3m, was leveled and mounted to the lab flooring to ensure experiments maintained stability. Other items added to ensure stability and proper leveling were Silicone adhesive/sealant into the space between the laboratory floor and the optical table, and aluminum shims to the table mounts, the linear stages and the four legs at the base of the bubble column.

The experiment was leveled to approximately 0.001 meters. Leveling the experiment will avoid reconstruction artifacts introduced by wobbling of the misaligned bubble column.

Secondly, we positioned the X-ray source, manufactured by YXLON, to allow flexibility in horizontal motion of the experiment and vertical motion of the source. To avoid any introduction of deflection, we mounted the X-ray source on an adjustable table, which was locked into position by external columns to prevent motion of the source. This setup maintains the source vertically adjustable without impacting the horizontal alignment of the source with the centerline path.

To collect sufficient projections, we installed linear stages and rotation stages to allow fine tuning of the detector and bubble column experiment. A linear stage is positioned under a rotation stage to allow movement of the experiment for collecting of flat field image

projections. The linear stages under the detector and bubble column also allows us to lineup the two items with the centerline of the X-ray source. The rotation stage under the bubble column is connected to a steel base board which holds the bubble column's weight and is perforated to allow zip ties to hold the bubble column legs and prevent horizontal motion during high air injection rates and repositioning for the collection of flat field images. The linear and rotation tables were leveled to within 0.1 degrees. The linear and rotation stages are operated from the operator's station via a National Instrument Labview program.

The Labview program controls operation of the rotation stage at a specified interval and provides the required external trigger for each increment. The Labview program allows incremental adjustments to fractions of an angle. Both rotation velocity and acceleration are set via the Labview program. Time delays are also programmed into the Labview program to ensure the rotation is complete before the X-ray source is triggered.

The THOR photon counter controls the number of frames collected and exposure rate once it receives the trigger signal from the Labview file. One single air hose of 0.5" inner diameter branches into four smaller hoses of 0.25" inner diameter to connect to four inlets positioned around the base of the bubble column. The large hoses branches into two hose which then branch into two other hoes of the same dimensions. The four hoses are connected to apply a uniform air injection to the chamber under the perforated brass plate.

The physical arrangement of the bubble column with respect to the X-ray source and detector are predicated on the principles of field of view magnification. The Source-Object, SOD, for our arrangement is 1180mm. The Object-Detector, OID, distance is 250mm. The Source-Image, SID, distance is 1430mm. The object magnification is the ration of SID to SOD, resulting in a value of 1.21. Since each pixel pitch is 100 microns, and a maximum of 2063 pixels lie across the detector active area horizontally, the inner diameter of the bubble column, 77.9mm, occupies 779 pixels. Our phantom was utilized to ensure this distance and magnification value was adequate to resolve a 1mm void area.

After evaluating our X-ray source and experiment against the magnification and resolution requirements, we evaluate the required X-ray source voltage and current to yield a sufficient photon flux to contrast the different materials in a single projection. The following equation characterizes the number of photons.

$$\frac{\#photons}{pixel} = 6x10^{10}\frac{photons}{KeVmAm^2} \cdot 100KeV \cdot 0.4mA \cdot (100x10^{-6}m)^2 \tag{6.10}$$

$$\frac{\#photons}{pixel} = 2.4x10^4 \tag{6.11}$$

Void Fraction Calculations

We can calculate phase fraction from X-rays by several ways each including different assumptions.

Option 1: If we assume monochromatic x-rays using our energy resolving detectors and only use data from a small range of energy such that a monochromatic source can be ap-

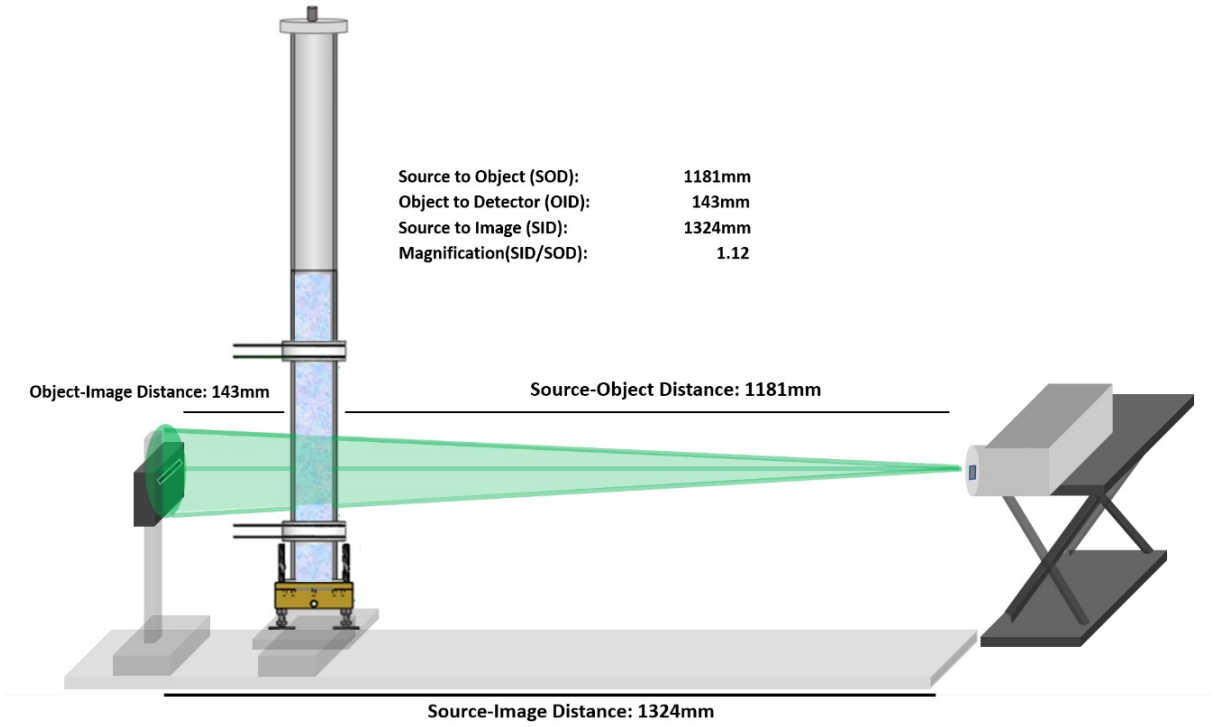

Figure 6.29: Bubble Column experiment setup with X-ray source and photon counter

proximated, we can then use 2D projections to calculate void fraction using the following equation:

$$\alpha = \ln \frac{\frac{I_m}{I_w}}{\frac{I_a}{I_w}} \tag{6.12}$$

where I_m is the intensity field for the projection of the mixture inside the bubble column, I_w is the intensity field for the projection of the water-filled bubble column, and I_a is the intensity field for the projection of the empty bubble column

We can then use a 2D projection with the Abel transform to provide a radial void fraction distribution, assuming a cylindrical and symmetric profile.

Option 2: We can reconstruct air, water and mixture CT scans and from the ratio of attenuation coefficients determine phase fraction. Note: if monochromatic or energy resolving detectors are used, then this should be straight forward. For polychromatic data with no energy resolution, we'll have 'effective attenuation coefficients'.

For monochromatic x-rays, we can utilize the following equation of attenuation maps to calculate the void fraction two-dimensional plot. The attenuation maps are comprised from

the attenuation coefficients gathered from the reconstruction of each medium. Using the appropriate geometry, these attenuation maps can be used in the following equation:

$$\alpha = \frac{\mu_{mixture} - \mu_{water}}{\mu_{air} - \mu_{water}} \tag{6.13}$$

Chapter 7

Wire Mesh Sensor Calibration

7.1 Wire Mesh Sensor Implementation and Construction

We will be utilizing wire mesh sensors to capture lateral void fraction across an empty bubble column with a hydrophilic and superhydrophobic inner wall and a simulated fuel cell assembly inserted into the bubble column. Wire mesh sensor technology was introduced by Horst-Michael Prasser in 1996. The impetus of his design was to visualize a cavitation bubble behind a fast acting shut-off valve in a pipeline with a time resolution of 1000 frames per second (Prasser, 1997). Our wire mesh sensors, based on Prasser's design, are designed to capture 1250 frames per second.

Figure 7.1 displays a layout of a wire mesh sensor to include the two grids of electrodes and the locations of the transmitter and receiver wires. Unlike Figure 7.1, our sensors have an ID of 77.9mm and a lateral spacing resolution of 3.254mm. The wire diameter is 100 microns. The sensors include two electrode grids with 24 electrodes each, which provide 24 x 24 sensitive points.

Figure 7.2 displays a simplified scheme of the signal acquisition layout of the wire mesh sensor. The wire mesh sensor function is based off the principle of local instantaneous conductivity of the two-phase system. The conductivity is measured at the intersection point of the wires of the two grids. The result is 24 x 24 sensitivity points, distributed equally across the the cross section. The system compensates for the grid intersections that are outside the bubble column, therefore the sensitivity points are less than expected with a 24 x 24 grid system.

During the signal acquisition, one plane of electrode wires is used as a transmitter, and the other as a receiver plane. The transmitter electrodes are activated by supplying them with voltage pulses in a successive order. The current at the receiver wire is a measure of conductivity of the fluid in the corresponding control volume, which is defined as the volume closest to the intersection of the two wires. The currents of all the wires are sampled simultaneously. After an analog to digital conversion is accomplished, the signals are recorded

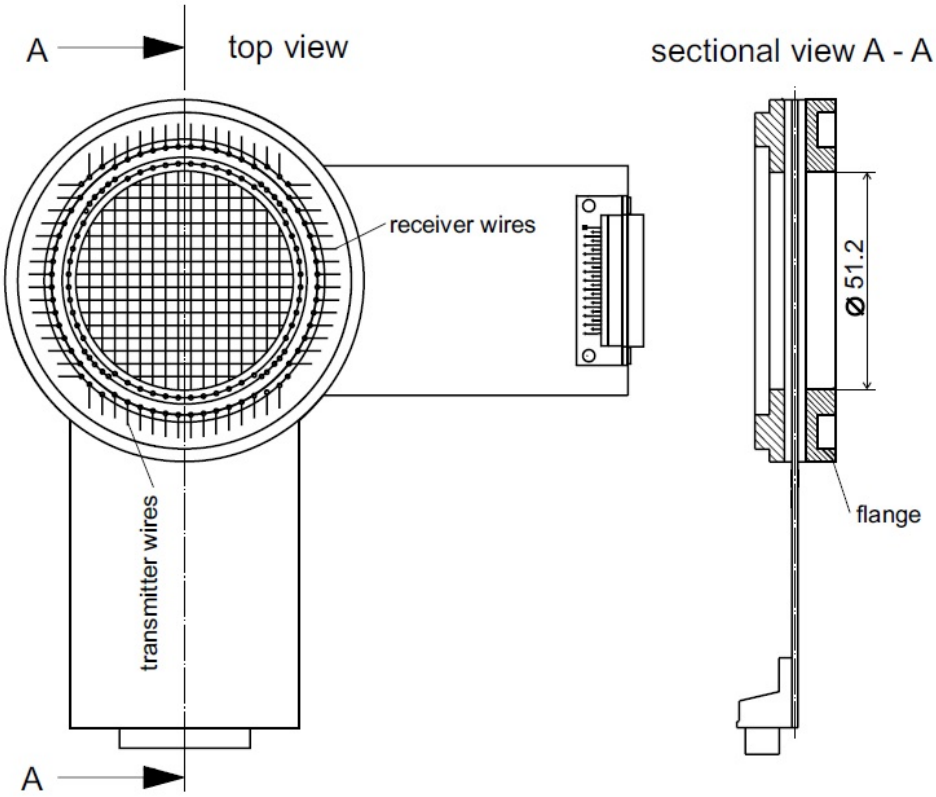

Figure 7.1: Wire mesh sensor layout (2 x 16 electrode wires)(Prasser, 1997)

by a data acquisition computer and stored for each receiver electrode separately.

Figure 7.3 displays the bubble column with four wire mesh sensors installed. Each pair of the sensors is positioned 25mm away from each other with a flange designed to not obstruct the flow between each measurement plane. This arrangement allows us to evaluate bubble velocity across the two measuring planes. Two wire mesh sensor pairs are separated by 33cm to measure the void fraction development before the simulated fuel assembly and right after the fuel assembly. This should give us an adequate void fraction measurement derived from the geometric constraints and superhydrophobic coating found in the fuel assembly. This particular measurement will furthermore be used to compare the lateral void fraction estimates against void fraction measurements derived from X-ray computed tomography.

The wire mesh sensor collects values in raw measurement data in 12-bit deep values. Our sensors are 24 x 24 (576) data values. Due to the curvature of the wire mesh sensor plane, we have 484 sensitivity points. Figure 7.4a displays the measurements of our sensor in millimeter units. Figure 7.4b displays a tilted view of the sensor displaying two wire mesh

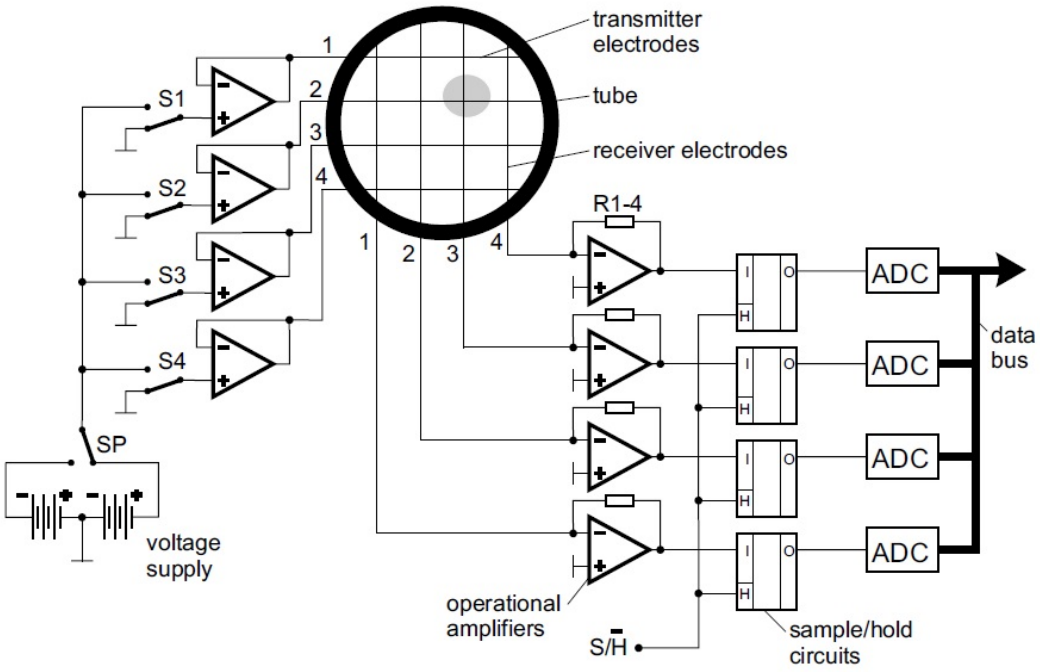

Figure 7.2: Simplified scheme of WMS signal acquisition system (Prasser, 1997)

grids.

The following figures were collected from the Wire Mesh Sensor Framework with an injection rate of 1SLPM. After activating the last transmitter wire, a complete matrix of measured values is stored in the computer, which represents the complete two-dimensional conductivity distribution in the sensor cross-section at the time of measurement.

Figure 7.5 is a single wire mesh sensor .dat file utilized to display a two-dimensional representation of a 24 x 24 sensitivity points. Items colored blue represent water and items colored white represent air. Any color between solid blue or solid white represent a mixture held between the phases of water and air. Figure 7.5 shows a display of a single wire mesh sensor grid, collected from the wire mesh sensor measurement system, WMS200. The figure displays the sensitivity point of the portions of a 24 x 24 grid that is exposed to the water in the bubble column. The center of the grid is white because a single bubble is rising, ejected from a single needle at the base of the bubble column. Since the edges of the squares on the sensor edge are not a full square, the software accounts for the difference in geometry so the void fraction measurements are not skewed based on the portions that are covered by the bubble column. You also notice that a portion of the sensor is displayed as a single gray

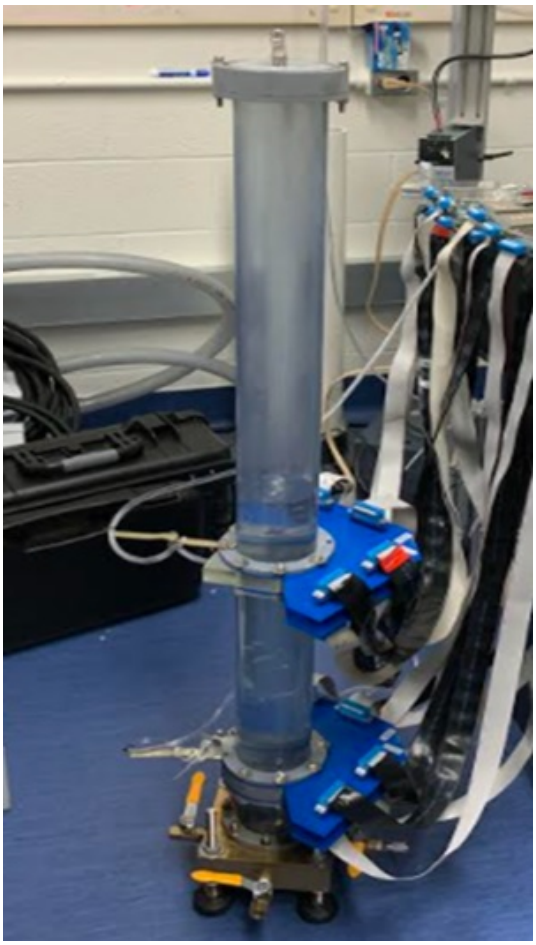

Figure 7.3: Bubble Column with four wire mesh sensors

line. This also serves as an example of a poor electrical connection caused by serial port misalignment or the presence of water in the vicinity of the cable connections.

Online mode displays several samples of images (taken at 1024Hz) averaged and displayed immediately after capturing the data for 30 seconds. Figure 7.6 displays four sensors utilized in the bubble column aligned from bottom of the bubble column to the top sensor. The bottom sensor is displayed at the top left of the figure and the top sensor is displayed in the right bottom of the figure.

Figure 7.7 shows a computer-aided design of the bubble column with the four sensors. The bottom pair of the wire mesh sensor is labeled Sensor 1 Top and Sensor 1 Bottom. The top pair of the wire mesh sensor is labeled Sensor 2 Top and Sensor 2 Bottom. For the remainder of my research, these sensors and accompanying measurements will be referred to using the labels displayed in Figure 7.7.

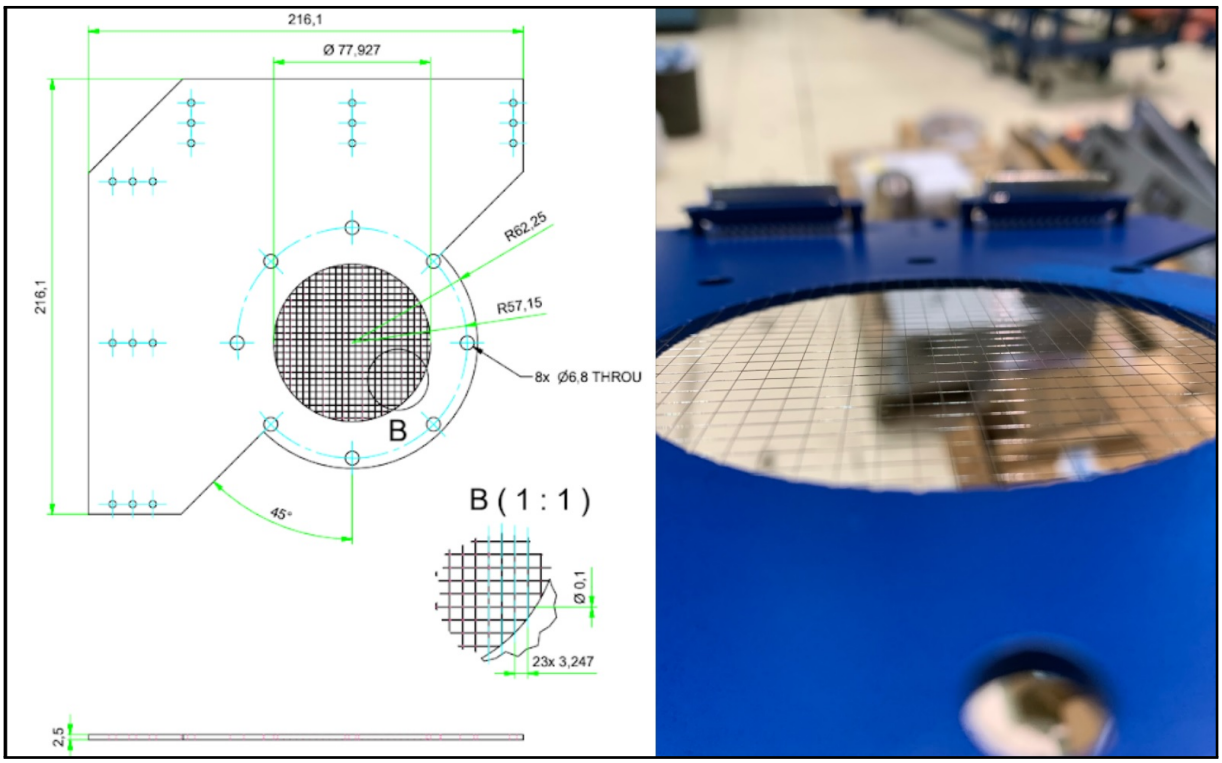

Figure 7.4: a) Wire mesh sensor computer aided design b) Wire mesh sensor in tilted view to show both wire grids

Our research will focus on evaluating bubbly flow to more physically mimic coalescing vapor bubbles in a departure from nucleate boiling approach. This flow will also allow us to differentiate bubble sizes using measurement techniques provided through wire mesh sensors, high speed cameras and primarily X-ray CT.

Figure 7.8 displays three images with measured bubbles, featuring the typical diameter of the flow regime we will be evaluating. These bubbles are not spheroid but ellipsoid or oblate spheroids. The majority of these bubbles either zig zag or spiral as predicted by several experiments and theories discussed by P.G. Saffman in his work titled, "On the Rise of Small Air Bubbles in Water."[34]

We calculated dimensionless equations (7.1), (7.2) and (7.3) to verify the bubble type which then allows us to measure the forces that control the dynamics of their movements under hydrostatic pressure, interfacial stresses and surface tension.

The highlighted box in Figure 7.7 displays the area where the bubble regime of interests reside for our research given the values for the following dimensionless equations of Bond number, Morton and Reynolds number:

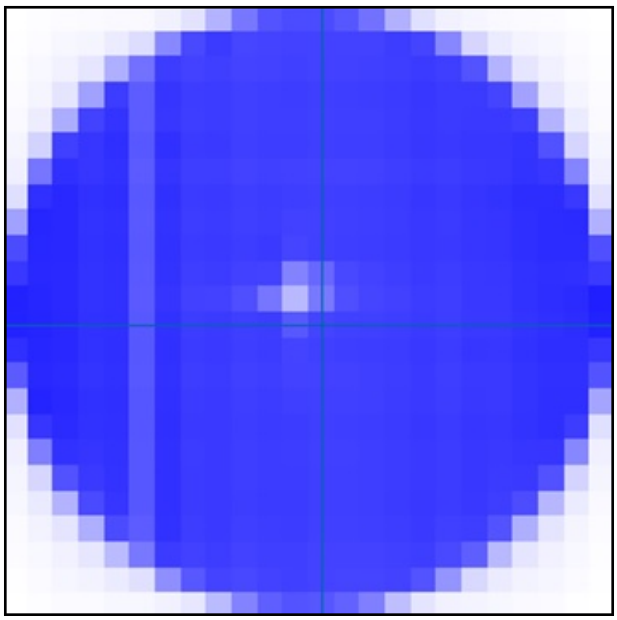

Figure 7.5: Wire Mesh Sensor 24 x 24 sensitive points (Real Time Grid Display)

$$E_o = \frac{g\Delta\rho d_e^2}{\sigma} \tag{7.1}$$

where E_o is the Eotvos number, which is the ratio of importance of gravitational force to surface tension force.

$$M = \frac{g\mu^4\Delta\rho}{\rho^2\sigma^3} \tag{7.2}$$

where M is the Morton number, which works with the Eotvos number to characterize shape of bubbles in a continuous phase.

$$Re = \frac{\rho d_e u}{\mu} \tag{7.3}$$

where Re is the Reynolds number, which defines the ratio of importance between inertial and viscous forces.

7.2 Wire mesh sensor calibration

In order to validate the utilization of our wire mesh sensors as a viable measuring tool for our experiment, we conducted several experiments to understand the wire mesh sensor

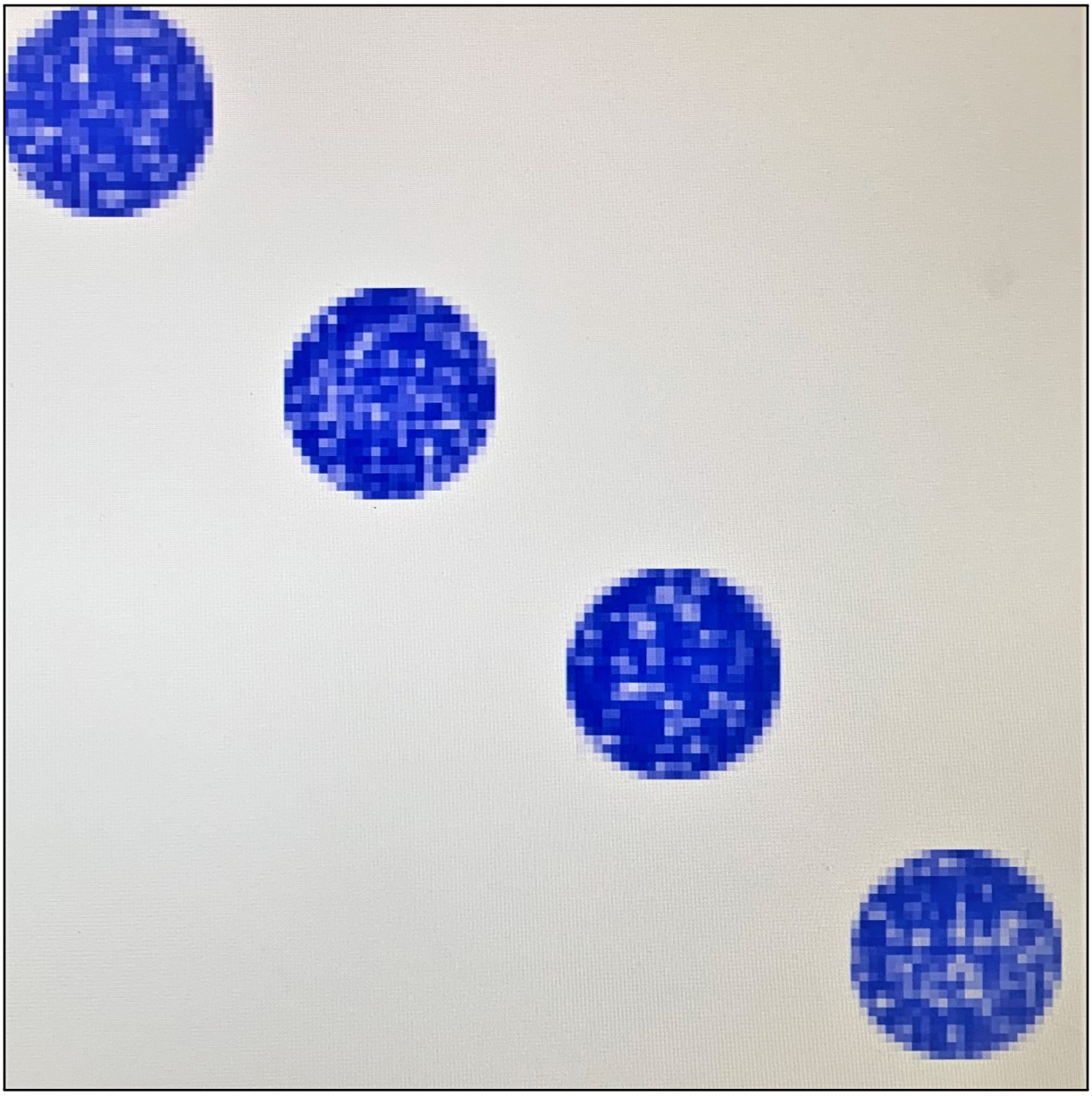

Figure 7.6: Wire Mesh Sensor acquisition software, WMS200, layout of four sensors (from top left to bottom right: Level 1 Bottom, Level 1 Top, Level 2 Bottom and Level 2 Top) where blue areas indicate water, white areas indicate air and grey areas indicate mixture of variable liquid and air

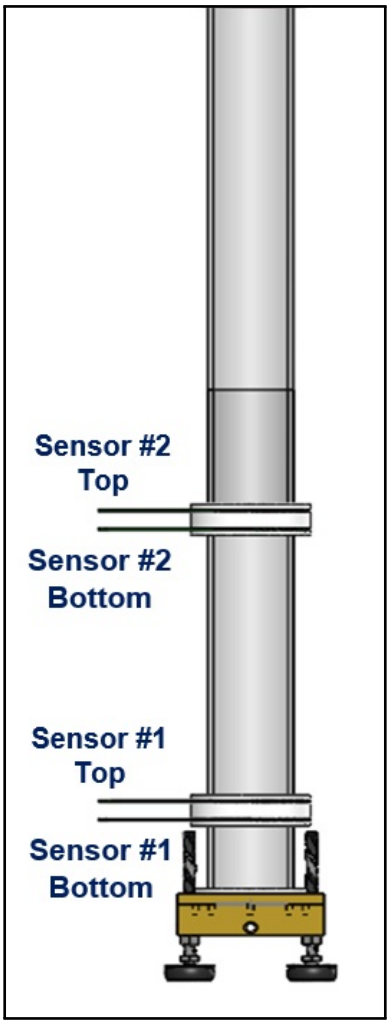

Figure 7.7: Labeled Wire Mesh Sensor Pairs

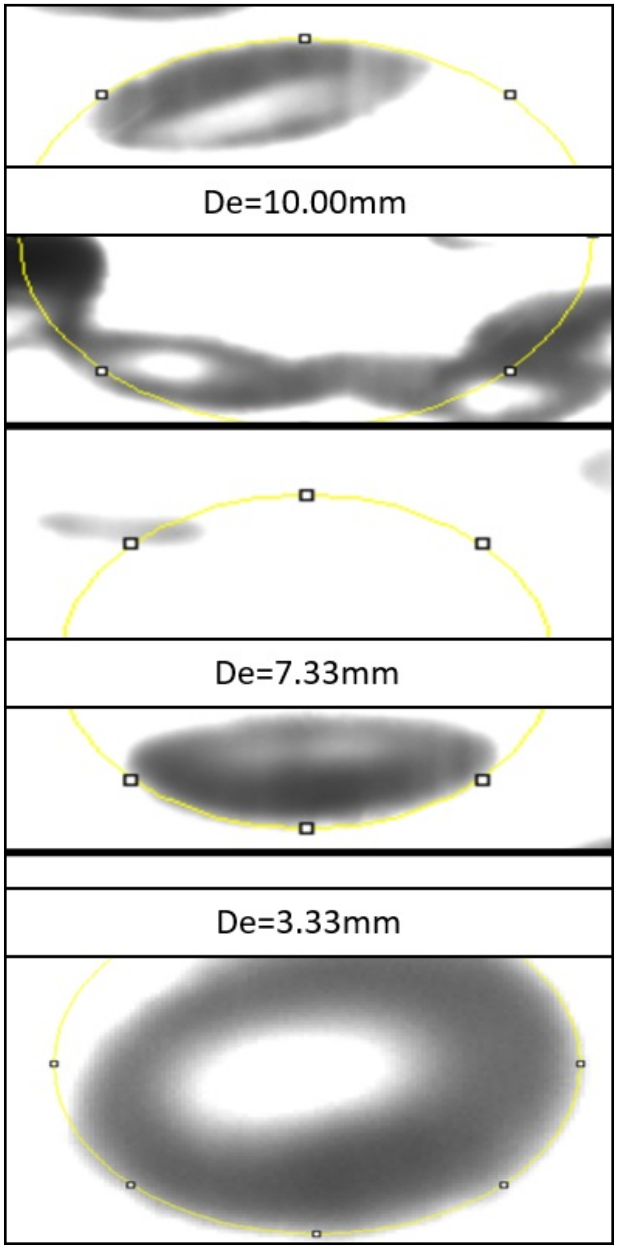

Figure 7.8: Expected Bubble Diameters

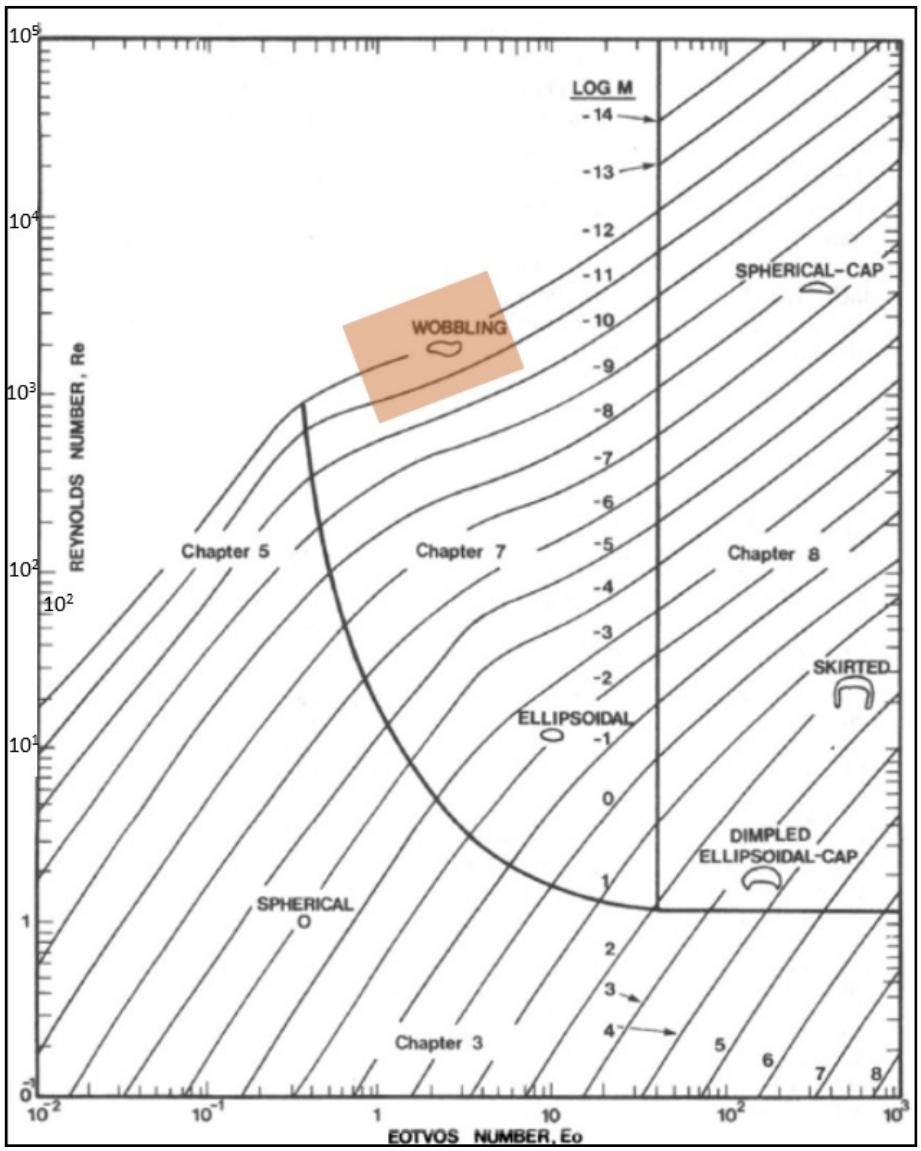

Figure 7.9: EOTVOS Number and Reynolds Number Comparison (Clift et al, 1978)[7]

measurements and processing software tools. We first attached the base of the bubble column with a single needle to control the injection of the bubbles to only a single bubble at a time. Using a high speed camera and the wire mesh sensor framework, we validated that the diameter of the bubbles were observed with regards to the spacing distance of a single bin represented in the void fraction display provided by the software. Secondly, we verified measurements of time-averaged void fraction with separate measurements calculated using

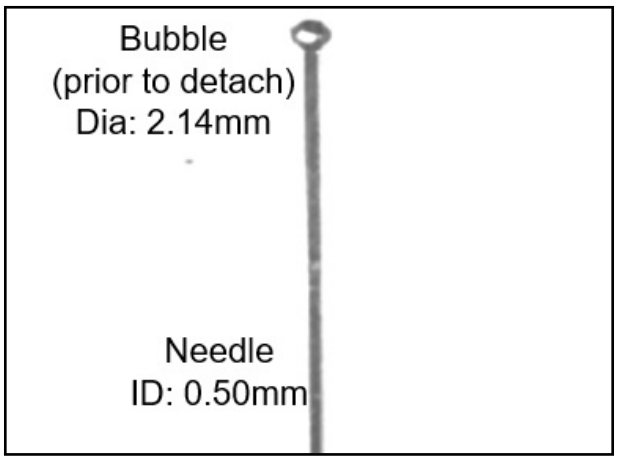

Figure 7.10: Bubble ejected from single needle (prior detachment)

a differential pressure transducer and height variation. Lastly, we continued to verify the Velocity modules and Bubble Size distribution module provided with the Wire Mesh Sensor Framework software. We have found that these modules are affected by backflow and become further inaccurate in a churn-turbulent flow.

Bubble evaluation from a single wire mesh sensor

To start evaluating the accuracy of the wire mesh sensors, we use a single needle with an inner diameter of 0.5mm, attached to the brass base plate. At a very slow injection rate, we use high speed cameras to capture the ejection of a single bubble. Figure 7.10 displays a still image of the needle and single bubble prior to detachment. This still image was collected using a Basler camera at 50fps. The diameter of the single bubble was measured at 2.14mm. Figure 7.11 displays a still image of the needle and the single bubble once it has detached from the needle. Following its detachment, the bubble measures a diameter of 3.14mm. These measurements coincide with an oblate spheroid, which is common throughout our flow regime of interest for our research.

Figure 7.12 displays an evaluation we conducted on the wire mesh sensor to evaluate its ability to capture expected bubble diameters. The highlighted box in Figure 7.12a shows the area where the still images of the bubbles were collected. These bubbles are captured in the still images displayed in Figure 7.12b. A measurement stick was inserted in the center of the bubble column and the outer limits of the bubble column to build a scale that we could use along with the high-speed camera to accurately measure the diameters of the single bubbles. Figure 7.12c is a vertical representation of the flow provided by the Wire Mesh Sensor Framework. In this figure, one bin represents a horizontal length of approximately

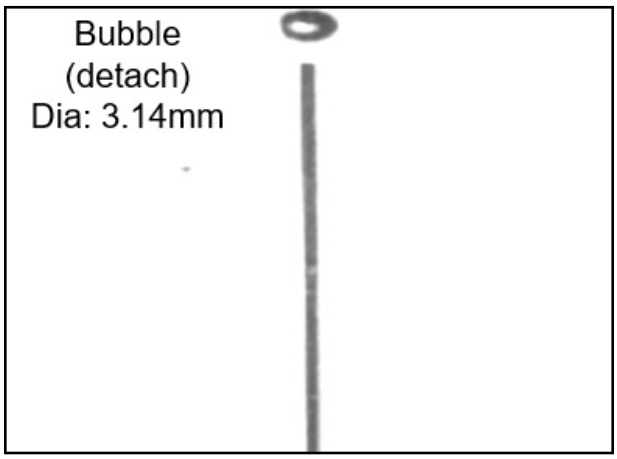

Figure 7.11: Bubble ejected from single needle (post detachment)

3.247mm. The vertical height of a bin represents a single frame and does not represent actual length as in the horizontal direction. The highlighted boxes (white bins) show a spectrum of capacitance that reflects the diameter of the bubble. One can notice how the individual bubbles in Figure 7.12b are displayed in the wire mesh sensor.

Figure 7.13 shows a side-by-side display of how the bubbles appear in the WMS based on variable air injection.

Velocity Module Evaluation

Figure 7.4 shows the WMS sensor used in the bubble column. Two of these sensors (e.g., Level 1 Bottom and Level 1Top) for a pair where there are nodes at nominally same x y (or r theta) locations but offset in z-direction. Velocity is calculated by the WMS based on cross-correlation of the signals from two sensor planes, with the understanding that a specific bubble crosses the sensor at the same x y-location with respect to each sensor. For a unidirectional flow with axial velocity being orders of magnitude larger than lateral, this is a good assumption (green bubble in Figure 7-15a, but in flows such as the churning flow and flows with significant backflow, this assumption is not always reasonable. For this reason, we will often calculate velocity also based on the cross-correlation of a void fraction from a group of nodes, as this way a bubble that moves e.g., one or two nodes laterally (red bubble in figure 7.15a) can still result in a signal that can be cross-correlated properly. Still, if time varying lateral motions of bubbles are significant, much uncertainty will accompany the velocity calculations in a non-unidirectional flow. The distance between the center of the sensors (30mm) is critical in this calculation, and as confirmed by the software supplier the velocity calculation of the wire mesh sensor software does not account for the thickness

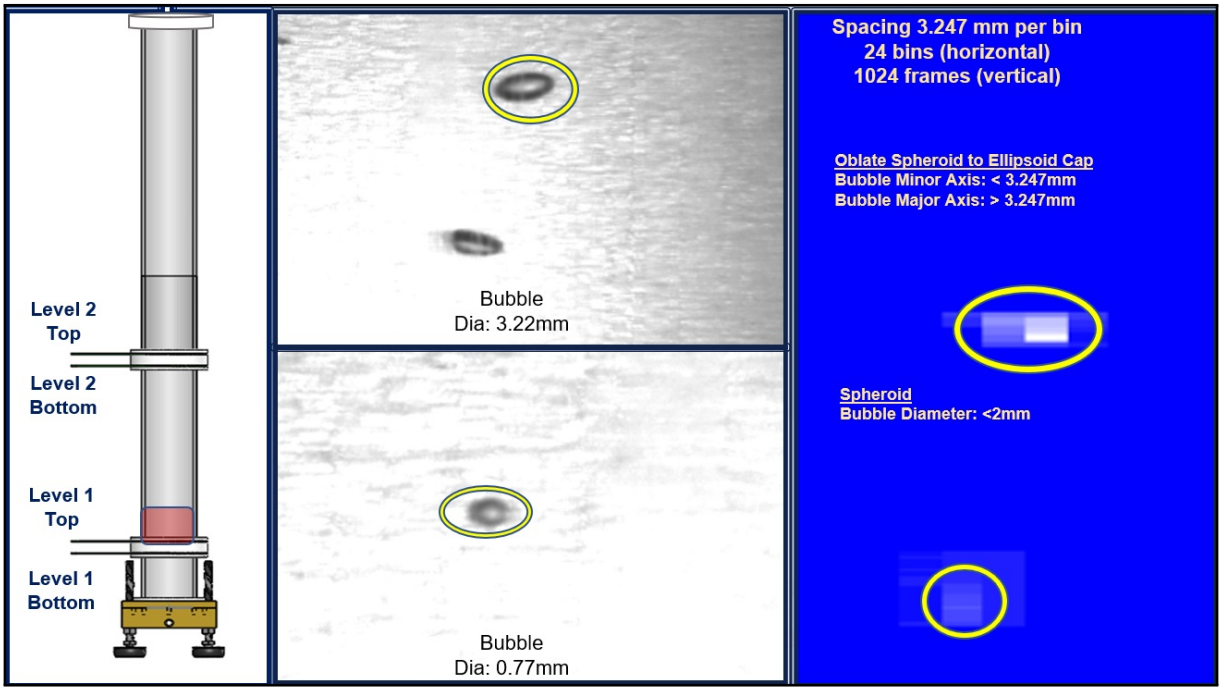

Figure 7.12: a) Bubble column with labeled wire mesh sensors and highlighted area captured by high-speed camera b) single bubbles rising with typical measured diameters c) diameter measurement using the void fraction vertical representation of flow provided by the Wire Mesh Sensor Framework software

of the sensors themselves, and hence the user MUST define the spacing between the actual distance of the sensor plane centers, and not the distance based on the thickness of the spacer alone. Even if the sensor thickness is entered elsewhere in the software modules, the value is NOT considered in the geometry module at all.

Figure 7.15a shows the exaggerated sensor cross-section and Figure 7.15b shows an average velocity profile from WMS measurements for a superficial gas velocity of 0.041 m/s. This average velocity profile is provided by the software Velocity module, which also uses a cross correlation technique.

Superficial gas velocity is defined as the ratio of the air injection flow rate and the cross-sectional area of the pipe.

$$U_g = \frac{Q}{A} \tag{7.4}$$

where U_g is the superficial gas velocity ($\frac{m}{s}$, Q is the air inejction rate ($\frac{m^3}{s}$ and A cross sectional area of the pipe (m^2

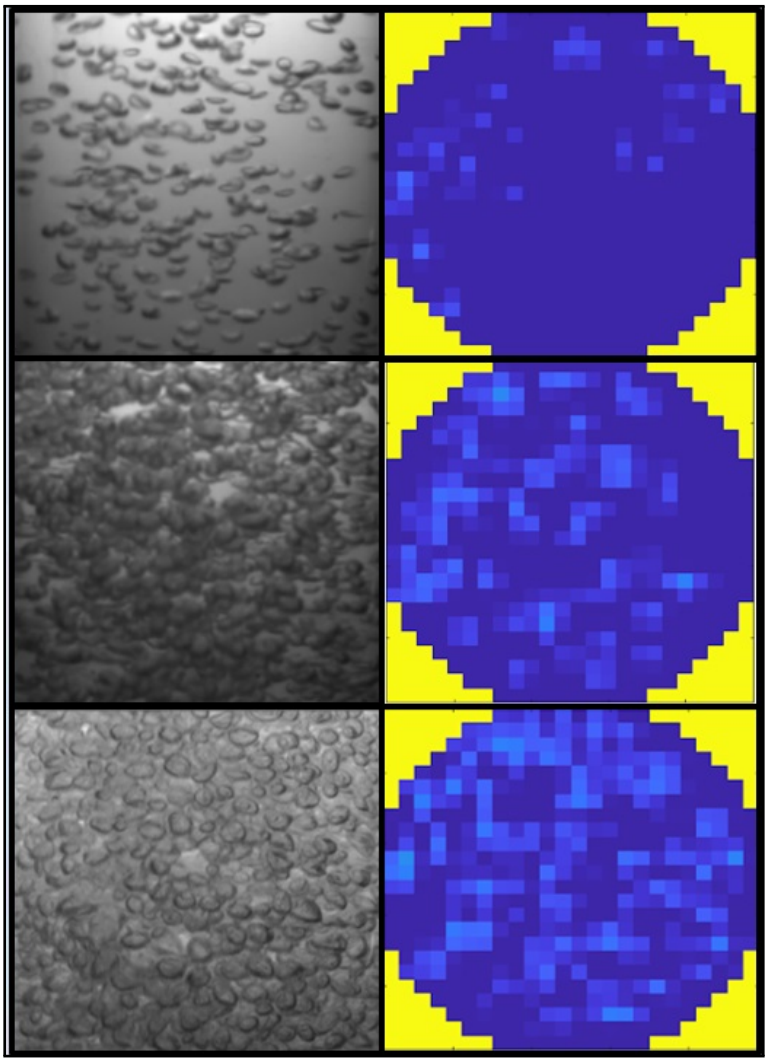

Figure 7.13: a) bubbles injected at 2000sccm (still image and WMS) b) bubbles injected at 9000sccm (still image and WMS) c) bubbles injected at 16000sccm (still image and WMS)

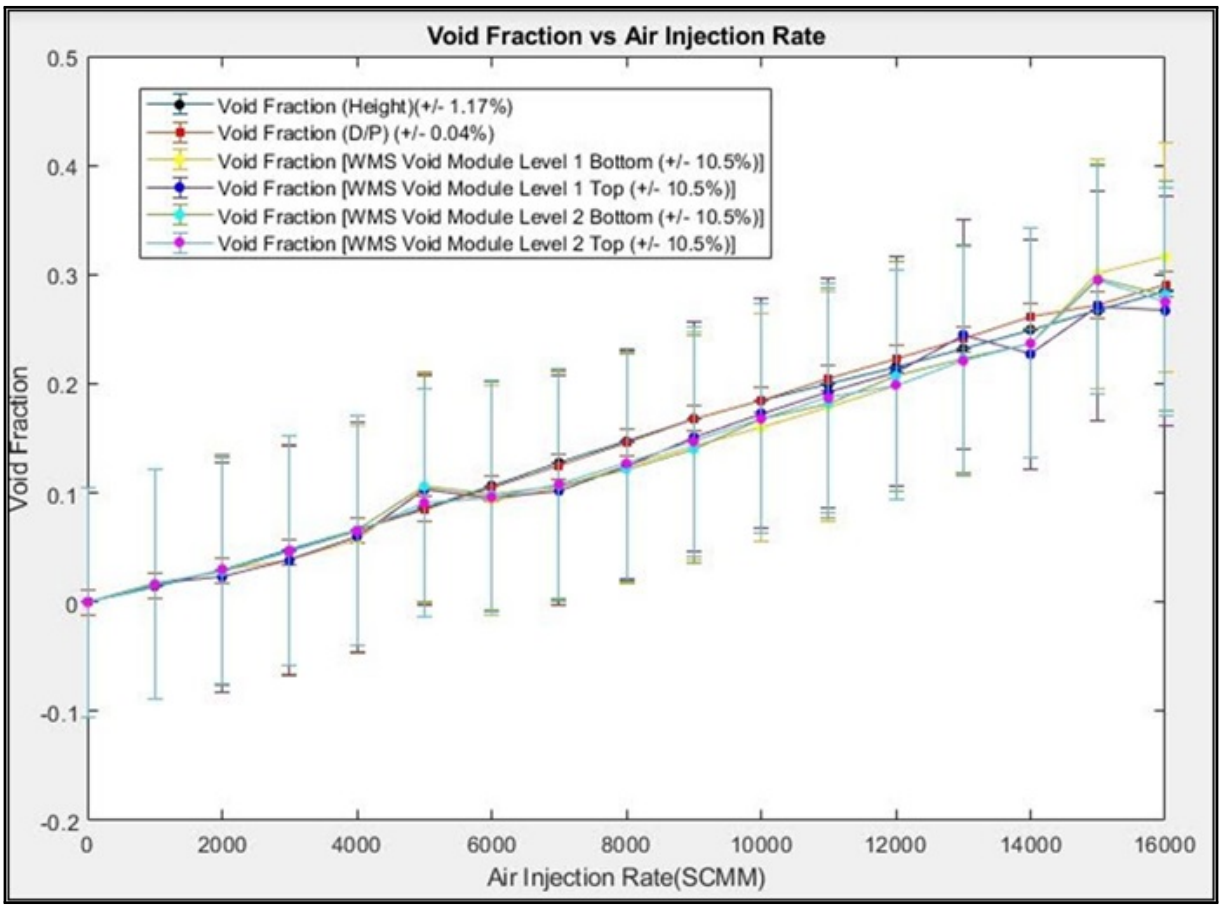

Figure 7.14: Void fraction measurements vs air injection rate, measured by height variation, differential pressure transducer and wire mesh sensors

The velocity is based on a cross-correlation of the void fraction time traces. Figure 7.16 shows two time traces from planes Level 2 Top and Bottom and their cross-correlation for the entire dataset of measurements. Looking at the cross-correlation and then individual time segments more closely we find the cross correlation is substantially affected by the churn turbulent flow as the superficial gas velocity increases. We find that cross correlation is more accurate when less nodes are used, or a specified neighborhood of nodes is preselected based on the lateral void fraction area of interest. An average velocity of the entire spatial dataset becomes less accurate with increasing superficial gas velocity.

Figure 7.16 shows for one node pair the two time traces and their cross correlation, which here indicates a lag of 0.001 seconds. Figure 7.17 shows the cross correlation for the full length of the average of the void fraction measurements from two sensors. Note the correlation value of the peak, and second highest correlation peaks. Had the peak ratio been

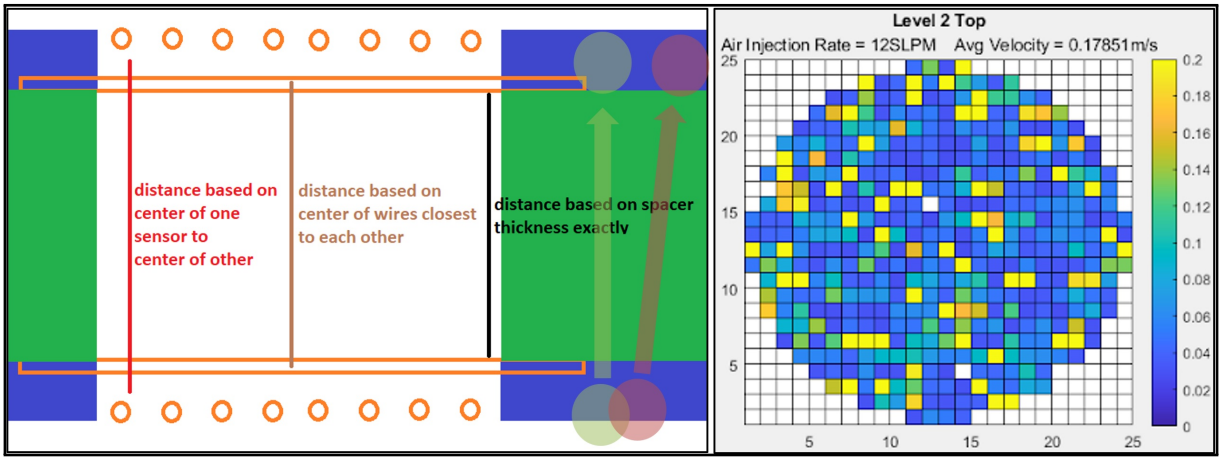

Figure 7.15: a) Sketch, not to scale of the different spacings between the WMS planes. Distance between sensor centers should be used for dx together with dt from the correlation, to get velocity U = dx/dt. Note, however, that a bubble not traversing axially (red bubble) would not produce a signal that can be cross correlated considering a single node pair. If the flow were to reverse, a time trace signal would need to be chopped in time to be able to get useful velocity correlation. b) The time-averaged velocity profile found in the Wire Mesh Sensor Framework for a superficial gas velocity of 0.041m/s exhibits many spurious seeming readings, and this can be understood to be due to the code attempting to cross-correlate signals between individual nodes averaged over duration of the run, whereas in reality notable fraction of bubbles also moved axially and velocity was not constant at given location over time (and may have even reversed). Hence in a churning flow found at higher injection rates in the bubble column, the basic WMS framework approach to velocity calculation is not accurate.

closer to unity or correlation value low, there would be an increased chance of this being a spurious correlation. Given the known spacing corresponds to air-water interfaces crossing the nodes at an average velocity of U = dx/dt = 0.20m/s.

As briefly noted above and sketched in Figure 7.15a, if the flow is not unidirectional (and in the bubble column significant lateral motion is also to be expected), node to node correlation can fail. Incorrect velocity may also result if flow is time varying and signals correlated are over a long time span (e.g. think of a flow with some bubbles crossing planes at 1m/s and others at 3 m/s). This will result in a correlation with two peaks, neither would be the average, and only one would be indicated as the velocity. Hence, we further explore correlation using our MATLAB code, developed jointly by University of Michigan and University of California Berkeley (UMBER), which enables averaging data from a cluster of nodes before correlation, and dividing time into predefined time segments. Figure 7.18

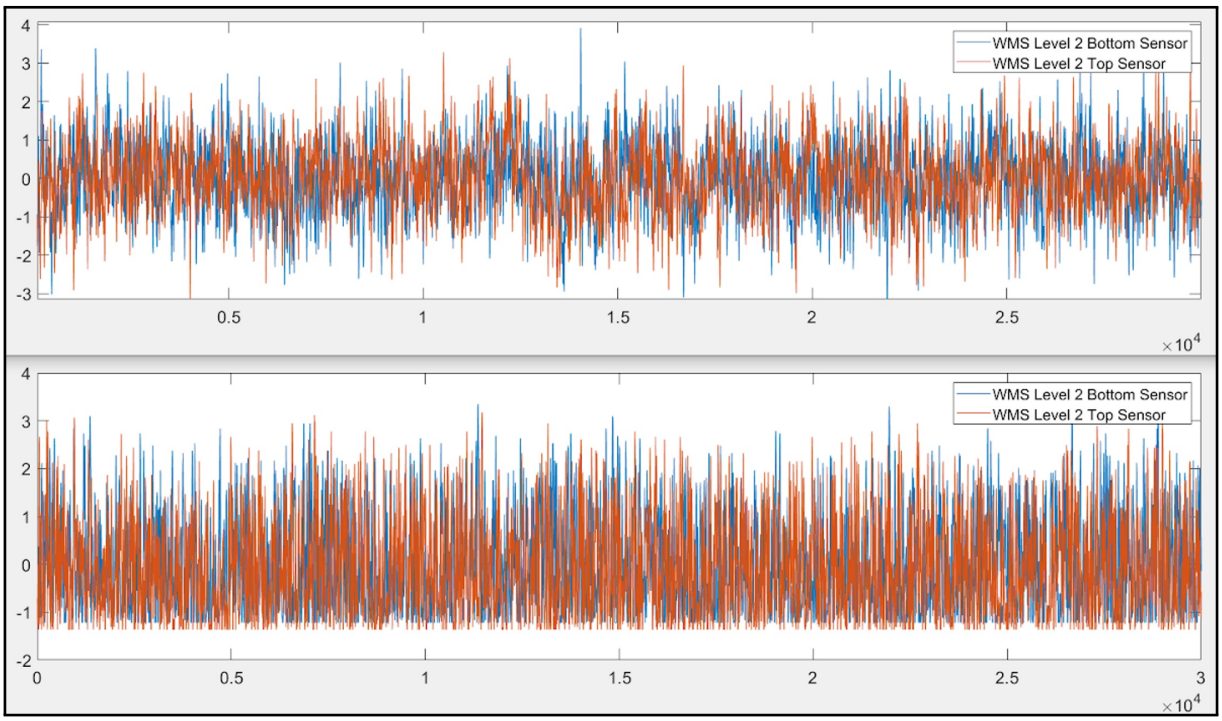

Figure 7.16: a) Average time traces for all collected frames and nodes b) Average time traces for a single node. These two time traces are for the top two wire mesh sensors with a superficial gas velocity of 0.041m/s.

shows the differences in lateral velocity distribution and average velocity derived from the Wire Mesh Sensor Framework software Velocity Module, our MATLAB code Velocity profile using the full time trace and our MATLAB code Velocity profile using the segmented time trace. Figure 7.19 displays the different lateral velocity distributions using different clusters prior to cross correlation.

The velocity is based on a cross-correlation of the void fraction time traces. Figure 6a shows the two time traces and their cross correlation for the entire dataset of measurements. Figure 7.16 shows for one node pair the two time traces and their cross correlation, which here indicates a lag of 0.001 seconds. Figure 7.17 shows the cross correlation for the full length of the average of the void fraction measurements from two sensors. Note the correlation value of the peak, and second highest correlation peaks. Had the peak ratio been closer to unity or correlation value low, there would be an increased chance of this being a spurious correlation. Given the known spacing corresponds to air-water interfaces crossing the nodes at an average velocity of U = dx/dt = 0.11m/s.

As the flow is not unidirectional and in the bubble column significant lateral motion is

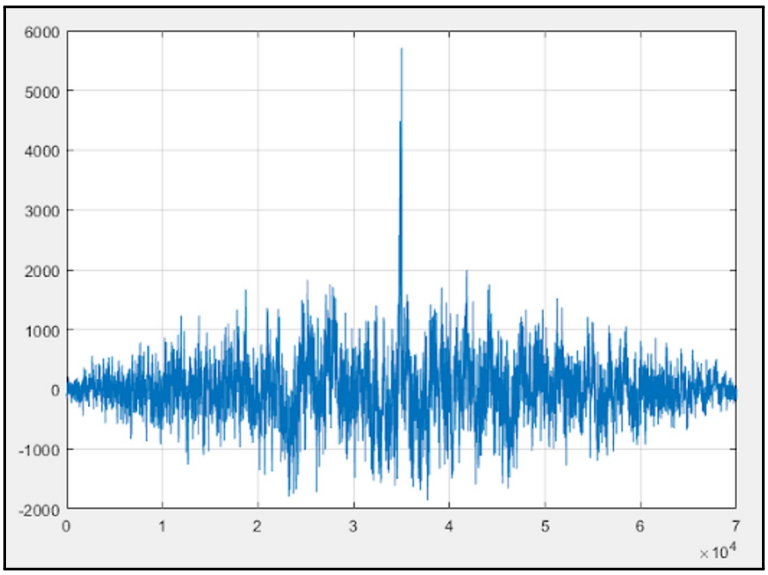

Figure 7.17: Display of cross correlation peak for the dataset comparisons.

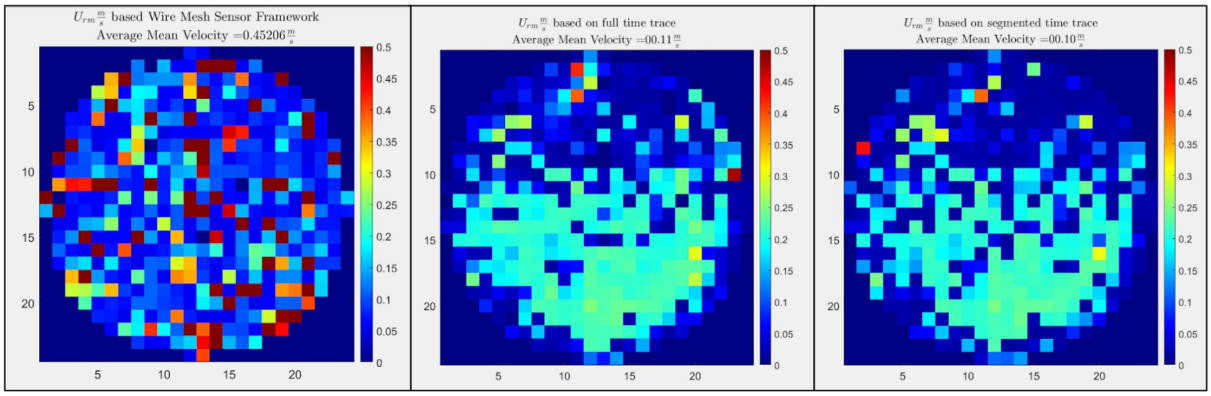

Figure 7.18: a) WMS Velocity profile for a superficial gas velocity of 0.041m/s with time-averaged mean velocity provided by the WMS Framework software b) WMS Velocity profile for a superficial gas velocity of 0.041m/s with time-averaged mean velocity provided by our MATLAB code for full time trace c) WMS Velocity profile for a superficial gas velocity of 0.041m/s with time-averaged mean velocity provided by our MATLAB code for segmented time traces

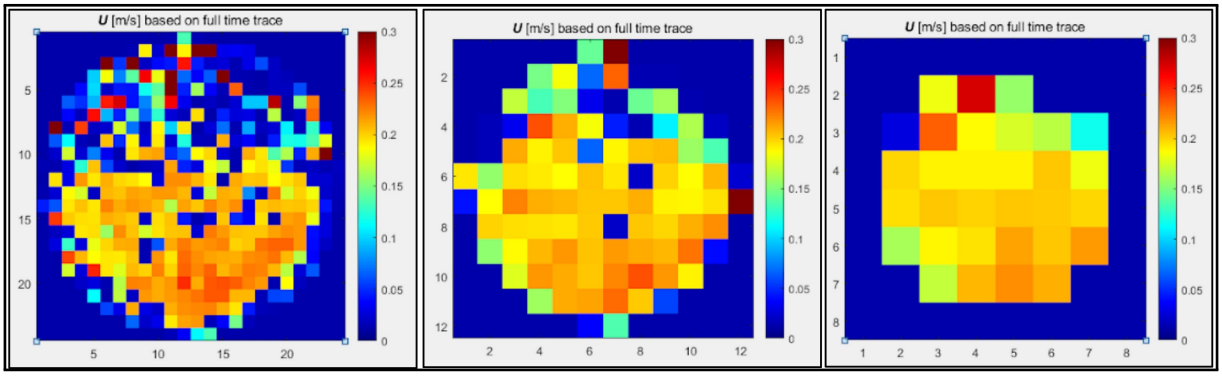

Figure 7.19: a) WMS Velocity profile using 24 x 24 nodes b) WMS Velocity profile using 12 X 12 clusters of 2 nodes each c) WMS Velocity profile using 6 x 6 clusters of 4 nodes each

also to be expected, node to node correlation can fail, especially if taken over long periods of time. Hence, we further explore correlation using our MATLAB code, which enables averaging data from a cluster of nodes before correlation, and also dividing time into used defined segments. Figure 7.18 shows the differences in lateral velocity distribution and average velocity derived from the Wire Mesh Sensor Framework software Velocity Module, our MATLAB code Velocity profile using the full time trace and our MATLAB code Velocity profile using the segmented time trace. Figure 7.19 displays the different lateral velocity distributions using different cluster prior to cross correlation.

Figure 7.20 displays the average velocity profile from the UMBER MATLAB code for a superficial gas velocity of 0.041m/s. Figure 7.20a displays the average velocity from a 24x24 cluster using spatial and time segment cross correlation for a data set of 35,000 frames at 1,000 Hz. At this high injection rate, the flow has substantial backflow, and you can notice the effects it has on the lateral velocity distribution as the northern half is significantly lower than the southern half of the profile. Understanding that there are portions of the profile that contain accurate velocity data, we can shift to an area where the velocity is more uniform. Figure 7.20b displays the average velocity for a 5x5 grid of the 24x24 cluster to calculate an average velocity for an that is not disrupted with spurious readings. In the small neighborhood of clusters, the average velocity between the spatial and time segment cross correlation are 0.206m/s and 0.294m/s respectively. Figure 7.20c displays the average velocity gathered for a 12x12 cluster of the dataset. Each node is calculated from the cross correlation of averaging two side-by-side nodes, located at the same location of each sensor, prior to cross-correlation. If the cluster was furthered lowered to 6x6 cluster, then the correlation will occur across the average of four nodes at the same location in each wire mesh sensor plane. The average velocity from the spatial cross correlation and time segment cross correlation yield a velocity of 0.174m/s and 0.267m/s, with the time-segment cross

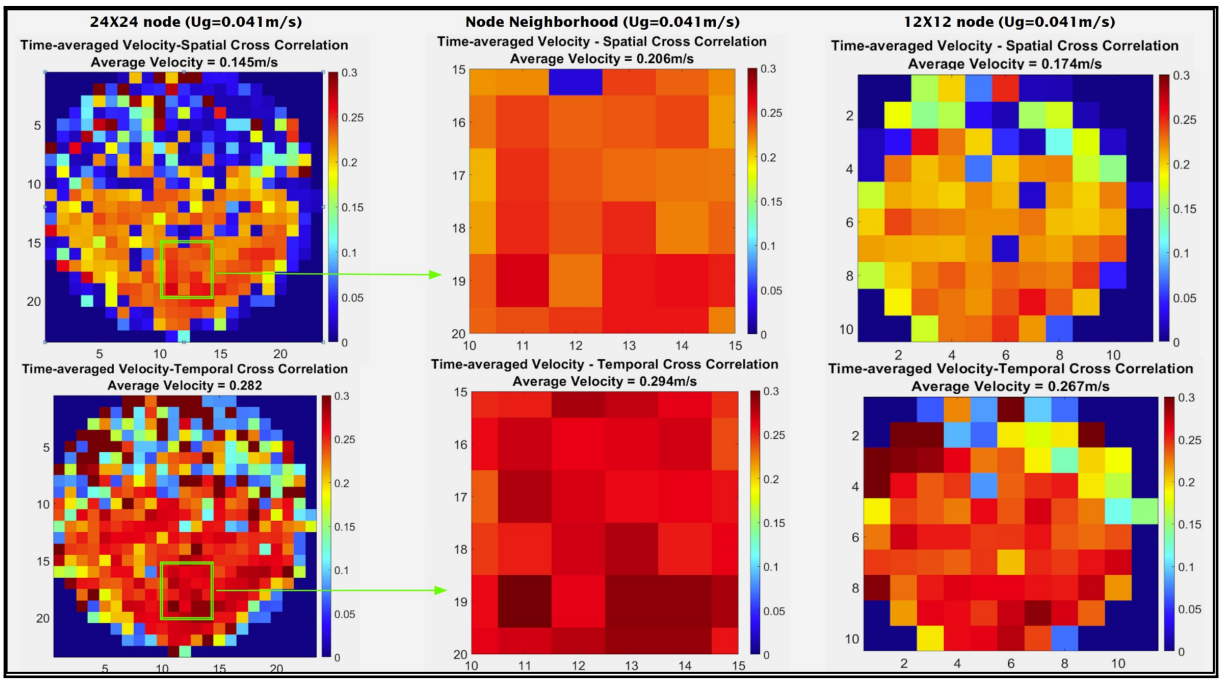

Figure 7.20: a) WMS Average Velocity profile using 24 x 24 nodes for Ug=0.041m/s b) WMS Average Velocity profile for a small box of nodes for Ug=0.041m/s c) WMS Average Velocity profile using 12 X 12 clusters of 2 nodes each for Ug=0.041m/s

correlation yielding a more uniform lateral display of the velocity profile and therefore a more accurate representation of the bubble regime velocity.

Figure 7.21 displays the average velocity profile from the UMBER MATLAB code for a superficial gas velocity of 0.020m/s, which we use to show why the effects observed in Figure 10 are driven by backflow and not necessarily software issues. Figure 11a displays the average velocity from a 24x24 cluster using spatial and time segment cross correlation for a data set of 35,000 frames at 1,000 Hz. At this lower injection rate, the flow rises more uniform, and backflow is minimal. The velocity profile across the bubble column is more uniform than the profiles at the higher injection rate discussed in Figure 7.18. Figure 7.21c displays the average velocity for a 12x12 grid of the 24x24 cluster to calculate an average velocity for an that is not disrupted with spurious readings. In the small neighborhood of clusters, the average velocity between the spatial and time segment cross correlation are 0.221m/s and 0.236m/s respectively. These velocities are closer in agreement, giving us more confidence in the results. Figure 7.19c displays the average velocity gathered for a 12x12 cluster of the dataset. The average velocity from the spatial cross correlation and time segment cross correlation yield a velocity of 0.203m/s and 0.230m/s. Both cross correlation methods yield

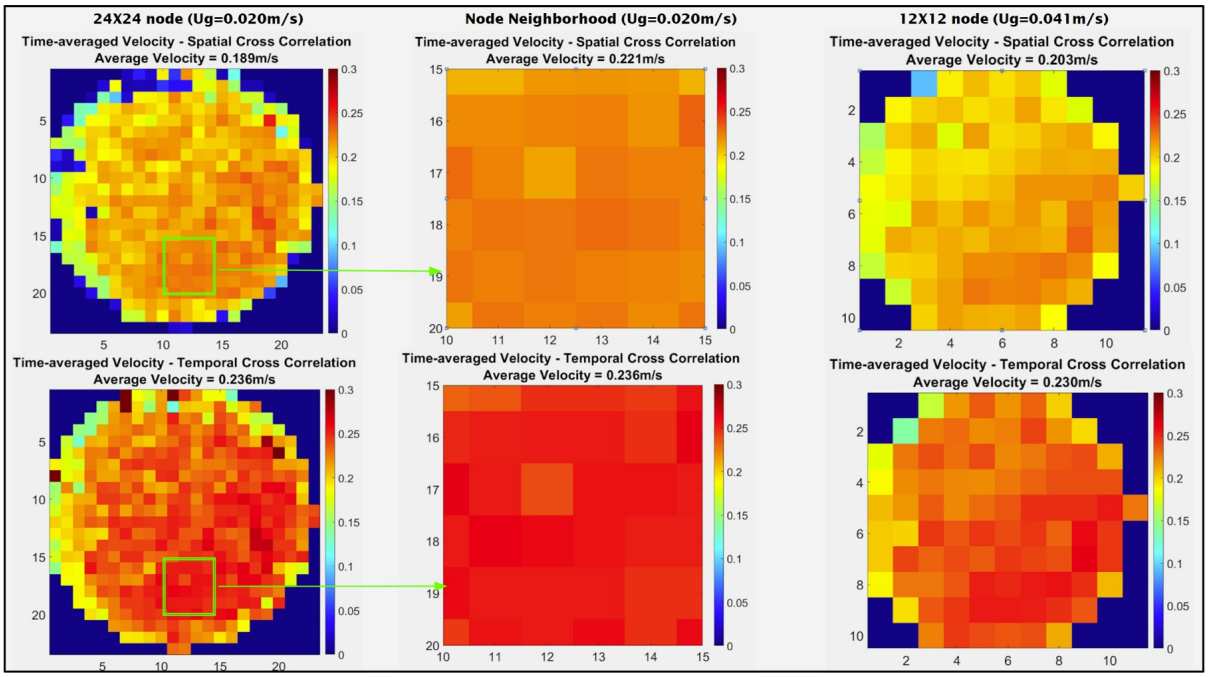

Figure 7.21: a) WMS Average Velocity profile using 24 x 24 nodes for Ug=0.020m/s b) WMS Average Velocity profile for a small box of nodes for Ug=0.020m/s c) WMS Average Velocity profile using 12 X 12 clusters of 2 nodes each for Ug=0.020m/s

a uniform lateral display of the velocity profile and therefore a more accurate representation of the bubble regime velocity.

Using the Wire Mesh Framework Software, we measured mean bubble diameter across the entire measurement dataset and display the results in a histogram shown in Figure 7.22. Figure 7.22 shows the mean bubble diameter for a superficial gas velocity of 0.041m/s, measured from the bottom and top WMS pairs. Note however that these bubble sizes are calculated based on the velocities indicated by the cross correlation, which may have errors for aforementioned reasons. If we substitute for the velocity field the average velocity calculated in our in-house MATLAB code we recover the modified curves shown in red. Later in this report, we will discuss how effective this tool is to assess if the bubble flow regime is homogeneous throughout all superficial gas velocity modifications.

Random bubble deformation is expected to always occur in a turbulent flow, the apparent flattening of the bubble may be attributed to its impact upon the WMS, whereas the fragmentation of its originally smooth interface contour to a cluster of connected small circles is attributable to the dissection of the bubble by the WMS, as displayed in Figure 7.23 (Prasser, 2001).

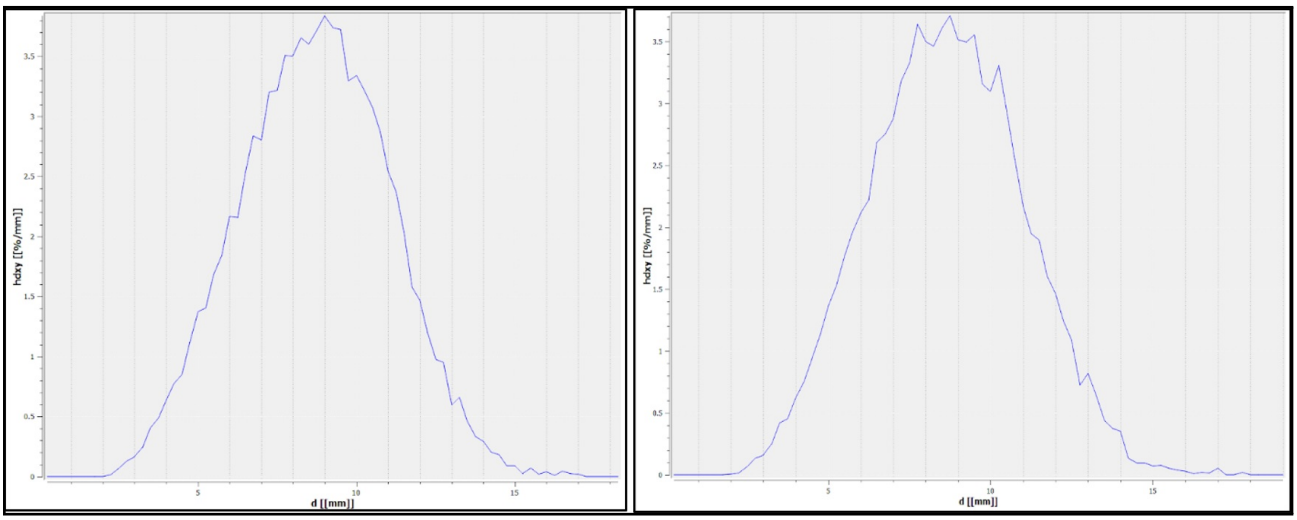

Figure 7.22: a) WMS Mean Bubble Diameter (histogram) for a superficial gas velocity of 0.041m/s Level 1 Pair b) WMS Mean Bubble Diameter (histogram) for a superficial gas velocity of 0.041m/s Level 2 Pair

Prasser et al. stated that bubble fragments tended to coalesce downstream of the sensor when the liquid flow rates was sufficiently high. Given the stagnant conditions that we have, we do not expect the fragments to coalesce downstream of the sensor. Further studies by Prasser also found that dual WMS unit will measure differently due mainly to the distortion of the bubbles by the upstream sensor. This will adversely effect interfacial velocity and bubble size estimates, and will bias the measurements towards a higher gas holdup.

We have concluded that WMS generally provides fairly accurate estimates of the void fraction and the interfacial velocity, but it is also subject to systematic errors in certain flow regimes and under certain flow conditions. The prediction of the gas flow rate in gas–liquid flows using the cross–correlation method was found to be accurate only for a very narrow range of flow conditions. The principles and successful applications of global wire-mesh tomography have also been presented. Several studies continue in this area to identify lingering issues related to wire–mesh tomography and to suggest procedures that may be used for resolving these issues in the future.

Shaban et al conducted a study where the void fraction measurements performed using WMS were compared to void fraction values calculated using a pressure gradient method. Figure 7.24 demonstrates performance of WMS for various flow regimes. One can notice that WMS measurements yeild higher void fraction for bubbly flows but lower for slug and churn flow as compared to the values calculated by the pressure gradient method. One can also note that the accuracy of the WMS is 10% throughout the bounds of the bubble regimes that we will measure (Shaban, 2017) [40].

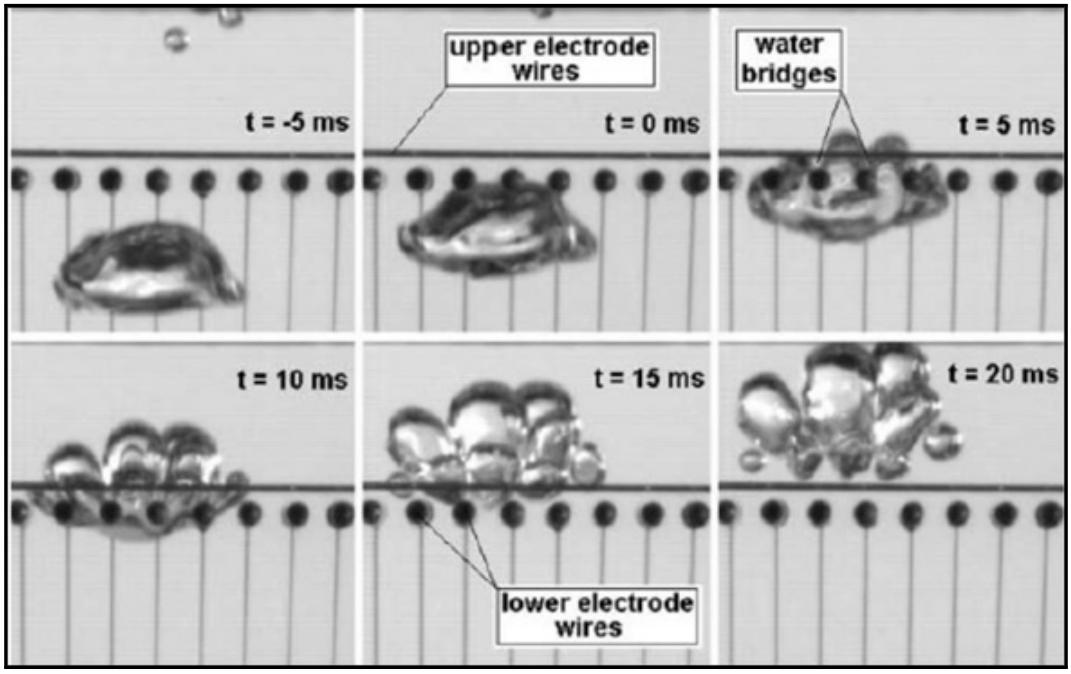

Figure 7.23: Bubble fragmentation caused by Wire Mesh Sensor (Prasser, 2001)[31]

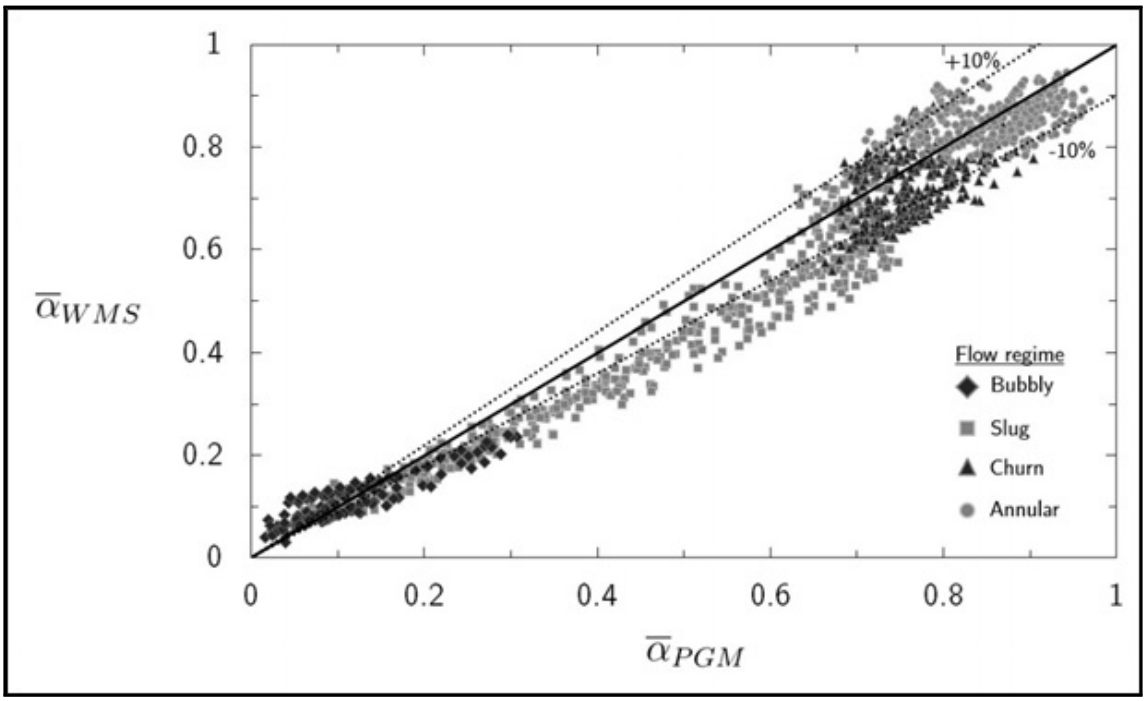

Figure 7.24: Void fraction measured using Wire Mesh Sensor vs that calculated using the pressure gradient method (Shaban, 2017) [40]

Chapter 8

X-Ray Computed Tomography Calibration

8.1 X-Ray Theory and Application

X-rays are utilized to determine structural properties of samples at a wide range of length scales. The role of the imaging methods is to replicate the location, amplitude, and spatial features of the original object. To achieve this, the X-rays must hold sufficient energy to penetrate the material or object of interest. We also need sufficient contrast between objects of interest and their surroundings, with sufficient resolution to distinguish features of interest. Techniques to image an object depend on the ability of radiation collection and quality of the image formulation. The manner of how X-rays are utilized is dependent on the interactions with the materials, primarily scattering and absorption (Attwood, 2016) [10].

Figure 8.1 displays the portion of the electromagnetic spectrum stemming from the infrared to the X-ray region, with approximate wavelengths across the top of the spectrum and photon energies across the bottom. The X-ray region of interest ranges from energies from 10 keV to 100 keV.

As we briefly review the basic process by which radiation interacts with matter, we will look at simplified models of the atom with point electrons in an orbit around a nucleus of positive charge $+Ze$. Using X-ray notation, the electron orbits are labeled K, L, and M, which correspond to the principal quantum numbers n = 1,2, and 3, respectively.

Figure 8.2a is a primary electron incident on a multi-electron atom, with an energy level that is sufficient to remove a core electron in close encounter. Figure 8.2b displays the photo-ionization process, where a photon of sufficient energy is absorbed by the atom. In this process the energy is transferred to an emitted photo-electron with a kinetic energy equal to the incident photon, minus the binding energy with less energy than a K-shell electron. In Figure 8.2c the atom is shown rearranging through a process known as fluorescence, where the electron transition is accompanied by the emission of a photon of characteristic energy equal to the difference between the initial and final atomic states. Figure 8.2d displays, in

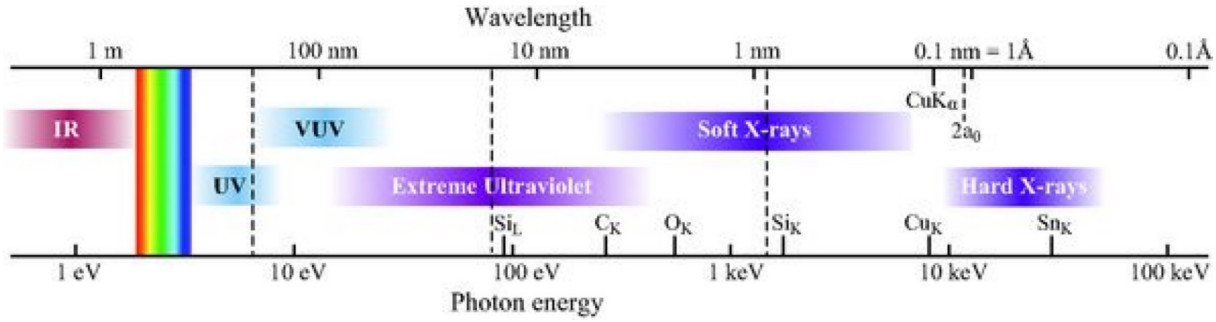

Figure 8.1: Electromagnetic Spectrum [10]

a competing effect with fluorescence, the atom rearranged through the emission of a second Auger and electron of characteristic energy (Attwood, 2016) [10].

The competition between fluorescent emission and the Auger process, depends on the Z atom numbers. The fluorescence process favors high Z atoms, and the Auger process for low Z atoms. Since Auger electrons have a fixed characteristic energy, they are used for elemental characterization in surface and interface analysis (Attwood, 2016) [10].

The emission spectrum regions are categorized by the presence of the primary atomic resonances and absorption edges of most elements, from low to high Z, where Z is the atomic number (the number of protons in the nucleus).

If the emitted photo-electron travels a particular distance in a material, it is likely to lose energy quickly due to interactions with other electrons. The interactions with electrons are governed by individual collisions or collective motion. As we observe the emission spectrum from a solid material bombarded by electrons is typical to observe both characteristic line emission and continuum emission. The later process is called bremsstrahlung, known as "braking radiation." Figure 8.3 shows a diagram of the bremsstrahlung process, where electrons of a given velocity, v, or energy, E, approach an electron or a nucleus at a close distance. The approach to close distance results in a wide range of accelerations and therefore emitting photons at a wide range of energies (Attwood, 2016) [10].

Given a large number of electrons that are incident and a wide variety of impact parameters, a broad continuum of radiation is produced. When the collision involved direct impact with bound electrons, a characteristic line emission is observed. Radiation intensity is a function of thickness. One observes that incremental increases in thickness, Δx , result in an incremental decrease in transmitted intensity, I, relative to the incident intensity, I_o, such that

$$\frac{I}{I_o} = -\rho\mu\delta x \tag{8.1}$$

where ρ is the mass density and μ is an energy-dependent and material-dependent ab-

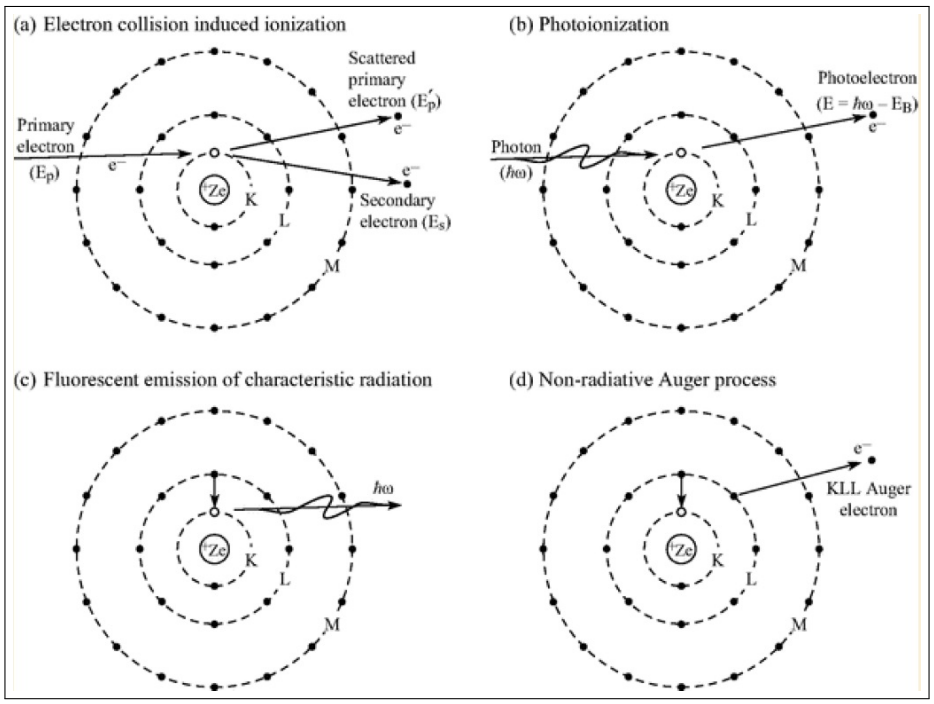

Figure 8.2: a) an incident primary electron of sufficiently high energy scattered by an atom as it knocks free a core electron from the K-shell. b) an incident photon of sufficient energy is absorbed by the atom with the emission of a photo-electron of kinetic energy equal to the energy minus the binding energy. c) Atom readjustment as a higher-lying electron makes a transition to a vacancy. d) The atom adjusts to core vacancy through non-radiative Auger process in which one electron makes a transition to the core vacancy.[10]

sorption coefficient.

$$\frac{I}{I_o} = e^{-\rho\mu x} \tag{8.2}$$

where μ is the linear absorption coefficient.

X-ray Scattering

X-ray scattering by water is caused by interactions of the incident X-ray photons with the electron density in the water molecule, located mostly in the oxygen atom. The X-ray diffraction signal is mostly dominated by oxygen-oxygen correlations. The majority of the measured X-ray signal undergoes either Thomson scattering or Compton scattering. Thomson scattering, or Rayleigh scattering, involves an X-ray photon interaction with the atom such that a photon is scattered with no change in energy. This type of scattering is a minor

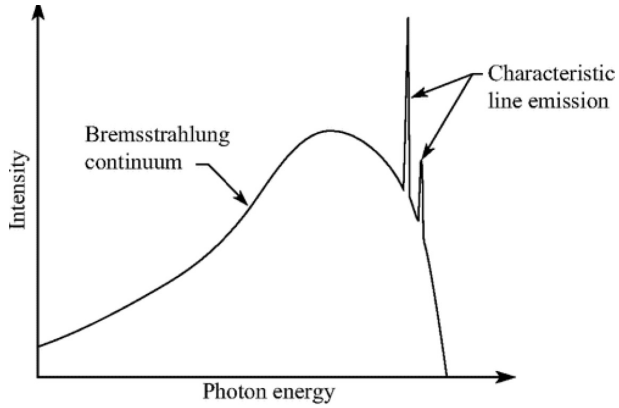

Figure 8.3: Continuum radiation and narrow line emission from a solid target (Attwood, 2016) [10]

contributor to the overall absorption coefficient. Compton scattering is the scattering of a photon after an interaction with a charged particle, usually an electron. Part of the energy of the photon is transferred to the recoiling electron. Compton scattering involves an X-ray shift caused by particle-like momentum of photons. Upon collision, the photon bounces off the electron, giving up some of its initial energy. The photon lowers its momentum since it cannot lower its velocity.

Figure 8.5 displays the attenuation length of X-rays in water based on photon energy. This shows the energy dependence of photoabsorption at low energy levels, as well as a leveling off at higher photon energies due to Compton scattering. The attenuation length is about four orders of magnitude longer for hard X-rays as compared to soft X-rays. Our experiments involve hard X-rays and have larger attenuation effects in water, primarily due to Compton scattering.

8.2 X-ray Source Tube

An X-ray tube, displayed in Figure 8.6, is composed of the following items: cathode, anode, X-ray window, filament leads and a ceramic vacuum envelope. The tube is maintained in a vacuum envelope to exclude air; and therefore permitting the unobstructed flow of electrons from the cathode to the anode. The cathode is maintained at a negative high voltage (kV) with respect the anode. The potential of the cathode is -10 to -500kV with respect to the anode. The potential between the cathode and anode is the accelerating force on electrons liberated from the cathode. Electrons are produced by passing a current through a filament. The current passing through filament causes the filament to heat to incandescence.

The target connected to the anode provides the necessary material to stop the electrons

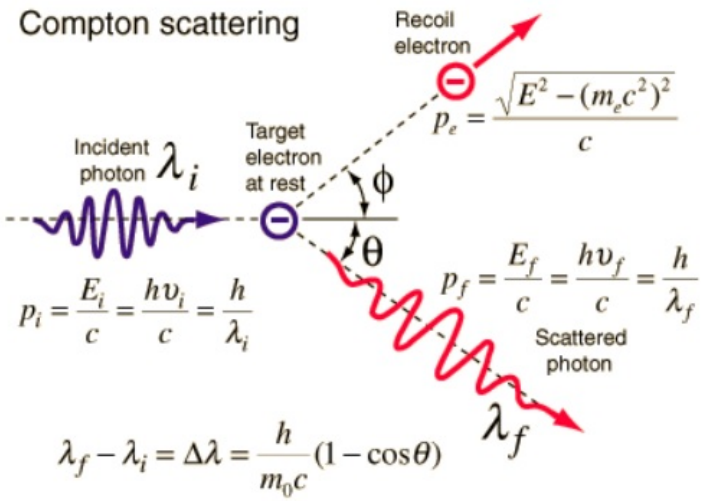

Figure 8.4: Compton Scattering
(http://hyperphysics.phy-astr.gsu.edu/hbase/hframe.html)

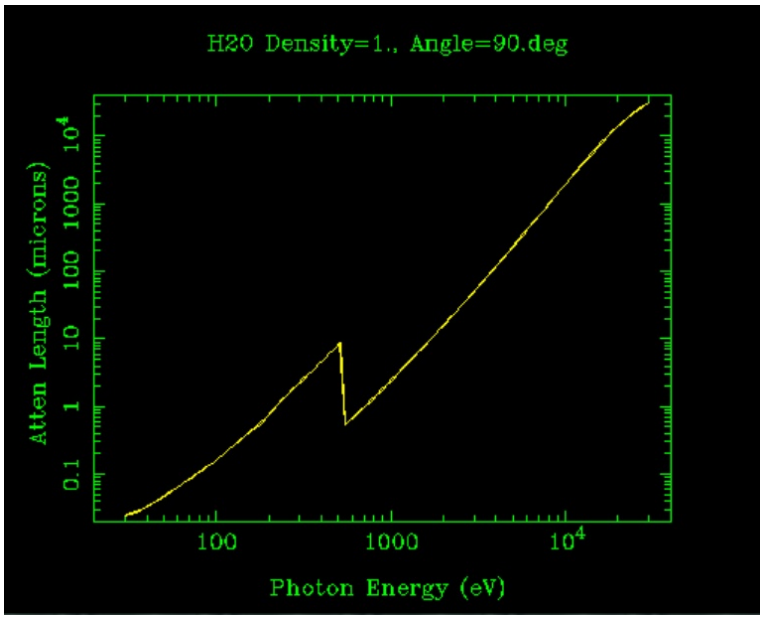

Figure 8.5: Water Attenuation Length vs Photon Energy

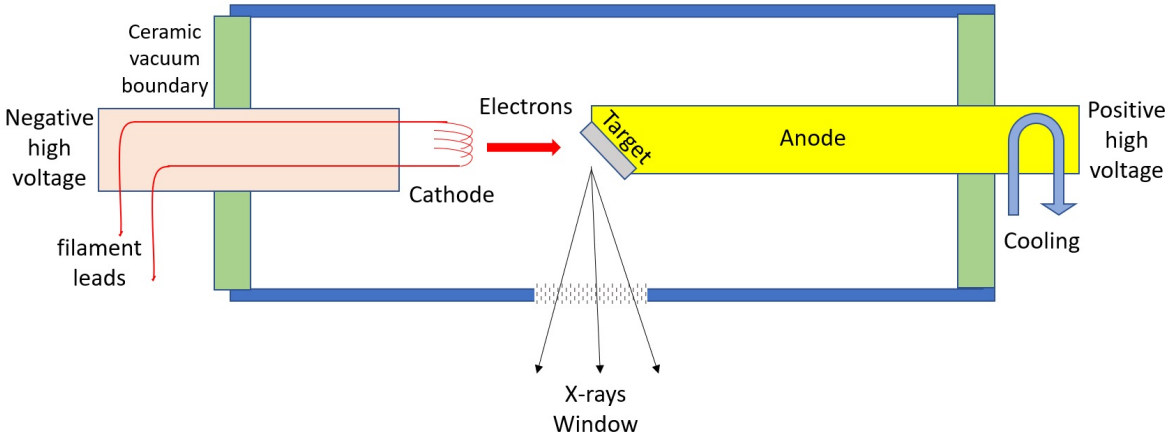

Figure 8.6: Schematic of an X-ray Directional Tube

and convert about 1% of their energy into the X-rays. The remaining energy appears as heat that is conducted through the anode to a coolant, water or air. The cooling must be in place to avoid melting or evaporization of the anode and ultimate destruction of the X-ray tube. Using an anode insert allows the anode material, Cu, to absorb the thermal effects and provide an electrical path. A Tungsten, W, material is used to provide X-rays, as a result of being bombarded with electrons.

The FXE-225.99 (51/48) microfocus tube is a low total power (64W) which is convected directly to air. Tungsten, W, is the most common anode material. It has a high melting point (3422°C) and adequate conductivity (1.74W/cm K). W produces intense bremsstrahlung and its characteristic K lines are at a useful energy levels.

The electrons experience acceleration from cathode to anode and will decelerate once they hit the anode. The energy spectrum emitted from the X-ray tube is a function of voltage potential between the cathode and anode, the target material, the angle at which the electron beam hits the target, the angle at which the X-rays are observed, and the material used for the X-ray tube window. X-ray transmission can be divided into "hard" X-rays and "soft" X-rays. "Hard" X-rays contain the short wavelength X-ray component which enhance the penetration into thick objects or objects with large densities. "Soft" X-rays components comprise the longer wavelength X-rays which enhance the image contrast (Heindel, 2011)[13].

A polychromatic X-ray beam contains both "hard" and "soft" X-rays. "Soft" X-rays are attenuated more readily than "hard" X-rays, producing an artifact called beam hardening. Beam hardening increases the average energy of the beam since the lower energy spectrum is preferentially absorbed.

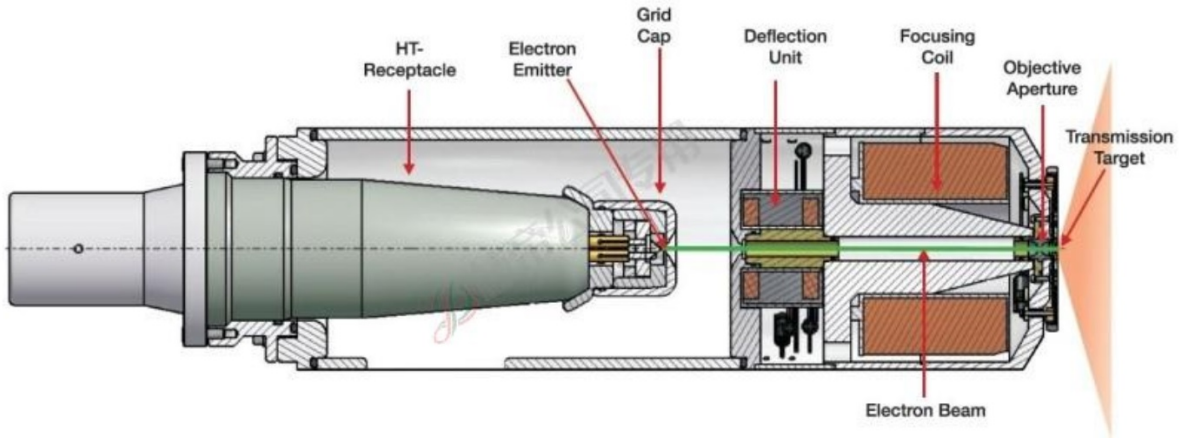

Figure 8.7: Transmission Tube Head Internal Parts
(credits: https://www.x-ray-worx.com/index.php/en/microfocus-x-ray-tubes-overview/microfocus-technology)

8.3 Microfocus Transmission Tubes

We will be using a microfocus X-ray tube, which has played an important role in industrial quality control and has advanced research methods. These X-ray tubes provide high resolution and high magnification X-ray scans. We will be using two types of microfocus X-ray tubes, transmission tube head and directional tube head. In areas where high resolution analysis is desired, high magnification tubes with a transmission tube head are used. If high power is required to analyze dense, mostly metallic materials, a directional tube head is used.

Transmission Head Tubes

The head of an X-ray transmission tube contains a "target" that can slide out. This target is covered with a very thin layer of Tungsten. Depending on the application, the Tungsten layer can range from 1-10 microns.

The target is bombarded with a focused electron beam in the so-called focal spot. The focal spot size defines the sharpness of the resulting X-ray image. A smaller focal spot results in better geometric sharpness.

The electron beam generates X-ray radiation in the Tungsten layer. Useful radiation is transmitted through a cone beam. The thickness of the transmission target has an impact on the maximum magnification in the X-ray microscopy. X-ray microscopy is a high magnification two-dimensional radiography. The closer the object is to the source of radiation the higher the geometric magnification. A thinner target yields a higher geometric magnification

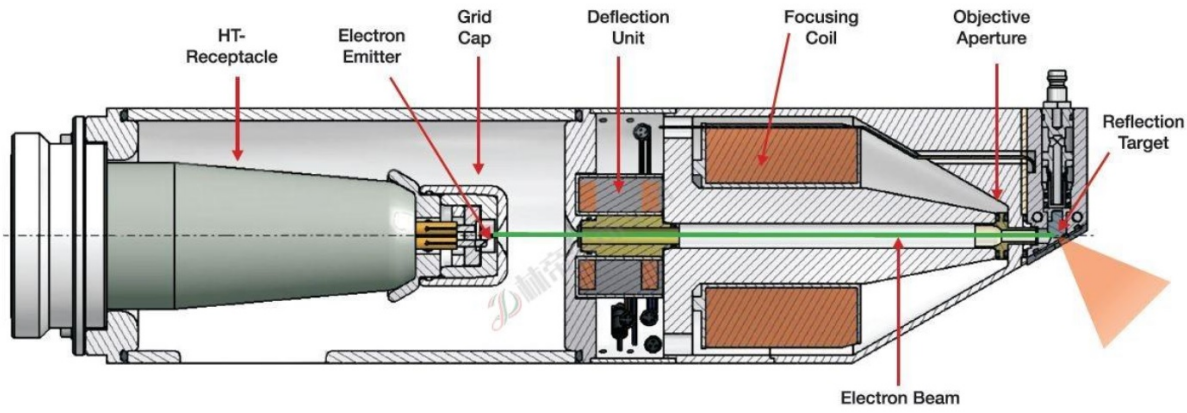

Figure 8.8: Directional Tube Head Internal Parts
(credits:https://www.x-ray-worx.com/index.php/en/microfocus-x-ray-tubes-overview/microfocus-technology)

for a given fixed focus-detector distance.

The maximum power of a transmission tube is limited to the heat conductivity of the transmission target. If the electron beam is focused on a single spot, it may exceed material temperature limits. Carbon is a material with the maximum heat conductivity in its three-dimensional crystalline form.

Directional Tube Head

The directional tube includes a denser metal target. There is also an integrated cooling system to provide cooling for the target to allow much higher electron consumption than a transmission head. The useful radiation is reflected in a 45°offset from the electron beam. The reflected cone beam is limited to 30°by the tube window. The directional tube has a higher magnification than the transmission tube due to the larger distance between the focal spot and the outer side of the tube window.

The following equation was utilized to calculate the penumbral blur (focal blur) of our X-ray experiment setup:

Focal blur calculation:

$$blur(pixel) = \frac{f(microns) * \frac{SID(mm) - SOD(mm)}{SOD(mm)}}{pixelwidth(microns)} \tag{8.3}$$

where f is the focal spot size from X-ray source manufacturer

$$blur(pixel) = \frac{6\mu m * \frac{1431mm - 1181mm}{1181mm}}{100\mu m} \tag{8.4}$$

Rotation and Translation of a Cone Beam

The X-ray source involves an X-ray tube that emits a single needle-like X-ray beam, forming a cone projection from a pin-hole collimator. This geometry is referred to as a "pencil beam". As the detector moves synchronously along with the X-ray tube, it displaces in a linear fashion over several projection angles. The differences in attenuation properties will result in variable intensities of the X-rays as it penetrates the object. As the object is rotated or the combination of the X-ray source and detector are rotated to maintain a perpendicular field, several projections of the same object must be collected to form a sinogram. Two-dimensional and three-dimensional reconstruction algorithms, such as filtered back projection, are used to account for the deviation from the center of the cone beam to produce an accurate depiction of the object. Although, this method is very effective in static environment, we will use it in dynamic multiphase flow environment to evaluate spatial resolution of time-averaged phase fraction of the flow.

8.4 THOR Photon Counter Detector Setup and Application

We purchased a THOR.FX.10.1.128.075.IP67.G2.A.WL photon counter as we learned that our X-ray detector suffered significant afterglow effects. The THOR detector is a dual energy photon counting detector assembly. The sensor is made up of CdTe and it has a pixel size of 100 microns with a pixel fill factor of 100%. It has an active area of 2048 X 128 pixels and adjusted to 2063 X 128 pixels by adding arbitrary pixels every 128 pixels to account for the tile gap and more closely approximate the actual dimensions of the object.

The detector is equipped with an external trigger that allows us to align our rotation device with our the photon counter. The detector's dual energy allows us to set a small window for our photon collection to get our polychromatic source closer to a monochromatic source, allowing us to utilize equations developed for monochromatic systems.

Figure 8.10 is an image of the detector mounted with the active area displayed by a white rectangle. Figure 8.11 is a layout of the photon counter from the manual displaying the side connections for the Ethernet cable and trigger cable that are both routed from the operator's station located approximately 30 feet from the detector.

Figure 8.12 displays the THOR photon counter positioned in between the two pairs of WMS. The distance between the bubble column and detector is approximately 250mm. The detector is mounted in such a way as to not interfere with the WMS and WMS cabling during bubble column rotation.

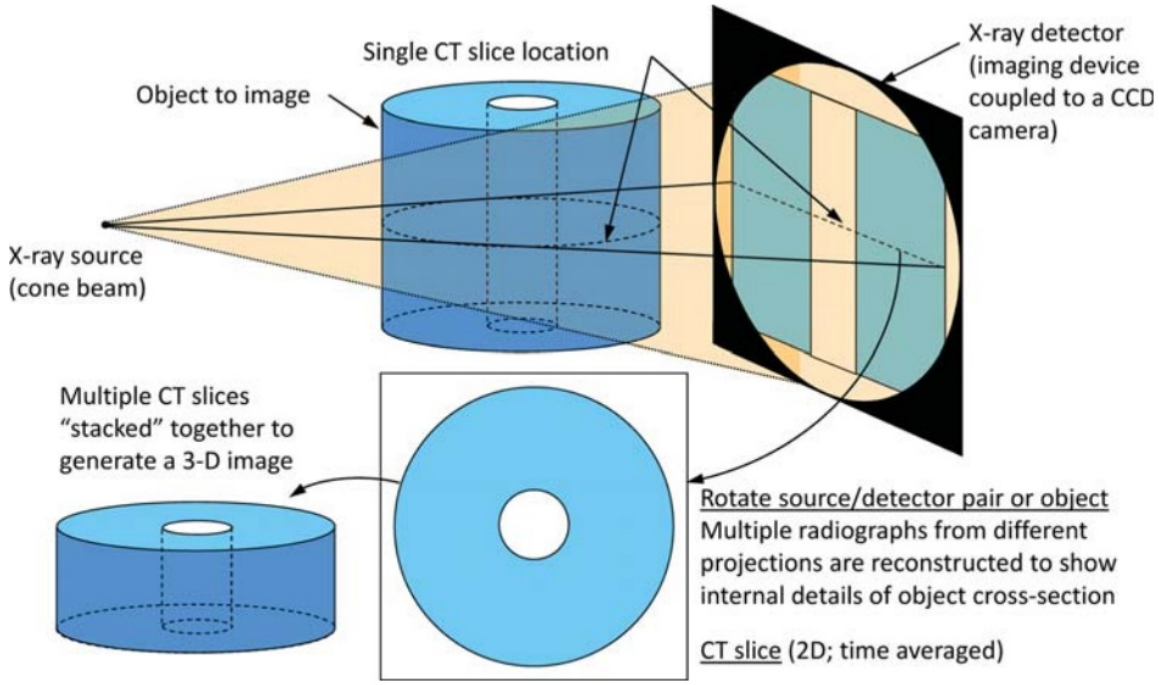

Figure 8.9: Schematic representation of X-ray Computed Tomography imaging (Heindel, 2011)[13]

We compensated for the pixel gap using MATLAB to add the missing pixel by interpolating the neighboring pixels. Figure 8.13 displays a typical intensity field with and without the pixel gap correction. You can see that the pixel gap correction applied in MATLAB renders a more uniform and geometrically correct intensity field. Figure 8.14 is a rendering of a reconstruction of a dimensional-specific phantom completed using the THOR photon counter detector.

8.5 X-ray Computed Tomography Calibration

In order to gain an understanding of the X-ray source, the imaging detector, the X-ray CT procedure and reconstruction algorithms, we performed several experiments that evaluated several parameters, such as power level (voltage and current of the X-ray source), spacing between the X-ray source, object and detector to achieve the proper magnification and evaluated the MATLAB-generated reconstruction code to render an adequate image that accounts for artificial artifacts. These particular considerations are time-consuming, but

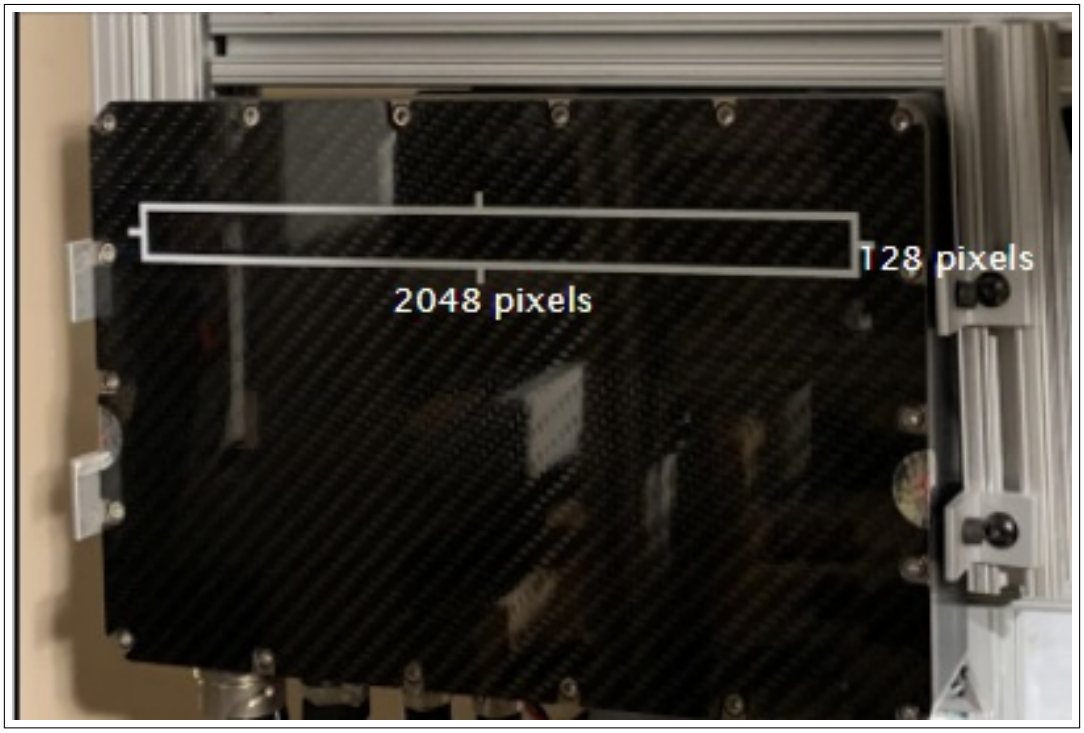

Figure 8.10: THOR Photon Counter Detector

essential to gain an appreciation for the technique and validate the results provided by this non-intrusive measurement tool.

Three-Acrylic cylinders computed tomography experiment to evaluate initial X-ray CT capability and challenges

The three-acrylic tube experiment was the first attempt to evaluate the phase fraction measurement in geometrical subsections of a vertical air-water column. The time varying local phase fractions and bubble sizes are of interest as they affect thermal performance of systems such as heat exchangers and Pressurized Water Reactors (PWR). As previously discussed, studies show that bubbles have a significant effect on wall drag and heat transfer in turbulent flows and may damage reactor core fuel cells. This phenomena is displayed in Figure 8.15. Depending on the conditions, bubbles may reduce or increase skin friction and heat transfer. Advanced measurement techniques are required to quantify the phase fractions in these processes. In these turbulent multiphase flow systems, it is necessary to improve understanding of the capabilities and limitations of the experimental techniques utilized to truly define the flow characteristics. With advances in high-speed cameras, wire mesh sensor

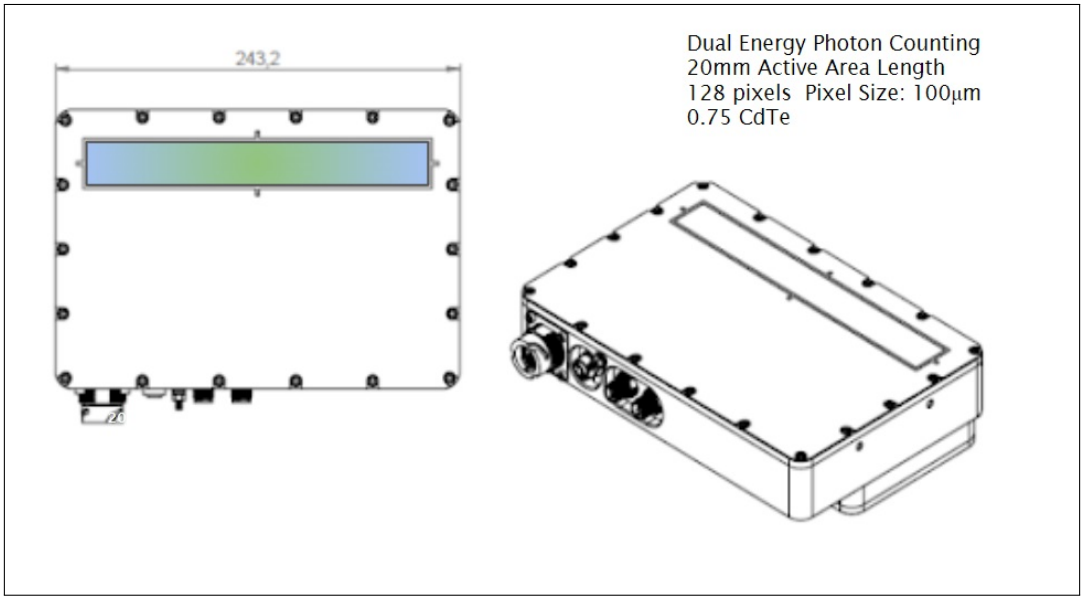

Figure 8.11: THOR Photon Counter Detector Layout

and X-ray Computed Tomography systems, the flow patterns in multiphase flow system can be better understood and further studied, to improve computer fluid dynamics modeling and inform or e.g. validate operational constraints on reactor core fuel systems.

Experiment motivation

Multiphase flows of interest are found in Pressurized Water Reactors (PWR), which operate in a cycle where the pressurized primary coolant is heated in the reactor core and cooled as it flows through the steam generator, where a secondary system recirculates water through the steam generator transferring heat from the primary coolant. The reactor coolant acts as a neutron moderator and forced to recirculate to cool the core with a single-phase flow with minimal occurrence of boiling.

Experiment setup

We used an acrylic cylinder enclosing three smaller acrylic tubes to have a static phantom mimicking a two-phase system with the addition of water to portions of the cylinder. The large acrylic tube measured a total diameter of 108.0mm and the smaller tubes measured 37.0mm outer diameter. The large acrylic tube was filled with water at room temperature and the three smaller acrylic tubes were left empty. Figure 8.16a displays an overhead image of the phantom utilized for these X-ray measurements. This ensured a static environment

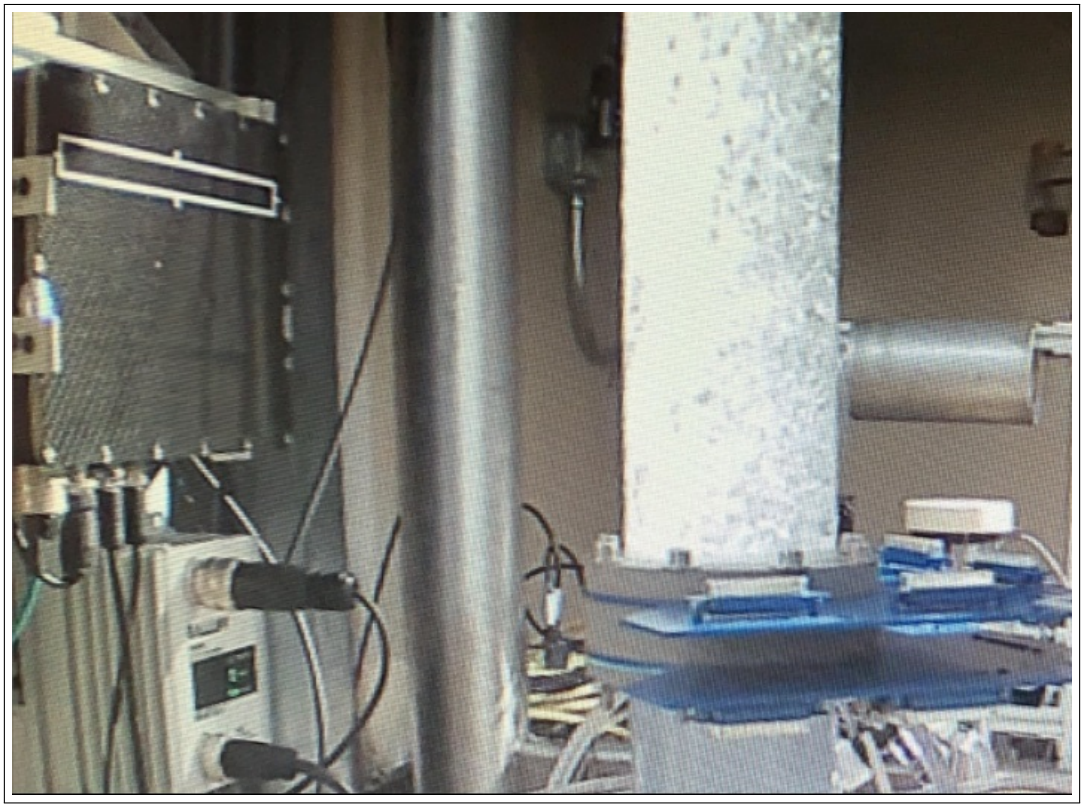

Figure 8.12: THOR Photon Counter Detector Location with respect to Bubble Column Experiment

where we could validate our system performance, examine artifacts, and improve the setup. We also use this experiment to evaluate the X-ray Computed Tomography algorithms utilized to reconstruct a two-dimensional slice of the phantom and later test-section with flow. Figure 8.16b shows the incremental measurements of the vertical section which allows us to compare the results of the reconstructed image with the actual geometry of the acrylic vertical section.

X-ray Computed-Tomography Reconstruction

The X-ray source utilized for this experiment is our FXE-225.99 YXLON, shown in Figure 8.17a. The FXE-225.99 (51/48) microfocus tube is a low total power (64W) source cooled by convection from ambient air, whereas the directional head is actively liquid cooled. With the micro focus head this X-ray source can operate at a maximum voltage of 225kV, a maximum tube current of 1mA and a maximum tube power of 64W. The experiment was conducted using a setting of 100kV and 200μA. The images were recorded with a PaxScan 4343R (Figure 8.17b) X-ray flat panel detector with a pixel pitch of 139μm.

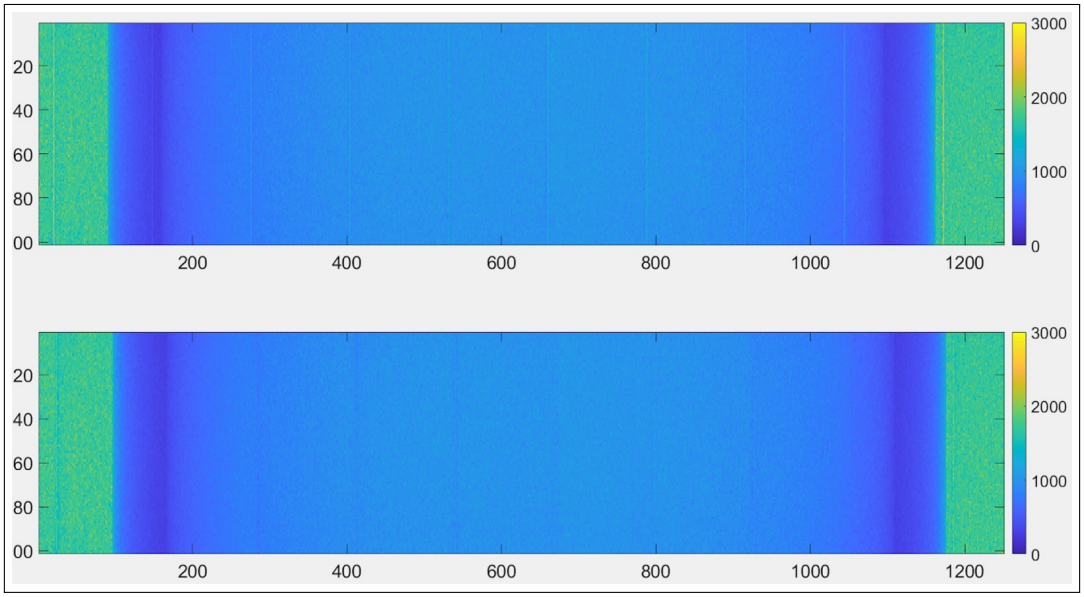

Figure 8.13: Intensity field before and after pixel gap intensity correction. Two changes were made. 1) an interpolated 'virtual pixel row' was added to replace the missing pixel row to recover exact relative spatial locations of pixels throughout the detector, and 2) the intensity of the pixels that collect charge over 125 instead of 100-micron width was accordingly multiplied by 0.7 to recover best estimate for what a 100-micron pixel would have provided as a signal.

X-rays are utilized to determine structural properties of samples at a wide range of length scales. The role of this imaging method is to replicate the location, amplitude, and spatial features of the original object (Attwood, 2016)[10]. To achieve this, the X-rays must hold sufficient energy to penetrate the material or object of interest with moderate attenuation, as there also needs to be contrast between objects of interest and their surroundings, with sufficient resolution to distinguish features of interest. In our experiment, we need to achieve contrast between water, air and the acrylic material.

With an extended collection of X-ray projections over incremental angles for a rotation of 180°or 360°, X-ray CT should acquire time-average and phase average void fraction distributions over the entire object cross-section. X-ray tomography is not intrusive and can perform as well as other void fraction calculation techniques that may be more intrusive, based on the accuracy and resolution (Prasser, 1998)[29]. This experiment is rotated as the intensity from the beam passes through the object and is measured by the PaxScan 4343R flat panel detector. With the understanding of projection distribution and material absorption properties, we can utilize tomographic reconstruction techniques to reconstruct the void inside the three smaller acrylic tubes. In our experiment, we utilized a Thor Lab Benchtop

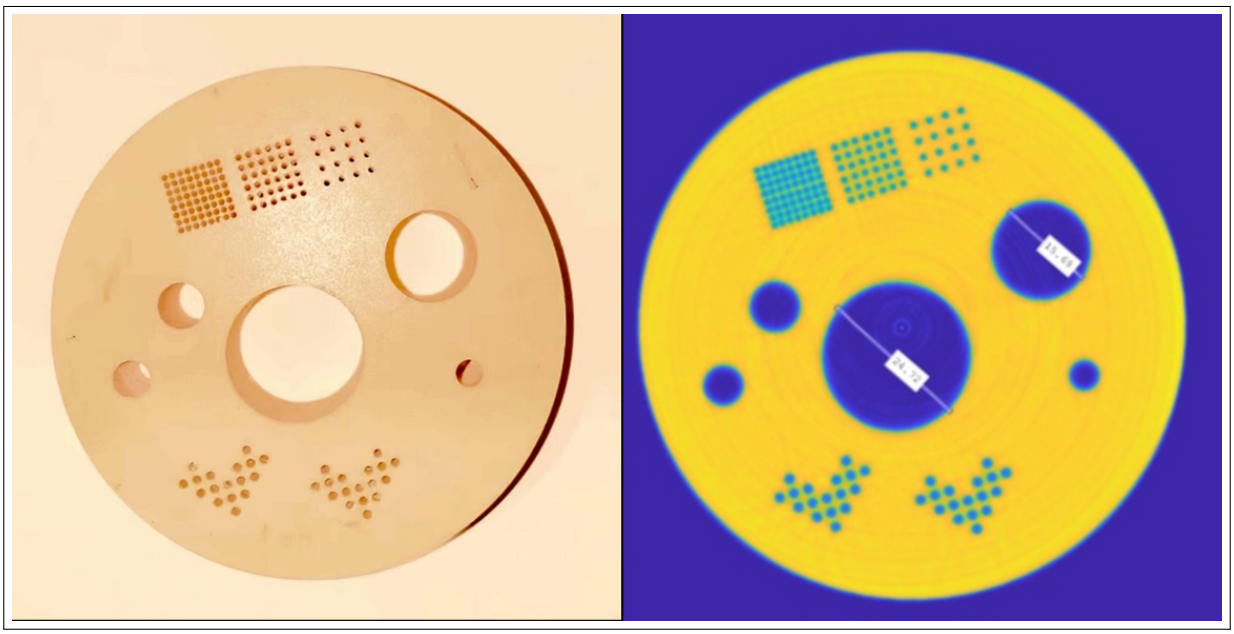

Figure 8.14: Bubble Phantom SIRT Reconstruction using the THOR Photon Counter

Stepper rotation stage to rotate the acrylic vertical tube 360 degrees at varying increments, initially as coarse as 5 degrees (with an accuracy of 820μrad) to collect 72 projections.

We used reconstruction algorithms implemented in the All Scales Tomographic Reconstruction Antwerp (ASTRA) Toolbox software program, which provides an efficient and flexible open source toolbox for tomographic projection and reconstruction (Aarle, 2016) [1].

X-ray Computed Tomography Experiment Results

To evaluate the number of projections required and performance of various reconstruction algorithms to render an adequate reconstruction of the acrylic cylinder, we constructed a phantom of the acrylic cylinder in MATLAB, simulating the phantom shown in Figure 8.18a. We then utilized ASTRA Toolbox [1] to render a sinogram (Figure 8.18b) and reconstructed results of the phantom (Figure 8.18c). For the first test, shown in Figure 8.19, a filtered back-projection reconstruction method was utilized to build the 2D slices. The reconstruction utilized 72 projections with an increment of 5 degrees.

Figure 8.19 displays the first measured sinogram and reconstructed image of the actual acrylic cylinder (phantom) using 72 projections. The disparity found on the outer edges of the reconstruction is very distinct and the circle boundaries are spatially offset and partially clipped due to the imperfect centering of the phantom apparatus on the vertical and horizontal plane. The data from this first test of our custom build system highlights the need

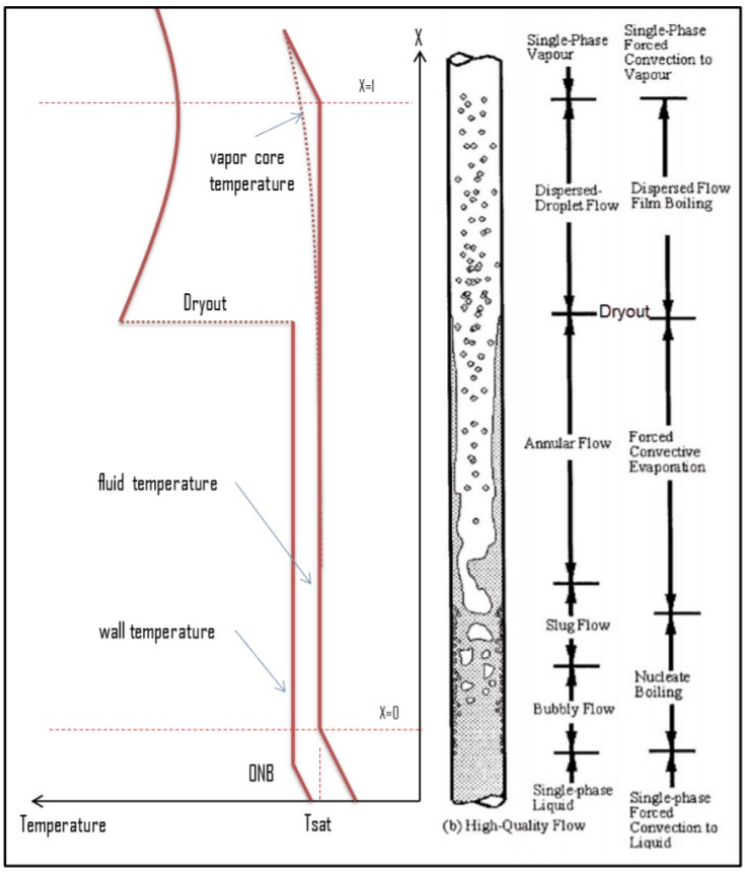

Figure 8.15: Flow Boiling Regime (www.nuclear-power.net)

for improved rotation angle accuracy, better centering, effect of uncontrolled lateral motions (seen as the spatial artifacts), effect of error in dataset (row 28 in sinogram repeated from row 29 due to system error), etc.

Figure 8.20a displays a phantom, constructed in MATLAB, simulating the acrylic cylinder filled with water in the areas between the large cylinder and each smaller cylinder. The accompanying sinogram and reconstructed image were built using 72 projections. Figure 8.21 displays the sinogram and reconstructed image of the actual acrylic cylinder, filled under the same conditions as the phantom, using 72 projections. Under these conditions, the acrylic cylinder presents a two-phase system to the X-rays. However, this dataset also has positioning errors, as well as artifacts from bean hardening, and finite spatial resolution, etc. The disparity found on the outer edges of the reconstruction result from poor centering of the experiment section. We expect resolution to improve with increased projections and improved centering of the object inside the X-ray beam.

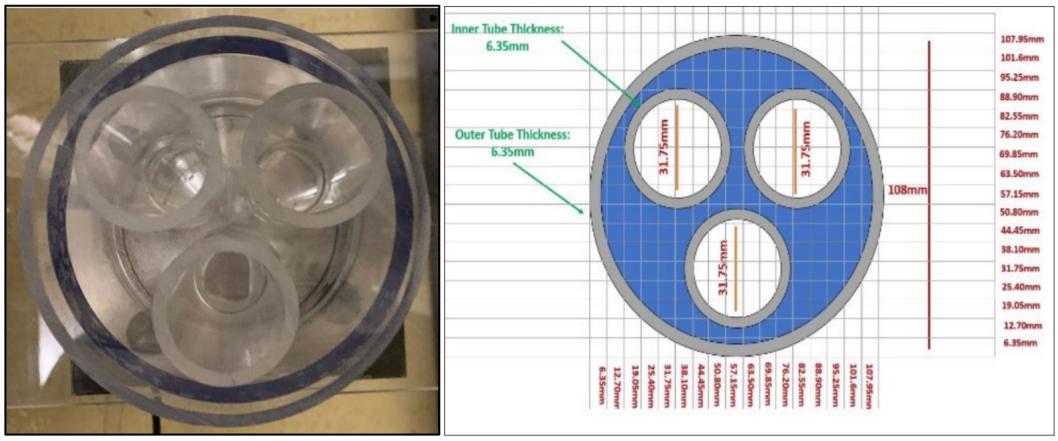

Figure 8.16: a) Image of Acrylic Cylinder with three-Acrylic inner tubes b) Cylinder Dimensions in further detail

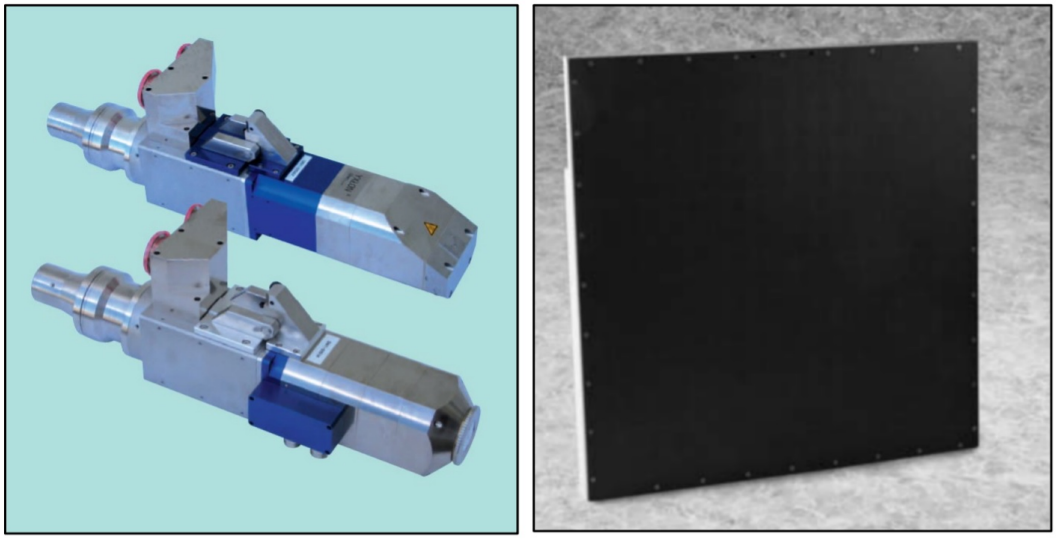

Figure 8.17: a) FXE-225 Microfocus Tube (YXLON) b) PaxScan 4343R Flat Panel Detector (PaxScan User Manual)

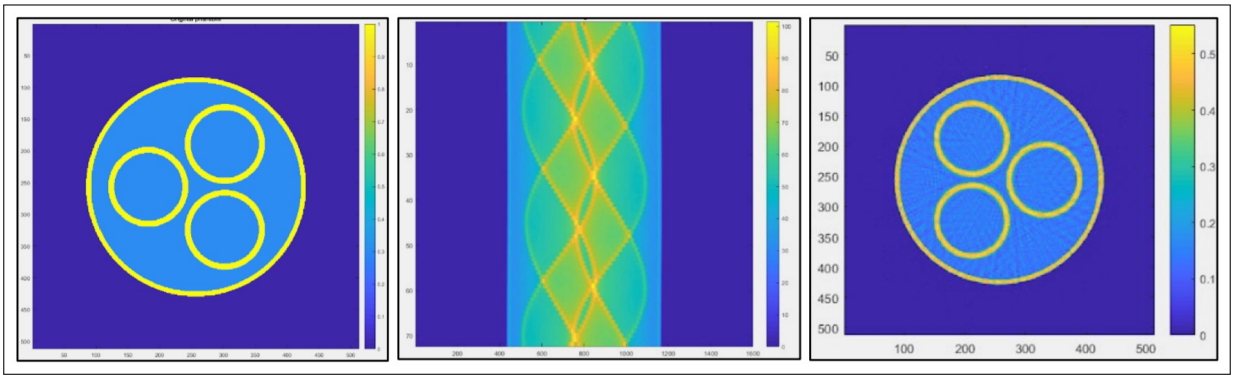

Figure 8.18: a) Original simulated Phantom-Water for cylinder b) sinogram c) ASTRA Toolbox FBP-CT Algorithm Reconstruction

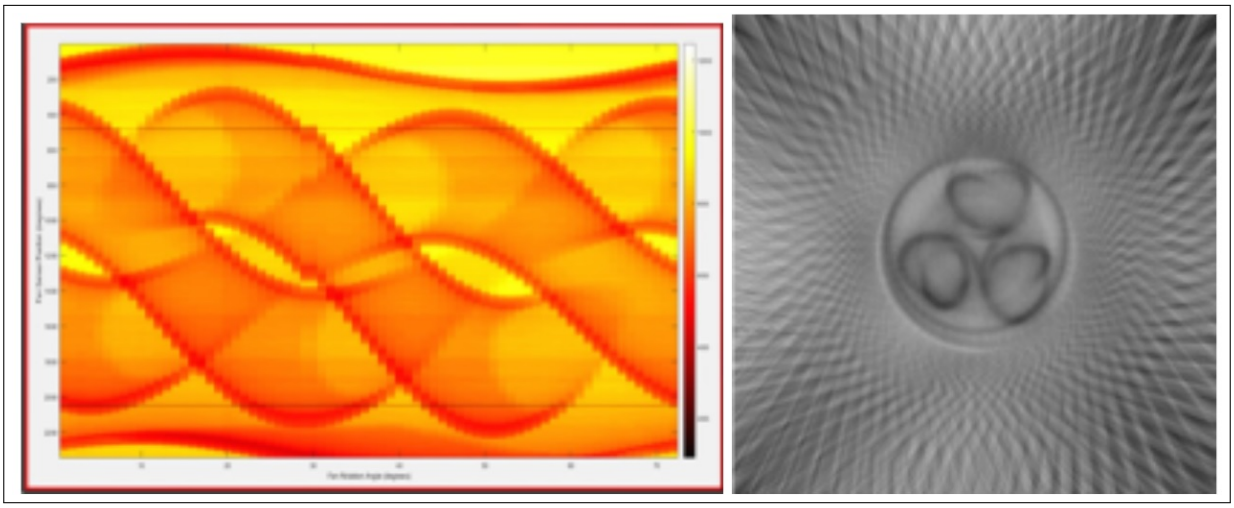

Figure 8.19: a) Water-free Cylinder Sinogram (72 projections) b) ASTRA Toolbox CT Algorithm Reconstruction (For this first test of the system, the idea was to also get familiarity to imaging artifacts like the one displayed in the reconstruction which is introduced by improper centering of the object).

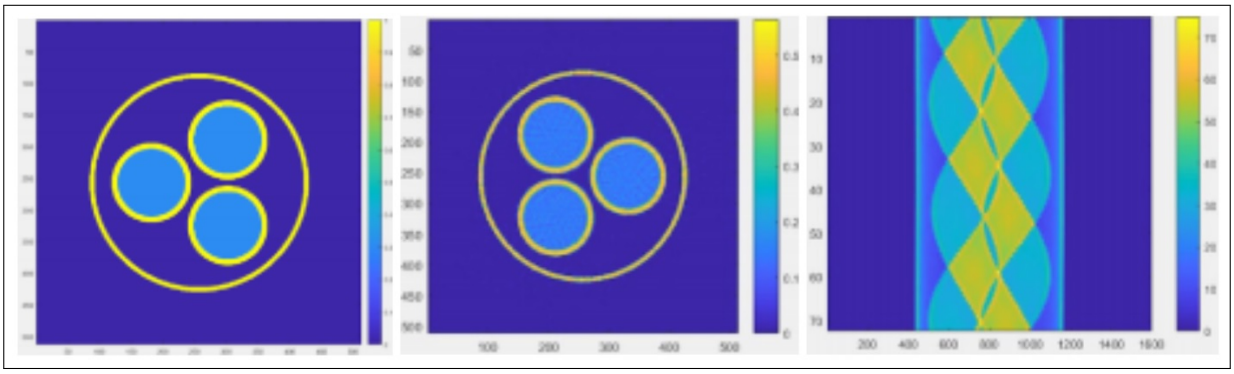

Figure 8.20: a) Original Phantom – Water-filled Cylinder b) Sinogram c) ASTRA Toolbox Phantom CT Reconstruction

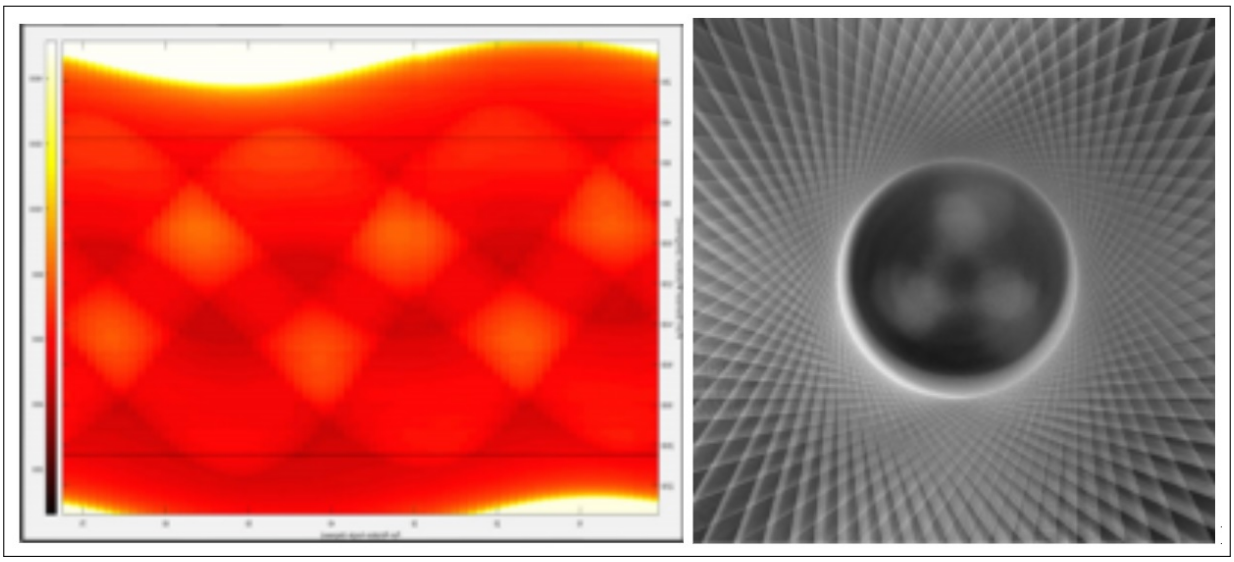

Figure 8.21: a) Water-filled Cylinder Sinogram (72 projections) (note that the imager also had bad pixel rows left uncorrected in initial system tests) b) ASTRA Toolbox CT Algorithm Reconstruction. As before, the goal at first was to get familiarity to imaging artifacts that may be produced.

Experiment Lessons Learned

Further reconstruction with a larger number of projections and smaller increment of degrees will result in a better reconstruction of the two-phase apparatus. We also learned from this experiment that centering and a higher current is essential to provide proper alignment and contrast to the reconstruction algorithms. As we continue to improve our custom built X-ray systems and the CT reconstruction algorithms, we can evaluate for more accurate measurements that will translate to an effective measurement tool of variable multiphase flows and will eventually allow us to compare flows of relevance to PWR and bubble column reactors. Utilization of improved X-ray system parameters, rotation accuracy and CT reconstruction algorithms to address artifacts will allow us to evaluate the flow regime inside fuel channels.

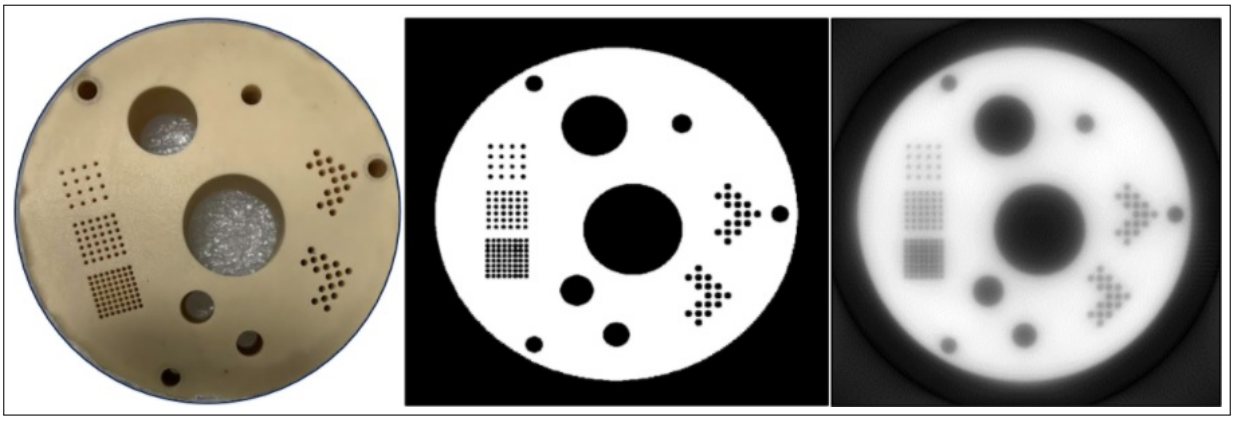

Figure 8.22: a) Actual Phantom b) simulated ideal phantom, and c) reconstructed Phantom

Rectangle Phantom Reconstruction

We used a rectangle of dimension 18mm by 22mm to use varying projection angles to reconstruct the rectangle to verify X-ray settings and reconstruction algorithms that yield optimal results for reconstruction. The rectangle phantom is made of water-equivalent material with attenuation characteristics similar to water, which is our primary medium. The rectangle was placed 1181mm from the directional tube head target and 143mm from the detector. Figure 8.23 depicts the actual phantom utilized during these X-ray calibration runs, with a green oval around the actual rectangle portion that was reconstructed.

Figure 8.24 displays a side-view X-ray projection of the rectangle phantom. This projection was calculated by using the mean of a series of projections. The averaged object projection was then filtered by utilizing a dark image (no X-ray source beam) and flat image (no object in the X-ray source cone beam) to eliminate noise introduced by the detector and the source.

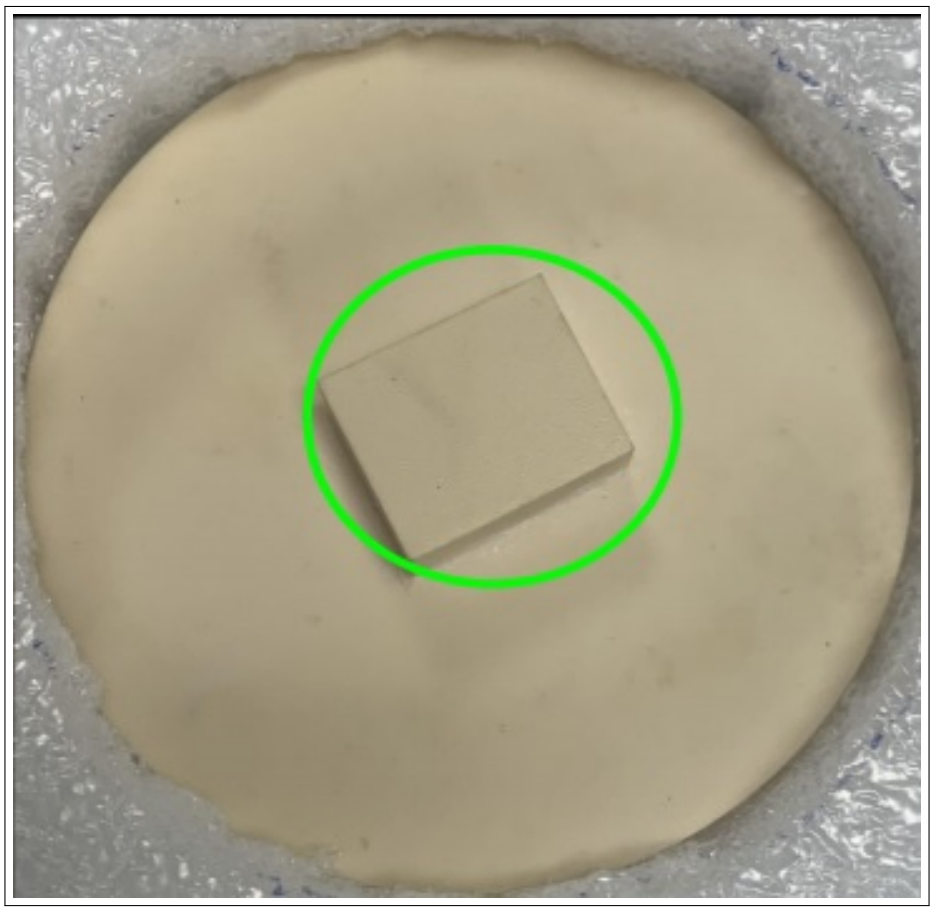

Figure 8.23: Actual Rectangle Phantom

Figure 8.25 displays the sinogram of 72 projections. Along the horizontal axis, the 72 angles are displayed. Along the vertical axis, the intensities along each projection are displayed. The sinogram is utilized to display the intensities for each angle. The reconstruction algorithm will utilize the sinogram to perform iterations using previous reconstruction as a weighing function and the original filtered back-projection.

Figure 8.26 is a display of the rectangle phantom reconstruction using SIRT CUDA ASTRA Toolbox reconstruction algorithm. This figure has several artifacts that require rectifying to produce a more accurate reconstruction. These artifacts are introduced by the inability to properly center the object in the cone beam field of view. Since each pixel is 100 microns, it is difficult to ensure the object stays completely in the center during rotation. Off-center problems will introduce artifacts and will affect the resolution of the reconstructed image.

Figure 8.27 displays what a difference adjusting the center of rotation will make to each

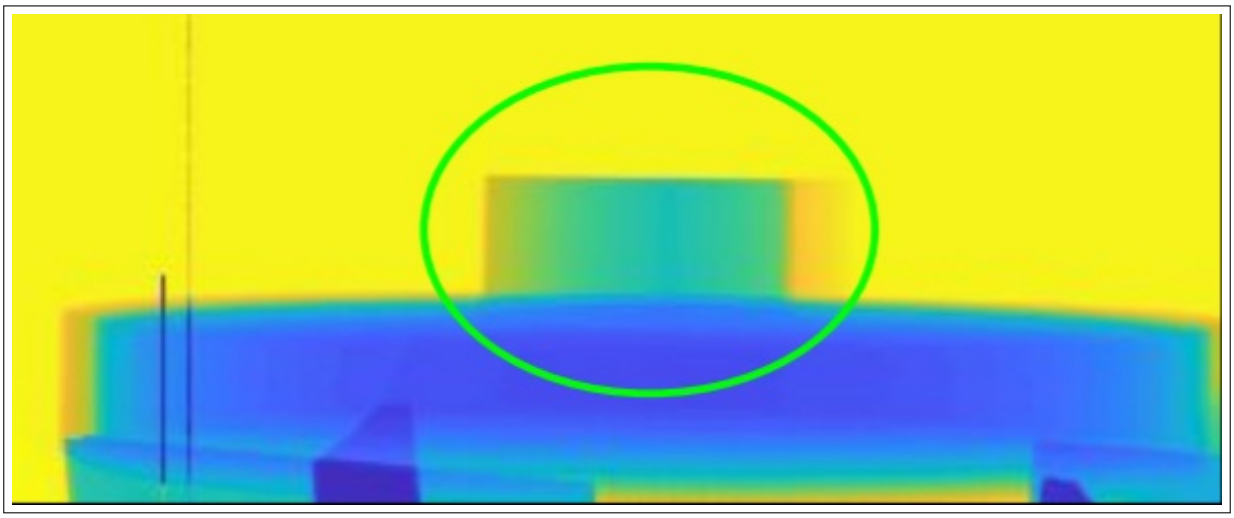

Figure 8.24: Side-view X-ray Image Projection of Rectangle Phantom

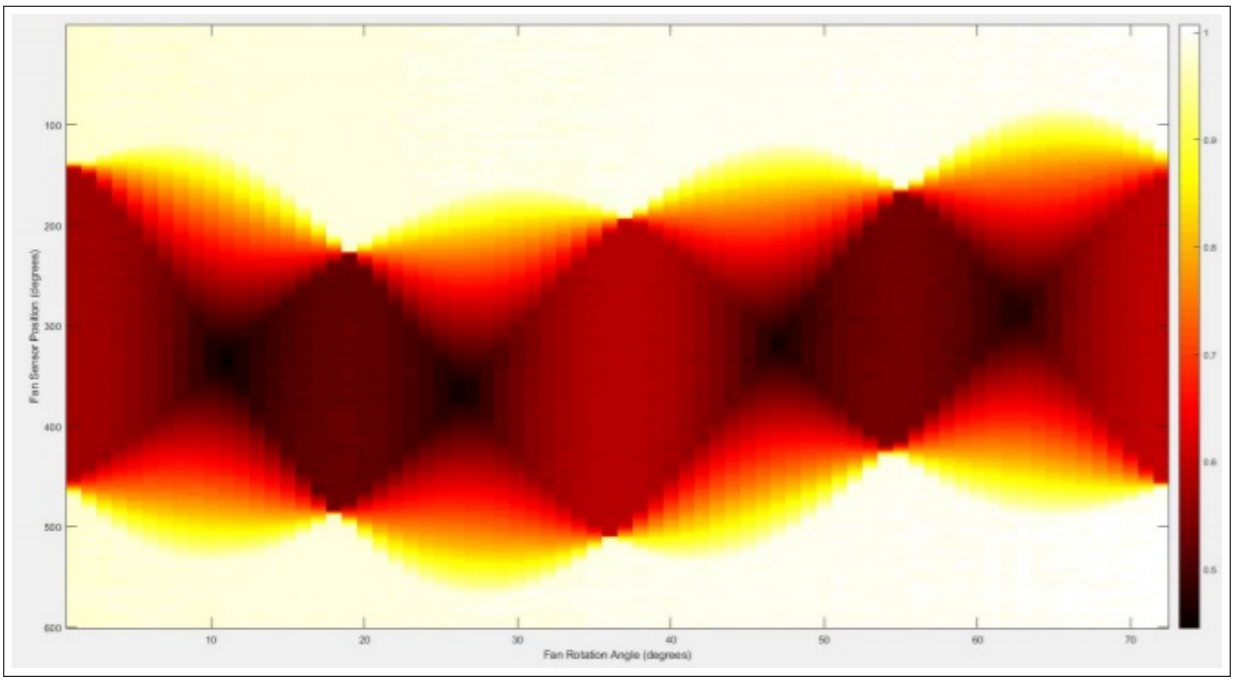

Figure 8.25: Side-view X-ray Image Projection of Rectangle Phantom

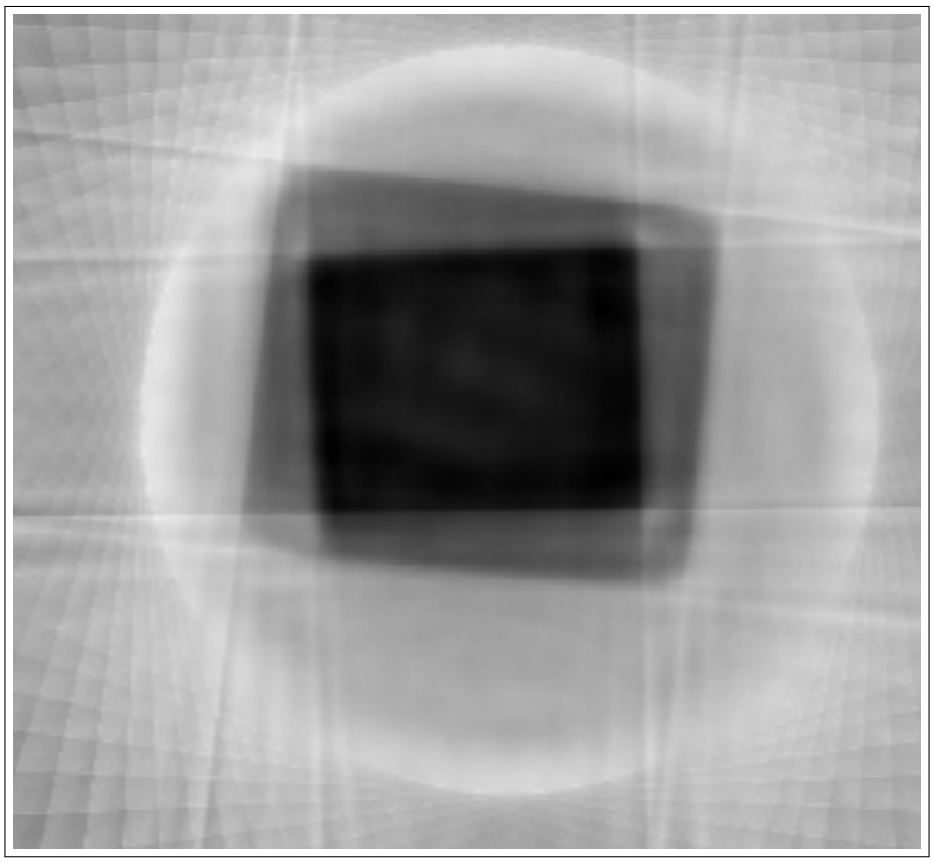

Figure 8.26: SIRT CUDA Reconstruction of Rectangle Phantom using 72 X-ray projections

reconstructed image. We apply a center of rotation offset by adjusting the pixel values by a prescribed pixel amount and apply that change to each projection. As you can see in the Figure 8.27, a center of rotation offset of 10 pixels will correct the image reconstruction. 10 pixels correlate to an offset of 1mm throughout a single rotation of the object. As you can infer from this, these corrections are necessary to correct the inaccurate placement of the object in the cone beam.

Figure 8.28 depicts a side view of the rectangle phantom using 360 projections. Figure 8.29 displays a sinogram of the same rectangle phantom using 72 projections. We used a different detector. Previous images were taken with PAXSCAN4343R detector with a pixel pitch of 139μm. These images were collected using a DT1412 detector with a pixel pitch of 100μm. The DT1412 detector allowed us to capture X-ray projections at a faster rate and collected all projections to a single file.

Figure 8.31 displays a sinogram constructed of 360 projections of variable intensity values displayed along a vertical axis.

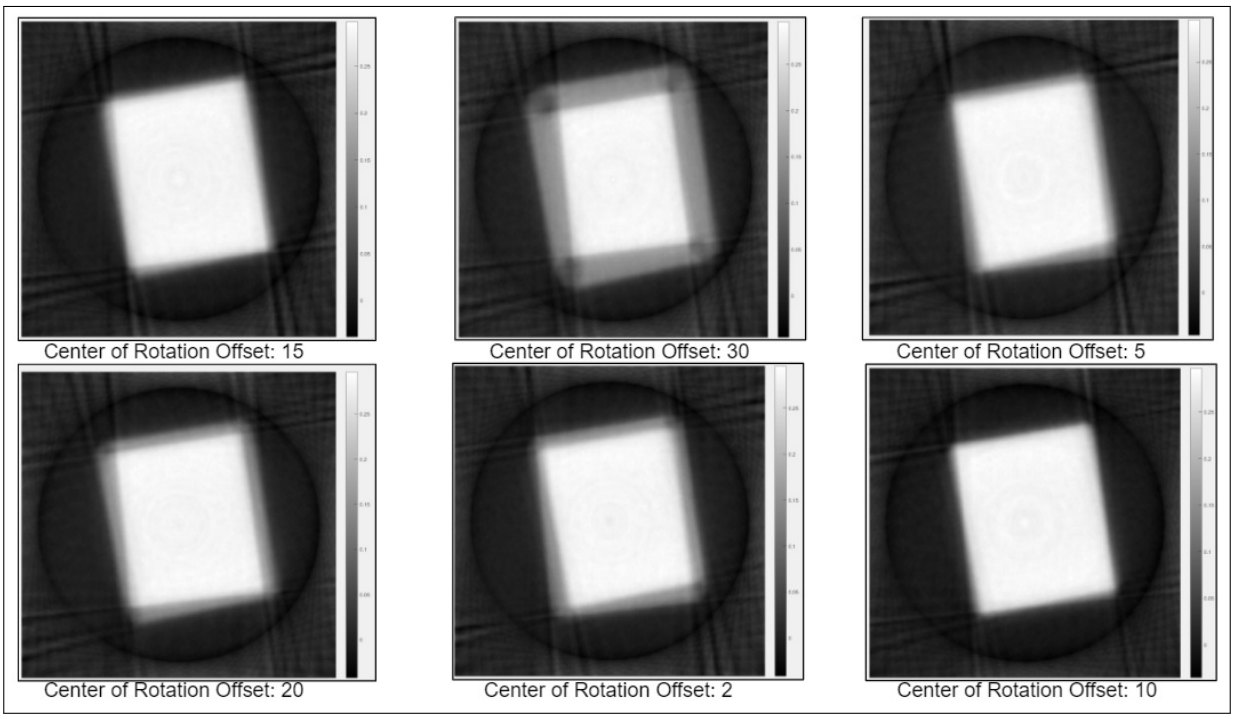

Figure 8.27: Rectangle Phantom SIRT CUDA Reconstruction (various center of rotation values)

Figure 8.30 displays a reconstruction of the rectangle using 72 projections. Here we applied thresholds to evaluate contrast and proximity to image saturation. The X-ray source was transmitting in High Power mode with 90kV and 125μm. The detector was operated continuously in Low Full Well with a frame period of 13300μsec.

Figure 8.31 displays a sinogram of the rectangle phantom with 360 projections. As a comparison with the sinogram composed from 72 projections, the sinogram is smoother and the boundaries of the rectangular features are more evident. The reconstruction of the rectangular phantom using these 360 projections is displayed in Figure 8.32. The reconstructed image was rendered using ASTRA toolbox SIRT CUDA algorithm, which makes use of the iterative reconstruction methods and graphics processing card. The reconstruction, as compared to Figure 8.30, shows a sharper edge at the corners of the rectangle and a more uniform attenuation coefficient for the entire rectangle.

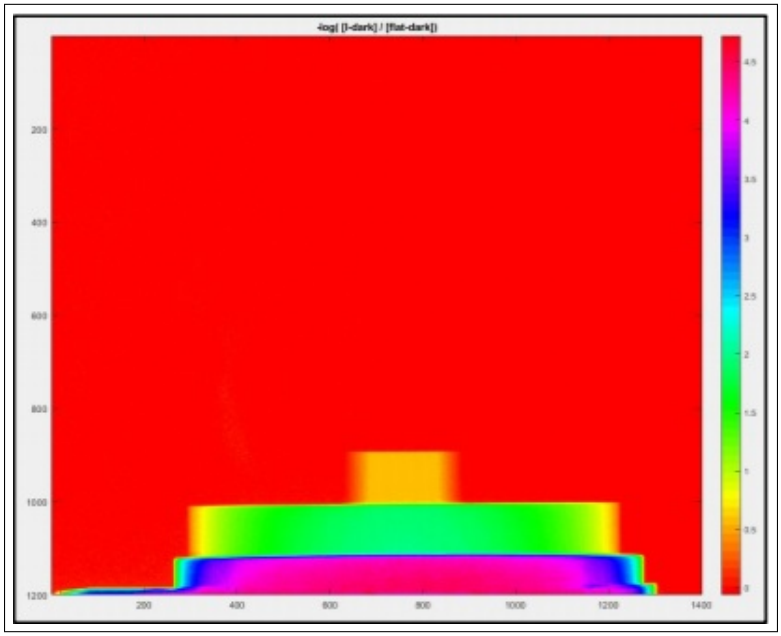

Figure 8.28: Side-view of Rectangle Phantom with 360 projections

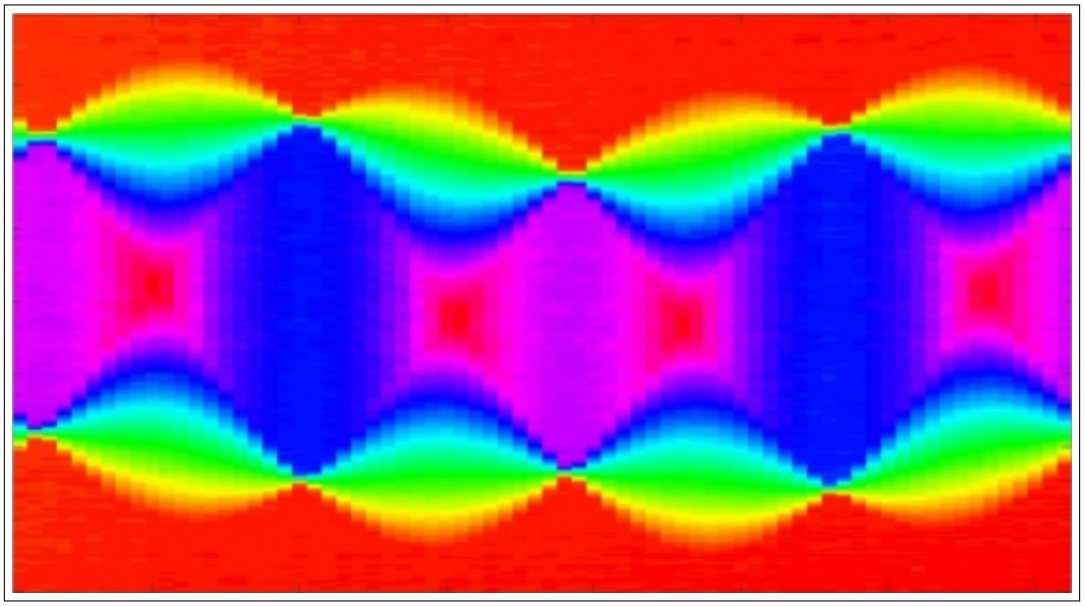

Figure 8.29: Sinogram of rectangle phantom with 72 projections

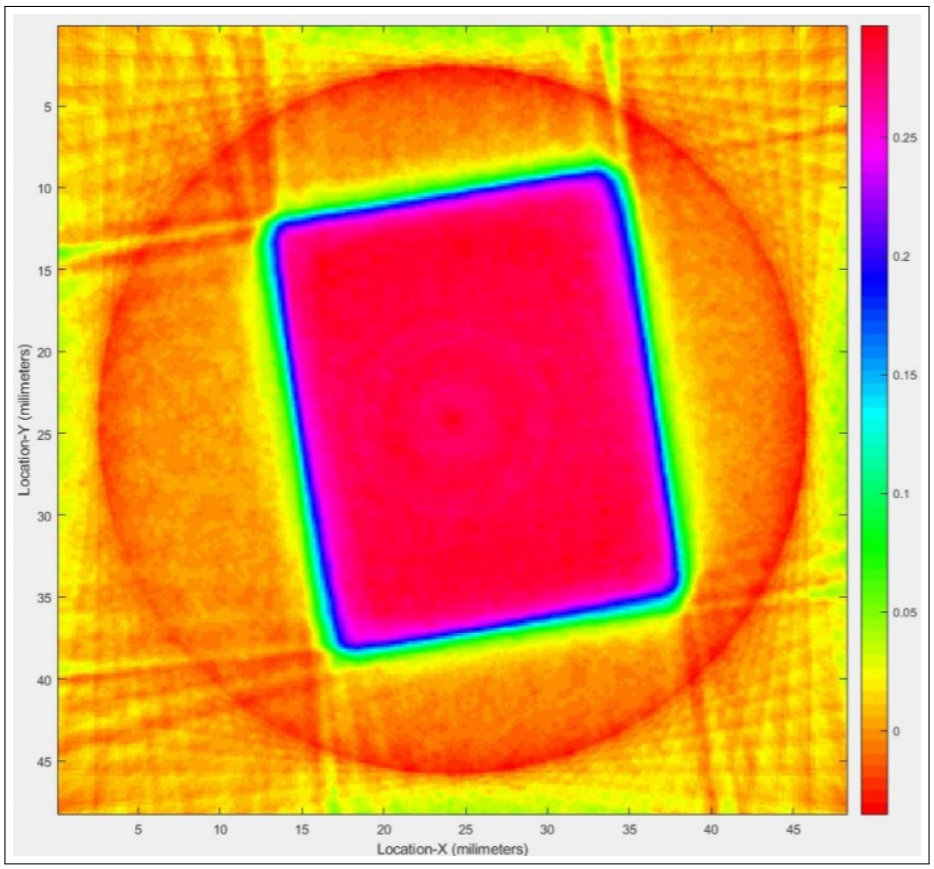

Figure 8.30: SIRT CUDA reconstruction of rectangle phantom with 72 projections(x-axis: angles; yaxis: projections)

8.6 Bubble Phantom Reconstruction

After gaining familiarity with the reconstruction algorithm and understanding the technique we will be utilizing for future X-ray CT measurements, we logically moved on to a more rigorous geometric shape that provided dimensions closer to our experiment. We designed a phantom, that will be referred to as the bubble phantom, since it mimics void areas in a material that has the same attenuation properties as water. The bubble phantom measures 76.2 mm in diameter and variable diameters for several voids. The smallest void is 1 mm in diameter. Figure 8.33 displays the bubble phantom positioned on the rotation stage.

Similar to the rectangular phantom, we built the bubble phantom in MATLAB, displayed in Figure 8.34, to evaluate the reconstruction algorithms and evaluate how many projections are required to render an adequate reconstruction. Figure 8.35 is a SIRT CUDA 3D reconstruction of the bubble phantom using 360 projections. Several of the artifacts are

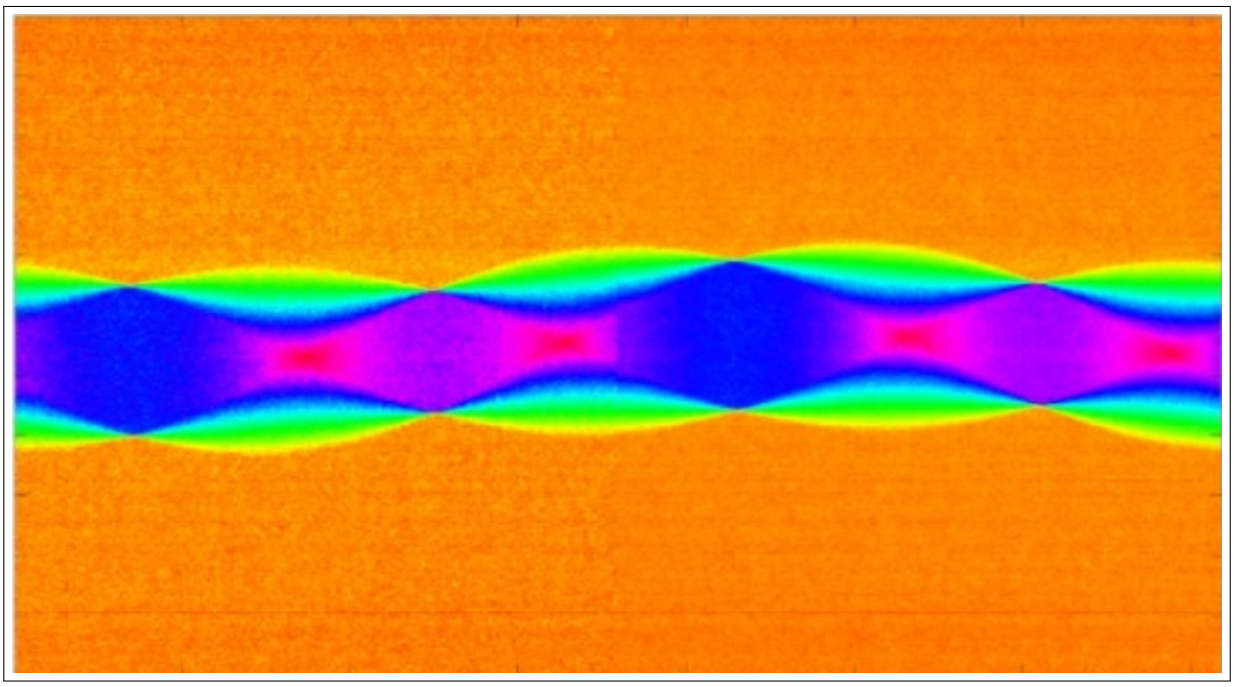

Figure 8.31: Sinogram of rectangle phantom with 360 projections (x-axis: angles; yaxis: projections)

introduced by the reconstruction software. Seeing how we can reconstruct the MATLAB-produced bubble phantom with the SIRT algorithm provided by ASTRA toolbox, we moved on to collect projections on the actual bubble phantom using the DT1412 detector.

Figure 8.37 was our fist attempt at reconstruction of the bubble phantom. Besides making adjustments to correctly align the bubble phantom in the X-ray beam, we also noticed that we have beam hardening effects visible in our reconstruction. These beam hardening effects show a non-uniform attenuation coefficient across the phantom and there is obscurity, deteriorating the resolution on the smaller holes. The striping is another artifact introduced by the misalignment of the phantom. We will discuss these artifacts in the last section of this chapter.

We positioned a 6.35 mm acrylic plate halfway between the object and the X-ray source to attempt to eliminate the beam hardening effects. We have a polychromatic source which is therefore susceptible to beam hardening effects. The polychromatic beam is comprised of a range of energy spectrum, and the energy spectrum is not attenuated uniformly when passing through an object. The lower energy photons are more easily attenuated or even completely adsorbed when traveling through a dense part. Beam hardening effects are observed in the reconstructed image by noticing a lower attenuation coefficient at the edge of the object

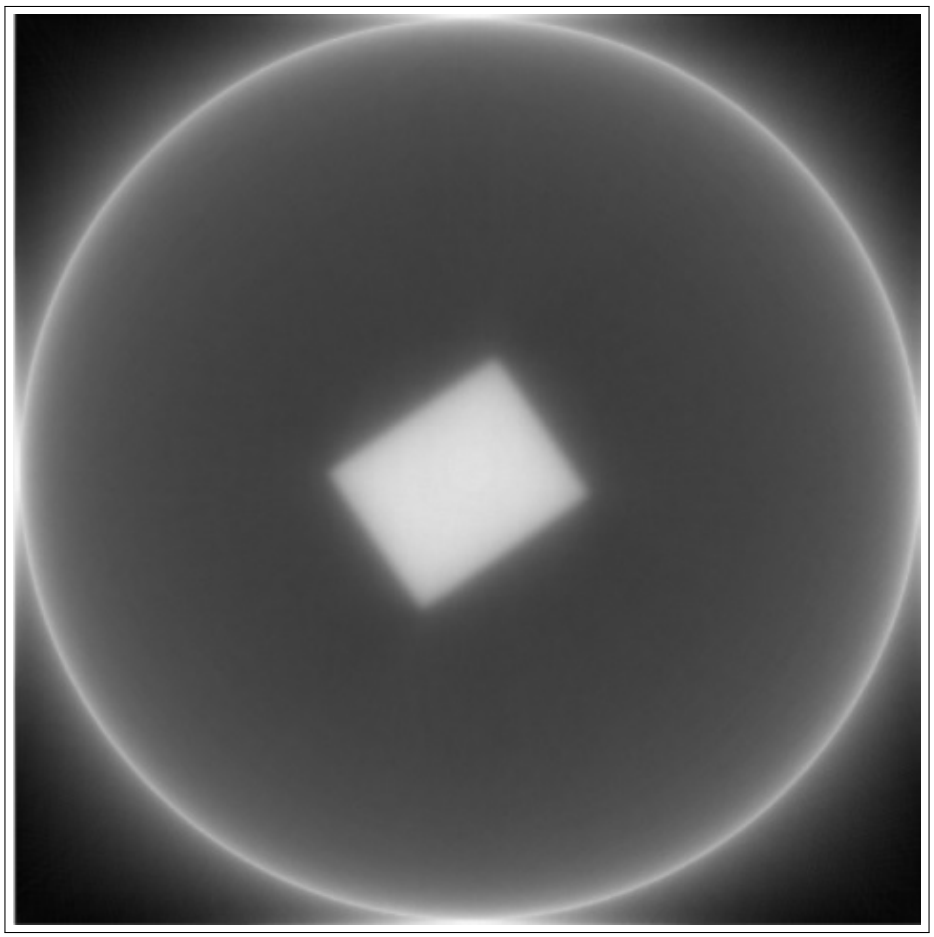

Figure 8.32: SIRT CUDA reconstruction of rectangle phantom with 360 projections

resulting in brighter voxels even if the object consists of homogeneous material. Figure 8.38 shows a reconstructed image after applying the acrylic plate. You can notice a substantial reduction in beam hardening effects. We have a better resolution resolved to 1mm based on the diameter of the smallest hole. Other artifacts that are evident and are not caused by beam hardening are ring artifacts and streaks, which we will address later.

As we continued to evaluate our images with the DT1412 detector, we noticed afterglow effects with longer duration scans. With a 1 second exposure, a collection of 3600 images took a lengthy time and intensity fields captured by the scintillation detector were not consistent over time and introduced afterglow effects. These afterglow effects introduce a non-uniform intensity field, producing a poor reconstruction image. We purchased a photon counter detector, which does not exhibit afterglow effects. The photon counter detector is equipped with cadmium telluride (CdTe) imaging modality which provides benefits to scintillation

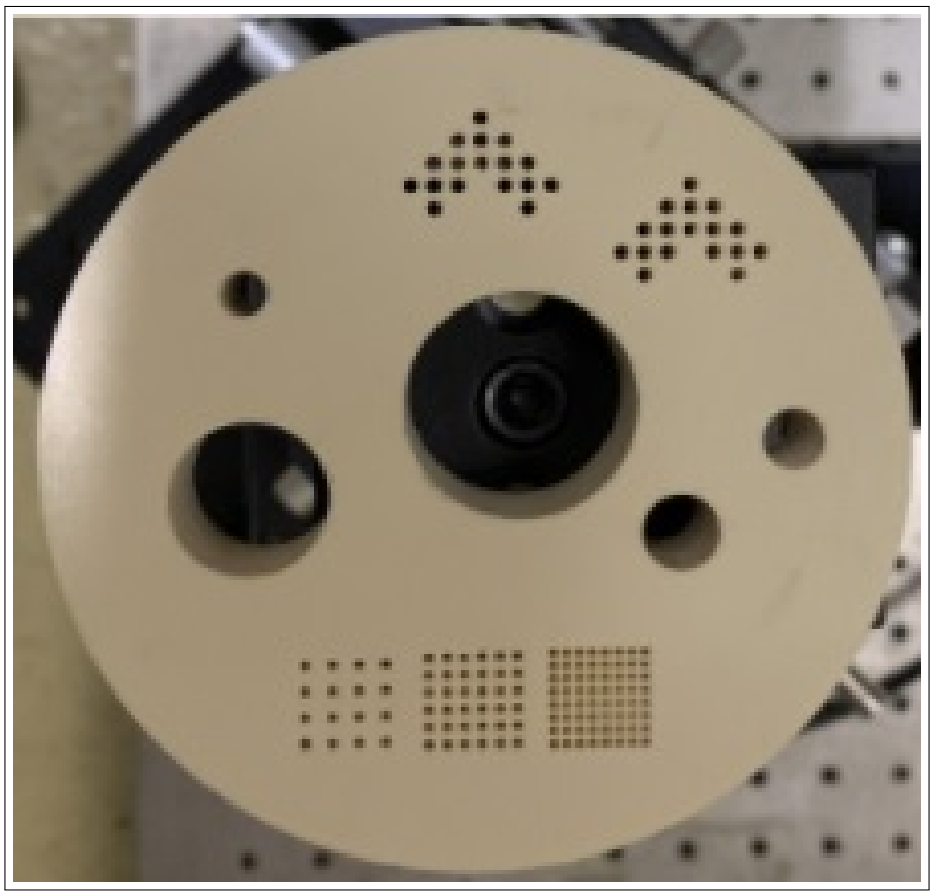

Figure 8.33: Original bubble phantom

detectors. Photon counters have an intrinsic resolution similar to the pixel size because the photon is collected individually by each pixel. The energy resolution of photon counting detector is higher than scintillation detectors because the energy is converted directly to a signal. Figure 8.39 is a SIRT CUDA reconstruction of the bubble phantom using 360 projections, collected by our photon counting detector, THOR FX20.1.128.075 model. This image has an improved resolution of the bubble phantom, with no striping but ring artifacts are still present. We modified our MATLAB reconstruction code to add algorithms to eliminate ring artifacts.

Ring artifact removal was accomplished in the present work utilizing the method of adaptive center determination for effective suppression, introduced by Jha et al (Jha, 2014) [15]. Jha et al's developed a method that is based on Gaussian localization of the ring center in the Hough parameter space so the proper origin could be assigned to the polar transformation. Once the rings are placed into linear stripes, existing methods are used to

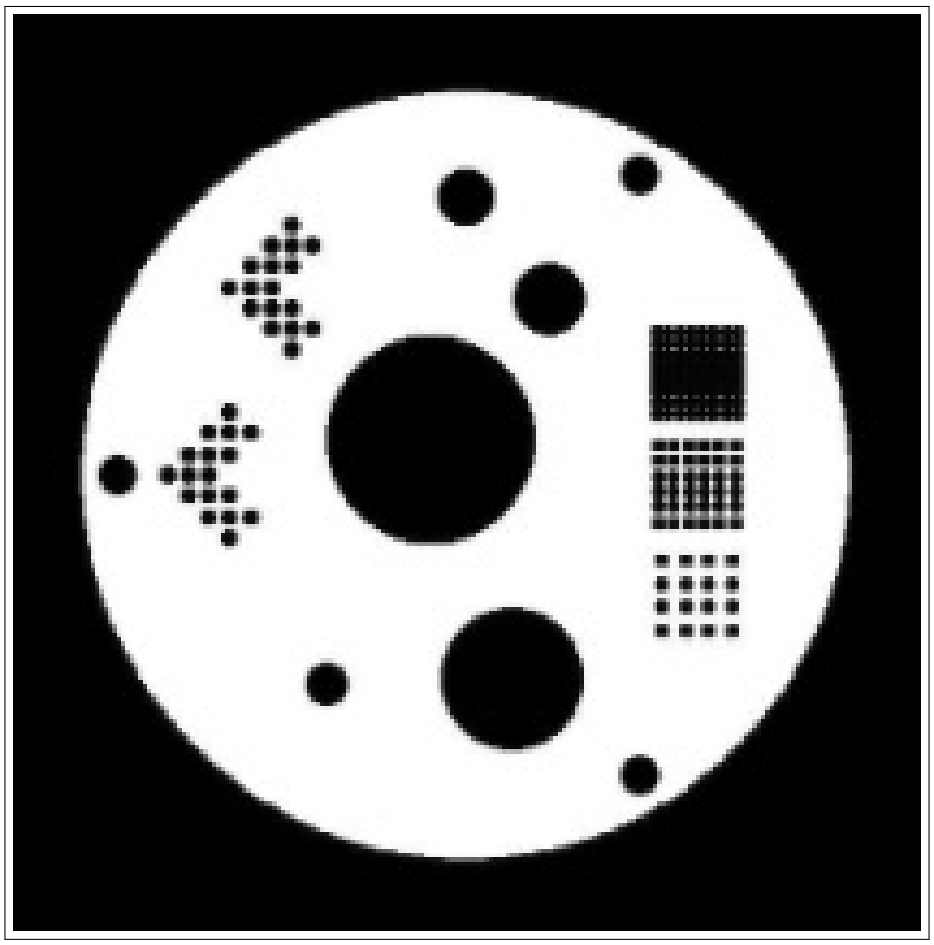

Figure 8.34: MATLAB-simulated bubble phantom

suppress those stripes and therefore suppress the ring artifacts[15].

Figure 8.40 is the same reconstructed image with a ring removal algorithm applied (Lee, 2013)[18].

X-ray Computed Tomography Artifacts

As detailed the reconstructions are and as efficient as third and fourth generations systems are at capturing internal spatial distribution, you still have artifacts that may be introduced due to factors that are not readily identifiable. The term *artifacts* is applied to any systematic discrepancy causing streaking, shading, rings and bands in a reconstructed volume that are not present in the original object (Martz, 2017)[24].

Table 8.1 lists known factors from different portions of a CT system that will introduce

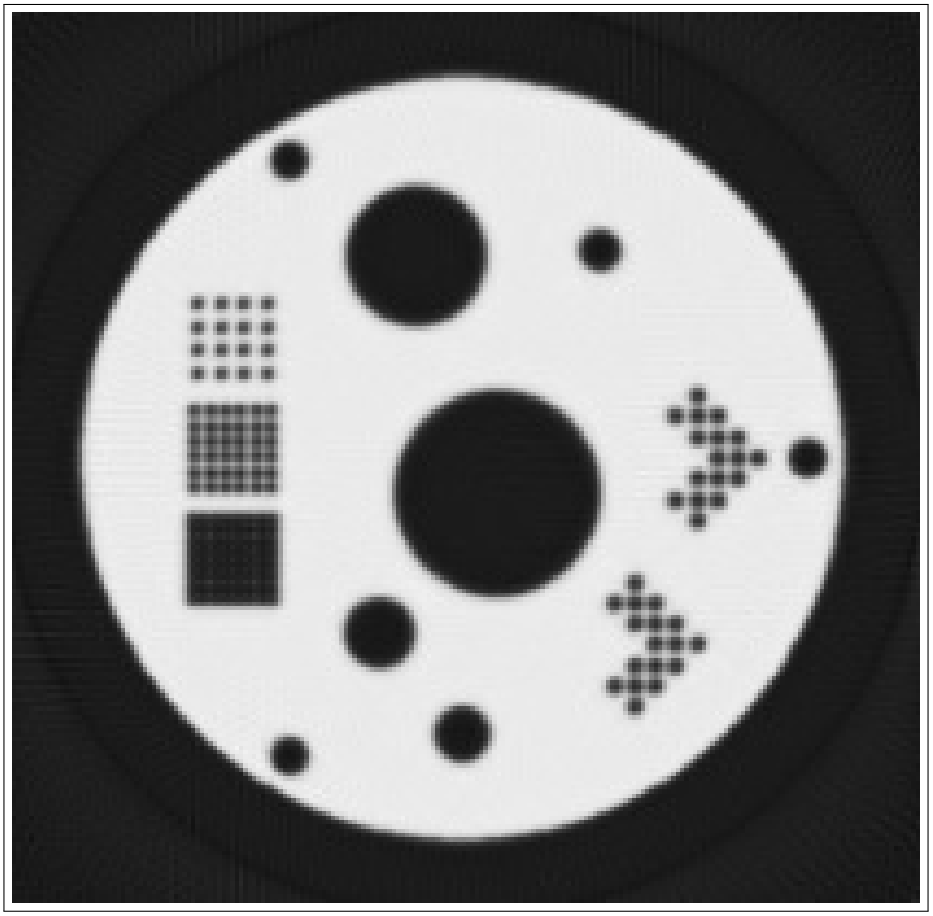

Figure 8.35: SIRT CUDA 3D Reconstruction of MATLAB Bubble Phantom

artifacts onto the reconstructed images. We will start off by explaining that the X-ray CT system can be broken down into the X-ray source, X-ray detector and the positioning system, which any one has the potential to introduce artifacts that may not immediately be indicative of any one of the three being the origin of the problem (Martz, 2017)[24].

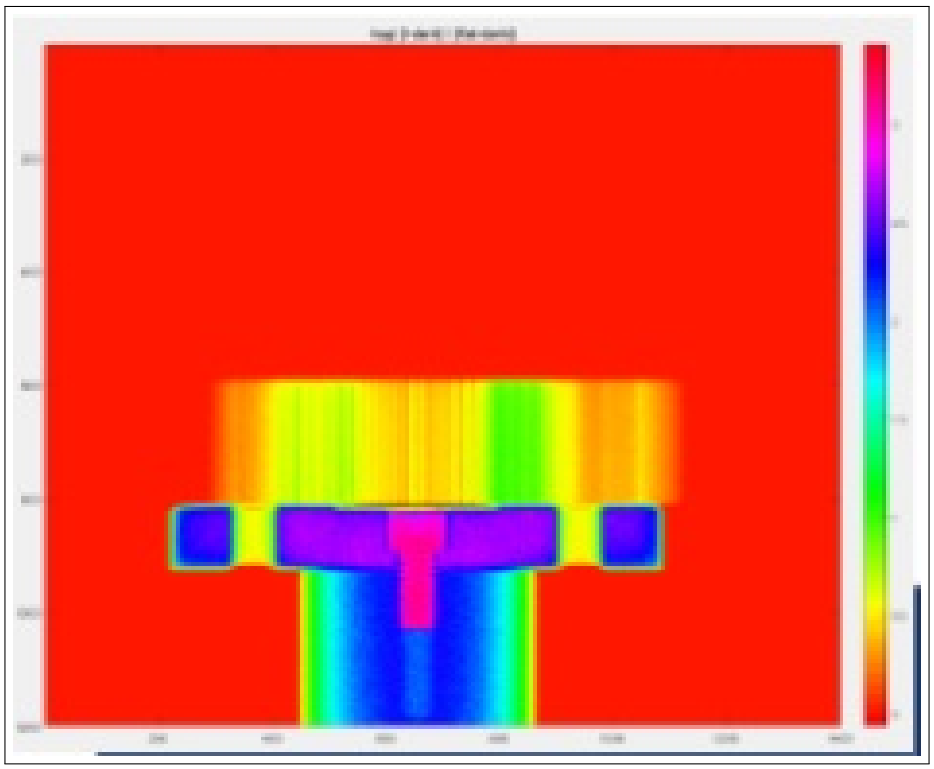

Figure 8.36: Side-view Single X-ray Projection of the Bubble Phantom

Properties of transmission images can be separated into three categories:

- factors impacting contrasting performance
- factors affecting spatial resolution
- sources of image noise

Differing sharpness in an image can be a result of magnification, positioning in the area between source and detector that could have bloomed in the image, and sufficient energy to adequately penetrate the object for that thickness.

Contrast in X-ray Images

Intrinsic contrast refers to the differences in X-ray attenuation that are resident in the object. The magnitude for this type of contrast are determined by the X-ray interactions in the material at the energy used in the inspection. Energy is a critical factor. At low energies

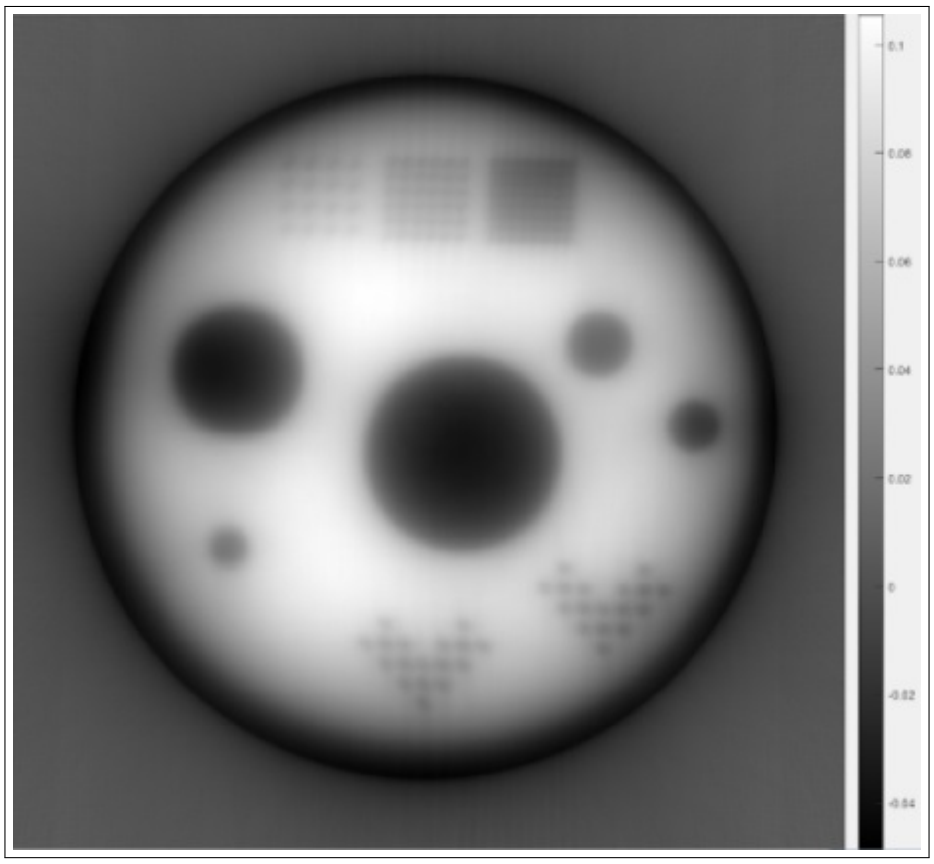

Figure 8.37: SIRT CUDA Original Bubble Phantom Reconstruction Image

where photo electric absorption is significant, the attenuation difference between two materials can be very large. At higher energies, where attenuation by Compton Scattering is more prevalent, the differences in material attenuation are less and more a result of differences found in the density of the material (Martz, 2017)[24].

In CT, scattered irradiation is deposited on interior edges of high attenuating materials with the result of additional blurring. Another impact of object scatter is that it can convolve with beam-hardening effects to result in scatter streaks.

Ring Artifacts

A ring artifact can result from an imbalance of the detector channels. These imbalance elements are a result of the detector and not the object. The sinogram will show these issues as vertical lines, which then generate reconstructed into rings. A number of techniques have been developed to remediate ring artifacts. Gain-offset adjustments can be estimated to

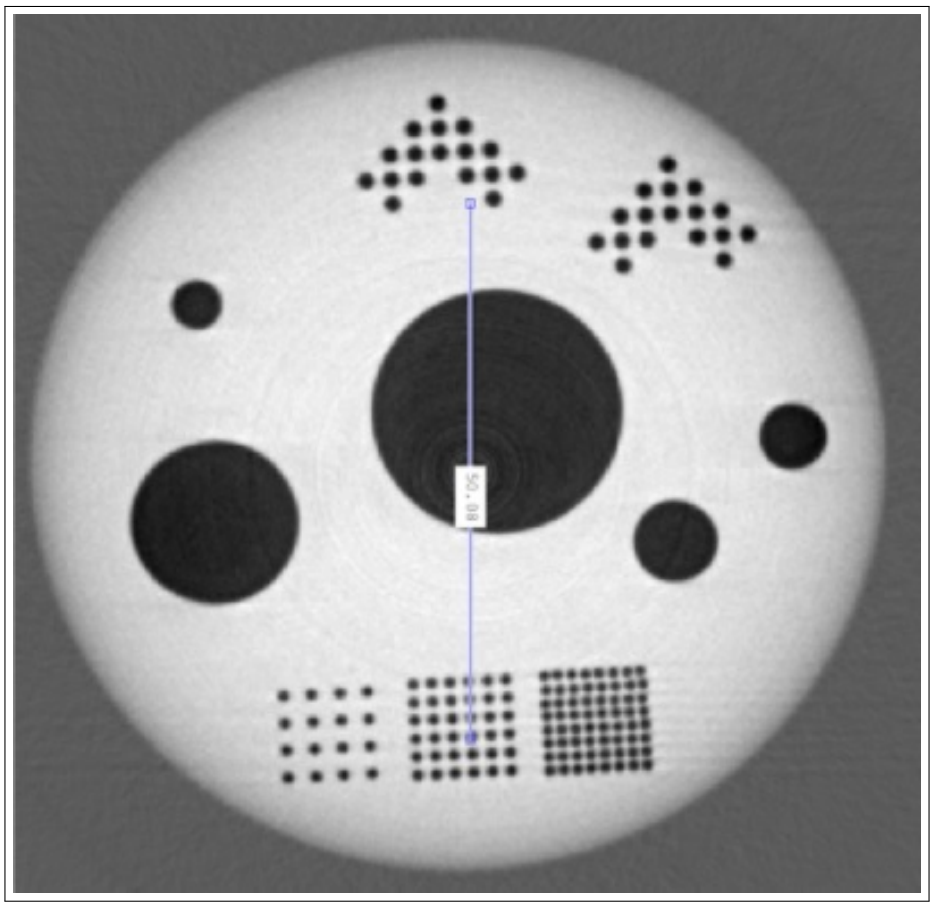

Figure 8.38: SIRT CUDA Original Bubble Phantom Reconstruction Image (with beam hardening filter)

remove the unique characterization of the digitization from the detector element (Martz, 2017)[24].

Angular Position Artifacts

Two types of artifacts can be found in angular position errors. The first type is the difference between assumed position of object relative to source and detector and the actual position. The second type is an error in the specified direction of the angular motion. These errors involve problems with poorly mounted objects (i.e. the object rotation slips on the mount or the position from the encoder does not rotate incrementally equal). Figure 8.41 displays what happens when when you have a non-parallel beam CT system with the wrong rotation direction. You can fix these errors by doing a reconstruction with the angular direction

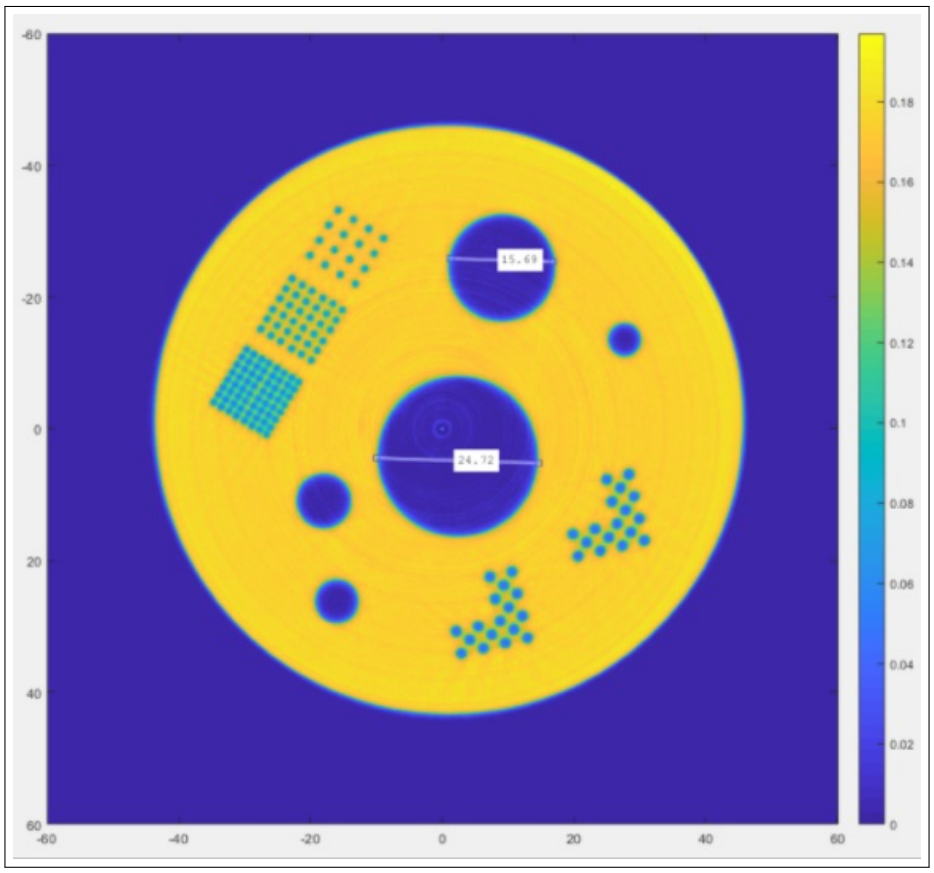

Figure 8.39: SIRT CUDA ASTRA Toolbox SIRT Bubble Phantom Reconstruction Image (THOR Photon Counter)

matching the direction of rotation relative to the order of the readout (Martz, 2017)[24].

Scatter Artifacts for High Aspect Ratio or High-Attenuating Objects

Scattering can result from photon absorption, Rayleigh scattering or Compton scattering. These photons are scattered and arrive at the detector with a different trajectory and possibly a different energy level. When we refer to scattering artifacts in our reconstruction, we cannot pinpoint the particular type of scattering but need to understand how to deal with the scattering artifact. Advances in filtering, energy threshold bands and collimators play a role in the reduction of scattering, but we will nonetheless need to still deal with correction of scattering artifacts in the images. Scattering is an artifact that is especially present during the X-ray sampling of high-aspect ratio or high-attenuating objects. Figure 8.41 shows a scatter effect problem and solution taken of a turbine blade. This artifact results from a

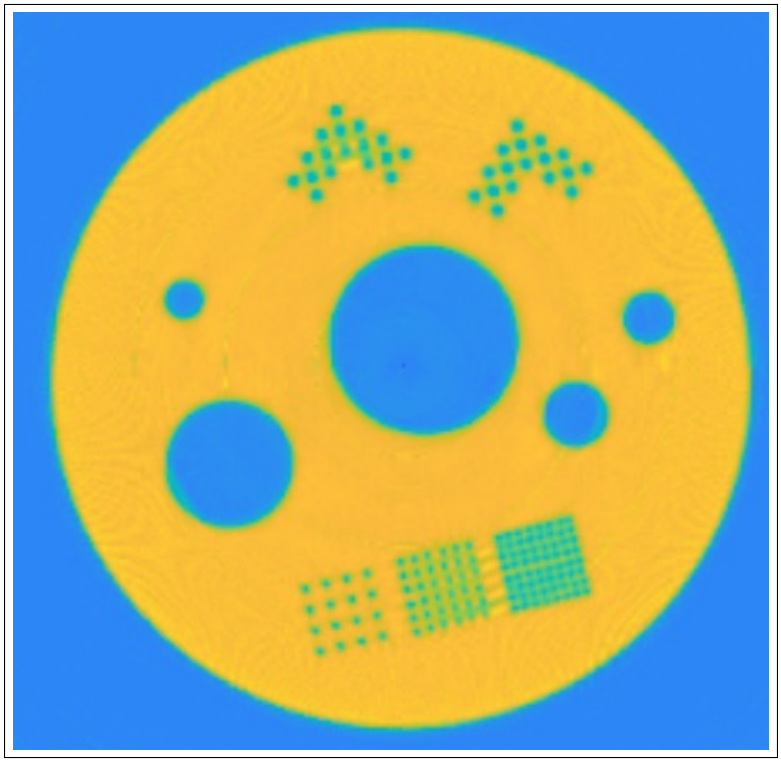

Figure 8.40: SIRT CUDA ASTRA Toolbox SIRT Bubble Phantom Reconstruction Image (THOR Photon Counter)(ring-removal algorithm applied)

lowering of attenuation of the material during long chords of the object. The source of the scatter stems from combinations of the following problems:

- lack of penetration through long chords of the object
- ineffective stopping power of the detector to avoid scattering from the back-face of the detector
- presence of background scatter that result on detector but are not part of the object

Solutions to this problem include thicker beam filtering, scanning at a higher energy, and utilization of collimators. When these techniques do not work, then an iterative code is necessary to filter out these artifacts (Martz, 2017)[24].

Bubble phantom in a titanium steel pipe

To prove how effective X-ray CT techniques are at reconstructing void areas in opaque systems, we inserted the bubble phantom inside a titanium pipe with a wall thickness of

Type of Artifact	Scan Geometry
Centering	Parallel, fan, cone
Bad or hot pixels	Parallel, fan, cone
Ring artifacts	Rotation-only scanning for any geometry
Angular positioning errors	Parallel, fan, cone
X-ray magnification	Only fan or cone geometry
Horizontal or in-plane midline offset	Fan or cone geometry
Vertical centering	Cone-beam geometry
Vertical midline offsets	Cone-beam geometry
Beam hardening	Parallel, fan, cone

Table 8.1: Type of artifact and scan (Martz, 2017)[24]

6.35 mm. We positioned the bubble phantom and pipe on our rotation stage to collect 1440 projections. We used a higher current flux to ensure adequate contrast between the bubble phantom components and the titanium pipe. We maintained the same power level as we did with the bubble phantom alone. We used the following parameters for this collection:

- Voltage: 95keV
- Current: 800μA
- Target current tracking mode enabled
- Detector: DT1412
- Projections: 1440

Figure 8.42 displays a side view and top view of the Titanium pipe positioned on the rotation stage. The bubble phantom was inserted into the Titanium pipe so as to leave no space between the bubble phantom and the pipe inner wall. We collected 1440 projections. This was comprised of collecting a single projection every 0.25˚increment. Figure 8.43 displays a single projection image and a reconstruction of the bubble phantom inside the pipe using SIRT algorithm. As is noticeable in the figure, several artifacts have bee introduced because of the presence of the metal wall. The boundaries of the metal walls has an artifacts that adds a darker ring overlapped over the bubble phantom. The smaller groups of holes are blurred and does not have a resolution as in the case absent the Titanium pipe. Nonetheless, the reconstruction resolution still offers an image close to the same geometrical arrangements found in the actual bubble phantom.

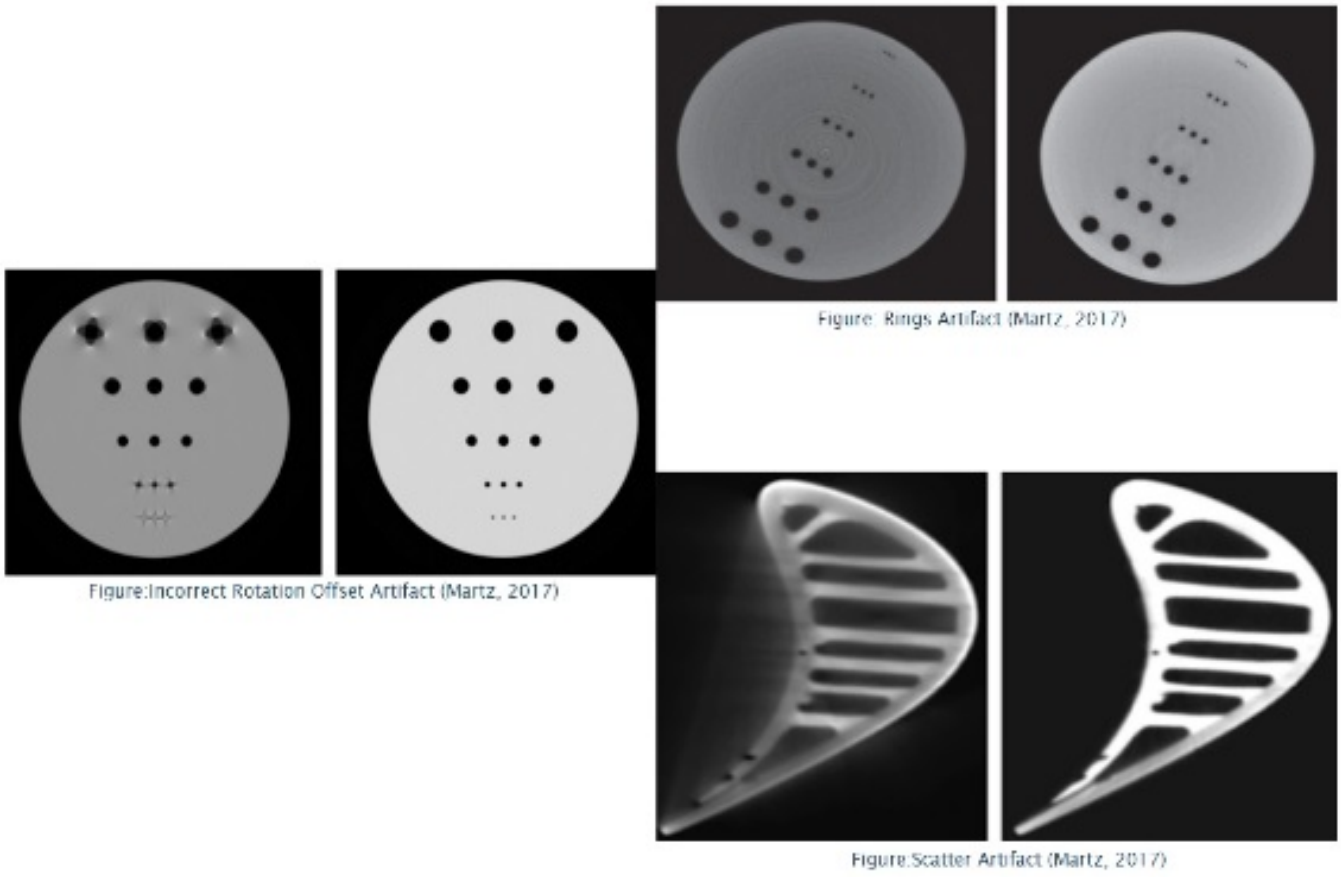

Figure 8.41: Examples of artifacts: left: incorrect rotation offset; right top: ring artifacts; right bottom: scatter artifacts (Martz, 2017)[24]

Noise Generations and Filtering in X-ray CT Reconstruction

An X-ray CT system is susceptible to multiple sources of noise. We will review the sources of noise to understand the limitations of the whole system. Our focus for noise filtering will be constrained to the actual reconstruction image.

- X-ray source signal: Our YXLON FXE Microfocus Directional Tube produces polyenergetic X-rays with a distribution of energies, which appears in a spectrum. This spectrum depends on the maximum applied tube potential and inherent filtration. The mean number of the quanta, interacting with the detector depends on the solid angle subtended by the detector element. The generation of the quanta in the CT scanner is a random process, governed by the probability of observing a specific number of

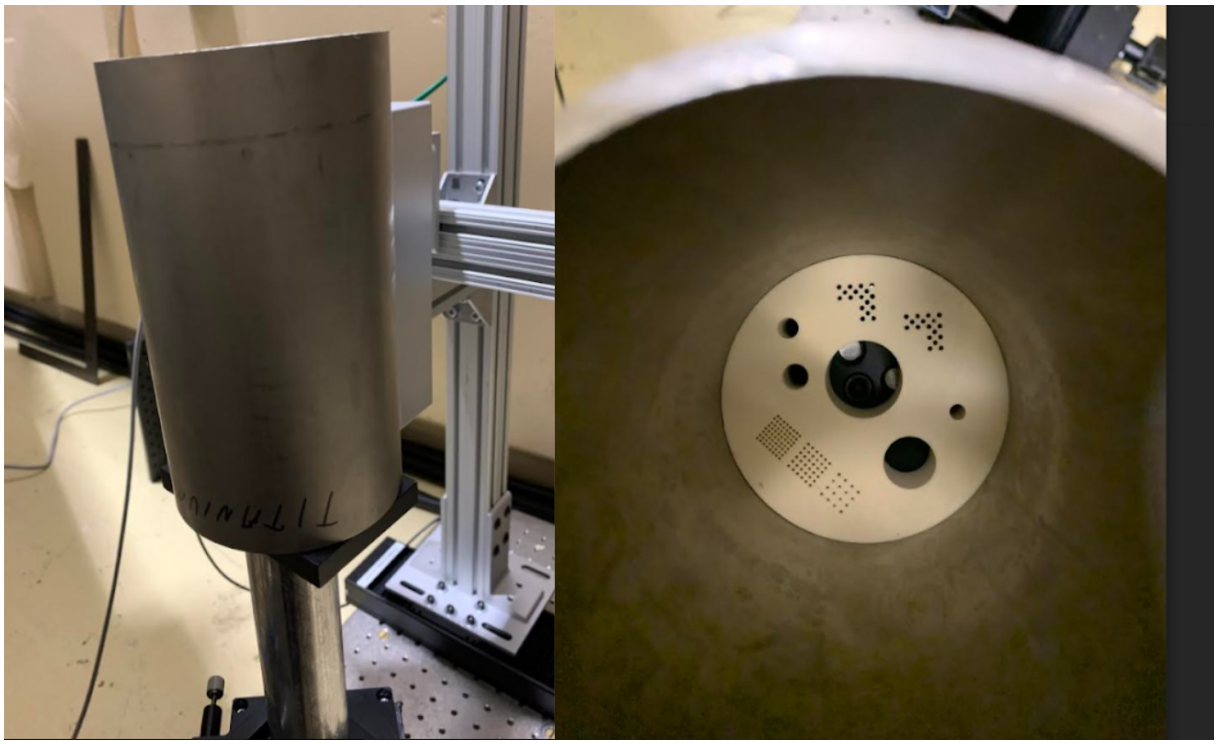

Figure 8.42: Bubble phantom inside titanium pipe (left: sideview; right: topview)

quanta within a particular energy range during a measurement period given by a Poisson distribution, characterized by the mean number of quanta per measurement. The attenuation of the beam through the material and resulting intensity field, identified in the Beer Lambert law, is also a random process, which makes it a Poisson process. By the time the projection is observed, the process is an additive Poisson process with a probability distribution function comprised from the convolution of the quanta and attenuation probability distribution functions (Whiting, 2006)[47].

- X-ray detector noise: Our THOR photon counter assigns equal weight to each photon, regardless of energy, and converts the counts into measurement units. Since the counter combines random Poisson processes at each energy level, the resulting signal from the counter is Poisson.

- Most studies on reconstruction algorithms have assessed that the probability distribution function is Poisson. The reconstruction noises that are observed in images are the following:

  – Salt and Pepper noise is a noise also known as impulse noise that can be caused by

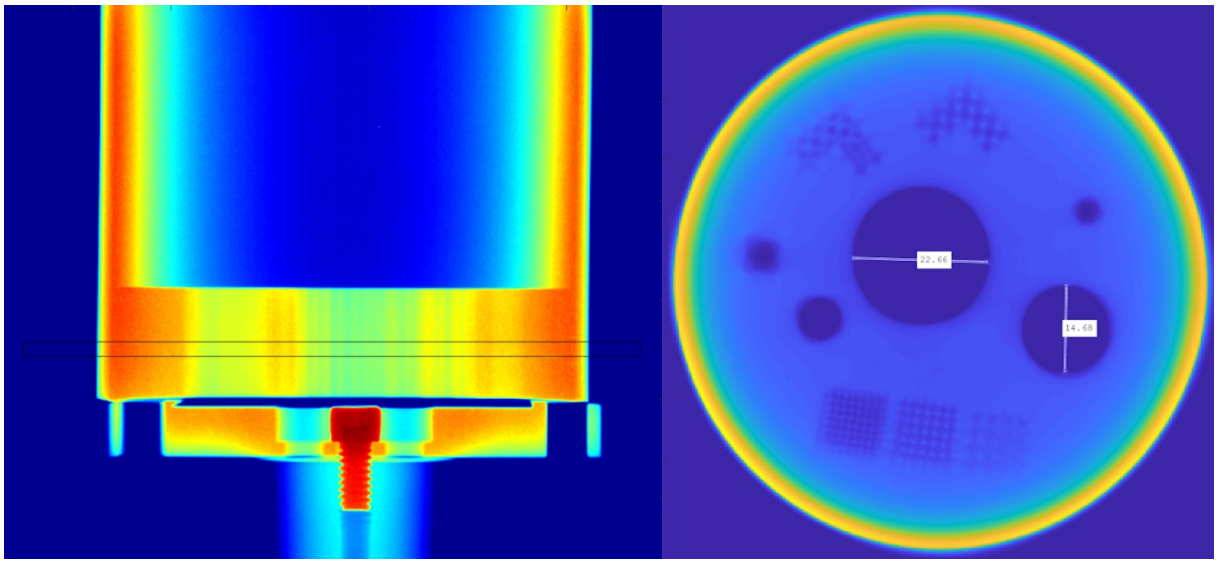

Figure 8.43: X-ray CT SIRT reconstruction of the bubble phantom inside titanium pipe (left: sideview; right: topview)

sharp and sudden disturbances in the image signal. It is represented by sparsely occurring white and black pixels.

- Poisson noise is generated by the Poisson distribution arising from quanta noise. This noise is signal dependent and there is generally a difficult process to design a noise reduction algorithm against this (Lee, 2018)[18].
- Speckle noise has a granular appearance resulting from random fluctuation in the return signal from an object which is not found greater than a single image processing element (Manson, 2019)[36].

Salt and Pepper noise

Figure 8.44 displays the reconstruction of our bubble phantom using SIRT CUDA reconstruction algorithm from ASTRA toolbox. Figure 8.45 includes three depictions of the bubble column with added noise from the three distinct categories. MATLAB provides a function called imnoise which will add noise from gaussian, local variable, Poisson, salt and pepper and speckle. After adding the noise, we evaluated different algorithms provided by MATLAB to attempt recover the original bubble phantom.

We evaluated medfilt2 which is a 2-D median filter that allows the user to set the predefined neighborhood of pixels. This filter has proven successful at improving the image quality of images affected by salt and pepper noise. As discussed previously, salt and pepper

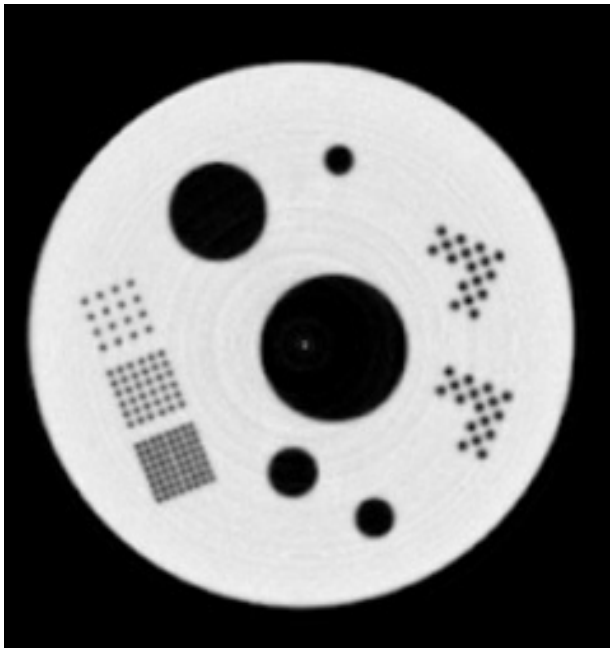

Figure 8.44: SIRT CUDA reconstruction of the bubble phantom

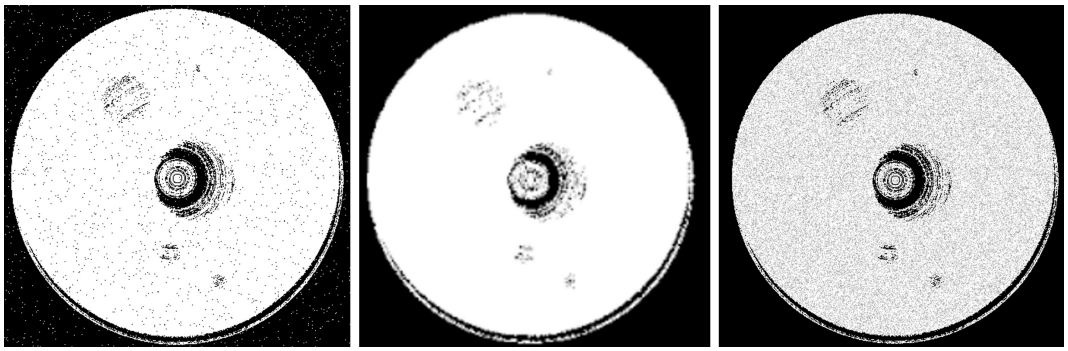

Figure 8.45: a) Salt & Pepper noise b) Poisson noise c) Speckle noise

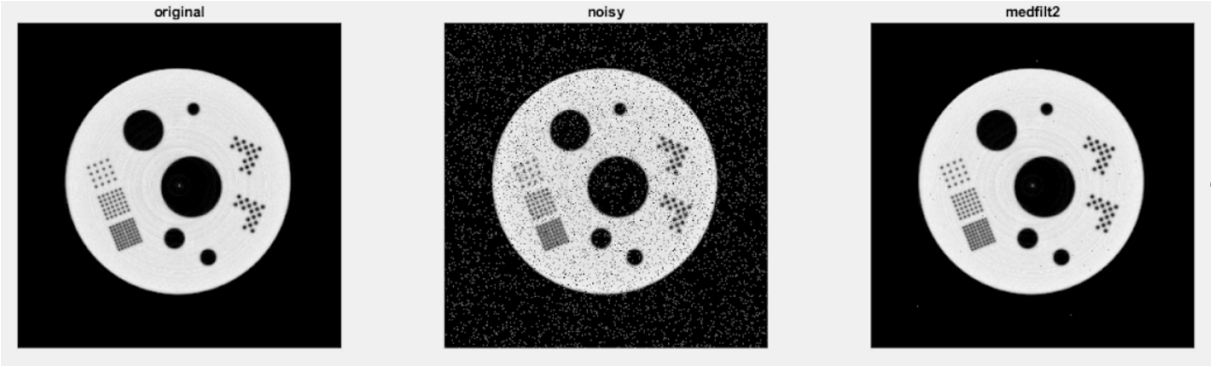

Figure 8.46: a) original bubble phantom b) bubble phantom with 10% salt & pepper image c) medfilt2 applied to the noisy image

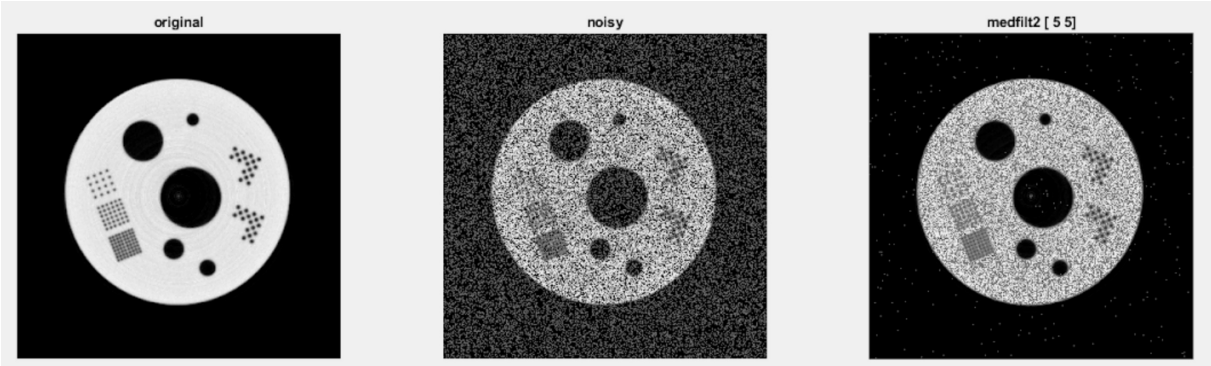

Figure 8.47: a) original bubble phantom b) bubble phantom with 50% salt & pepper image c) medfilt2 applied to the noisy image

noise include a few noisy pixels which are noisy enough to degrade the image as a whole. Salt and pepper noise generation is associated with how the bits are altered to minimum and maximum values which appear as black and white dots sprinkled over the image. Median filters are effective at reducing random noise, especially when the noise amplitude probability density has periodic patterns. Median filtering works by placing a window over the image. The median values of the input window are shifted to the center of the window at the output range. Figure 8.46 includes an application of the median filter provided in MATLAB. The original image was distorted by adding 10% of salt and pepper noise using a code separate from the imnoise function in MATLAB.

In Figure 8.47, we added 50% salt and pepper noise to the original image. We noticed

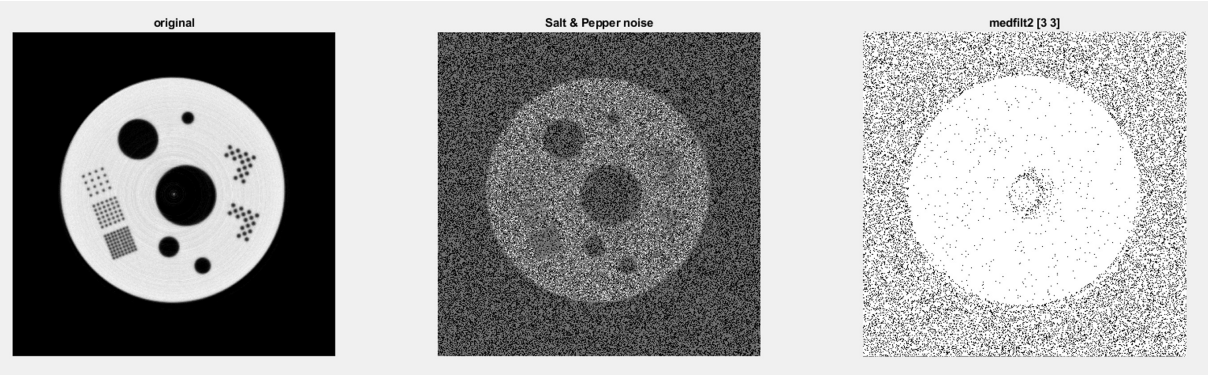

Figure 8.48: a) original bubble phantom b) bubble phantom with 80% salt & pepper image c) medfilt2 applied to the noisy image

the medfilt2 function alone was not adequate to restore the original image, so we modified the neighborhood of pixels to be affected in the calculation to a 5x5 matrix throughout the 3600x3600 original matrix size.

In Figure 8.48, we added 80% salt and pepper noise to the original image. We noticed the medfilt2 function alone was not adequate to restore the original image.

Noise Reduction Algorithms

We found that noise is introduced from the X-ray CT procedure regardless of the noise that is added due to the X-ray source, photon counter and dynamic object. Increasing the current to produce a larger photon flux should yield a more resolved image. Requiring a higher contrast resolution will require a larger photon flux. The original bubble phantom requires the resolution to measure a 1mm inner diameter hole. We selected a 100keV and 350µA setting for the X-ray source to provide the required contrasting to the bubble phantom. The number of photons required to produce an image has a linear relationship with the slice thickness. A thicker slice allows more photons for consideration, improving SNR but yielding a poorer resolution. Reconstruction algorithms are non-linear processes that introduce noise in a non-uniform manner. This means that the intensity of the noise varies across the image.

We evaluated different reconstruction techniques provided with ASTRA toolbox. There are other reconstruction algorithms that also reduce noise, such as statistical image reconstruction and regularization techniques discussed by Zhang et al[50]. The Simultaneous Iterative Reconstruction Technique yielded effective spatial resolution results using the bubble phantom, providing a spatial resolution of 1mm. We decided to use this technique for our experiments due to the spatial resolution results from our calibration experiments.

The Simultaneous Iterative Reconstructive Technique is a reconstruction algorithm based

off the algebraic techniques introduced by Stefan Kaczmarz in 1937. The main principle behind this algorithm is to see the process as a system of equations, where $\mathbf{f}$ is the object, $\mathbf{p}$ is the data and $\mathbf{W}$ is the system matrix. $\mathbf{f}$ is the vector of unknowns. $\mathbf{p}$ is the set of projections that are gathered and averaged at each angle for one projection dataset for the single angle. In our experiment, we collected 30 to 35 frames per angle to account for the dynamic nature of our experiment. We specifically selected a region of interest in the bubble column to limit processing time and took a mean of all the projections for a single angle. The mean projection was then used as the representation of the projection for a single angle out of 360 angles. $\mathbf{p}$ is 360 projections, which were actually mean projections of a larger collection set as discussed above.

$$\mathbf{Wf} = \mathbf{p} \tag{8.5}$$

We will look at the two-dimensional case for the sake of simplicity. Equation 8.5 can be rewritten to include the number of iteration and projection slices:

$$\Sigma_{j=1}^{M} w_{i,j} f_j = p_i, i = 1, 2, ..., N \tag{8.6}$$

where M is the number of pixels and N is the number of lines from projections.

$w_{i,j}$ will be utilized as the weighing factor that gives the contribution of pixel j to the projection value of i, and f_j is the value of the object at pixel j.

Kaczmarz's method includes the following formula where an initial guess is made for the equation of unknowns and the difference between the initial guess and the first reconstruction image is utilized as the weighing function [43].

$$\mathbf{f}^{k+1} = \mathbf{f}^{k} - \frac{\mathbf{f}^{k} \cdot \mathbf{w}_i - p_i}{\mathbf{w}_i \cdot \mathbf{w}_i} \mathbf{w}_i \tag{8.7}$$

The SIRT reconstruction technique includes the following iteration method:

These algebraic reconstruction algorithms usually suffer from salt and pepper noise, caused by inconsistencies introduced in the set of equations that consist of approximations commonly used for w_i. These approximations show inconsistencies between the computed ray-summation images and the measured ray-summation images. This is further exacerbated because the reconstruction algorithm uses the previous function as a weighing parameter. SIRT suffers from these inconsistencies in the forward process but results in smoother reconstruction as it eliminates the continual and competing pixels at each update of the equation (Kak, 1999)[43].

Other areas that can add noise are the number of projections used and the number of iterations. We have found that higher projections yield more resolved reconstructions for both a static and dynamic collection. We found that an increase in the number of iterations for dynamic objects worsens the reconstruction due to the iteration of the salt and pepper noise. Figures 8.50-8.52 display a reconstruction of the bubble phantom, which is a static object. The resolution improves with an increase on the iterations. Increased iterations

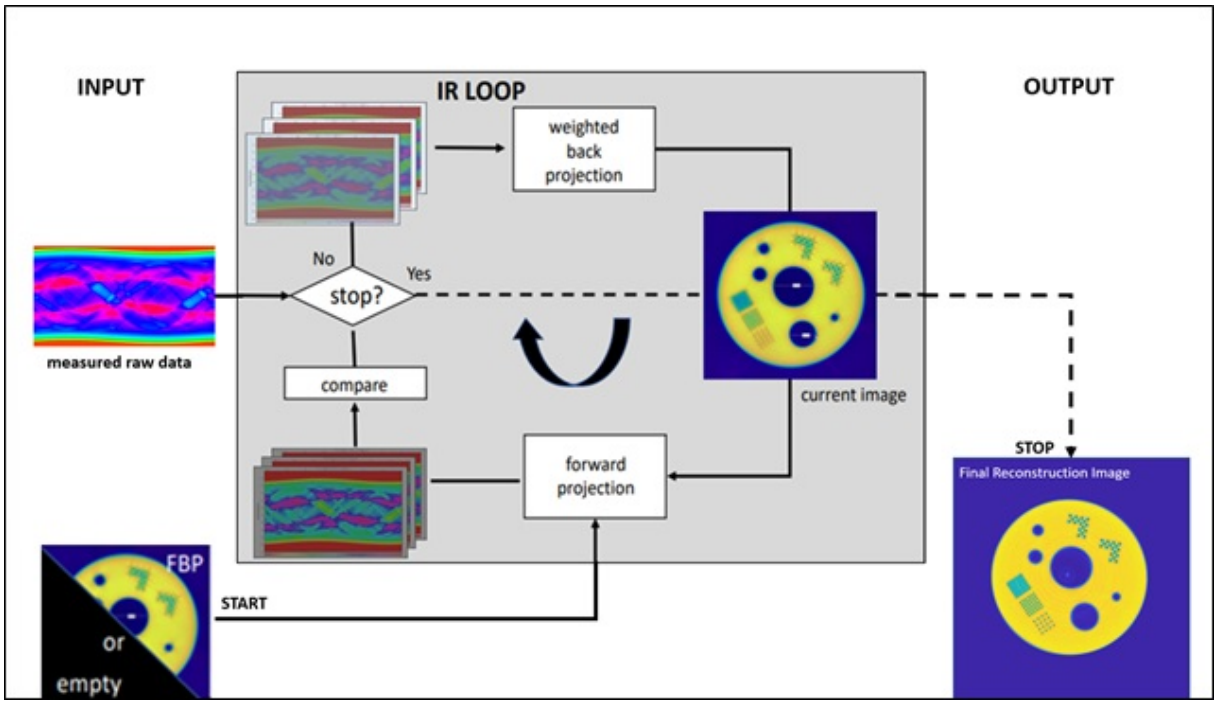

Figure 8.49: SIRT process for a bubble phantom with 1400 projections and 150 iterations

show a larger convergence and result in a more uniform attenuation coefficient across the reconstructed image.

To more closely evaluate the resolution of a static object with an increased number of iterations, we zoomed in to the smallest cluster of holes in the bubble phantom. These holes have an inner diameter of 1mm. Figure 10 displays the small cluster of holes from reconstruction images for 50, 150 and 250 iterations. The reconstruction with 250 iterations shows a more resolved image but introduces stronger ring artifacts due to the iteration of the ring artifacts from previous reconstruction iterations. This perturbation is apparent in the static object reconstructions and shows up as salt and pepper noise with a larger number of iterations. Figure 8.54 displays the reconstruction of the bubble phantom with 1400 iterations. The area of reconstruction is the same area from Figure 8.53. You can notice a more resolved image but with a stronger amount of noise. We applied the medfilt2 algorithm to the image and you can notice a significant reduction in salt and pepper noise.

Since the area of interest for our research is focused on void areas ranging from 5mm to 20mm, we shifted to a different area of the bubble phantom. The void areas displayed in the reconstructed image after 1400 iterations show a noisy image. When the medfilt2 was applied to the reconstructed image, the noise is significantly less, and the attenuation coefficients are more uniform. Medfilt2, as previously discussed, is an excellent filtering tool

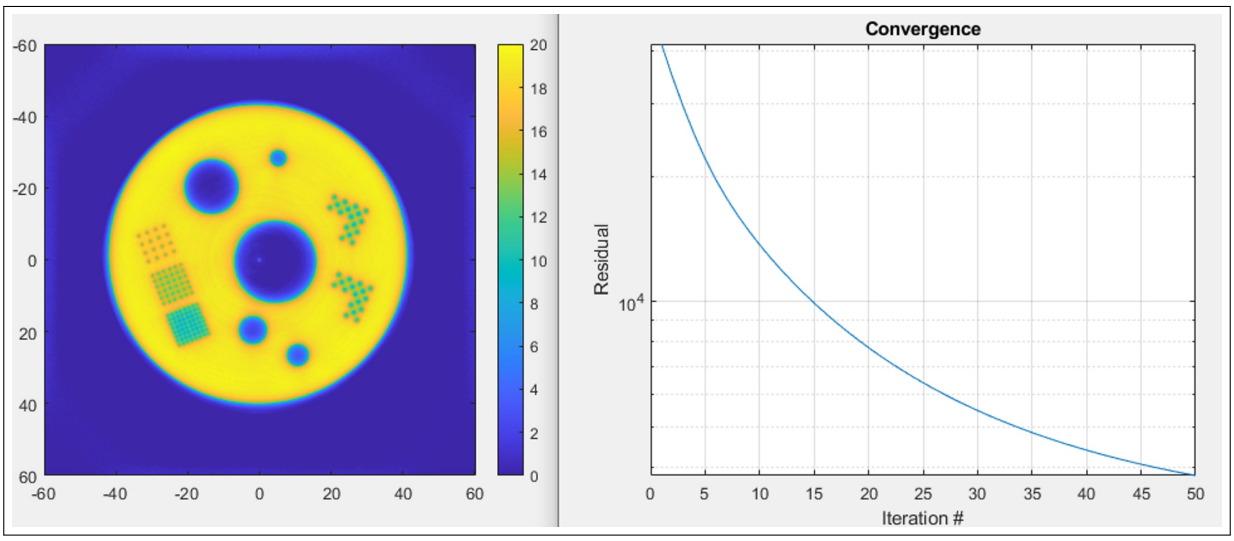

Figure 8.50: SIRT reconstruction of a bubble phantom with 1400 projections and 50 iterations

against salt and pepper noise.

We want to now focus on other artifacts that may impact our reconstruction and understanding of the void areas. We zoomed in closely into the edges of the largest void area in Figure 8.56. Figure 8.57 shows the same area of the void area edge. Figure 8.57a is the original area, Figure 8.57b is the image with an applied filter of medfilt2, and Figure 8.57c is the applied medfilt2 with a neighborhood of 6 x 6. The applied filter shows the padded '0' applied to the corner of the images expected from the median filter. The edge is marked by the distinction of a transition from the yellow to green to blue area. The goal is to create a distinction between the yellow (solid) and blue (air) area. The green area is an artifact and our goal is to minimize the green area to create a more accurate distinction. In Figure 8.57, we applied medfilt2(6 6) and it proved slightly successful at eliminating the green area artifact but not successful at completely characterizing the edge. In Figures 8.58 and 8.59, SIRT reconstruction was performed at 3000 iterations, which introduced an observable amount of salt and pepper noise. A median filter was applied to recover a more uniform attenuation coefficient, while preserving spatial resolution. The spatial resolution was improved from 150 iterations, and therefore these high number of iterations will serve detrimental to noise corrections.

Now we transition to our experiments to evaluate noise sources and validate the application of the medfilt2 filter on the reconstructed images. Figure 8.60 shows the reconstruction of the bubble column with the inner walls coated with NeverWet. The noise in the reconstructed image after 1000 iterations makes it difficult to evaluate the lateral distribution of

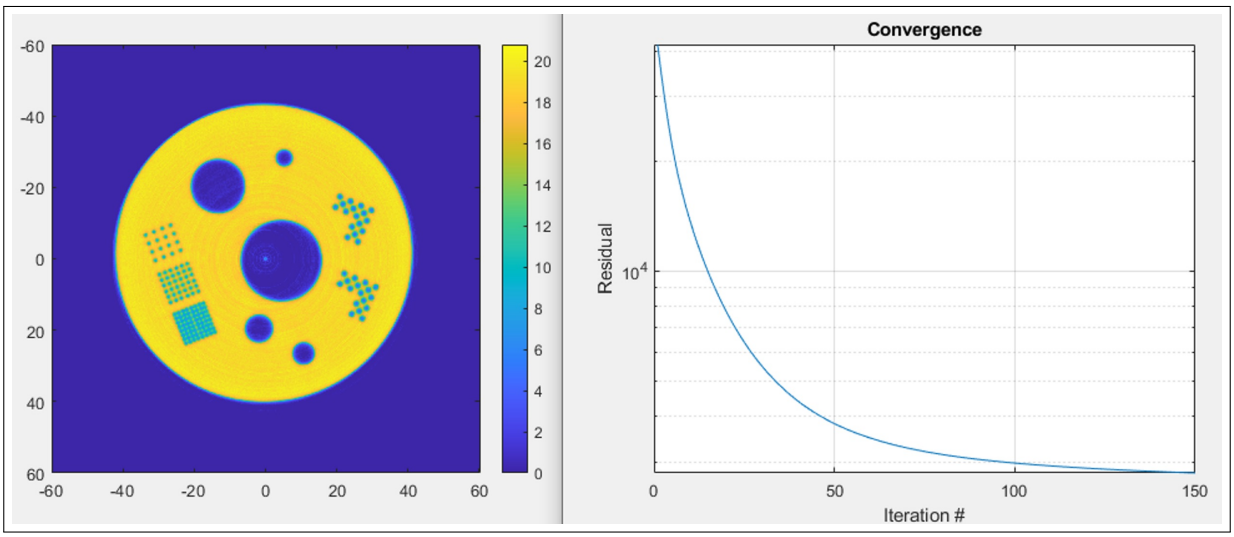

Figure 8.51: SIRT reconstruction of a bubble phantom with 1400 projections and 150 iterations

void fraction across the bubble column. When we apply medfilt2 you get a lateral distribution of the void fraction that resembles something we would expect. We first want to make sure that the filter has not removed information that is important to our understanding of the bubble dynamics. We observe this by evaluating the wire mesh measurements for the experiments and observe the lateral distribution and void fraction comparison to see if the filter tool works adequately. Figures 8.60 and 8.61 display the SIRT reconstruction for the two bubble column experiments without and with superhydrophobic coated inner wall, respectively. The images prior to the implementation of the medfilt2(50 50) shows a substantial amount of salt and pepper noise due to both the dynamic environment and the iteration of previous noise of the same kind. While the noise has been substantially removed in the right images of Figures 8.60 and 8.61, we still don't know if the filtered reconstructed images are representative of the actual bubble dynamics in each situation.

We now turn to Figure 8.62 to validate our reconstructed image against the wire mesh sensor measurements which have been previously validated against height, differential pressure measurements and previous calibration measurements from single bubble experiments. The colorbars of Figure 8.62 have been adjusted to display 0.15 to better evaluate the lateral void fraction distribution. The measurements are actually 15.25 centimeters apart. Both images display similarities of a centralized higher void fraction developing due to larger diameter bubbles that form from coalescing of bubbles at the wall driven by the NeverWet coating. While it is difficult to compare the individual value similarity between a 24 x 24 matrix from WMS and a 777 x 777 matrix from the X-ray Reconstructed image, you can

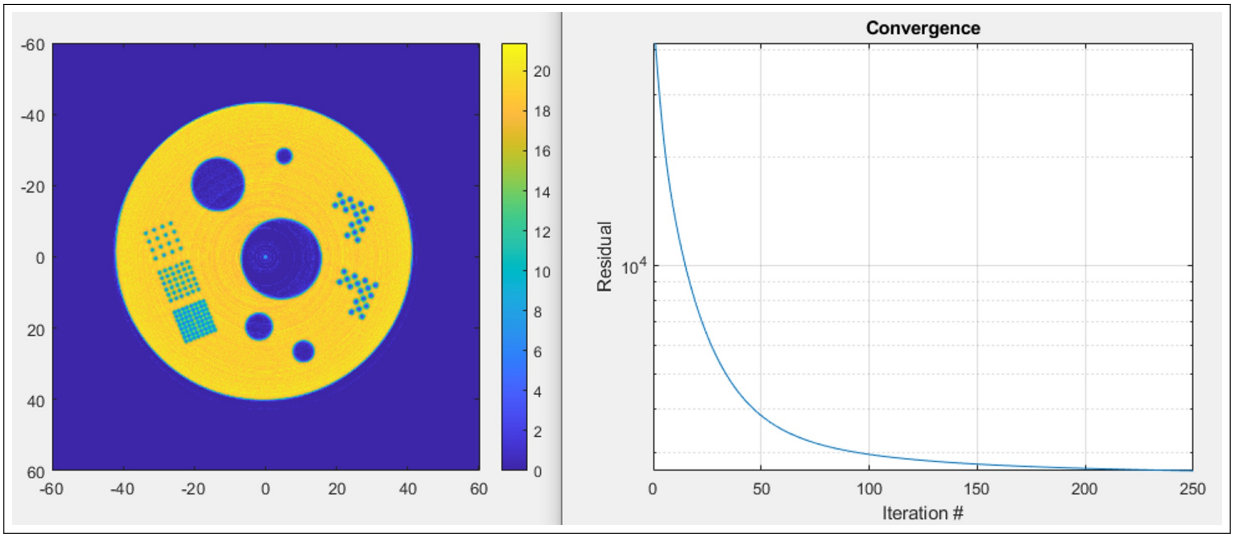

Figure 8.52: SIRT reconstruction of a bubble phantom with 1400 projections and 250 iterations

get a general idea that the filtered image is commensurate with the lateral distribution provided by WMS. Additionally, the WMS measured a void fraction of 0.095 and the X-ray CT reconstruction yielded a void fraction of 0.097 which are in a fair agreement. Figure 8.63 displays the same type of measurements for the non-coated case. The iterations of the X-ray CT were kept at 100 iterations since there was a central noise area that got perturbated at 1000 iterations to the point that it threw off the void fraction calculation. Void fraction measurements for the WMS and X-ray CT were 0.226 and 0.231 respectively with a very accurate agreement in lateral void fraction distribution.

To continue our evaluation of the median filter utilization on the bubble column void fraction experiments, we also want to evaluate whether an increased number of iterations and over-iterated salt & pepper noise are detrimental to our void fraction assessments. Figure 8.64 displays two images reconstructed from 100 and 1000 iterations. The 1000 iterations do get rid of artifacts that we believe are not representative of the flow at the inner wall, but it does introduce perturbations of the central void areas.

X-ray CT Iterative Reconstruction Evaluation on Suspended PVC Tubes inside a Bubble Column

We transition to look at a separate experiment where we coat a single PVC tube out of four suspended PVC tubes to evaluate void fraction lateral distribution across the bubble column and an array of 2 x 2 PVC tubes. The 1000 iteration reconstruction (Figure 8.65b), as compared to the 100 iteration reconstruction (Figure 8.65a), shows a perturbation of noise

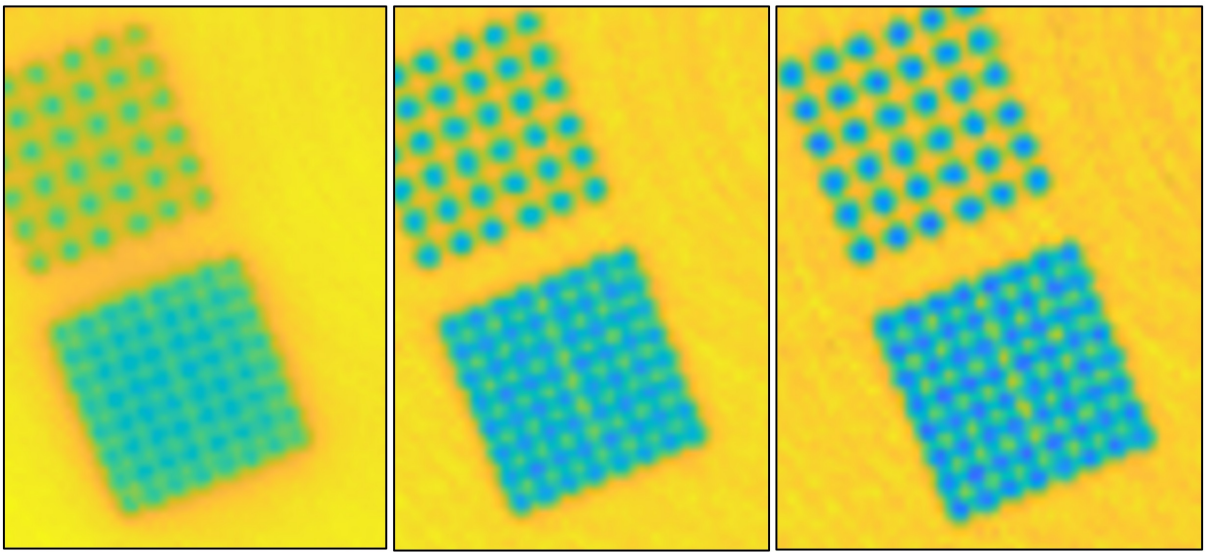

Figure 8.53: SIRT reconstruction of a bubble phantom small grid of 1mm ID holes at 50, 150 and 250 iterations.

that results in a larger void fraction, probably driven by the bright areas along the inner wall, displayed in Figure 8.65. The reconstruction with a medfilt2(15 15) is adequate to yield an accurate representation of void fraction validated by WMS measurements displayed in Figure 8.66. In other words, more iterations is not necessarily better since iteration of dynamic experiments introduces an iteration of noise, which introduces measurement inaccuracies.

Additionally, Figure 8.66 shows how powerful the non-intrusive X-ray CT time-averaged void fraction method is at capturing void areas that are impeded at the WMS because of suspension brackets.

Figure 8.67 displays the time-averaged void fraction measurements from X-ray CT for two experiments conducted with the same parameters with the only exception of a substituted PVC tube coated with NeverWet superhydrophobic coating. These measurements render a filtered reconstruction using the MATLAB median filter over a 15 x 15 localized pixel area. Colorbars were modified to each particular experiment based on the large difference in void fraction between the two images. The X-ray CT system is non-intrusive and has proven capable of rendering time-averaged void fraction measurements based on averaged void fraction from localized void fraction values. This measurement method also produces an accurate lateral void fraction distribution that shows the affinity of air to the SHS-tube, resulting in an overall lower void fraction and maximizing wetted areas on the hydrophilic tubes.

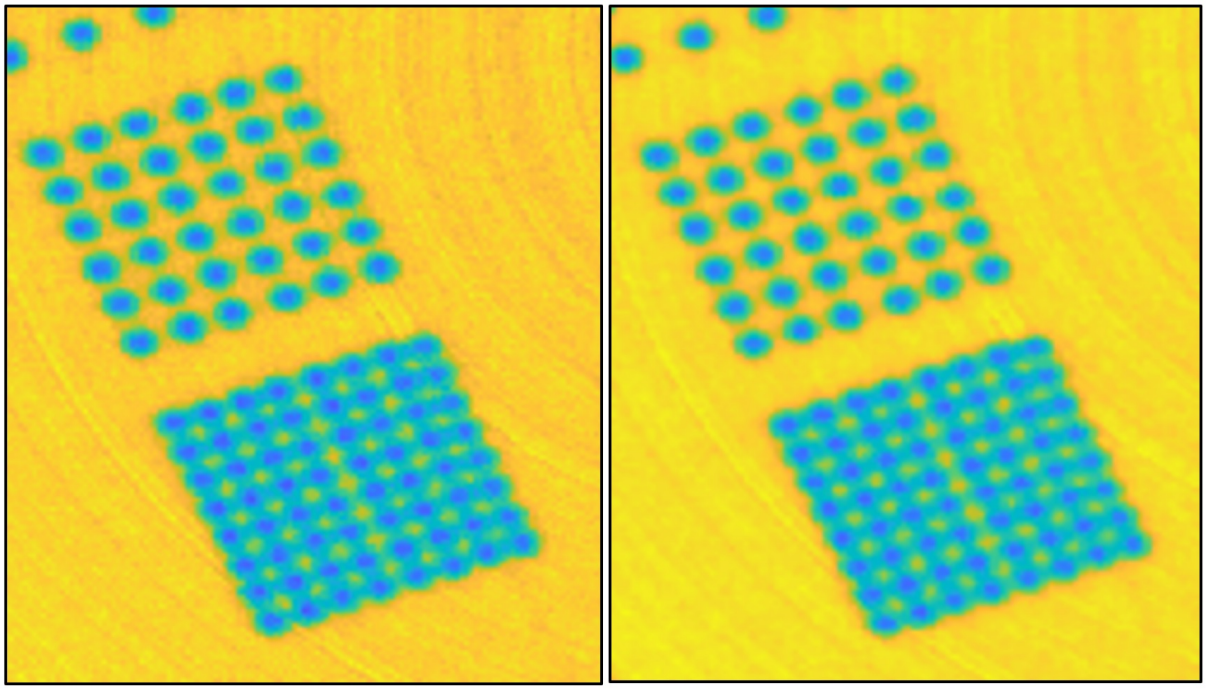

Figure 8.54: a) SIRT reconstruction with 1400 projections and 250 iterations b) SIRT reconstruction with 1400 projections and 250 iterations with medfilt2 applied

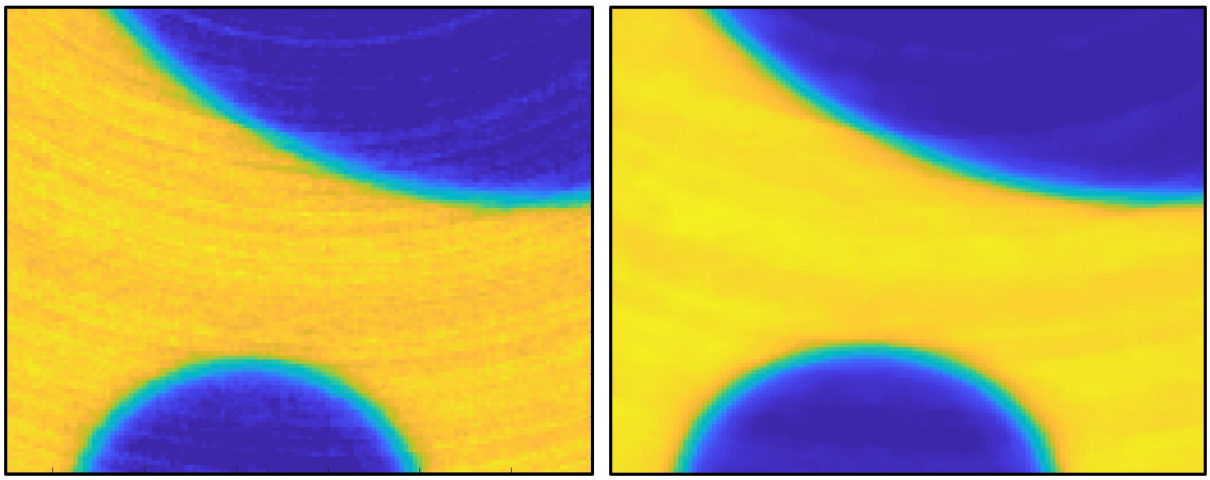

Figure 8.55: a) SIRT reconstruction with 1400 projections and 250 iterations large void reconstruction b) SIRT reconstruction with 1400 projections and 250 iterations large void reconstruction with medfilt2 applied

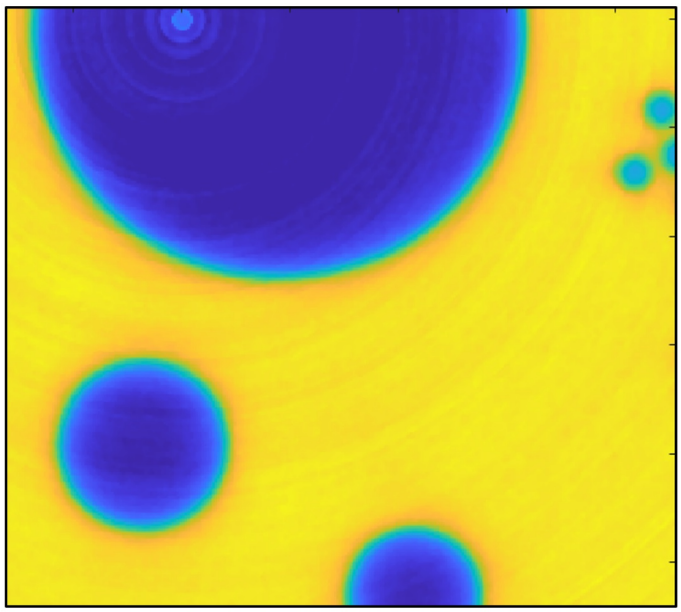

Figure 8.56: SIRT reconstruction of the bubble phantom after 1400 iterations

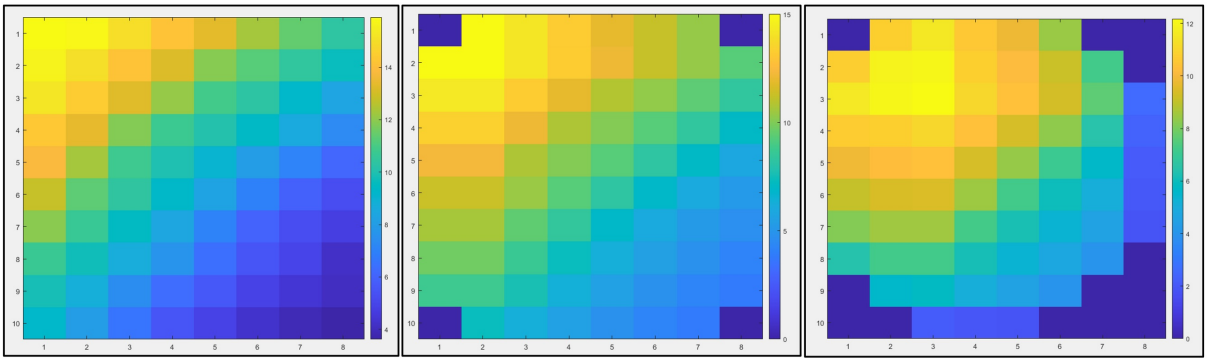

Figure 8.57: SIRT reconstruction of the bubble phantom: a) Original phantom b) Median filter 2D application c) Median filter applied with a matrix of 6 x 6

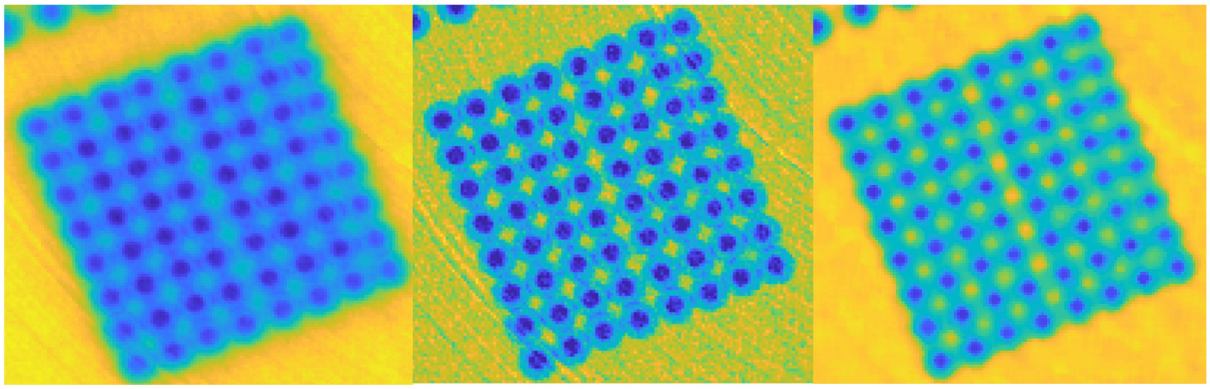

Figure 8.58: SIRT reconstruction of the bubble phantom: a) Original phantom b) 3000 iterations c) 3000 iterations with a median filter applied with a matrix of 6 x 6

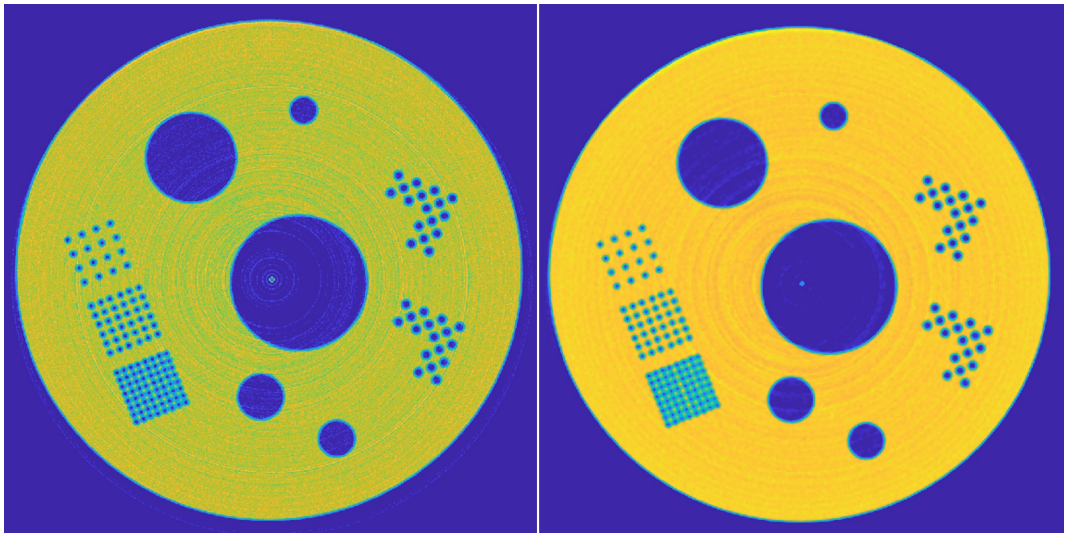

Figure 8.59: a) SIRT reconstruction of the bubble phantom with 3000 iterations b) SIRT reconstruction of the bubble phantom with 3000 iterations with a median filter 2D

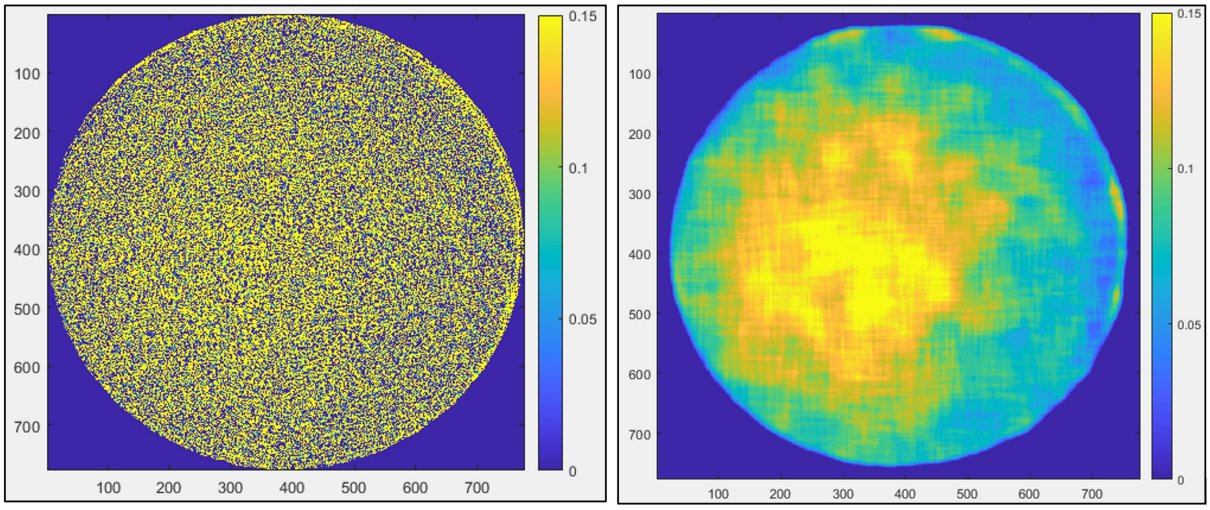

Figure 8.60: a) SIRT reconstruction (1000 iterations) of the bubble column with NeverWet coating b) SIRT reconstruction (1000 iterations) of the bubble column with NeverWet coating (medfilt2 [50 50] applied)

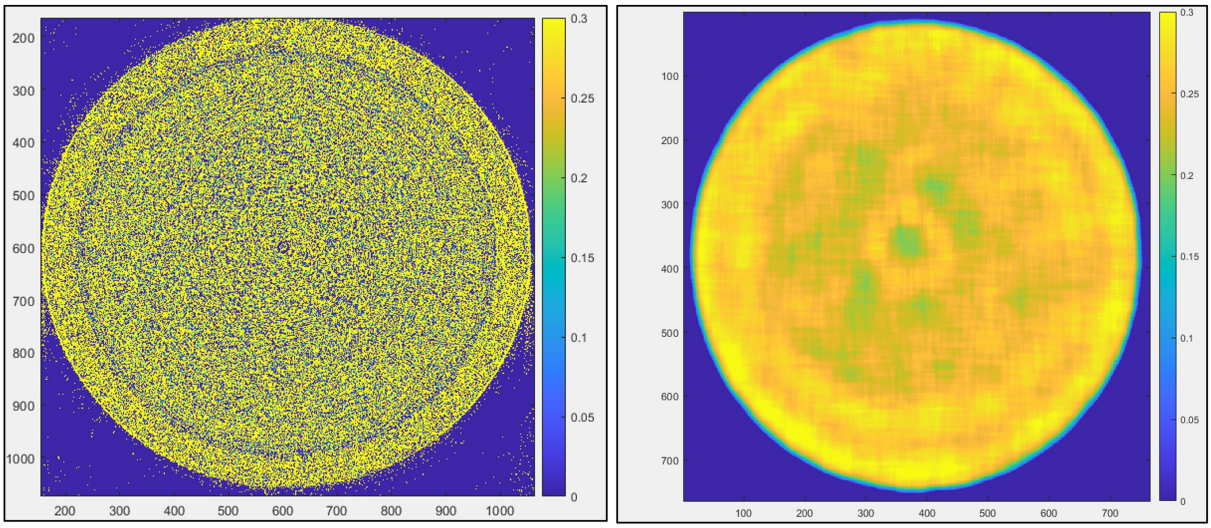

Figure 8.61: a) SIRT reconstruction (1000 iterations) of the bubble column without NeverWet coating b) SIRT reconstruction (1000 iterations) of the bubble column without NeverWet coating (medfilt2 applied)

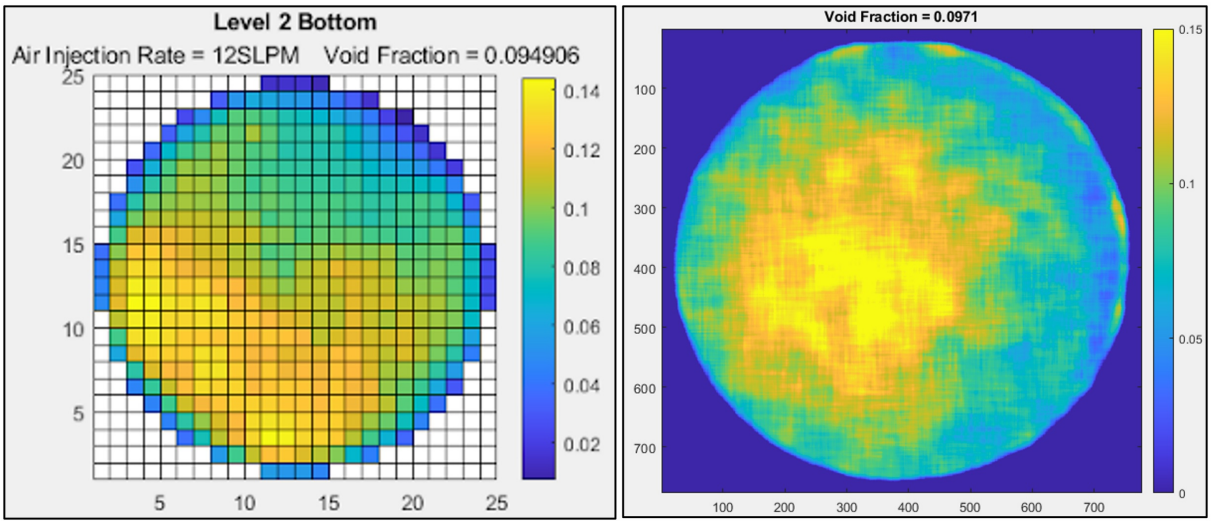

Figure 8.62: a) Wire Mesh Void Fraction measurements of the bubble column with NeverWet coating b) SIRT reconstruction (1000 iterations) of the bubble column with NeverWet coating

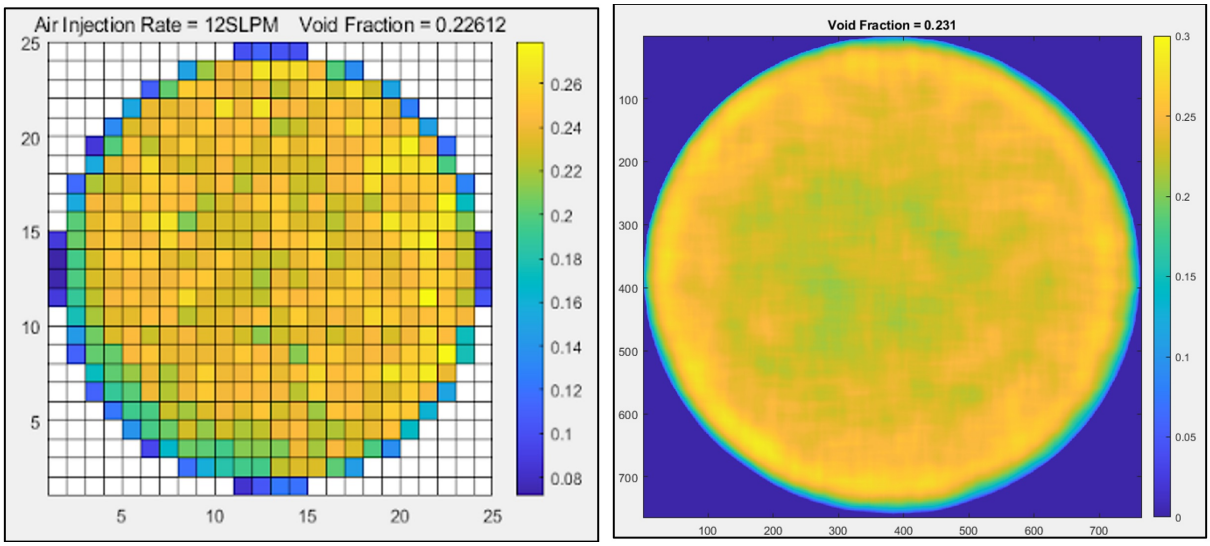

Figure 8.63: a) Wire Mesh time-averaged Void Fraction measurements of the bubble column b) SIRT reconstruction (100 iterations) of time-averaged Void Fraction across the bubble column

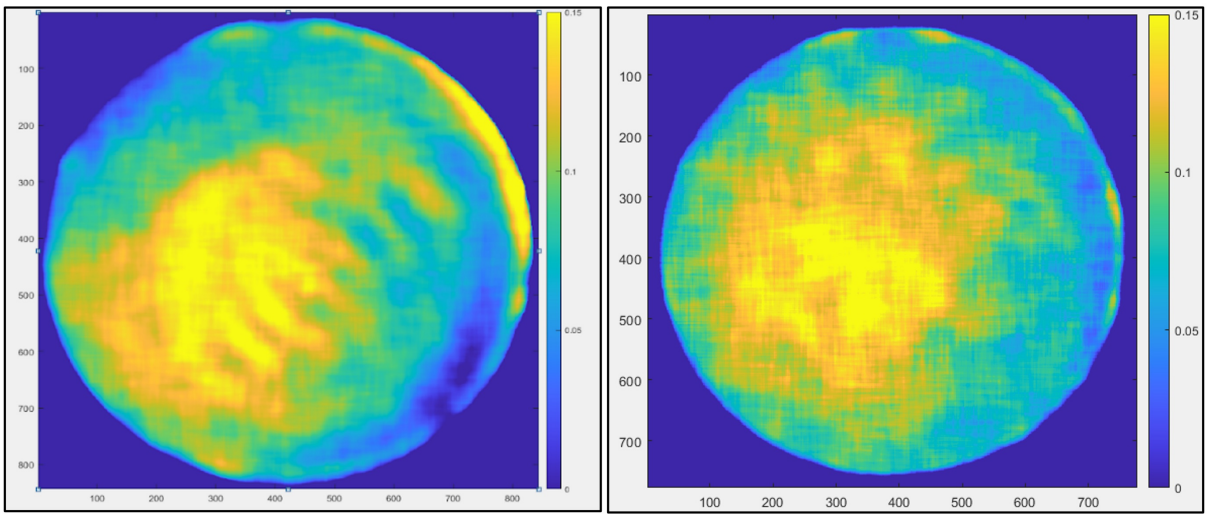

Figure 8.64: a) SIRT reconstruction (100 iterations) of the bubble column with NeverWet coating b) SIRT reconstruction (1000 iterations) of the bubble column with NeverWet coating

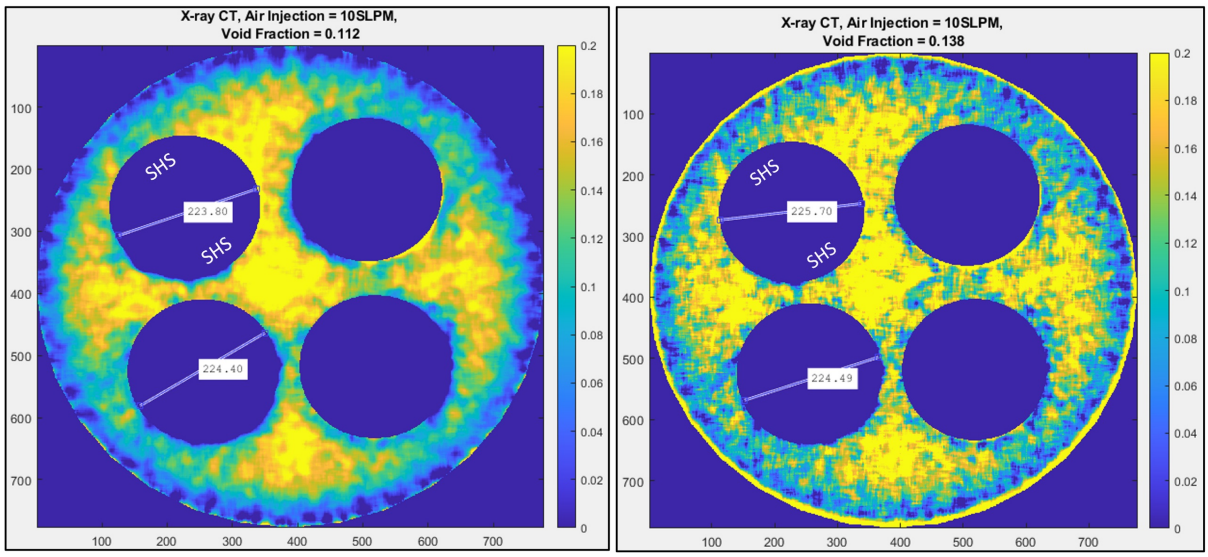

Figure 8.65: a) SIRT reconstruction (100 iterations) of the bubble column with NeverWet coating b) SIRT reconstruction (1000 iterations) of the bubble column with NeverWet coating

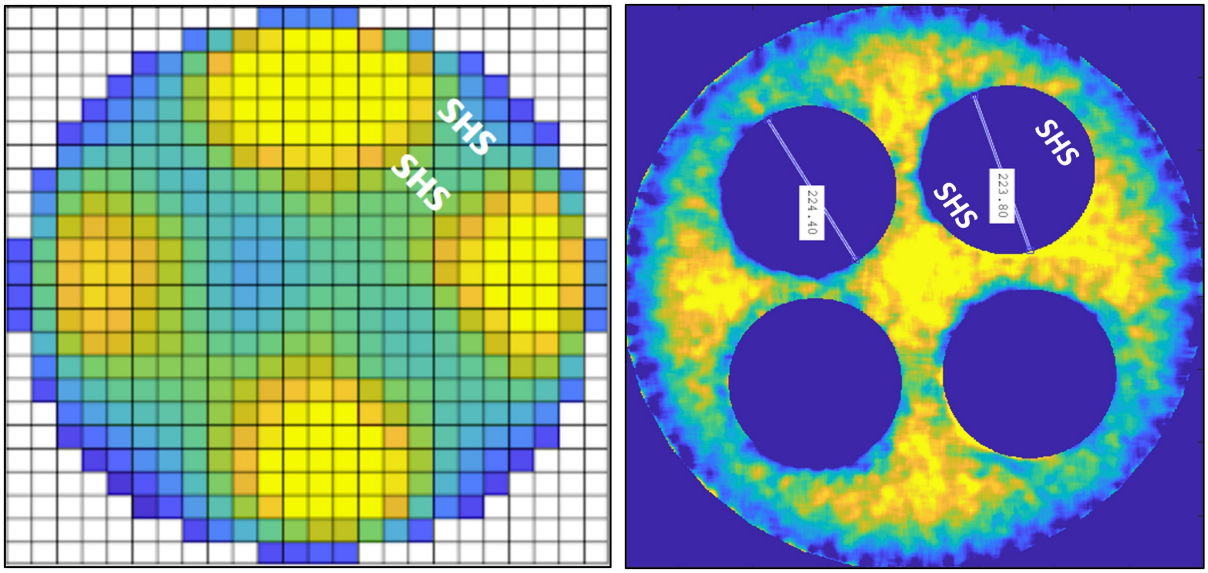

Figure 8.66: a) SIRT reconstruction (100 iterations) of the bubble column with NeverWet coated PVC Tube b) SIRT reconstruction (1000 iterations) of the bubble column with NeverWet coated PVC tube

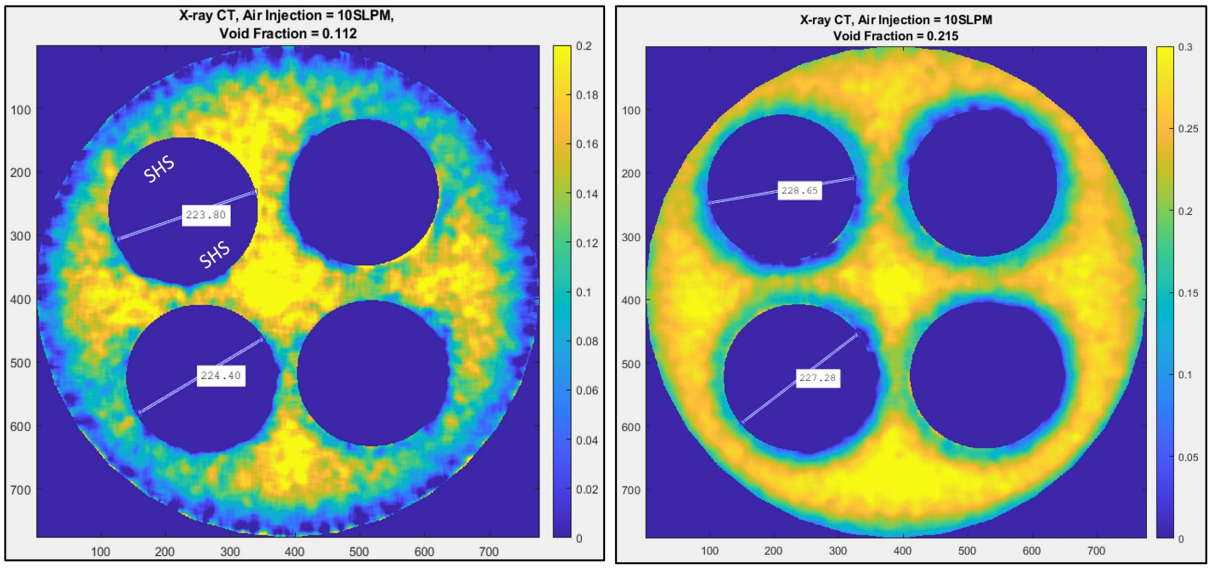

Figure 8.67: a) Time-averaged Void Fraction (SIRT reconstruction using100 iterations) with one substituted SHS-coated PVC tube b) Time-averaged Void Fraction (SIRT reconstruction using100 iterations) with hydrophilic PVC tubes

Chapter 9

Effect of Hydrophobicity of walls on bubble column dynamics

9.1 Background

Bubble columns are utilized in multiple facets of engineering industry from chemical, nuclear, biochemical, and petrochemical industries. These engineering applications offer excellent heat and mass transfer characteristics, minimal maintenance, low operating costs, and provide simplified engineering construct and compactness. Due to these advantages, gaining an understanding of hydrodynamic and operating parameters that characterize their operations, is essential to continue to improve the efficiency if these design parameters. We will study how the addition of superhydrophobic surfaces affect bubble dynamics and regime as observed in gas holdup, bubble velocity and bubble sizes. The characteristics define the bubble regime, which would then influence mass transfer and heat transfer coefficients. The design of bubble column reactors depends on the quantification of heat and mass transfer characteristics, mixing phenomena, and chemical kinetics of the reacting system. We will evaluate the following parameters, which are usually considered in the design of bubble column: axial dispersion coefficient of gas in liquid, mean bubble diameter, and gas holdup.

Fluid dynamics has a significant effect on the operation and performance of bubble columns. The flow regimes in bubble columns are classified according to superficial gas velocity and grouped into three types of regimes: homogeneous (bubbly flow), heterogeneous (churn-turbulent flow), and slug flow. This flow regimes are depicted in Figure 1 to visually show the different bubble patterns. Bubbly flow regimes, in a setting with no water flow, exhibit homogeneous flow regime at low superficial gas velocity. The bubbles in this flow regime are characterized by uniform small sizes and rise velocity. This flow regime is also characterized by uniform small sizes and rise velocities. This flow regime is also characterized by its uniform bubble distribution, subtle mixing and little to no observable bubble coalescing or bubble breakup. Kawagoe et al. found that gas holdup in bubbly regimes have a linear relationship with increasing superficial gas velocity. The churn-turbulent regime in-

volves the disturbance of the bubbly regime due to enhanced turbulent motion of gas bubbles and liquid recirculation. Many of the bubbles coalesce and breakup resulting in a bimodal distribution of bubble density and bubble size distribution (Lehr, 2002)[21].

The onset of transition from bubbly flow regime, homogeneous, to churn-turbulent, heterogeneous, is characterized by the onset of upward liquid circulation in the column center and downward circulation near the column wall., therefore more gas holdup takes place at the center of the bubble column.

Superficial gas velocity is the averaged velocity of gas dispersed from the sparger mechanics, expressed as the volumetric flow rate divided by the cross-sectional area of the bubble column. Studies in this area discuss how void fraction increases with superficial gas velocity. The increase of void fraction is proportional to superficial gas velocity in a homogenous regime. The increase of void fraction in a heterogeneous regime is defined by the increase in large bubbles vice smaller bubbles, which play a constant contribution to gas holdup.

Column dimension, such as diameter and height, can affect hydrodynamics. Shah et al. reported that, in bubble columns, the effect of column size on void fraction is negligible for diameters greater than 10-15 cm. Luo et al. found that dimensions are negligible on void fraction when the ratio of the column height to the diameter (aspect ratio) is greater than 5. Our bubble column has an aspect ratio of 12.84. Bubble characteristics are important to void fraction development.

Superhydrophobic surfaces are characterized by their high contact angles in the presence of water drops. This material is used for its water repellency. The characteristic of high contact angle is associated with the Cassie state, which consists of a surface topography with a stabilized layer of air underneath the water. When a condition exists where there is no entrapped air and the whole surface of the substrate is in direct contact with the water, the surface is said to be in a Wenzel state. For applications of drag reduction in capillaries, the superhydrophobic surface must be submerged. With these surfaces in the Cassie state, drag reduction is reduced because the hydrodynamic boundary conditions change. The no slip boundary usually found between the solid to water interface is replaced by a water to air interface that cannot support shear stresses. When the superhydrophobic surface is submerged, the air on the surface is no longer connected to the atmosphere and the Cassie state durability is limited to hydrostatic pressure and dissolution of gas in water. As the pressure in the entrapped gas increases with hydrostatic pressure, the gas starts to dissolve in water and requires a source of replenishment to maintain its state. The gas may also be depleted based on the saturation conditions of the water. Bubbles dispersed in a liquid and flowing by the superhydrophobic surface can be used to replenish the air on the superhydrophobic surface to maintain the Cassie state. The bubbles must meet a particular criterion to merge with the air layer (Shi, 2015) [42].

Chen Shi et al. conducted force measurements for the interaction of bubbles with submerged superhydrophobic surfaces in the Cassie state. Their experiment included the use of an Atomic Force Microscope (AFM) and a theoretical model based on Reynold's lubrication theory and Young-Laplace equation to interpret the measured pressure curves. Their findings for soot-templated (600°C) sample of ¿ 158 +/- 4°contact angle revealed, from microscopy,

that the bubble would disappear at a critical force of approximately 1nN with the surface. This force changes for each operating condition. It was observed that this interaction was fast and only caught with video microscopy vice the naked eye. The experiment revealed that submerged superhydrophobic surfaces have superaerophilic properties in water. The air layer along the superhydrophobic surface acts like one large bubble, which allows us to evaluate the relationship between bubbles and superhydrophobic surfaces using bubble to bubble interaction theory (Shi, 2015) [42].

9.2 Bubble Column Comparisons between Hydrophobic and Hydrophilic Inner Walls Time-Averaged Void Fraction Measurements

We conducted an evaluation of bubble flow dynamics against areas of different surface characteristics. We constructed two different bubble columns made of polycarbonate material. One of the bubble columns was coated with GenToo coating inside the inner walls to add a hydrophobic characteristic to the inner wall. GenToo is a corrosion-resistant and easy clean coating which stands up to harsh environments. GenToo is a transparent coating that has a hydrophobic quality that repels water and most oils and solvents. The second bubble column was constructed to maintain a hydrophilic characteristic in the inner walls. The purpose of this experiment was to compare how hydrophobic and hydrophilic surfaces affect bubble dynamics inside the bubble column. This comparison was evaluated using wire mesh sensor measurements from four different sensors positioned along the vertical direction of each bubble column.

Experimental Setup

Figure 9.1 displays a layout of a wire mesh sensor to include the two grids of electrodes and the locations of the transmitter and receiver wires. Our sensors have an ID of 77.927 mm and a lateral spacing resolution of 3.247mm. The wire diameter is 100 microns. The sensors include two electrode grids with 24 electrodes each, which provide 24 x 24 sensitive points.

Figure 9.2 displays a simplified scheme of the signal acquisition layout of the wire mesh sensor. The wire mesh sensor function is based off the principle of local instantaneous conductivity of the two-phase system. The conductivity is measured at the intersection point of the wires of the two grids. The result is 24 x 24 sensitivity points, distributed equally across the cross section. The system compensates for the grid intersections that are outside the bubble column, therefore the sensitivity points are less than expected with a 24 x 24 grid system.

Figure 9.3 displays the bubble column with four wire mesh sensors installed. Each pair of the sensors is positioned 27.5 mm away from each other with a flange designed to not obstruct the flow between each measurement plane. This arrangement allows us to evaluate

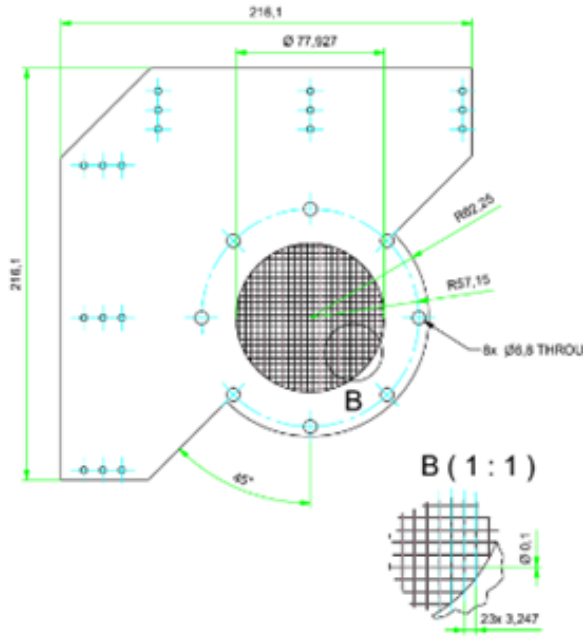

Figure 9.1: Wire mesh sensor layout (24 x 24 electrode wires)

bubble velocity across the two measuring planes. Two wire mesh sensor pairs are separated by 35.5 cm to measure the void fraction development. This should give us an adequate void fraction measurement derived from the geometric constraints and hydrophobic and hydrophilic characteristics of the inner walls. This measurement will furthermore be used to compare the lateral void fraction estimates against void fraction measurements derived from X-ray computed tomography.

Figure 9.4 displays the layout of the sensors in an order as displayed in the measurements. The lower plane arrangement of wire mesh sensors is positioned approximately 10 cm above the air injection openings. The lower plane sensors are labeled Level 1 Bottom and Level 1 Top. Level 1 Bottom is positioned reversed and rotated 90 degrees to align with the upper sensor. The measurement field compensates for this arrangement that was solely arranged based on limitations of space for electrical connections to the transmitter and receiver wires. The upper plane arrangement of the wire mesh sensors is positioned approximately 35.5 cm above the lower plane arrangement. The upper plane sensors are labeled Level 2 Bottom and Level 2 Top. Level 2 Bottom is positioned reversed and rotated 90 degrees to align with the upper sensor. The measurement field compensates for this arrangement that was solely arranged based on limitations of space for electrical connections to the transmitter and receiver wires of both sensors.

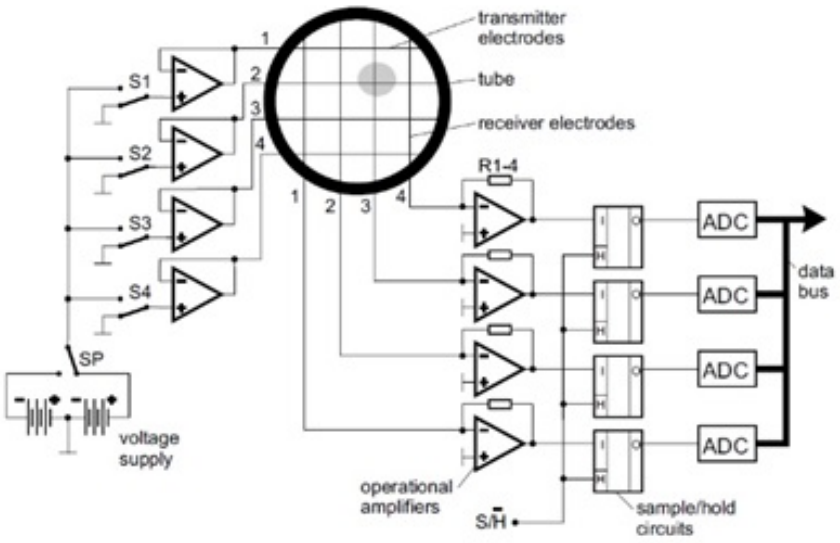

Figure 9.2: Simplified scheme of WMS signal acquisition system (Prasser, 1997)

Wire mesh acquisition software provides the electrical connections to each of the wire mesh sensor grids. There are a total of 16 connections which provide 8 transmitter wire connections and 8 receiver wire connections. The Wire Mesh Sensor Framework software contains a void fraction module, which is utilized to process the collected time-averaged display of lateral void fraction distribution. For the comparison collection, we collected 17,500 frames at 500Hz to ensure the collected points converged within 1 % of the running frame average for all collected frames.

Figure 9.5 displays time-averaged void fraction estimates for the two bubble columns using variable air injection rates from 1000 SCCM to 16000 SCCM and superficial gas velocity $0.34\frac{cm}{s}$ to $5.47\frac{cm}{s}$. These void fraction measurements were compiled from evaluation of height differences between the initial height and the height at the selected injection rate. Figure 9.6 displays time-averaged void fraction measurements compiled from 17,500 frames captured at 500Hz from each of the four wire mesh sensors. The histogram files provided with the Wire Mesh Sensor Framework software was utilized as the calibration dataset for these measurement sets. Histogram calibration files were yielding better results than water calibration files along the wall boundaries and were used as a primary source for calibration files. Eventually we realized that the diameter of the inner tubes was slightly shorter in diameter than the wire mesh sensor diameters. Based on this realization, we utilized a region of interest, provided in the software, which would result in masking the sensitivity points that were obstructed by the tubes and therefore not consider those values for void

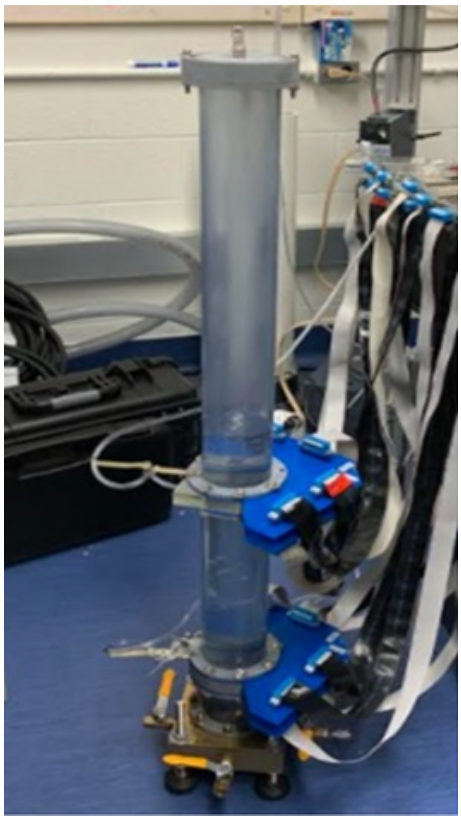

Figure 9.3: Bubble column with four Wire Mesh Sensors installed

fraction calculations.

Time-averaged Void Fraction Measurement Findings

Figure 9.5 shows the bubble column with hydrophobic inner walls provide lower void fraction estimates at values greater than 10000 SCCM (Superficial Gas Velocity: $3.42\frac{cm}{s}$) as compared to void fraction measurements from the bubble column with hydrophilic inner walls. We believe the lowering void fraction values are associated with bubbles coalescing near the wall and escaping faster along the inner wall of the bubble column, thus resulting in a lower void fraction. As expected, you see the air bubbles start to disperse closer to the inner walls that are coated with hydrophobic characteristics. The affinity to the wall occurs pass a superficial gas velocity of $3.42\frac{cm}{s}$ when we assess that the geometric constraint of the inner wall is near the air bubbles as they move laterally based on interactions with other bubbles rising through the column. Below a superficial gas velocity of $3.42\frac{cm}{s}$, the bubbles can disperse without succumbing the constraints of the inner walls of the bubble column. At

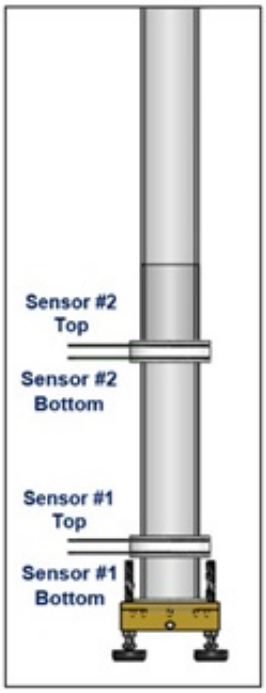

Figure 9.4: Bubble column with four Wire Mesh Sensors labeled

injection rates higher than a superficial gas velocity of $3.42\frac{cm}{s}$, the bubbles disperse towards the inner wall of the bubble column based on interfacial forces between each bubble that causes them to repel off each other or coalesce into larger air bubbles.

At a superficial gas velocity of $3.42\frac{cm}{s}$, the bubbles in the hydrophobic column are more dispersed than the bubbles in the hydrophilic bubble column. The void fraction values are very similar for both columns. Figures 9.6-9.10 were compiled from all four wire mesh sensors and displayed from the bottom sensor on the bottom left to the top sensor in the upper right. Each subset figure contains the estimated time-average void fraction for its designated sensor. The colorbar was maintained the same for both columns within each figure to allow for a comparison of lateral void fraction measurements between both columns.

At (U_g) of $3.07\frac{cm}{s}$, as displayed in Figure 9.7, displays how the bubbles in the hydrophobic column are more uniformly dispersed in the top pair of wire mesh sensors. This is the first time we see the void fraction values start to separate from each other, clearly displaying a distinction in flow regime most likely caused by the force interactions between the inner wall of the bubble column and interfacial forces between rising bubbles.

At (U_g) of $3.76\frac{cm}{s}$, as displayed in Figure 9.8, you continue to see a more dispersed bubble dynamic. The void fraction is still locally higher in the center of the bubble column

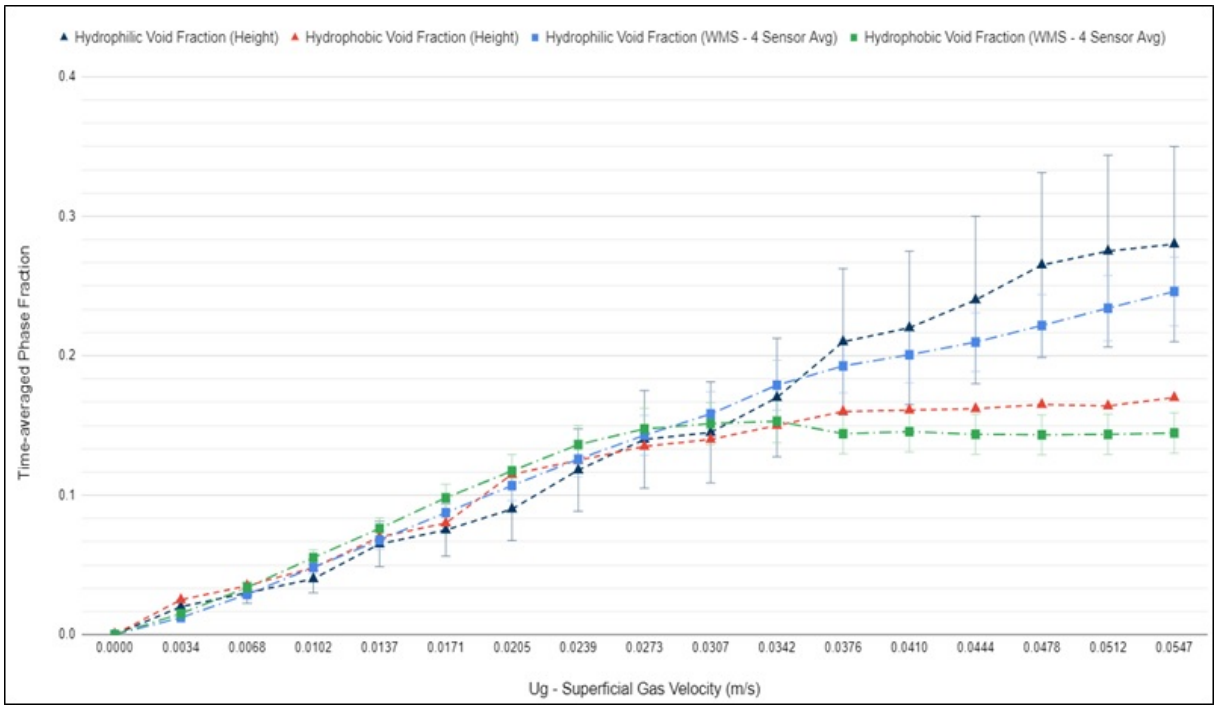

Figure 9.5: Hydrophobic Bubble Column (lower 2 lines) vs Hydrophilic Bubble Column (upper 2 lines) Time-averaged Void Fraction measurements (using Wire Mesh Sensor Framework and height measurements)

but the time-averaged void fraction is considerably less than the time-averaged void fraction measurements for the hydrophilic bubble column.

Figure 9.10 displays the time-averaged void fraction estimates for each sensor at (U_g) of $4.44\frac{cm}{s}$. The hydrophilic time averaged void fraction starts to skew towards one side of the bubble column. The hydrophobic bubble column continues to spread evenly across the column horizontally and continue to maintain a very low void fraction.

Figure 9.11 displays the time-average void fraction for both columns at an air injection rate of 16000 SCCM (16 SLPM). The void fraction for the hydrophobic bubble column maintains its lowered void fraction and uniformly dispersed bubble dynamics.

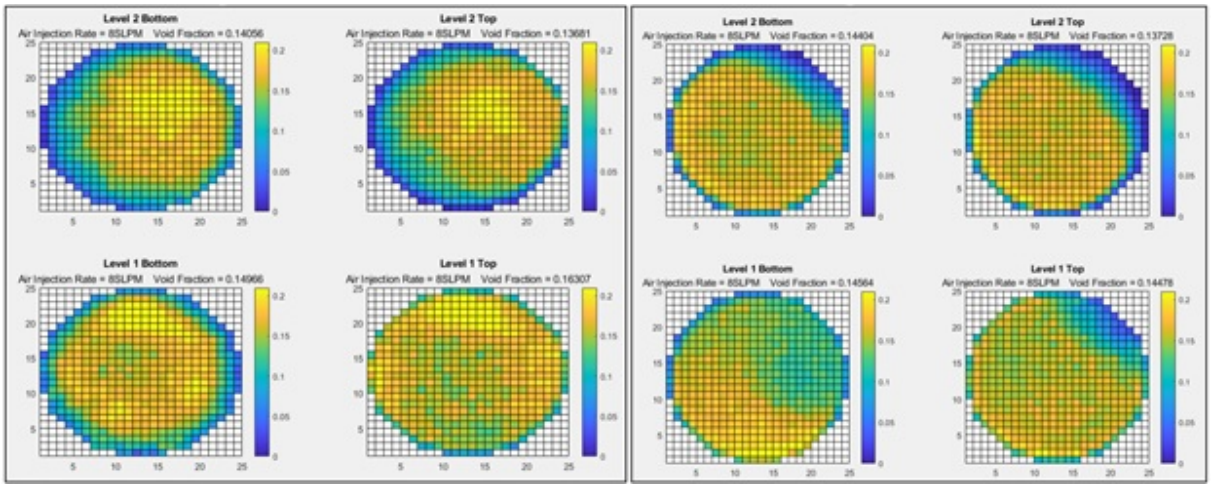

Figure 9.6: Superficial gas velocity (U_g) of $2.73\frac{cm}{s}$ Hydrophobic Bubble Column (left) vs Hydrophilic Bubble Column (right) lateral display of time-averaged void fractions

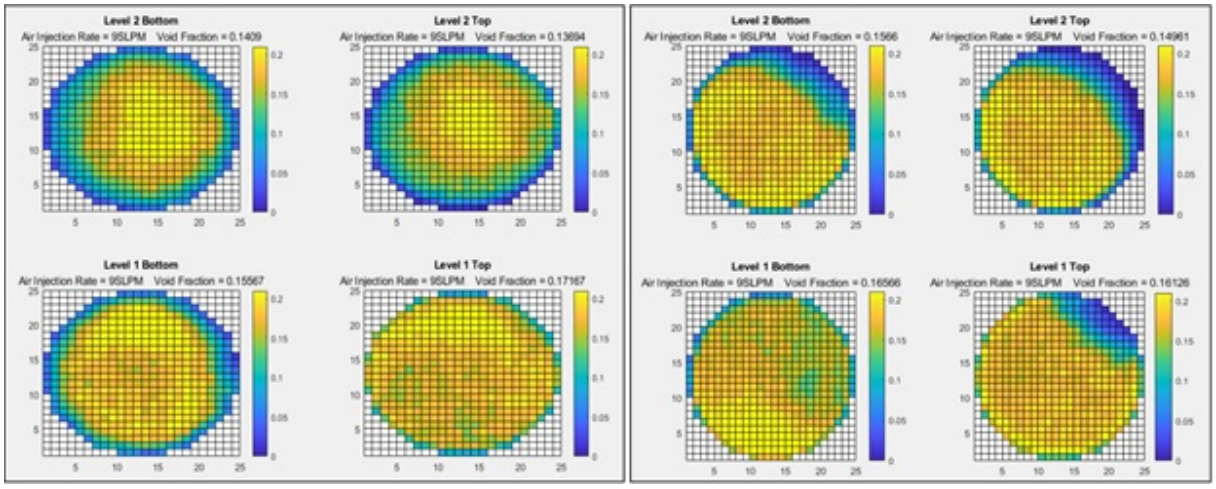

Figure 9.7: Superficial gas velocity (U_g) of $3.07\frac{cm}{s}$ Hydrophobic Bubble Column (left) vs Hydrophilic Bubble Column (right) lateral display of time-averaged void fractions

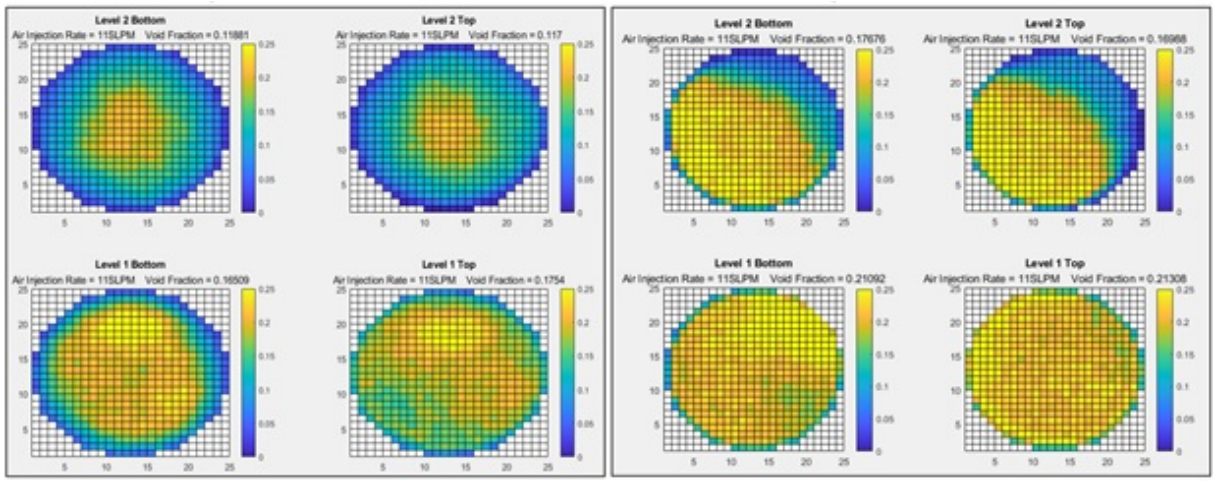

Figure 9.8: (U_g) of 3.76$\frac{cm}{s}$ Hydrophobic Bubble Column (left) vs Hydrophilic Bubble Column (right) lateral display of time-averaged void fractions

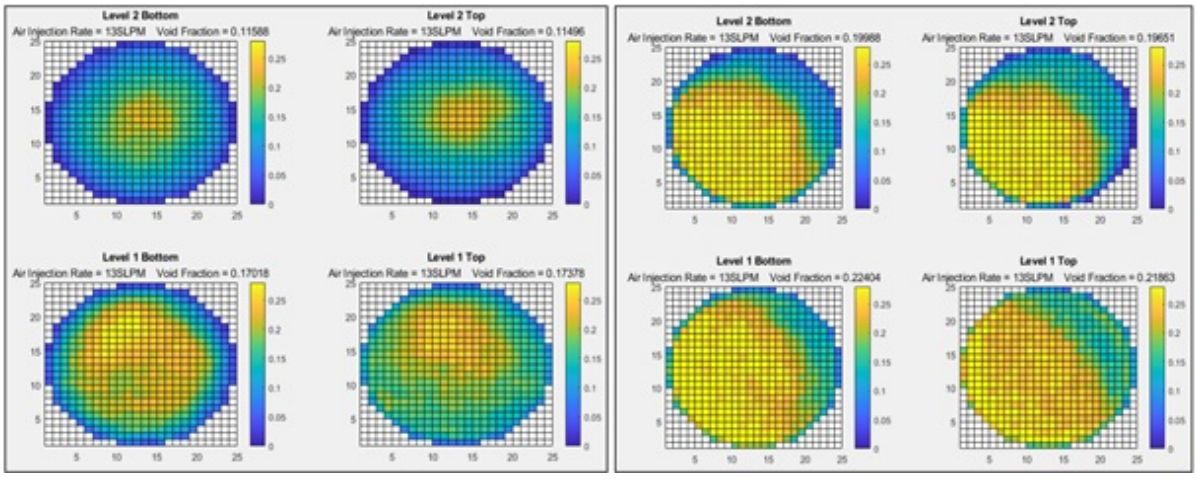

Figure 9.9: (U_g) of 4.44$\frac{cm}{s}$ Hydrophobic Bubble Column (left) vs Hydrophilic Bubble Column (right) lateral display of time-averaged void fractions

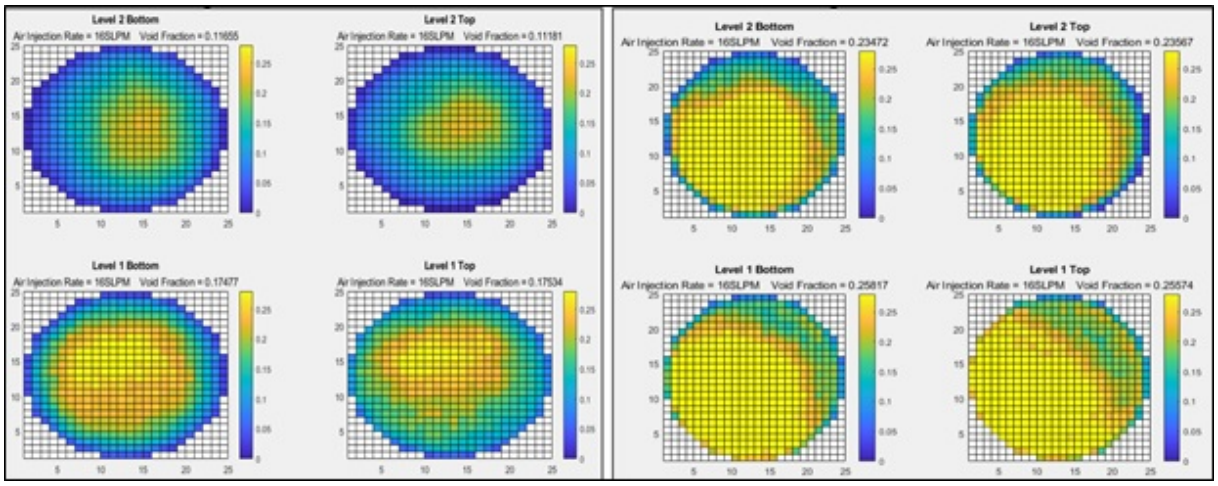

Figure 9.10: (U_g) of 5.47$\frac{cm}{s}$ Hydrophobic Bubble Column (left) vs Hydrophilic Bubble Column (right) lateral display of time-averaged void fractions

9.3 Bubble Column Comparisons between Superhydrophobic and Hydrophilic Inner Walls Time-Averaged Void Fraction measurements

Experiment Setup

In this experiment, we transitioned to evaluate superhydrophobic coatings applied to the inner walls of a bubble column constructed from a polyvinyl chloride (PVC) pipe. The bubble column was constructed of three PVC sections glued to PVC flanges, which provided 8 holes for bolt access to secure the sections into a single water-tight column. The PVC sections were glued to the flanges using GOOP adhesive and allowed to cure for 24 hours. Clear Silicon was applied to the outside seam connection between the flange and PVC pipe to add another layer of protection against water leakage. The clear Silicon application was allowed to cure for 24 hours. Figure 9.11 displays the bubble column setup and instrumentation used in this experiment.

Wire Mesh Sensor, Height and X-ray Measurements were conducted on the hydrophilic and superhydrophobic-coated bubble column. Four time-averaged phase fraction measurement techniques were utilized on both bubble columns through a range of 1SLPM to 18SLPM. The following techniques have variable accuracy but their agreement proved valuable to understand how each technique measures time-averaged phase fraction:

- Void Fraction calculation by height difference. Both columns maintained a clarity, although at different levels, to allow us to measure height differences. We utilized an

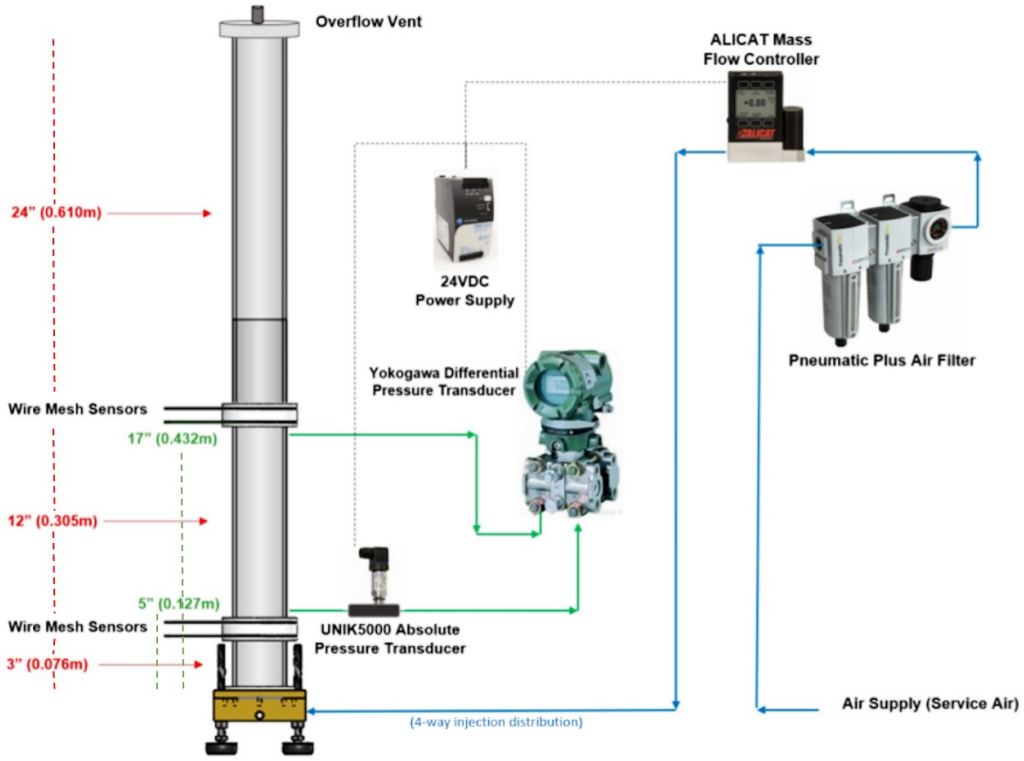

Figure 9.11: Bubble Column Display with Instrumentation

electrical tape to align along the top portion of the bubble column. A measurement tape was used to measure the height from the base of the bubble column. We measured the initial height with no air injection and measured the height at each air injection increment. Figure 9.12 displays the water level used for the height difference calculation. The following equation was used to measure the difference:

$$\alpha = \frac{Height_{final} - Height_{initial}}{Height_{final}} \tag{9.1}$$

- Void Fraction calculation by Wire Mesh Sensor measurements were performed using the WMS200 acquisition system connected to 8 transmitter and 8 receiver modules. The transmitter and receiver modules are connected to two separate grids along the center of the wire mesh sensor. The Wire Mesh Sensor Framework software was utilized to process the data from the WMS200 software.

  Figure 9.13 displayed the running frame average computation results utilized to evaluate the number of frames required to arrived at a converged set with a difference of

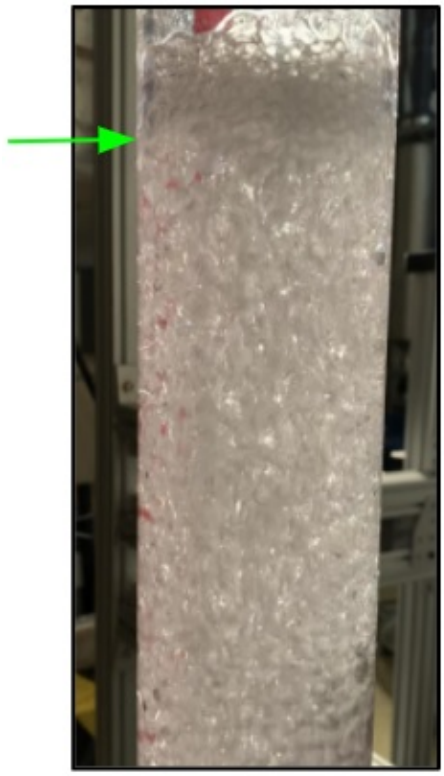

Figure 9.12: Bubble Column display with water level for a specific height

running average to final value by 1%. The running average used the void fraction files from the data set to compare each subsequent 24x24 grid frame to a running average of the previous frames. When the difference value between a particular dataset and the running average reach under a specific tolerance, the dataset was considered converged up to a specified accuracy. We determined 17,500 frames yielded a converge dataset that met the criteria of 1% for a 500Hz frame rate.

The Wire Mesh Sensor framework uses two types of calibration methods: histogram and water only dataset. Histogram proved beneficial to us but we utilized Water Calibration to validate which calibration was effective for our measurements. The following equation was utilized with a measured water-only dataset.

$$\alpha_{i,j,k} = \frac{U^{w}_{i,j} - U^{meas}_{i,j,k}}{U^{w}_{i,j}} \tag{9.2}$$

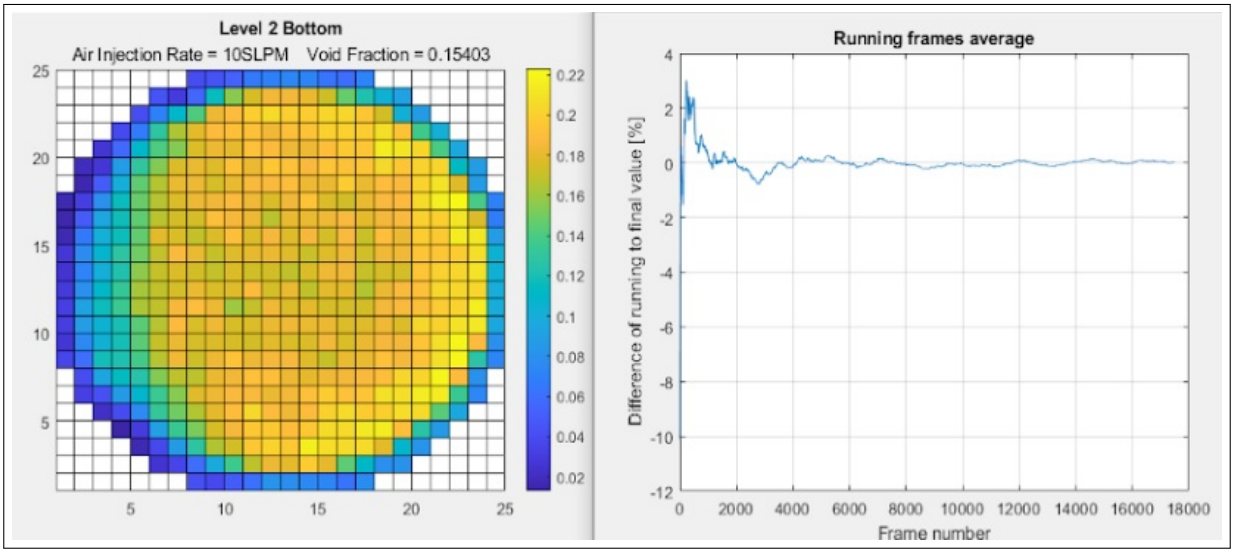

Figure 9.13: Converged Wire Mesh Sensor Dataset for WMS Time-averaged Void Fraction Measurements

- Void Fractions were measured by evaluating the intensity field at each projection angle for mixture, water-only and air-only. Each local void fraction was collected and the mean was used as the time-averaged void fraction value. The Intensity field of the mixture is a mean of the number of frames taken per run. In this case, we took 30 frames per angle at a frame rate of 1 second. Figure 9.14 displays the different intensity fields for the three mediums. The difference in intensity fields, coupled with approximations for a monochromatic X-ray source, allow using an intensity field relationship for void fraction calculations. The following equation was utilized to measure time-averaged void fraction from intensity field variations across the three different mediums.

$$\alpha = \frac{log\frac{I_{mixture}}{I_{water}}}{log\frac{I_{air}}{I_{water}}} \tag{9.3}$$

- Void Fraction calculation were also computed from the reconstruction dataset attenuation values for the three mediums: Mixture, Water-only, and Air-only. By using the following equation and ensuring proper centering of the bubble column, you can calculate the void fraction, that is rendered in a two-dimensional lateral display.

$$\alpha = \frac{\mu_{mixture} - \mu_{water}}{\mu_{air} - \mu_{water}} \tag{9.4}$$

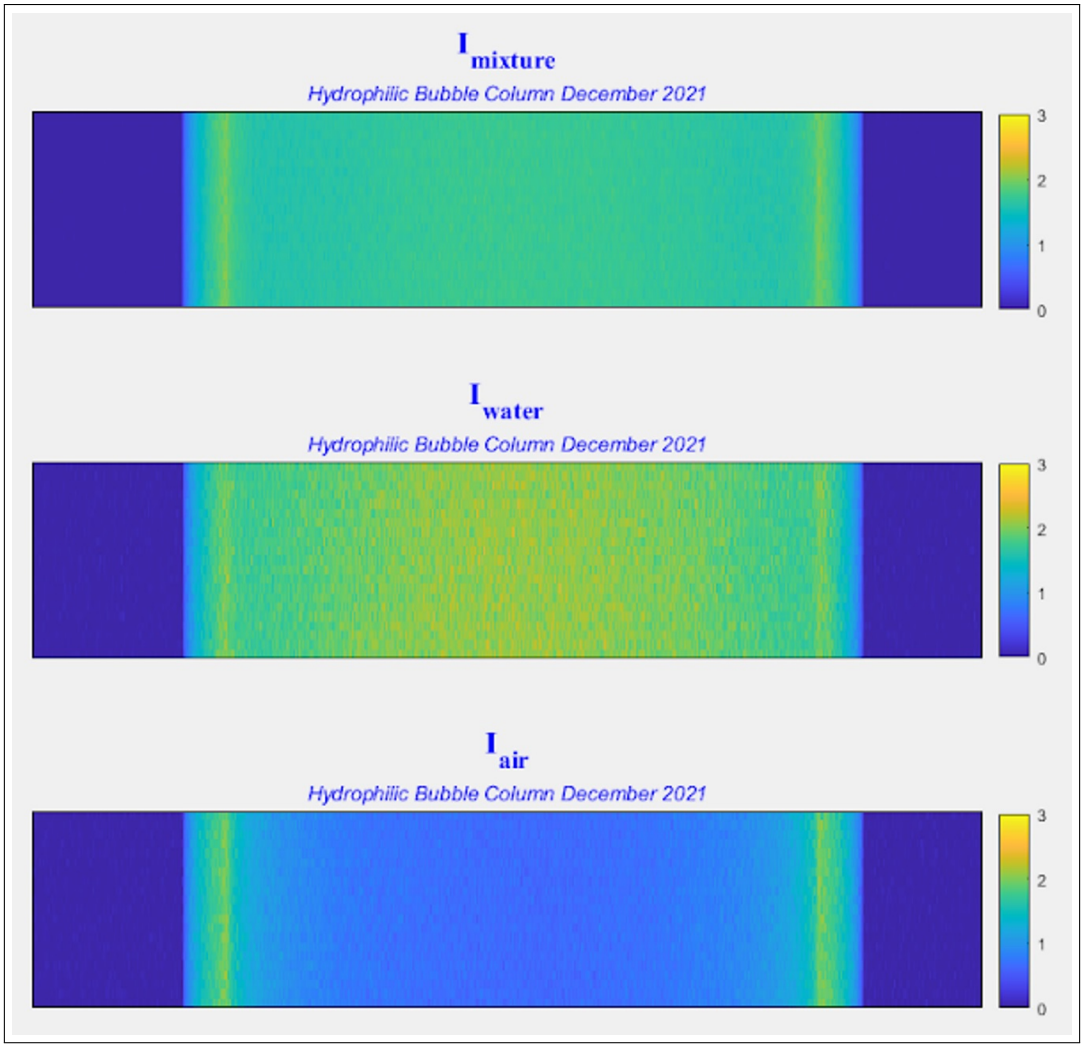

Figure 9.14: Mean Intensity fields for Mixture (top), Water (center), and Air (bottom)

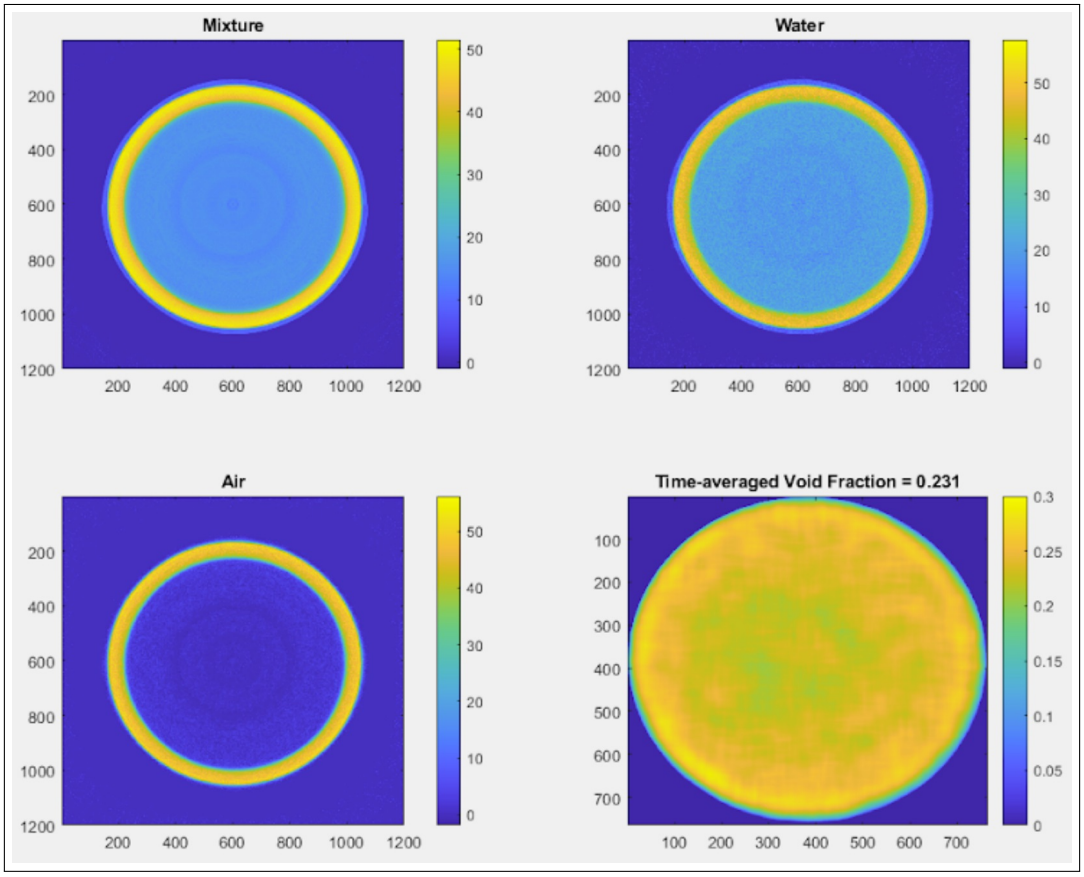

Figure 9.15: Two-dimensional SIRT Reconstruction of three mediums (Mixture, Water, and Air) and Void Fraction calculations from the attenuation coefficients gathered from the reconstruction of each medium.

Figure 9.15 displays the reconstruction attenuation coefficients for the mediums of water, air and mixture. The Void Fraction results from equation 9.4 are displayed in the lower right figure of Figure 9.15. The display is a 2 dimensional representation of the time-averaged phase fraction calculations which include the other three reconstructions.

Figure 9.16 displays a single bubble photographed inside the bubble column following coating of the bubble column with NeverWet Multisurface Liquid Repelling Treatment. The contact angle was measured using ImageJ software angle measuring tool. The measurement was performed from a line parallel to the curved wall of the tube and the first deviated line that runs tangential to the bubble curvature.

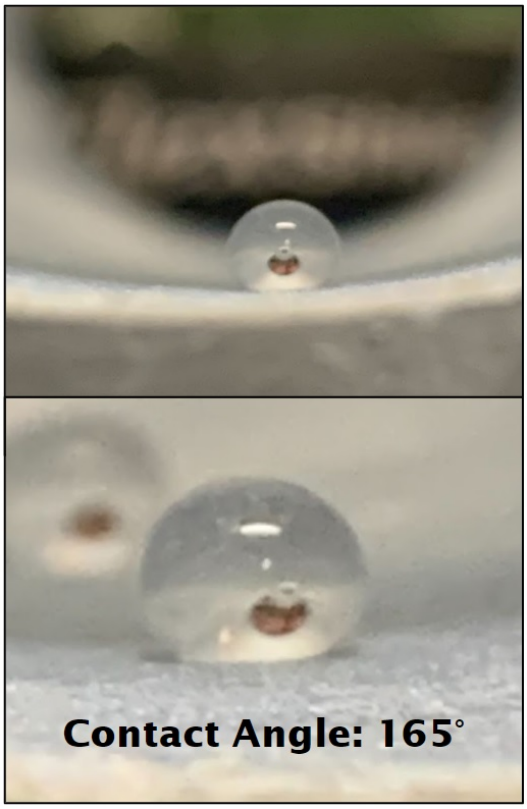

Figure 9.16: Single Bubble on Superhydrophobic Coating inside the PVC Bubble Column

Hydrophilic PVC Tube Void Fraction Measurement Results

The YXLON X-ray Source parameters were set at 100kV and 350μA in TXI mode, which provides automatic tracking of the target current to maintain a consistent intensity field.

The THOR X-ray Detector is a photon counter with parameters set at a Low keV of 40keV and High keV of 60keV. The exposure time was set at a frame rate of 1 second. We collected 35 frames per angle for 360 degree increments for a complete rotation.

The Bubble Column is made up of PVC material with an inner tube diameter of 77.927mm and a tube wall thickness of 6.35mm.

The measurement sequence included the following:

- 1 360 rotation Bubble Column for water-only medium, 1 frame per degree
- 1 360 rotation Bubble Column for air-only medium, 1 frame per degree
- 1 360 rotation Bubble Column for mixture medium at 0.041m/s superficial gas velocity, 30 frames per degree

We measured the bubbly flow regime through the hydrophilic bubble column using two pairs of wire mesh sensors, varying superficial gas velocity from 0.0034m/s to 0.0615m/s. These measurements are displayed in Figure 9.17, compared with void fraction measurements calculated from height differences. We also highlighted the specific measurement values that correspond with the X-ray CT measurements. The bottom pair of WMS measurements are displayed in the blue and red lines. The top pair of WMS measurements are displayed as the green and yellow lines. The void fraction measurements from height differences is displayed as a dashed orange line. WMS measurements have an error bar of 10%. Height measurement has an error bar of 25%. The WMS measurements are in accurate agreement throughout all superficial gas velocities and deviate from height measurements at a superficial gas velocity of 0.0450, but stay within error bar accuracy through all superficial gas velocities. Based on these measurements, void fraction measurements rise to 0.30 at the maximum superficial gas velocity of the experiment.

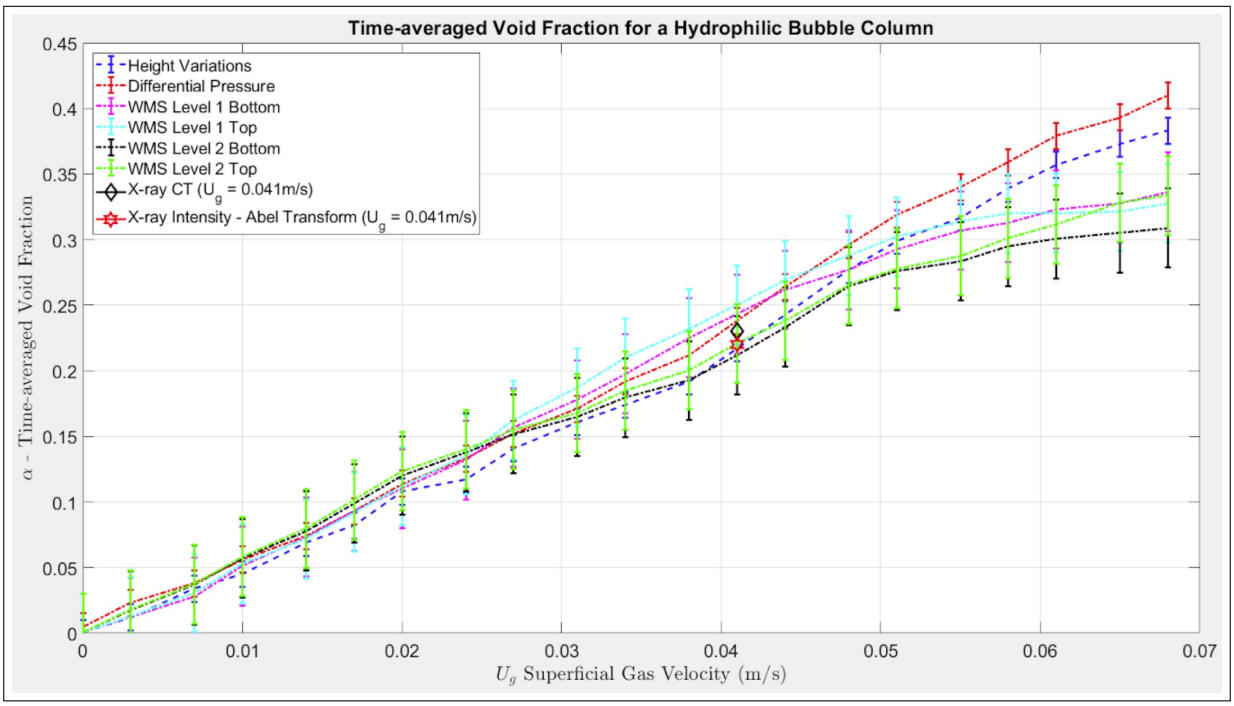

Figure 9.17: Time-averaged Void Fraction measurements summary for hydrophilic bubble column

Figure 9.18 displays time averaged void fraction measurements for a superficial gas velocity of 0.041m/s, which is the same setting used for X-ray CT measurements. Due to electronic cabling constraints during rotation motion and length of X-ray CT measurements, we decided to take the WMS measurements separately from X-ray CT measurements. The

time-averaged void fraction measurements at this superficial gas velocity averaged at 0.222, measured by taking the average of the Level 2 Bottom and the Level 1 Top WMS. The WMS void fraction coincides with a calculated void fraction from height differences of 0.237.

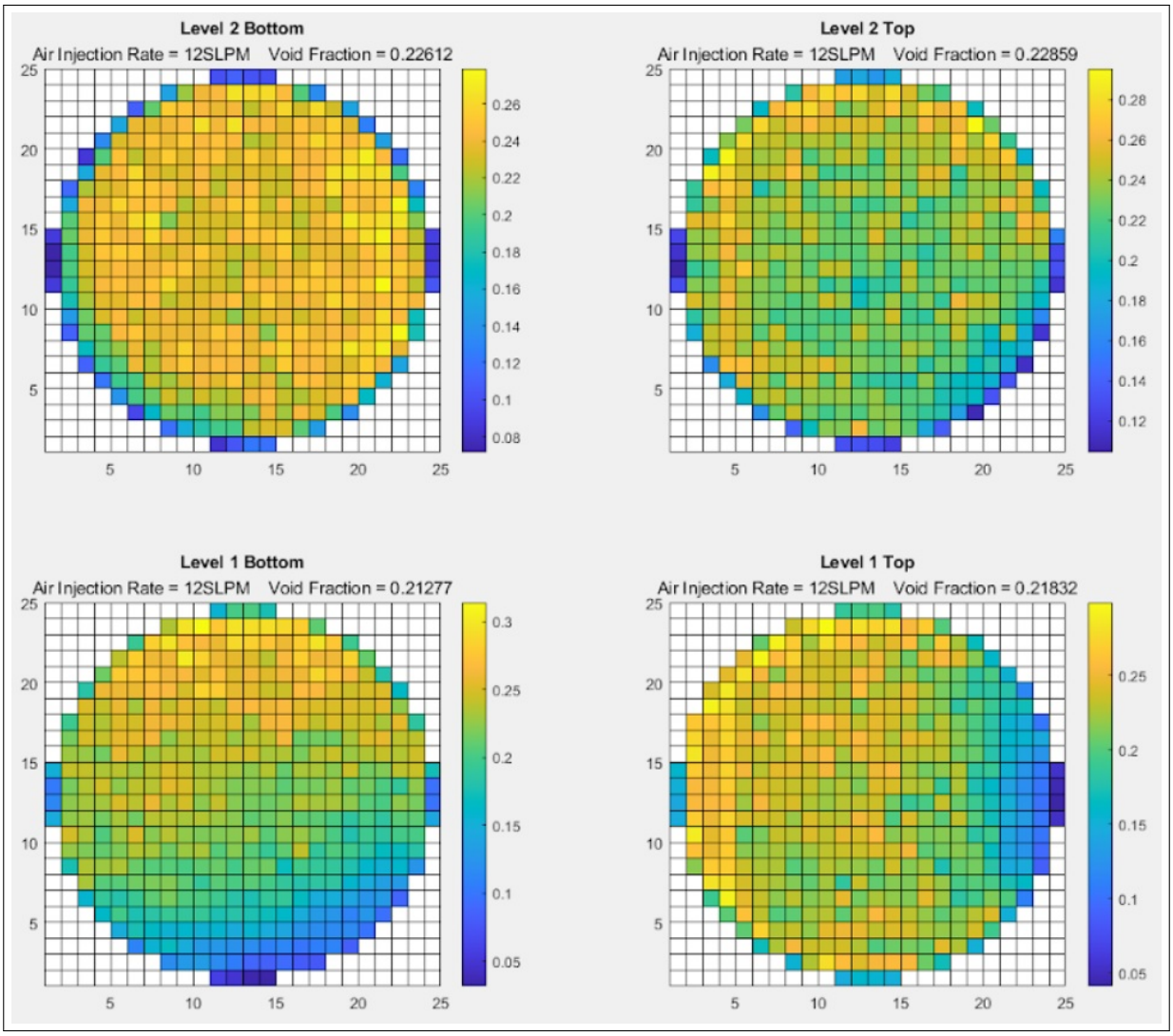

Figure 9.18: Time-averaged Void Fraction measurements for four wire mesh sensors at a superficial gas velocity of 0.041m/s

Figure 9.19 displays the time-averaged void fraction calculated by using the two-dimensional intensity projection variation from the water, air and mixture mediums. As previously discussed, the time-averaged void fraction is calculated using Equation 9.3. We collected 30 frames per angle and calculated a mean intensity field using MATLAB. The mean intensity

field of the mixture was used in the equation along with the intensity field measured for the mediums of water and air. The calculation is conducted at each angle for a total of 360 void fraction measurements, where the mean is used as the final time-averaged void fraction of 0.225. This value is in agreement with both void fraction measurements from the WMS and height differences. This shows that intensity measurements gathered from our X-ray source and photon counter settings are adequate to measure two-dimensional void fraction of the bubble column over an entire rotation.

This measurement is beneficial to prove the efficiency of Equation 9.3. There is one difficulty encountered with this technique that can make the measurement troublesome. The centering of the experiment is important for this measurement because you have to select the two-dimensional range of the intensity field. As you rotate the experiment, the intensity field projection may shift in pixel due to off-centering effects. Based on how well you have centered the experiment, you may need to apply a more constrained two-dimensional range for your area of interest so calculations are constrained to the portion of the intensity field that is the mixture and not the bubble column wall. If the bubble column wall is introduced into the calculation, artifacts introduced by the wall boundaries may lead to inaccurate void fraction measurements using Equation 9.3.

Figure 9.20 displays a time-averaged void fraction measurement calculated from the reconstruction values for the three mediums using Equation 9.4. The calculated attenuation coefficients that are rendered in a two-dimensional lateral representation using the SIRT algorithm, provided in the ASTRA toolbox, are entered into Equation 9.4 and the result is displayed in the lower right figure. The mean of the attenuation coefficients from the reconstructed void fraction data set yield a time-averaged void fraction of 0.234, which is in agreement with the three previous measurements discussed.

Figure 9.21 displays the X-ray CT time-averaged void fraction reconstruction with a median filter applied. This reconstruction suggests that more air accumulates against the walls as they rise. Bubble coalescing against the wall is expected in a homogeneous bubble regime. Furthermore, Figure 9.22 shows the time-averaged void fraction measurements from X-ray CT and the Level 2 Bottom wire mesh sensor. Both displays agree with respect to showing a larger void fraction along the walls. The X-ray CT system measurement is 17.8cm below the wire mesh sensor measurement. Even though they are not exactly at the same location, they show a uniform bubble lateral distribution with a strong affinity to the inner walls.

Superhydrophobic-coated PVC Tube Void Fraction Measurement Results

A separate bubble column constructed from the same material and arranged with the same measurements and arrangements was coated with NeverWet in the inner walls to make the inner walls superhydrophobic.

The measurement sequence included the following:

- 1 360 rotation of the Bubble Column for water-only medium; 1 frame per degree

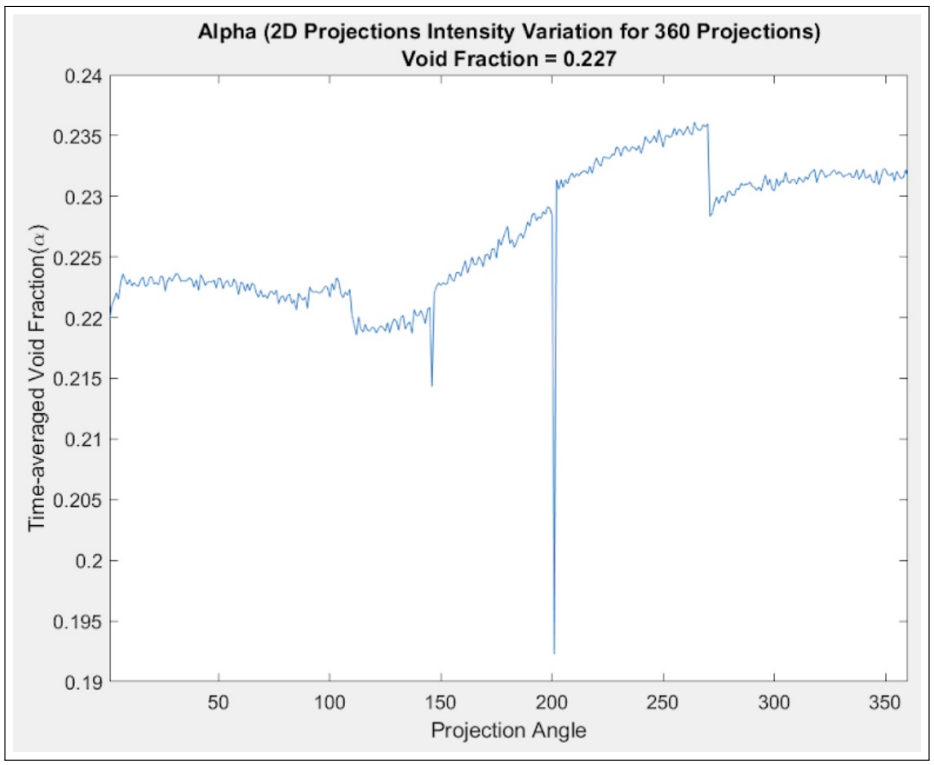

Figure 9.19: Time-averaged Void Fraction measurements from X-ray two-dimensional intensity fields at a superficial gas velocity of 0.041m/s

- 1 360 rotation of the Bubble Column for air-only medium; 1 frame per degree
- 1 360 rotation of the Bubble Column for mixture medium at 0.041m/s superficial gas velocity; 30 frames per degree

We measured the bubbly flow regime through the superhydrophobic bubble column using two pairs of wire mesh sensors, varying superficial gas velocity from 0.0034m/s to 0.0615m/s. Void fraction measurements from all techniques are displayed in Figure 9.23. We also annotated with symbols the time-averaged void fraction values that correspond with the X-ray CT measurements. The bottom pair of WMS measurements are displayed in the cyan and magenta. The top pair of WMS measurements are displayed as the green and black lines. The void fraction measurements from height differences is displayed as a blue line. WMS measurements have an error bar of 10%. Height measurement has an error bar of 25%. The WMS measurements for Level 1 sensors are in accurate agreement throughout all superficial gas velocities with height measurements but deviate from the Level 2 sensors when superficial gas velocity exceeds 0.014m/s. Based on these measurements, void fraction measurements

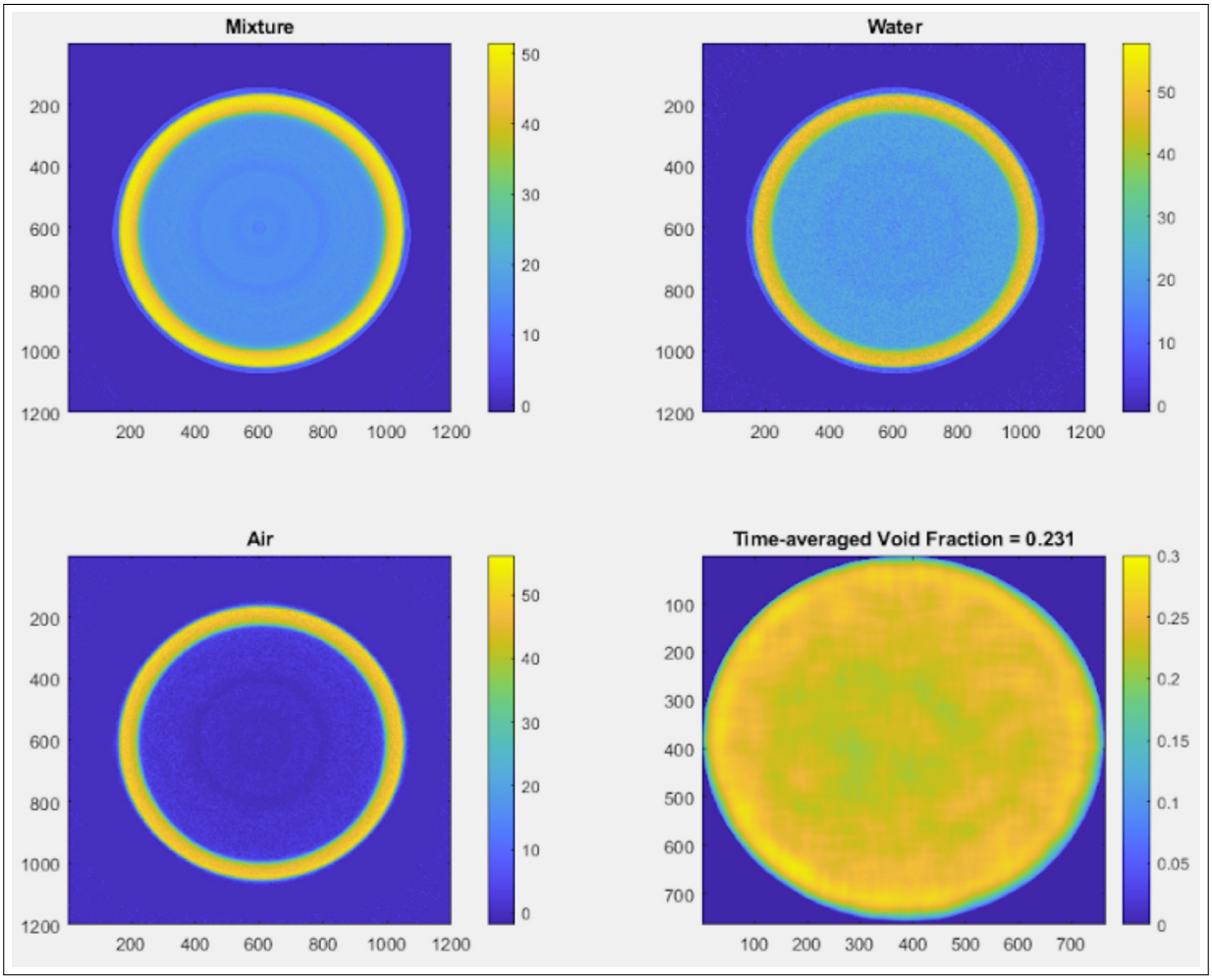

Figure 9.20: Time-averaged Void Fraction measurements from X-ray CT Attenuation Coefficients at a superficial gas velocity of 0.041m/s

rise to 0.15 at the maximum superficial gas velocity of the experiment for the bottom WMS pair and plateau at 0.09 for the top WMS pair and X-ray CT measurements agree with the Level 2 WMS measurements for void fraction.

Figure 9.24 displays time averaged void fraction measurements for a superficial gas velocity of 0.041m/s, which is the same setting used for X-ray CT measurements. Due to electronic cabling constraints during rotation motion and length of X-ray CT measurements, we decided to take the WMS measurements separately from X-ray CT measurements. The time-averaged void fraction measurements at this superficial gas velocity averaged at 0.120, measured by taking the average of the Level 2 Bottom and the Level 1 Top WMS. The WMS

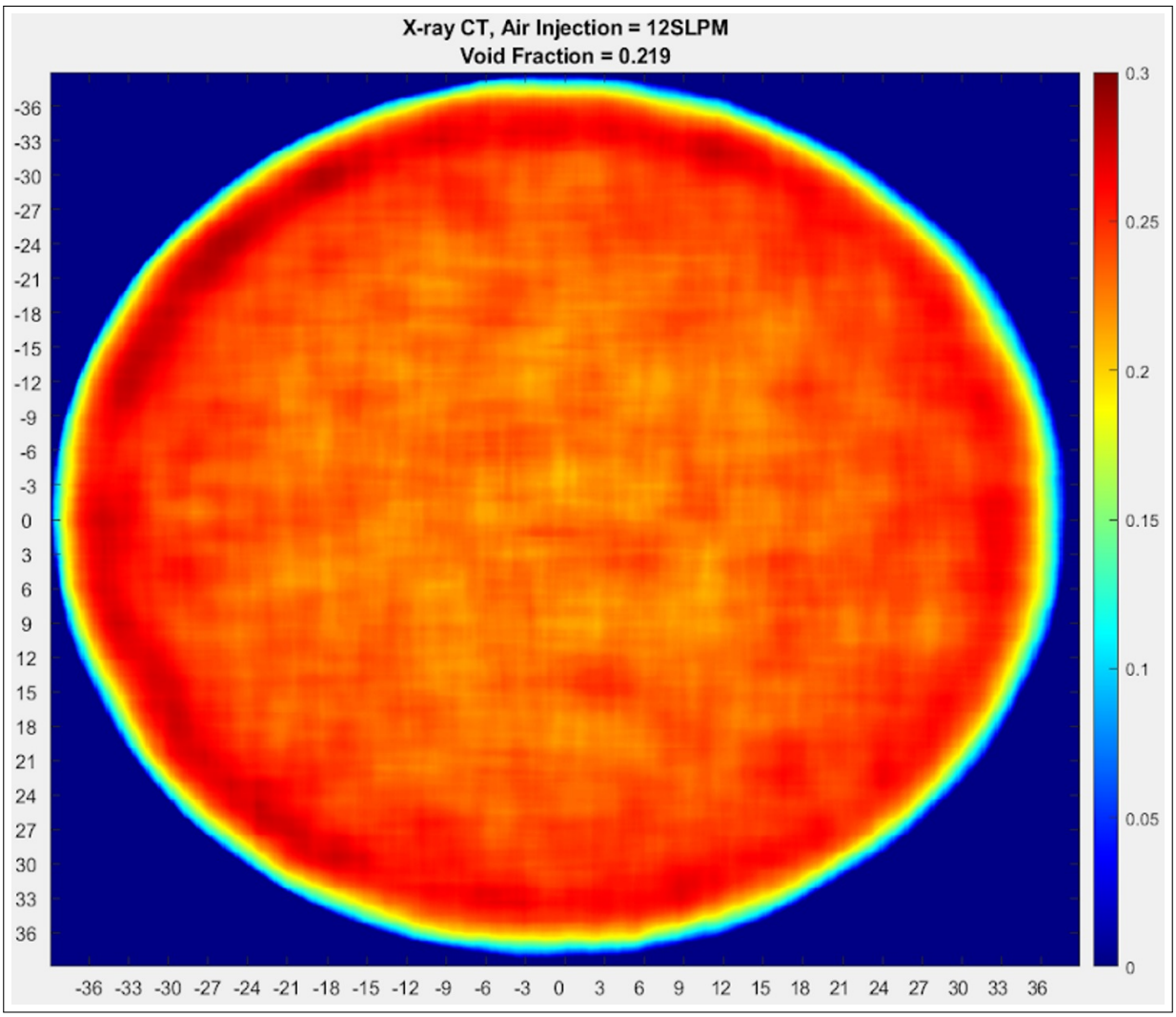

Figure 9.21: Time-averaged Void Fraction measurements from X-ray CT Attenuation Coefficients at a superficial gas velocity of 0.041m/s - Hydrophilic Bubble Column

void fraction coincides with a calculated void fraction from height differences of 0.130.

Figure 9.25 displays the time-averaged void fraction calculated by using the two-dimensional intensity projection variation from the water, air and mixture mediums. As previously discussed, the time-averaged void fraction is calculated using equation 9.3. We collected 30 frames per angle and calculated a mean intensity field using MATLAB. The mean intensity field of the mixture was used in the equation along with the intensity field measured for the mediums of water and air. The calculation is conducted at each angle for a total of 360 void fraction measurements, where the mean is used as the final time-averaged void fraction of

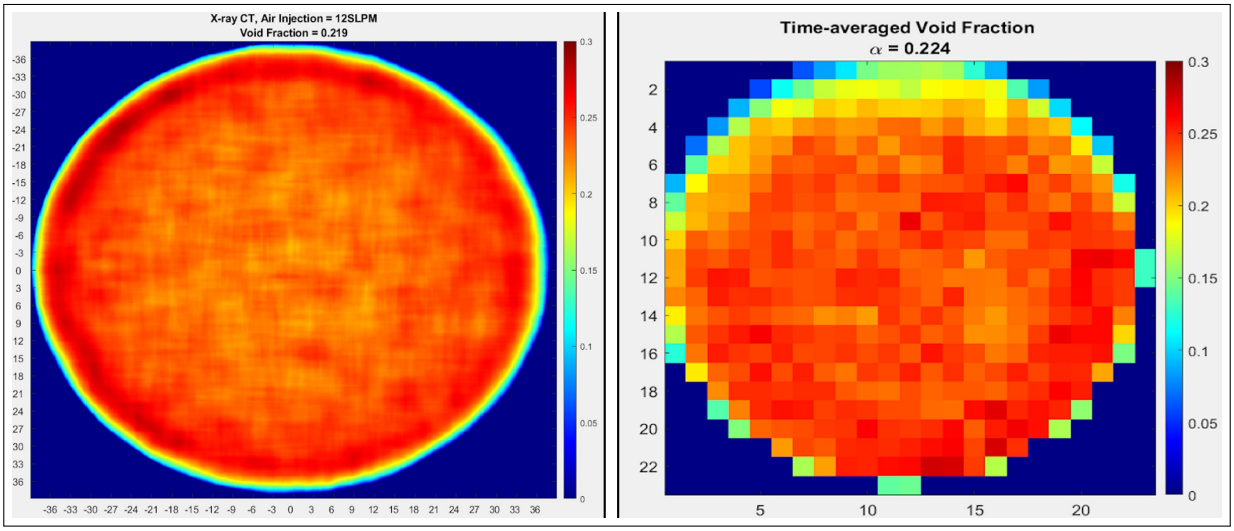

Figure 9.22: a) X-ray CT Time-averaged Void Fraction collected using SIRT reconstruction algorithm using 30 frames per angle with 1sec exposure $\alpha = 0.219$ b) WMS time-averaged Void Fraction on Level 2 Bottom Sensor $\alpha = 0.224$

0.100. This value is in agreement with both void fraction measurements from the WMS and height differences. This shows that intensity measurements gathered from our X-ray source and photon counter settings are adequate to measure two-dimensional void fraction of the bubble column over an entire rotation.

Figure 9.26 displays a time-averaged void fraction measurement calculated from the reconstruction values for the three mediums using Equation 9.4. The calculated attenuation coefficients that are rendered in a two-dimensional lateral representation using the SIRT algorithm, provided in the ASTRA toolbox, are entered into Equation 9.4 and the result is displayed in the lower right figure. The mean of the attenuation coefficients from the reconstructed void fraction data set yield a time-averaged void fraction of 0.092, which is in agreement with the three previous measurements discussed. Figure 9.27 displays the X-ray CT SIRT Reconstruction with the measured Time-averaged Void Fraction displayed in the figure title. Figure 9.28 displays the time-averaged void fraction reconstruction from both X-ray CT and WMSs, geometrically aligned.

Evaluation of Bubble Dynamics within a Hyrdrophilic and Superhydrophobic Inner Wall Coating

We will discuss the difference on void fraction measurements calculated by X-ray CT and wire mesh sensors between the hydrophilic and superhydrophobic-coated bubble column

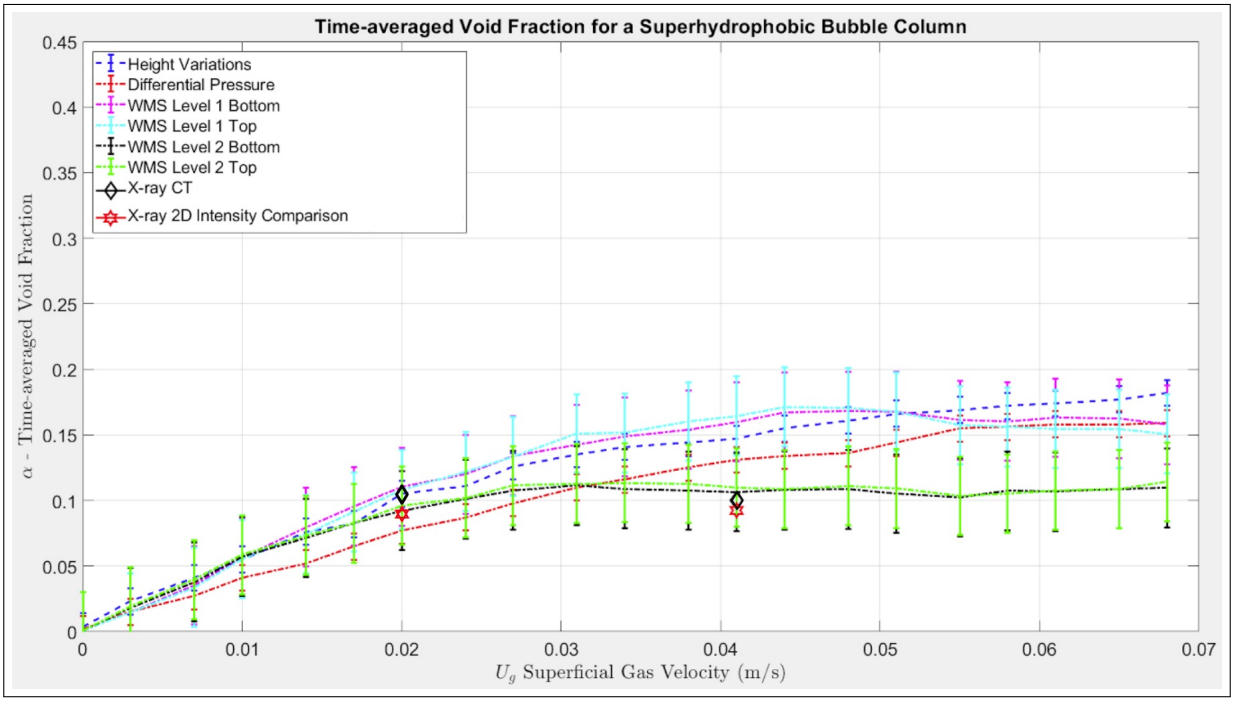

Figure 9.23: Time-averaged Void Fraction measurements summary for superhydrophobic bubble column

inner walls. We will also show variability of differential pressure measurements in each condition. The only difference between the two constructed bubble columns was the applied coating to one of the two bubble columns. We selected a superficial velocity of 0.041m/s to observe an obvious difference among the time-averaged void fraction measurements in the different techniques previously discussed.

Figure 9.29 displays the WMS measurements from the Level 2 Bottom sensor of WMS datasets for the two different bubble columns. At a superficial gas velocity of 0.0140m/s, the time-averaged void fraction deviates between the two bubble columns. We assess that at the point of deviation, the characteristics of the inner wall coating affect the evolution of gas holdup along the bubble column.

The superhydrophobic coating creates an air layer along the inner wall. The bubbles coalesce at the inner wall as the density of the bubbles push them against the air layer generated by the superhydrophobic coating. The coalescing bubbles join to form larger bubbles which rise as one larger bubble under buoyancy forces. Based on the buoyancy forces, the larger bubbles migrate towards the center of the bubble column as they continue to rise. Figure 9.29a displays the time-averaged void fraction measured by the Level 2 Bottom WMS located in the upper portion of the bubble column. We can notice that the

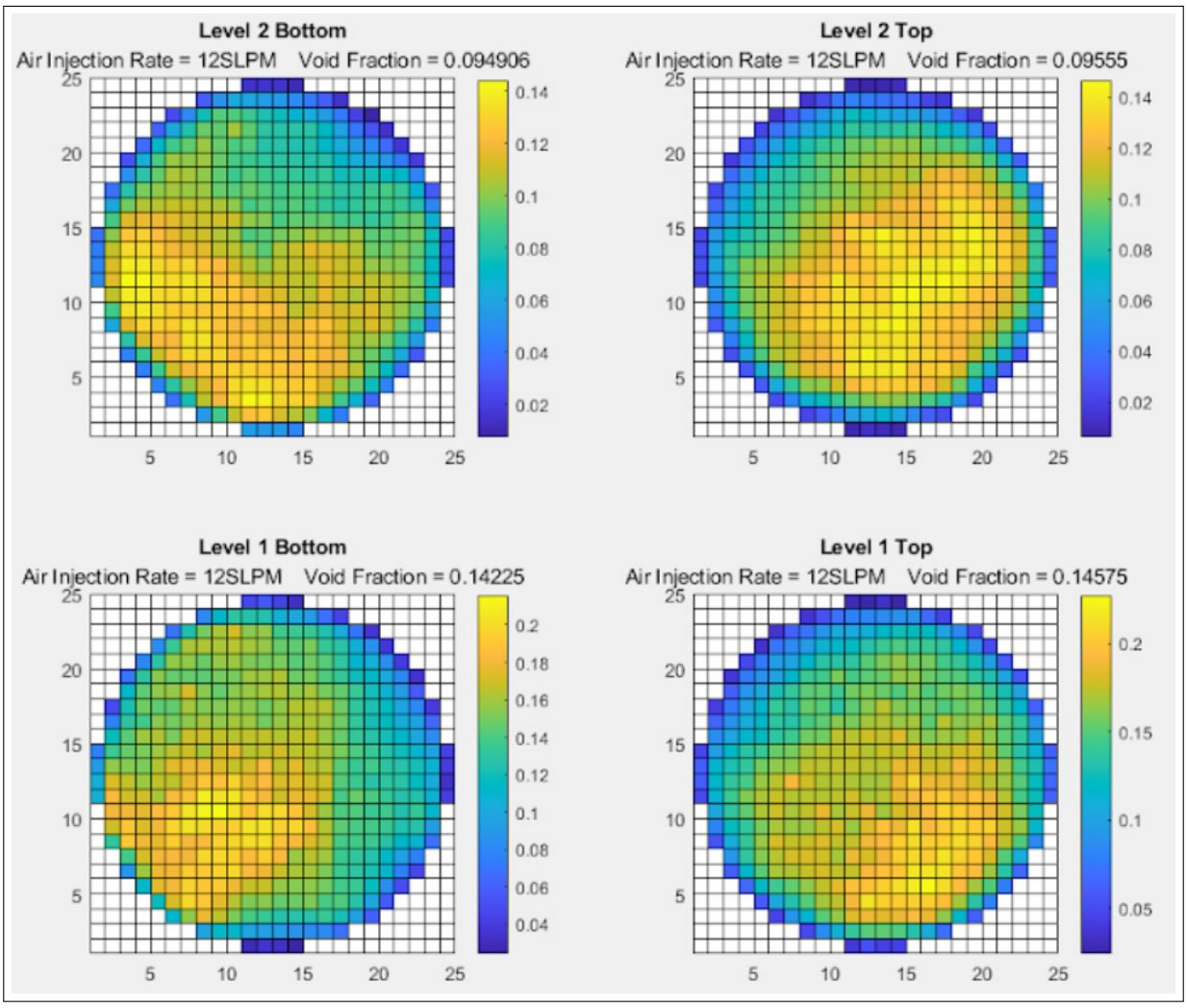

Figure 9.24: Time-averaged Void Fraction measurements for four wire mesh sensors at a superficial gas velocity of 0.041m/s

void fraction is fairly uniform across the bubble column and there are void areas located along the wall of the bubble column. Figure 9.29b displays the time-averaged void fraction from Level 2 Bottom WMS located in the upper portion of the bubble column. As opposed to Figure 9.29a, Figure 9.29b shows the void fraction is lower as previously discussed and the bubble distribution is closer to the center than in the hydrophilic case. The lower void areas along the wall is also noticeable. This suggests that less bubbles accumulate against the wall. In a churn-turbulent flow regime, smaller diameter bubbles are recirculated onto the walls from the liquid circulation driven by the buoyancy forces acting on the larger

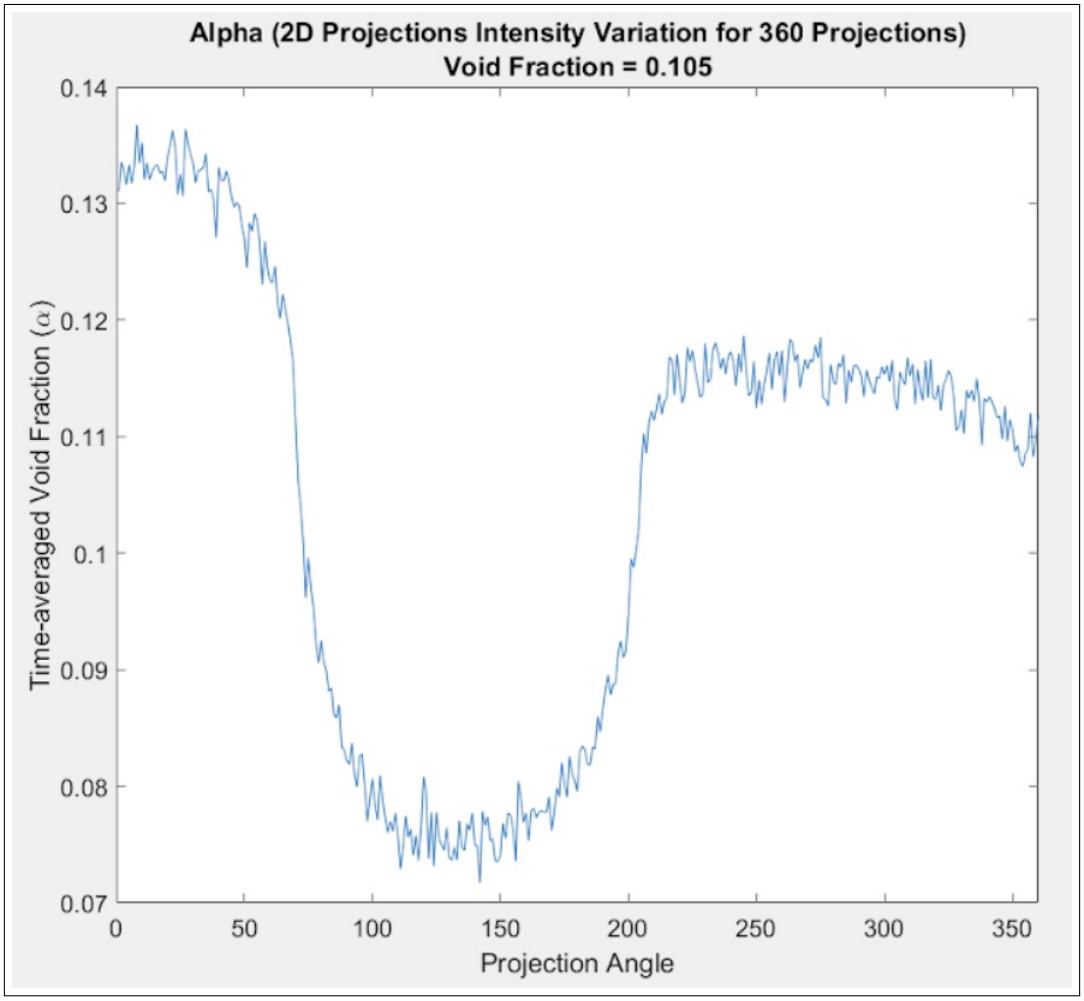

Figure 9.25: Time-averaged Void Fraction measurements from X-ray two-dimensional intensity fields at a superficial gas velocity of 0.041m/s

diameter bubbles and induced lateral pressure variation. The substantial bubble coalescence was observed in the 35-second WMS collection.

We also include a vertical void fraction distribution shown along with each measurement technique and location along the bubble column. This plot was built by adding two additional differential pressure transducer taps. The measurements are color-coded to reflect the measurements listed in the legend from top to bottom. "Waterline" refers to the void fraction measurement from height variation. "WMS (position designator)" measurements are distributed into all four sensors. Three differential pressure measurement along a distance of 15.8cm, 30.5cm and 52.1cm are labeled "D/P (location)". "X-ray CT" displays the void

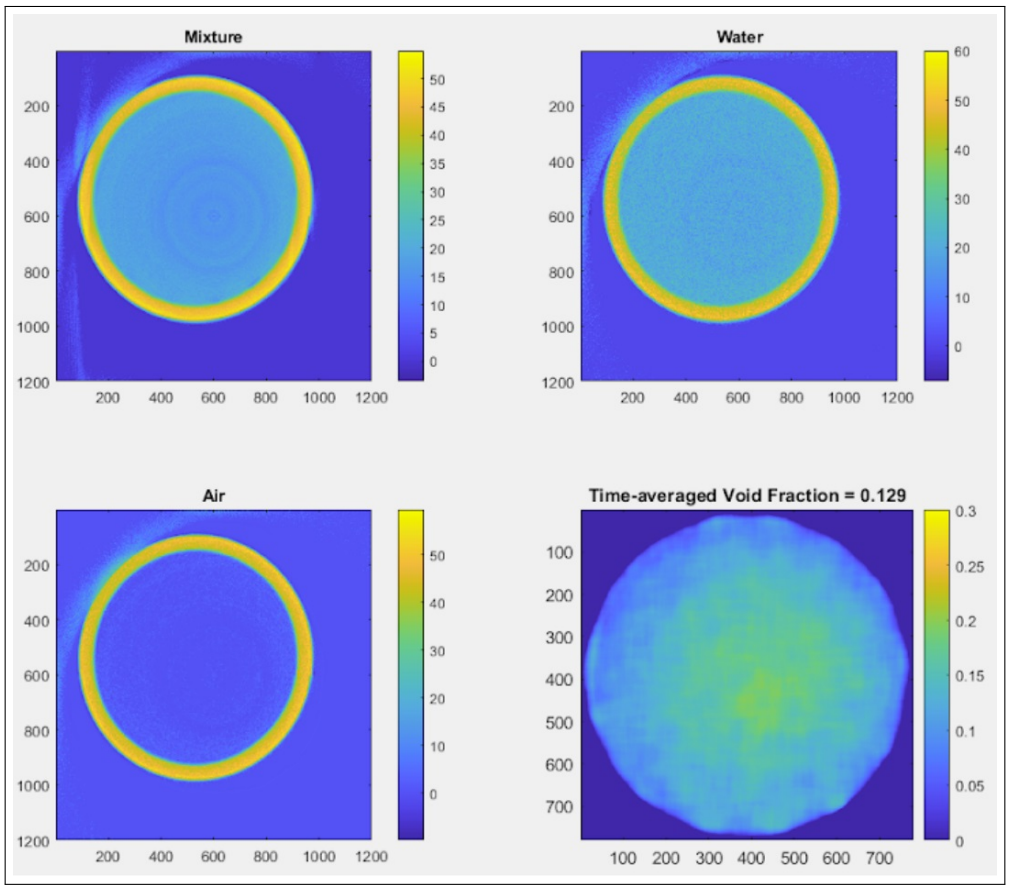

Figure 9.26: Time-averaged Void Fraction measurements from X-ray CT Attenuation Coefficients at a superficial gas velocity of 0.041m/s

fraction measurement at the specified location right below the lowest differential pressure tap to avoid interference. Figure 9.30a displays the vertical void fraction distribution for the hydrophilic bubble column. The time-averaged void fractions are fairly consistent along the bubble column which suggests that the flow is homogeneous and the bubble column wall has minimal impact on time-averaged void fraction. Unlike Figure 9.30a, Figure 9.30b displays void fraction measurements decreasing significantly along the height of the bubble column, suggesting that the bubbles are interacting with the superhydrophobic surface. The lower void fraction suggests that the air layer is coalescing bubbles along the length of the bubble column forcing the phenomena of absorption of large bubble coalescing, which causes a larger buoyancy force and higher mean bubble velocity. These flow features would suggest that the bubble regime is no longer homogeneous and has transition to heterogeneous via a churn-turbulent flow.

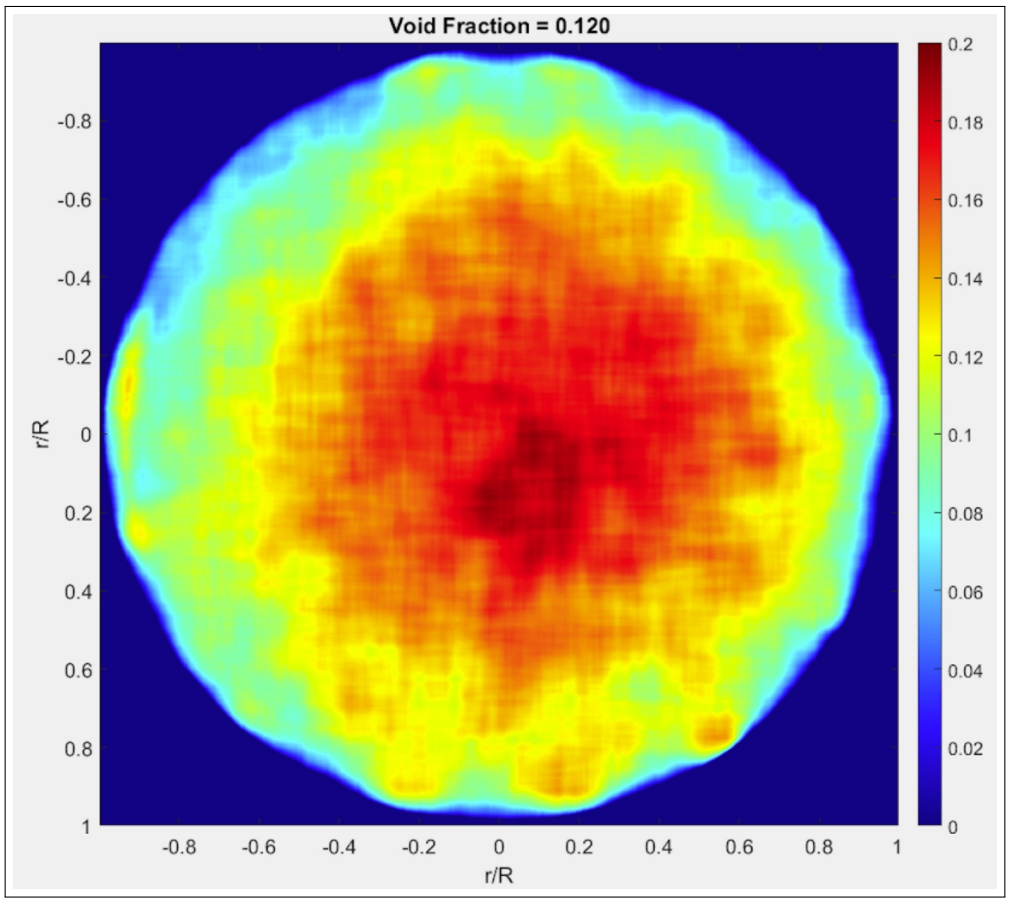

Figure 9.27: Time-averaged Void Fraction measurements from X-ray CT Attenuation Coefficients at a superficial gas velocity of 0.041m/s - Superhydrophobic Bubble Column

Figure 9.31 displays the X-ray CT reconstructions for both cases. We adjusted the axis to include distance in millimeters to reflect the actual dimensions. We also use colorbars with the same color axis. Figure 9.31a displays the superhydrophobic case where the larger void areas are in the center. A portion of the bubble coalesce at one fourth of the wall. This perhaps suggests a heterogeneous bubble regime where larger diameter bubbles migrate to the center of the bubble column while smaller bubbles travel along the wall. Figure 9.31b displays a uniform bubble distribution with a larger concentration along the inner wall. This suggests a homogeneous regime of bubble flow.

Figure 9.32 displays a still image of the bubbly flow inside the superhydrophobic-coated bubble column. We notice that the coating makes the bubble column partially opaque but very difficult to evaluate the bubble coalescing with high-speed cameras. We can continue to measure the height variation using a light positioned directly behind the waterline of the

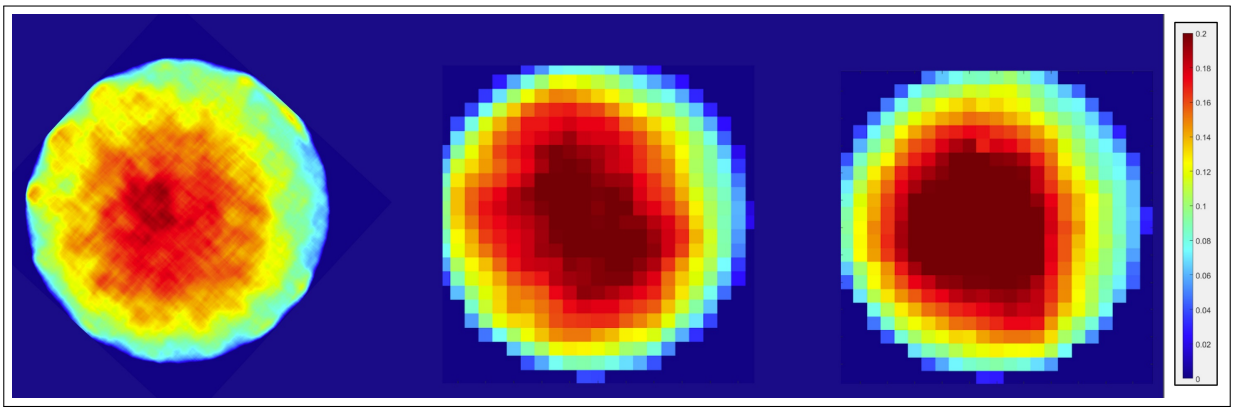

Figure 9.28: Time-averaged Void Fraction measurements from X-ray CT and wire mesh sensors at a superficial gas velocity of 0.041m/s - Superhydrophobic Bubble Column (geometrically aligned)

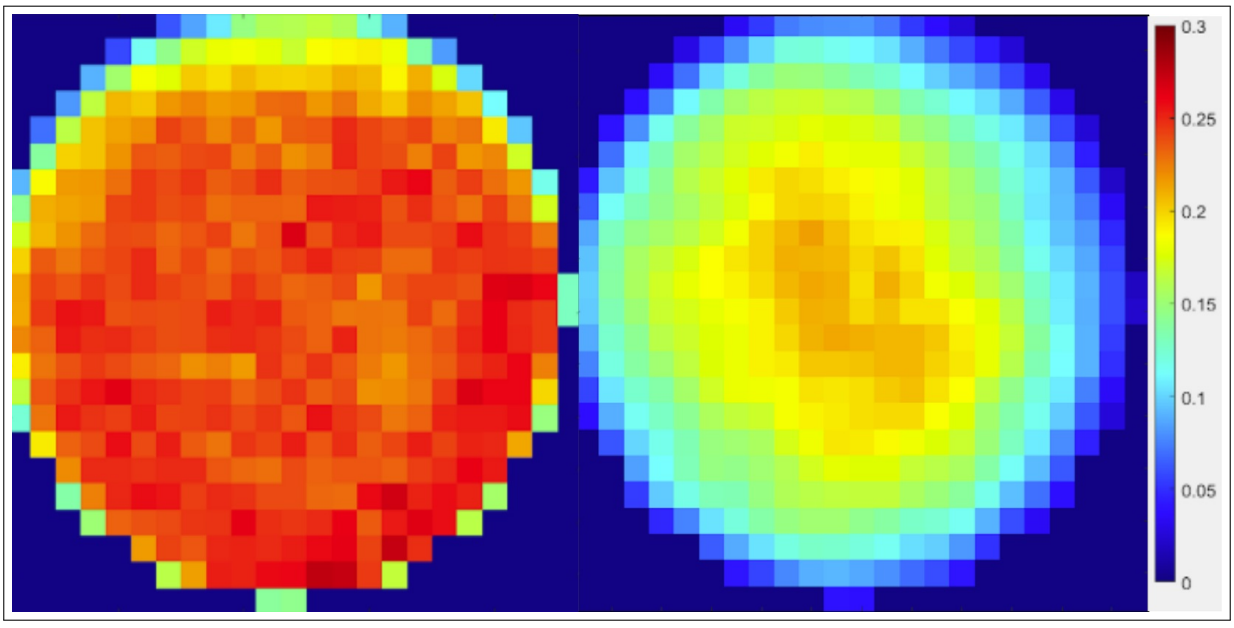

Figure 9.29: a) Time-averaged Void Fraction measurements from wire mesh sensor for hydrophilic bubble column ($\alpha = 0.224$) b) Time-averaged Void Fraction measurements from wire mesh sensor for superhydrophobic bubble column ($\alpha = 0.135$)

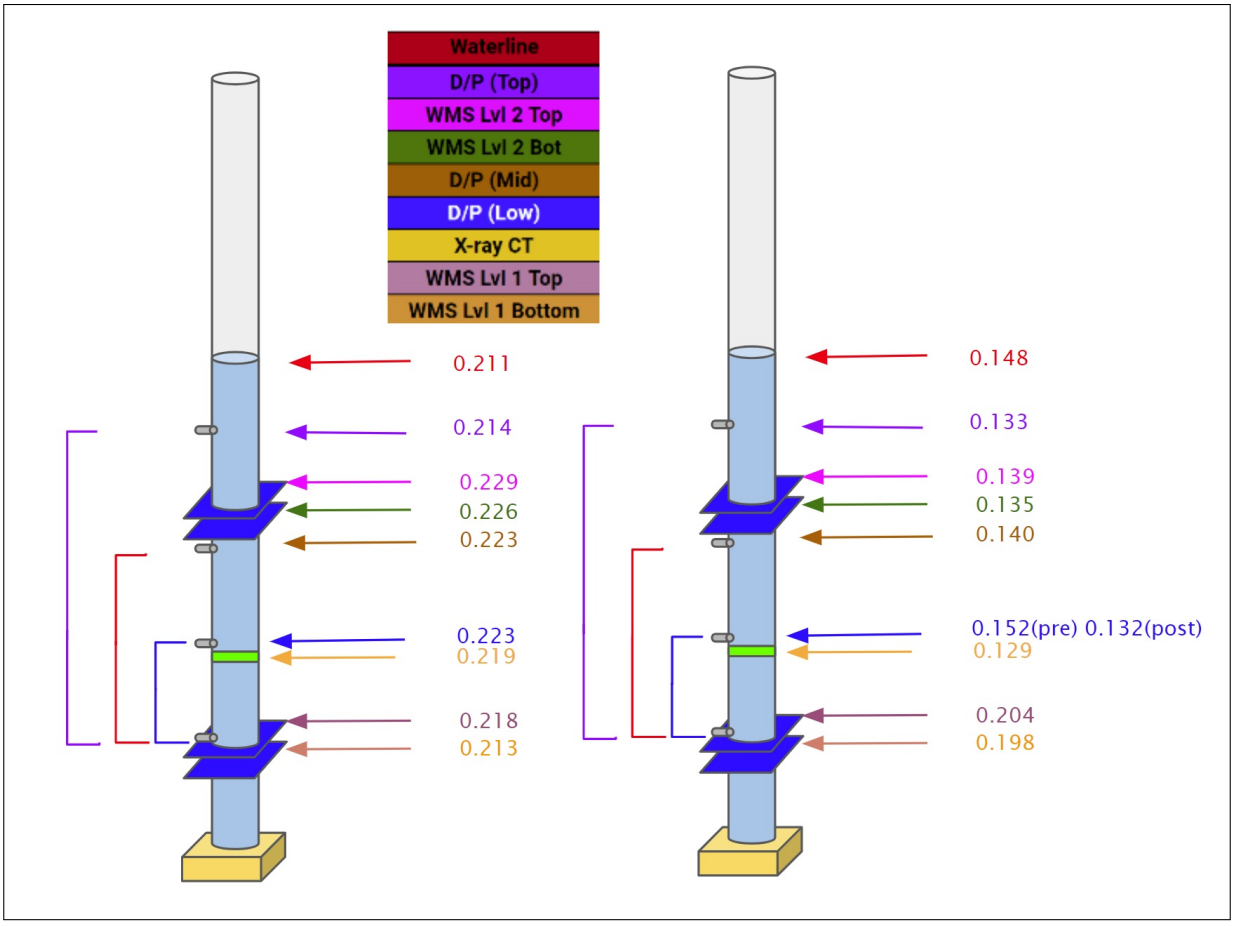

Figure 9.30: a) Time-averaged Void Fraction vertical distribution for hydrophilic bubble column b) Time-averaged Void Fraction vertical distribution for superhydrophobic bubble column

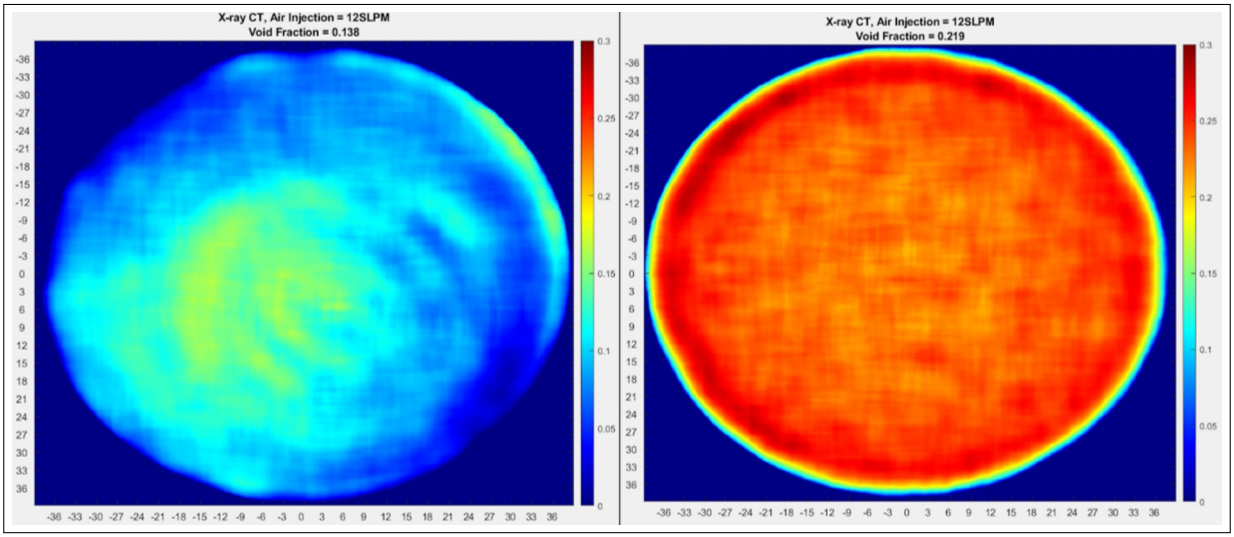

Figure 9.31: a) Time-averaged Void Fraction using X-ray CT Reconstruction using SIRT reconstruction with 100 iterations and medfilt2 filter (NeverWet Coated Inner Wall Bubble Column) b) Time-averaged Void Fraction using X-ray CT Reconstruction using SIRT reconstruction with 100 iterations and medfilt2 filter (Hydrophilic Inner Wall Bubble Column)

bubble column. Fortunately, we can utilize the Wire Mesh Sensor Framework Bubble Size Distribution module to get an idea of the mean bubble diameter and validate our findings that the superhydrophobic-coated inner wall changed the bubble regime from a dispersed bubble regime to a churn-turbulent flow.

Figures 9.33 and 9.34 are probability density functions displaying bubble density versus bubble diameter. These figures are produced by the Wire Mesh Sensor Framework Bubble Size Distribution module. This modules uses void fraction, bubble size and property module, and velocity module to produce a histogram figure with the highest value displaying the mean bubble diameter for the entire dataset. Figure 9.33 shows the probability density function for four superficial gas velocities, 0.003m/s, 0.020m/s, 0.041m/s and 0.061m/s, in the hydrophilic bubble column. The scatter plot for each probability density function shows that mean diameter increases through out the range of superficial gas velocities for our experiment range. The mean bubble diameter values range from 4 to 12mm and maintains the flow homogeneous based on the single peak observed on the density function. Figure 9.34 shows the probability density function for four superficial gas velocities, 0.003m/s, 0.020m/s, 0.041m/s and 0.061m/s, in the superhydrophobic bubble column. The scatter plot for each probability density function shows that mean diameter increases through out the range of superficial gas velocities for our experiment range. The bubble density function displays a bimodal curve, which is indicative of a heterogeneous flow pattern. The mean bubble

Figure 9.32: Picture of Opaque Bubble Column - Inner Wall coated with Superhydrophobic Coating (NeverWet)

diameter value for smaller bubbles range from 4 to 8mm and the mean bubble diameter for the larger bubbles range from 10-40mm. This bubble size distribution confirms a churn-turbulent flow.

Figures 9.36 and 9.37 display the time-averaged velocity for the hydrophilic and superhydrophobic bubble columns, respectively. Figure 9.35 displays the time averaged velocity calculated using cross correlation over 24 x 24 nodes, 12 x 12 nodes and 6 x 6 nodes to evaluate an average velocity that is representative of the bubble flow in the midst of inaccuracies that may be introduced by churn-turbulent flow and substantial backflow. Figure 9.36 displays the time averaged velocity calculated using cross correlation over 24 x 24 nodes, 12 x 12 nodes and 6 x 6 nodes to evaluate an average velocity in a superhydrophobic bubble column. The time-averaged velocity for the hydrophilic bubble column is 0.27m/s and the average velocity for a superhydrophobic bubble column is 0.47m/s. As expected the bubbles with larger diameters will rise faster in the center of the bubble column and yield a higher

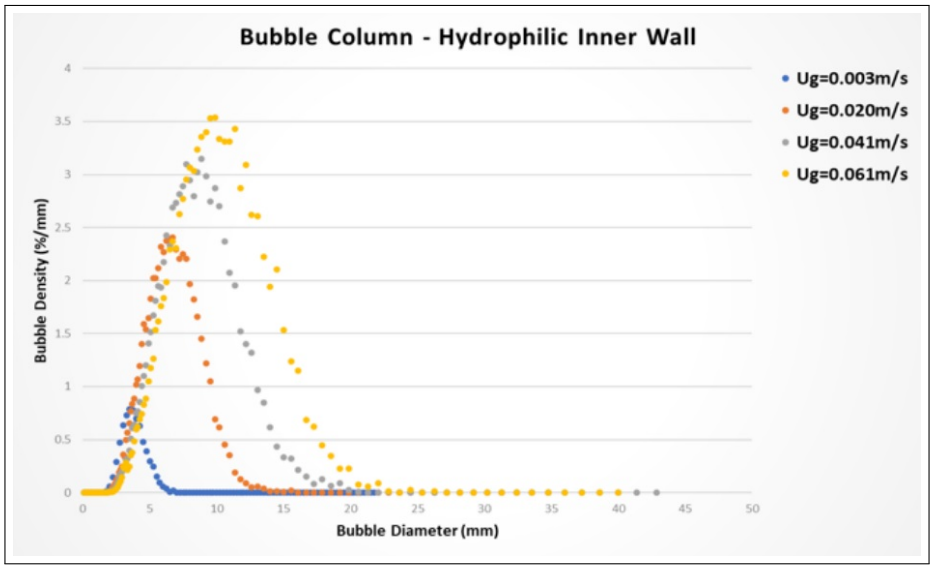

Figure 9.33: Probability Density Function - Bubble Diameter in Hydrophilic Bubble Column

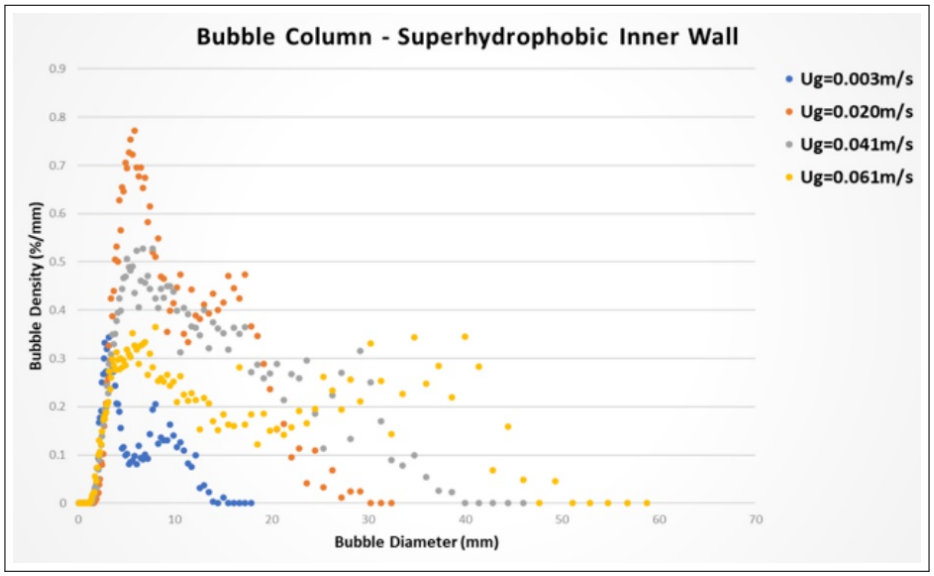

Figure 9.34: Probability Density Function - Bubble Diameter in Superhydrophobic Bubble Column

average flow velocity than the hydrophilic case.

9.4 Conclusions

Knowing how bubble column reactors rely on bubble flow to promote mixing to meet chemical requirements for their applications, we have shown, through advanced non-intrusive measurement techniques, how to capture the effects of superhydrophobic characteristics on bubble regime transitions within a bubble column. We find that superhydrophobic-coated material that is introduced into a bubble column will cause bubbles to escape faster from the bubbly flow regime, resulting in a 30-60% reduction in gas holdup at variable injection rates and earlier transition to churn-turbulent flow. Depending on application, these superhydrophobic characteristics may modify the bubble regime to promote larger mixing with minimal changes in superficial gas velocity and no changes in bubble column geometry. These surfaces have been evaluated in a submerged boiling setting to show how effective the vapor layer improves heat transfer via film boiling (Li, 2016)[23].

Advanced measurement techniques, such as X-ray computed tomography and iterative reconstruction algorithms, are required to measure the effects of superhydrophobicity on bubble flow regimes at high injection rates, which cause the flow regime to become opaque for optical measurement techniques. Five time-averaged phase fraction measurement techniques were utilized on a bubble column with a hydrophilic inner wall and a bubble column with a superhydrophobic inner wall from a range of 0.003 m/s to 0.061 m/s. We have validated X-ray CT time-averaged void fraction reconstruction results against measurement techniques offered by height variation, differential pressure transducer, and wire mesh sensors. Their agreement proved valuable to understand how each technique measures time-averaged void fraction and allowed us to validate our X-ray CT void fraction measurements. With respect to time-averaged void fraction measurements, we have shown how X-ray CT reconstruction is a measurement technique that offers spatial resolution comparable to wire mesh sensors and a more effective measurement tool because of its non-intrusiveness to the flow regime.

To further evaluate the transition from a homogeneous to heterogeneous bubble regime, we utilized the Velocity and Bubble Size Distribution modules, provided in the Wire Mesh Sensor Framework, to evaluate mean bubble diameters and bubble flow velocity to validate our hypothesis that the superhydrophobic-coated inner wall changes the bubble regime from a dispersed bubble regime to a churn-turbulent flow. In a hydrophilic bubble column, the bubble flow throughout our experiment remained homogeneous with an 8mm change in mean bubble diameter from a superficial gas velocity of 0.003m/s to 0.061m/s. In a superhydrophobic bubble column, the bubble flow transitioned from homogeneous to heterogeneous at low superficial gas velocity with two mean bubble diameters averaging between 8mm and 30mm from a superficial gas velocity of 0.003m/s to 0.061m/s. With utilization of these modules and our vertical display of time-averaged void fraction along the vertical height of the bubble column, we show how the superhydrophobic coatings in the bubble column inner walls continue to effect bubble dynamics as the bubbles rise and continues to lower the

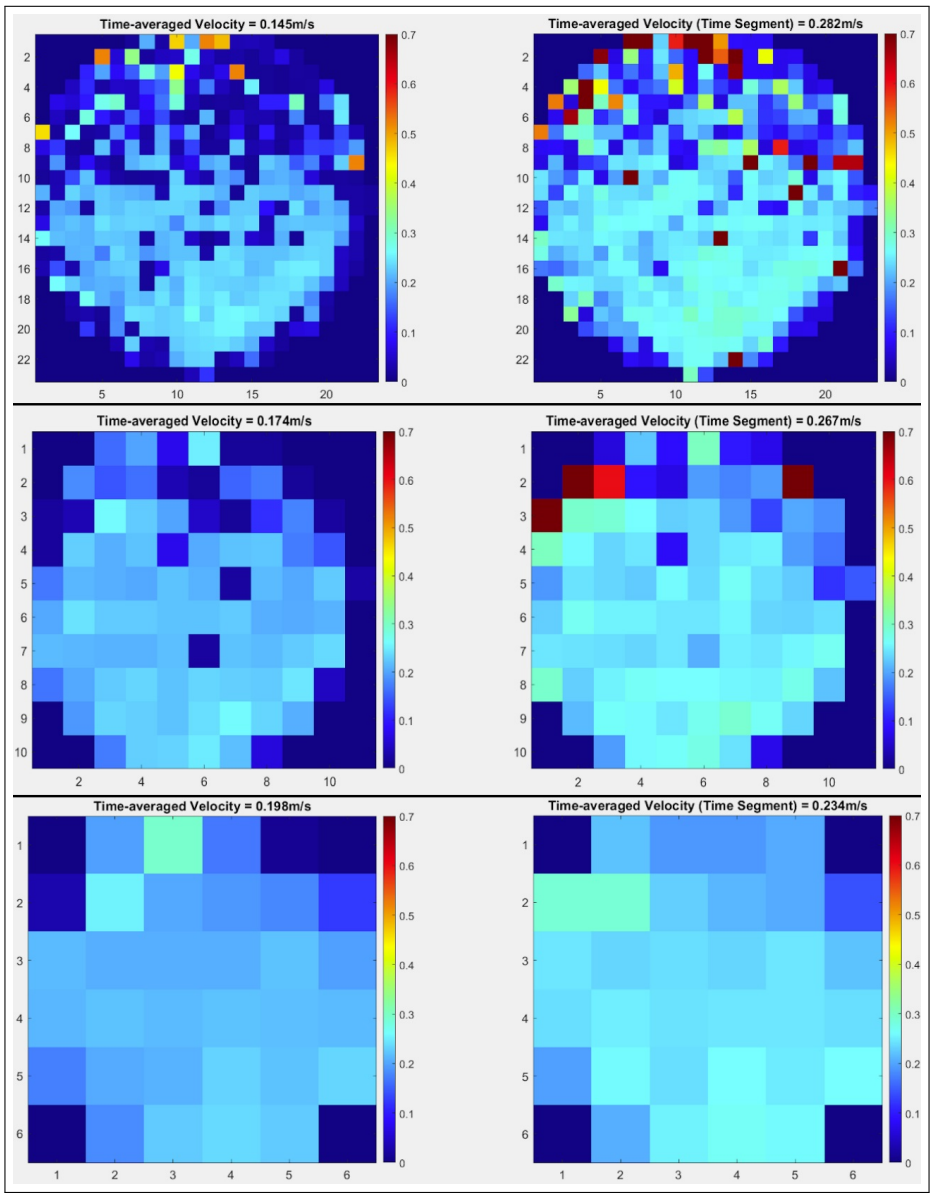

Figure 9.35: Time-averaged velocity for hydrophilic bubble column at Ug=0.041m/s a) 24 x 24 nodes b) 12 x 12 nodes c) 6 x 6 nodes

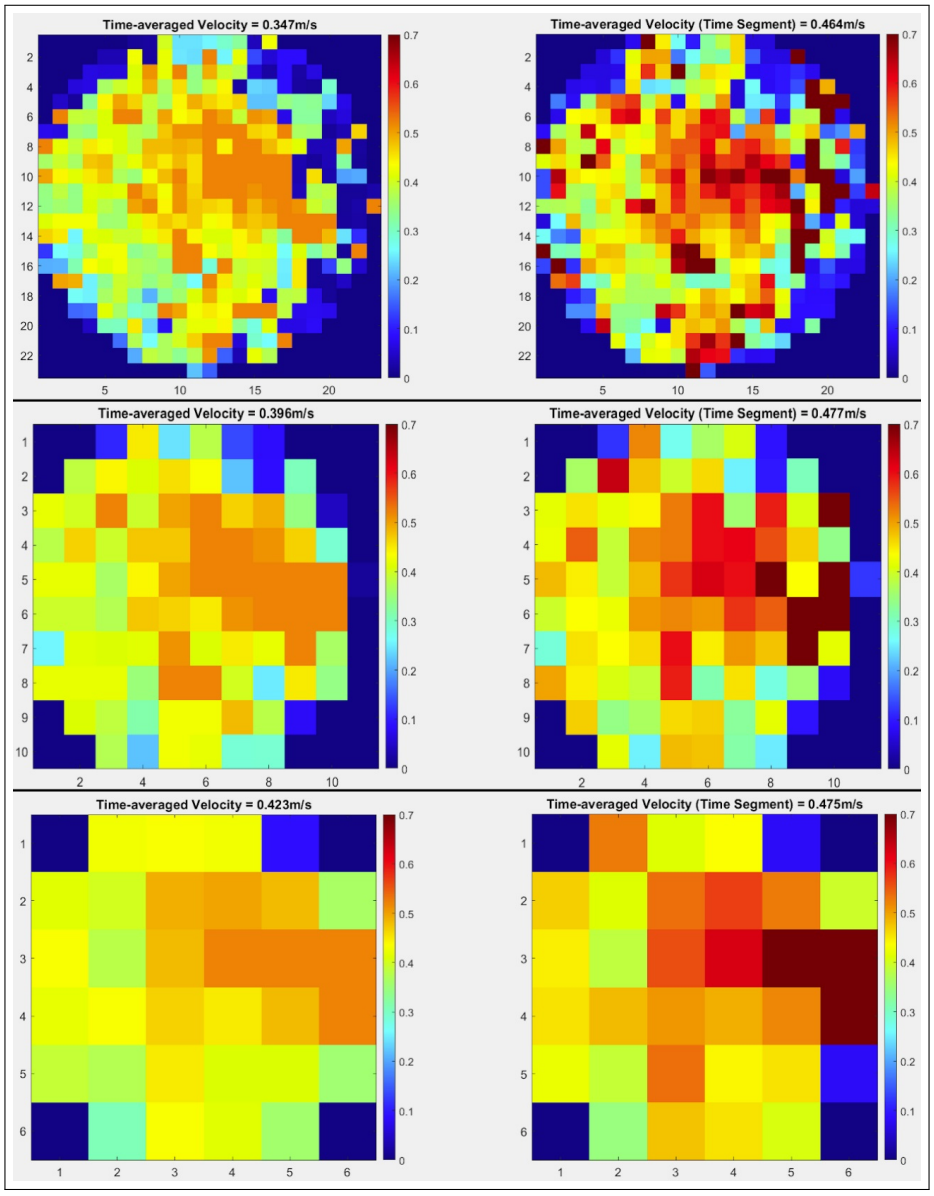

Figure 9.36: Time-averaged velocity for superhydrophobic bubble column at Ug=0.041m/s a) 24 x 24 nodes b) 12 x 12 nodes c) 6 x 6 nodes

void fraction even further as the spacing between the bubble diameter and the inner wall decreases.

These findings suggests that lower void fractions are achievable with a modification of surface wall characteristics to promote superhydrophobicity. Additionally, superhydrophobic coatings promote transition to churn-turbulent flow without any modification to superficial gas velocity or bubble column dimensions. Lastly, advanced measurement techniques, such as X-ray computed tomography, have proven effective at providing a non-intrusive and spatial and temporal resolved void fraction measurements of dynamic multiphase flow systems.

Chapter 10

Hydrophobicity and Hydrophilicity Measurements in Bubble Columns with Superhydrophobic Internals

10.1 Bubble Dynamics in Simulated 2 x 2 Hydrophilic Fuel Cell Array with Internal Superhydrophobic-coated Material-Run 1

We utilized four wire mesh sensors to evaluate variations in bubble flow regime inside a bubble column as the bubbles interact with surfaces that are superhydrophobic. We speculate that bubbles interact with the superhydrophobic surface air layer on the material and coalesce to form larger bubbles and therefore rise faster under buoyancy forces. We believe this motion will then act as an area of low pressure behind the wake of the larger and faster rising bubbles, attracting nearby bubbles onto the bubble wake and encourage further interaction with the air layer on the superhydrophobic PVC tube.

Experiment Setup

A 33cm section of the bubble column was modified to include four PVC tubes of 23mm diameter each. The PVC tubes extended the entire length of the 33cm section. The bubble column diameter is 77.9mm. With a bubble diameter averaging approximately 2.5mm, the free space not occupied by the four PVC tubes allow interaction between bubbles and the surfaces. The bubble column has a cross-sectional area of $0.00477m^2$. The cross-sectional area of the four PVC tubes is $0.00166m^2$, allowing $0.00311m^2$ of free space for the multiphase flow regime to rise under hydrostatic pressure.

The four PVC tubes are held together at the bottom and top of the test section by stainless steel bolts and modified PVC flange to include PVC cross-shape extension to support

and align the PVC tubes.

The experiment included four runs total to measure time-averaged void fraction and velocity:

- 2 runs with four hydrophilic tubes
- 2 runs with three hydrophilic tubes and one superhydrophobic tube

Figure 10.1 displays the four PVC tube arrangement inside the bubble column. The clear tube allows the ability to visualize the bubble interaction along the PVC tube surfaces. This allows us to visualize the different bubble sizes and bubble flow regime that develop as a result of the superhydrophobic material introduced into the 2 x 2 array simulated fuel rod bundle.

The PVC tubes are held together at the top and bottom by smaller stainlees steel tubes that do not traverse the length of the tube but are securely held at each end of the PVC tube. A hex 1-inch bolt is used to hold the metal inserts to the flanges on the top and the bottom, displayed in Figure 10.2. This allows for water to protrude into the tubes and minimize any possible vibrations caused by the turbulent bubble flow and pressure differential across the submerged PVC tube. If significant vibrations are introduced into the pole assembly, they might possibly render X-ray computed tomography reconstruction inaccurate. We notice X-ray CT reconstructions introduce additional artifacts around the shape of the PVC wall due to excessive vibrations and the higher injection rates of our experiment range.

When a surface is immersed in water, the superhydrophobic coating displays an air layer along the tube surface. The air layer appears like a mirror-sheen across the surface. The green box in Figure 10.3 displays the mirror-like sheen. It may appear difficult to see but the difference is noticeable once compared to the other three PVC tubes that are not coated with superhydrohphobic polymer.

A mask file and modified geometry file were developed using the Wire Mesh Sensor framework software to ensure bubbles inside these areas were not counted in the void fraction estimates. Since the tube diameter was 2 mm less than the diameter of the wire mesh sensor, the mask editor tool was also used to generate a region of interest to encompass the cross-sectional area of the tube and prevent the algorithms from including the areas outside the diameter of the tube that were covered by the wire mesh sensors. This method is displayed in Figure 10.4.

Air flow into the bubble column was controlled using an ALICAT Flow Control unit, with a range from 0 to 20 SLPM. An air compressor unit was utilized to maintain air pressure at 100 psia. Air was injected into the bubble column through a series of 800 holes perforated on a brass plate positioned 12.7cm under the 4 PVC tubes. The height of the water level in the bubble column varies with changes in air flow. Using the difference between a specific height at a given air injection and an initial height with no air injection, the void fraction can be calculated to get an initial estimate of difference between four hydrophilic tubes and the modified setup including a superhydrophobic tube, replacing a hydrophilic tube. Figure 10.5 displays the void fraction measured from height and WMS for both cases. The lines

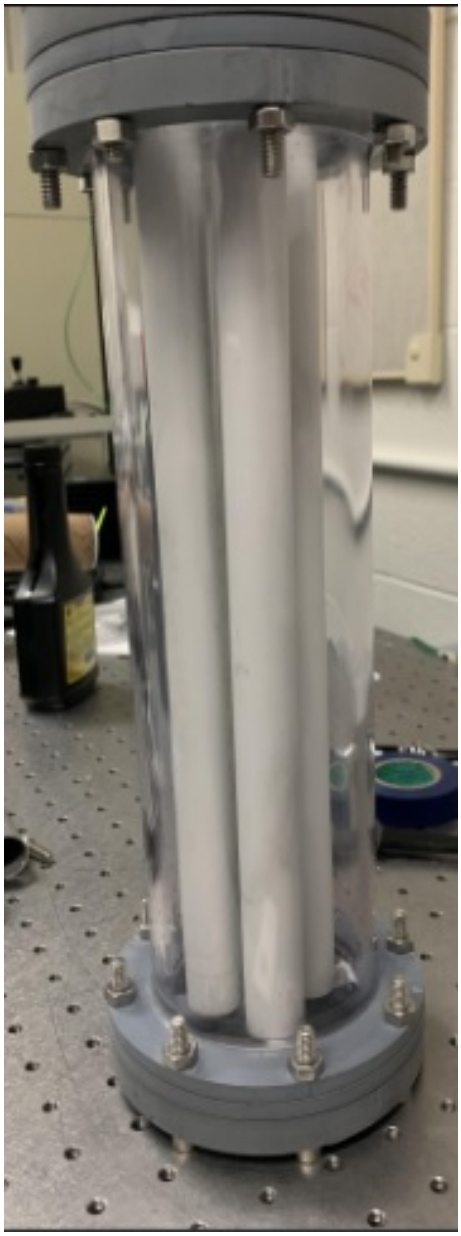

Figure 10.1: Experiment Section with Four PVC Tubes

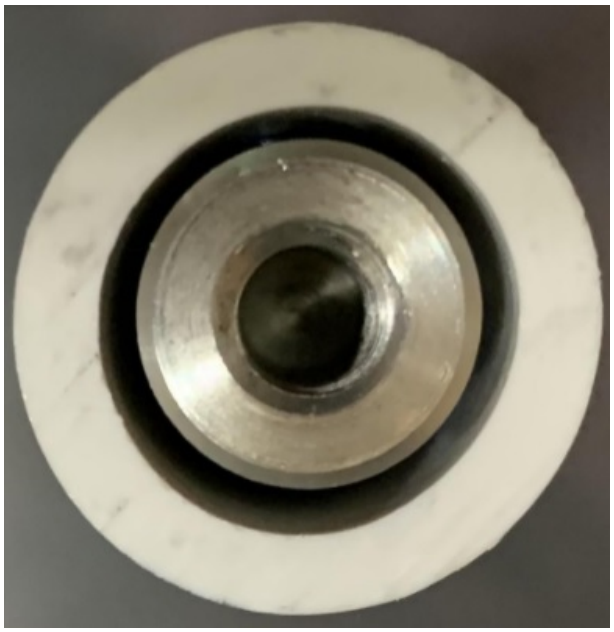

Figure 10.2: Top View Cross Section of PVC tube with Inner Metal Support Tube

highlighted in green and blue represent the void fraction calculations (y-axis) for injection rates stemming from 1 SLPM to 16 SLPM (x-axis) for four hydrophilic PVC tubes. The lines highlighted in red and yellow represent the void fraction calculations (y-axis) for injection rates stemming from 1 SLPM to 16 SLPM (x-axis) for three hydrophilic PVC tubes and one superhydrophobic tube. You can notice the significantly lower void fraction for the case with a single substituted SHS-coated PVC tube, captured by void fraction measurements from height variation method and Level 2 WMS.

Time-averaged Void Fraction WMS Measurements of the Bubble Column with Four Tubes (with and without a substituted SHS-coated PVC Tube)

Figure 10.6 displays the deviation from void fraction measurements pass 4SLPM. The void fraction measurements for the 4 PVC tubes show void fractions reaching 0.3 at approximately 16SLPM. Void fraction measurements remain much lower than the void fraction for four hydrophilic PVC tubes. This suggests that a single superhydrophobic tube can significantly affect overall void fraction for the entire simulated rod assembly. Observations suggest that the bubbles are coalescing and escaping the system at a faster rate than the bubble dynamics found in a set-up with four hydrophilic PVC tubes.

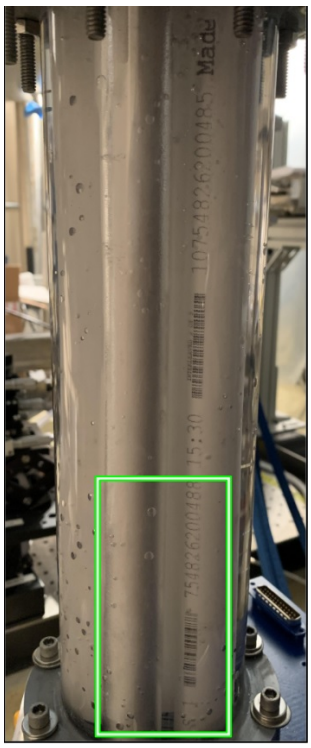

Figure 10.3: Experiment Section with Four PVC Tubes (with one Superhydrophobic PVC tube)

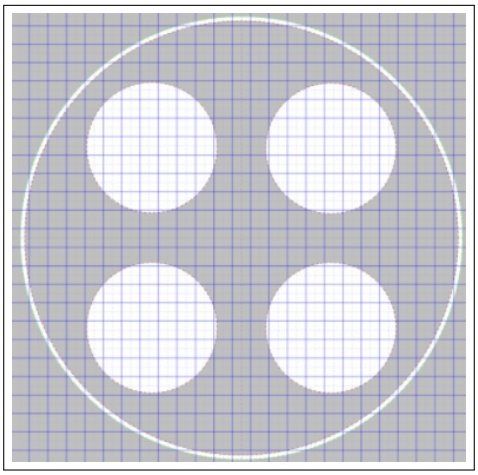

Figure 10.4: Mask file Geometry (Wire Mesh Sensor Framework - Mask Editor tool)

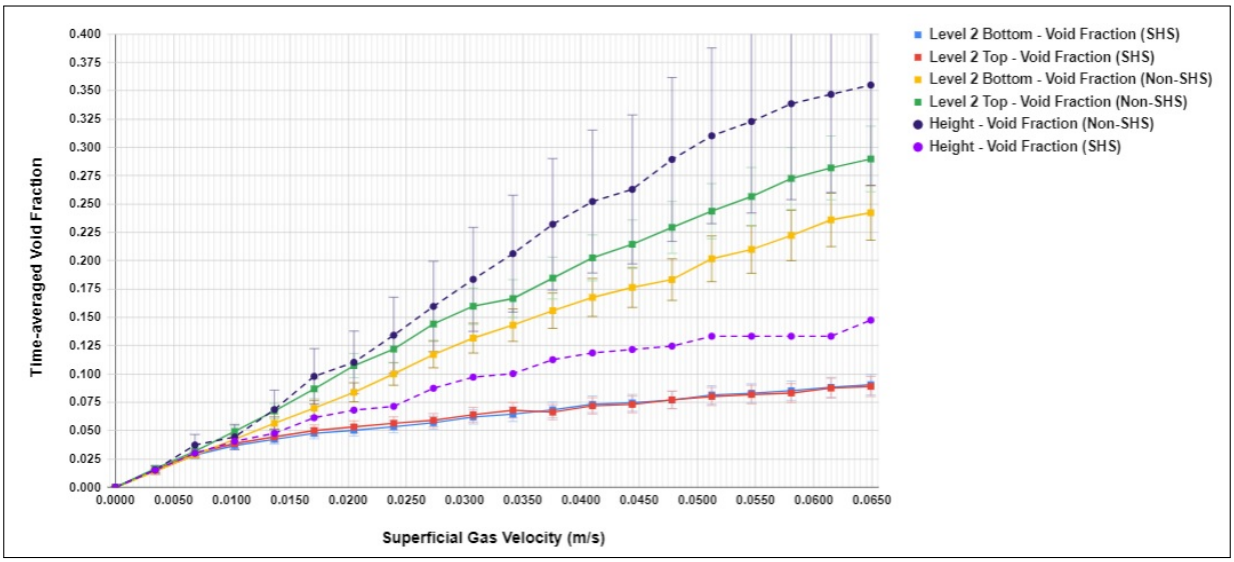

Figure 10.5: Void Fraction measurements calculated by bubble column height variation and wire mesh sensor from the Level 2 pair

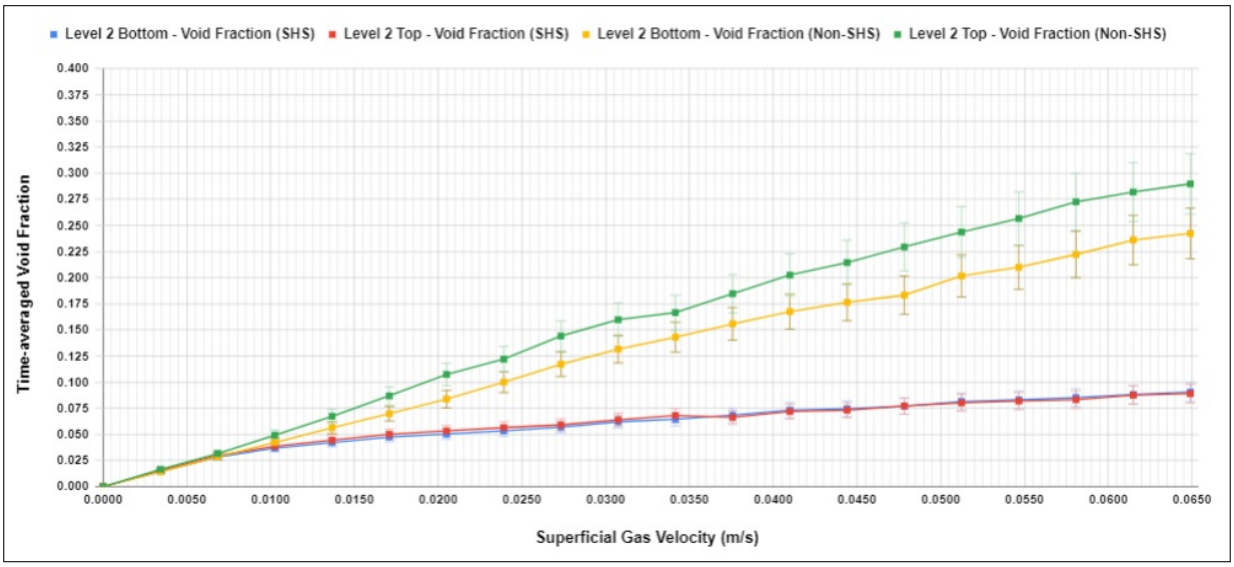

Figure 10.6: Void Fraction measurements from Level 2 WMS pair, calculated by Wire Mesh Sensor Framework software

The calculation for void fractions using the wire mesh sensors is a more accurate measurement of the void fraction across the cross section of the four PVC tubes. Since the PVC tubes do not extend throughout the entire length of the bubble column, the void fractions calculated from height only serve to suggest a qualitative understanding of the differences between the bubble dynamics across the two separate tube configurations. Nonetheless, the time-averaged void fraction measured by the wire mesh sensor directly above the PVC tubes (Level 2 Bottom WMS) yields a reduction in void fraction similar to the deviation observed using height differences. Figure 10.6 displays the deviation from void fraction measurements pass 5 SLPM. The void fraction measurements for the 4 PVC tubes show void fractions reaching 0.15 at approximately 16 SLPM. Void fraction measurements remain much lower than the void fraction for four hydrophilic PVC tubes. The reduction in void fraction ranges from 30-40% across an air injection rate from 5 to 16 SLPM. This suggests that a single superhydrophobic tube can significantly affect overall void fraction for the entire rod assembly.

In a nominal hydrophilic situation, the boundary condition between two fluids, e.g. a liquid and a gas, is the continuity of the shear stress at the interface. Since an air layer is introduced with a superhydrophobic surface, the maximum velocity shifts to the air layer from water where the frictional drag is significantly lower. The higher frictional drag usually observed at the walls is replaced by a lower frictional drag along the surface. In our case, we intuitively expect the rising bubbles will join the air layer along the superhydrophobic tube, driving the formation of a larger bubble, which in turn will rise faster due to lower viscosity at the wall, or an absorption of the air bubble to replenish the air layer in the plastron of the superhydrophobic coating. With a larger bubble diameter, you may expect a larger frictional drag that will act against the upper momentum of the larger rising bubble, but we expect buoyancy forces to dominate. We expect the generated wake from larger bubbles will create a lower pressure below the bubble will attract nearby bubbles. This may have the effect of attracting more bubbles to the superhydrophobic surface.

Figure 10.7 displays the time-averaged lateral void fraction for a total collection time of 35 seconds, which equates to 17,500 frames at a rate of 500 Hz. This figure shows the time-averaged void fraction measurements for the bubble column with a superhydrophobic tube inserted, displayed in Figure 10.7a and the time-averaged void fraction measurements for the bubble column with only hydrophilic tubes, displayed in Figure 10.7b. To fully understand the strength of the superhydrophobic characteristics of the material, we will look for consistency as the air injection rate increases.

Figures 10.8 and 10.9 displays a consistency along the superhydrophobic PVC tubes that is not seen in the void fraction measurements of the four hydrophilic tubes.

Figure 10.10 displays time-averaged void fraction for an air injection of 16SLPM (Ug = 0.0547m/s). 16SLPM (Ug = 0.0547m/s) is the highest air injection we could put into the bubble column to avoid overflowing the bubble column. At this rate, the void fraction measurements of the bubble column with a superhydrophobic tube have reached a plateau and remain considerably less than the void fraction measurements for the bubble column with all hydrophilic tubes. The reduction in void fraction reached a 50% value.

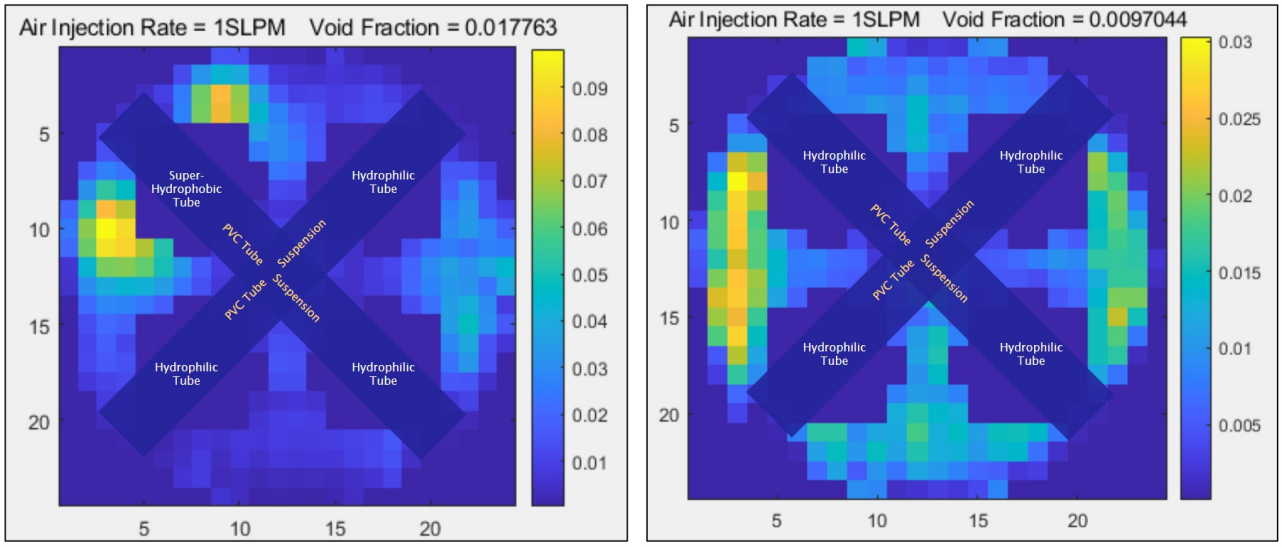

Figure 10.7: Time-averaged Void Fraction Lateral Representation (Wire Mesh Sensor Framework software) at 1SLPM (Ug = 0.0034m/s) Air Injection a) 3 hydrophilic and 1 superhydrophobic tubes; b) 4 hydrophilic tubes

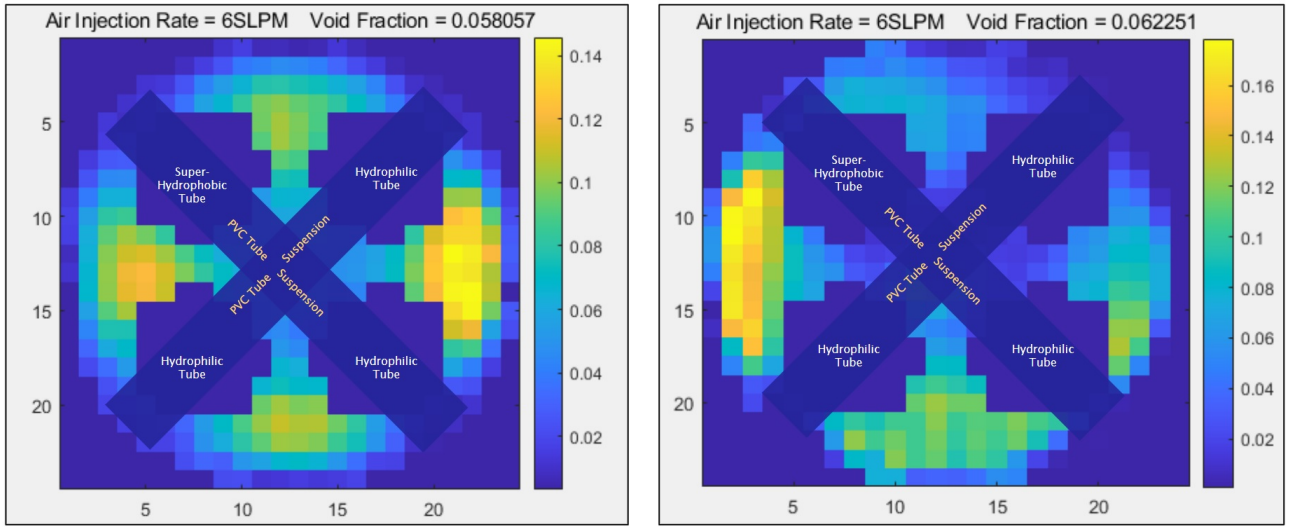

Figure 10.8: Time-averaged Void Fraction Lateral Representation (Wire Mesh Sensor Framework software) at 6SLPM (Ug = 0.0205m/s) Air Injection a) 3 hydrophilic and 1 superhydrophobic tubes; b) 4 hydrophilic tube

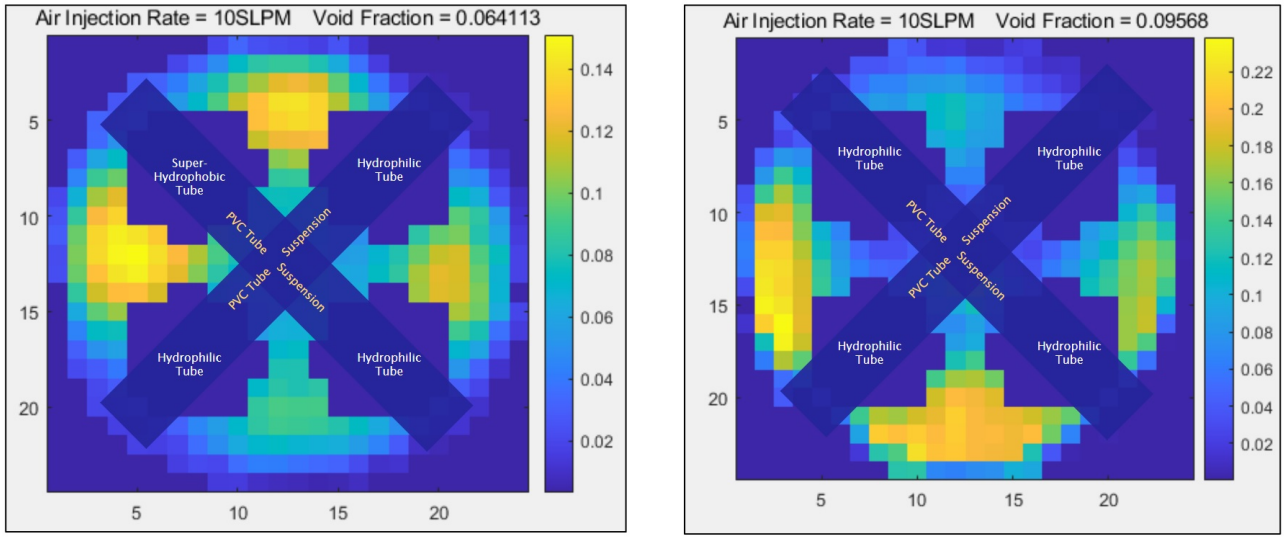

Figure 10.9: Time-averaged Void Fraction Lateral Representation (Wire Mesh Sensor Framework software) at 10SLPM (Ug = 0.0342m/s) Air Injection a) 3 hydrophilic and 1 superhydrophobic tubes; b) 4 hydrophilic tube

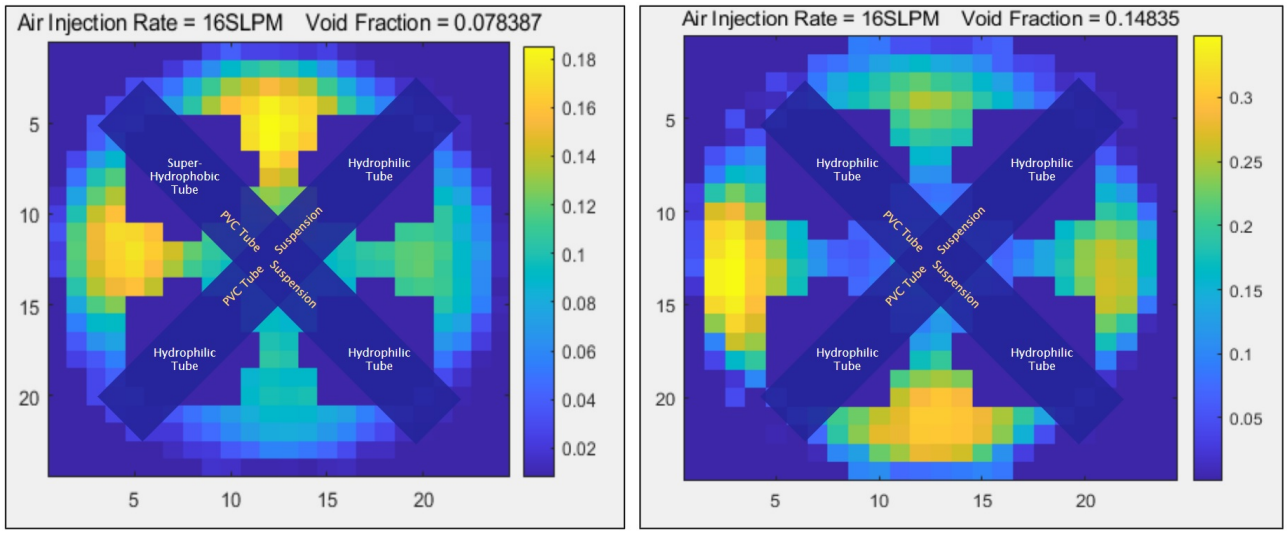

Figure 10.10: Time-averaged Void Fraction Lateral Representation (Wire Mesh Sensor Framework software) at 16SLPM (Ug = 0.0547m/s) Air Injection a) 3 hydrophilic and 1 superhydrophobic tubes; b) 4 hydrophilic tube

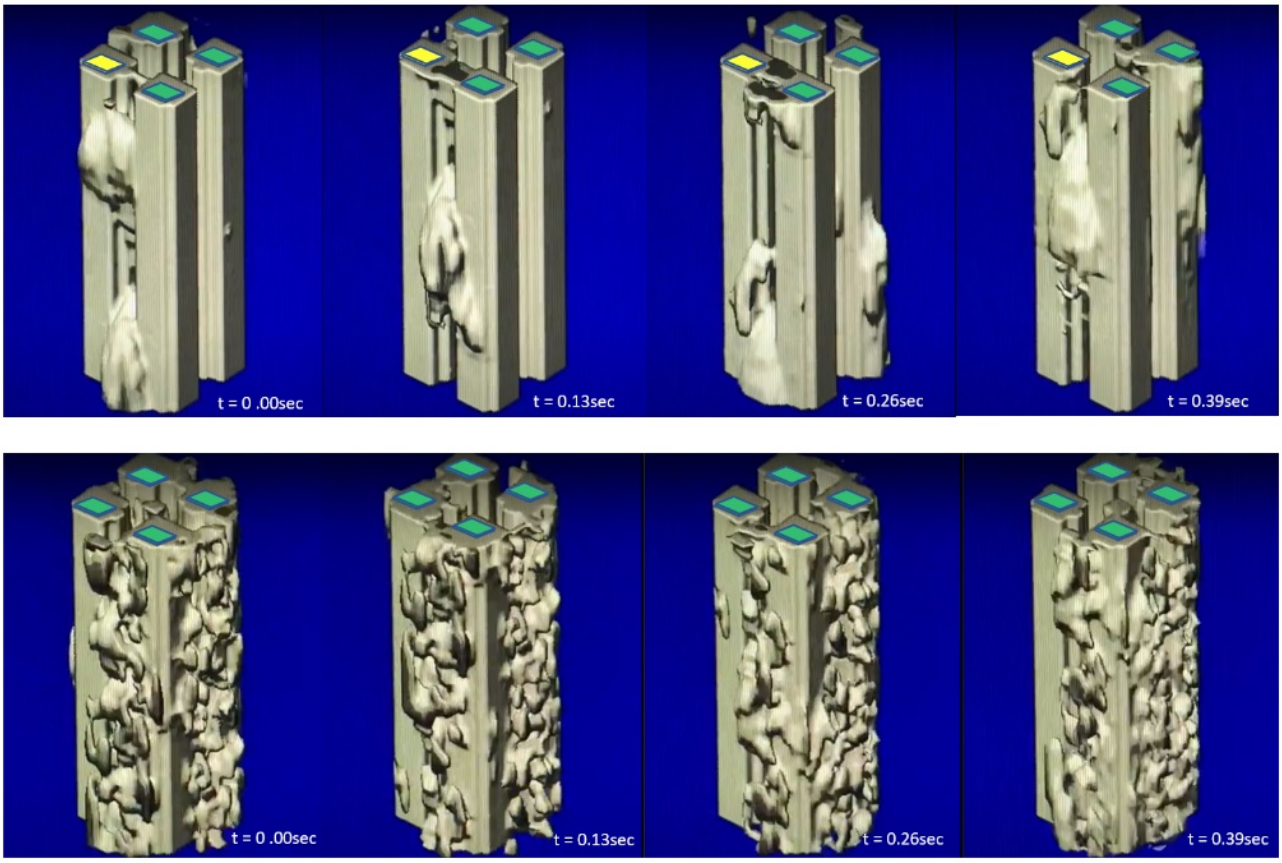

Figure 10.11: a) Bubble Dynamics 3D Isosurface Still Images (30fps) 3 Hydrophilic Tubes (green) and 1 Superhydrophobic (yellow) Tube (Air injection: 10SLPM); b) Bubble Dynamics 3D Isosurface Still Images (30fps) 4 Hydrophilic Tubes (green) (Ug = 0.0342m/s)

Figure 10.11 displays a 3D voxel video sequence of bubble dynamics rising along the mask geometrical constraints for the PVC tubes. This figure shows a 3D comparison of the differences in bubble flow an regime between these two separate configurations at the same superficial gas velocity. Figure 10.11a shows a considerably less bubble population for the configuration with a superhydrophobic PVC tube. The bubble regime in Figure 10.11a shows a churn regime, while the bubble regime in Figure 10.11b displays bubbly flow regime. The churn bubble regime remains closer to the area with superhydrophobic coating, which allows the other tubes to remain wetted. Figure 10.11b clearly shows more bubbles, which means there is less wetted area on the surfaces of the PVC tubes, which may result in a higher temperature along the fuel rods in a real world application.

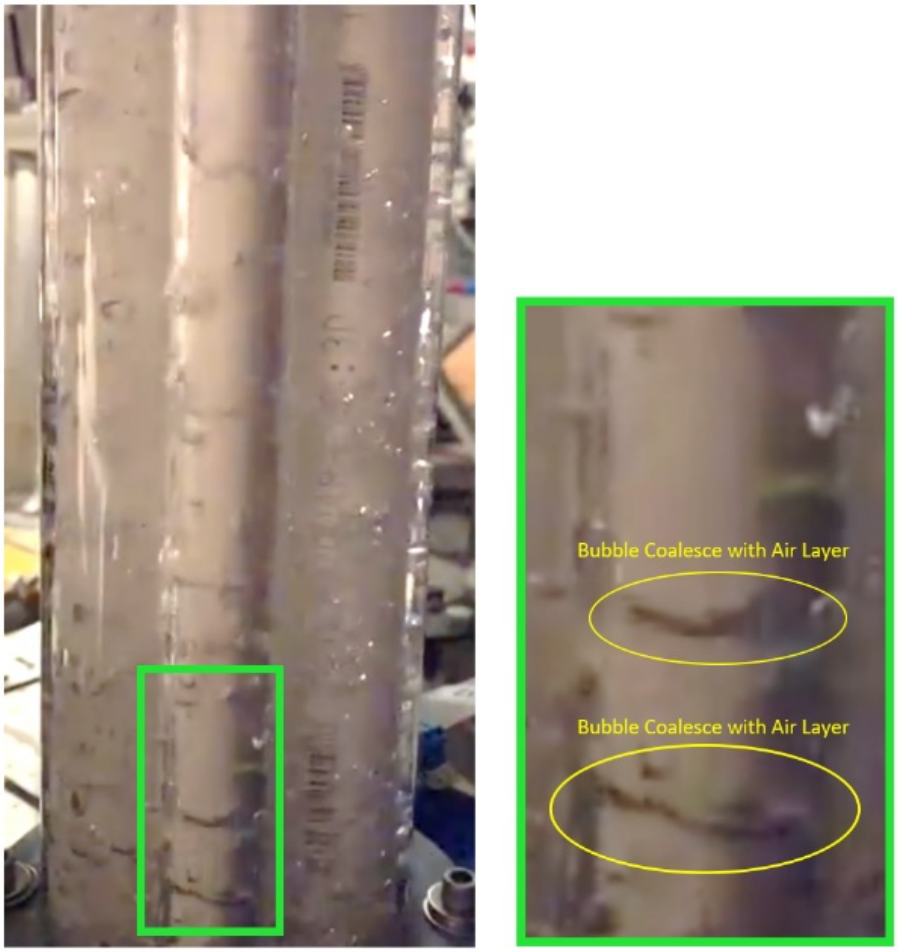

Figure 10.12: Indications of Bubble Coalescence with Air Layer along Superhydrophobic PVC Tube

Bubble Dynamics alongside SHS-coated PVC Tube

Figure 10.12 is an image that captures the effects of superhydrophobic coatings. The center tube in the image is coated with a superhydrophobic polymer using NeverWet. The bubbles along the superhydrophobic-coated tube continue to coalesce and ride along the air layer of the coated tube. The hydrophilic tube to the right and left of the coated tube in the figure has multiple bubbles rising along it, but you can notice that several of the bubbles were attracted to the center tube and continue rising along the coated tube. It is difficult to tell from this figure, whether the air bubbles are being absorbed by the air layer or growing to a point of detachment.

Figure 10.13 displays the advantage of the bubble regime that ensues from superhydrophobic tubes. The air bubbles shown in the upper portion of the bubble column are caused by the bubble coalescing into larger bubbles that occurs along the coated tube. These larger bubbles are not occurring on the hydrophilic tubes, and may further be carried away by natural circulation if a pipe flow was developed vice a bubble column. This is advantageous to maintain the hydrophilic tubes wetted for continued heat transfer which maintains the conditions of the fuel rods below peak central temperature limits.

Figure 10.14 is a still frame collected at 50fps to evaluate the bubble affinity to the SHS-coated PVC tube. A bubble in Figure 10.14 attaches itself to the coated tube and stretches and elongates under drag forces applied at the water to air layer boundary. Figure 10.15 is a separate still frame displaying a large bubble that has formed from the coalescing of smaller bubbles as it continues to experience elongation due to the interaction with the PVC inner wall and the air layer of the coated PVC tube. This bubble will continue to expand and rise at a faster velocity due to its volume expansion and buoyancy forces.

Figure 10.16 displays a single bubble balanced on an SHS-coated PVC tube prior to immersing the tube in water. We used the available angular measurement tool found in ImageJ imaging software to measure the contact angle of the bubble to prove that the conditions are superhydrophobic. We measured a contact angle greater than 150°, which is within the range of superhydrophobic characteristics.

Evaluation of Time-averaged Void Fraction, Bubble Velocity and Bubble Diameter for the Four Tube (with and without substituted SHS-coated PVC Tube)

We performed X-ray CT scans of the bubble column with a superficial gas velocity of 0.034m/s. The X-ray CT scan was performed first on the bubble column with the middle section modified with suspended four hydrophilic PVC tubes. The second X-ray CT scan was performed on the bubble column with the middle section modified with suspended three hydrophilic PVC tubes and one superhydrophobic-coated PVC tube. The configuration and superficial gas velocity were maintained the same for both measurements. The X-ray source was maintained at 100kV and 350μA with TXI mode set to on. The photon counter was modified to include a threshold of 40kV and 60kV with an exposure time of 1 second. The Void Fraction results for three void fraction measurement techniques discussed previously are displayed in Table 10.1. We see a fairly good agreement between the three measurement techniques which validates our hypothesis that gas holdup is significantly reduced by introducing a superhydrophobic internal to a confined channel of a vertical aerated system.

We performed time-averaged void fraction measurements for both cases collecting 17,000 frames at 500Hz. Figures 10.17 and 10.18 display the results for both cases. Figure 10.17 displays the setup of the 24x24 time-averaged void fraction rendering processed using the Wire Mesh Sensor Framework program. The measurement was generated using histogram

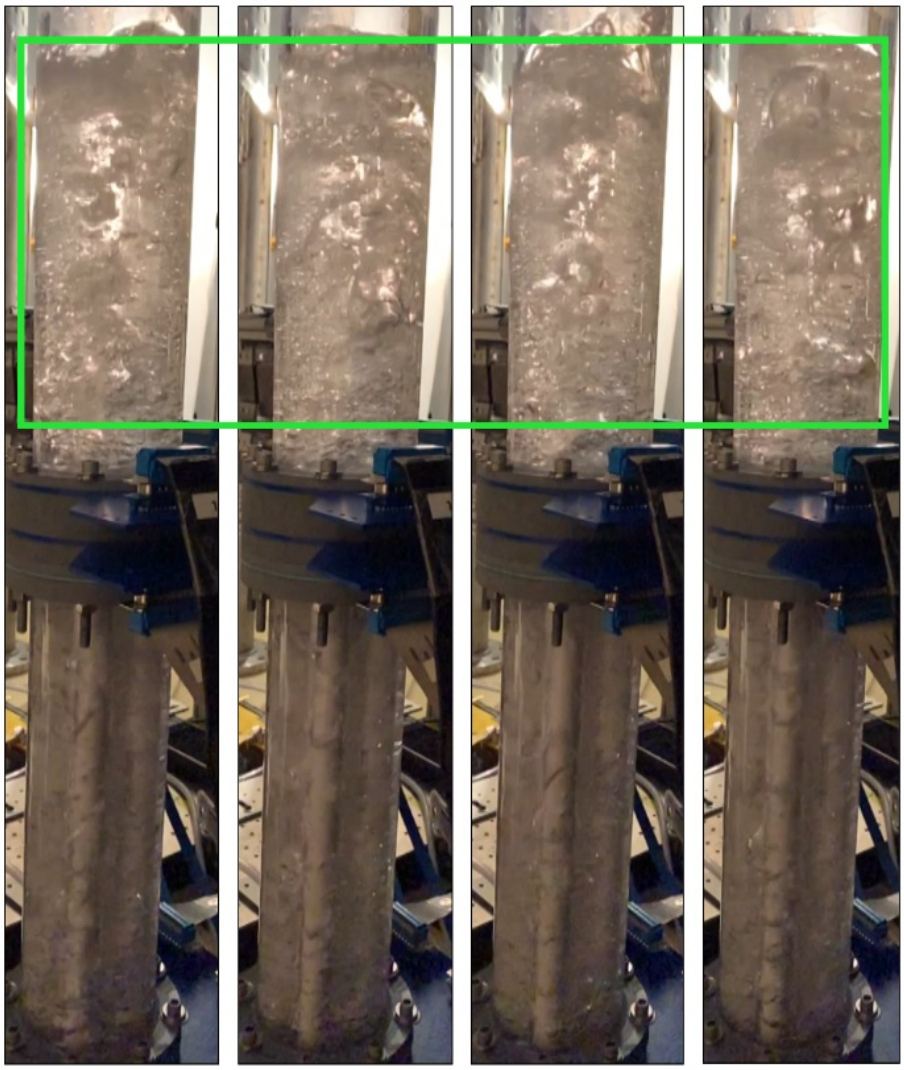

Figure 10.13: Multiple still images of large bubble formations in the upper section of bubble column due to bubble coalesce with air layer along the superhydrophobic PVC Tube in the lower section of the bubble column

calibration. We superimposed the suspension cross-bar above the rendering since they lie approximately 10mm below the bottom WMS of the top pair (Level 2). This clarifies the void fraction measurements to the viewers and allows us to specify where the SHS-coated PVC tube is located. We notice that the void areas, specified by brighter colors of the color scheme, reach values of 0.180 in proximity of the SHS-coated PVC tube. The average void fraction of all measured data points is 0.078. Figure 10.18 displays the same cross bar and

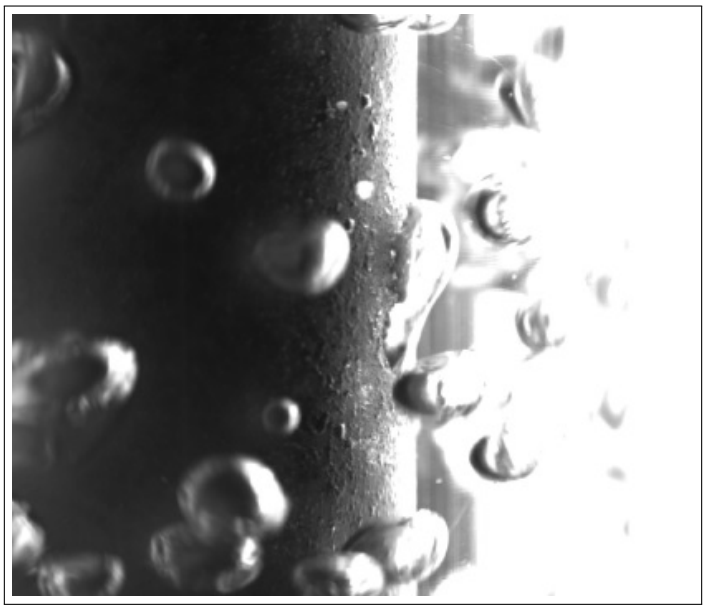

Figure 10.14: Single bubble rise along an SHS-coated PVC Tube to show bubble affinity to air layer and coalescence on PVC-coated tube

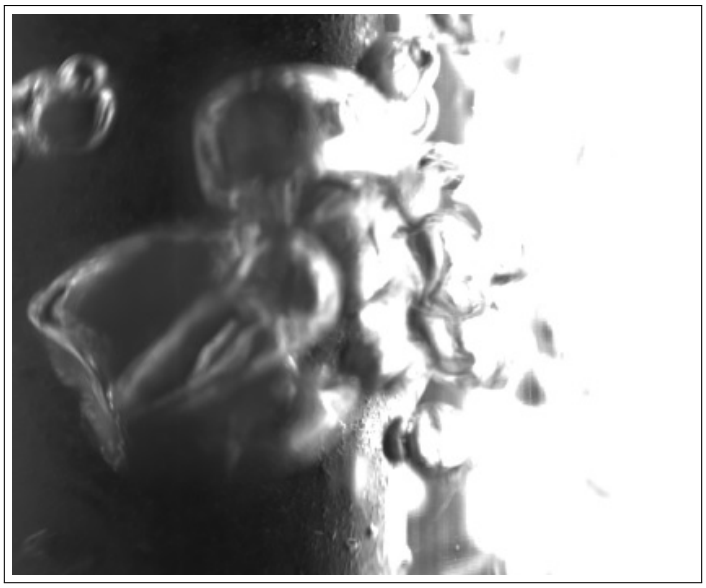

Figure 10.15: Single bubble rise along an SHS-coated PVC Tube to show bubble coalescence on PVC-coated tube leading to larger diameter bubbles

Figure 10.16: Single Bubble on SHS-coated PVC Tube with Contact Angle measured by ImageJ imaging software.

Void Fraction Measurement Method	Void Fraction with Four Hydrophilic Tubes	Void Fraction with Three Hydrophilic and One SHS-coated Tubes
Height Difference	0.188	0.076
Wire Mesh Sensor (average of Level 1 Top and Level 2 Bottom)	0.181	0.078
X-ray Intensity Field (Mixture, Water and Air)	0.183	0.074

Table 10.1: Time-averaged Void Fraction Measurements for Bubble Column with Four PVC Tubes suspended (with and without one substituted SHS-coated PVC Tube)

specifies that all tubes are hydrophilic. Using the same colorbar range used in Figure 10.17, we notice void areas reaching 0.300, which is 40% higher than the void areas seen in Figure 10.17. Additionally, the time-averaged void fraction value for the entire dataset is 0.125 for the case with only hydrophilic tubes, which is 44% greater than the case with one of four hydrophilic tubes replaced with an SHS-coated PVC Tube.

Figure 10.19 displays a wire mesh sensor located approximately 10mm above the suspension cross bar for the four tubes. It also shows the location of the top pair of WMS utilized in these measurements so we understand how the PVC tubes are situated only between the two WMS pairs. The Void Fraction measurements, rendered in MATLAB vice the Wire

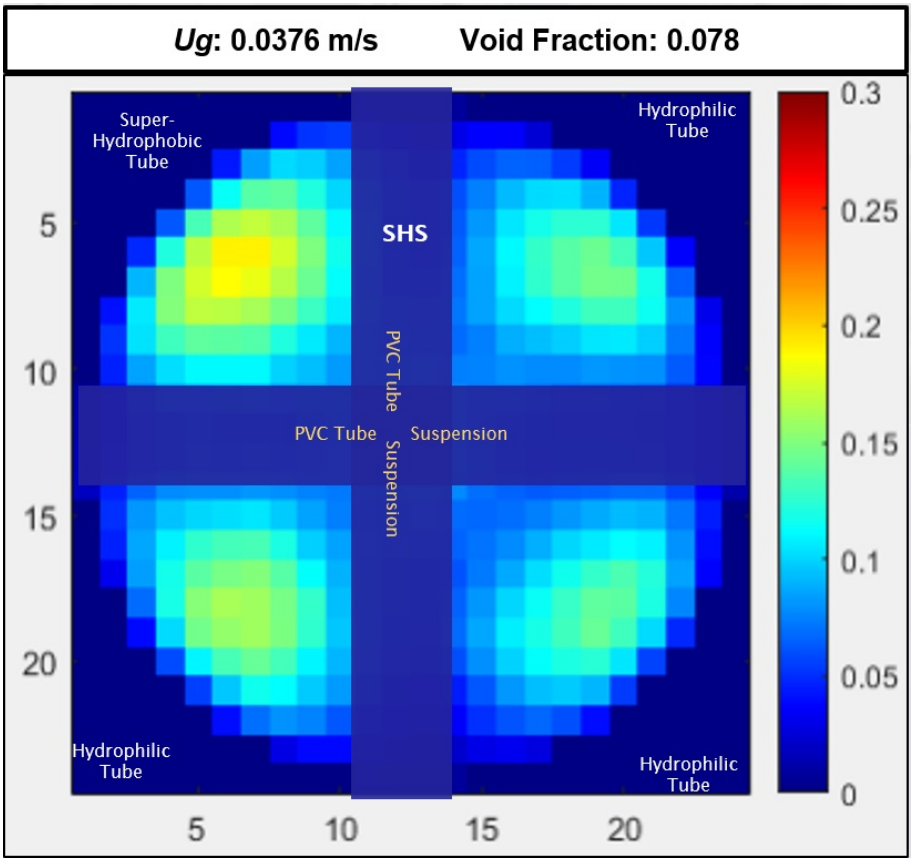

Figure 10.17: Time-averaged Void Fraction Lateral Distribution for Bubble Column with 3 hydrophilic tubes and 1 SHS-coated tube at U_g=0.0376$\frac{m}{s}$

Mesh Sensor Framework, with no superimposed cross bar is displayed so we can get an idea of the void fraction measurement without any modifications or introduced mask elements. You can see that the results are consistent with Figure 10.17. The substitution of a single hydrophilic PVC tube with a SHS-coated PVC tube results in larger localized void areas in vicinity of the SHS-coated tube but a substantially reduced average void fraction across all other areas. This is important since our focus in this scenario is to maintain zero to minimal void areas in vicinity of tubes that simulate fuel rods.

Figure 10.20 displays a wire mesh sensor located approximately 10mm above the suspension cross bar for the four tubes. It also shows the location of the top pair of WMS utilized in these measurements so we understand how the PVC tubes are situated between the two WMS pairs. The Void Fraction measurements, rendered in MATLAB vice the Wire Mesh Sensor Framework, with no superimposed cross bar is displayed so we can get an idea of the void fraction measurement without any modifications or imposed mask elements. You

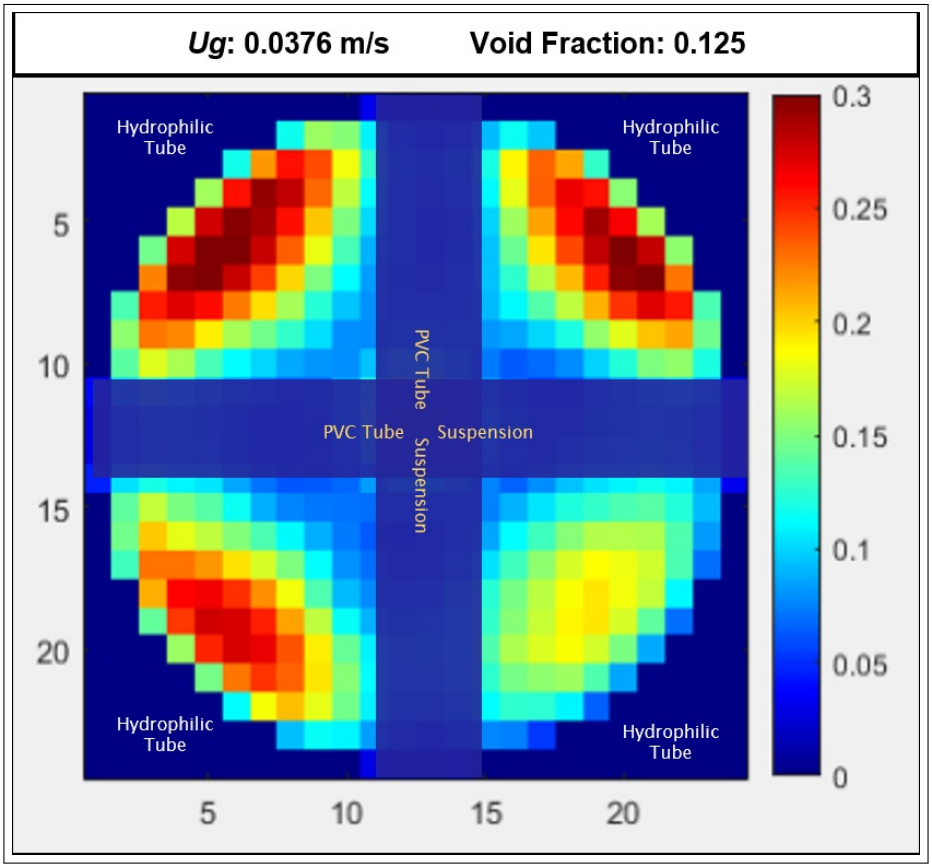

Figure 10.18: Time-averaged Void Fraction Lateral Distribution for Bubble Column with 4 hydrophilic tubes at U_g=0.0376$\frac{m}{s}$

can see that the results are consistent with Figure 10.18. The void areas are greater in all quadrants and have a substantially higher average void fraction across all other areas than the case with a substituted SHS-coated PVC tube. Along with the previous case, these results are important to show how these large void areas in vicinity of simulate fuel rods can pose detrimental effects with respect to super-heating and Critical Heat Flux violations.

To validate the modification of the bubble regime in both cases, we also measured mean bubble velocity and mean bubble diameter. We hypothesize that the introduction of an SHS-coated internal surface will change the bubble regime from homogenous to heterogenuous. Figure 10.21 is a velocity profile processed in MATLAB using cross-correlation functions, using a measurement frequency of 500Hz. The areas in green display areas with larger velocity profiles than neighboring areas. The average bubble velocity for the entire dataset with an SHS-coated tube was 0.56m/s. Figure 10.22 displays the average velocity profile for the case with four hydrophilic PVC tubes. In this case, the green highlighted areas are

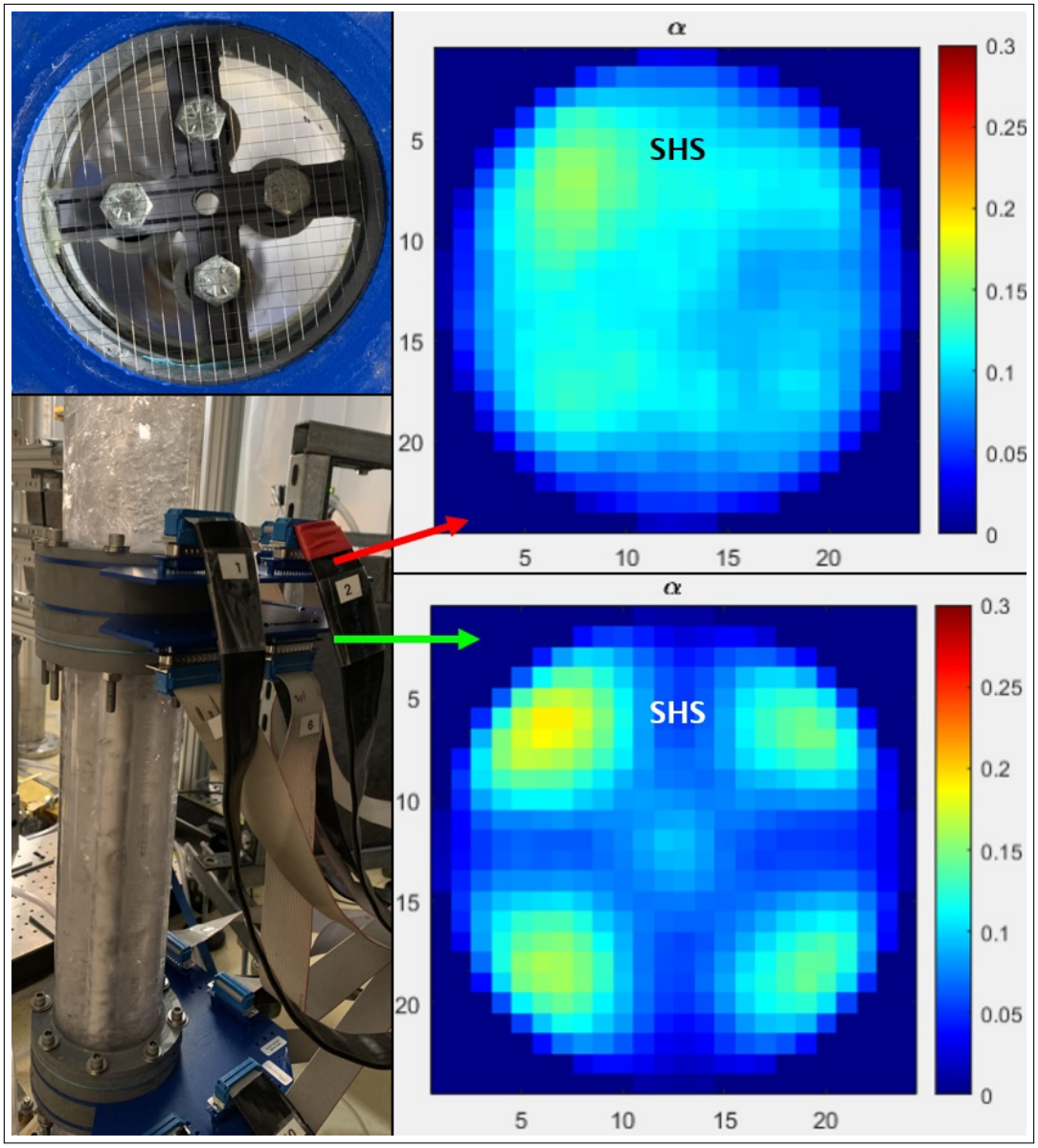

Figure 10.19: (Upper Left) Top View photo of WMS above suspended PVC tubes (Lower Left) Location of Upper WMS Pair (Right) Time-averaged Void Fraction Lateral Distribution for Bubble Column with substituted SHS-coated tube at U_g=0.0376$\frac{m}{s}$

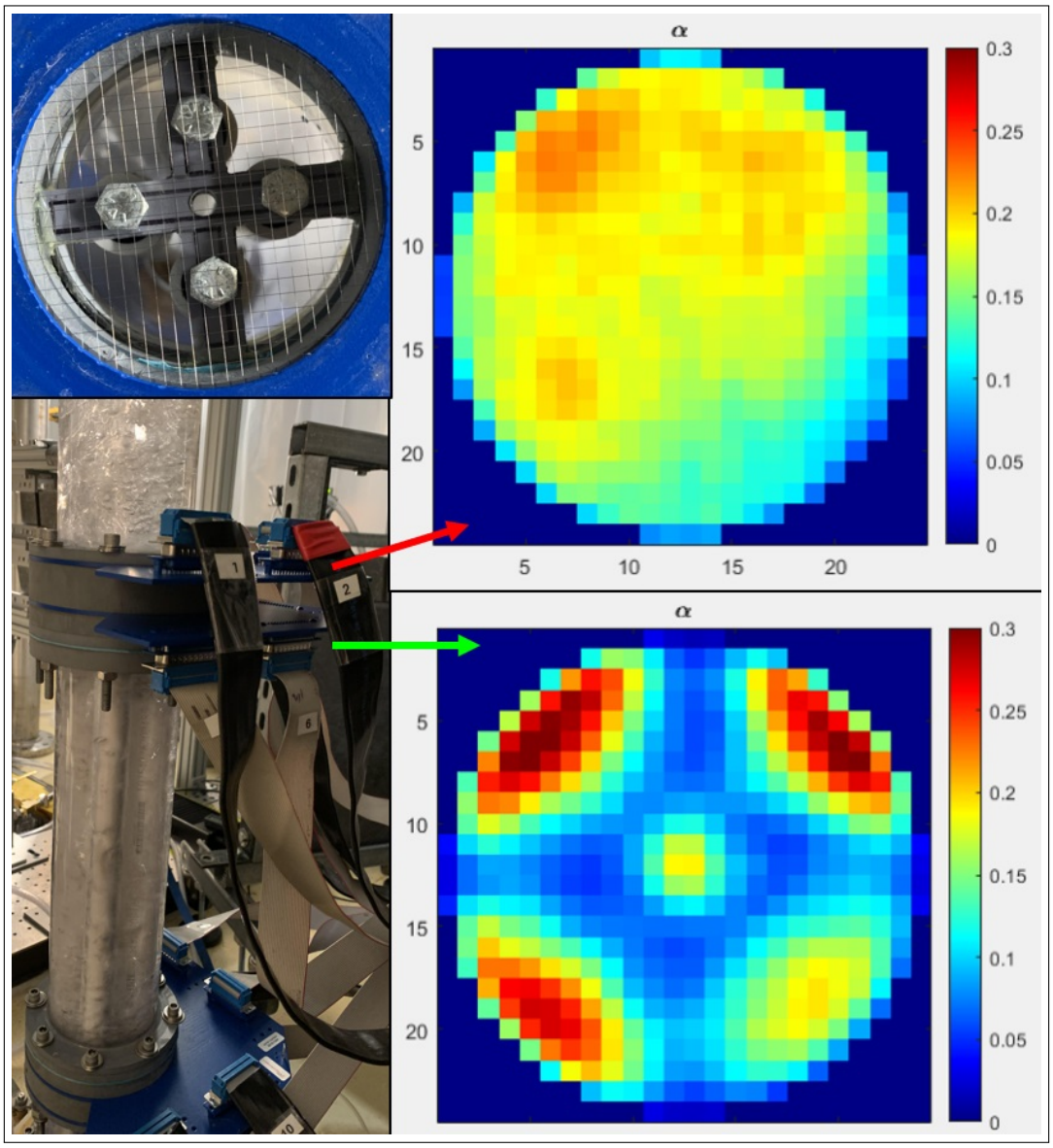

Figure 10.20: (Upper Left) Top View photo of WMS above suspended PVC tubes (Lower Left) Location of Upper WMS Pair (Right) Time-averaged Void Fraction Lateral Distribution for Bubble Column with no substituted SHS-coated tube at U_g=0.0376$\frac{m}{s}$

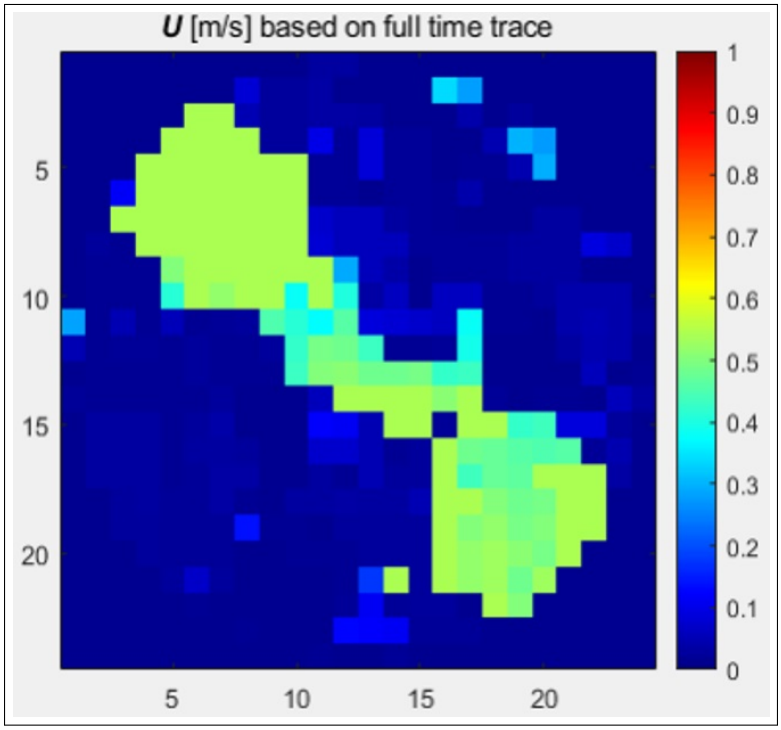

Figure 10.21: Time-averaged Velocity Lateral Distribution for Bubble Column with substituted SHS-coated tube at U_g=0.0376$\frac{m}{s}$

minimal which would suggest either smaller bubbles or lower speed. The average bubble velocity for this case was 0.26m/s.

We used a mean bubble velocity equation derived from Shah et al's paper,"Design Parameters Estimations for Bubble Column Reactors," to calculate expected mean bubble rise velocity given the superficial gas velocity and gas hold-up[12]. Although this equation applies to homogeneous flow in an empty bubble column reactor, we use it to get a qualitative idea of how bubble velocity will change given the relationship of superficial gas velocity to void fraction for both cases.

$$U_b = \frac{U_g}{\alpha} \tag{10.1}$$

where: U_b = mean bubble rise velocity U_g = superficial gas veloicty α = void fraction/gas holdup

In Figure 10.23, we calculate that mean bubble rise velocity using the superficial gas velocity and void fraction relationship for the case with a substituted SHS-coated PVC tube is 0.52m/s and 0.34m/s for the case with only hydrophilic tubes. As we compare Figures

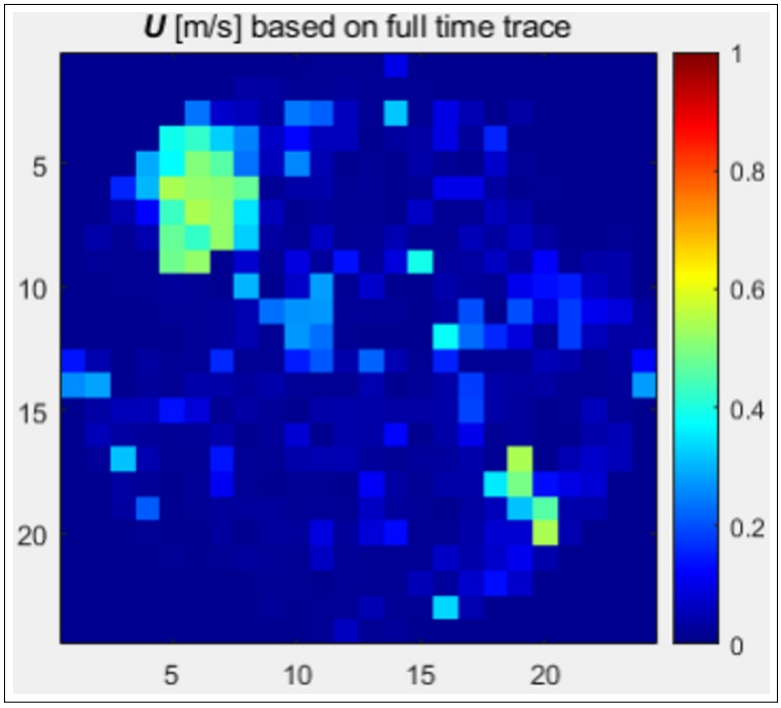

Figure 10.22: Time-averaged Velocity Lateral Distribution for Bubble Column with no substituted SHS-coated tube at U_g=0.0376$\frac{m}{s}$

10.21 and 10.22 to Figure 10.23, we see a fair agreement in our measured results as compared to our calculations.

Using the Wire Mesh Framework Software, we measured mean bubble diameter across the entire measurement frames and displayed the results in a histogram shown in Figures 10.24 ad 10.25. Figure 10.24 shows the mean diameter for the case of four hydrophilic tubes. Figure 10.25 shows the histogram for the mean bubble diameter for the case with a substituted SHS-coated PVC tube. We can clearly see that the bubble regime is no longer homogeneous and there are two consistent bubble diameters observed. While the hydrophilic case has a mean bubble diameter of 8mm, the case with the superhydrophobic tube has a mean bubble diameter of 6mm and 19mm. In this case you have larger bubbles forming and smaller bubbles also rising. The flow is no longer in the bubbly flow regime but has transitioned to churn-turbulent flow.

The larger bubbles cause churn and higher mixing across the bubble column. Figure 10.26 is a still image of the bubbles from this experiment rising amidst a hydrophilic and superhydrophobic PVC tube. We notice more bubble coalesce in vicinity of the SHS-coated tube and larger bubble formation as a result of coalescing as the bubbles are attached to the air layer on the SHS-coated tube. Figure 10.27 is a still image of the upper portion of the

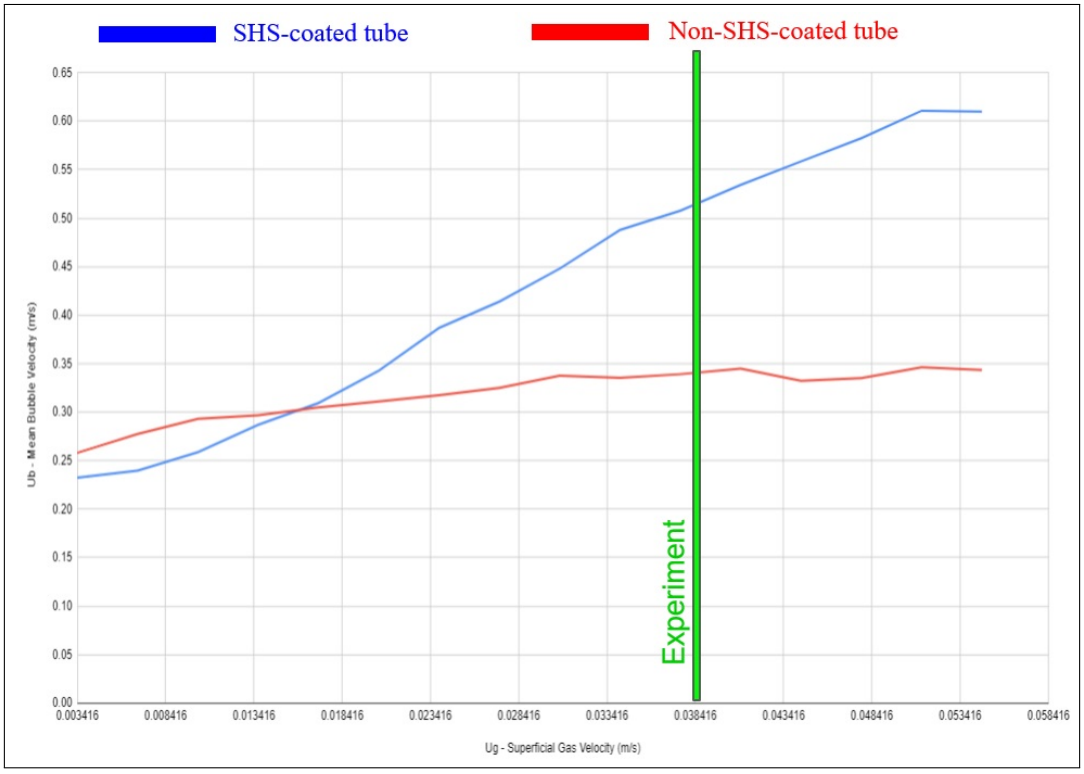

Figure 10.23: Mean Bubble Velocity

bubble column, taken above the four PVC tubes, to show how large these bubbles develop into and validate that the flow is no longer homogeneous.

Figure 10.28 displays the X-ray CT reconstruction of the bubble column under the same superficial gas velocity as the measurements taken with WMS. The colorscale is the same for both figures and the location of the SHS tube has been specified. The attenuation coefficient for the mixture with the SHS-coated tube is lower for the case with hydrophilic tubes. This was only collected with 5 frames per angle so the void fraction values have a higher uncertainty since projections are less converged. These reconstructions serve as a qualitative comparison of how an X-ray CT scan with limited time-resolved void fraction estimates can still resolve larger void areas around the SHS tube and an overall lower void fraction as compared to the hydrophilic case.

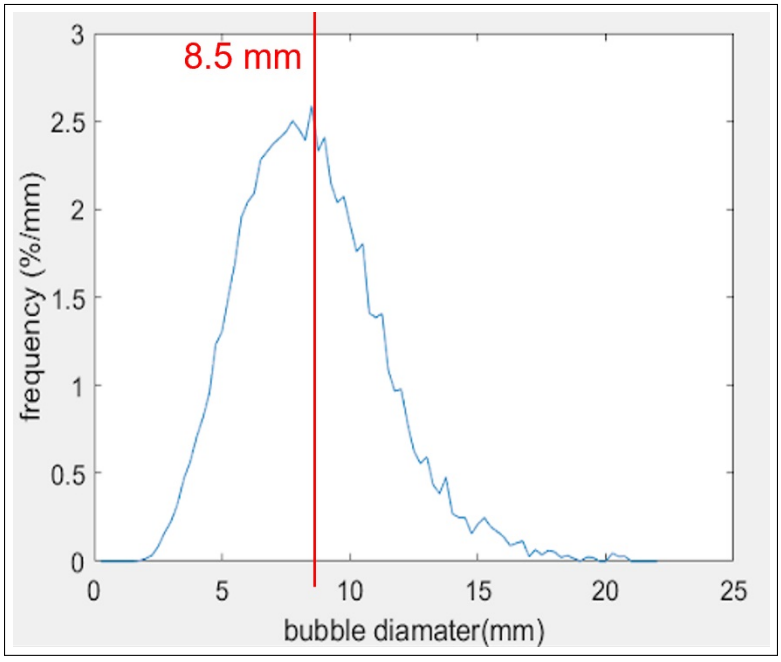

Figure 10.24: Mean Bubble Diameter Bubble Dynamics within four hydrophilic tubes

10.2 Bubble Dynamics in Simulated 2 x 2 Hydrophilic Fuel Cell Array with Internal Superhydrophobic-coated Material-Run 2

We performed a second run with 35 frames collected per angle using our X-ray source and photon counter. We increased our X-ray source to a setting of 100kV and 400μA in TXI mode. The threshold applied to our photon counter were 40keV and 60keV with an exposure time of 1 second. We performed one rotation for a total of 1 frame per angle for the mediums of water and air. We performed one rotation and collected 35 frames per angle at a 1 second exposure for a total of 12,600 projection frames. A new software was applied to our photon counter to allow us to collect 35 frames per angle based on one trigger pulse per angle vice a trigger pulse per individual projection. This minimizes electronic problems that may arise from the trigger pulse signal. Run 1 was collected using a trigger response that depended on pulse signal duration. Although the proper exposure time was verified, this has the potential to introduce a skipped signal or lowered signal pulse value that can result in frame collection problems, such as skipped pixel. With our new software applied, we successfully collected 35 frames per angle with no disruption in data transfer. We picked 35 frames per angle at a 1 second exposure since we obtained converged dataset observed through the wire mesh

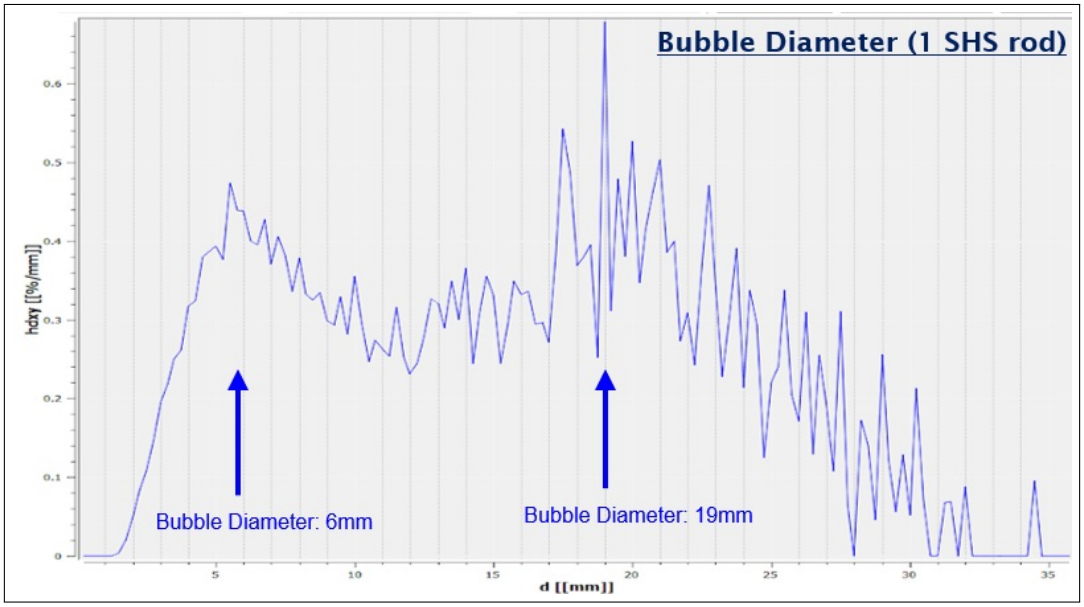

Figure 10.25: Mean Bubble Diameter Bubble Dynamics within four PVC tubes (3 hydrophilic and 1 SHS-coated)

measurements for a 35 second collection at 1000Hz frame rate. We also selected a different superficial velocity from the first run. We used a superficial velocity of 0.034m/s. Table 2 summarizes the time-averaged void fraction results.

Time-averaged Void Fraction Measurements for Four Hydrophilic Tubes in a 2x2 Array Configuration

Air flow into the bubble column was controlled using an ALICAT Flow Control unit, with the range from 0 to 19 SLPM. Shop air with an air pressure reduced to 30psig was utilized to maintain a constant applied air pressure. Air was injected into the bubble column through a series of 800 holes perforated on a brass plate positioned 12.7 cm under the 4 PVC tubes. The height of the water level in the bubble column varies with changes in air flow. Using the difference between a specific height at a given air injection and an initial height with no air injection, the void fraction can be calculated to get an initial estimate of difference between four hydrophilic tubes and the modified setup including a superhydrophobic tube, replacing a hydrophilic tube. Four WMS were positioned in pairs referenced as Level 1 and Level 2. Level 1 is the WMS pair under the PVC tubes. Level 2 is the WMS pair above the PVC tubes. Figure 10.29 displays the time-averaged void fraction calculated by all previously discussed measurement techniques for superficial gas velocity ranging from 0.003 to 0.068m/s.

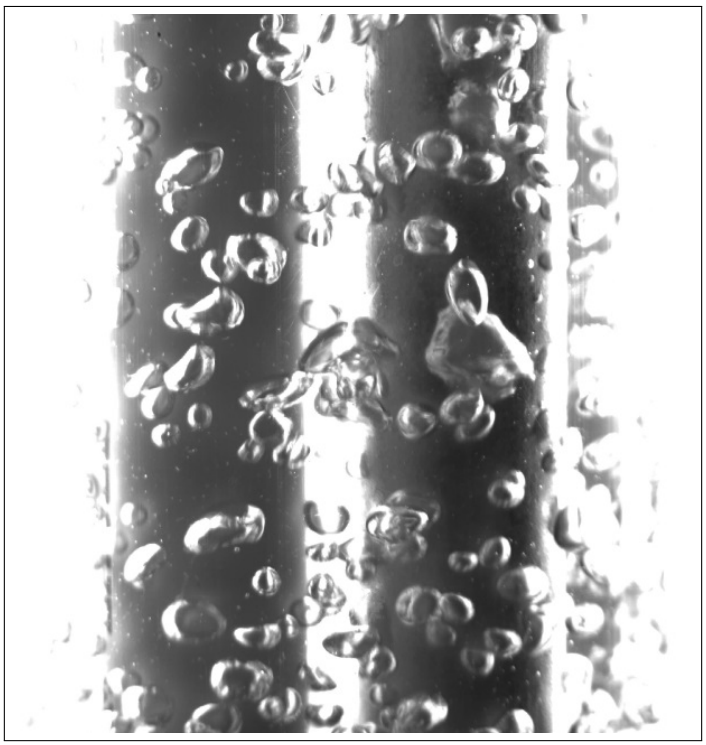

Figure 10.26: Bubble Flow Amidst hydrophilic (left) and superhydrophobic (right) PVC Tubes

Void Fraction Measurement Method	Void Fraction with Four Hydrophilic Tubes	Void Fraction with Three Hydrophilic and One SHS-coated Tubes
Height Difference	0.250	0.130
Differential Pressure transducer	0.256	0.115
Wire Mesh Sensor (Level 2)	0.168	0.098
X-ray Intensity Field (Mixture, Water and Air)	0.202	0.110
X-ray CT Reconstruction (ASTRA/SIRT)	0.202	0.113

Table 10.2: Time-averaged Void Fraction Measurements for Bubble Column with Four PVC Tubes suspended (with and without one substituted SHS-coated PVC Tube)

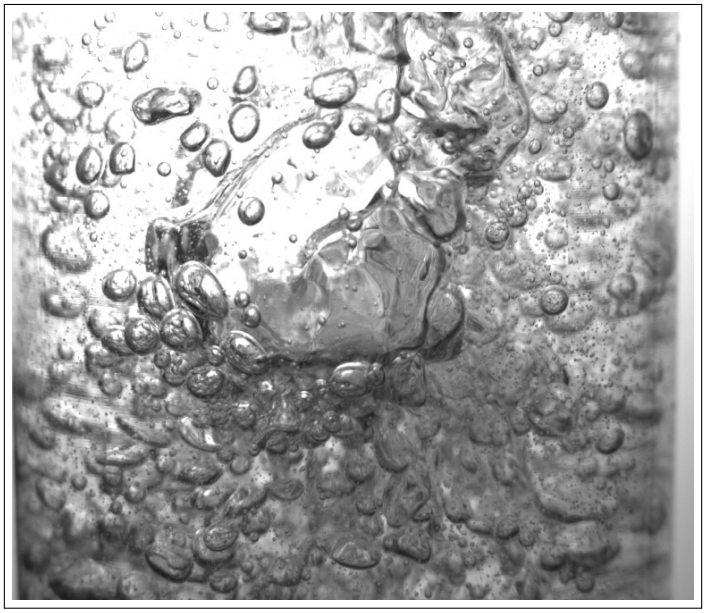

Figure 10.27: Mean Bubble Diameter Bubble Dynamics within four PVC tubes (3 hydrophilic and 1 SHS-coated)

Figure 10.30 displays the time-averaged void fraction measured by the four wire mesh sensors for a superficial gas velocity of 0.034m/s. The bottom pair of WMS display the lateral void fraction distribution prior to entering the geometric constraints of the four PVC tubes. The top pair of WMS display the lateral void fraction measurements right above the four PVC tubes. In this case, we notice a reduction in void fraction as the bubble encounter interference introduced by the confined geometric area around the tubes. This obviously affects void fraction as the bubbles may coalesce under the confined space constraints into a more vertical distribution vice horizontal. The Level 2 Bottom WMS is positioned 10mm above the PVC tubes which is our best measurement of lateral distribution around the PVC tubes. The Level 2 Top WMS gives lateral distribution but is not adequate to identify the individual effects of the tubes on a particular void area since it is 40mm above the PVC tubes. The WMS Void Fraction calculated for Table 10.2 was gathered by taking the average of the void fractions from the Level 1 Top WMS and the Level 2 Bottom WMS. This is an approximate void fraction used to validate the X-ray CT void fraction calculations considering that the X-ray CT scan is in the center of both the Level 1 Top WMS and Level 2 Bottom WMS.

We used the varying X-ray intensity fields for the three mediums (mixture, water and air) at each frame to calculate the time-averaged void fraction for the hydrophilic case. The intensity field for the mixture is averaged at each angle from the collected 35 frames. Figure

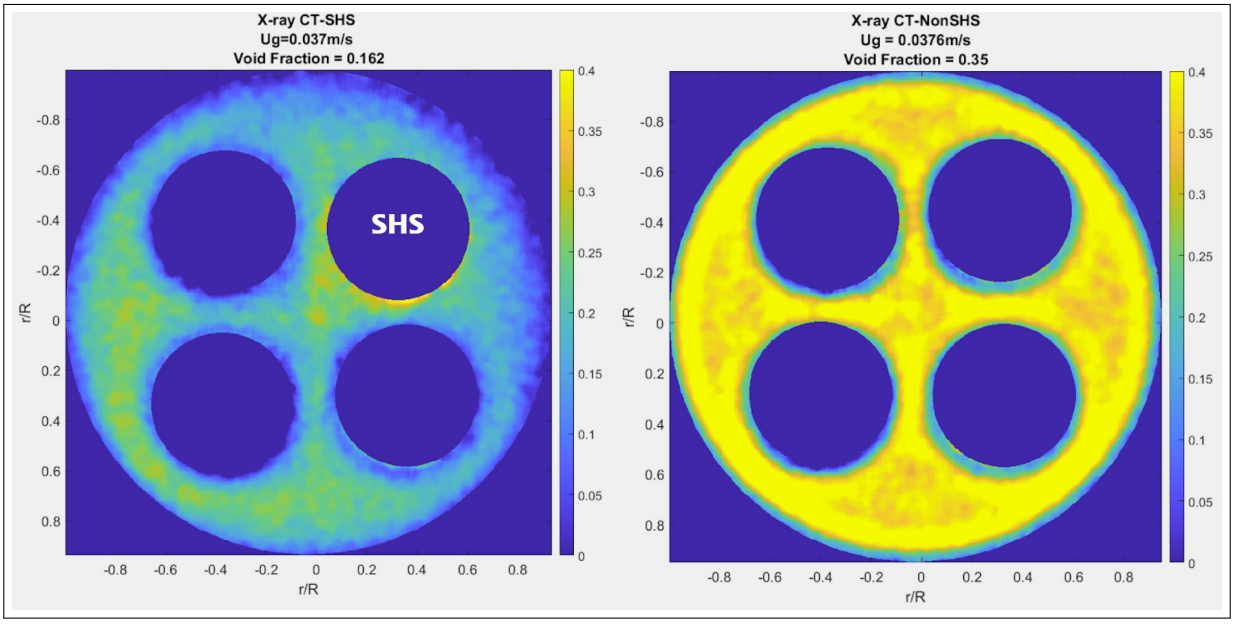

Figure 10.28: X-ray CT Reconstruction using SIRT algorithm with ASTRA Toolbox. a) SHS-coated PVC Tube. b) Hydrophilic Tubes

10.31 displays the time-averaged void fraction calculated at each angle using Equation 9.3. The average of the 360 time-averaged void fraction is 0.202, which is used as the time-averaged void fraction for the entire measurement run.

We used the X-ray Computed Tomography reconstruction for the three mediums and Equation 9.4 to render a two-dimensional time-averaged void fraction displayed in the lower right of Figure 10.32. This reconstructed time-averaged void fraction yielded a void fraction of 0.202.

The time-averaged void fraction measurement from X-ray computed tomography is displayed in Figure 10.33 with all areas exterior to the inner wall omitted. In order to calculate the time-averaged void fraction from this graph we need to eliminate the reconstructed PVC tubes so their void fraction values are not included in the calculation. Figure 10.34 displays the same void fraction reconstruction with mask implemented for the PVC tubes and median filter application. The time-averaged void fraction, calculated by taking a mean of all the void fraction values contained within the bubble column and external to the PVC tubes, is 0.205.

Figure 10.35 displays both the X-ray CT Void Fraction reconstruction and the Level 2 Bottom WMS measurement. This figure displays the strength of both measurement techniques. The X-ray CT reconstruction gives a more accurate average void fraction as compared to height and X-ray intensity projection variation. As we still have not achieved the

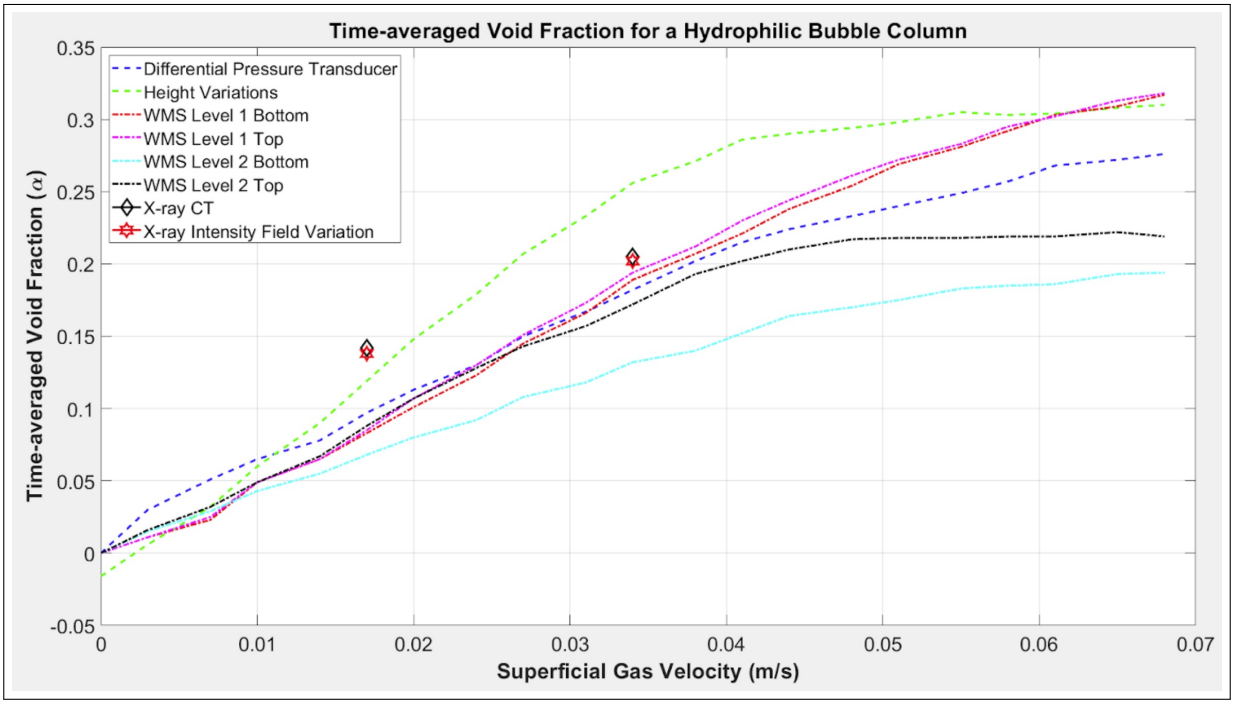

Figure 10.29: Void Fraction measurements for the hydrophilic case calculated by all four WMSs, height variation, differential pressure transducer and X-ray CT and intensity variation

resolution to show dynamic localized VF to a fine degree in X-ray CT as observed in WMS, the WMS continues to provide better spatial resolution. The intrusion of the WMS on the flow and positioning of the WMS above the tubes suggest that X-ray CT provides a more accurate localized assessment of time-averaged void fraction across the four PVC tubes.

Time-averaged Void Fraction Measurements for Three Hydrophilic Tubes and One Superhydrophobic Tube in a 2x2 Array Configuration

Air flow into the bubble column was controlled using an ALICAT Flow Control unit, with a range from 0 to 19 SLPM. Shop air with an air pressure reduced to 30psig was utilized to maintain a constant applied air pressure. Air was injected into the bubble column through a series of 800 holes perforated on a brass plate positioned 12.7cm under the 4 PVC tubes. The height of the water level in the bubble column varies with changes in air flow. Using the difference between a specific height at a given air injection and an initial height with no air injection, the void fraction can be calculated to get an initial estimate of difference between four hydrophilic tubes and the modified setup including a superhydrophobic tube, replacing

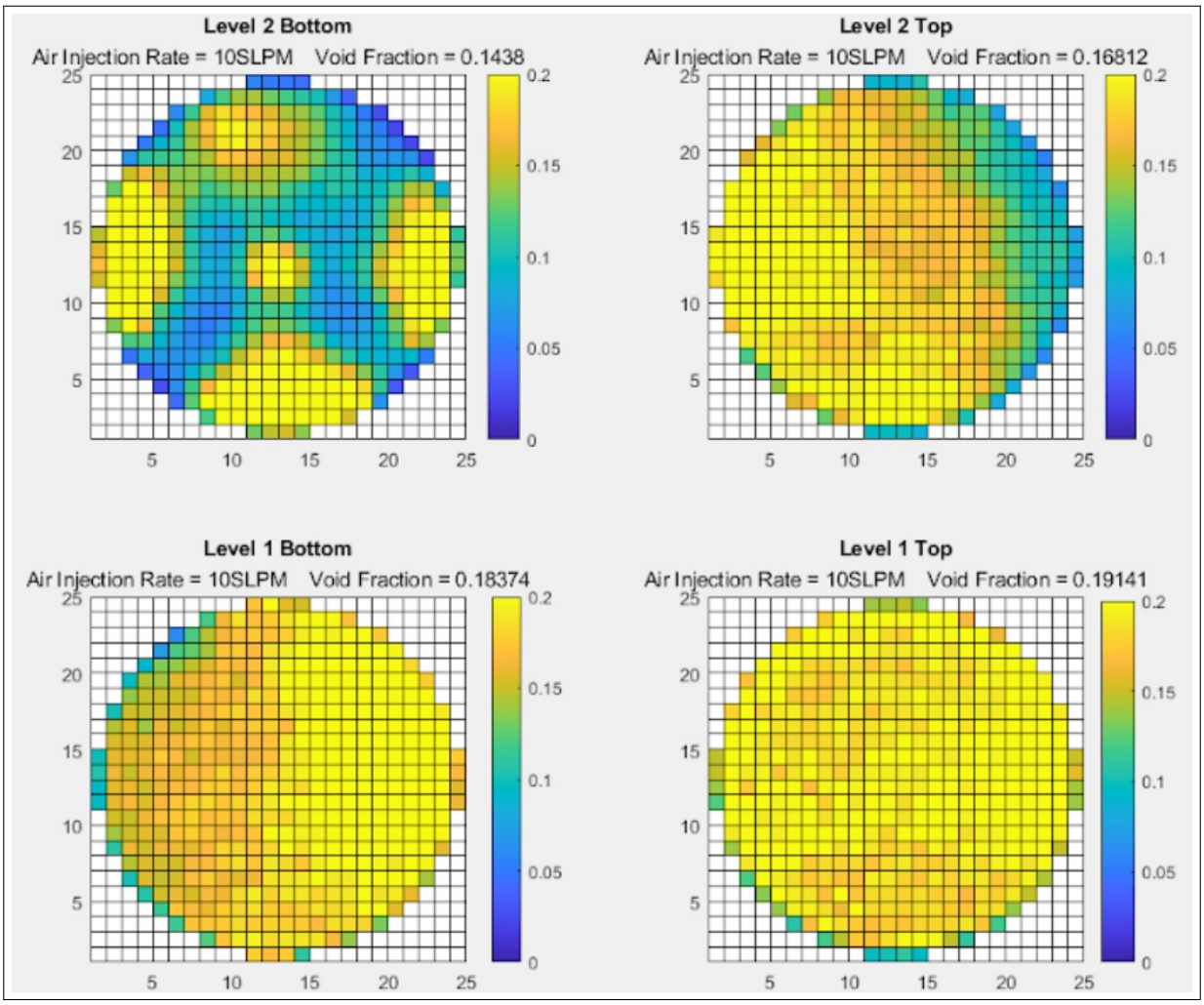

Figure 10.30: Void Fraction measurements for the hydrophilic case calculated by all four WMS and bubble column height difference - Ug = 0.034m/s

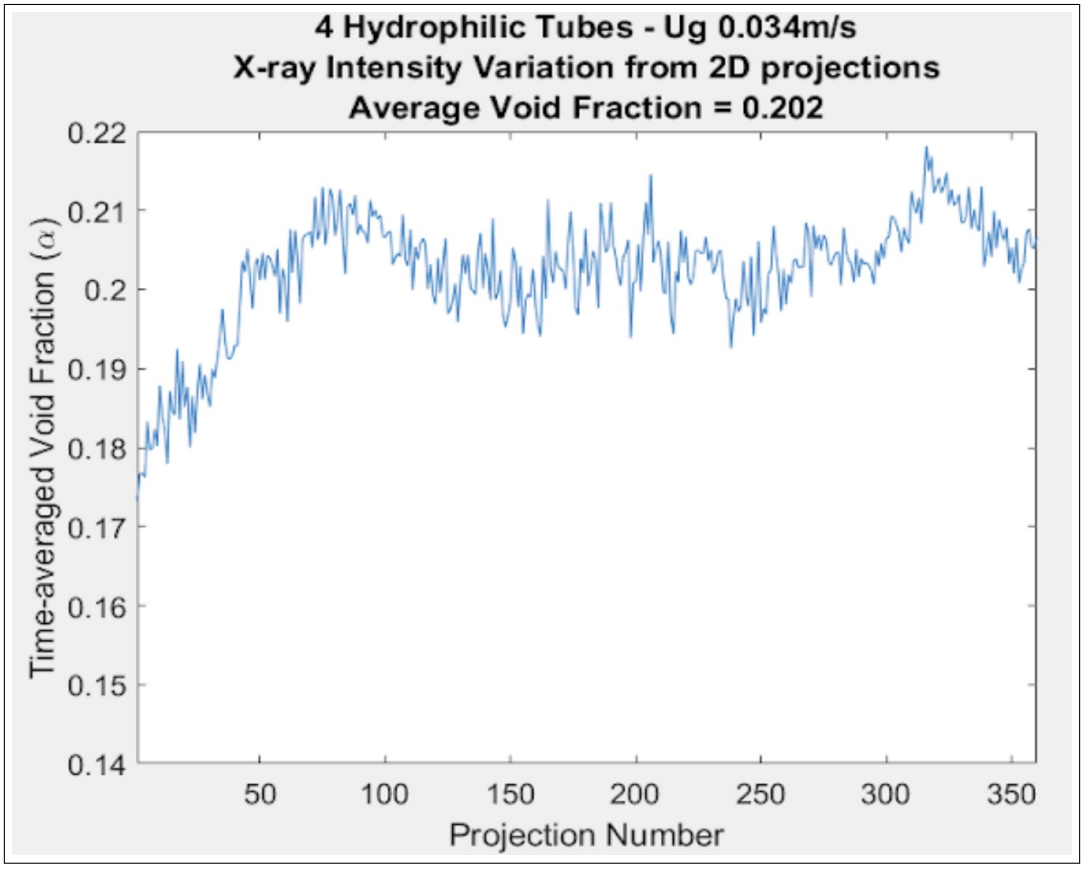

Figure 10.31: Void Fraction measurement for the hydrophilic case calculated by X-ray Intensity Fields for Mixture, Water and Air - Ug = 0.034m/s

a hydrophilic tube. Four WMS were positioned in pairs referenced as Level 1 and Level 2. Level 1 is the WMS pair under the PVC tubes. Level 2 is the WMS pair above the PVC tubes. Figure 10.36 displays the time-averaged void fraction calculated by WMS and height differences for air injection rate ranging from 1 to 19SLPM.

Figure 10.37 displays the time-averaged void fraction measured by the four wire mesh sensors for a superficial gas velocity of 0.034m/s. The bottom pair of WMS display the lateral void fraction distribution prior to entering the geometric constraints of the four PVC tubes. The top pair of WMS display the lateral void fraction measurements right above the four PVC tubes. In this case, we notice a reduction in void fraction as the bubble encounter interference introduced by the confined geometric area around the tubes and the superhydrophobic-coated PVC tube. The Level 2 Bottom WMS is positioned 10mm above the PVC tubes which is our best measurement of lateral distribution around the PVC tubes. The Level 2 Top WMS gives lateral distribution but is not adequate to identify the individual

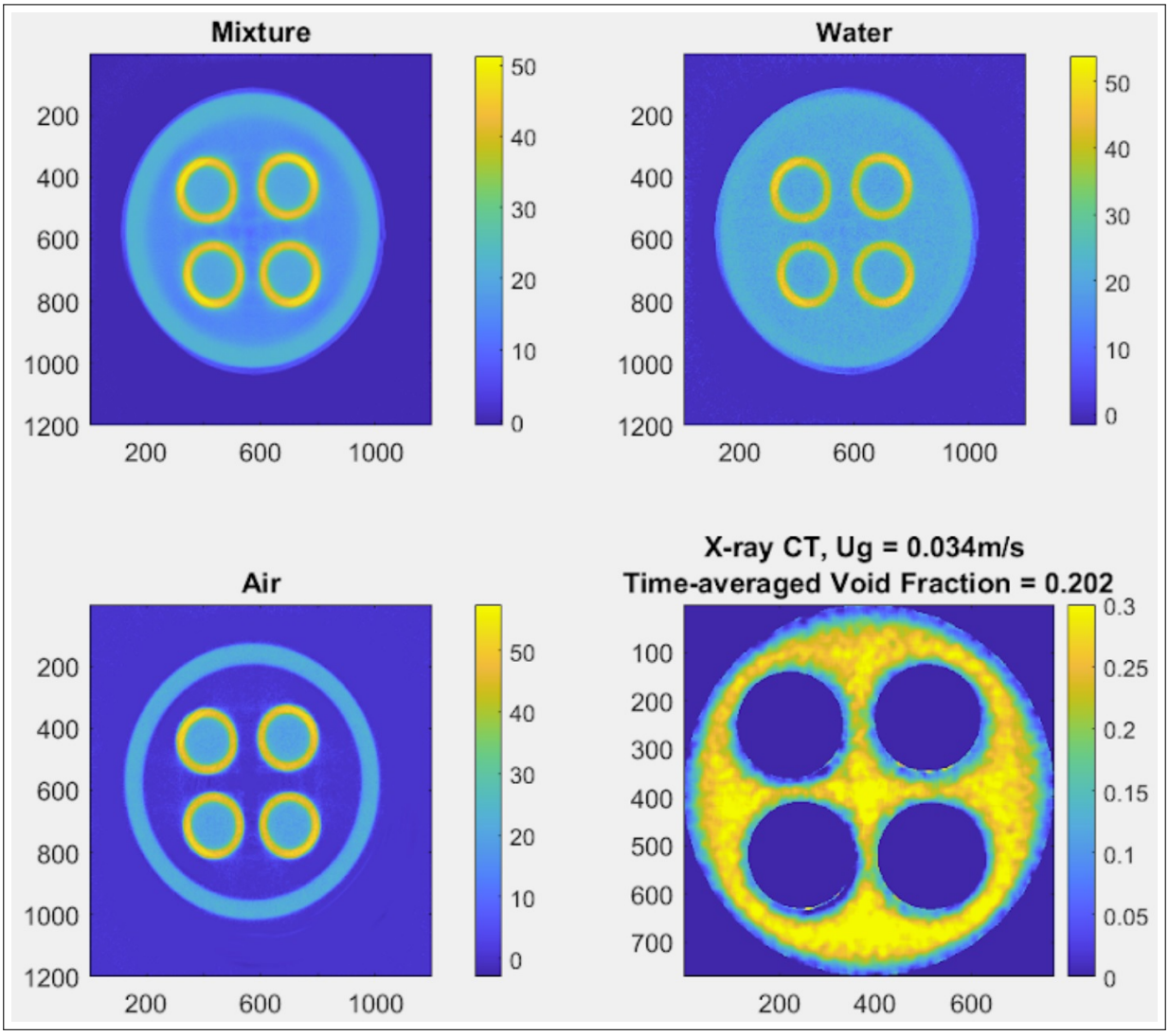

Figure 10.32: X-ray CT Reconstruction for Mixture, Water and Air. Bottom Right: Void Fraction measurement for the hydrophilic case calculated by X-ray Computed Tomography Reconstruction - Ug = 0.034m/s

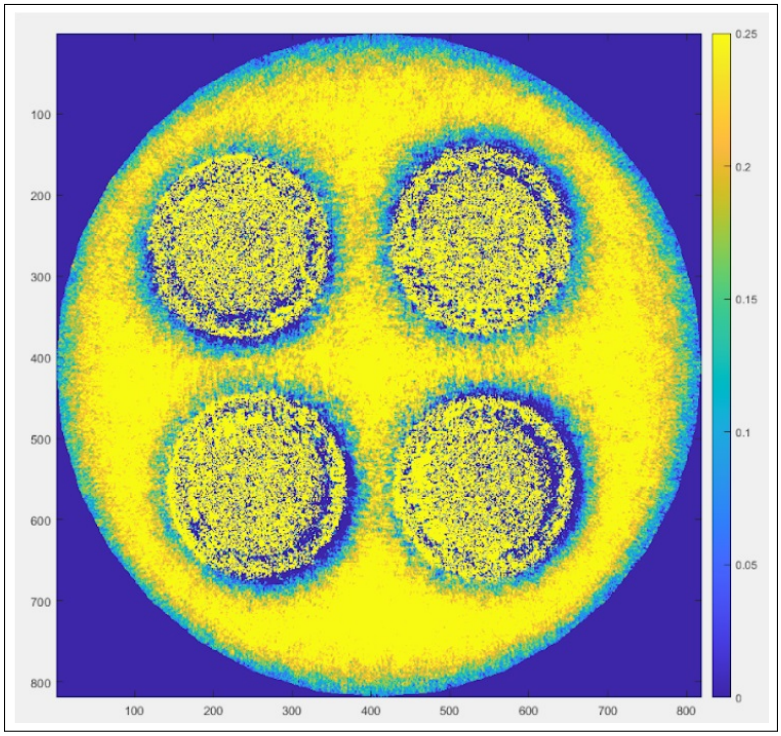

Figure 10.33: Time-averaged Void Fraction measurement for the hydrophilic case calculated by X-ray Computed Tomography Reconstruction (no mask and no filter applied) - Ug = 0.034m/s

effects of the tubes on a particular void area since it is 40mm above the PVC tubes. The WMS Void Fraction calculated for Table 10.2 was gathered by taking the average of the void fractions from the Level 1 Top WMS and the Level 2 Bottom WMS. This is an approximate void fraction used to validate the X-ray CT void fraction calculations considering that the X-ray CT scan is in the center of both the Level 1 Top WMS and Level 2 Bottom WMS.

We used the varying X-ray intensity fields for the three mediums (mixture, water and air) at each frame to calculate the time-averaged void fraction for the hydrophilic case. The intensity field for the mixture is averaged at each angle from the collected 35 frames. Figure 10.38 displays the time-averaged void fraction calculated at each angle using Equation 9.3. The average of the 360 time-averaged void fraction is 0.111, which is used as the time-averaged void fraction for the entire measurement run.

We used the X-ray Computed Tomography reconstruction for the three mediums and Equation 9.4 to render a two-dimensional time-averaged void fraction displayed in the lower right of Figure 10.39. This reconstructed time-averaged void fraction yielded a void fraction of 0.114.

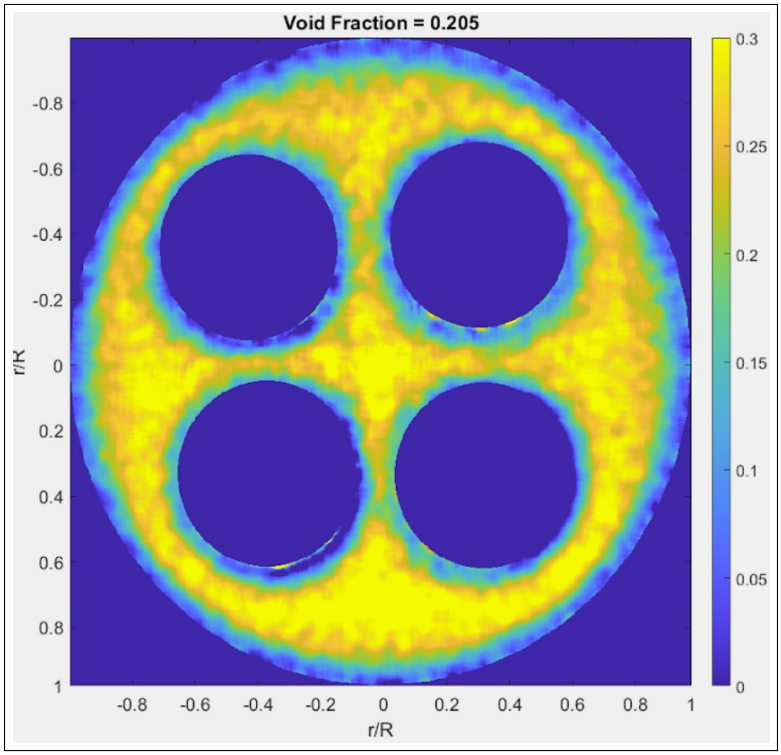

Figure 10.34: Time-averaged Void Fraction measurement for the hydrophilic case calculated by X-ray Computed Tomography Reconstruction (mask-included and medfilt2 applied) - Ug = 0.034m/s

The time-averaged void fraction measurement from X-ray computed tomography is displayed in Figure 10.40 with all areas exterior to the inner wall omitted. In order to calculate the time-averaged void fraction from this graph we need to eliminate the reconstructed PVC tubes so their void fraction values are not included in the calculation. Figure 10.41 displays the same void fraction reconstruction with mask implemented for the PVC tubes and median filter applied to eliminate salt and pepper noise. The time-averaged void fraction, calculated by taking a mean of all the void fraction values contained within the bubble column and external to the PVC tubes, is 0.114.

Figure 10.42 displays both the X-ray CT Void Fraction reconstruction and the Level 2 Bottom WMS measurement. This figure displays the strength of both measurement techniques. The X-ray CT reconstruction gives a more accurate average void fraction than WMS as validated by height difference and X-ray intensity projection variation void fraction calculations. The intrusion of the WMS on the flow and positioning complexity of the WMS above the tubes suggest that X-ray CT provides a more accurate assessment of localized time-averaged void fraction around the SHS tube.

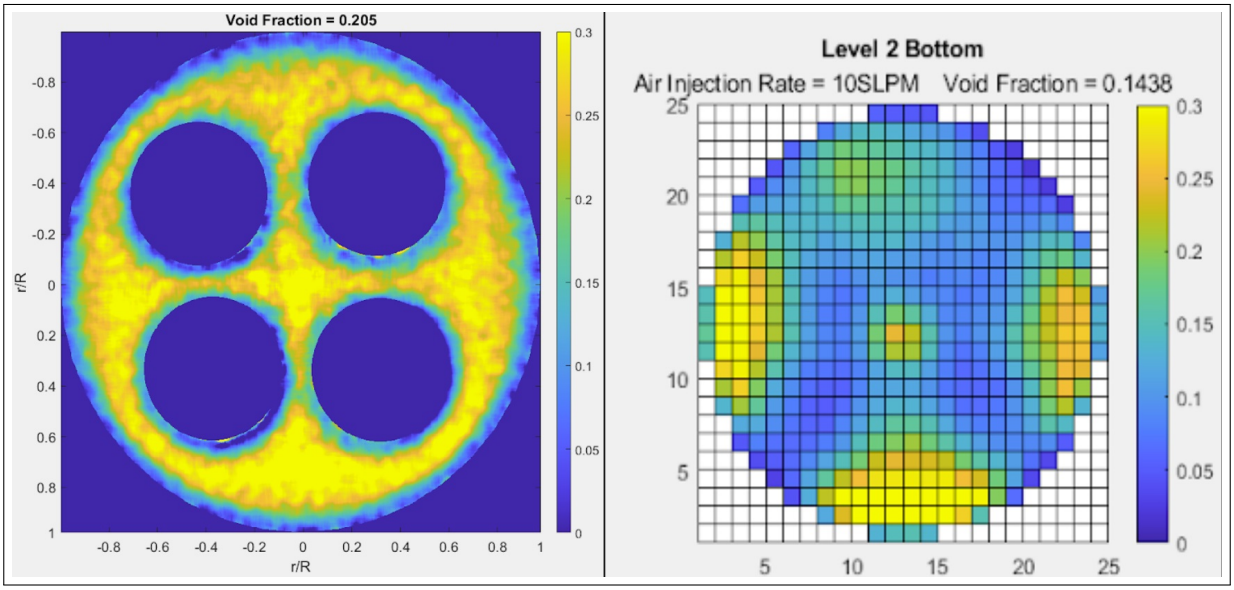

Figure 10.35: Time-averaged Void Fraction measurement for the hydrophilic case calculated by X-ray Computed Tomography Reconstruction and Level 2 Bottom Wire Mesh Sensor - Ug = 0.034m/s

We also realized that increased iterations of the SIRT algorithm is not necessarily helpful in these dynamic situations. A large number of iterations is helpful for improved resolution in static environments. In our dynamic case, multiple iteration add noise to the reconstruction so we evaluated the best iterations to produce the required resolution of the the system. Figure 10.43 displays the best resolved reconstructions from a reduced number of iterations applied to the ASTRA toolbox SIRT algorithm.

Evaluation of Time-averaged Void Fraction, Bubble Velocity and Bubble Diameter for Four PVC Tubes (with and without substituted SHS-coated PVC Tube)

Using the Wire Mesh Framework Software, we measured mean bubble diameter across the entire measurement frames and displayed the results in a histogram shown in Figure 10.44. Figure 10.44a shows the mean diameter for the case of four hydrophilic tubes. Figure 10.44b shows the histogram for the mean bubble diameter for the case with a substituted SHS-coated PVC tube. We can clearly see that the bubble regime is no longer homogeneous and there are two consistent bubble diameters observed. While the hydrophilic case has a mean bubble diameter of 8mm, the case with the superhydrophobic tube has a mean bubble diameter of 23mm and 27mm. In this case you have larger bubbles forming and smaller

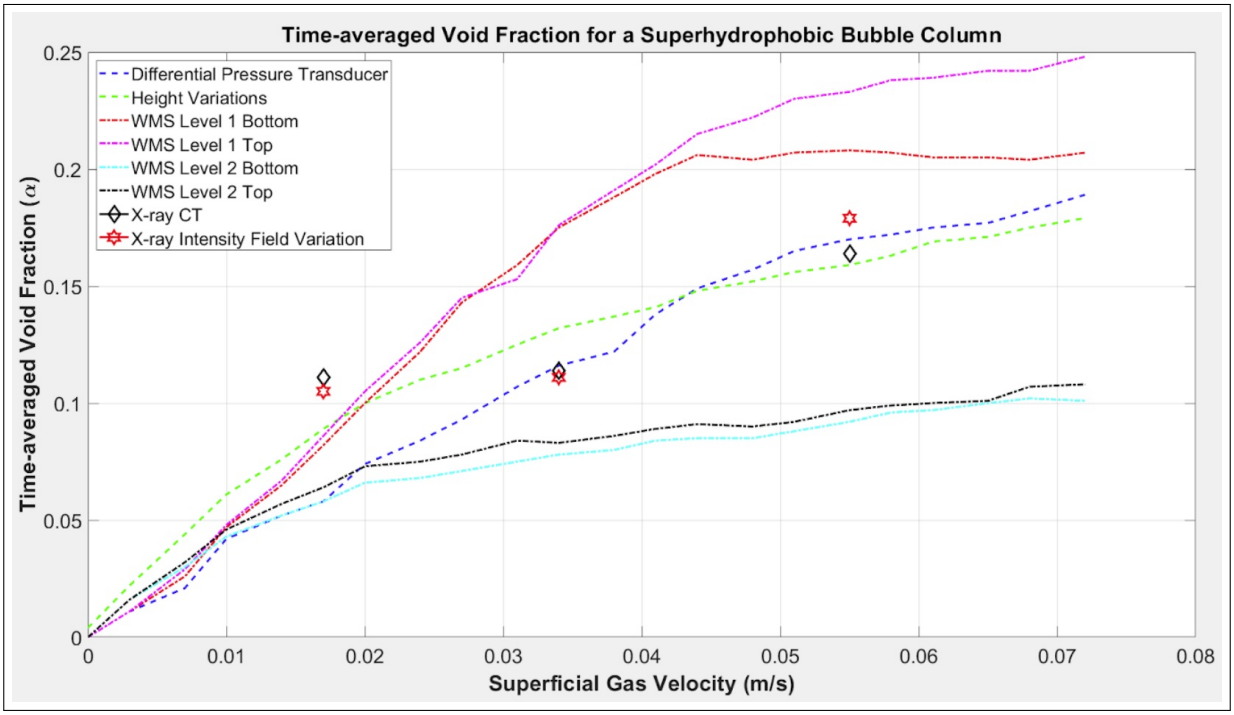

Figure 10.36: Void Fraction measurements for the superhydrophobic case calculated by all four WMS and bubble column height difference

bubbles also rising. The flow is no longer in the bubbly flow regime but has transitioned to churn-turbulent flow.

We evaluated the bubble diameter at variable air injections to see how the bubble diameter changes with increased superficial gas velocity. Figure 10.45 displays the mean bubble diameter histograms for cases at 6, 10 and 15SLPM air injection. Here we see that the bubble regime still remains homogeneous but the diameter size increases from 5mm at 6SLPM to 10mm at 15SLPM. Figure 10.46 displays the mean bubble diameter for the case with a substituted superhydrophobic-coated PVC tube at 6, 10, and 15SLPM air injection. The mean bubble diameter in all cases is larger than in the hydrophilic case with values reaching 17mm diameter to a 39mm diameter at higher air injection rates. We also notice that the histogram for the superhydrophobic case reveals the bubble regime is heterogeneous.

We compared the average velocity for the system. Figure 10.47 provides the time-averaged velocity results calculated from MATLAB's cross correlation functions. The average bubble velocity for the superhydrophobic case in 0.54m/s across the entire WMS. The average bubble velocity for the hydrophilic case is 0.20m/s with localized pockets reaching velocity values of approximately 0.50m/s.

Figure 10.48 displays the time-averaged void fraction measurements for all four WMS

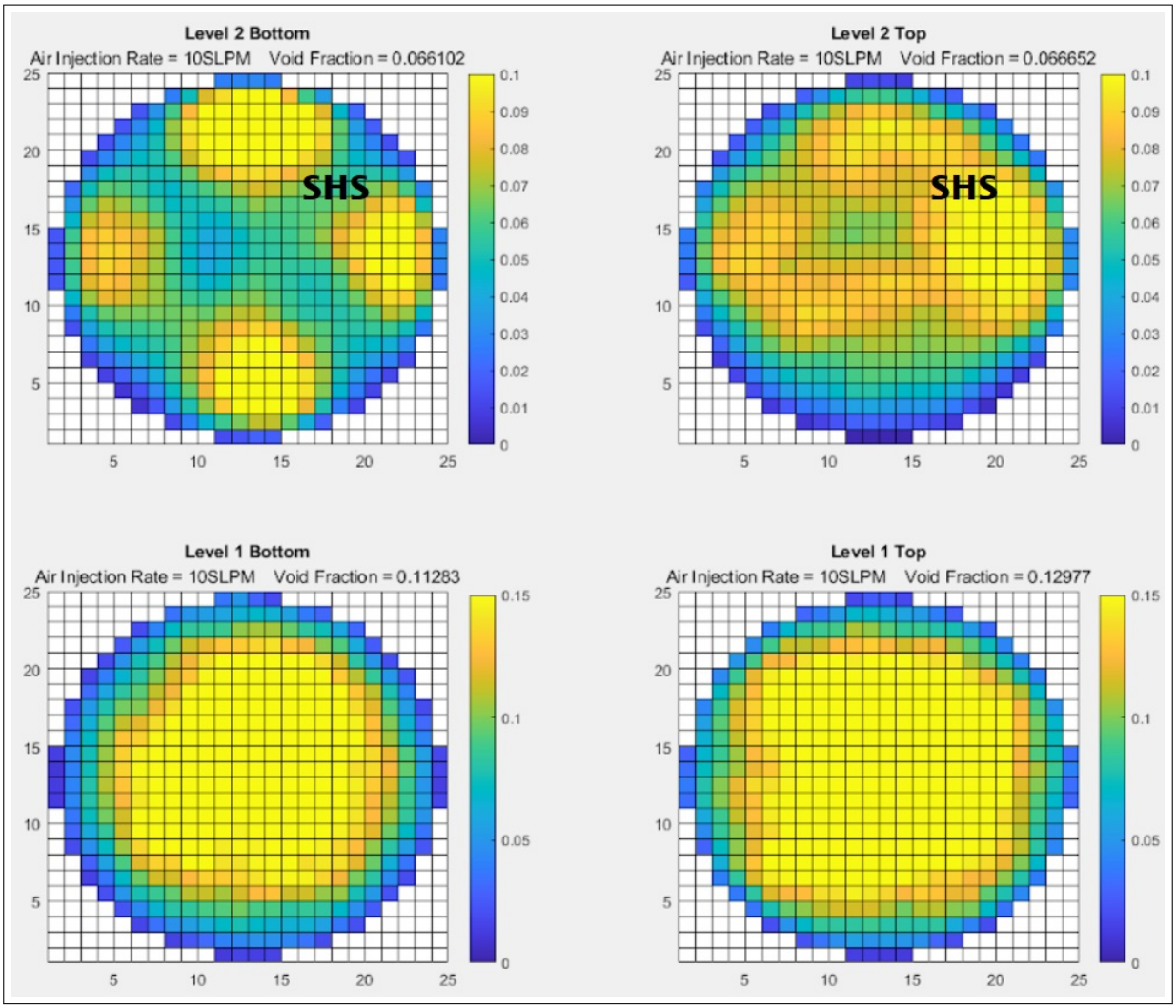

Figure 10.37: Void Fraction measurements for the superhydrophobic case calculated by all four WMS and bubble column height difference - Ug = 0.034m/s

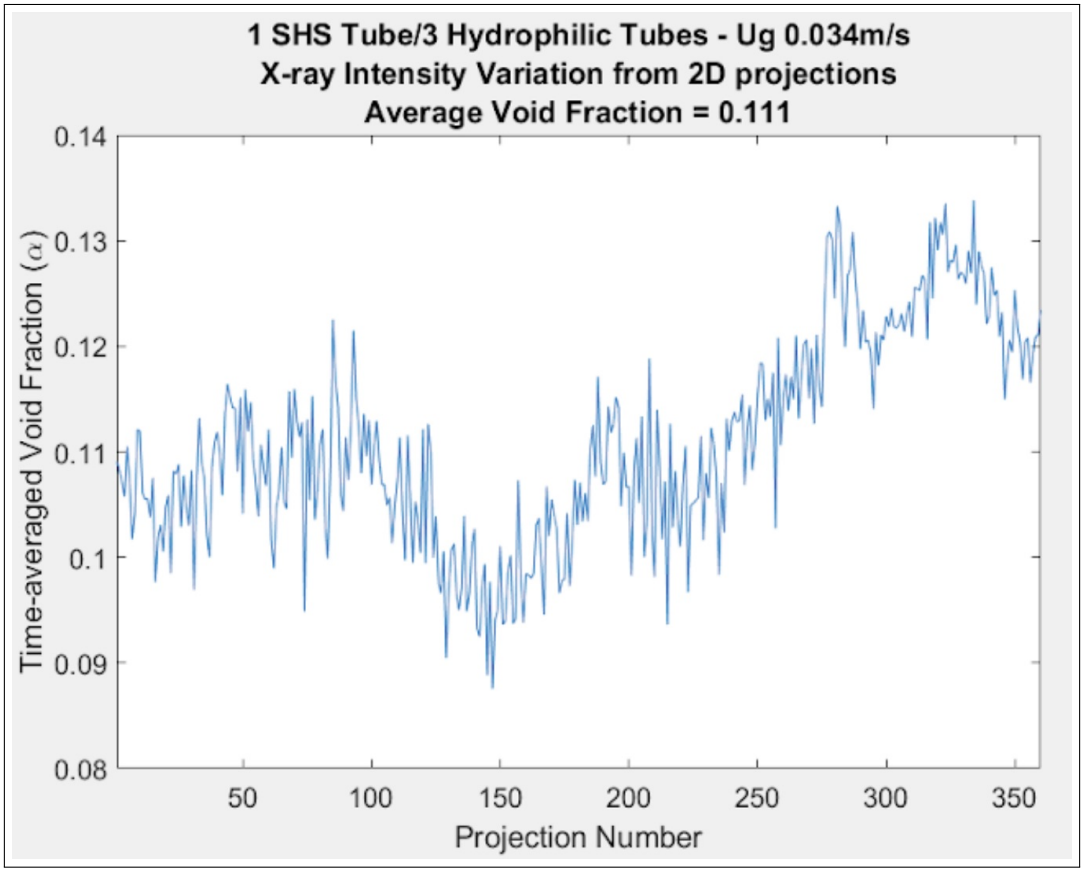

Figure 10.38: Void Fraction measurement for the superhydrophobic case calculated by X-ray Intensity Fields for Mixture, Water and Air - Ug = 0.034m/s

in both cases. The Level 2 WMS for hydrophilic cases show void fraction values that are twice the values of those provided in the superhydrophobic case. We notice that the bubble dynamics caused by the heterogeneous case also affects the bubble dynamics below the four PVC tubes, as depicted in the lower void fraction values provided in the Level 1 WMS.

Figure 10.49 displays the X-ray CT reconstruction for time-averaged void fraction for both cases. Overall, the superhydrophobic-coated PVC tube reduces total average void fraction for the system and also lowers localized void fraction around the simulated fuel rods by concentrating the higher void areas around the superhydrophobic-coated simulated rod. Figure 10.50 displays an X-ray CT reconstruction of time-averaged void fraction for half the superficial gas velocity of Figure 10.49. This reconstruction shows a definitive concentration of larger void areas around 75% of the SHS-coated tube. The average lateral void fractions are similar but the X-ray CT reconstruction is spatially resolved to show the differences in localized void fractions that may not be observed using our other measurement techniques.

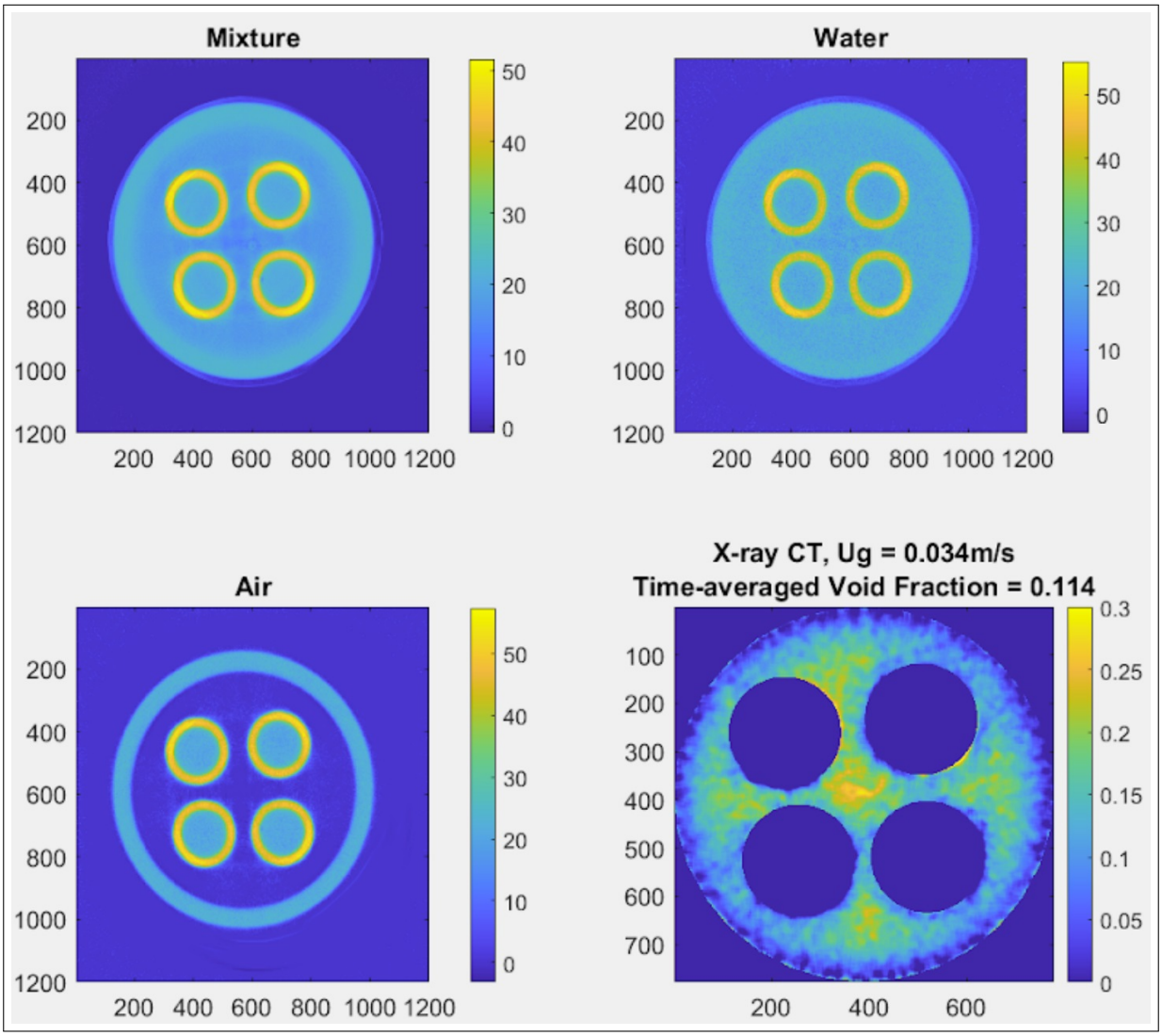

Figure 10.39: X-ray CT Reconstruction for Mixture, Water and Air. Bottom Right: Void Fraction measurement for the superhydrophobic case calculated by X-ray Computed Tomography Reconstruction - Ug = 0.034m/s

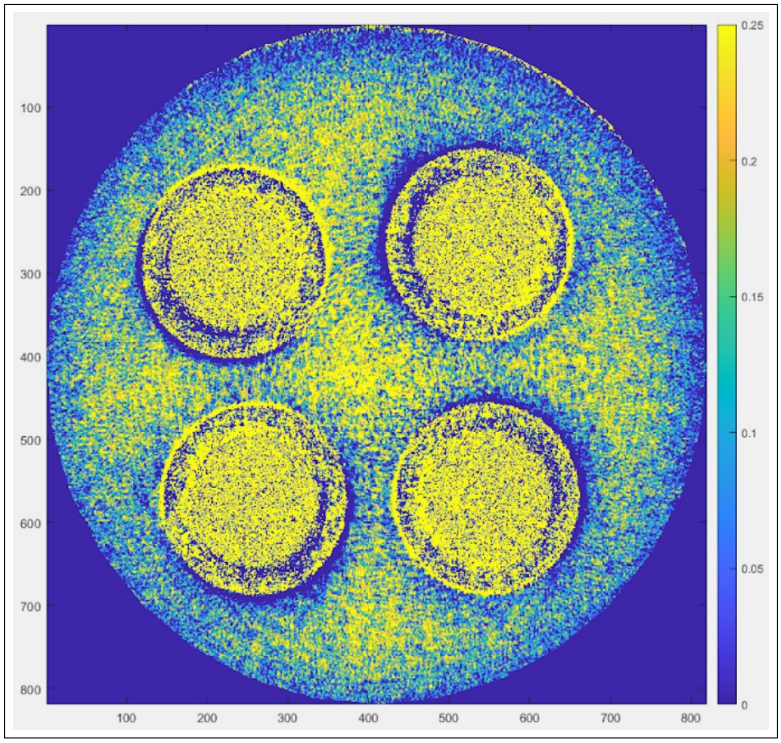

Figure 10.40: Time-averaged Void Fraction measurement for the superhydrophobic case calculated by X-ray Computed Tomography Reconstruction (No Mask) - Ug = 0.034m/s

Figure 10.51 is a still image of the SHS-coated tube in the system with bubble rising along the vertical tube. Figure 10.52 is the same still image but the figure has been modified to only show the edge finder feature using ImageJ image processing software. You can notice that there are less small bubbles rising along the SHS-coated tube, but a larger presence of large bubbles caused by coalescing that happened lower on the SHS-coated tube. If you look closely at the edge finder, you can notice that it captures some of the curvature of the larger bubbles although not completely because of interference with smaller bubbles.

Figures 10.53 and 10.54 show time-averaged void fraction measurements for the techniques discussed to include, Differential Pressure sensors, Wire Mesh Sensors, Height variation, X-ray Intensity variation and X-ray Computed Tomography. The X-ray measurements are displayed for a superficial gas velocity of 0.034m/s. Figure 10.52 shows differential pressure sensor void fraction measurements that rise much higher than the void fractions for all other measurements. Since the area is more constrained between the sensor ports and the PVC tubes, we suspect that the measured pressures may vary larger than the other sensors. As expected, Level 2 WMS data is lower than the Level 1 WMS since the four PVC tubes change the dynamics of the bubbles by spreading the bubbles more in line than lateral dis-

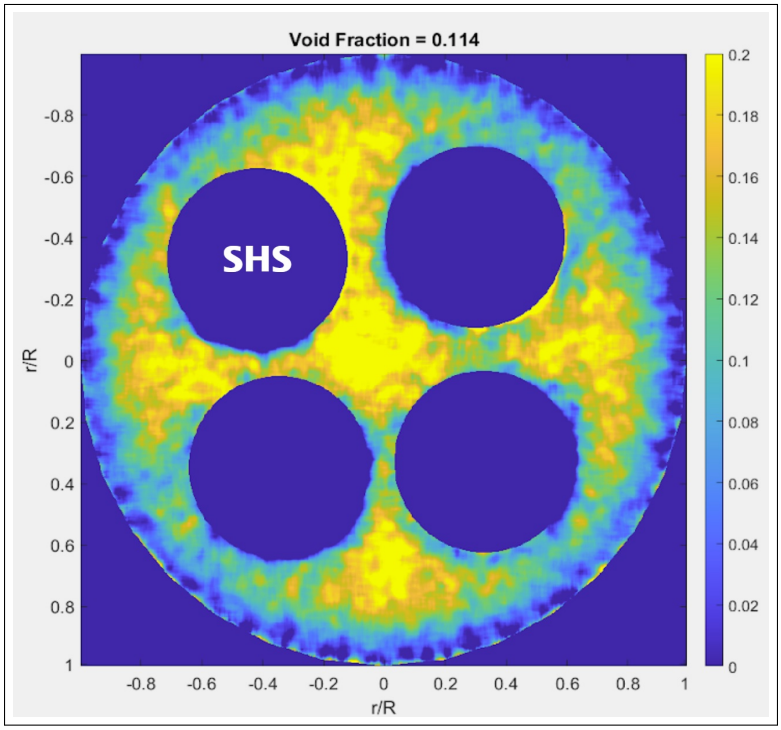

Figure 10.41: Time-averaged Void Fraction measurement for the superhydrophobic case calculated by X-ray Computed Tomography Reconstruction (mask included and medfilt2 applied) - Ug = 0.034m/s

tribution. Height variation measurements follow as similar slope and between both WMS pairs. We report Void Fraction as an average of both pairs so we can evaluate this Void Fraction against the Void Fraction calculated from the X-ray measurement, which focuses on the middle column between the WMS pairs.

Both Figures 10.52 and 10.53 have the same vertical and horizontal scale so we can show the noticeable contribution 1 superhydrophobic-coated PVC tube substitution can do to a change in bubble dynamics. You can see the Void Fraction measurement reductions between the two WMS pairs. The Void Fraction WMS Sensor-Level 2 Top for the hydrophilic case reaches a maximum of 0.220, but the Void Fraction WMS Sensor-Level 2 Top for the superhydrophobic case reaches a maximum of 0.120. The differential pressure sensor and height measurements line up along the average of each WMS pair. The X-ray CT also lines up along the center of the WMS pairs. This gives us confidence in our differential pressure measurements and height measurements. It is interesting to spend some time on why the upper WMS pair shows a very low estimate of void fraction. The bubbles coalesce and elongate along the PVC tube which may explain why the upper WMS do not capture the

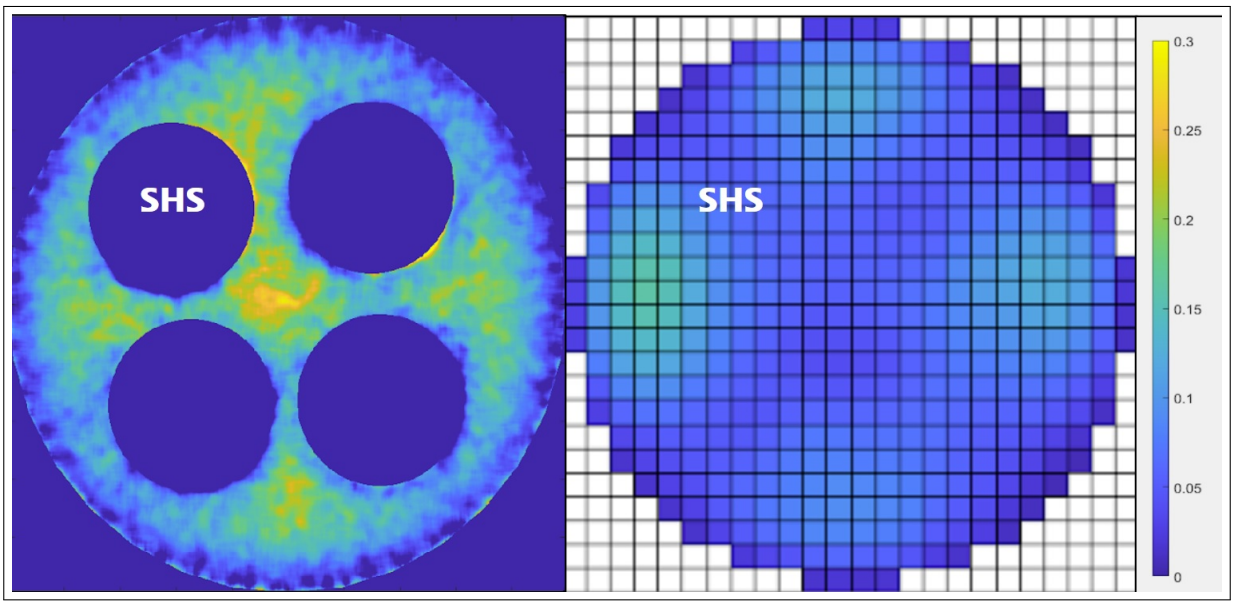

Figure 10.42: Time-averaged Void Fraction measurement for the superhydrophobic case calculated by X-ray Computed Tomography Reconstruction and Level 2 Bottom Wire Mesh Sensor - Ug = 0.034m/s

breadth of the lateral distribution. The large ellipsoid void has a major axis in the vertical direction and that may cause a lower recorded lateral void area as the bubbles come out of the rod bundle. We will showcase our evaluation of geometric constraints on the rod bundle and find where the superhydrophobic coating plays a critical role.

10.3 Relationship between geometric constraints, superhydrophobicity and void fraction

When the superhydrophobic surface is submerged, the air on the surface is no longer connected to the atmosphere and the Cassie state durability is limited to hydrostatic pressure and dissolution of gas in water. As the pressure in the entrapped gas increases with hydrostatic pressure, the gas starts to dissolve in water and requires a source of replenishment to maintain its state. The gas may also be depleted based on the saturation conditions of the water. Bubbles dispersed in a liquid and flowing by the superhydrophobic surface can be used to replenish the air on the superhydrophobic surface to maintain the Cassie state. The bubbles must meet a particular criterion to merge with the air layer [42].

Figure 10.55 displays a qualitative depiction of bubble interaction with the air layer along the SHS-coated tube. We want to evaluate void fraction calculations for varying

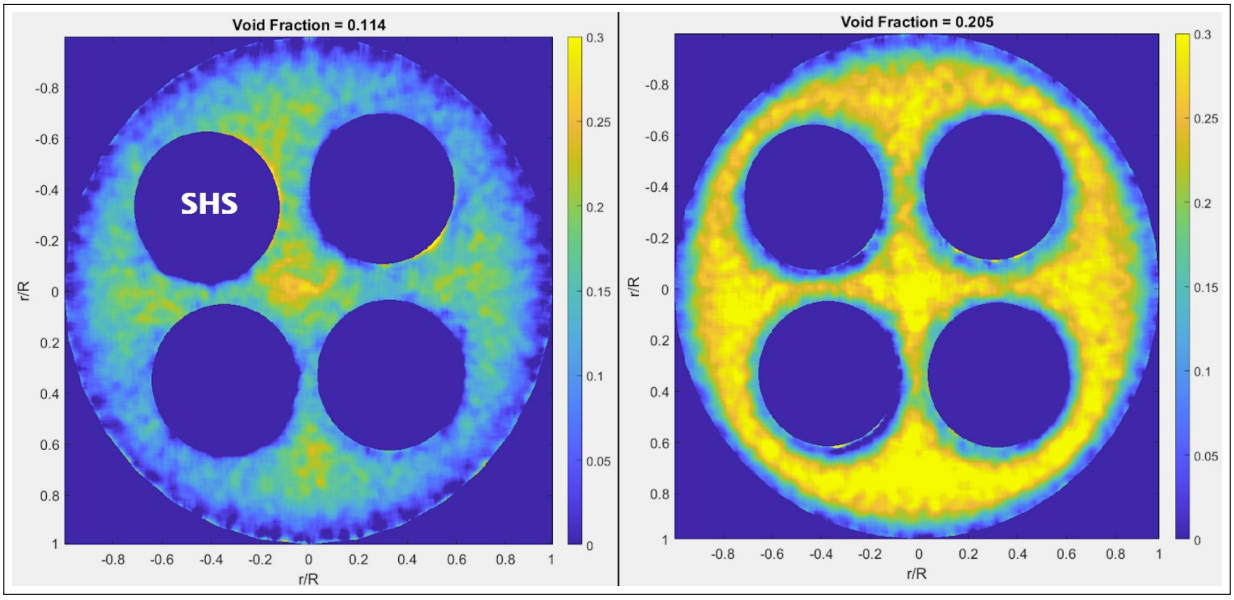

Figure 10.43: Time-averaged Void Fraction measurement for the superhydrophobic (Right) and hydrophilic (Left) cases calculated by X-ray Computed Tomography Reconstruction - Ug = 0.034m/s

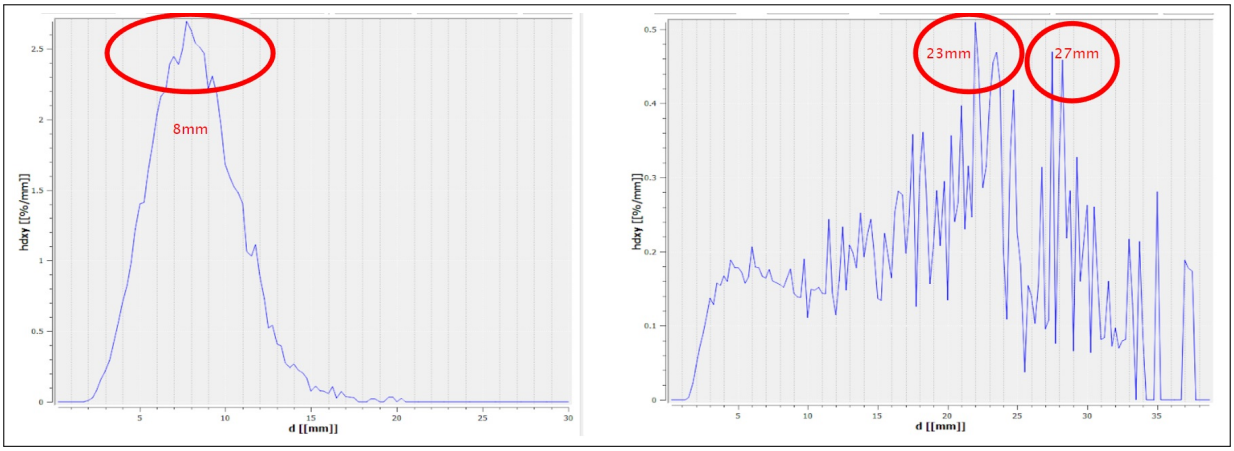

Figure 10.44: Mean Bubble Diameter for a) hydrophilic cases and b) superhydrophobic case calculated by Wire Mesh Sensor Framework - Ug = 0.034m/s

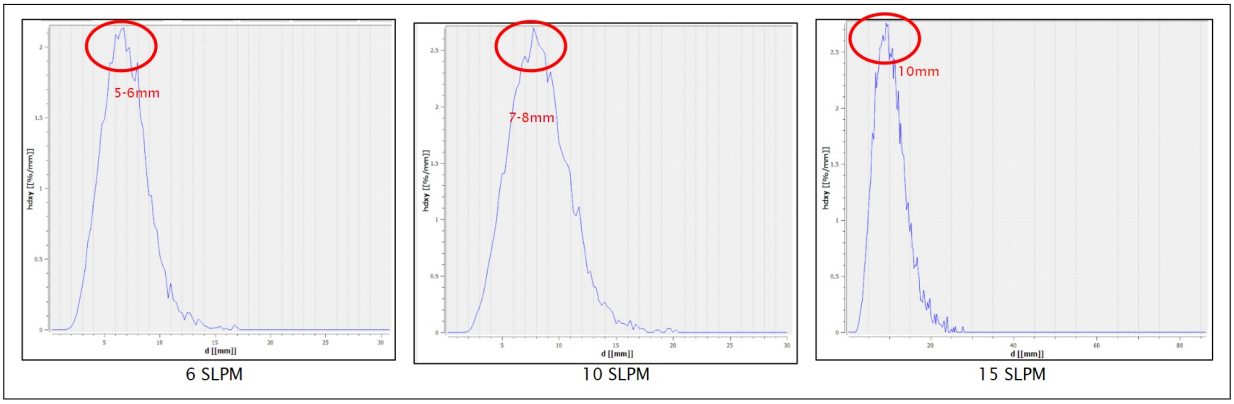

Figure 10.45: Mean Bubble Diameter for the hydrophilic case calculated by Wire Mesh Sensor Framework for variable air injections

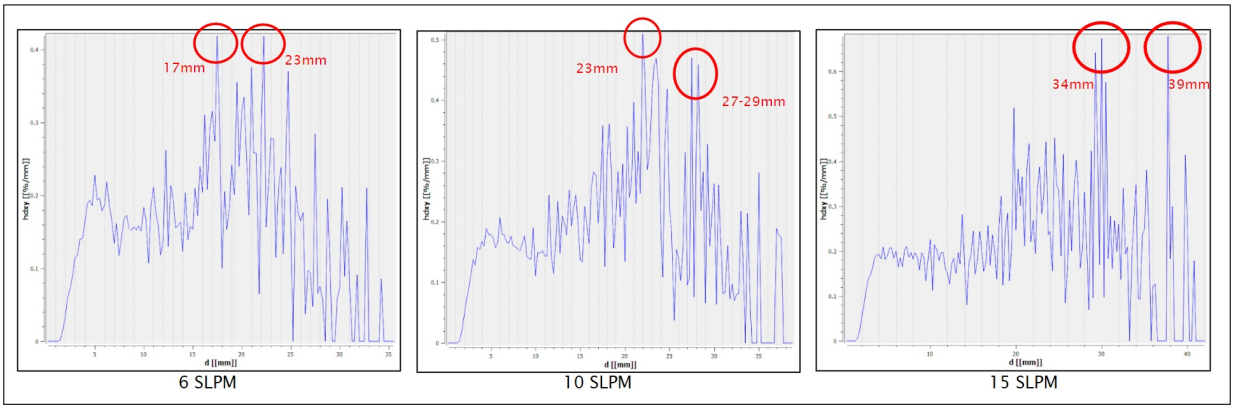

Figure 10.46: Mean Bubble Diameter for the superhydrophobic case calculated by Wire Mesh Sensor Framework for variable air injections

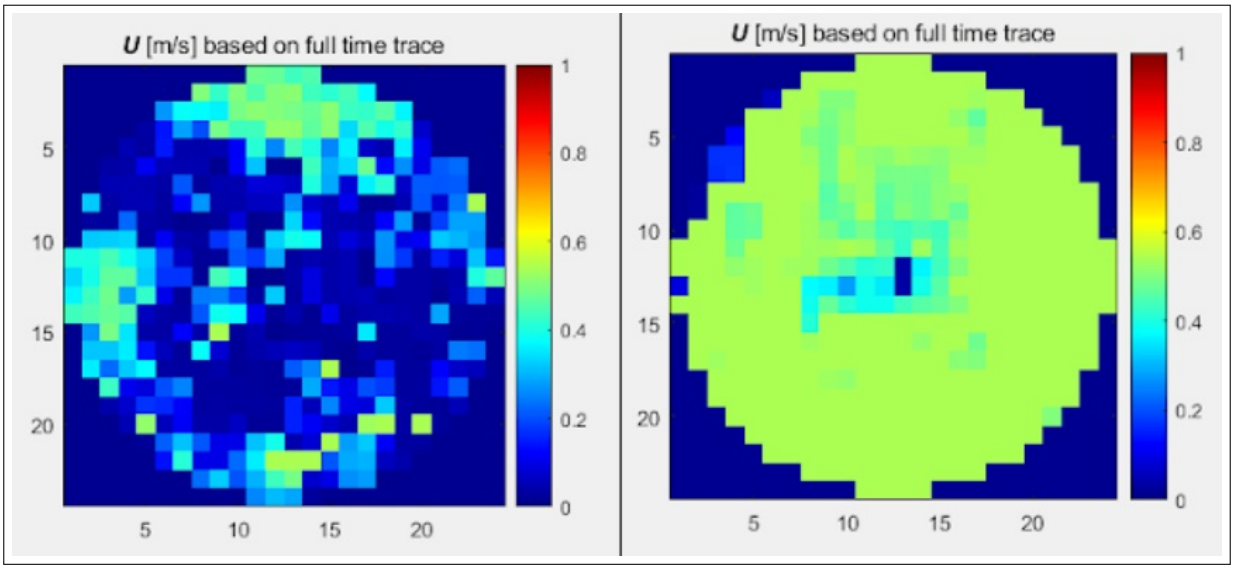

Figure 10.47: Mean Bubble Velocity for a) hydrophilic case and b) superhydrophobic case calculated by MATLAB cross-correlation function

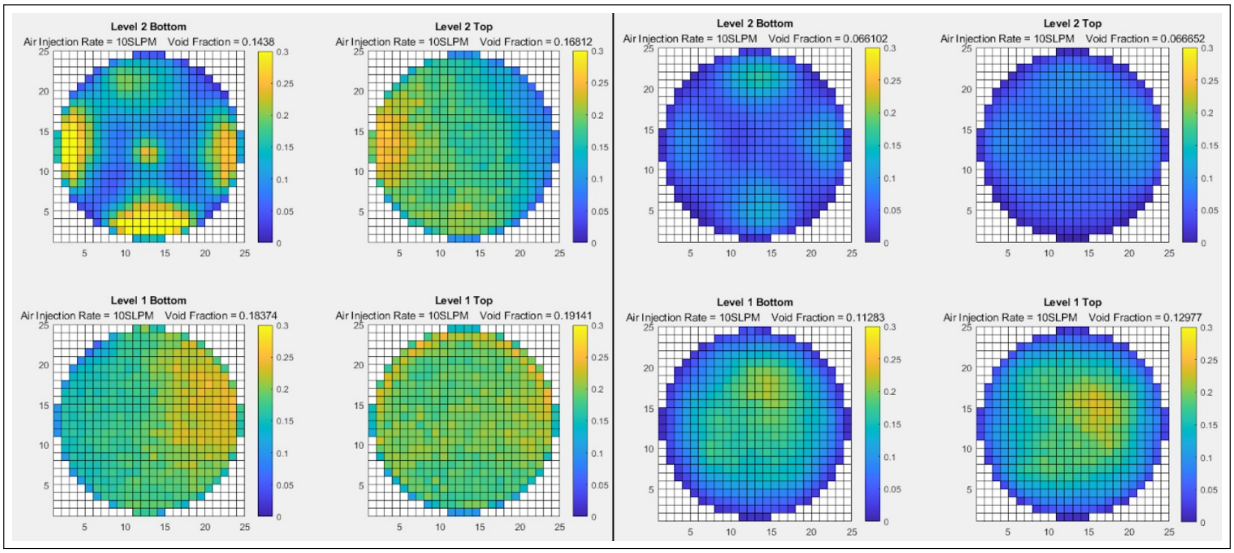

Figure 10.48: Time-averaged Void Fraction WMS measurements for the hydrophilic (Left) and superhydrophobic (Right) cases

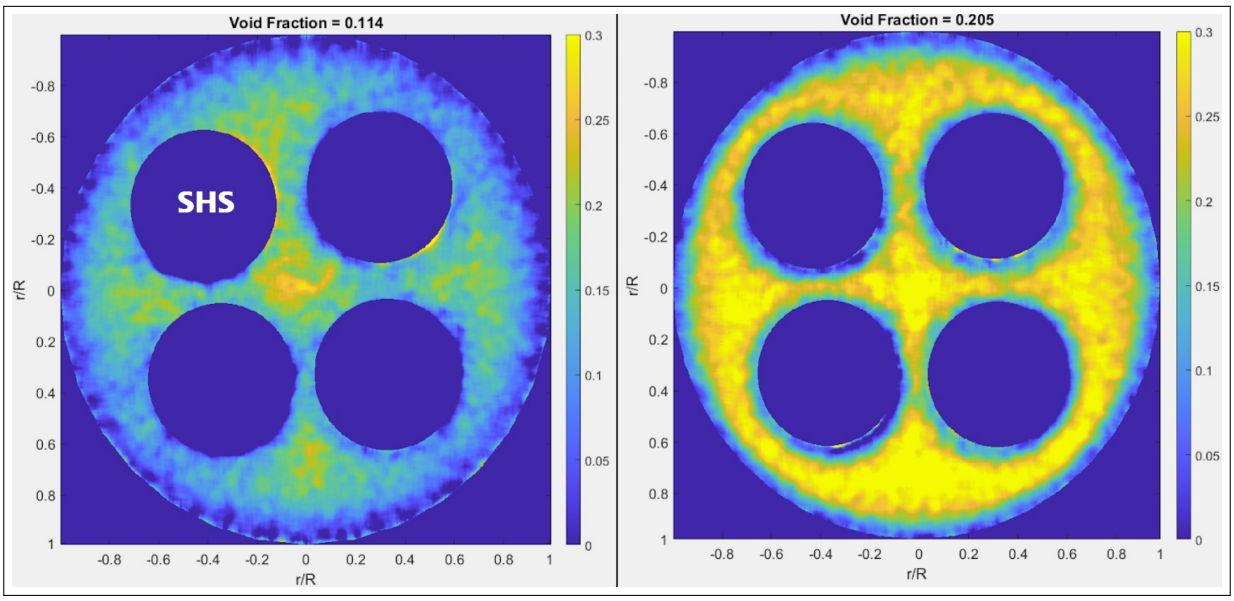

Figure 10.49: Time-averaged Void Fraction X-ray CT Reconstruction measurements for the hydrophilic (Left) and superhydrophobic (Right) cases for Ug=0.034m/s

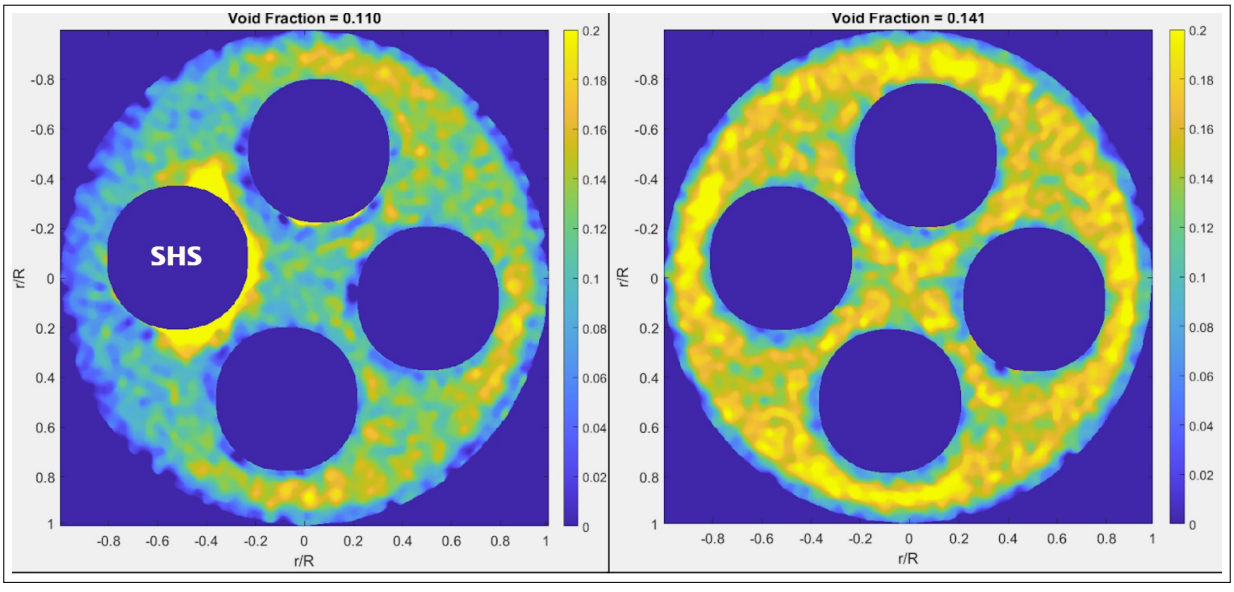

Figure 10.50: Time-averaged Void Fraction X-ray CT Reconstruction measurements for the hydrophilic (Left) and superhydrophobic (Right) cases for Ug=0.017m/s

Figure 10.51: SHS-Tube Immersed in Water-filled Bubble Column Still Photo (Color Photo)

Figure 10.52: SHS-Tube Immersed in Water-filled Bubble Column Still Photo (Edge Finder)

geometric arrangement of the rod bundle to gain an understanding whether geometry or superhydrophobicity cause the dramatic changes in time-averaged void fraction. We want to determine at what superficial gas velocity, the gas holdup is significantly impacted by geometric constraints provided by the rod bundle configuration. Figure 10.56 displays the Level 2 Top sensor wire mesh sensor measurement for several geometric cases to include the following:

- bubble column with no tubes
- bubble column with 1 SHS tube
- bubble column with 1 non-SHS tube
- bubble column with 1 SHS and 1 non-SHS tube
- bubble column with 2 non-SHS tubes
- bubble column with 1 SHS and 2 non-SHS tubes
- bubble column with 3 non-SHS tubes
- bubble column with 1 SHS and 3 non-SHS tubes

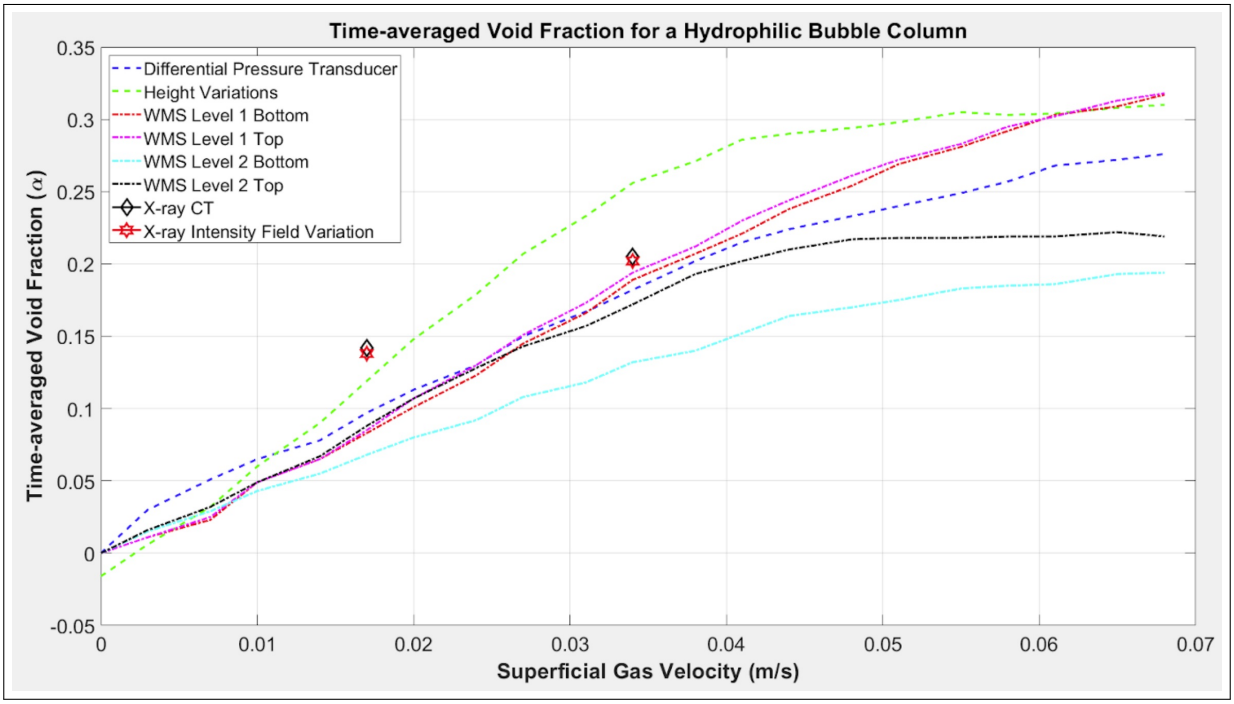

Figure 10.53: Time-averaged Void Fraction measurements for the hydrophilic from all measurement techniques

- bubble column with 4 non-SHS tubes

If you refer to Figure 10.56, we can see how the 4 non-SHS rod configuration has a significant effect on gas holdup pass a superficial gas velocity of 0.025m/s. We suspect that this is die to the elongation of the bubbles as their major axis shifted to vertical and therefore measuring shorter for the horizontal void fraction measurement of the WMS. In a four rod bundle configuration, the superhydrophobic coating has the least effect. This may be partially due to the less exposure the bubbles have to the surface, since three other tubes block the bubbles from reaching the SHS-tube. In the comparison case between 1 SHS tube and 1 non-SHS tube, the variation in gas holdup is solely due to the superhydrophobic coating and the effects start at a superficial gas velocity of 0.014m/s. This suggests that maximizing exposed area of superhydrophobicity will have a variable effect on void fraction. The figure also suggests that there is a relationship between void fraction and geometrical constraints that become significant once the volume ratio (tube volume to bubble column volume) and bubble density reach a particular point.

Figure 10.57 only displays the 1 SHS-tube, 1 non-SHS tube and the empty bubble column. This is provided to give a clear concise plot of the scenario with the largest change

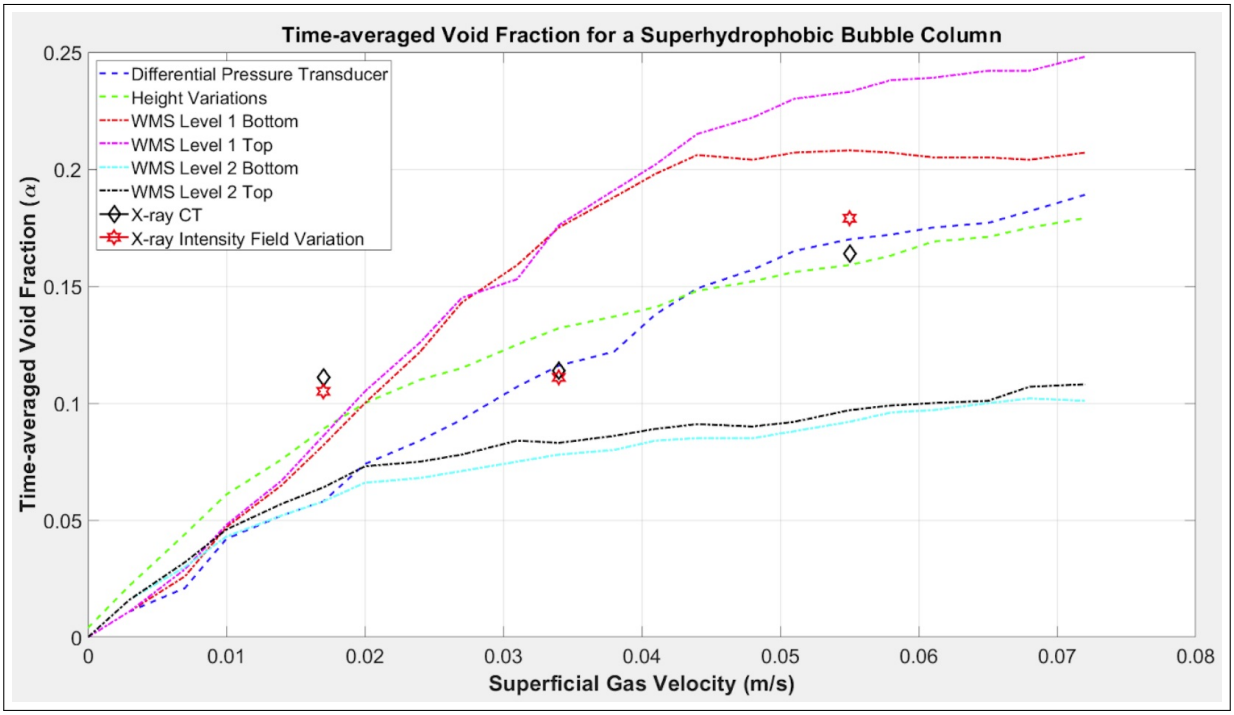

Figure 10.54: Time-averaged Void Fraction for the superhydrophobic-PVC tube substitution from all measurement techniques

in void fraction due to changing the surface from hydrophilic to superhydrophobic. Figure 10.58 shows the scenarios with different rod configurations and a single SHS-coated rod. Figure 10.59 displays the time-averaged void fraction measurements for variable configurations with PVC tubes, with and without SHS-coatings, to show how both geometric constraints and SHS coatings affect lateral void fraction distribution. These figures show how the geometric constraints affect the void fraction for an increasing superficial gas velocity but the superhydrophobic characteristic remains dominant as the leading reason for the lower void fraction values.

Further investigation, outside of this thesis, would lend itself to evaluate how viscosity along the superhydrophobic surface affects the bubble interaction. Additionally, different types of measurement techniques are required to evaluate if the void fraction is lower due to the phenomena of absorption onto the air layer to continuously replenish the air layer.

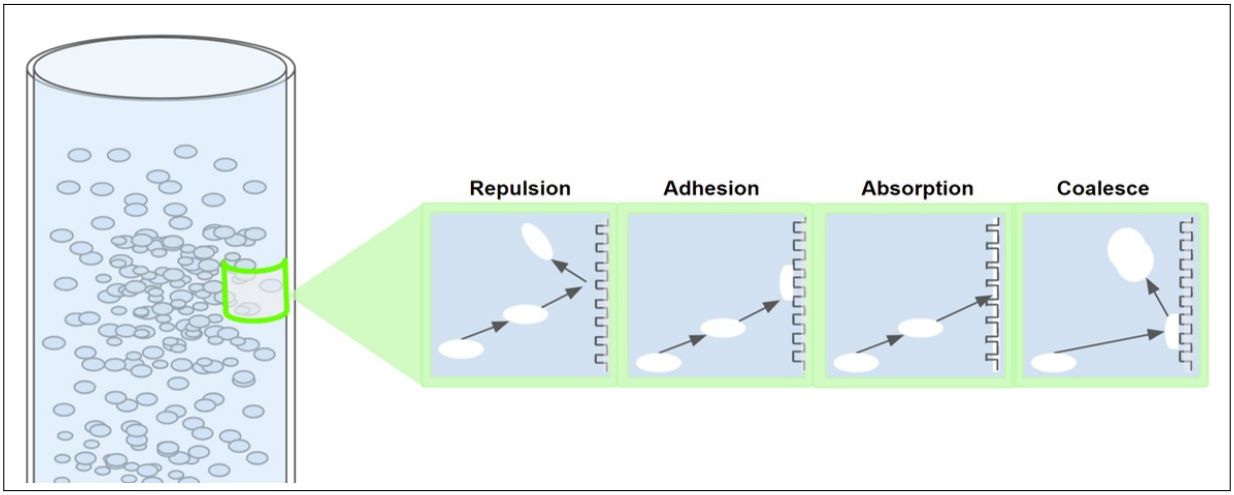

Figure 10.55: Qualitative depiction of bubble interactions with submerged superhydrophobic surfaces

10.4 Conclusions

We have discussed how pressurized water reactors operate in a single-phase flow with localized nucleation sites that recondense in the bulk liquid flow. Localized nucleation sites arise to promote convectional heat transfer to the bulk liquid. During an event of flow loss or any condition that can result in bulk liquid temperatures exceeding saturation temperatures, bubbles will form more frequently, creating a boiling casualty called Departure from Nucleate Boiling. A Departure from Nucleate Boiling condition results from the bulk liquid temperature reaching and exceeding Critical Heat Flux. Any attempt to lower the amount of vapor formation along the superheated liquid will minimize the margin to Critical Heat Flux. If a superhydrophobic-coated material is introduced into a fuel cell as a substitute to a fuel rod, the bubbles will localize to the superhydrophobic-coated tube and will likely escape faster from the flow regime, resulting in a larger margin to reach Critical Heat Flux.

Based on the characteristics of vapor bubbles in saturated and superheated systems, we used gas bubbles, which shows similar growth patterns to vapor bubbles in superheated liquids. We have shown, through advanced non-intrusive measurement techniques, how to capture the effects of superhydrophobic characteristics on localized bubble regime characteristics and bubble flow regime transitions within a simulated fuel rod assembly. We find that a single superhydrophobic-coated rod substitution, which is $\frac{1}{4}$ of our simulated fuel rod assembly, has a significant impact on void fraction reduction, resulting in a 30% reduction in gas holdup and earlier initiation of transition to churn-turbulent flow from a bubbly flow regime. These superhydrophobic characteristics may modify the bubble regime to promote larger removal of bubbles from the systems via the formation of a lower density of larger

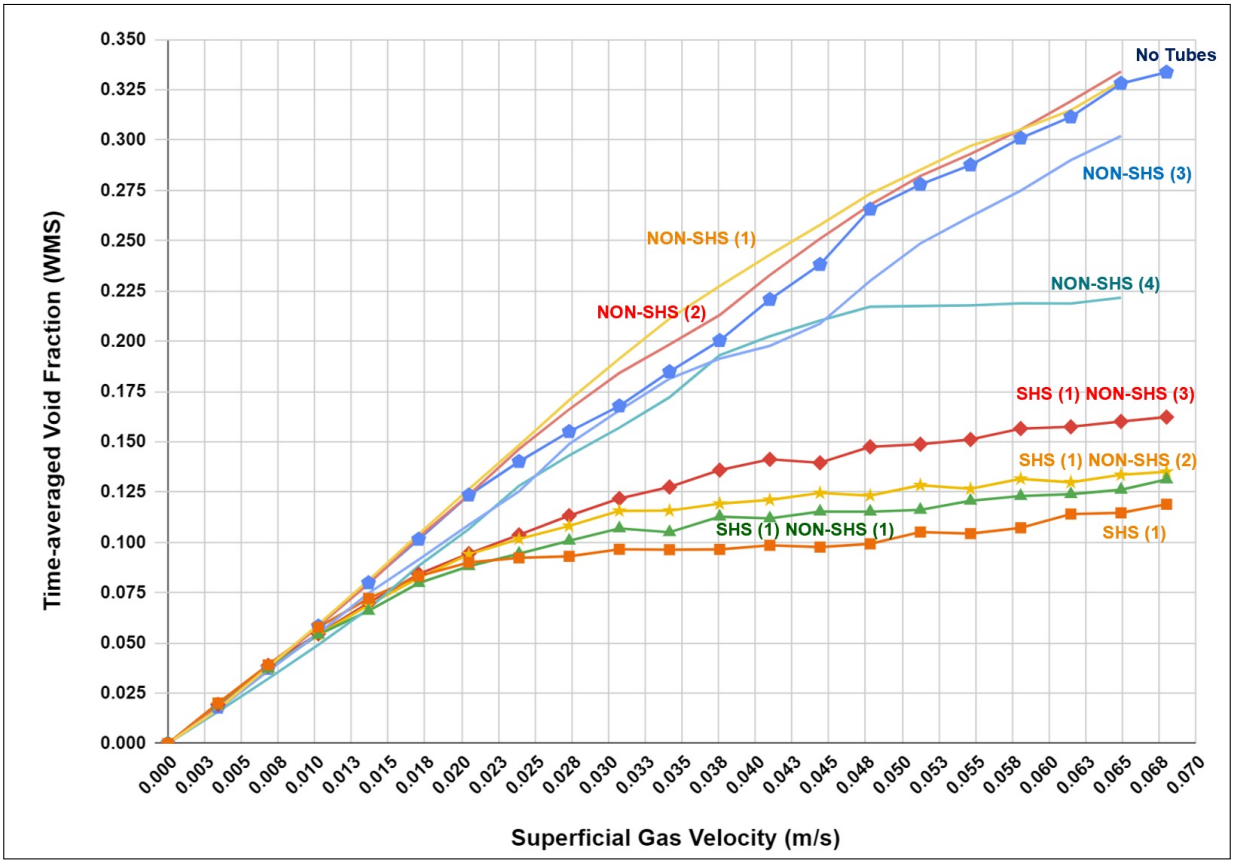

Figure 10.56: Variable SHS and Non-SHS Tube - time-averaged void fractions calculated by wire mesh sensors

bubbles or possible SHS-tube air layer absorption, with minimal changes in superficial gas velocity and no changes in fuel rod configuration.

Advanced measurement techniques, such as X-ray computed tomography and iterative reconstruction algorithms, are required to measure the effects of superhydrophobicity within fuel rod assemblies at variable injection rates. Since the fuel rod assembly is already an obstructed view, visualization of flow regimes by optical measurement techniques and wire mesh sensors becomes very difficult. With advances in X-ray Computed Tomography, these flow patterns within a fuel rod assembly can be realized and further studied, to offer experimental observations for the effects of superhydrophobic-coated surfaces on void fraction distribution across the fuel cell assembly. Five time-averaged phase fraction measurement techniques were utilized on both bubble columns from a range of 0.003 m/s to 0.068 m/s. We have validated X-ray CT time-averaged void fraction reconstruction results against measurement techniques offered by height variation, differential pressure transducer, and wire

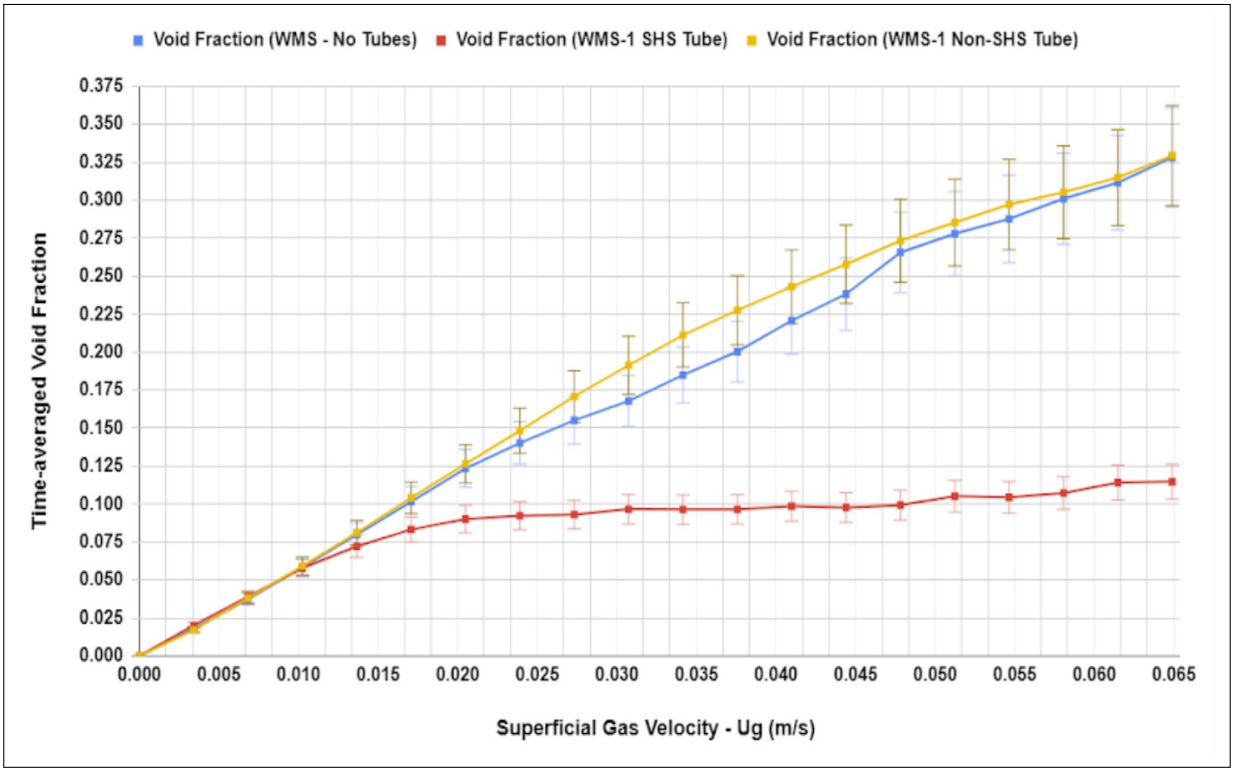

Figure 10.57: Single SHS and Non-SHS Tube - time-averaged void fractions calculated by wire mesh sensors

mesh sensors. Their agreement proved valuable to understand how each technique measures time-averaged void fraction and allowed us to identify advantages and disadvantages of each technique. With respect to time-averaged void fraction measurements, we have shown how X-ray CT reconstruction is a measurement technique that offers spatial resolution comparable to wire mesh sensors and a more effective measurement tool because of its non-intrusiveness.

To further evaluate localized transition from a homogeneous to heterogeneous bubble regime, we utilized the Velocity and Bubble Size Distribution modules, provided in the Wire Mesh Sensor Framework, to evaluate mean bubble diameters and bubble flow velocity in order to validate our hypothesis that the superhydrophobic-coated rod changed the bubble regime from a dispersed bubble regime to a churn-turbulent flow. In a hydrophilic bubble column, the bubble flow throughout our experiment remained homogeneous with a 20-30mm change in mean bubble diameter from a superficial gas velocity of 0.003m/s to 0.061m/s. In a fuel assembly with a single superhydrophobic tube, the bubble flow transitioned from homogeneous to heterogeneous at a very low superficial gas velocity with two mean bubble diameters averaging between 17mm and 23mm from a superficial gas velocity of 0.003m/s

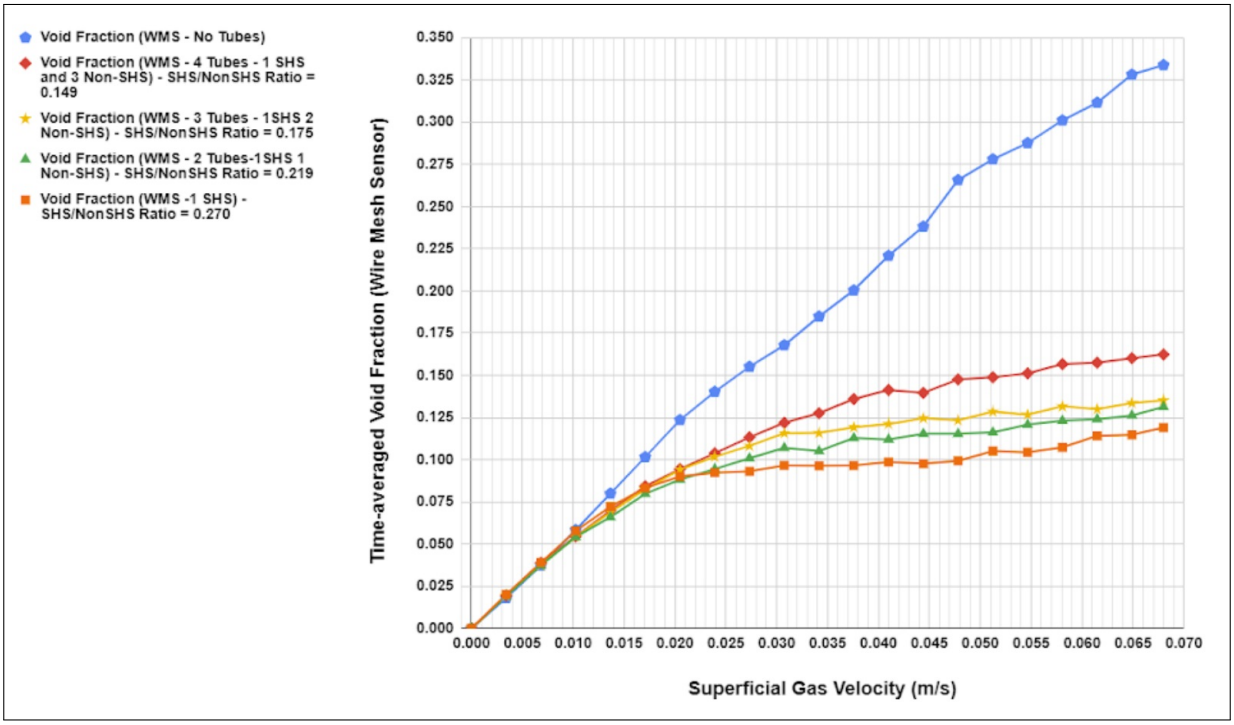

Figure 10.58: Volume Ratio and variable SHS tube bundle arrangement time-averaged void fractions calculated by wire mesh sensors

to 0.061m/s. Bubble flow regime transition to churn-turbulent was observed based on the increase in bubble diameter, bimodal histogram profile of bubble density and an increase in localized velocity along the area with a SHS-coated rod. We learned that geometric constraints, varied by adjusting the rod configuration also plays a role in localized gas holdup but not as substantial as replacing a single fuel rod with a a SHS-coated rod.

These findings suggests that lower void fractions are achievable with a modification of rod surface wall characteristics to promote superhydrophobicity. Additionally, superhydrophobic coatings promote transition to churn-turbulent flow without any modification to superficial gas velocity or bubble column dimensions. Thirdly, advanced measurement techniques, such as X-ray computed tomography, have proven effective at providing a non-intrusive and spatial and temporal resolved void fraction measurement in dynamic multiphase flow systems with optically obstructed fields of view. Lastly, further studies are warranted to evaluate if the substantially lower void fraction offered by a submerged SHS-coated rod is due to the phenomena of absorption onto the air layer in the Cassie-Baxter state or other bubble to air layer interactions.

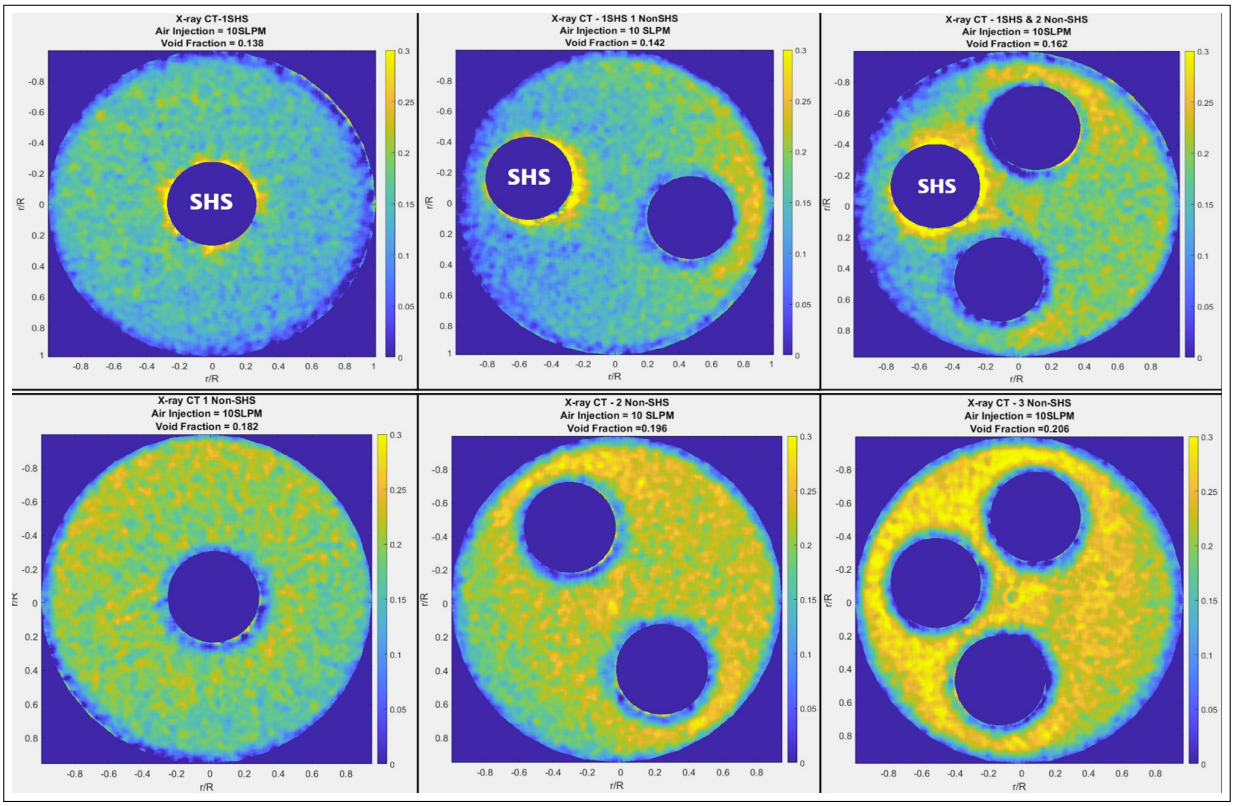

Figure 10.59: Xray CT Time-averaged Void Fraction for variable rod configurations with and without a substituted SHS-coated rod

References

[1] W.V. Aarle et al. "Fast and flexible X-ray tomography using ASTRA toolbox". In: *Optical Society of America* -.- (2016), pp. 1–19.

[2] T. Allen, J.Busby, and M. Meyer. "Material Challenges for Nuclear Systems". In: *Materials Today* 13.12 (2010), pp. 14–23.

[3] A. Avdeev. *Bubble Systems*. Springer, 2016.

[4] A. Bejan. *Convection Heat Transfer*. John Wiley Sons, INC, 2004.

[5] C. Brennen. *Fundamentals of Multiphase Flows*. Cambridge University Press, 2005. ISBN: 0521848040.

[6] C. Brucker. "Structure and Dynamics of the wake of bubbles and its relevance for bubble interaction". In: *Physics of Fluids* 11.7 (1999), pp. 1781–1796.

[7] R. Clift, J. Grace, and M. Weber. *Bubbles, Drops, and Particles*. Dover Publications, 1978.

[8] J. Collier and J. Thorne. *Convective Boiling and Condensation*. Oxford University Press, 1994.

[9] J. Fan Z. Cui. "Effect of Acoustic Standing Wave in a Bubble Column". In: *Industrial and Engineering Chemistry Research* 44.17 (2005), pp. 7010–7018.

[10] Attwood D and A. Sakdinawat. *X-rays and Extreme Ultraviolet Radiation*. Cambridge University Press, 2016.

[11] M. Dziubinski, H. Fidos, and M. Sosno. "The flow pattern map of a two-phase non-Newtonian liquid-gas flow in the vertical pipe". In: *International Journal of Multiphase Flow* 30.5 (2004), pp. 551–563.

[12] Y. Shah B. Kelkar S. Godbole. "Design Parameters Estimate for Bubble Column Reactors". In: *American Institute of Chemical Engineers* 28.3 (1982), pp. 353–379.

[13] T. Heindel. "A Review of X-Ray Flow Visualization With Applications to Multiphase Flows". In: *Journal of Fluids Engineering* 133.74 (2011), 074001_1–074001_16.

[14] S. Hosokawa, K. Hayashi, and A. Tomiyama. "Void distribution and bubble motion in bubbly flows in a 4x4 rod bundle. Pat 1: Experiments". In: *Journal of Nuclear Science and Technology* 51.2 (2013), pp. 220–230.

[15] D. Jha et al. "Adaptive center determination for effective suppression of ring artifacts on tomography images". In: *Applied Physics Letters* 105.0 (2014), pp. 143107-1 - 143107–4.

[16] A. Kamei. "Void Fraction in a Four by Four Rod Bundle under a Stagnant Condition". In: *Journal of Power and Energy Systems* 4.2 (2010), pp. 315–326.

[17] R. Knief. *Nuclear Engineering: Theory and Technology of Commercial Nuclear Power-Second Edition*. American Nuclear Society, 2014.

[18] Y. Lee et al. "Comparison of photon counting and conventional scintillation detectors in pinhole SPECT system for small animal imaging". In: *Proceeding of SPIE* 8668.1 (2013), pp. 8668-1 - 8668–6.

[19] D. Legendre, J. Boree, and J. Magnandet. "Thermal and Dynamic Evolution of a Spherical Bubble moving steadily in a superheated or subcooled liquid". In: *Physics of Fluids* 10.6 (1998), pp. 1256–1272.

[20] G. Riboux F. Risso D. Legendre. "Experimental Characterization of the agitation generated by bubbles rising at high Reynolds number". In: *Journal of Fluid Mechanics* 643.1 (2010), pp. 509–539.

[21] F. Lehr, M. Millies, and D. Mewes. "Bubble-size distributions and flow fields in bubble columns". In: *American Institute of Chemical Engineers* 48.11 (2002), pp. 2426–2443.

[22] L. Li, B. Breedveld, and D. Hess. "Creation of Superhydrophobic Stainless Steel Surfaces by Acid Treatment and Hydrophobic Film Deposition". In: *American Chemical Society - Applied Materials and Interfaces* 4.0 (2012), pp. 4549–4556.

[23] Y. Li et al. "Single bubble dynamics on spuerheated superhydrophobic surfaces". In: *International Journal of Heat and Mass Transfer* 99.0 (2016), pp. 521–531.

[24] H. Martz et al. *X-ray Imaging - Fundamentals, Industrial Techniques and Applications*. CRC Press, 2017.

[25] G. Mchale, M. Newton, and N. Shirtcliffe. "Immersed superhydrophobic surfaces: gas exchange, slip and drag reduction properties". In: *Royal Society of Chemistry* 6.4 (2010), pp. 714–723.

[26] T. Anklam R. Miller. "Void Fraction under High Pressure, Low Flow Conditions in Rod Bundle Geometry". In: *Nuclear Engineering and Design* 75 (1983), pp. 99–108.

[27] Yoshiaki Oka. *Nuclear Reactor Design*. Springer, 2014.

[28] S. Pope. *Turbulent Flows*. Cambridge University Press, 2000.

[29] H-M. Prasser. "A new electrode-mesh tomography for gas-liquid flows". In: *Flow Measurement and Instrumentation* 9 (1998), pp. 111–119.

[30] H-M. Prasser, M. Misawa, and I. Tiseanu. "Comparison between wire-mesh sensor and ultra-fast X-ray tomograph for an air–water flow in a vertical pipe". In: *Flow Measurement and Instrumentation* 16.2 (2005), pp. 73–83.

[31] H-M. Prasser, D. Scholz, and C. Zippe. "Bubble size measurement using wire mesh sensors". In: *Flow Measurement and Instrumentation* 12.0 (2001), pp. 299–312.

[32] A. Prosperetti. "Vapor Bubbles". In: *Annual Review of Fluid Mechanics* 49.1 (2017), pp. 221–248.

[33] F. Risso. "Agitation, mixing and transfers induced by bubbles." In: *Annual Review of Fluid Mechanics* 50 (2018), pp. 25–48.

[34] P-G. Saffman. "On the rise of small air bubbles in water". In: *Trinity College* (1956), pp. 249–275.

[35] T. Schafer et al. "Ultrafast X-ray Computed Tomography Imaging for Hydrodynamic Investigations of Gas-Liquid Two-Phase Flow in Centrifugal Pumps". In: *Journal of Fluids Engineering* 142.4 (2020), pp. 041502.1–041502.9.

[36] E. Manson A. Ampoh E. Fiagbedzi J. Flether C. Schandorf. "Image Noise in Radiography and Tomography: Causes, Effects and Reduction Techniques". In: *Current Trends in Clinical Medical Imaging, Juniper Publishers* (2019), pp. 86–91.

[37] E. Fermi E. Amaldi O. D'Agostino F. Rasetti E. Segre. "Artificial Radioactivity produced by Neutron Bombardment". In: *Royal Society* 146.857 (1934), pp. 483–500.

[38] W. Sha and V. Shah. *Bubble Dynamics in a Superheated Liquid*. Argonne National Laboratory, 1977.

[39] H. Shaban. *Experimental Investigation of Internal Air-Water Flows*. Ottawa-Carleton Institute for Mechanical and Aerospace Engineering, 2015.

[40] H. Shaban and S. Tavoularis. "Performance evaluation of conductivity wire-mesh sensors in vertical channels". In: *Flow Measurement and Instrumentation* 54.1 (2017), pp. 185–196.

[41] A. Shafquet. "Study of Bubble Flow in an Air-Water Two-Phase Flow by Using Electrical Capacitance Tomography". In: *Proceedings for the 3rd International Conference on Intelligent and Advanced Systems* (2010).

[42] C. Shi et al. "Interraction between air bubbles and superhydrophobic surfaces in aqueous solutions". In: *Langmuir* 31.26 (2015), pp. 7317–7327.

[43] A. Kak M. Stanley. *Principles of Computerized Tomographic Imaging*. IEEE Press, 1999.

[44] L. Tong and J. Weisman. *Thermal Analysis of Pressurized Water Reactors*. American Nuclear Society, 1996.

[45] I. Vakarelski, D. Chan amd J. MArston, and S. Thoroddsen. "Dynamic Air Layer on TExtured Superhydrophobic Surfaces". In: *Langmuir* 31.29 (2013), pp. 11074–11081.

[46] L. Wang et al. "Fabrication of superhydrophobic surfaces on stainless steel mesh substrates via electrobrush flow plating technology". In: *19th CIRP Conference on Electro Physical and Chemical Machining* 68.1 (2018), pp. 232–236.

[47] B. Whiting J. O'Sullivan J. Williamson. "Properties of preprocessed sinogram data in X-ray Computed Tomography". In: *American Association of Physical Medicine* 33.9 (2006), pp. 3290–3303.

[48] S. Yoon et al. "Image reconstruction for limited-angle electron beam X-ray computed tomography with energy-integrating detectors for multiphase flows". In: *IEEE Transactions on Computational Imaging* 4.1 (2017), pp. 112–124.

[49] S. Morooka T. Ishizuka M. Iizuka K. Yoshimura. "Experimental Study in Void Fraction in a Simulated BWR Fuel Assembly (Evaluation of Cross-Sectional Averaged Void Fraction". In: *Nuclear Engineering and Design* 114 (1989), pp. 91–98.

[50] H. Zhang et al. "Statistical image reconstruction for low-dose CT using nonlocal means-based regularization". In: *Computerized Medical Imaging and Graphics* 38.- (2013), pp. 423–435.

Appendix A

Multiphase Flow Laboratory Standard Operating Procedures and Safety Handling

A.1 Experimental Description and Laboratory Setup

The X-ray Tomography Multiphase Flow Measurements laboratory has a radiation shielded space accommodating a vertical and horizontal flow loop, and enabling a wide variety of experiments utilizing radiation producing machines, without the need to redo shielding. For each experiment for the Computed Tomography (CT) system, a rotation table and eight linear stages control the relative position of the X-ray source and detector, as it rotates around a flow loop, bubble column or other experiment. An X-ray source and photon counting imager are used for proof-of-concept of in-lab X-Ray Particle Image Velocimetry (PIV) measurement. The system also enables code validation from time-averaged X-ray Computed Tomography.

The X-ray Tomography Measurements laboratory is comprised of three components that require adherence to different procedures to ensure proper safety controls are in place prior to transmitting X-rays. The system includes an X-ray source and detector, mounted on six linear stages, which are assembled and attached to a rotation table that will maneuver around any experiment that will be positioned in the center of the rotation table.

Figure 1 displays a side view of the laboratory setup, including a side view of the shielding, the steel frame which holds a steel tank and the rotation table with linear stages located in the center of the steel frame. The system is located in the southeast corner of Room 1140 in Etcheverry Hall.

Figure 2 displays a top view of the laboratory. The stainless-steel tank and optical table depicted in Figure 2 are separate setups that will not entirely be dedicated to the X-ray tomography system. During X-ray operations, personnel assigned to various lab setups must exit the area prior to any X-ray operation. A concrete wall (20ft by 15ft), a lead brick wall

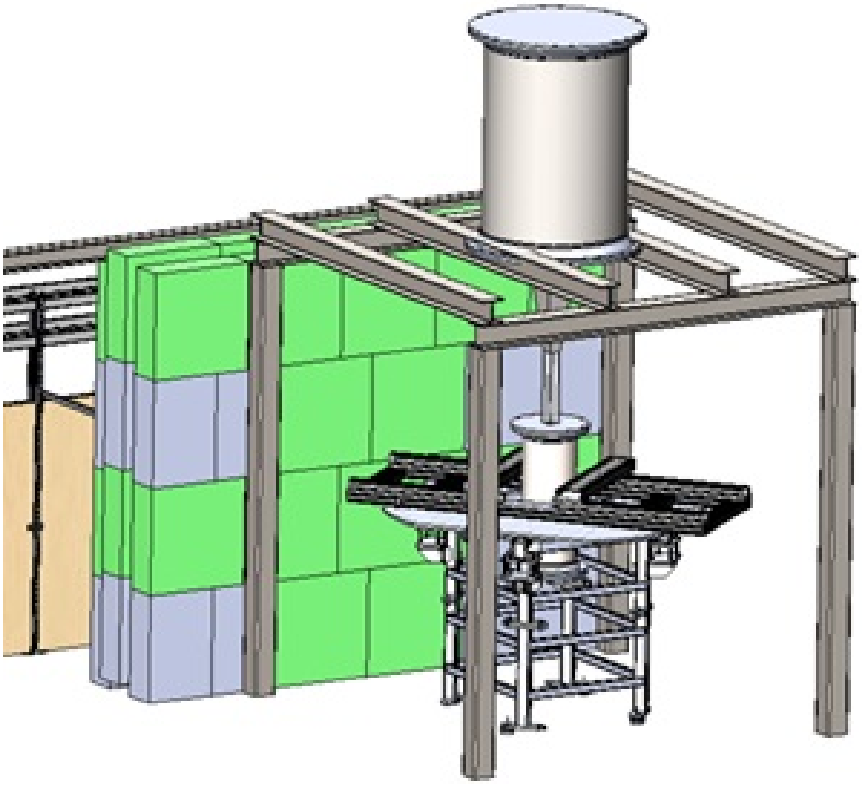

Figure A.1: X-ray Tomography Laboratory Setup (Side View)

(9ft by 8ft) and aluminum door provide the primary boundary for the designated area of X-ray operations. The concrete wall and the lead brick wall with the adjoining three walls in the southeast corner and neutron generator room boundary provide primary shielding to prevent exposure to the operators and personnel throughout the other areas of Etcheverry Room 1140. The square symbols in red display safeguard locations associated with the rotation table, linear stages and the X-ray source.

The rotation table is a 90inch X 96inch table operated by a motor, with electric power provided by a servo controller and command signals from a CPU. The servo and CPU are located outside of the designated area. The servo controller is provided 400VAC power from an electric cabinet located inside the designated space. Figure 3 displays the rotation table which rotates from a motor located under the table, powered from a servo controller.

Figure 4 displays the electrical connections associated with the rotation table. The 400VAC power is provided from an electric cabinet. The operator must plug the system in and turn on the breaker to energize the servo controller. The CPU and associated circuitry on the ACOPOS 1180 are powered by a 24VDC power supply. This power supply is also situated

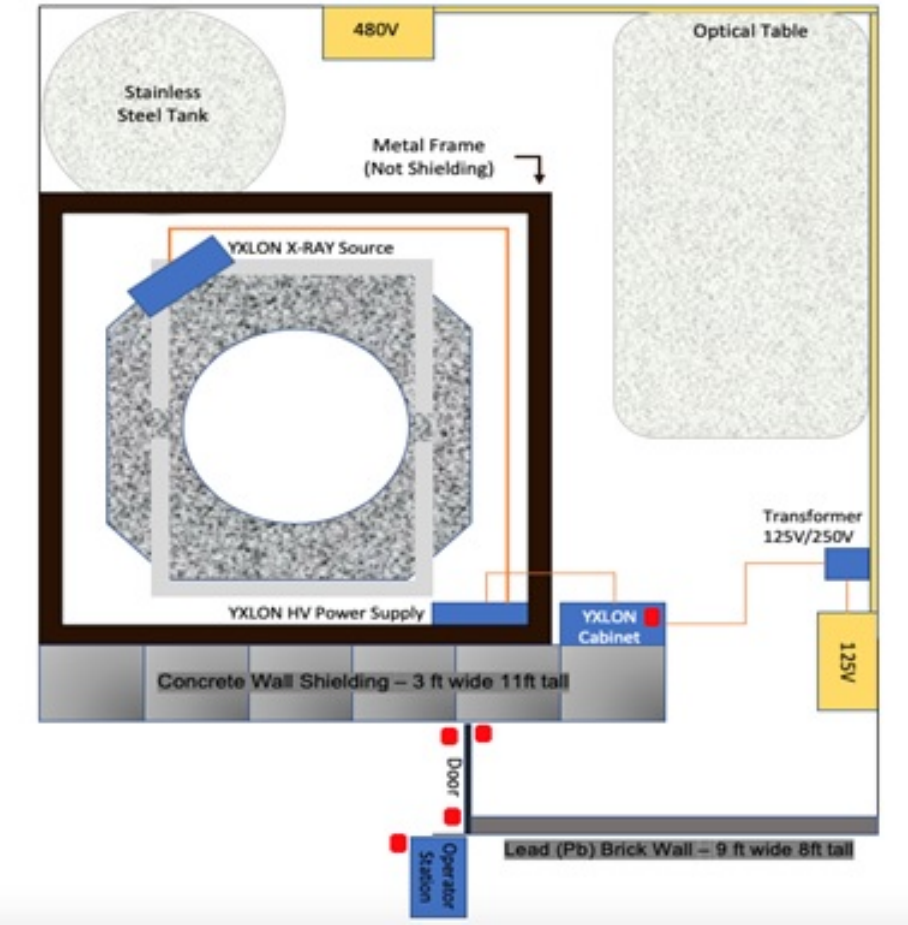

Figure A.2: X-ray Tomography Laboratory Setup (Side View)

outside of the designated area along with the CPU and ACOPOS 1180 servo controller. Figure 5 lays out the electrical plug and breaker associated with the rotation table. The operator will not leave the rotation table plugged in if not in use.

Eight linear stages are utilized to provide an XYZ axis control to position the X-ray source (FXE-992X) and detector. An XYZ axis is formed utilizing linear stages as depicted in Figure 6. Each group of four linear stages is controlled by a separate computer system displayed in Figure 7. The controllers can function independently or remotely from the operator station to make ease during troubleshooting and normal operations. Steel slides are connected to each linear stage and further connected to each other to form an XYZ axis of operation. The Z linear stages have a brake in addition to the motor to protect the motor from the weight of the X-ray source (150lbs) when assembled into a vertical position.

The linear stages are controlled through a LABVIEW program built specifically to move

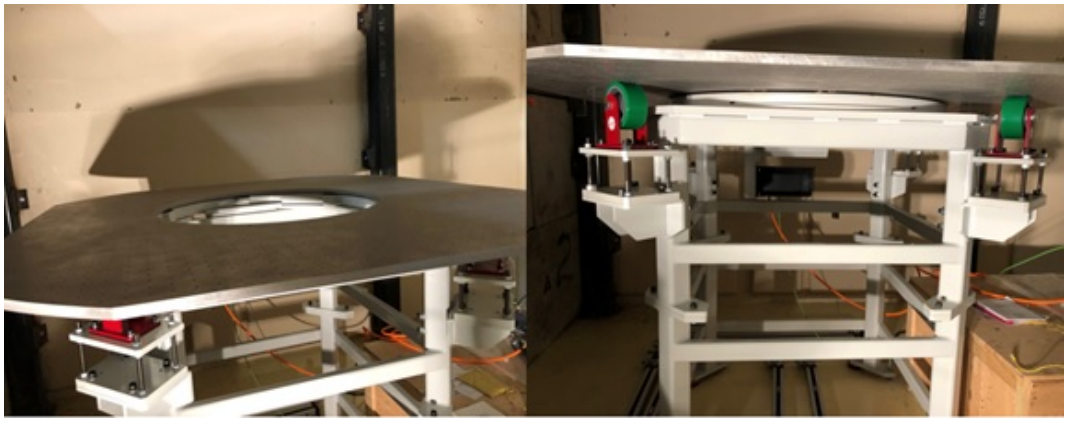

Figure A.3: NR1500ZAG Weiss Rotation Table

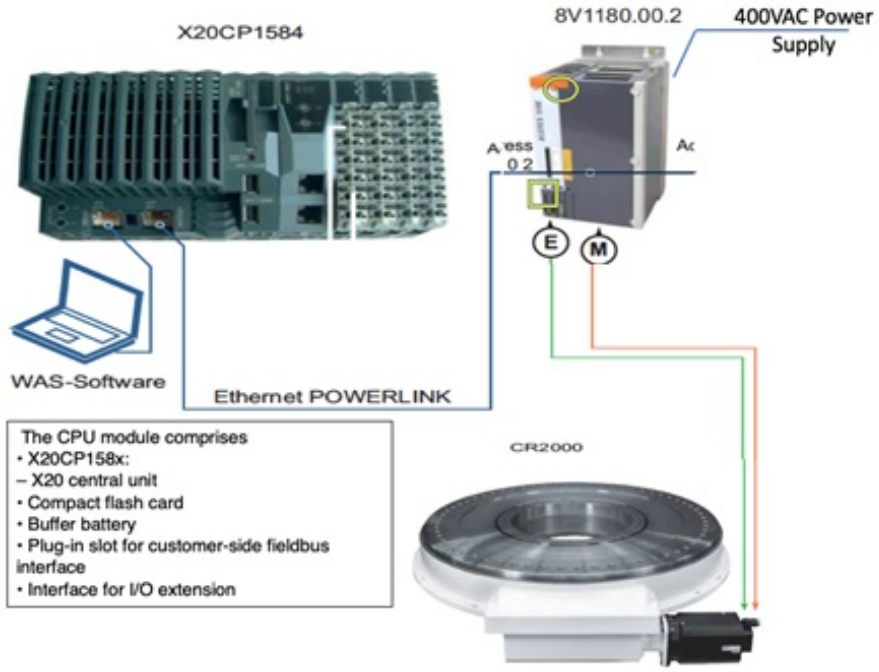

Figure A.4: ACOPOS 1180 NR1500ZAG Rotation Table and Controls

Figure A.5: Electrical Plug and Breaker for NR1500ZAG Rotation Table

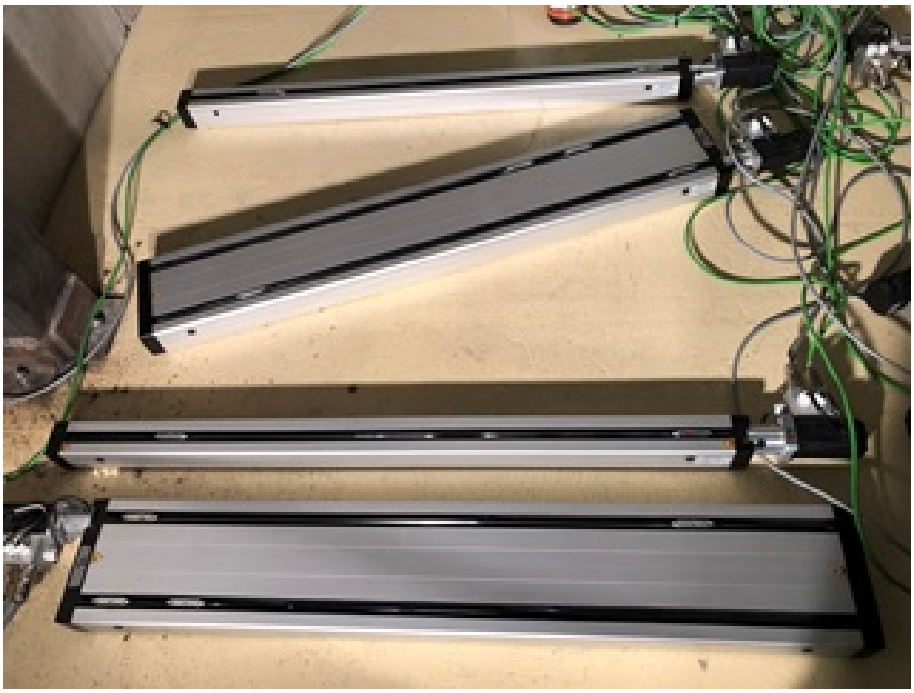

Figure A.6: Group Linear Stages (X,Y,A Z)

Figure A.7: Linear Stage Controller Front Panel (1 of 2 controllers depicted)

Figure A.8: Linear Stage Controller Back Panel (1 of 2 controllers depicted)

all eight linear segments in one motion. The positions of the linear stages are dependent on the experiment setup and measurement requirements. The linear stages will lock out if you exceed hard stops located in the system. Emergency Stop buttons are located in the front panel of each computer. An Emergency Stop is also located at the operator station to allow the operator to quickly stop the movement prior to reaching a hard stop or damaging associated cable and the experiment located in the center of the rotation table.

Figure 7 displays the front panel of the linear stage controllers. The Red Emergency Stop button will stop the four linear stages associated with the respective controller. BOTH EMERGENCY STOP BUTTONS MUST BE PRESSED TO STOP ALL LINEAR STAGES. The Power button and the PC Start button must be pressed to power on the computer and the controller. Both lights will display a green light when the controller and computer are energized.

Figure 8 displays the back panel of the linear stage controllers. Each grey and green cable

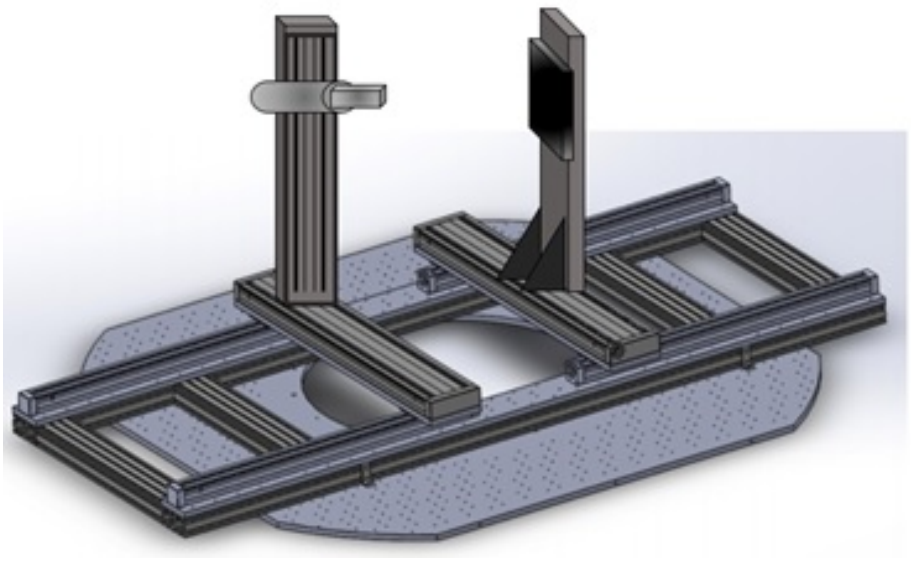

Figure A.9: Linear Stages Projected Assembly with X-ray Source and Detector

are connected to each one of four linear stages. The gray cables provide electrical power to each linear stage and green cables (serial cables) provide control inputs to each linear stage. The top left corner of the back panel displays the ethernet connection from the controller to the associated PCI card at the back of the operator station computer. The small yellow ethernet cable must remain in the current configuration displayed in Figure 8 for the system to operate. Next to the power cable connection, a switch is located that is required to be pressed to power on the system from the Power and PC start buttons in the front panel. Figure 9 depicts a projection of the complete linear-stage assembly.

The X-ray source is a FXE-99X twin head setup system with a directional and transmission head. The laboratory will mount the X-ray source with one head at a time. The directional head is available for more precise image measurements. The source will be mounted to the Z-axis linear stage using two steel THOR LABS brackets, which will be attached to the steel slide associated with the Z-axis. Figure 10 displays the two heads available with the X-ray source.

Figure 11 displays the X-ray source with the associated cooling connections, vacuum hose and turbo pump. The blue cables are coolant hoses which are only connected to the directional head. The transmission is cooled by ambient cooling. The clear vacuum hose is braided with steel to prevent the hose from collapsing under vacuum pressure. Prior to head removal, the pressure must be bled off to equalize pressure and allow replacement of the attached head. The current depiction in Figure 11 shows the transmission head connected and the directional head is hinged up with its cooling hose connected to each

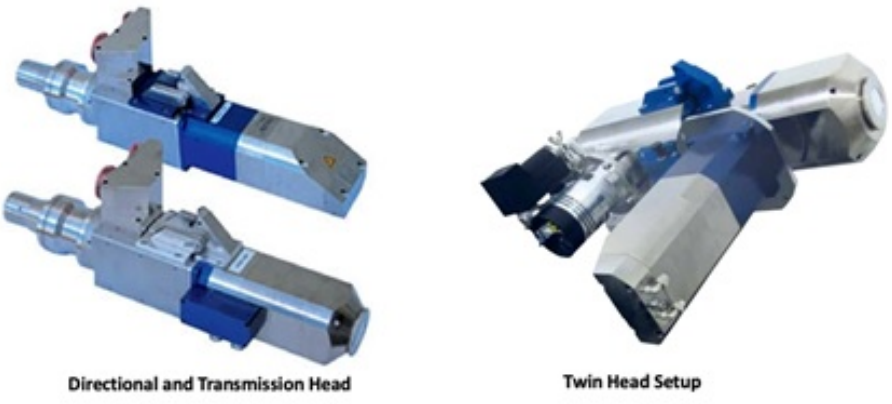

Figure A.10: FXE-992X Directional and Transmission X-ray Source

other to avoid leakage of coolant. Prior to replacing the heads, allow sufficient time for cooling, bleed the pressure by turning the black knob next to the vacuum connection, ensure high power generator is de-energized and utilize a support to hold the weight of the head while removing the screws. The internals of the head and vacuum chamber are cleaned with isopropyl alcohol using a white lint-free cloth and latex gloves. CAUTION: THE VACUUM CHAMBER CAN HAVE EXCESSIVE HEAT AFTER SECURING X-RAY OPERATIONS. ALLOW SUFFICIENT TIME FOR THE X-RAY SOURCE UNIT TO COOL BEFORE ATTEMPTING TO REMOVE THE HEAD.

The following safeguards are put in place to avoid inadvertent radiation exposure to personnel. These safeguards should be verified prior to operation of the X-ray source.

Prior to X-ray operations, the following interlocks and indications will be tested: - Limit Switches - Emergency Stop Plunger - “X-ray On” Sign - Preliminary light

Prior to testing, the room, as defined by the space in the southeast corner of Room 1140, bounded by the concrete wall, lead brick wall and aluminum security door, will be vacated and verified free of personnel by the operator. The mezzanine above the neutron generator will also be verified free of personnel and a sign will be placed at the bottom of ladder to ensure no access is allowed during X-ray operations.

Limits switches:

- The operator will attempt to operate the X-ray machine with the door open.
- Expected Result: With the door open, the X-ray machine should not operate, and a red alarm will be displayed in the X-ray software general window.
-

Emergency Stop plunger:

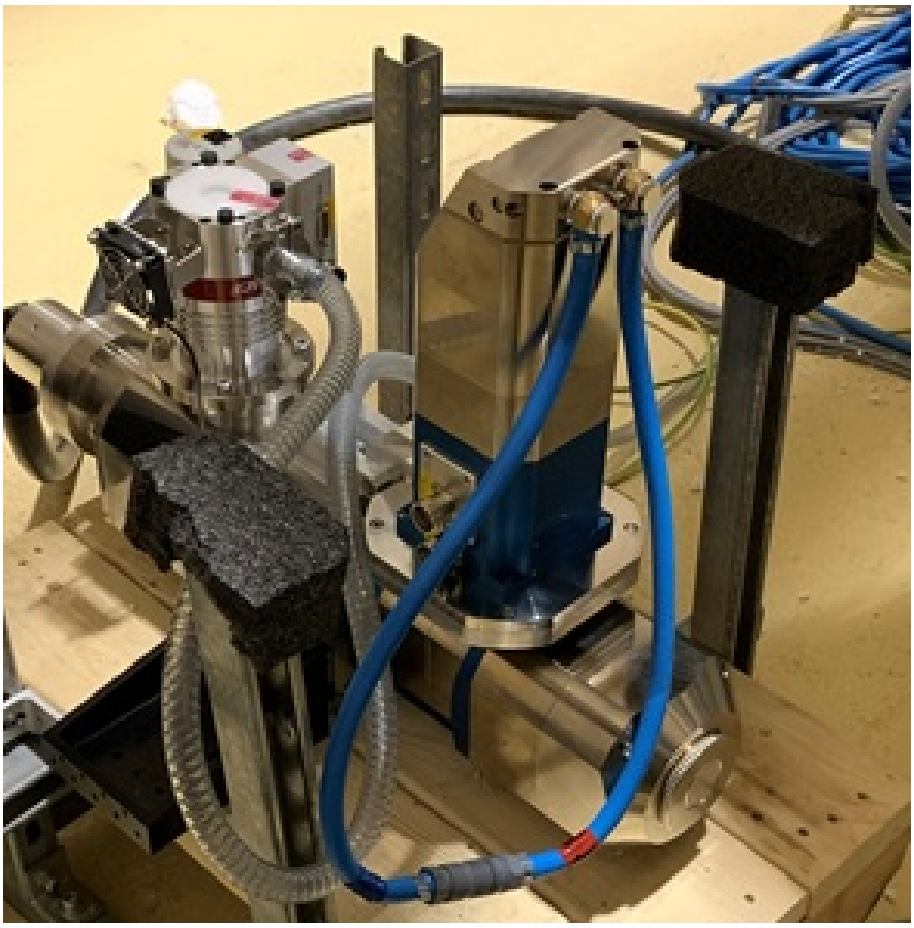

Figure A.11: FXE-992X Directional and Transmission X-ray Source Turbo Pump System

- The operator will push in the plunger and attempt to operate the X-ray machine.
- Expected Result: With the door open, the X-ray machine should not operate, and a red alarm will be displayed in the X-ray software general window.

The operator will also verify that the "X-ray On" sign and preliminary light (blue light) are energized during system operation.

The aluminum door must be closed prior to X-ray operations and following verification by operator that the space is cleared of personnel. The door closed will engage two limit switches which will close an electrical interlock circuit to allow X-ray operations. Upon opening the door, the interlock will disengage, and a red alarm condition will be displayed in the X-ray software at the operator station. Additionally, the X-ray system will not function. The system can be RESET by closing the door and pressing the RESET button at the

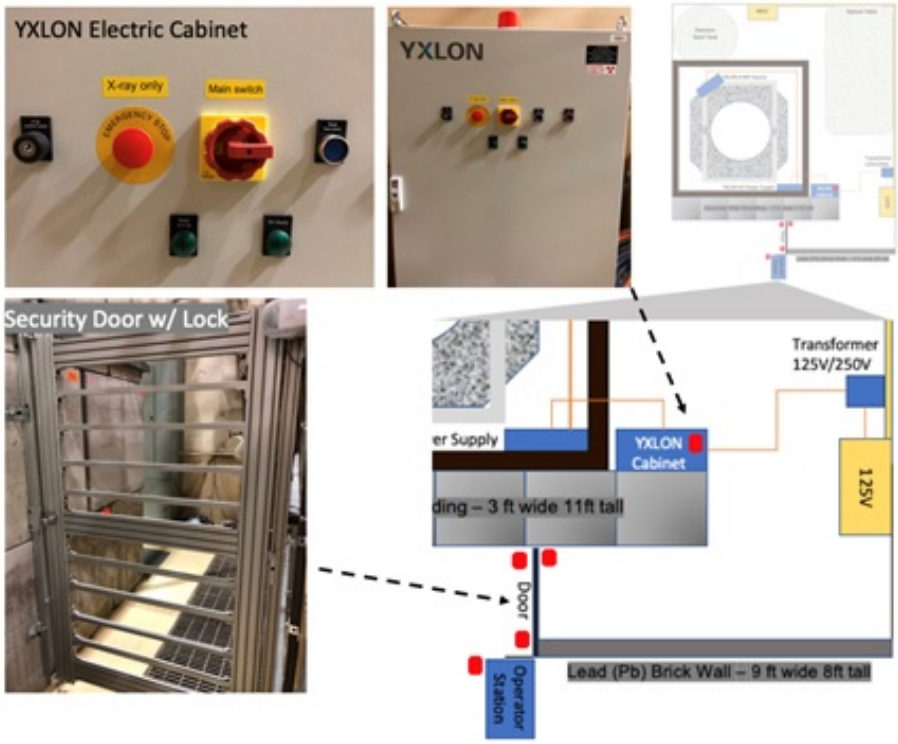

Figure A.12: YXLON X-ray Source Power Cabinet Safeguards

operator station. After pressing the RESET button, the red alarm will clear on the X-ray software status board.

Figure 13 displays the X-ray door sign and Preliminary Light. The Preliminary light will shine in blue and will stay energized for 10 seconds at which point the X-ray sign will stay energized as long as the X-ray source stays energized. The X-ray sign will shut-off during arcing of the system throughout the warmup cycle.

Figure 14 displays the Emergency Stop Plunger utilized to stop the X-ray machine. The plunger is located at the operator station. Unlike the Door limit switches, the Emergency Stop cannot be RESET from the RESET button at the operator station alone. The operator will need to pull out the plunger, enter the designated area to press the RESET button on the X-ray cabinet, close the door and then press the RESET button. After fully resetting the system, the alarm will clear on the X-ray software status window.

Following radiation surveys of the adjoining areas during maximum power operations, the mezzanine area above the neutron generator has been designated as inaccessible during X-ray operations. Figure 15 is the sign that needs to be posted at the bottom of the ladder to the mezzanine prior to operating the X-ray source. The sign is currently attached to a chain hanging from the ladder. In order to prohibit access, the sign and chain must be

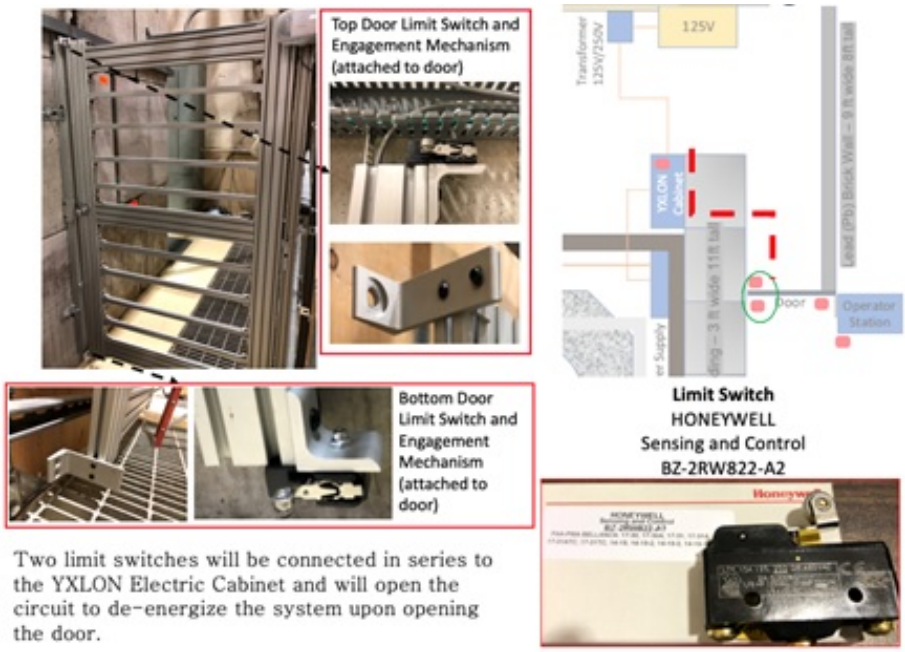

Figure A.13: YXLON X-ray Source Door Limit Switches

connected across the ladder entrance.

Figure 16 is the Startup and Safety Checklist that will be performed by the operator prior to X-ray operations to ensure personnel safeguards are functioning correctly.

A.2 Hazardous Materials

Isopropyl Alcohol is stored in the space for ease of use during cleaning of the X-ray chamber prior to transmission or directional head change out.

A.3 Potential Hazards

Electrical shock: from X-ray HV supply and instrumentation Physical hazard: moving traverse stages and rotation table on CT system Chemicals: see Section 2 Sharps: if glass ware breaks, from sharp corners of experimental setups under construction Water: if flow loops leak, significant quantities of water may be discharged and increase risk of electrical shock or slip and fall Inhalation: few of the smallest PIV/LDV seeding particles may present an inhalation hazard. If such is indicated on the MSDS of the material, a suitable mast must be used. Compressed Gas: The lab may have TBD compressed nitrogen cylinders. Radioactive

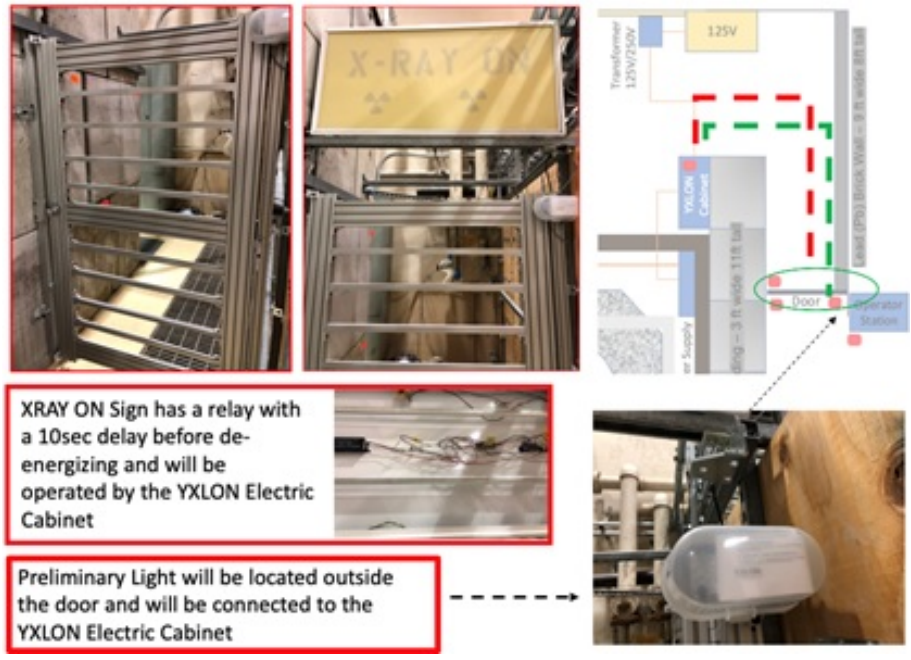

Figure A.14: YXLON X-ray Door Sign and Preliminary Light

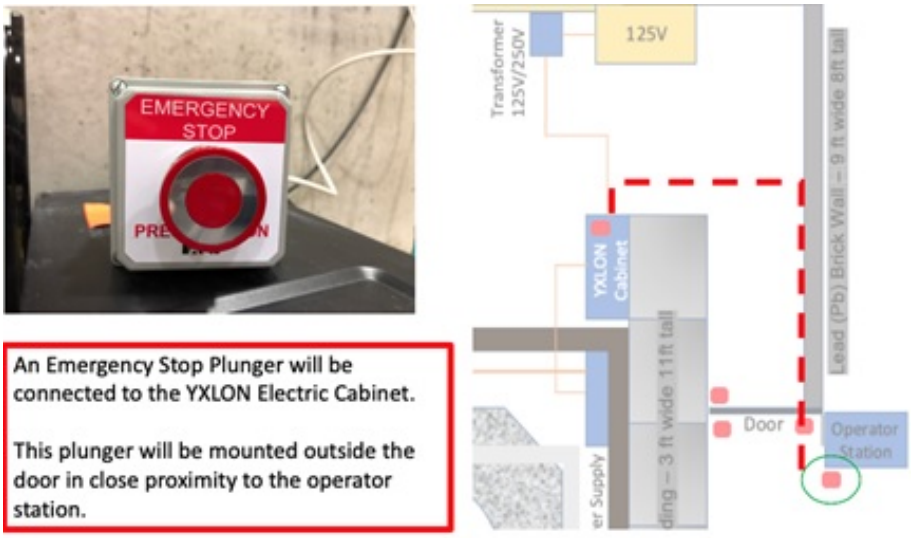

Figure A.15: YXLON X-ray Emergency Stop Plunger

Figure A.16: YXLON X-ray Access Prohibited Sign

material: None are believed to be present. However, EHS has notified the PI that the area must periodically be inspected for traces of Tritium that may be present from past experiments utilizing the same space. In particular, if a major (i.e. ¿10 gallons) water leak occurs resulting in trenches / room being inundated, the water to be pumped out must be inspected for traces of Tritium prior to discharging it to drain.

A.4 Required Training

ALL USERS MUST GO THROUGH RADIATION SAFETY TRAINING AND BE LISTED ON THE LAB RUA.

NO EXPERIMENTS INVOLVING HUMANS, ANIMALS OR LIVING TISSUE ARE TO BE CONDUCTED IN THIS SPACE WITHOUT PRIOR APPROVAL FROM BOTH EHS PI.

Training by experienced lab member and supervision during first use(s) of this protocol.

If no experienced lab member is qualified to supervise the initial uses of X-ray source, then arrangements should be made to have someone from EHS Radiation Safety present during initial operations of the X-ray source.

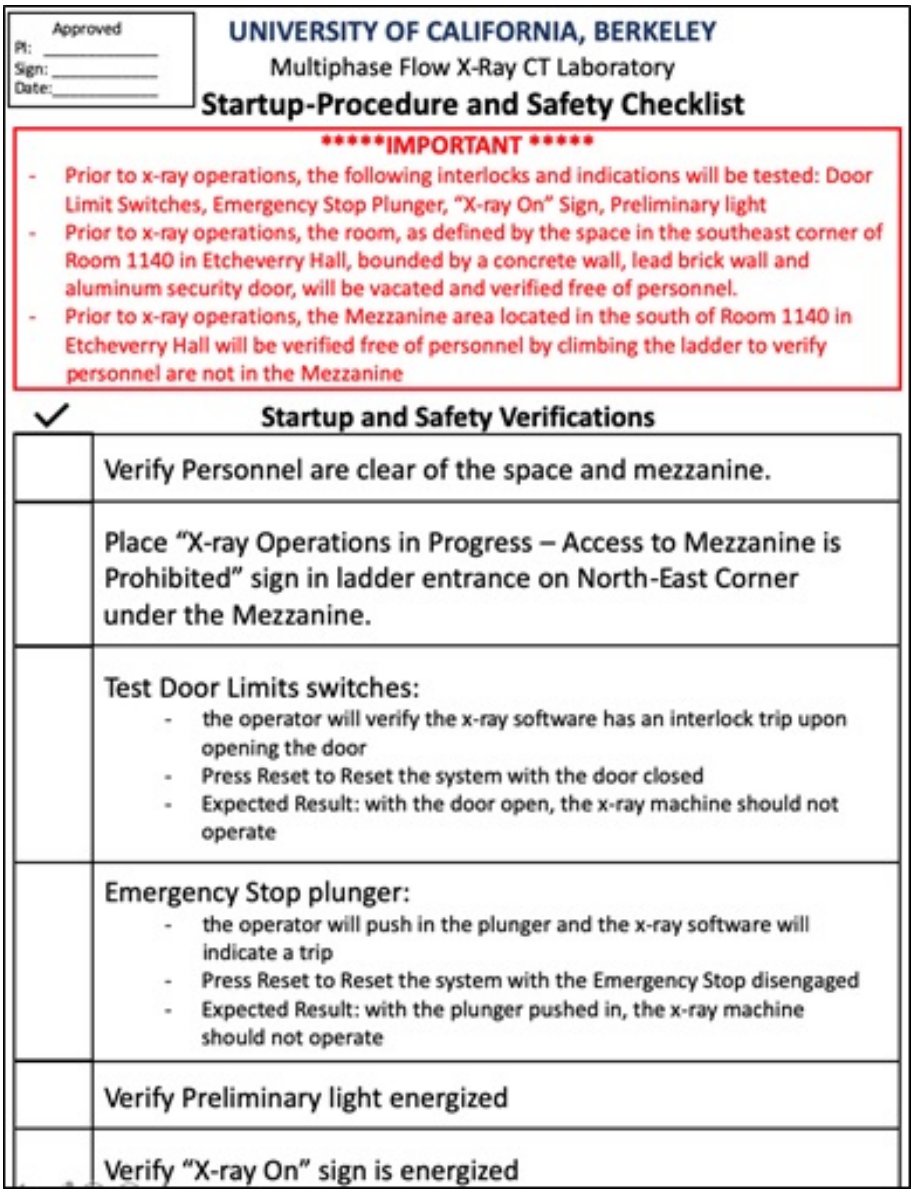

Approved
PI: _____
Sign: _____
Date: _____

UNIVERSITY OF CALIFORNIA, BERKELEY

Multiphase Flow X-Ray CT Laboratory

Startup-Procedure and Safety Checklist

*****IMPORTANT *****

- Prior to x-ray operations, the following interlocks and indications will be tested: Door Limit Switches, Emergency Stop Plunger, "X-ray On" Sign, Preliminary light
- Prior to x-ray operations, the room, as defined by the space in the southeast corner of Room 1140 in Etcheverry Hall, bounded by a concrete wall, lead brick wall and aluminum security door, will be vacated and verified free of personnel.
- Prior to x-ray operations, the Mezzanine area located in the south of Room 1140 in Etcheverry Hall will be verified free of personnel by climbing the ladder to verify personnel are not in the Mezzanine

✓	Startup and Safety Verifications
	Verify Personnel are clear of the space and mezzanine.
	Place "X-ray Operations in Progress – Access to Mezzanine is Prohibited" sign in ladder entrance on North-East Corner under the Mezzanine.
	Test Door Limits switches: - the operator will verify the x-ray software has an interlock trip upon opening the door - Press Reset to Reset the system with the door closed - Expected Result: with the door open, the x-ray machine should not operate
	Emergency Stop plunger: - the operator will push in the plunger and the x-ray software will indicate a trip - Press Reset to Reset the system with the Emergency Stop disengaged - Expected Result: with the plunger pushed in, the x-ray machine should not operate
	Verify Preliminary light energized
	Verify "X-ray On" sign is energized

Figure A.17: Start-up Procedure and Safety Checklist

A.5 Special Handling Procedure, Interlocks, and Shielding

The shielding consists of

- heavy concrete walls and floor on four sides,
- "wall" of heavy Barite keyed concrete shielding blocks with physical path between two rows of them (and interlocked door at the start of the physical path, and
- Heavy concrete ceiling (thickness ¿ TBD) above the room and TBD (¿24ft) afar from any RPM.

Monte Carlo simulations and radiation survey have been conducted to ensure dose to all personnel is ALARA.

No shielding is to be altered or interlock defeated without ALL of the following:

- permission from PI (and EHS, when applicable), AND
- without ensuring the RPM power is disabled with lockout, AND
- posting a sign on the lockout stating specifically what work is being conducted on the shielding or interlocks.

Any and all alterations to the shielding, non-standard changed to the system configuration, or installation of new system components or safeguard mechanics require prior approval from BOTH EHS and PI.

Even after changing the instrument or general facility configuration in a pre-approved manner, the user MUST use a survey/other meter to check that no unexpected radiation is detectable outside the designated area. User must conduct measurements in adjoining areas of the designated area.

NO personnel are allowed inside the shielded room during X-ray operations.

NO unnecessary personnel (and nobody without dosimeter and radiation safety training) are allowed by the operator station (denoted by a yellow and black tape on the floor) when the X-ray system is in use.

All FLOW-lab (and other authorized) personnel must wear whole body dosimeters in the designated area, whenever experiments utilizing the X-ray systems are conducted.

A.6 Personal Protective Equipment Individual Monitoring Devices

- Safety glasses (when handling chemicals, power tools or conducting other activity that may present and eye hazard)

- Filter/mask (if handling material that presents an inhalation hazard)
- Clothing that fully covers the legs
- Close-toed shoes
- Gloves (as necessary)
- Dosimetry (all personnel must wear whole body dosimeters in the designated area, whenever experiments utilizing the x-ray systems are to be conducted)

A.7 Engineering, Security and Ventilation Controls

Person with the key(s) to the RPM power lock-out must ensure the power is off and system locked down whenever they are not conducting an experiment.

Personnel must lock the laboratory door whenever being the last person to leave the room.

A.8 Accident Procedures

Radiation Safety must be notified immediately of any of the following situations:

- An interlock failure
- Unexpected personnel exposure
- Airborne radioactivity
- Loss of control, unauthorized use, or theft of radiation producing machines

In the event of an exposure:

- During business hours call the EHS main line at (510) 642-3073. After hours and on the weekends, call UCPD at (510) 642-3333. Shut down and secure the machine.
- Await further instructions from EHS Radiation Safety on how to proceed.

A.9 Maintenance/Removal

All machine repairs will be performed by qualified personnel. Interlocks will be tested, and radiation leakage surveys will be performed before returning the machine to service. Beam alignment operations require specific authorization *and/or* supervision by EHS.

Machines that are moved from their current approved location require prior notification to EHS to verify that the new location is appropriate for use and change of registration with

the State of California. Transfer, sale, or disposal of machines to another user or institution similarly requires notification to the State of California within 30 days.

Appendix B

X-ray Tomography using ASTRA Toolbox and MATLAB iFanBeam Reconstruction Techniques

B.1 X-ray Computed Tomography

Due to complexities with high speed cameras and particle image velocimetry, X-ray computed tomography (CT) can capture time-averaged void fraction distribution in a quasi-steady pipe flow. Visible light is scattered at the vapor-liquid boundary layer, but x-rays can be utilized for these measurements without succumbing to scattering at the vapor-liquid interface. By examining x-ray images, one can derive void fraction in a quantitative manner. A CT scanner advantageously measures spatial average of the void fraction but also provides an understanding of void fraction along a cross section of the pipe.

X-ray coherent diffractive imaging (CDI) records the scattering of spatially coherent X-rays using a function of the angle in the far-field with a distant 2D detector, such as a CCD (Attwood, 2016). In order to reconstruct an image from a scattering object, we need to know intensity and phase as a function of position. We will utilize recorded X-rays images from incremental angular positions. The measured intensities can be Fourier transformed back to the object plane, which allows for numerical reconstruction. An iterative process is utilized through a projection algorithms. Fourier transforms are calculated iteratively and sequentially between the detector and the object. The iterations are continued until a convergence is reached, at which moment point image reconstruction is a possibility.

The idea of the CT system is to create an image of the interior of an object using large number of line integrals over attenuation coefficients. The CT system provides a 3D flat slice of the target object. A fan of X-ray line integrals are shaped by a collimator in a way that outputs as a flat x-ray fan. Utilizing a tube and array's simultaneous rotation around an object will provide instantaneous intensity values at fixed angles called projections. If attenuation coefficients are understood, the reconstruction process will result in a gray scale

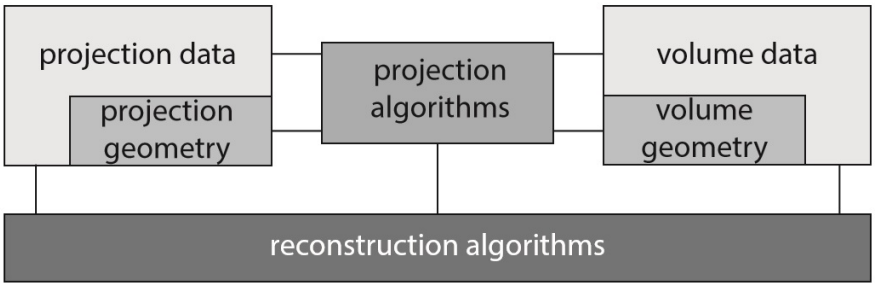

Figure B.1: Overview of ASTRA Toolbox concepts

image. Each slice is represented in a so-called voxel, which is a 3D pixel. A brighter voxel results in a higher attenuation coefficient.

The All Scales Tomographic Reconstruction Antwerp (ASTRA) Toolbox provides an efficient and flexible open source toolbox for tomographic projection and reconstruction. ASTRA Toolbox was developed in 2010 by the Vision Lab, University of Antwerp, Belgium, and jointly with Centrum Wiskunde Informatica (CWI) in Amsterdam, Netherlands, since 2014. Most of the code is open source and written in C++. The core processing is offloaded to a GPU card using the CUDA language. The toolbox is accessible via both Python and MATLAB, which makes it more familiar and allows the user to delve into most algorithms (Aarle, 2016).

The flexibility in the utilization of ASTRA Toolbox comes in the following forms:

- Non-conventional geometries are supported for versatility,
- modular design affords the ability to individually used each of the sub-components so they can be personalized for your specific application,
- using it scalability feature offers reconstruction methods that can be quickly evaluated on small-sized problems with local computational platforms.

The concepts and modules available in ASTRA Toolbox:

- Volume and projection data objects, linked to their corresponding geometry information;
- the geometry information for the data objects are linked together in a projection algorithm building block;
- the algorithm building block is used together with the data in the reconstruction algorithm object

Projection and Volume Data

The ASTRA toolbox data modules store and manage projection and volume datasets. Memory is allocated first and the data has to be copied from interface layer to the actual toolbox. The operation returns a unique identifier that can be utilized to reference the data.

Geometry

The volume geometry provides a description of the pixel or voxel grid on which the reconstructed object is depicted. A voxel is usually isotropic but can be specified as anisotropic as well. This is useful in cases where the effective resolution in a reconstruction is not the same in each dimension.

The projection geometry defines the trajectory if the X-ray source and the detector relative to the volume geometry. This parameter includes the the number and size of the detectors' pixels and specification of the X-ray source and detector that rotate around the object. The available projection geometries include parallel beam and fan beam for 2D data and parallel beam and cone-beam for the three dimensional data.

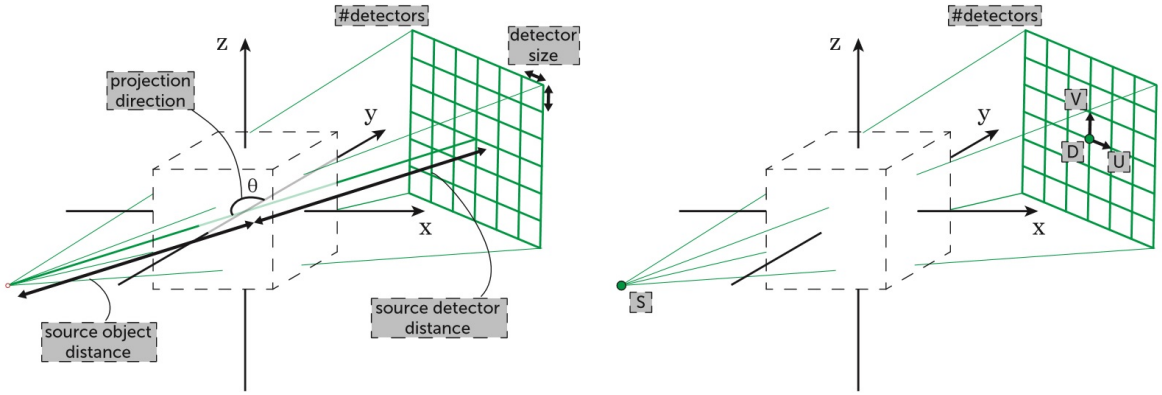

(a) default (b) vector-based

Figure B.2: Approaches to specification of a cone-beam projection geometry

The projection geometry can be conducted using two method, as displayed in Figure (B.2). The default mechanism involved the source and detector following a circular trajectory around an origin of the volume coordinate system, where the detector plane is perpendicular to the line through the source and origin. In a 3D tomographic reconstruction system, there are five sets of parameters required: the number of detector pixels, the detector pixel size, the distance from the center of rotation, the distance from the center of rotation to the center of the detector and a list of projection angles.

Instead of the method where you need to specify the parameters above and ensure a proper point of centering, the ASTRA Toolbox allows the users to specify each projection separately, referred to as the vector-based geometry. In a cone beam projection model, each projection image is defined by four 3D vectors in the volume coordinate system. This specification may be more difficult as the computation of the source and detector trajectory has to be meticulously specified.

Projection Operations

Projection operations are essential parts of the reconstruction process. The forward projection operator simulates projection images from a 2D or 3D volume by computing a sparse matrix vector multiplication:

$$p := Wv \tag{B.1}$$

where p is a vector that represents 2D or 3D projection data, v is a vector that represents 2D or 3D volume data, and W is the projection matrix, defined by both volume geometry are projection geometry.

The backprojection operation melds the projection data through a reconstruction volume by computing:

$$v := W^T p \tag{B.2}$$

The projection building blocks is where the values w_{ij} of W are calculated and used to compare projection and backprojection images. the designers of ASTRA Toolbox put effort into making this portion of the reconstruction computationally efficient.

Reconstruction Algorithms

Tomographic reconstruction algorithms are formed from the basic projection and back projecting building blocks. The reconstruction methods available in ASTRA Toolbox include Forward Backprojection (FBP) for parallel and fan beam and FDK for cone beam datasets.

B.2 Michigan Phantom Reconstruction

A phantom developed by the University of Michigan was utilized to calibrate the X-ray source. The phantom was utilized to build sinograms and test reconstruction algorithm with ASTRA Toolbox. The phantom depicts air bubbles at multiple dimensions to evaluate the necessary projections required to reconstruct the bubble column to a specific accuracy. Figure B.3 displays the Michigan phantom utilized for calibration of the reconstruction process.

Figure B.4 displays a comparison between parallel-beam and fan-beam geometry using a simple phantom of three objects. The thick red lines display the X-ray beam paths. In

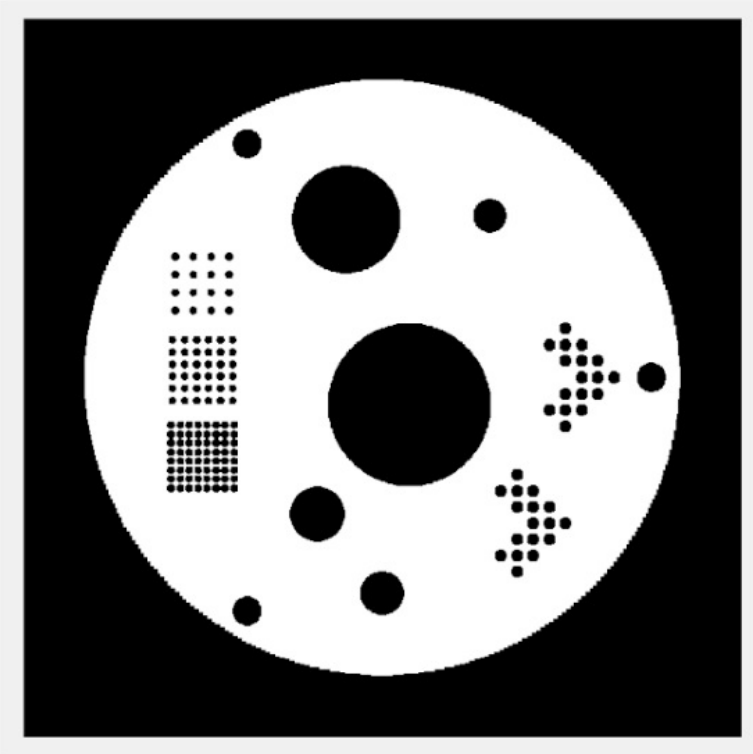

Figure B.3: University of Michigan Phantom

a parallel-beam geometry the beams are under a single projection angle. In a fan-beam geometry, these rays are located in fans from different projection angles.

Figure B.5 displays a comparison between the Radon spaces of parallel-beam and fan-beam geometry. The upper left hand side of Figure B.5 shows a simple phantom. It has two squares of variable sizes and one circle. The object have the same attenuation coefficients. The upper right side of Figure B.5 displays the Radon spaces of parallel-beam geometry with its polar representation. The lower left side displays the sinogram projection of the phantom using a parallel-beam geometry. The lower right side displays the sinogram of the phantom using fan-beam geometry. The two lower pictures look similar because the highest attenuation values are at 135° and 315° are located at the same point. A dashed line shows the prominent positions and therefore show the disparity between the two Radon spaces (sinogram representations).

Figure B.6 displays a sinogram constructed from 180 projections using a parallel-beam geometry. Figure B.7 displays a sinogram from 360 projections using parallel-beam geometry.

Figure B.8 is a two-dimensional reconstruction of a phantom. The top left figure is the original phantom. ASTRA Toolbox offers the following two-dimensional algorithms:

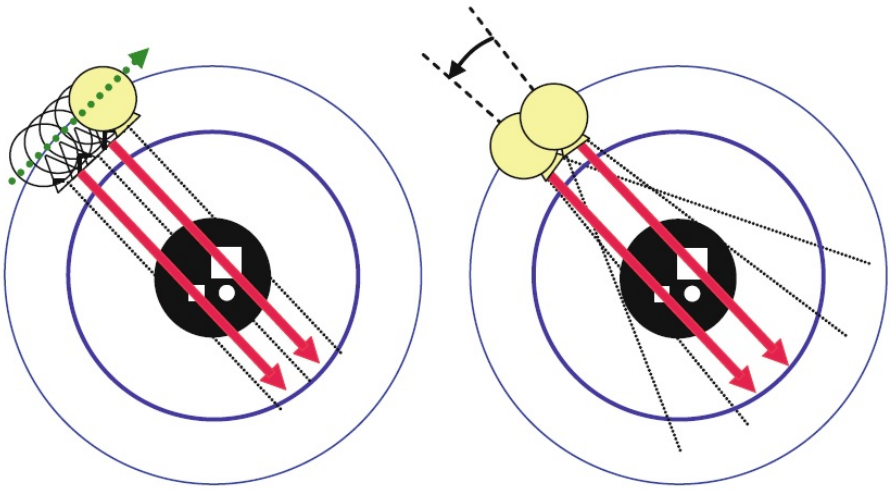

Figure B.4: Comparison of Parallel Beam and Fan Beam Geometry (Buzug, 2008)

- Back Projection (BP) - it utilizes a projector and projection data as input to return a back projection of the data
- Filtered Back Projection (FBP) - utilizes a projector, projection data and initial reconstruction as input and then returns the reconstruction.
- Simultaneous Iterative Reconstruction Technique (SIRT) - it utilizes projection data and an initial reconstruction as input, and returns the reconstruction after a specific number of iterations.
- Simultaneous Algebraic Reconstruction Technique (SART) - it utilizes projection data, initial reconstruction as input and SART iterations, which each consist of a Forward Projection and Back Projection of a single projection direction.
- Conjugate Gradient Least Squares (CGLS) - it utilizes projection data and an initial reconstruction and returns the reconstruction after a specified number of CGLS iterations. The CGLS algorithm is the most time consuming of the reconstruction algorithms.

Figure B.9 is a two-dimensional Graphical Processing Unit (GPU) reconstruction of a phantom. The top left figure is the original phantom. ASTRA Toolbox offers the following two-dimensional GPU algorithms:

- Back Projection CUDA (BP CUDA) - the GPU utilizes a projector and projection data as input to return a back projection of the data

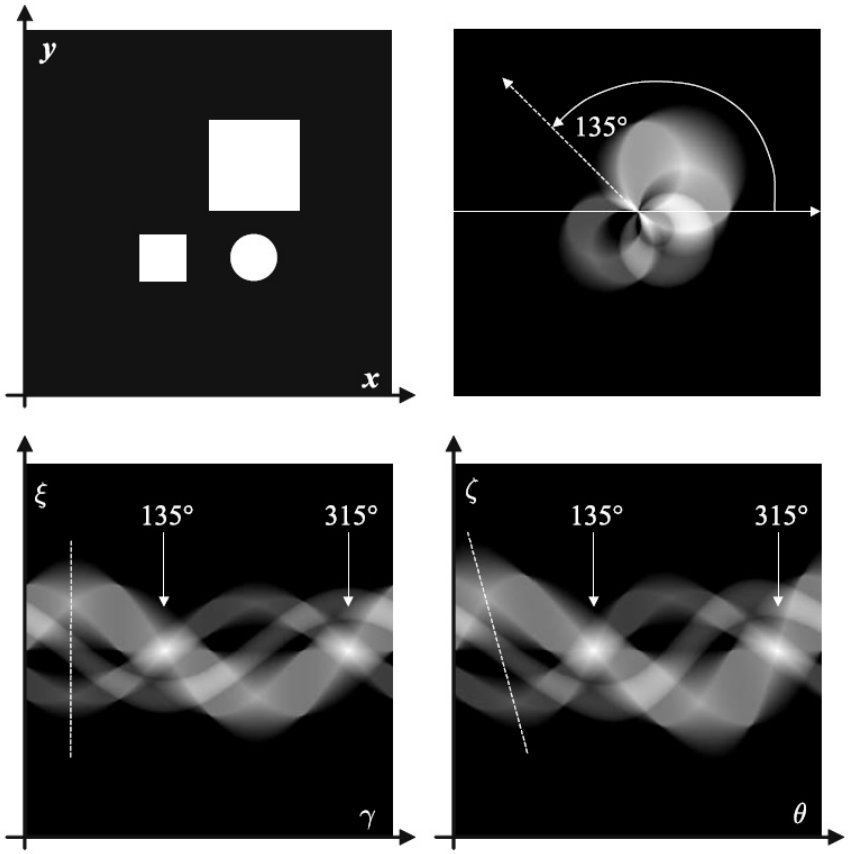

Figure B.5: Comparison between Radon spaces of parallel-beam and fan-beam geometry (Buzug, 2008)

- Filtered Back Projection CUDA (FBP CUDA) - the GPU utilizes a projector, projection data and initial reconstruction as input and then returns the reconstruction.
- Simultaneous Iterative Reconstruction Technique CUDA (SIRT CUDA) - the GPU utilizes projection data and an initial reconstruction as input, and returns the reconstruction after a specific number of iterations.
- Simultaneous Algebraic Reconstruction Technique CUDA (SART CUDA) - the GPU utilizes projection data, initial reconstruction as input and SART iterations, which each consist of a Forward Projection and Back Projection of a single projection direction.
- Conjugate Gradient Least Squares CUDA (CGLS CUDA) - the GPU utilizes projection data and an initial reconstruction and returns the reconstruction after a specified

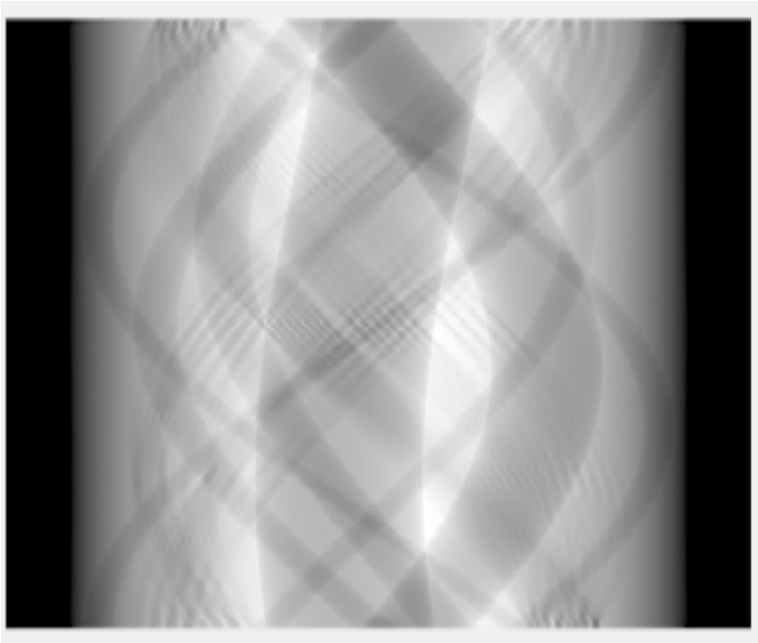

Figure B.6: University of Michigan Phantom Sinogram 180 Projections

number of CGLS iterations. The CGLS algorithm is the most time consuming of the reconstruction algorithms.

Figure B.10 is a three-dimensional Graphical Processing Unit (GPU) reconstruction of a phantom. The top left figure is the original phantom. ASTRA Toolbox offers the following three-dimensional GPU algorithms:

- Back Projection 3D CUDA (BP3D CUDA) - the GPU utilizes a projector and projection data as input to return a back projection of the data
- Filtered Back Projection CUDA (FBP CUDA) - the GPU utilizes a projector, projection data and initial reconstruction as input and then returns the reconstruction.
- Simultaneous Iterative Reconstruction Technique 3D CUDA (SIRT3D CUDA) - the GPU utilizes projection data and an initial reconstruction as input, and returns the reconstruction after a specific number of iterations.
- Conjugate Gradient Least Squares 3D CUDA (CGLS3D CUDA) - the GPU utilizes projection data and an initial reconstruction and returns the reconstruction after a specified number of CGLS iterations. The CGLS algorithm is the most time consuming of the reconstruction algorithms.

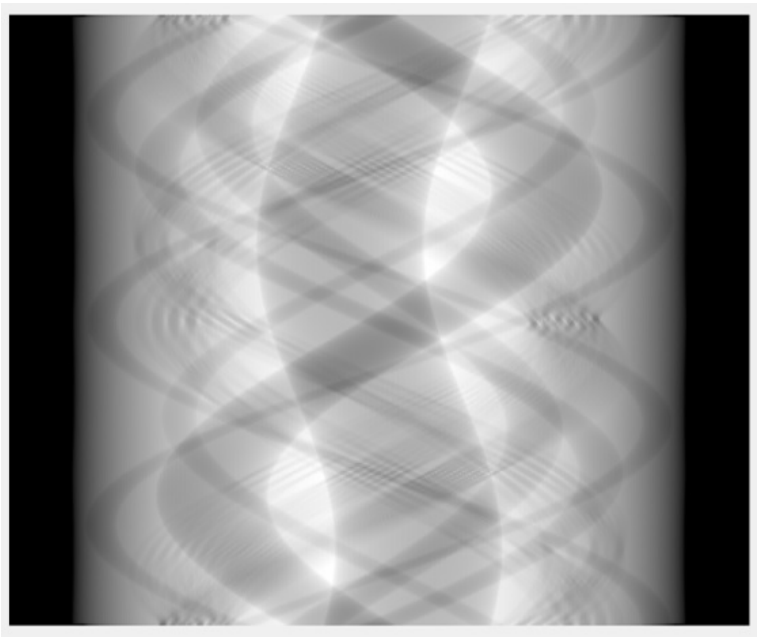

Figure B.7: University of Michigan Phantom Sinogram 360 Projections

B.3 Three-Dimensional Computed Tomography Results for a Fixed Measured Cylinder

To start evaluating the sinogram development of the X-rays, we designed a simple experiment with three acrylic cylinders inserted inside of one larger acrylic cylinder. The cylinder is a diameter of 5.25 inches. The diameter of the three cylinders within the larger cylinder is 1.25 inches. The three acrylic cylinders of 1.25 inches are maintained empty and the 5.25 acrylic cylinder is filled with water. This allows us to have an accurate assessment of the required projections to accurately calculate the voids within the large cylinder during the reconstruction process.

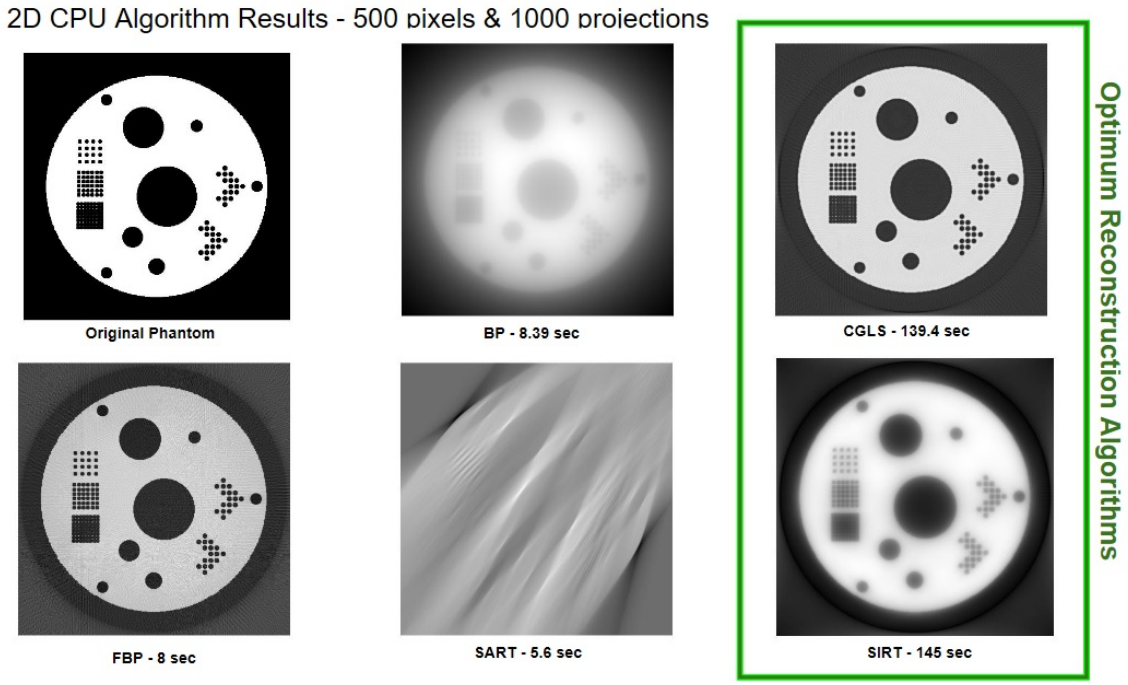

Figure B.8: Two-Dimensional CPU Reconstruction Algorithms

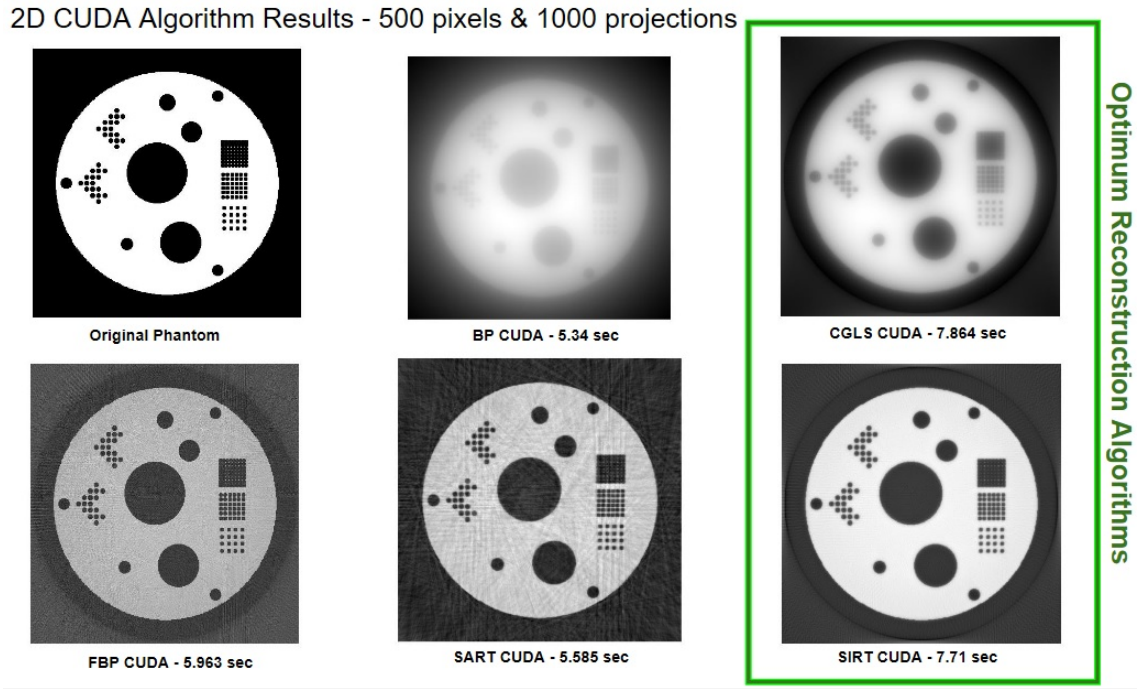

Figure B.9: Two-Dimensional GPU Reconstruction Algorithms

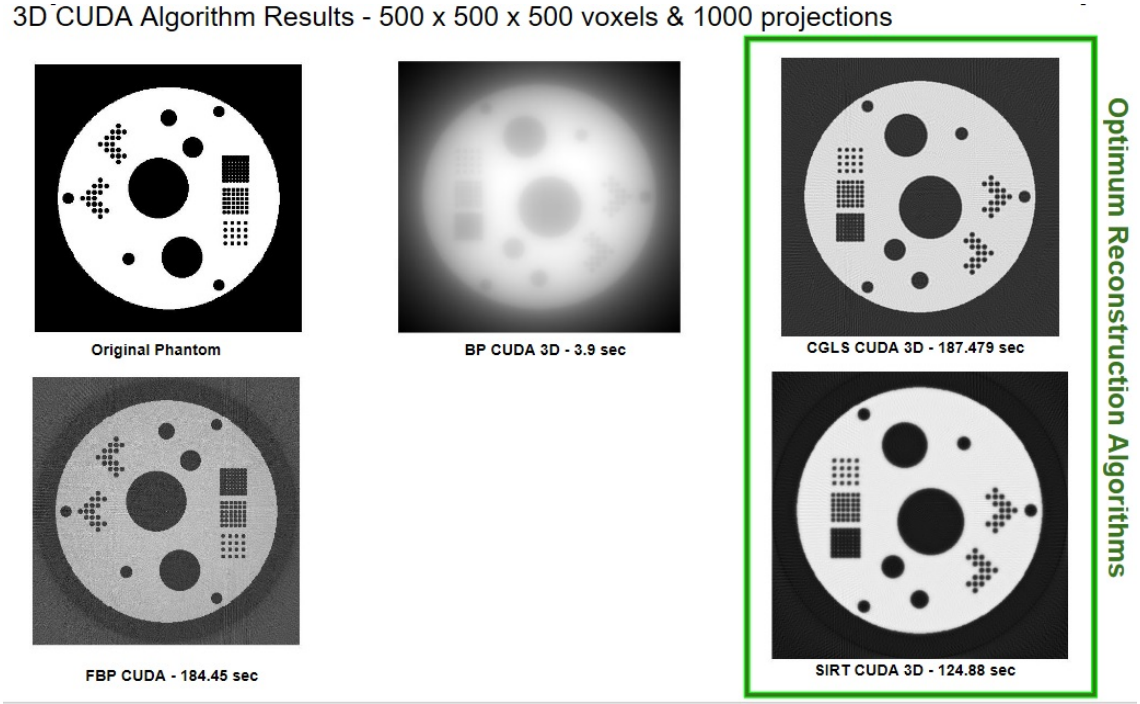

Figure B.10: Two-Dimensional GPU Reconstruction Algorithms

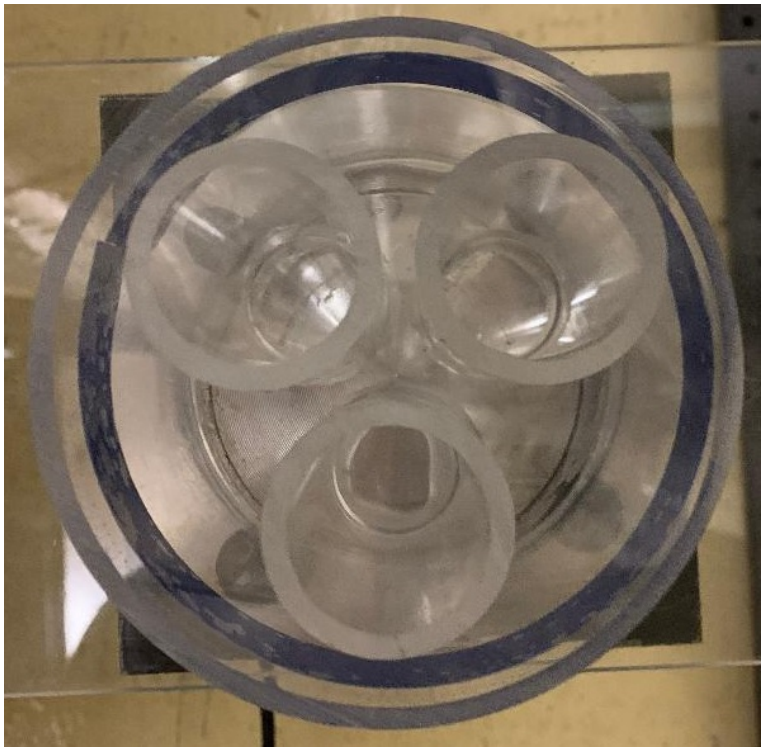

Figure B.11: Three-Dimensional Image of Acrylic Cylinder with Three Acrylic Inner Tubes

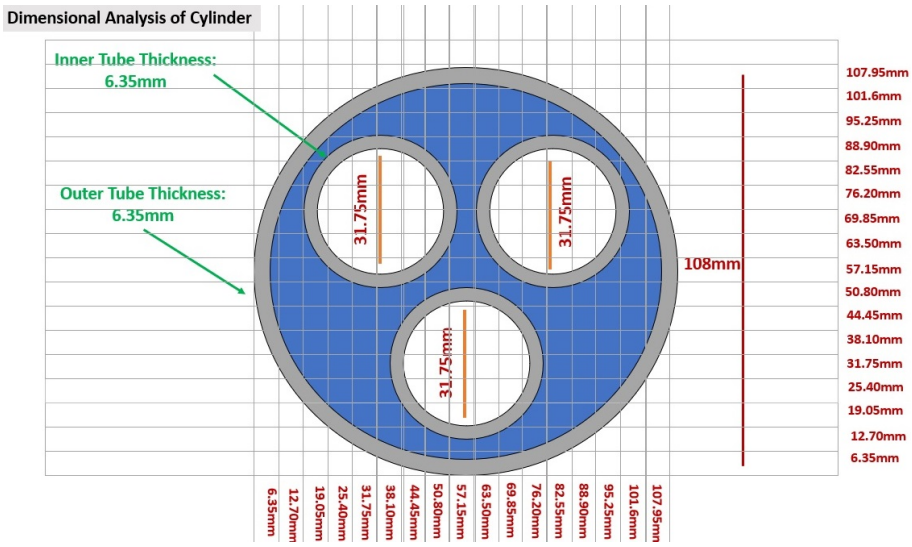

Figure B.12: Acrylic Cylinder Fixed Measurement Phanton

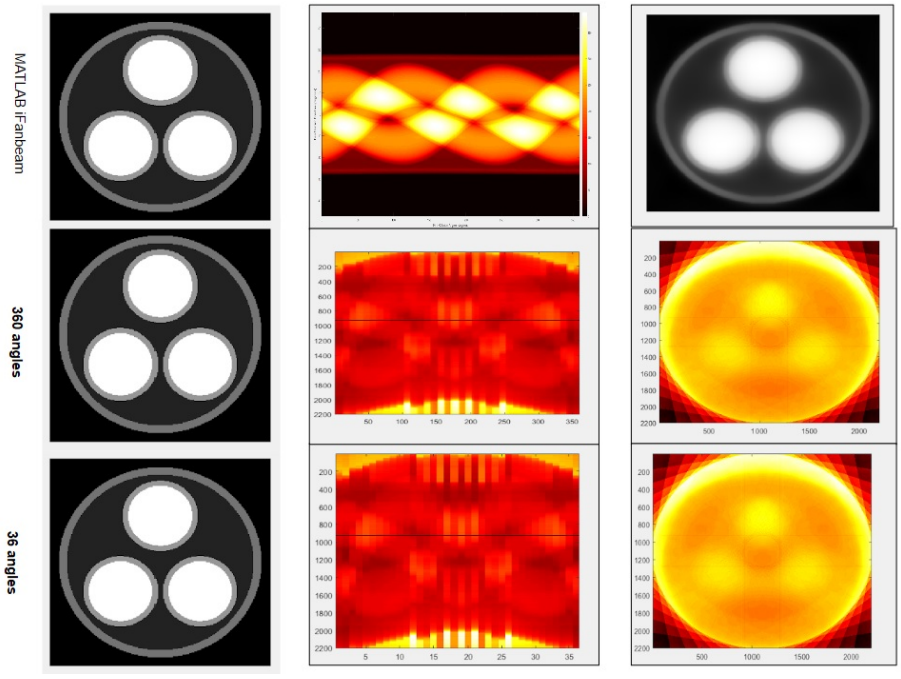

Figure B.13: Sinograms for 36 vs 360 Projections

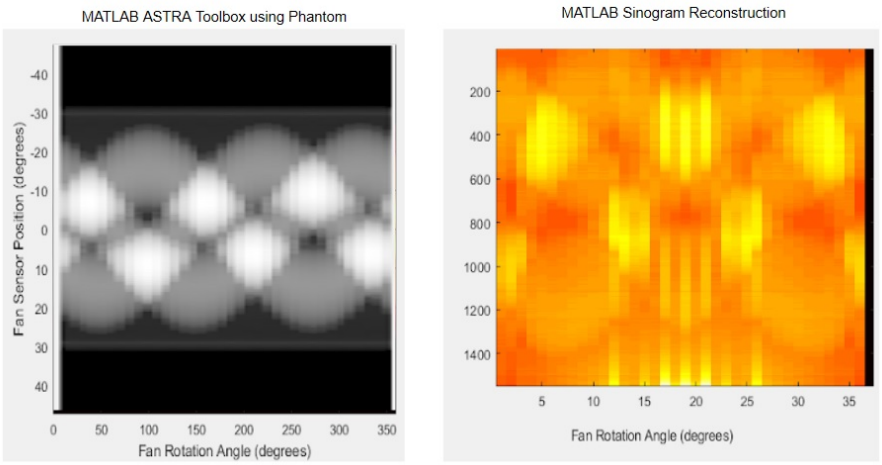

Figure B.14: Sinograms for Phanton and Cylinder Projections (ASTRA Toolbox)

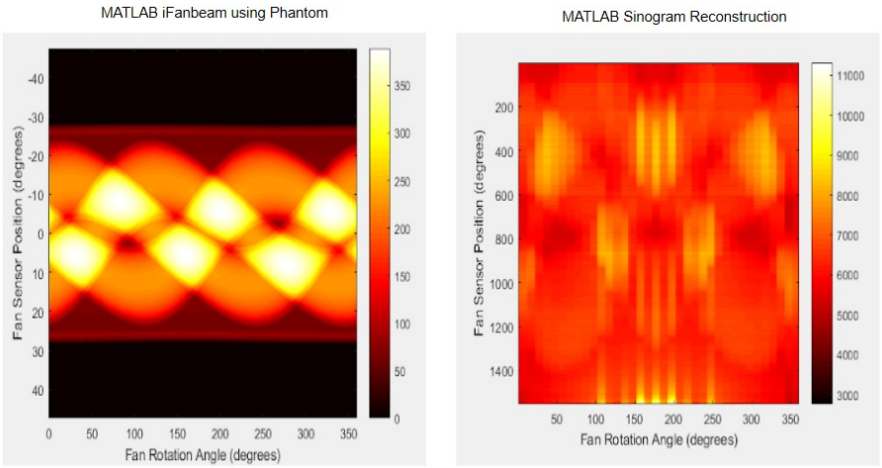

Figure B.15: Sinograms for Phanton and Cylinder Projections (iFanbeam)

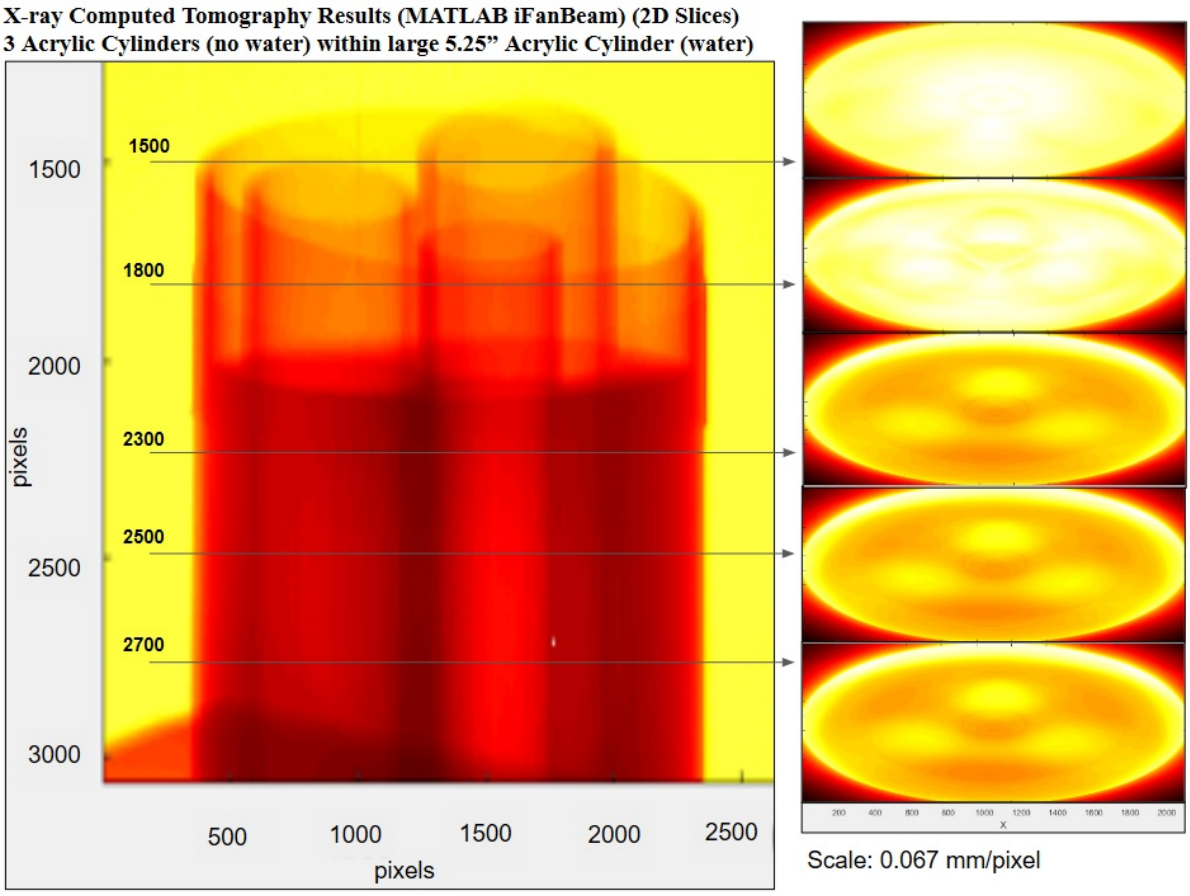

Figure B.16: Reconstructed 2D Slices for X-ray Tomographic Results - Feb 28, 2020

Appendix C

MATLAB Reconstruction File Explanation

C.1 X-ray Image File Management

We used MATLAB to interface with ASTRA Toolbox's reconstruction algorithms. The MATLAB code was built in such a way to allow one script per run. The MATLAB file includes three different parts: a section that reads the image data from the detector, a second section that builds the sinogram from the images and the third part which references the powerful reconstruction algorithms available with ASTRA Toolbox.

Since Detector 1412 collects one single .dat extension file, we need to restructure the string of values into individual frames. Detector 1412 has a 1200x1400 pixel frame.

The following function is written to perform a function where the .dat file is restructured into individual frame by reading the text file that is created by the detector. This text file is of the same name as the .dat file.

MATLAB Image File Reader Code

MATLAB Code:

```
A = [Folder 'XrayImageRun.dat'];
B = [Folder 'XrayImageRun.txt'];
[FinalImage]=ImagesIn(A,B);
function [FinalImage]=ImagesIn(A,B)
file = textread(B, "whitespace', ");
Width=str2double(strrep(file(8,1),'*',"));
Height=str2double(strrep(file(10,1),'*',"));
PixelDepth=str2double(strrep(file(12,1),'*',"));
NumberOfImages=str2double(strrep(file(14,1),'*',"));
sizeA = [Width*Height*NumberOfImages];
fileID = fopen(A);
```

```
A=(fread(fileID,sizeA,'*uint16'));
fclose(fileID);
FinalImage = zeros(1200,1400,NumberOfImages,'uint16');
for frameNB = 1:NumberOfImages
j1 = (frameNB-1)*(Width*Height)+1;
j2 = j1+(Width*Height)-1;
FinalImage(:,:,frameNB) =
reshape(A(j1:j2),[1400,1200])';
end
end
```

This function is also utilized with the generation of Flat and Dark images. A Flat Image is acquired by maintaining the same settings for the X-ray Detector, with the exception of moving the object away from the field of view. A Dark image is acquired with the X-ray source off. We usually collected 10 frames for Flat and Dark image projections.

MATLAB Image File Reader Code - Dark and Flat Images

MATLAB Code:

```
A = [Folder 'XrayImageRun17Dark.dat'];
B = [Folder 'XrayImageRun17Dark.txt'];
[FinalImage]=ImagesIn(A,B);
Dark = mean(FinalImage,3);
A = [Folder 'XrayImageRun17Flat.dat'];
B = [Folder 'XrayImageRun17Flat.txt'];
[FinalImage]=ImagesIn(A,B);
Flat = mean(FinalImage,3);
```

C.2 Region of Interest and Image Filtering

Based on the area of interest, we need to find the row that coincides with the object. We select two pixel values that define the boundaries of the object. This saves computing time and focuses the reconstruction on the intensity values of interest.

MATLAB Code for Area of Interest

MATLAB Code:

```
line = 760;
FirstColumn = 100;
LastColumn = 1350;
rowaverage = 15;
CenterOfRotationOffset = -40+27;
```

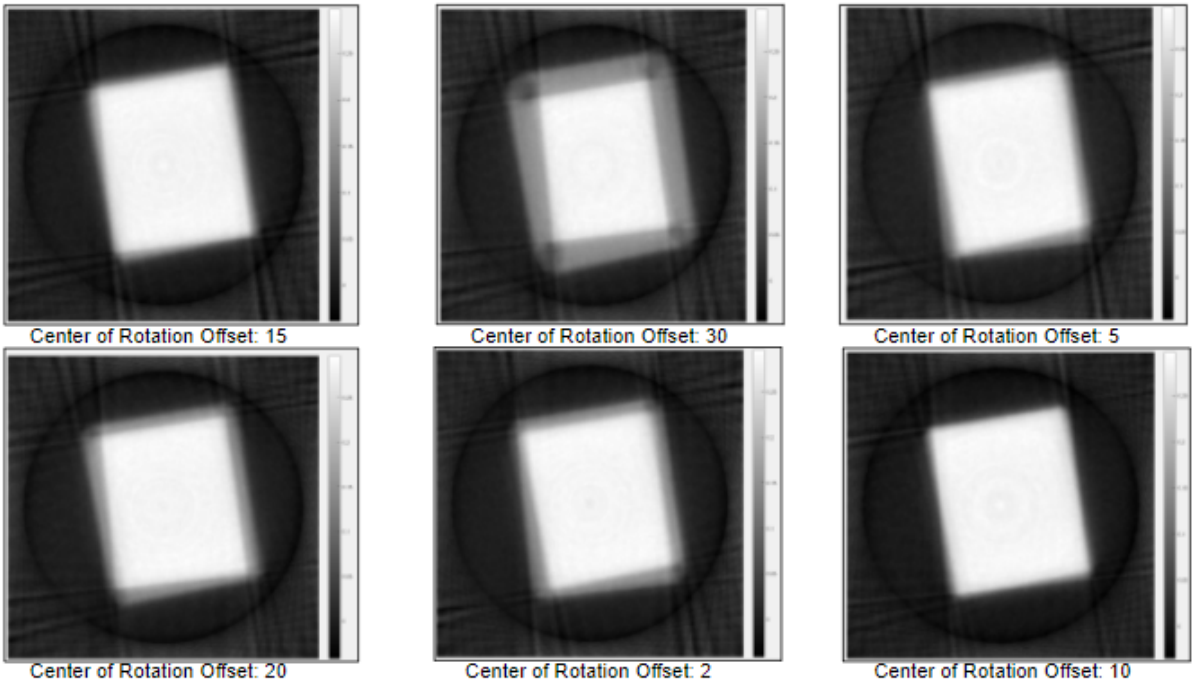

Figure C.1: Center of Rotation Offset Examples

Center of Rotation

We apply a center of rotation adjustment to correct for placing the object off-center. Based off a detector with a pixel pitch of 100 microns introduces difficulties in aligning the object on the center of rotation axis. Center the object is not achievable by the naked eye and requires a sufficient amount of time to place the object as close to center as possible. By introducing a center of rotation offset to the MATLAB code, we were able to correct all pixel lines and produce a reconstruction image that is accurate.

Figure C.1 displays the type of artifacts that are visualize if the object is reconstructed off rotation.

The images from the X-ray projections are read from a single file. We then separate the images from a single file and take the average value of each projection.

We use the following equation to calculate the intensity values at each projection angle.

$$I = -log\left[\frac{ProjectionImage - DarkImage}{FlatImage - DarkImage}\right] \tag{C.1}$$

We calculate the intensity value for each image using 30 rows for averaging.

MATLAB Code - Center of Rotation Offset

MATLAB Code:

```
counter = 0;
A = [Folder 'XrayImageRun17.dat'];
B = [Folder 'XrayImageRun17.txt'];
[FinalImage]=ImagesIn(A,B);
for AngleNB = 1:1440
Data1 = mean(FinalImage(:,:,AngleNB+1),3);
I = -log((Data1-Dark)./(Flat-Dark));
counter = counter + 1;
Data(AngleNB).a = mean(I(((line-row_average) : (line + row_average)), (FirstColumn : LastColumn) + CenterOfRotationOffset), 1);
DataRAW(AngleNB).a = mean(Data1(((line-row_average) : (line+row_average)), (FirstColumn : LastColumn) + CenterOfRotationOffset), 1);
end
```

C.3 Building Sinogram from Image Projections

We need to get the intensity values lined up into a sinogram, which is used by ASTRA tomographic algorithms for reconstruction. The sinogram is oriented with the vertical axis displaying the projection angle and the horizontal axis displaying the horizontal area of interest of the object. The different lines depict varying intensity values changing as the X-rays transmit through the object of variable densities.

MATLAB Code for Building Sinogram

MATLAB Code:

```
NBangles = 1440;
LastAngle = 360-360/NBangles;
Turn = 90;
thetas = [linspace(0,LastAngle,NBangles)-Turn]*pi/180;
sinogram = zeros(length(thetas),(LastColumn-FirstColumn)+1);
for n = 1:length(thetas)
sinogram(n,:) =(Data(n).a)';
sinogramRAW(n,:) =(DataRAW(n).a)';
end
SinogramSize=size(sinogram,2);
```

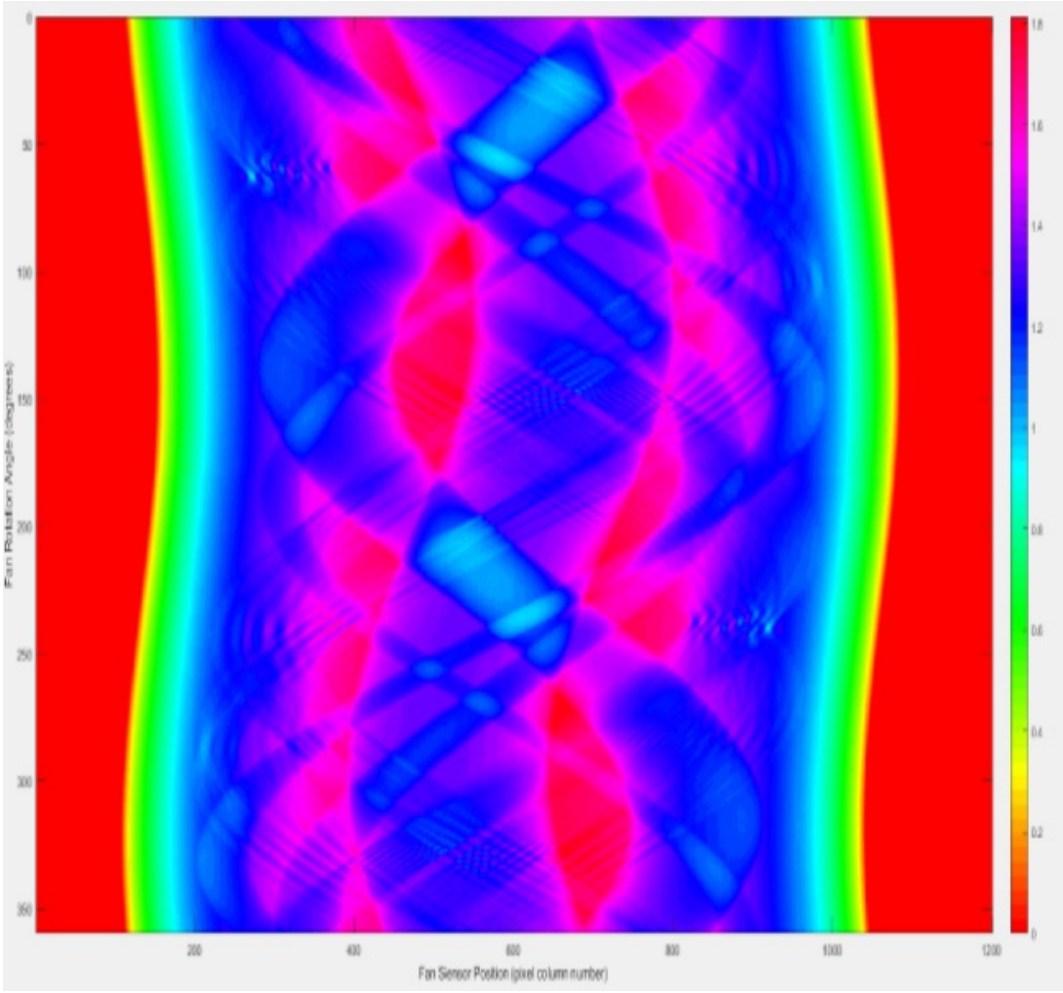

Figure C.2: Sinogram Examples

ASTRA Toolbox Reconstruction Algorithms

The construction of the sinogram is the final step and necessary to get accurate since it will be the item used by ASTRA Toolbox iterative reconstruction algorithm to reconstruct the image. The next step is to provide a volume geometry utilized to delineate the available space where the object will be reconstructed. We define a domain size in millimeters.

xmin = -50
xmax = 50
ymin = -50
ymax = 50
voxels in x = 600
voxels in y = 600

The particular detector selected, DT1412, has a pixel pitch of 100 microns, which is defined as the number of microns represented in one pixel. We then define the length between the X-ray source and the object and the distance between the object and the detector. These parameters referred to as SOD (Source to Object Distance) and ODD (Object to Detector Distance) are used in the ASTRA algorithm that creates the projection geometry.

Both the volume geometry and the projection geometry

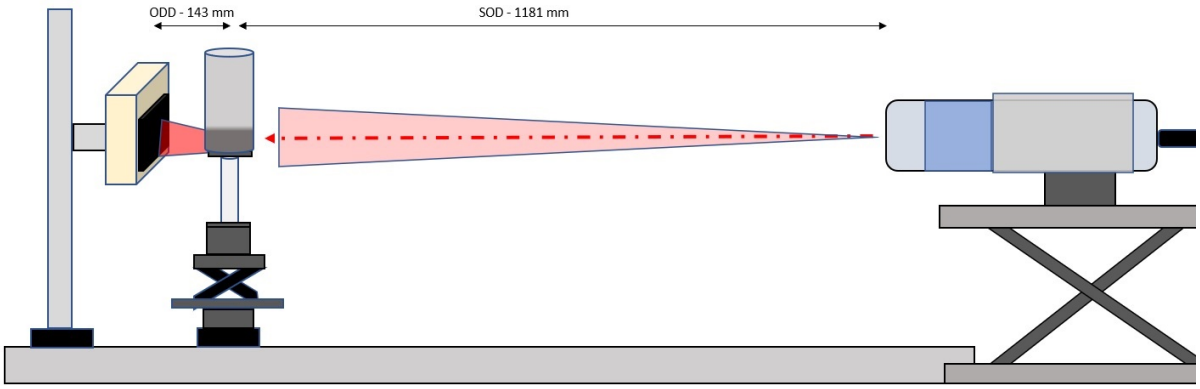

Figure C.3: Reconstruction Distance Parameters

MATLAB Reconstruction Algorithm Selection Code

recontype = 'GPU';
xmin = -50;
xmax = 50;
ymin = -50;

ymax = 50;
voxels$_x$ = 1200/2;
voxels$_y$ = $voxels_i n_x$;
volgeom = astracreatevolgeom(voxels$_x$, $voxels_y$, $xmin$, $xmax$, $ymin$, $ymax$);
PixelPitch = 0.1;
SOD = 1181;
ODD = 143;
NB iterations = 250;
switch recontype case 'CPU'
projgeom = astracreateprojgeom('fanflat', PixelPitch ,SinogramSize, thetas,SOD,ODD);
projid = astracreateprojector('stripfanflat', projgeom, volgeom);
case 'GPU'
projgeom = astracreateprojgeom('fanflat', PixelPitch ,SinogramSize, thetas,SOD,ODD);
sinogram$_i d = astramexdata2d('create','-sino', proj_geom, sinogram)$;

ASTRA Toolbox Reconstruction Algorithms

The two GPU ASTRA Toolbox reconstruction algorithms that have rendered the optimal reconstruction graphics are the SIRT and CGLS CUDA algrotihms. SIRT CUDA and CGLS CUDA are defined below:

- Simultaneous Iterative Reconstruction Technique 3D CUDA (SIRT3D CUDA) - the GPU utilizes projection data and an initial reconstruction as input, and returns the reconstruction after a specific number of iterations.
- Conjugate Gradient Least Squares 3D CUDA (CGLS3D CUDA) - the GPU utilizesprojection data and an initial reconstruction and returns the reconstruction after aspecified number of CGLS iterations. The CGLS algorithm is the most time consumingof the reconstruction algorithms

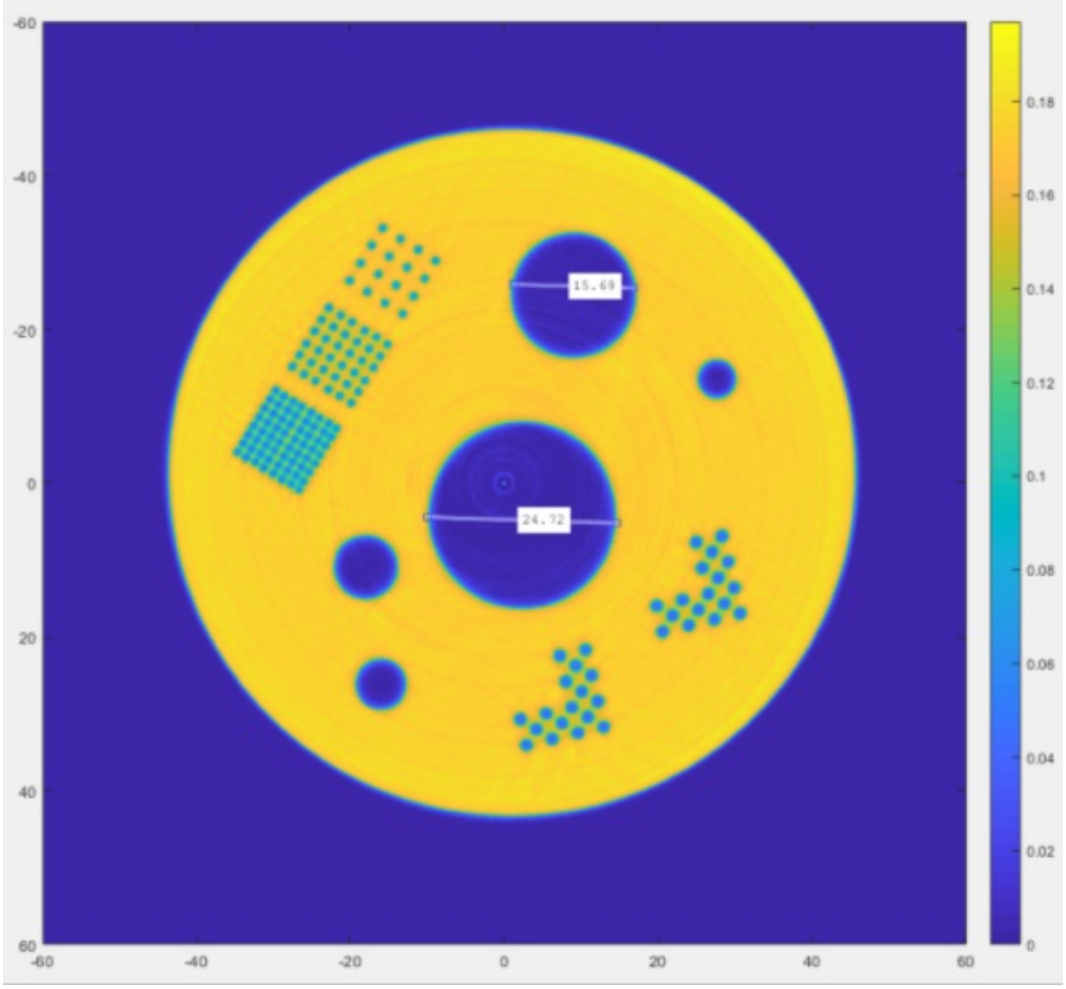

Figure C.4: Simultaneous Iterative Reconstruction Technique Bubble Phantom Reconstruction

Appendix D

MATLAB Codes for Wire Mesh Sensor Void Fraction and Velocity Measurements

Wire Mesh Sensor Void Fraction and Velocity Calculation MATLAB Code

```
clear all, clc, close all
% WMS data post-processing
% Simo Makiharju and Angel Rodriguez, UC Berkeley
% Last edited 1/24/2022

%% WMS Preset Settings
frames = 30000;          % number of frames to read
frames_cal = 30000;      % number of CALIBRATION frames
x_num = 24;              % number of wires in x direction
y_num = 24;              % number of wires in y direction
SensorFPS = 1000;        % frames per second used in WMS measurements
SensorSpace = 0.028;     % Spacing in meters between sensor measurement planes
SLPM = 12;               % Air Injection
ColorBarVFMax = 0.3;     % max colorbar setting for Voif Fraction
MaxFlowSpeed = 0.3;      % max colorbar setting for Velocity
caltype = 'Histogram';   % 'WaterCal' or 'Histogram'
Area = 0.003247^2;       % area of nodes, m^2
DiameterSensor = 0.0779;% diameter of the sensor (meters)
% Folder containing measurement data
folder = 'D:\Rodriguez_WMS_Files\UncoatedBCWMSvsDP\12SLPM\';
% Folder containing calibration data. Can be same as above.
folder_cal = 'D:\Rodriguez_WMS_Files\SHSWMS1_21_2022_Expert\WaterCal\';
%% read calibration data (*.dat-file)
FID = fopen([folder_cal,'WaterCal_X_Level1 Bottom_transformed_mirror_vertically_
transformed_rotate.dat'],'rb');
ddata1 = fread(FID,x_num * y_num * frames_cal,'uint16');
ddata1 = reshape(ddata1, [x_num y_num frames_cal]);
fclose(FID);
FID = fopen([folder_cal,'WaterCal_X_Level1 Top.dat'],'rb');
```

```
ddata2 = fread(FID,x_num * y_num * frames_cal,'uint16');
ddata2 = reshape(ddata2, [x_num y_num frames_cal]);
fclose(FID);

cdata1 = ddata1; %rename for algorithm
cdata2 = ddata2; %rename for algorithm
%% Read raw data (*.dat-file) from a single pair of WMS
FID = fopen([folder num2str(SLPM), 'SLPM1_12_2034_X_Level1 Bottom_transformed_mirror_vertically_
transformed_rotate.dat'],'rb');
ddata1 = fread(FID,x_num * y_num * frames_cal,'uint16');
ddata1 = reshape(ddata1, [x_num y_num frames]);
fclose(FID);

FID = fopen([folder num2str(SLPM),'SLPM1_12_2034_X_Level2 Top.dat'],'rb');
ddata2 = fread(FID,x_num * y_num * frames_cal,'uint16');
ddata2 = reshape(ddata2, [x_num y_num frames]);
fclose(FID);

rawdata1 = ddata1;
rawdata2 = ddata2;

%% Read data from *.v-file from a single pair of WMS
FID = fopen([folder num2str(SLPM),'SLPM1_12_2034_X_Level1 Bottom_transformed_mirror_vertically_transf
vdata1 = fread(FID,x_num * y_num * frames,'uint8');
vdata1 = reshape(vdata1, [x_num y_num frames]);
fclose(FID);

 for m = 1:24
        for n = 1:24
            for l = 1:frames
            if vdata1(m,n,l) == 255
               vdata1(m,n,1) = NaN;
            else
               vdata1(m,n,l) = vdata1(m,n,l);
            end
            end
        end
 end

FID = fopen([folder num2str(SLPM),'SLPM1_12_2034_X_Level1 Top.v'],'rb');
vdata2 = fread(FID,x_num * y_num * frames,'uint8');
vdata2 = reshape(vdata2, [x_num y_num frames]);
fclose(FID);

 for m = 1:24
        for n = 1:24
            for l = 1:frames
            if vdata2(m,n,l) == 255
               vdata2(m,n,1) = NaN;
            else
               vdata2(m,n,l) = vdata2(m,n,l);
            end
            end
        end
 end

%% Comments
% cdata1   = cal data for plane 1
% rawdata1 = raw data for plane 1
% vdata1   = vf data for plane 1
```

```
% cdata2   = cal data for plane 2
% rawdata2 = raw data for plane 2
% vdata2   = vf data for plane 2

%% Section that can be used to plot frames & volumes for initial inspection
figure(1),clf
subplot(1,2,1),imagesc((mean(vdata1(:,:,:),3)/100))
axis equal, axis tight
caxis([0 ColorBarVFMax])
colorbar
title(['Time-averaged Void Fraction Level Bottom'])
subplot(1,2,2),imagesc(mean(vdata2(:,:,:),3)/100)
axis equal, axis tight
caxis([0 ColorBarVFMax])
colorbar
title(['Time-averaged Void Fraction Level Top'])
%% Find peaks for histogram calibration
for i=1:24
    for j = 1:24
        [f,xi] = ksdensity(permute(rawdata1(i,j,:),[3 2 1]));
        [pks loc] = findpeaks(f,xi,'SortStr','descend');
        Uw1(i,j) = loc(1);
        [f,xi] = ksdensity(permute(rawdata2(i,j,:),[3 2 1]));
        [pks loc] = findpeaks(f,xi,'SortStr','descend');
        Uw2(i,j) = loc(1);
    end
end

%% Time average Calculations
switch caltype

case 'WaterCal'
    for i=1:24
    for j = 1:24
        tave1(i,j)=mean(vdata1(i,j,:));
        tave2(i,j)=mean(vdata2(i,j,:));
        ctave1(i,j)=mean(cdata1(i,j,:));
        ctave2(i,j)=mean(cdata2(i,j,:));
        rawtave1(i,j)=mean(rawdata1(i,j,:));
        rawtave2(i,j)=mean(rawdata2(i,j,:));
%         NEWCAL_tave1(i,j) = mean( 1- rawdata1(i,j,:) ./ ctave1(i,j));
%         NEWCAL_tave2(i,j) = mean( 1- rawdata2(i,j,:) ./ ctave2(i,j));

   % If using histogram cal, comment two rows above and uncomment 4 rows below
        NEWvdata1(i,j,:) =  (1- rawdata1(i,j,:) ./ Uw1(i,j))*100;
        NEWvdata2(i,j,:) =  (1- rawdata2(i,j,:) ./ Uw2(i,j))*100;

        NEWCAL_tave1(i,j) = mean(NEWvdata1(i,j,:));
        NEWCAL_tave2(i,j) = mean(NEWvdata2(i,j,:));
    end
    end

tave1 = NEWCAL_tave1;
tave2 = NEWCAL_tave2;
figure(2),clf
subplot(1,2,1)
imagesc(ctave1/100)
axis equal, axis tight, colormap(jet),colorbar
caxis([0 ColorBarVFMax])
title(['\alpha'])
```

```
subplot(1,2,2)
imagesc(ctave2/100)
axis equal, axis tight, colormap(jet),colorbar
caxis([0 ColorBarVFMax])
title(['\alpha'])

% Plot makes it easy to see if data scrambled
figure(3)
subplot(3,2,1)
imagesc(NEWCAL_tave1/100),colorbar,colormap(jet)
axis equal, axis tight
caxis([0 ColorBarVFMax])
title(['\alpha 1, data set '])
subplot(3,2,2)
imagesc(NEWCAL_tave1/100),colorbar,colormap(jet)
axis equal, axis tight
caxis([0 ColorBarVFMax])
title(['\alpha 2, data set '])

case {'Histogram'}
    for i=1:24
    for j = 1:24
        tave1(i,j)=mean(vdata1(i,j,:));
        tave2(i,j)=mean(vdata2(i,j,:));
        rawtave1(i,j)=mean(rawdata1(i,j,:));
        rawtave2(i,j)=mean(rawdata2(i,j,:));
        NEWvdata1(i,j,:) =  (1- rawdata1(i,j,:) ./ Uw1(i,j))*100;
        NEWvdata2(i,j,:) =  (1- rawdata2(i,j,:) ./ Uw2(i,j))*100;

        NEWCAL_tave1(i,j) = mean(NEWvdata1(i,j,:));
        NEWCAL_tave2(i,j) = mean(NEWvdata2(i,j,:));
    end
    end


figure(4),clf
subplot(1,2,1)
imagesc(tave1/100)
axis equal, axis tight, colormap(jet),colorbar
caxis([0 ColorBarVFMax])
title(['\alpha'])
subplot(1,2,2)
imagesc(tave2/100)
axis equal, axis tight, colormap(jet),colorbar
caxis([0 ColorBarVFMax])
title(['\alpha'])
% Plot makes it easy to see if data scrambled
figure(5)
subplot(3,2,1)
imagesc(NEWCAL_tave1/100),colorbar,colormap(jet)
axis equal, axis tight
caxis([0 ColorBarVFMax])
title(['\alpha 1, data set '])

subplot(3,2,2)
imagesc(NEWCAL_tave1/100),colorbar,colormap(jet)
axis equal, axis tight
caxis([0 ColorBarVFMax])
title(['\alpha 2, data set '])
end
```

```
switch caltype
case 'WaterCal'
subplot(3,2,3)
imagesc(ctave1/100),colorbar,colormap(jet)
axis equal, axis tight
caxis([0 ColorBarVFMax])
title(['Cal 1, data set '])

subplot(3,2,4)
imagesc(ctave2/100),colorbar,colormap(jet)
axis equal, axis tight
caxis([0 ColorBarVFMax])
title(['Cal 2, data set '])

subplot(3,2,5)
imagesc(NEWCAL_tave1/100),colorbar,colormap(jet)
axis equal, axis tight
caxis([0 ColorBarVFMax])
title(['New Cal \alpha 1, data set '])

subplot(3,2,6)
imagesc(NEWCAL_tave2/100),colorbar,colormap(jet)
axis equal, axis tight
caxis([0 ColorBarVFMax])
title(['New Cal \alpha 2, data set '])

    case {'Histogram'}
subplot(3,2,3)
imagesc(rawtave1/100),colorbar,colormap(jet)
axis equal, axis tight
caxis([0 ColorBarVFMax])
title(['Raw 1, data set '])

subplot(3,2,4)
imagesc(rawtave2/100),colorbar,colormap(jet)
axis equal, axis tight
caxis([0 ColorBarVFMax])
title(['Raw 2, data set '])

subplot(3,2,5)
imagesc(NEWCAL_tave1/100),colorbar,colormap(jet)
axis equal, axis tight
caxis([0 ColorBarVFMax])
title(['New Cal \alpha 1, data set '])

subplot(3,2,6)
imagesc(NEWCAL_tave2/100),colorbar,colormap(jet)
axis equal, axis tight
caxis([0 ColorBarVFMax])
title(['New Cal \alpha 2, data set '])
end
%% Replace vdata if you want to Xcorr on our vf instead of Wire MEsh Sensor Framework software output
%vdata1 = NEWvdata1;
%vdata2 = NEWvdata2;
%%%%%%%%%%%%%%%%%%%%%%%%%%%%%%%%%%%%%%%%%%%%%%%%%%%%%%%%%%%%%%%%%%%%%%%%%%%%%%%%%%%%%%%%%%%%%%%%%%%%
%% View t-traces of full frame average for initial troubleshooting
for i=1:frames
    ave1(i) = mean2(vdata1(:,:,i));
    ave2(i) = mean2(vdata2(:,:,i));
```

```
end
ave1 = ave1./mean(ave1,'omitnan');
ave2 = ave2./mean(ave2,'omitnan');

ave1 = normr(ave1);
ave2 = normr(ave2);

ave1 = (ave1-mean(ave1,'omitnan'))/std(ave1,'omitnan');
ave2 = (ave2-mean(ave2,'omitnan'))/std(ave2,'omitnan');

figure(6),clf
plot(1:frames,ave1,1:frames,ave2)
axis([1 frames -10 10])
legend('Wire Mesh Sensor Bottom','Wire Mesh Sensor Top')

%% Test X-cor of full frame average for initial troubleshooting
figure(7)
r = xcorr(ave1,ave2);
subplot(1,2,1)
plot(r), grid on
Fs = SensorFPS;
[acor,lag] = xcorr(ave1,ave2);
[~,I] = max(abs(acor));
lagDiff = lag(I);
timeDiff = lagDiff/Fs;
FlowSpeed = -SensorSpace/timeDiff;
subplot(1,2,2)
plot(lag,acor)

%% Windowing aproach
% Integer node groupings from [1:48; 48./[1:48]]
% nodes squared 1     2     3     4     6     8    12     24
%              24    12     8     6     4     3     2     1

%Template_Size = [1 2 3 4 6 8 12 24];
Template_Size = [1];
NB_Templates = size(Template_Size,2);
tic
for J = 1:NB_Templates % template #
    Template = Template_Size(J);
    for i = 1:(24/Template)
        for j = 1:(24/Template)
            for t = 1:frames
                ia = 1+(i-1)*Template; ib = i*Template;
                ja = 1+(j-1)*Template; jb = j*Template;
                WindowAve(J).plane1(i,j,t) = mean2(vdata1(ia:ib,ja:jb,t));
                WindowAve(J).plane2(i,j,t) = mean2(vdata2(ia:ib,ja:jb,t));
            end
        end
    end
end
toc
%% Flow Speed Calculations
Fs = SensorFPS;          % samples per second
clear FlowSpeed FlowSpeed_Pxcor
PiecewiseCorr = 1;
windowSize = 10;
b = (1/windowSize)*ones(1,windowSize);
a = 1;
```

```
tic
for J = NB_Templates:-1:1 % template #. FOR QUICK TEST, USE e.g. just 5
    Template = Template_Size(J);
    k = 0; % subplot #
    for i = 1:(24/Template)
        for j = 1:(24/Template)
            k = k+1; % subplot #

            ave1 = WindowAve(J).plane1(i,j,:);
            ave2 = WindowAve(J).plane2(i,j,:);

            WindowAve(J).norm1(i,j,:) = (ave1-mean(ave1))/std(ave1);
            WindowAve(J).norm2(i,j,:) = (ave2-mean(ave2))/std(ave2);

            norm1 = permute(WindowAve(J).norm1(i,j,:),[3 2 1]);
            norm2 = permute(WindowAve(J).norm2(i,j,:),[3 2 1]);

            % Sliding average filter
            %norm1 = filter(b,a,norm1);
            %norm2 = filter(b,a,norm2);

            % Median filter
            %norm1 = median(norm1,windowSize);
            %norm2 = median(norm2,windowSize);
            if i==12 && j==12
            figure(8),clf
            plot(1:frames,norm1,1:frames,norm2)
            legend('WMS Bottom Sensor','WMS Top Sensor')
            ax=gca;
            ax.FontSize = 15;
            else
            end
%           figure(30)
%           subplot((24/Template),(24/Template),k),plot(1:frames,norm1,1:frames,norm2)

            [acor,lag] = xcorr(norm1,norm2,3000);
            c0 = floor(size(acor,1)/2)-2000; c1=floor(size(acor,1)/2)-50; %limit speed to 0.25 m/s to
            [~,I] = max((acor(c0:c1)));
            lagDiff = lag(c0+I-1);
            timeDiff = lagDiff/Fs;
            FlowSpeed(i,j) = -0.0246/timeDiff;

%           figure(40)
%           subplot((24/Template),(24/Template),k),plot(lag,acor),grid on
            if PiecewiseCorr == 1 % also do piece xcor and average
            PieceLength = 2000;
            Smax=2000; % maximum shift
            Pmax = floor((frames-Smax)/PieceLength); % # of segments to shift
            Pxcor = NaN(Pmax,Smax);
             for p = 1:Pmax
               ia = 1+(p-1)*PieceLength; ib = p*PieceLength;
               Piece1 = norm1(ia:ib);
               Piece1 = (Piece1-mean(Piece1))/std(Piece1); %re-normalize piece

              for s = 50:Smax % shift
               Piece2 = norm2((ia+s):(ib+s));
               Piece2 = (Piece2-mean(Piece2))/std(Piece2); %re-normalize piece
               Pxcor(p,s) = sum(Piece1.*Piece2);
               end
             end
```

```
            end
%             figure(50),clf
%             imagesc(Pxcor),colorbar,colormap(jet)
%             figure(60)
%             subplot((24/Template),(24/Template),k),plot(sum(Pxcor)),grid on
             [~,I] = max(sum(Pxcor));
             timeDiff = I/Fs;
             FlowSpeed_Pxcor(i,j) = SensorSpace/timeDiff;
             Area = (Template*DiameterSensor/24)^2; %area of nodes, m^2
             Flow(J).vf1(i,j) =  mean(ave1)/100;
             Flow(J).vf2(i,j) =  mean(ave2)/100;
             Flow(J).Speed(i,j) =  FlowSpeed(i,j);
             Flow(J).Rate(i,j) =  (mean(ave1)+mean(ave2))/2 * FlowSpeed(i,j) * Area;
             Flow(J).SpeedXcor(i,j) =  FlowSpeed_Pxcor(i,j);
             Flow(J).RateXcor(i,j) =  (mean(ave1)+mean(ave2))/2 * FlowSpeed_Pxcor(i,j) * Area;
        end
    end
    Flow(J).Volumerate = sum(sum(Flow(J).Rate(i,j)));                    % total volume flow rate m^3/s
    Flow(J).VolumerateXcor = sum(sum(Flow(J).RateXcor(i,j)));            % total volume flow rate m^3/s

    %FlowSpeed
    figure(8),clf
    subplot(1,2,1)
    imagesc(FlowSpeed),colorbar,colormap(jet)
    for i=1:24
    for j=1:24
    if FlowSpeed(i,j) < 0.0125
    FlowSpeed(i,j)=nan;
    else
    end
    end
    end
    FlowSpeedAverage = mean(mean(FlowSpeed,'omitnan'));
    axis equal, axis tight
     title(['$U_{rm} \frac{m}{s}$ based on full time trace'],'interpreter','latex')
    subtitle(['Average Mean Velocity =', num2str(FlowSpeedAverage,'%05.2f'),'$\frac{m}{s}$'],'interpr
    caxis([0 0.5])
    ax=gca;
    ax.FontSize = 15;
    subplot(1,2,2)
    imagesc(FlowSpeed_Pxcor),colorbar,colormap(jet)
    for i=1:24
    for j=1:24
    if FlowSpeed_Pxcor(i,j) > 24
    FlowSpeed_Pxcor(i,j)=nan;
    else
    end
    end
    end
    FlowSpeed_PxcorAverage = mean(mean(FlowSpeed_Pxcor,'omitnan'));
    axis equal, axis tight
    title(['$U_{rm} \frac{m}{s}$ based on segmented time trace'],'interpreter','latex')
    subtitle(['Average Mean Velocity =', num2str(FlowSpeed_PxcorAverage,'%05.2f'),'$\frac{m}{s}$'],'
    caxis([0 0.5])
    ax=gca;
    ax.FontSize = 15;
%% Radial Distribution of Velocity
N=x_num;
    [X,Y] = meshgrid(-1:2/(N):1);
    Z=FlowSpeed;
```

```
    Nmid = (N)/2;
    X = X(1,:);
    Y = Y(:,1);
    Zx = Z(Nmid,Nmid:end);
    Zy = Z(Nmid:end,Nmid)';
    M=(N)/2+1;
    [Zr,r] = radialavg(Z,M);
    err = Zr-(Zx+Zy)/2;
    alpha=Zr;
figure(9);
subplot(2,1,1)
    imagesc(X,Y,Z);colormap(jet);colorbar;title('Lateral Distibution of Velocity');
    xlabel('X');ylabel('Y');
    caxis([0 0.25]);
subplot(2,1,2)
    plot(r,Zr,'o');
    title('Average Radial Distibution of Velocity');
    xlabel('r'); ylabel('alpha');
    legend('Void Fraction');
    axis([0 1 0 0.3])
figure(10);
plot(r,err);
title(sprintf('%s Error=%0.1g', t, std(err,'omitnan')))
xlabel('rho'); ylabel('Z');
    savefig(gcf,['Template' num2str(Template) '_Climited.fig'])
    saveas(gcf,['Template' num2str(Template) '_Climited.png'])
% Void Fraction
figure(11),clf
subplot(1,2,1)
imagesc(Flow(J).vf1),colorbar,colormap(jet)
axis equal, axis tight
title('\it\alpha\rm_1', num2str(mean(mean(Flow(J).vf1,'omitnan'))))
subplot(1,2,2)
imagesc(Flow(J).vf2),colorbar,colormap(jet)
axis equal, axis tight
title('\it\alpha\rm_2', num2str(mean(mean(Flow(J).vf2,'omitnan'))))
savefig(gcf,['Summary_Template' num2str(Template) '_Climited.fig'])
saveas(gcf,['Summary_Template' num2str(Template) '_Climited.png'])
end
toc
```

Appendix E

MATLAB Codes for X-ray Computed Tomography and Intensity Variation of Void Fraction Measurements

X-ray Computed Tomography and Intensity Variation Void Fraction Measurement MATLAB Code

```
%%MATLAB Code
% using ASTRA Toolbox
% developed by Simo Makiharju and Angel Rodriguez
clear all;
close all;
clc;
%% Initial Parameters

% Xray kV = 100
% Xray uA = 350
% Xray TXI = On
% Xray Mode = Microfocus
% Detector Thresholds: 40keV and 60keV

%%Reading Images

%%  With Dual Threshold (Low kV = 40kV High kV = 90)

%% Preset Values

framescollected = 30;          % frames collected per angle
numthetas = 360;               % number of angles
line = 80;                     % center line of interest
FirstColumn = 600;             % first pixel boundary to left
LastColumn = 1900;             % last pixel boundary to right
row_average = 10;              % average of rows from center
line in both directions (cannot be greater than 125
after summing to 'line' value
```

```
CenterOfRotationOffset = 49;   % center or rotation applied to all projections
recontype = 'GPU';             % CPU or GPU
PixelRegion = {[line-row_average,line+row_average],[1,2048]};
voxeladjust=1;
VoxelSize=1200;
NB_iterations=100;

% Files for reading
filename = [cd '\UncoatedPVCBCMixture12SLPM\UncoatedPVCBCMixture_W2048X256X2047_bits16_TE_000.tif'];
tic
numimgs = 2047;
XrayImageTE = zeros(((line+row_average)-(line-row_average))+1,2048,10861,'uint16');
for i = 30:numimgs
    if (i >= 1272) && (i <= 1291)
      I = imread(filename,'PixelRegion',PixelRegion,1271);
      XrayImageTE(:,:,i-29) = I;
    else
      I = imread(filename,'PixelRegion',PixelRegion,i);
      XrayImageTE(:,:,i-29) = I;
    end
end

filename = [cd '\UncoatedPVCBCMixture12SLPM\UncoatedPVCBCMixture_W2048X256X2047_bits16_TE_001.tif'];

numimgs = 2047;
for i = 1:numimgs
      I = imread(filename,'PixelRegion',PixelRegion,i);
      XrayImageTE(:,:,i+2018) = I;
end

filename = [cd '\UncoatedPVCBCMixture12SLPM\UncoatedPVCBCMixture_W2048X256X2047_bits16_TE_002.tif'];

numimgs = 2047;
for i = 1:numimgs
      I = imread(filename,'PixelRegion',PixelRegion,i);
      XrayImageTE(:,:,i+4065) = I;
end

filename = [cd '\UncoatedPVCBCMixture12SLPM\UncoatedPVCBCMixture_W2048X256X2047_bits16_TE_003.tif'];

numimgs = 2047;
for i = 1:numimgs
      I = imread(filename,'PixelRegion',PixelRegion,i);
      XrayImageTE(:,:,i+6112) = I;
end

filename = [cd '\UncoatedPVCBCMixture12SLPM\UncoatedPVCBCMixture_W2048X256X2047_bits16_TE_004.tif'];

numimgs = 2047;
for i = 1:numimgs
      I = imread(filename,'PixelRegion',PixelRegion,i);
      XrayImageTE(:,:,i+8159) = I;
end

filename = [cd '\UncoatedPVCBCMixture12SLPM\UncoatedPVCBCMixture_W2048X256X655_bits16_TE_005.tif'];

numimgs = 655;
for i = 1:numimgs
      I = imread(filename,'PixelRegion',PixelRegion,i);
      XrayImageTE(:,:,i+10206) = I;
```

```
end

for i = 1:10861
      XrayImagePixelShiftTE(:,:,i)=PixelShift(XrayImageTE(:,:,i));
end

FinalImageTE = zeros(size(XrayImageTE,1),2063,numthetas,'uint16');

counter = 0;
for p = 1:numthetas
    counter = counter + framescollected;
    FinalImageTE(:,:,p) = mean(XrayImagePixelShiftTE(:,:,(counter-(framescollected-1)):counter),3);
end

% Reading Flat Image
filename = [cd '\UncoatedPVCBCFlat\UncoatedPVCBCFlat_W2048X256X36_bits16_TE_000.tif'];
numimgs = 10;
FlatImageTE = zeros(size(XrayImageTE,1),2063,numimgs,'uint16');
for j = 1:10
      J = imread(filename,'PixelRegion',PixelRegion,j);
      XrayImageFlatTE(:,:,j) = J;
      XrayImagePixelShiftTE(:,:,j)=PixelShift(XrayImageFlatTE(:,:,j));
      FlatImageTE(:,:,j) = XrayImagePixelShiftTE(:,:,j);
end

FlatImageTE(:,:,1) = mean(FlatImageTE,3);


% Files for reading
filename = [cd '\UncoatedPVCBCMixture12SLPM\UncoatedPVCBCMixture_W2048X256X2047_bits16_HE_000.tif'];
tic
numimgs = 2047;
XrayImageHE = zeros(((line+row_average)-(line-row_average))+1,2048,10861,'uint16');
for i = 30:numimgs
    if (i >= 1272) && (i <= 1291)
      I = imread(filename,'PixelRegion',PixelRegion,1271);
      XrayImageHE(:,:,i-29) = I;
    else
      I = imread(filename,'PixelRegion',PixelRegion,i);
      XrayImageHE(:,:,i-29) = I;
    end
end

filename = [cd '\UncoatedPVCBCMixture12SLPM\UncoatedPVCBCMixture_W2048X256X2047_bits16_HE_001.tif'];

numimgs = 2047;
for i = 1:numimgs
      I = imread(filename,'PixelRegion',PixelRegion,i);
      XrayImageHE(:,:,i+2018) = I;
end

filename = [cd '\UncoatedPVCBCMixture12SLPM\UncoatedPVCBCMixture_W2048X256X2047_bits16_HE_002.tif'];

numimgs = 2047;
for i = 1:numimgs
      I = imread(filename,'PixelRegion',PixelRegion,i);
      XrayImageHE(:,:,i+4065) = I;
end

filename = [cd '\UncoatedPVCBCMixture12SLPM\UncoatedPVCBCMixture_W2048X256X2047_bits16_HE_003.tif'];
```

```
numimgs = 2047;
for i = 1:numimgs
      I = imread(filename,'PixelRegion',PixelRegion,i);
      XrayImageHE(:,:,i+6112) = I;
end

filename = [cd '\UncoatedPVCBCMixture12SLPM\UncoatedPVCBCMixture_W2048X256X2047_bits16_HE_004.tif'];

numimgs = 2047;
for i = 1:numimgs
      I = imread(filename,'PixelRegion',PixelRegion,i);
      XrayImageHE(:,:,i+8159) = I;
end

filename = [cd '\UncoatedPVCBCMixture12SLPM\UncoatedPVCBCMixture_W2048X256X655_bits16_HE_005.tif'];

numimgs = 655;
for i = 1:numimgs
      I = imread(filename,'PixelRegion',PixelRegion,i);
      XrayImageHE(:,:,i+10206) = I;
end

for i = 1:10861
      XrayImagePixelShiftHE(:,:,i)=PixelShift(XrayImageHE(:,:,i));
end

FinalImageHE = zeros(size(XrayImageHE,1),2063,numthetas,'uint16');

counter = 0;
for p = 1:numthetas
    counter = counter + framescollected;
    FinalImageHE(:,:,p) = mean(XrayImagePixelShiftHE(:,:,(counter-(framescollected-1)):counter),3);
end



% Reading Flat Image
filename = [cd '\UncoatedPVCBCFlat\UncoatedPVCBCFlat_W2048X256X36_bits16_HE_000.tif'];
numimgs = 10;
FlatImageHE = zeros(size(XrayImageHE,1),2063,numimgs,'uint16');
for j = 1:10
      J = imread(filename,'PixelRegion',PixelRegion,j);
      XrayImageFlatHE(:,:,j) = J;
      XrayImagePixelShiftHE(:,:,j)=PixelShift(XrayImageFlatHE(:,:,j));
      FlatImageHE(:,:,j) = XrayImagePixelShiftHE(:,:,j);
end

FlatImageHE(:,:,1) = mean(FlatImageHE,3);


FinalImageMixture = FinalImageTE-FinalImageHE;
FinalImage=FinalImageMixture;
FlatImage = FlatImageTE-FlatImageHE;

figure(1),clf
[recmixture,imgCorrectedmixture,Imixture]=TwoDimensionalReconstruction(FinalImage,FlatImage,
numthetas,line,FirstColumn,LastColumn,row_average,CenterOfRotationOffset,recontype,
VoxelSize,NB_iterations);
```

```
% Mean and Std Deviation
figure(11)
imagesc(imgCorrectedmixture)
hEllipse = imellipse(gca,[198/voxeladjust 160/voxeladjust 818/voxeladjust 823/voxeladjust]);
maskImage = hEllipse.createMask();
imshow(maskImage)
maskedImage = imgCorrectedmixture .* cast(maskImage, class(imgCorrectedmixture));
imshow(maskedImage);
column1 = find(sum(maskImage, 1), 1, 'first');
column2 = find(sum(maskImage, 1), 1, 'last');
row1 = find(sum(maskImage, 2), 1, 'first');
row2 = find(sum(maskImage, 2), 1, 'last');
croppedImagemix = maskedImage(row1:row2, column1:column2);
imagesc(croppedImagemix)
m=numel(croppedImagemix)
counter=0;
som=0;
for i=1:m;
    if croppedImagemix(i) == 0
        som=som+0;
    else
        som=som+croppedImagemix(i);
        counter=counter+1;
    end
end
avg=som/counter;
o=numel(croppedImagemix)
% avg=mean(nonzeros(croppedImagewater));
sd=0;
for i=1:o;
    if croppedImagemix(i) == 0
        sd=sd+0;
    else
        sd=sd+(croppedImagemix(i)-avg)^2;
    end
    end
sdfinalmix=(sd/(o-1))^(1/2)
avgmix = avg
title(['Mean =    ', num2str(avgmix),'     Standard Deviation =     ', num2str(sdfinalmix)])



%% Water Only

%% Reading Images - Water Only
CenterOfRotationOffset = -9+58;

filename = [cd '\UncoatedPVCBCWaterOnly\UncoatedPVCBCWaterOnly_W2048X256X361_bits16_TE_000.tif'];
tic
numimgs = 360;
XrayImageTE = zeros(((line+row_average)-(line-row_average))+1,2048,numimgs,'uint16');
for i = 1:numimgs
       I = imread(filename,'PixelRegion',PixelRegion,i+1);
      XrayImageTE(:,:,i) = I;
end

for i = 1:360
      XrayImagePixelShiftTE(:,:,i)=PixelShift(XrayImageTE(:,:,i));
end
```

```
FinalImageTE = zeros(size(XrayImageTE,1),2063,numimgs,'uint16');
FinalImageTE = XrayImagePixelShiftTE;
FinalImageWaterTE = FinalImageTE;

% Reading Flat Image
filename = [cd '\UncoatedPVCBCFlat\UncoatedPVCBCFlat_W2048X256X36_bits16_TE_000.tif'];
numimgs = 10;
FlatImageTE = zeros(size(XrayImageTE,1),2063,numimgs,'uint16');
for j = 1:10
      J = imread(filename,'PixelRegion',PixelRegion,j);
      XrayImageFlatTE(:,:,j) = J;
      XrayImagePixelShiftTE(:,:,j)=PixelShift(XrayImageFlatTE(:,:,j));
      FlatImageTE(:,:,j) = XrayImagePixelShiftTE(:,:,j);
end

FlatImageTE(:,:,1) = mean(FlatImageTE,3);


filename = [cd '\UncoatedPVCBCWaterOnly\UncoatedPVCBCWaterOnly_W2048X256X361_bits16_HE_000.tif'];
tic
numimgs = 360;
XrayImageHE = zeros(((line+row_average)-(line-row_average))+1,2048,numimgs,'uint16');
for i = 1:numimgs
       I = imread(filename,'PixelRegion',PixelRegion,i+1);
      XrayImageHE(:,:,i) = I;
end

for i = 1:numimgs
      XrayImagePixelShiftHE(:,:,i)=PixelShift(XrayImageHE(:,:,i));
end

FinalImageHE = zeros(size(XrayImageHE,1),2063,numimgs,'uint16');
FinalImageHE = XrayImagePixelShiftHE;
FinalImageWaterHE = FinalImageHE;

% Reading Flat Image
filename = [cd '\UncoatedPVCBCFlat\UncoatedPVCBCFlat_W2048X256X36_bits16_HE_000.tif'];
numimgs = 10;
FlatImageHE = zeros(size(XrayImageHE,1),2063,10,'uint16');
for j = 1:10
      J = imread(filename,'PixelRegion',PixelRegion,j);
      XrayImageFlatHE(:,:,j) = J;
      XrayImagePixelShiftHE(:,:,j)=PixelShift(XrayImageFlatHE(:,:,j));
      FlatImageHE(:,:,j) = XrayImagePixelShiftHE(:,:,j);
end

FlatImageHE(:,:,1) = mean(FlatImageHE,3);
FinalImage = FinalImageWaterTE-FinalImageWaterHE;
FinalImageWater=FinalImage;
FlatImage = FlatImageTE-FlatImageHE;

figure(2),clf
[recwater,imgCorrectedwater,Iwater]=TwoDimensionalReconstruction(FinalImage,FlatImage,
numthetas,line,FirstColumn,LastColumn,row_average,CenterOfRotationOffset,recontype,
VoxelSize,NB_iterations);

% Mean and Std Deviation
figure(22)
imagesc(imgCorrectedwater)
hEllipse = imellipse(gca,[198/voxeladjust 160/voxeladjust 818/voxeladjust 823/voxeladjust]);
```

```
maskImage = hEllipse.createMask();
imshow(maskImage)
maskedImage = imgCorrectedwater .* cast(maskImage, class(imgCorrectedwater));
imshow(maskedImage);
column1 = find(sum(maskImage, 1), 1, 'first')
column2 = find(sum(maskImage, 1), 1, 'last')
row1 = find(sum(maskImage, 2), 1, 'first')
row2 = find(sum(maskImage, 2), 1, 'last')
croppedImagewater = maskedImage(row1:row2, column1:column2);
imagesc(croppedImagewater)
m=numel(croppedImagewater)
counter=0;
som=0;
for i=1:m;
    if croppedImagewater(i) == 0
        som=som+0;
    else
        som=som+croppedImagewater(i);
        counter=counter+1;
    end
end
avg=som/counter;
o=numel(croppedImagewater)
% avg=mean(nonzeros(croppedImagewater));
sd=0;
for i=1:o;
    if croppedImagewater(i) == 0
        sd=sd+0;
    else
        sd=sd+(croppedImagewater(i)-avg)^2;
    end
    end
sdfinalwater=(sd/(o-1))^(1/2)
avgwater = avg
title(['Mean =    ', num2str(avgwater),'     Standard Deviation =     ', num2str(sdfinalwater)])

%% Reading Images - Air Only
CenterOfRotationOffset = -7+58;

filename = [cd '\UncoatedPVCBCAirOnly\UncoatedPVCBCAirOnly_W2048X256X361_bits16_TE_000.tif'];
tic
numimgs = 360;
XrayImageTE = zeros(((line+row_average)-(line-row_average))+1,2048,numimgs,'uint16');
for i = 1:numimgs
       I = imread(filename,'PixelRegion',PixelRegion,i+1);
      XrayImageTE(:,:,i) = I;
end

for i = 1:360
      XrayImagePixelShiftTE(:,:,i)=PixelShift(XrayImageTE(:,:,i));
end

FinalImageTE = zeros(size(XrayImageTE,1),2063,numimgs,'uint16');
FinalImageTE = XrayImagePixelShiftTE;
FinalImageAirTE = FinalImageTE;

% Reading Flat Image
filename = [cd '\UncoatedPVCBCFlat\UncoatedPVCBCFlat_W2048X256X36_bits16_TE_000.tif'];
numimgs = 10;
FlatImageTE = zeros(size(XrayImageTE,1),2063,numimgs,'uint16');
```

```
for j = 1:10
      J = imread(filename,'PixelRegion',PixelRegion,j);
      XrayImageFlatTE(:,:,j) = J;
      XrayImagePixelShiftTE(:,:,j)=PixelShift(XrayImageFlatTE(:,:,j));
      FlatImageTE(:,:,j) = XrayImagePixelShiftTE(:,:,j);
end

FlatImageTE(:,:,1) = mean(FlatImageTE,3);


filename = [cd '\UncoatedPVCBCAirOnly\UncoatedPVCBCAirOnly_W2048X256X361_bits16_HE_000.tif'];
tic
numimgs = 360;
XrayImageHE = zeros(((line+row_average)-(line-row_average))+1,2048,numimgs,'uint16');
for i = 1:numimgs
       I = imread(filename,'PixelRegion',PixelRegion,i+1);
      XrayImageHE(:,:,i) = I;
end

for i = 1:360
      XrayImagePixelShiftHE(:,:,i)=PixelShift(XrayImageHE(:,:,i));
end

FinalImageHE = zeros(size(XrayImageHE,1),2063,numimgs,'uint16');
FinalImageHE = XrayImagePixelShiftHE;
FinalImageAirHE = FinalImageHE;

% Reading Flat Image
filename = [cd '\UncoatedPVCBCFlat\UncoatedPVCBCFlat_W2048X256X36_bits16_HE_000.tif'];
numimgs = 10;
FlatImageHE = zeros(size(XrayImageHE,1),2063,numimgs,'uint16');
for j = 1:10
      J = imread(filename,'PixelRegion',PixelRegion,j);
      XrayImageFlatHE(:,:,j) = J;
      XrayImagePixelShiftHE(:,:,j)=PixelShift(XrayImageFlatHE(:,:,j));
      FlatImageHE(:,:,j) = XrayImagePixelShiftHE(:,:,j);
end

FlatImageHE(:,:,1) = mean(FlatImageHE,3);

FinalImage = FinalImageAirTE-FinalImageAirHE;
FinalImageAir=FinalImage;
FlatImage = FlatImageTE-FlatImageHE;

figure(3),clf
[recair,imgCorrectedair,Iair]=TwoDimensionalReconstruction(FinalImage,FlatImage,
numthetas,line,FirstColumn,LastColumn,row_average,CenterOfRotationOffset,recontype,
VoxelSize,NB_iterations);

% Mean and Std Deviation
figure(33)
imagesc(imgCorrectedair)
hEllipse = imellipse(gca,[198/voxeladjust 160/voxeladjust 818/voxeladjust 803/voxeladjust]);
maskImage = hEllipse.createMask();
imshow(maskImage)
maskedImage = imgCorrectedair.* cast(maskImage, class(imgCorrectedair));
imshow(maskedImage);
column1 = find(sum(maskImage, 1), 1, 'first')
column2 = find(sum(maskImage, 1), 1, 'last')
row1 = find(sum(maskImage, 2), 1, 'first')
```

```
row2 = find(sum(maskImage, 2), 1, 'last')
croppedImageair = maskedImage(row1:row2, column1:column2);
imagesc(croppedImageair)
m=numel(croppedImageair)
counter=0;
som=0;
for i=1:m;
    if croppedImageair(i) == 0
        som=som+0;
    else
        som=som+croppedImageair(i);
        counter=counter+1;
    end
end
avg=som/counter;
o=numel(croppedImageair)
sd=0;
for i=1:o;
    if croppedImageair(i) == 0
        sd=sd+0;
    else
        sd=sd+(croppedImageair(i)-avg)^2;
    end
    end
sdfinalair=(sd/(o-1))^(1/2)
avgair = avg
title(['Mean =   ', num2str(avgair),'      Standard Deviation =   ', num2str(sdfinalair)])

%% Void Fraction Calculation
figure(4),clf

alpha = (recmixture-recwater)./(recair-recwater);
imagesc(alpha);
hEllipse = imellipse(gca,[186 166 813 813]);
% Create a binary image ("mask") from the ROI object.
maskImage = hEllipse.createMask();
% Display the ellipse mask.
imshow(maskImage);
% Mask the image with the ellipse.
maskedImage = alpha .* cast(maskImage, class(alpha));
% Display the image with the "burned in" ellipse.
imshow(maskedImage);
% Find the bounding box
column1 = find(sum(maskImage, 1), 1, 'first')
column2 = find(sum(maskImage, 1), 1, 'last')
row1 = find(sum(maskImage, 2), 1, 'first')
row2 = find(sum(maskImage, 2), 1, 'last')
croppedImage = maskedImage(row1:row2, column1:column2);
imagesc(croppedImage)
colorbar
caxis([0 0.25])

t = 'Time-averaged Void Fraction Radial Distribution'
N=813;
[X,Y] = meshgrid(-1:2/(N-1):1);
[Q,R] = cart2pol(X,Y);
Z=croppedImage;
Nmid = (N-1)/2+1;
X = X(1,:);
Y = Y(:,1);
```

```
Zx = Z(Nmid,Nmid:end);
Zy = Z(Nmid:end,Nmid)';
M=(N-1)/2+1;
[Zr,r] = radialavg(Z,M);
err = Zr-(Zx+Zy)/2;

figure(122);
subplot(2,1,1)
    imagesc(X,Y,Z);colormap(jet);colorbar;title(t);
    xlabel('X');ylabel('Y');
    caxis([0 0.25]);
subplot(2,1,2)
    plot(r,Zr,'o');
    title(t)
    xlabel('r'); ylabel('Z');
    legend('Zr');
    axis([0 1 0 0.3])

figure(123);
plot(r,err);
title(sprintf('%s Error=%0.1g', t, std(err)))
xlabel('rho'); ylabel('Z');


figure(5),clf

alpha = (imgCorrectedmixture-imgCorrectedwater)./(imgCorrectedair-imgCorrectedwater);
imagesc(alpha);
hEllipse = imellipse(gca,[198/voxeladjust 173/voxeladjust 818/voxeladjust 803/voxeladjust]);
% Create a binary image ("mask") from the ROI object.
maskImage = hEllipse.createMask();
% Display the ellipse mask.
imshow(maskImage);
% Mask the image with the ellipse.
maskedImage = alpha .* cast(maskImage, class(alpha));
% Display the image with the "burned in" ellipse.
imshow(maskedImage);
% Find the bounding box
column1 = find(sum(maskImage, 1), 1, 'first')
column2 = find(sum(maskImage, 1), 1, 'last')
row1 = find(sum(maskImage, 2), 1, 'first')
row2 = find(sum(maskImage, 2), 1, 'last')
croppedImage = maskedImage(row1:row2, column1:column2);
imagesc(croppedImage)
colorbar
caxis([0 0.3])
alphamean = mean(nonzeros(croppedImage),'omitnan');
title('X-ray CT, Air Injection = 11SLPM, Void Fraction =', num2str(alphamean))

%% Void Fraction Measurements
% Void Fraction Reconstruction

for i = 1:360
    alpha1(i) = log((mean(FinalImageMixture(:,880:1770,i)))/
    (mean(FinalImageWater(:,880:1770,i))))/
    log((mean(FinalImageAir(:,880:1770,i)))/
    (mean(FinalImageWater(:,880:1770,i))));
end
figure(7)
plot(alpha1)
```

```
title({'Alpha (2D Projections)',num2str(mean(alpha1))})

figure(8)
subplot(2,2,1)
imagesc(imgCorrectedmixture)
colorbar
title('Mixture')

subplot(2,2,2)
imagesc(imgCorrectedwater)
colorbar
title('Water')

subplot(2,2,3)
imagesc(imgCorrectedair)
colorbar
title('Air')

subplot(2,2,4)
imagesc(croppedImage)
colorbar
caxis([0 0.30])
alphamean=mean(nonzeros(croppedImage),'omitnan');
title('X-ray CT, Air Injection = 11SLPM, Void Fraction =', num2str(alphamean))


%% Abel Transform
i=10;
k=180;
     for j=1:2063
         alphaAbel(1,j)=log(double(Imixture(i,j,k))/double(Iwater(i,j,k)))/
         log(double(Iair(i,j,k))/double(Iwater(i,j,k)));
     end

A=alphaAbel;
A=real(A);
A(A<0)=0;
A(isnan(A))=0;
A(isinf(A))=0;
figure(110)
B = A(:,925:1730);
imagesc(B)
colorbar
caxis([0 0.3])
R=0.0779;
f = abel_inversion(B,R,10,1);
figure(111),clf
imagesc(f'/max(max(f)))
colorbar
caxis([0 1])
save('result.mat')

% Abel to Hankel - take FFT of data,
% but keep only positive Fourier coefficients since function
% real and even
N = length(f);
im = f;
data2 = f; data2 = data2';
Delta = X(2)-X(1);
F = real( fft(fftshift(f')) ); F = F(1:N/2);
```

```
q = [0:N/2-1]/N/(Delta);
% Inverse Hankel Transform, approximated by
% sum_{i=1} N /2 F(q_i) q_i J0(2 pi q_i r) Delta q
r = [0:N/2-1]*(Delta*sqrt(2));
f = zeros(size(r));
for k=1:length(r)
f(k) = sum(F(:).*Delta.*q(:).*besselj(0,2*pi*r(k).*q(:)));
end
% plot recovered 1D function
figure(2); plot(r, f); grid on;
h=gca;set(h,'FontSize',20); xlabel('spatial variable');
h1=title({'recovered 1D profile of','circularly-symmetric function'});
set(h1,'FontSize',20);
% create 2D function from 1D profile
rmax = max(r); NN = 4*ceil(rmax./Delta/sqrt(2));
horiz = [-NN/2:NN/2-1]*Delta; vert = [-NN/2:NN/2-1]*Delta;
theta = linspace(0,2*pi,2*length(f));
f2D = zeros(NN,NN); counts = zeros(NN,NN);
for k = 1:length(f)
if(r(k) ~= 0)
Rows = round( r(k)*sin(theta)./Delta/1 ); Rows = Rows + NN/2 + 1;
Cols = round( r(k)*cos(theta)./Delta/1 ); Cols = Cols + NN/2 + 1;
ind = find((Rows <= NN) & (Cols <= NN) );
Rows = Rows(ind); Cols = Cols(ind);
f2D(sub2ind(size(f2D),Rows,Cols)) = f2D(sub2ind(size(f2D),Rows,Cols)) + f(k);
counts(sub2ind(size(f2D),Rows,Cols)) = counts(sub2ind(size(f2D),Rows,Cols)) + 1;
else
f2D(ceil(NN/2),ceil(NN/2)) = f(k);
end
end
f2D(find(counts~=0)) = f2D(find(counts~=0))./counts(find(counts~=0));
figure(3); imagesc(horiz,vert,f2D); grid on;
h=gca;set(h,'FontSize',20); xlabel('horizontal distance');
ylabel('vertical distance'); axis image;
h1=title('recovered 2D circularly symmetric function');
set(h1,'FontSize',20); colorbar
```

Supporting Document: Two-Dimensional Reconstruction

```
function [rec,imgCorrected,Intensity]=TwoDimensionalReconstruction(FinalImage,FlatImage,
numthetas,line,FirstColumn,LastColumn,row_average,CenterOfRotationOffset,recontype,
VoxelSize,NB_iterations)
% Separate Images from a Single File
for AngleNB = 1:numthetas %Depends on the number of files and number of projection
    Data1 = mean(FinalImage(:,:,AngleNB),3);
    I = -log((Data1)./(mean(FlatImage(:,:,1),3)));
    Intensity(:,:,AngleNB)=I;
%   Data(AngleNB).a = mean(I(((line-row_average):(line+row_average)),(FirstColumn:LastColumn)+
CenterOfRotationOffset),1);
    Data(AngleNB).a = mean(I(size(FinalImage,1),(FirstColumn:LastColumn)+
    CenterOfRotationOffset),1);
    DataRAW(AngleNB).a = mean(Data1(size(FinalImage,1),(FirstColumn:LastColumn)+
    CenterOfRotationOffset),1);
end
%% Build sinogram
disp('Building sinogram...')
NBangles = numthetas; % Number of Projections
```

```
LastAngle = numthetas-numthetas/NBangles;
% Rotete sinogram to change rotation of object in reconstruction
Turn = 0; % degrees or rotation to orient reconstruction as desired
thetas = [linspace(0,LastAngle,NBangles)-Turn]*pi/180;
sinogram = zeros(length(thetas),(LastColumn-FirstColumn)+1);
sinogramRAW = zeros(length(thetas),(LastColumn-FirstColumn)+1);
% Build
for n = 1:length(thetas)
    sinogram(n,:) =(Data(n).a)';
    sinogramRAW(n,:) =(DataRAW(n).a)';
end % loop sinogram
sinogram = imgaussfilt(sinogram);
SinogramSize=size(sinogram,2); %Use size instead of length because length will not pick
the largest number to define length
%%
sinogram = circshift(sinogram,numthetas,1);% circularly shifts the values in array A by
K positions along dimension dim. Inputs K and dim must be scalars.
subplot(2,3,1)
imagesc(1:SinogramSize,thetas*180/pi,sinogram)
colormap(hsv); colorbar
ylabel('Fan Rotation Angle (degrees)')
xlabel('Fan Sensor Position (pixel column number)')
toc
sinogramRAW = circshift(sinogramRAW,2*numthetas,1);% circularly shifts the values in array A by
K positions along dimension dim. Inputs K and dim must be scalars
imagesc(1:SinogramSize,thetas*180/pi,sinogramRAW)
colormap(hsv); colorbar
ylabel('Fan Rotation Angle (degrees)')
xlabel('Fan Sensor Position (pixel column number)')
title('Sinogram');
toc
%% Find center of mass to ensure cener of rotation correct
subplot(2,3,2)
r_coord = (1:SinogramSize)-SinogramSize/2;
plot(r_coord,mean(sinogram,1),'b')
grid on
%center of mass calculation
r_center = sum(r_coord.*mean(sinogram,1))/sum(mean(sinogram,1));
hold on
plot([r_center r_center],[min(mean(sinogram,1)) max(mean(sinogram,1))])
plot(r_coord,flip(mean(sinogram,1)),'r')
legend('Original', 'CoR axis', 'Flipped')
hold off
title('If CoR correct, lines should overlapp and be centered around CoR')
%% CT reconstruction
% Domain size in mm
xmin = -60;
xmax = 60;
ymin = -60;
ymax = 60;
voxels_in_x = VoxelSize;
voxels_in_y = voxels_in_x;%
vol_geom = astra_create_vol_geom(voxels_in_x, voxels_in_y, xmin, xmax, ymin, ymax);
% Thor pixel pitch is 100 microns
PixelPitch = 0.1;   % [mm]
SOD = 1181;         % [mm]
ODD = 143;          % [mm], ODD = SID - SOD
switch recontype
    case 'CPU'
%%%%% NOTE - PRESENTLY RUNS ONLY ON ONE CORE - SLOW
```

```
% ASTRA Toolbox Processing
disp('Reconstructing - CPU...')

proj_geom = astra_create_proj_geom('fanflat', PixelPitch ,SinogramSize, thetas,SOD,ODD);

proj_id = astra_create_projector('strip_fanflat', proj_geom, vol_geom);

% We now re-create the sinogram data object as we would do when loading
% an external sinogram
sinogram_id = astra_mex_data2d('create', '-sino', proj_geom, sinogram);

% Create a data object for the reconstruction
rec_id = astra_mex_data2d('create', '-vol', vol_geom);

% Set up the parameters for a reconstruction algorithm using the CPU
% The main difference with the configuration of a GPU algorithm is the
% extra ProjectorId setting.
cfg = astra_struct('SIRT');
cfg.ReconstructionDataId = rec_id;
cfg.ProjectionDataId = sinogram_id;
cfg.ProjectorId = proj_id;
cfg.option.MinConstraint = 0;
%cfg.option.MaxConstraint = 255;

UseMask = 1;
if UseMask == 1
%%% MASK
% create a reconstruction in a circular region instead of the usual rectangle.
% This is done by placing a circular mask on the square reconstruction volume:
    c = -((voxels_in_x-1)/2):((voxels_in_x-1)/2);
    [x, y] = meshgrid(c,c);
    mask = (x.^2 + y.^2 < ((voxels_in_x-1)/2)^2);
    % Create a data object for the mask
    mask_id = astra_mex_data2d('create', '-vol', vol_geom, mask);
    cfg.option.ReconstructionMaskId = mask_id;
end

% Available algorithms:
% ART, SART, SIRT, CGLS, FBP

% Create the algorithm object from the configuration structure
alg_id = astra_mex_algorithm('create', cfg);

%%% ITERATE
PlotResiduals = 0; % 1 to plot
if PlotResiduals == 1
    % Run the iterations one at a time, keeping track of errors
    phantom_error = zeros(1, NB_iterations);
    residual_error = zeros(1, NB_iterations);
    for i = 1:NB_iterations
      % Run a single iteration
      astra_mex_algorithm('iterate', alg_id, 1);

      residual_error(i) = astra_mex_algorithm('get_res_norm', alg_id);
    end
    figure(40); plot(residual_error)
else
    % Run NB_iterations of the algorithm
    astra_mex_algorithm('iterate', alg_id, NB_iterations);
end
```

```
    % Get the result
    rec = astra_mex_data2d('get', rec_id);
    toc

    case {'GPU'}

        % create geometries
        proj_geom = astra_create_proj_geom('fanflat', PixelPitch ,SinogramSize, thetas,SOD,ODD);

        % We now re-create the sinogram data object as we would do when loading
        % an external sinogram
        sinogram_id = astra_mex_data2d('create', '-sino', proj_geom, sinogram);

        % Create a data object for the reconstruction
        rec_id = astra_mex_data2d('create', '-vol', vol_geom);

        cfg = astra_struct('SIRT_CUDA'); %or CGLS_CUDA
        cfg.ReconstructionDataId = rec_id;
        cfg.ProjectionDataId = sinogram_id;
        cfg.option.MinConstraint = 0;

        % Create the algorithm object from the configuration structure
        alg_id = astra_mex_algorithm('create', cfg);

        %%% ITERATE
        PlotResiduals = 1; % 1 to plot
        if PlotResiduals == 1
            % Run the iterations one at a time, keeping track of errors
            phantom_error = zeros(1, NB_iterations);
            residual_error = zeros(1, NB_iterations);
            for i = 1:NB_iterations;
              % Run a single iteration
              astra_mex_algorithm('iterate', alg_id, 1);

              residual_error(i) = astra_mex_algorithm('get_res_norm', alg_id);
           end
            subplot(2,3,5); semilogy(residual_error)
            grid on
            title('Convergence')
            xlabel('Iteration #')
            ylabel('Residual')
        else
            % Run NB_iterations of the algorithm
            astra_mex_algorithm('iterate', alg_id, NB_iterations);
        end
        % Get the result
        rec = astra_mex_data2d('get', rec_id);
        toc

    otherwise
        warning('Unexpected reconstruction type. SKIPPED')
        toc
end

%%
subplot(2,3,3)
imagesc([xmin xmax],[ymin ymax],rec)
colormap parula  % jet% gray %hsv
colorbar
```

```
axis equal tight
% Include lines to masure objects in reconstruction
imdistline;
imdistline;

%% Ring Removal
 ang_sampling=8;
[imdata,imgCorrected] = ringremoval(rec,ang_sampling);
 subplot(2,3,4)
 imagesc(imgCorrected);
 title('Ring corrected Image');
   axis square
% Thresholded reconstruction
%subplot(2,3,5)
rec_t = rec;
rec_t(rec<0.1)=0;
rec_t(rec>=0.1)=0.20;
imagesc([xmin xmax],[ymin ymax],rec_t)
title('Threshold Reconstruction');
axis equal tight
colormap parula % jet% gray %hsv
colorbar
imdistline; imdistline;


%% Plot original image and identify area used in reconstruction
subplot(2,3,6)
imagesc(I)
colormap parula% gray hsv
colorbar
title({'-log( [I] / [flat])',...
       '+Region reconstructed in rectangle'})
hold on
rectangle('position',[FirstColumn 1 LastColumn-FirstColumn size(FinalImage,1)])
hold off

%% Clean up.
if (exist('proj_id'))==1
    astra_mex_projector('delete', proj_id);
end
astra_mex_algorithm('delete', alg_id);
astra_mex_data2d('delete', rec_id);
astra_mex_data2d('delete', sinogram_id);

toc
end %function
```

Appendix F

Void Fraction Measurement Techniques

F.1 Void Fraction Measurement Techniques

Based on differential pressure

The gas phase fraction based on pressure difference in a section of pipe:

$$\Delta P = (\rho_{water} - \rho_{mix}) g \Delta h \tag{F.1}$$

where Δh is the height over which ΔP is measured, and by definition for two phase mixture of air and water.

$$\rho_{mix} = \rho_{air}\alpha + \rho_{water}(1 - \alpha) \tag{F.2}$$

Hence the gas phase fraction, α, is:

$$< \overline{\alpha_{dp}(Z)} >_{x,y} = \frac{\rho_{mix} - \rho water}{\rho_{air} - \rho_{water}} = \frac{\Delta P}{(\rho_{water} - \rho_{air}) g \Delta h} \tag{F.3}$$

Based on holdup

A measurement tape was used to measure the height from the base of the bubble column. We measured the initial height with no air injection h_{water} and measured the height of the liquid free surface (ignoring any foam on top) at each air injection increment ($h_{water} + \delta h$). Figure F.2 displays the water level used for the height difference calculation. The following equation was used to measure the difference:

$$< \overline{\alpha_h} >_{x,y} = \frac{\delta h}{h_{water} + \delta h} \tag{F.4}$$

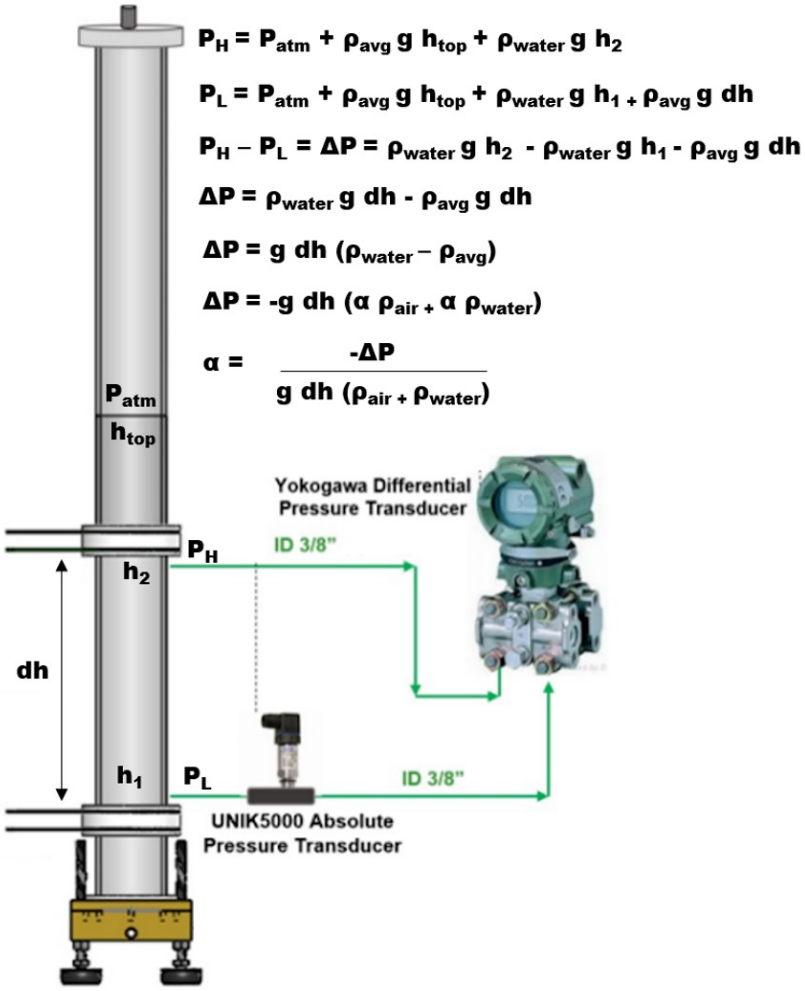

Figure F.1: Void fraction measurement based on differential pressure transducer data. Schematics and calculations

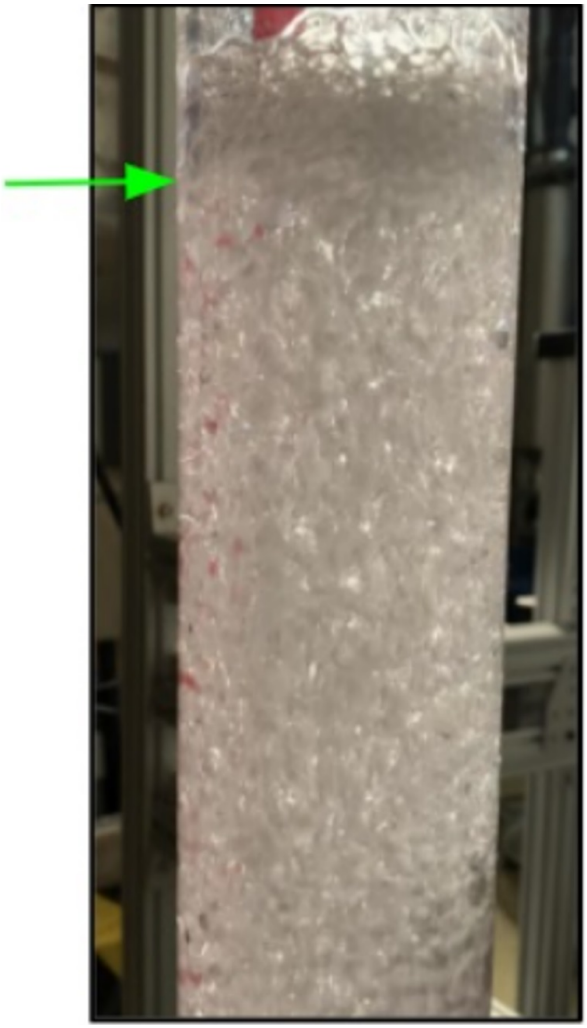

Figure F.2: Bubble Column display with water level for a specific height. The maximum deflection that can be seen at higher injection rates is +/- 0.25 inches, which results in an accuracy deflection of 5%.

Due to the motion of the interphase and accuracy with which the elevation can be read in the first place we estimate the uncertainty in height with gas is +/- 0.25 inches (+/- 6.4mm), and +/- 0.125 inches (+/- 3.2mm) without gas. This leads to an uncertainty of 5% on void fraction calculations based on uncertainty propagation by Gauss' method.

Based on wire mesh sensor

The Wire Mesh Sensor framework uses two types of calibration methods: histogram (nodes water value based on cutoff from histogram, and requires a flow where for each node – there are moments where node truly feels no air influence) and water only dataset (nodes water value based on case where no air is supposed to be present, and can be effected by a bubble stuck on the node, especially occurring near walls). Histogram proved beneficial to us, but we utilized Water Calibration to validate which calibration was effective for our measurements. The following equation was utilized with a measured water-only dataset:

$$\overline{\alpha_{WMS}(x,y,z)} = \frac{U^{w}_{i,j} - U^{meas}_{i,j,k}}{U^{w}_{i,j}} \tag{F.5}$$

Figure F.3 displays the contour of final time average and running frame average computation results utilized to evaluate the number of frames required to arrive at a converged set with a difference of running average to final value by 1%.

The running average calculation uses the void fraction files from the data set to compare each subsequent 24x24 grid frame to a running average of the previous frames. When the difference value between a particular dataset and the running average reached a specified tolerance, the dataset was considered converged up to a specified accuracy. For the flow condition of the bubble column with variable superficial gas velocity from 0.003m/s to 0.068m/s, we sampled at 1,000Hz to collect 35,000 frames yielding a converge dataset that met the criteria of 1%. We verified convergence across all flow rates and determined a collection of 35 seconds at 1,000Hz was satisfactory to achieve a converged dataset within 0.1% for all experiment superficial gas velocities.

Based on X-ray

Void fractions were measured by evaluating the intensity field at each projection angle for mixture, water-only, and air-only. Each local void fraction was collected, and the mean was used as the time-averaged void fraction value. The intensity field of the mixture is a mean of the number of frames taken per run. In this case, we took 30 frames per angle at a frame rate of 1 second. Figure F.4 displays an example of different intensity fields for the three mediums. The difference in intensity fields, coupled with approximations for a monochromatic X-ray source, allow using an intensity field relationship for void fraction calculations. The following equation was utilized to measure time-averaged void fraction from intensity field variations across the three different mediums. We can calculate phase fraction by several ways each including different assumptions. Option 1, if we assume monochromatic x-rays (or energy

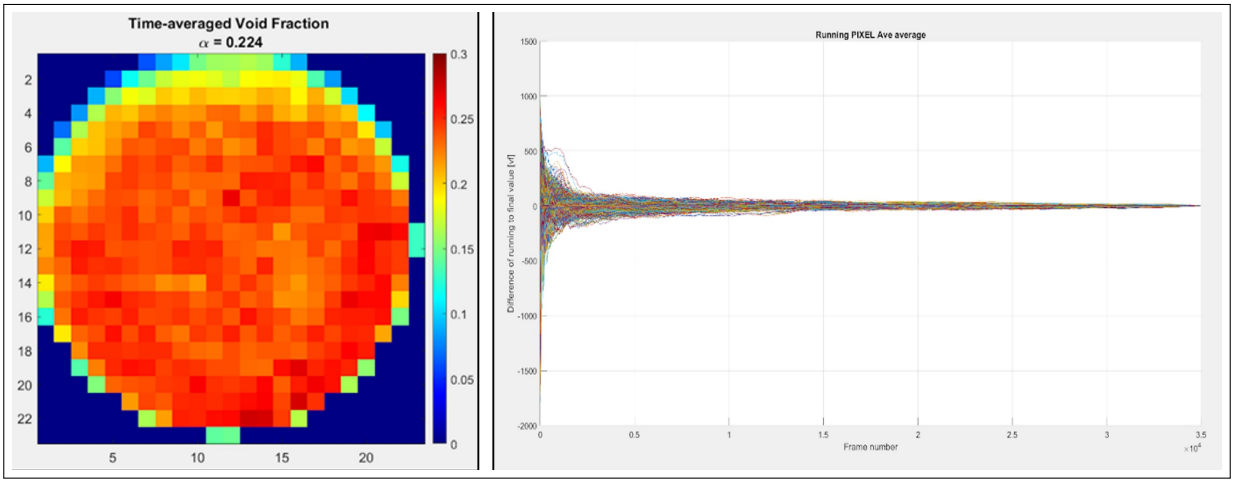

Figure F.3: Bubble Column Wire Mesh Sensor measurement with running frame average

resolving detectors and only use data from chosen energy level) then in the 2D projections we could calculate:

$$\overline{\alpha_{X-rayprojection}(x,y)} = \frac{ln(\frac{I_m(x,y)}{I_w(x,y)})}{ln(\frac{I_a(x,y)}{I_w(x,y)})} \tag{F.6}$$

From this 2D projection if there is radial variation in the time averaged dataset, we must also correct for the mapping from a projection to a cross section. From the 2D projections of phase fraction and reconstruction of 2D phase fraction either by Abel transform if we assume axial symmetry. Figure 17a shows the projected void fraction and Figure 17b shows it after the Able transform in a two-dimensional rendering of the void fraction distribution, assuming symmetrical void fraction.

We can also reconstruct air, water and mixture CT scans and from the ratio of attenuation coefficients determine phase fraction. Note if monochromatic or energy resolving detectors used that this should be straight forward, and for polychromatic data with no energy resolution we'll have effective attenuation coefficients.

For monochromatic x-rays:

$$\overline{\alpha_{X-rayCT}(x,y,z)} = \frac{\mu_{mixture}(x,y,z) - \mu_{water}(x,y,z)}{\mu_{air}(x,y,z) - \mu_{water}(x,y,z)} \tag{F.7}$$

where the subscripts note cases with all water, air or mixture in the bubble column.

With the THOR photon-counting dual threshold detector we have data from two thresholds and as first approximation for given range assume nominally uniform attenuation to calculate void fraction. The dual thresholds (in our example were 40keV and 60keV) allow

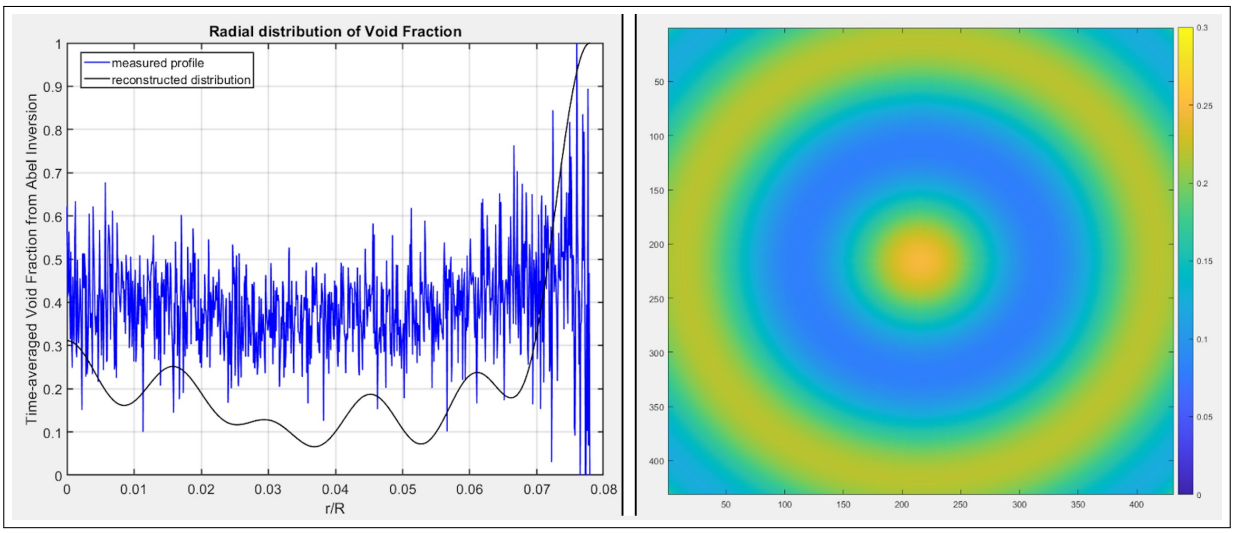

Figure F.4: a) Radial distribution of time-averaged void fraction calculated from Abel transform. b) Two-dimensional display of Abel transform void fraction, assuming symmetry

us to generate a data set of photon counts that are closer to monochromatic data. We will consider reconstruction based on high threshold, low threshold, and (low-high) data. Figure 18 shows the difference using the different threshold datasets yields for a single projection frame. Figure F.6 displays the reconstruction using SIRT algorithm for each of the three energy thresholds (¿40keV, 40-60keV, ¿60keV). Since we are utilizing equation 3.7, usually reserved for monochromatic sources, we use frames collected from the energy threshold between 40keV and 60keV for our reconstruction algorithms and final calculation of void fraction by X-ray CT iterative reconstruction method.

F.2 Uncertainty Estimates

Since we can calculate phase fraction from five different methods, we estimate uncertainty for each measurement technique using Monte Carlo algorithm. We calculate mean and standard deviation for each parameter that plays a role in the void fraction calculation used in each measurement technique. We utilize the MATLAB function, normrnd, which generates a random number from the normal distribution with a mean parameter and standard deviation parameter. We then use 100,000 points to simulate the function for void fraction calculations. Following the simulation and construction of the probability density functions for each measurement technique, displayed in Figure F.8, we calculate the mean and standard deviation for the entire simulation. These values are displayed in Table 1. The parameters used in the simulation are displayed in Table 2. Figure F.9 includes the results of our Monte

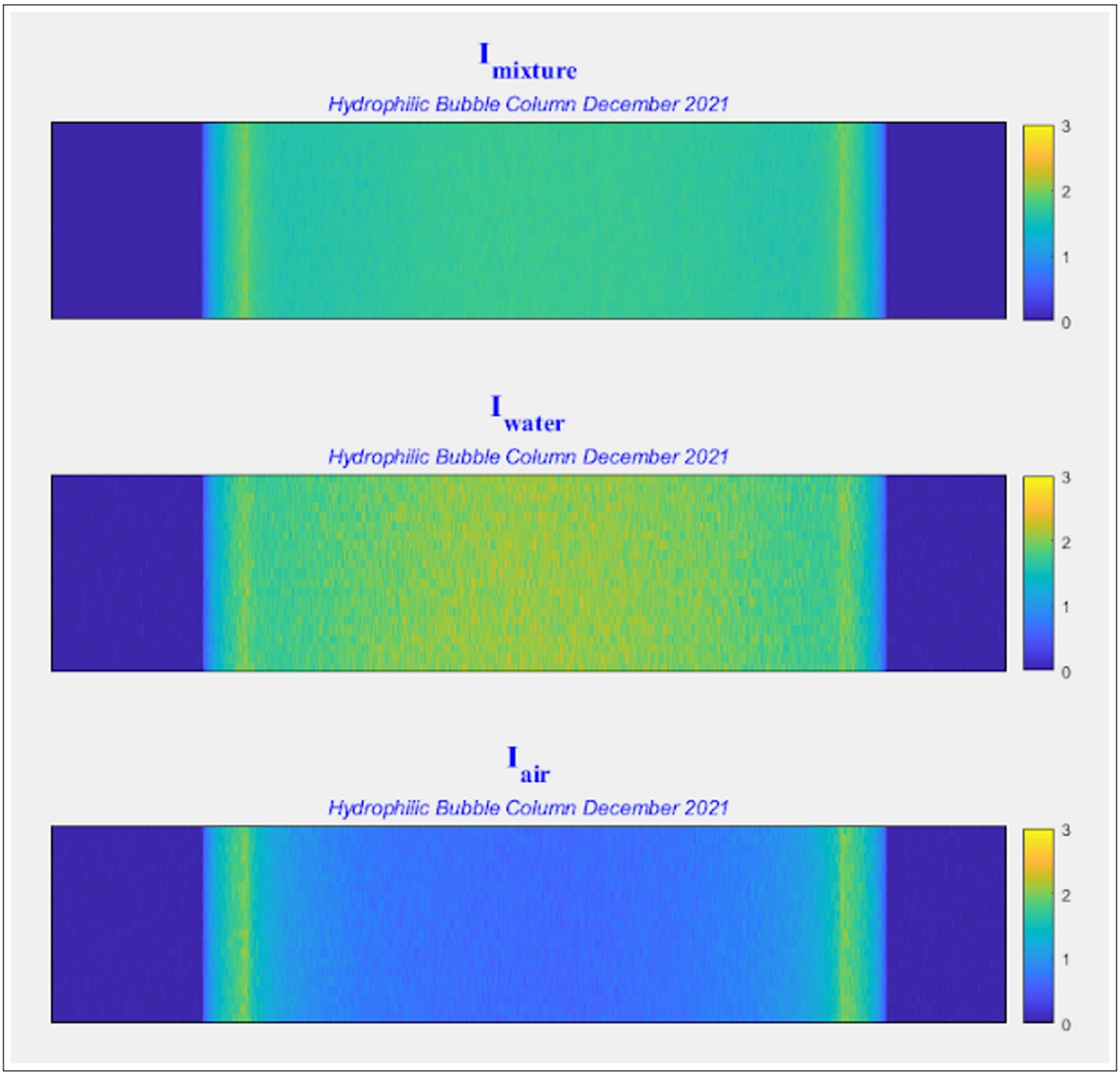

Figure F.5: X-ray intensity fields (calculated by taking a log of the ratio of the average raw projection image over the average flat field image) for Mixture, Water, and Air mediums inside a bubble column. These intensity fields are captured by using the dual threshold (photon energies between 40KeV and 60KeV, on the photon counter.

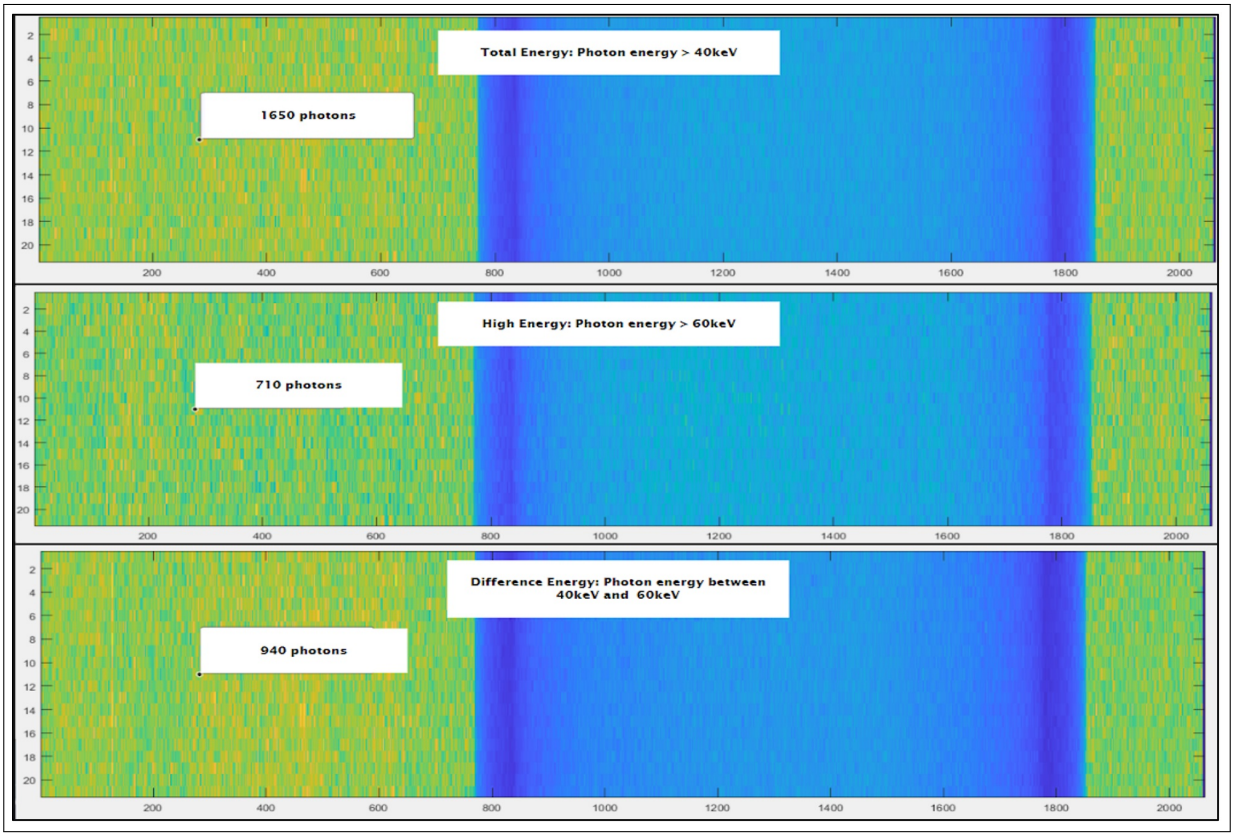

Figure F.6: X-ray intensity fields with cursor point in the same pixel location a) Total Energy (photon energy ¿ 40keV) b) High Energy (photon energy ¿ 60keV) c) Difference Energy (photon energy between 40keV and 60keV)

Carlo evaluation of each technique.

The following MATLAB code was utilized for our calculations:

```
%Alpha by Variable Measurement Techniques -  Monte Carlo
clc, clear all
% sample code by S.A. Makiharju, 2021

%Alpha by Differential Pressure Detector -  Monte Carlo
height_mean = 0.3048;    height_std = 0.00635;  %meter
rhomix_mean = 710;     rhomix_std = 10;  %Pa
T_mean = 15.5;         T_std = 2;        %C

I = 100000; %number of points to simulate
for i=1:I
    % see https://www.mathworks.com/help/stats/
    normrnd.html
```

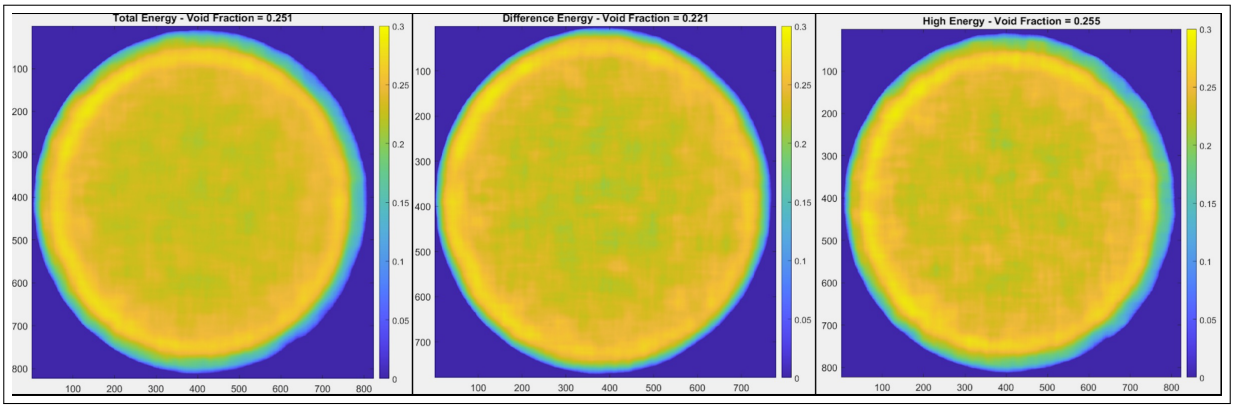

Figure F.7: X-ray CT Time-averaged Void Fraction Reconstruction a) using Total Energy (photon energy > 40keV) b) using Difference Energy (photon energy between 40keV and 60keV) c) using High Energy (photon energy > 60keV)

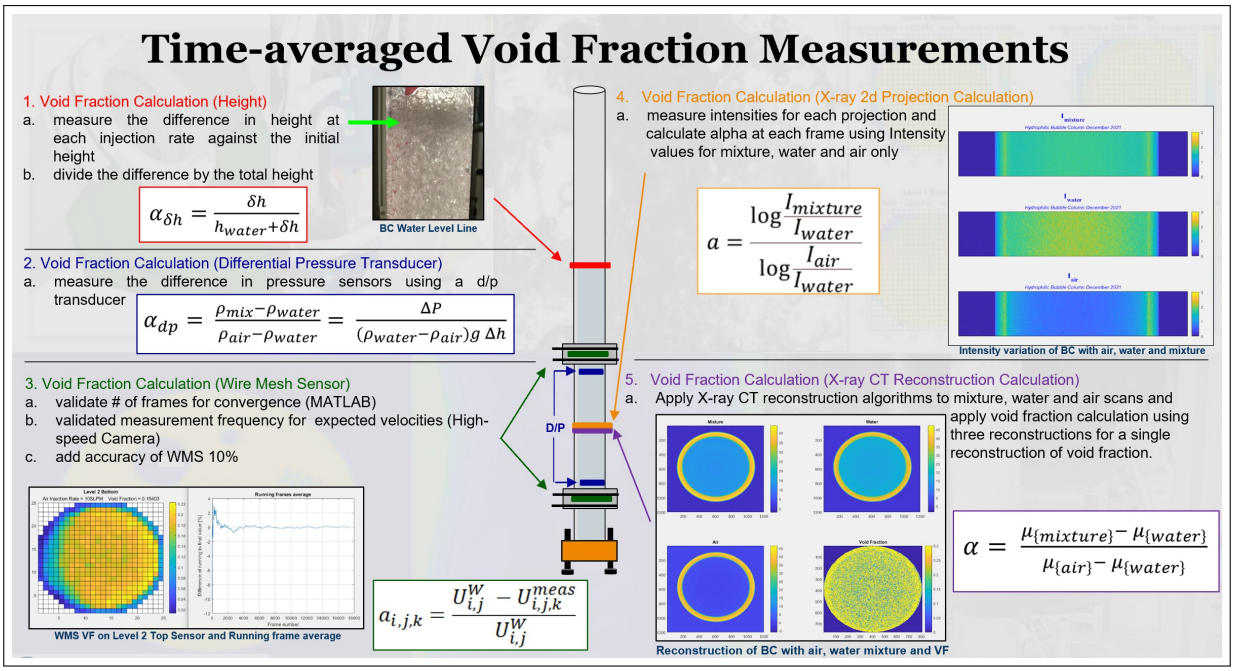

Figure F.8: Time-averaged Void Fraction measurement techniques

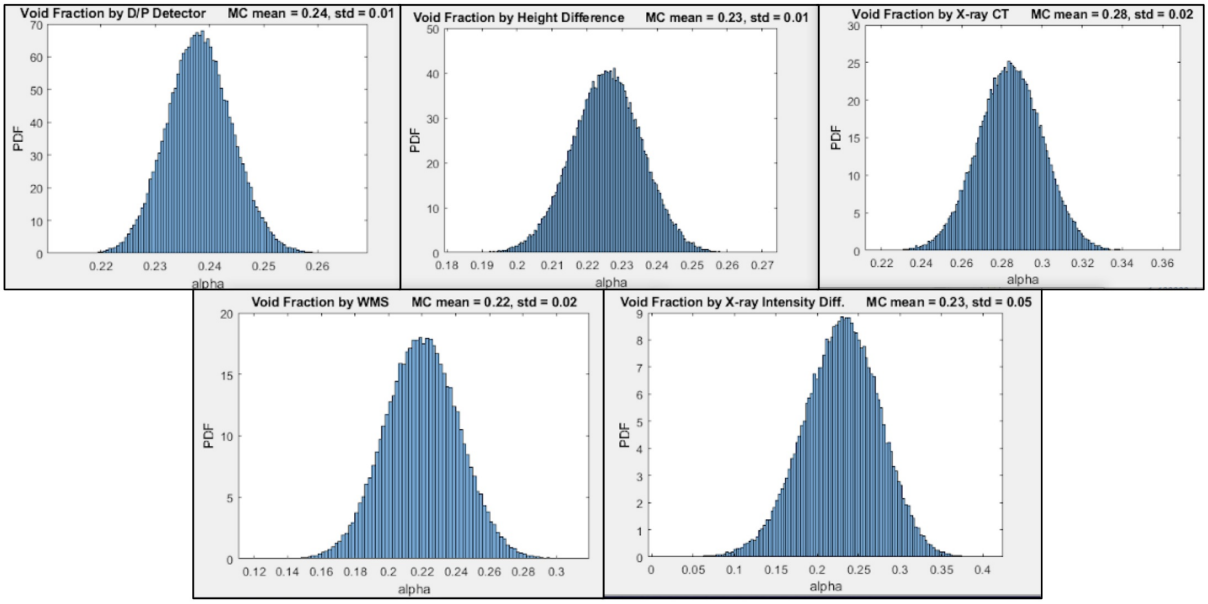

Figure F.9: Monte Carlo evaluation of measurement techniques.

Measurement Type	Void Fraction	Uncertainty
Height Variation	0.24	0.01
Differential Pressure	0.24	0.01
Wire Mesh Sensor (avg)	0.22	0.02
X-ray 2D Projections	0.23	0.05
X-ray CT Reconstruction	0.21	0.02

Table F.1: Monte Carlo simulations for void fraction measurement techniques

Measurement Technique	Parameters ('normrnd' applied to all parameters)			
D/P Transducer	$Height_{(mean,std)}$	$dP = \rho_{mixture(mean,std)}$	$T_{(mean,std)}$	$\alpha = \frac{-dP}{9.81\ (1.2-988)Height}$
Height Difference	$Height_{Final}$	$Height_{Initial}$		$\alpha = \frac{Height_{Final} - Height_{Initial}}{Height_{Final}}$
X-ray Intensity Variation	$Imix_{(mean,std)}$	$Iwater_{(mean,std)}$	$Iair_{(mean,std)}$	$\alpha = \frac{log\frac{Imix}{Iwater}}{log\frac{Iair}{Iwater}}$
X-ray Computed Tomography	$recmix_{(mean,std)}$	$recwater_{(mean,std)}$	$recair_{(mean,std)}$	$\alpha = \frac{recmix-recwater}{recair-recwater}$
Wire Mesh Sensor	$WMS_{(mean,std)}$			$\alpha = WMS_{normrnd}$

Table F.2: Parameters utilized for each measurement technique's Monte Carlo accuracy calculations

```
    T(i) = normrnd(T_mean,T_std);
    height(i) = normrnd(height_mean,height_std);
    rhomix(i) = normrnd(rhomix_mean,rhomix_std);
%     rhow(i) = Fun_rho_w(T(i));

    dP(i) = rhomix(i);
    alphadP(i) = -dP(i)/(9.81*(1.2-998)*height(i));
end
alphadP = real(alphadP);
figure(1),clf
% see https://www.mathworks.com/help/matlab/ref/
matlab.graphics.chart.primitive.histogram.html?searchHighlight=histogram&s_tid=doc_srchtitle
histogram(alphadP,'Normalization','pdf')
title(['Void Fraction by D/P Detector   ','   MC mean = ' num2str(mean(alphadP),'%0.2f') ',
std = ' num2str(std(alphadP),'%0.2f')])
xlabel('alpha'),ylabel('PDF')


%Alpha by Height Difference -  Monte Carlo
heightfinal_mean = 0.81026;    heightfinal_std = 0.00635;  %meter
heightinitial_mean = 0.62736;    heightinitial_std = 0.00635;  %meter

I = 100000; %number of points to simulate
for i=1:I
    % see https://www.mathworks.com/help/stats/
    normrnd.html
    heightfinal(i) = normrnd(heightfinal_mean,heightfinal_std);
    heightinitial(i) = normrnd(heightinitial_mean,heightinitial_std);
    alphah(i) = (heightfinal(i) - heightinitial(i))/heightfinal(i);
end
alphah = real(alphah);
figure(2),clf
% see https://www.mathworks.com/help/matlab/ref/
matlab.graphics.chart.primitive.histogram.html?searchHighlight=histogram&s_tid=doc_srchtitle
histogram(alphah,'Normalization','pdf')
title(['Void Fraction by Height Difference   ','   MC mean = ' num2str(mean(alphah),'%0.2f') ',
std = ' num2str(std(alphah),'%0.2f')])
xlabel('alpha'),ylabel('PDF')
```

```
%Alpha by X-ray CT -  Monte Carlo
mumix_mean = 14.3899;    mumix_std = 0.24;  %non-dimensional
muwater_mean = 19.73;    muwater_std = 0.24;  %non-dimensional
muair_mean = 0.946;    muair_std = 0.24;  %non-dimensional
I = 100000; %number of points to simulate
for i=1:I
    % see https://www.mathworks.com/help/stats/
    normrnd.html
    mumix(i) = normrnd(mumix_mean,mumix_std);
    muwater(i) = normrnd(muwater_mean,muwater_std);
    muair(i) = normrnd(muair_mean,muair_std);
    alphaxrayct(i) = (mumix(i) - muwater(i))/(muair(i) - muwater(i));
end
alphaxrayct = real(alphaxrayct);
figure(3),clf
% see https://www.mathworks.com/help/matlab/ref/
matlab.graphics.chart.primitive.histogram.html?
searchHighlight=histogram&s_tid=doc_srchtitle
histogram(alphaxrayct,'Normalization','pdf')
title(['Void Fraction by X-ray CT   ','
xlabel('alpha'),ylabel('PDF')
MC mean = ' num2str(mean(alphaxrayct),'%0.2f') ',std = num2str(std(alphaxrayct),
%Alpha by X-ray 2D -  Monte Carlo
Imix_mean = 180;    Imix_std = 11.13;  %non-dimensional
Iwater_mean = 139;    Iwater_std = 13.73;  %non-dimensional
Iair_mean = 444;    Iair_std = 32.14;  %non-dimensional
I = 100000; %number of points to simulate
for i=1:I
    % see https://www.mathworks.com/help/stats/
    normrnd.html
    Imix(i) = normrnd(Imix_mean,Imix_std);
    Iwater(i) = normrnd(Iwater_mean,Iwater_std);
    Iair(i) = normrnd(Iair_mean,Iair_std);
    alphaxray2d(i) = log(Imix(i)/Iwater(i))./log(Iair(i)/Iwater(i));
end
alphaxray2d = real(alphaxray2d);
figure(5),clf
% see https://www.mathworks.com/help/matlab/ref/
matlab.graphics.chart.primitive.histogram.html?searchHighlight=histogram&s_tid=doc_srchtitle
histogram(alphaxray2d,'Normalization','pdf')
title(['Void Fraction by X-ray Intensity Diff.   ',' MC mean = ' num2str(mean(alphaxray2d),'%0.2f')
xlabel('alpha'),ylabel('PDF')

%Alpha by WMS -  Monte Carlo
WMS_mean = 0.22;    WMS_std = 0.022;  %non-dimensional
I = 100000; %number of points to simulate
for i=1:I
    % see https://www.mathworks.com/help/stats/
    normrnd.html
    WMS(i) = normrnd(WMS_mean,WMS_std);
    alphaxraywms(i) = WMS(i);
end
alphaxraywms = real(alphaxraywms);
figure(4),clf
% see https://www.mathworks.com/help/matlab/ref/
matlab.graphics.chart.primitive.histogram.html?searchHighlight=histogram&s_tid=doc_srchtitle
histogram(alphaxraywms,'Normalization','pdf')
title(['Void Fraction by WMS   ','
xlabel('alpha'),ylabel('PDF')
MC mean = ' num2str(mean(alphaxraywms),'%0.2f') ', std = '
num2str(std(alphaxraywms),
```